INSTITUT FÜR KONSTRUKTIVEN INGENIEURBAU

LEHRSTUHL FÜR TUNNELBAU, LEITUNGSBAU UND BAUBETRIEB

PROF. DR.-ING. M. THEWES

Doctoral Thesis

STABILITY OF SLURRY SUPPORTED TUNNEL FACE CONSIDERING THE TRANSIENT SUPPORT MECHANISM DURING EXCAVATION IN NON-COHESIVE SOIL

submitted in fulfilment of the requirements for the degree of Doctor of Engineering (Dr.-Ing.) to the Department of Civil and Environmental Engineering of the Ruhr-Universität Bochum

BY

ING. ZDENEK ZIZKA

SFB 837
Interaction Modeling in Mechanized Tunneling

Doctoral Thesis

STABILITY OF SLURRY SUPPORTED TUNNEL FACE CONSIDERING THE TRANSIENT SUPPORT MECHANISM DURING EXCAVATION IN NON-COHESIVE SOIL

submitted in fulfilment of the requirements for the degree of Doctor of Engineering (Dr.-Ing.) to the Department of Civil and Environmental Engineering of the Ruhr-Universität Bochum

BY

ING. ZDENEK ZIZKA

Reviewers:

Prof. Dr.-Ing. Markus Thewes
Institute for Tunnelling and Construction Management, Ruhr-Universität Bochum (Germany)

Prof. Dr. Adam Bezuijen
Laboratory of Geotechnics, University of Gent (Belgium)

Date of submission: 16th October 2018

Date of oral examination: 13th February 2019

PREFACE

The present study was developed in my time as research assistant at the Institute for Tunnelling and Construction Management ("TLB") of the Ruhr-Universität Bochum.

My special thanks goes first to Prof. Dr.-Ing. Markus Thewes for his guidance of the thesis. Further, I want to thanks to Prof. Thewes for his intensive scientific support and the trust placed in me during my work at the institute. To Dr.-Ing. Britta Schoesser and deceased Prof. Dr.-Ing. habil. Tom Schanz, I want to thank for their intensive promotion and scientific leading of the "SFB 837 subproject A6", in frame of which, this thesis was developed. Additionally, I explicitly acknowledge Prof. Dr. Adam Bezuijen for his deep interest in my work, the countless and informative discussions, and his active participation in my examination. To Prof. Dr. Markus Knobloch I thank for his friendly willingness to take on the tasks of a non-specialist examiner.

Furthermore, I have to thank my colleagues at the TLB for outstanding years of co-working. Numerous discussions, sharing time together and mutual help when solving any problems were amazing. The same can be said to the colleagues from the Collaborative Research Center SFB 837. In particular, I thank to Dr.-Ing. Jakob Küpferle for his collaboration on joint experiments conducted with the RUB tunnelling device. Another special thank goes to Dr.-Ing. Anna-Lena Hammer for countless discussions during the last phases of the thesis writing. Experimental investigation needs experimental devices. Therefore, I want to thank also to the technicians involved in the construction of the experimental equipment that I have used for the investigation in this thesis.

Additionally, the work of numerous students and the support of the student assistants has to be acknowledged here. Especially, I would like to thank to my student assistant Samy Tong for his invaluable help during development of this thesis.

A big thank goes also to my former colleagues from the company MTC - Maidl Tunnelconsultants GmbH & Co. KG where I had the pleasure to work simultaneously

during the time at the TLB. This developed thesis has significantly benefited from the practical knowledge I have obtained during my work in the company.

Last but not least, I thank to my parents for their endless support and encouragement for working abroad in Germany. Within the time in Bochum, I met a lot of great people among them also my girlfriend Gabriela. To her I want to express my deep thanks for always motivating me to finish this thesis.

Ruhr-Universität Bochum, October 2018 Zdenek Zizka

ACKNOWLEDGEMENTS

The German Research Foundation DFG (Deutsche Forschungsgemeinschaft) facilitated this research financially through subproject A6 “Locally transient face support within hydroshield excavation” as part of the Collaborative Research Center 837 “Interaction modeling in mechanized tunneling” at the Ruhr-Universität Bochum.

This support is gratefully acknowledged.

ABSTRACT

Tunnel face stabilization is one of the three key elements of the soft ground tunnelling. Slurry shields are known to be a reliable excavation method in non-cohesive soils under groundwater level. In such conditions, they can actively support the tunnel face while minimising of the support pressure fluctuations. Two fundamental conditions must be fulfilled to stabilize a tunnel face: A sufficient face support pressure in the excavation chamber and an efficient pressure transfer of slurry excess pressure onto the soil skeleton. At the time of introduction of the slurry shield, the theories to describe the pressure transfer were transferred from diaphragm wall technology, in which the bentonite slurry supports the open trench. In the past, however, increased pore water pressures above the hydrostatic level were measured in front of the tunnel face during excavation. The measurements could not be explained by the pressure transfer theories from diaphragm wall technology. The increased pore pressure significantly reduces the efficiency of the face support. It is expected that the increased pore pressures result from the continuous disturbance of the pressure transfer mechanism by rotating cutting tools at the tunnel face during excavation. The objectives of this thesis are to understand the consequences of simultaneous slurry penetration and tool excavation process at the tunnel face. A further aim is to characterize the pressure transfer and resulting tunnel face support efficiency for various combinations of slurry penetration and excavation scales.

Considering the state of the art of slurry face support and of face stability assessment, two hypotheses about the pressure transfer during slurry shield excavation resulting from the interaction between cutting tools and pressure transfer mechanism are formulated. Case A and Case B of the interaction at the tunnel face are introduced based on local comparison between slurry penetration and tool cutting depth. The Case A stands for higher cutting depth than slurry penetration depth, while Case B represents shallower cutting depth than slurry penetration depth. It is concluded that each case requires different approach of characterization due to repeated primary slurry penetration in Case A and slurry re-penetration in Case B. To obtain the basis for

the further comparison with slurry penetration scale, the typical relationship between cutting depth of a tool and the timespan between subsequent tool passing was determined from reference excavation projects. Following on this the slurry penetration was investigated experimentally. Time-dependent permeability of soil for slurry and slurry penetration depth were evaluated for the Case A of interaction. In contrast, the focus of the investigation for Case B was set on the distribution and development of pore pressure and effective stress inside and outside of slurry penetrated zone during the slurry penetration. The investigations for both cases were conducted using originally designed column tests. Case B was additionally investigated using the RUB tunnelling device. A transient FE seepage analysis utilizing the experimentally determined transient permeability coefficients for slurry was necessary to determine the pressure transfer in Case A due to mutual cutting tracks interaction. In Case B, the slurry stagnation gradient determined in the experiments could be directly transferred to the tunnel face conditions to assess the transfer due to presence of slurry re-penetration.

It is concluded that the pressure transfer efficiency in Case A is significantly reduced due to increased pore water pressures outside of slurry penetrated zone during excavation. The methods originating from diaphragm wall technology to predict pressure transfer are not valid in Case A. Based on the obtained results, it is recommended to conduct the excavation with a type of interaction according to Case B. Finally, an integrated approach for the design of minimal required slurry pressure to stabilize the tunnel face is suggested.

INDEX

Preface ..... **I**

Acknowledgements ..... **III**

Abstract ..... **V**

Index ..... **VII**

1. Introduction **1**

1.1 Motivation 1

1.2 Problem statement and objectives 3

1.3 Methodology and structure 4

2. Face stability of slurry shield driven tunnels **7**

2.1 Fundamentals of slurry shield tunnelling method 8

2.1.1 Slurry shield construction and application range 9

2.1.2 Fundamental requirements for the support medium and pressure 11

2.1.3 Cutting tools used in slurry shield tunnelling 12

2.2 Failure modes of the slurry supported tunnel face 14

2.2.1 Local failure modes 14

2.2.2 Global failure modes 15

2.3 Local stability assessment 15

2.4 Global stability assessment 16

2.4.1 Limit equilibrium solutions 17

2.4.2 Limit state solutions 19

2.4.3 Comparison and evaluation of the models 22

2.5 German safety concept for the face stability analysis 23

2.6 Practice oriented calculation of minimal support pressure in non-cohesive soils using Horn's failure mechanism 27

2.7 Conclusions about face stability assessment of slurry shield driven tunnels 34

3. Slurry-soil interaction and the slurry pressure transfer 36

3.1 Basic properties of interacting materials 37

3.1.1 Definition of non-cohesive soils 37

3.1.2 Basic properties of bentonite slurries 38

3.2 Characterization of flow processes in soil by the theory of porous media .. 47

3.2.1 Continuum approach of flow characterization in porous media 49

3.2.2 Capillary bundle approach of flow characterization in porous media 52

3.3 Fundamentals of suspension filtration and flow through porous media 55

3.3.1 General types of suspension filtrations 55

3.3.2 Standard blocking filtration (deep bed filtration) 57

3.4 Theories of support pressure transfer at the tunnel face 64

3.4.1 Theories not considering time factor 65

3.4.2 Theories considering time factor 76

3.4.3 Theories considering time factor and the interaction with cutting tools globalized over the entire tunnel face 81

3.5 Conclusion about state of the art of the slurry-soil interaction and the slurry pressure transfer 86

4. Theoretical considerations concerning the adaptations of pressure transfer models 89

4.1 Case A - Tool penetration deeper than pressure transfer mechanism 91

4.2 Case B - Tool penetration shallower than pressure transfer mechanism 95

5. Analysis of excavation scale 101

5.1 Analysis of tool layout on cutting wheels 103

5.2 Tool penetration and timespans between tool passes 104

6. Experimental investigations: Case A – shallow slurry penetration scale 109

6.1 Experimental set-up & methodology 109

6.2 Experimental programme and materials 113

6.3 Results and Interpretation 115

6.3.1 Experiments without back-pressure 115

6.3.2 Experiments with back-pressure 122

6.4 Comparison of tool cutting with slurry penetration scale for the Case A .. 125

6.5 Summary of experimental investigation for the Case A 128

7. Experimental investigations: Case B – deep slurry penetration scale 131

7.1 Experimental set-up & methodology 132

7.1.1 Primary penetration of slurry 132

7.1.2 Re-penetration of slurry 134

7.1.3 Re-penetration of slurry with soil cutting – RUB Tunnelling device 137

7.2 Experimental programme and materials 139

7.2.1 Primary penetration and re-penetration 139

7.2.2 Re-penetration with soil cutting – RUB Tunnelling device 143

7.3 Results and Interpretation 145

7.3.1 Primary penetration of slurry within the column test 145

7.3.2 Re-penetration of slurry within the column test 157

7.3.3 Re-penetration with soil cutting – RUB Tunnelling device 163

7.4 Summary of experimental investigation for the Case B 170

8. Case A – Pressure transfer analysis and the implementation into tunnel face stability assessment 173

8.1 Methodology and the numerical models used in the pressure transfer analysis 173

8.1.1 Model for the parametric investigation of the tunnel face segmentation 174

8.1.2 Model for evaluation of the pressure transfer and simplified cutting wheel 179

8.1.3 Model for evaluation of the pressure transfer and realistic cutting wheel 183
8.2 Results and interpretation for the pressure transfer analysis 185
8.2.1 Parametric study for investigation of the segmentation of the tunnel face 185
8.2.2 Investigation considering experimental results for slurry penetration and a simplified cutting wheel 186
8.2.3 Investigation considering experimental results for slurry penetration and a realistic cutting wheel 193
8.2.4 Comparison of the calculated pressure transfer with other theories 198
8.3 Face stability assessment for Case A 200
8.3.1 Face stability assessment for excavation with simplified and with realistic cutting wheels 200
8.3.2 Additional notes to the face stability in Case A 201
9. Case B – Implementation of the experimental results into analytical face stability assessment 205
9.1 Conditions at the tunnel face during excavation and resulting model adaptation 206
9.1.1 Slurry penetration depth 206
9.1.2 Stagnation gradient development 208
9.1.3 Development of effective stress 213
9.2 Resulting adaptation of the face stability calculation model 214
9.3 Additional check of the self-bearing capacity of the wedge 217
9.3.1 Parametric study 218
9.3.2 Limitations of the additional check 219
10. Recommendations for practice 221
10.1 Efficiency of the pressure transfer mechanism and measures to its increase. 221
10.2 Integrated design approach for the required face support pressure 224

10.2.1 Scenario with fixed parameters 225

10.2.2 Scenario without fixed parameters 230

11. Conclusion & outlook 231

References XI

List of Figures XXI

List of Tables XXXI

List of Symbols XXXV

List of Abbreviations XLVII

Curriculum Vitae XLIX

Appendix LI

1. INTRODUCTION

1.1 Motivation

Soft ground tunnelling has three specific key elements: tunnel face stabilization, segmental lining installation and grouting of the annular gap between the lining and ground, which can be critical for the tunnel stability. This thesis focuses on the first element – tunnel face stabilization. Specifically, the thesis concentrates on tunnel face stabilization during slurry shield excavations. Slurry shields are known to be reliable excavation method in non-cohesive soils under groundwater level. In such conditions, they are able to actively support the tunnel face including the minimization the deviations of support pressure. Thus, disturbances to the surroundings due to the excavation can be minimised. The technology of using bentonite slurry (suspension) as a support medium was adapted from diaphragm wall technology. In diaphragm wall technology, the slurry is used to support the open trench.

Jacob (1975) reported the up to date development of slurry shields and the first application in Germany. He expressed concerns regarding the application of the diaphragm wall support technology to slurry shields. The concerns were focused on the interaction of slurry supported tunnel face with periodically rotating cutting tools. According to him, experiments were conducted for clarification purposes. The results of the slurry penetration experiments were that the slurry stagnated between 1 and 2 seconds after the experiment start. Further details about the experiments were not published. He concluded that the slurry would offer a safe support, despite the periodical disturbance of the transfer mechanism by cutting tools. With this statement, concerns were dispelled for a long time. The topic was not touched again even when Krause (1987) investigated filter cake formation and concluded that it takes between 1 – 2 minutes (in fact he meant slurry stagnation stage during penetration).

The community was still convinced that the local dynamic pressure changes caused by cutting tools are negligible due to the low rotation speed of the cutting wheel

(Anheuser, 1987). Anheuser (1989) assumed that the acting thickness of the pressure transfer mechanism is formed within a few seconds, and that the distance between cutting tools is in comparison large enough to omit any local disturbances of the pressure transfer mechanism. Hence, Anheuser (1987) assumed that the adjacent cutting tools are not influencing each other. Consequently, the application of unadjusted principles of slurry support from diaphragm wall technology was further promoted by Babendererde (1991), Maidl et al. (1994) and Jancsecz & Steiner (1994).

Jancsecz & Steiner (1994) reviewed up-to-date applications of the diaphragm wall principles based on previously conducted shield excavation projects (Table 1-1). They did not report any problems resulting from the interaction of the pressure transfer mechanism with cutting tools. Janczecs & Steiner (1994) instead focused on the issue of avoiding deep slurry intrusion into soil for excavations in permeable ground. The Grauholz Tunnel is an example of such an excavation. The tunnel was excavated in coarse soil with a characteristic grain size (d_{10}) up to 2 mm. According to Jancsecz & Steiner (1994) and Anagnostou & Kovari (1994), in order to guarantee the efficient support of the imaginary soil wedge at the face in such projects, it is important to avoid deep slurry penetration. For the assessment of slurry penetration depth, the authors again adopted the principles previously known from diaphragm wall technology.

Table 1-1: Projects used to review the functionality of slurry face support by Jancsecz & Steiner (1994)

Project	Location	Year
City rail, U8	Berlin, Germany	1987
City rail TA6, Lot 22N	Duisburg, Germany	1988 - 1989
Grauholz Tunnel	Bern, Switzerland	1990 - 1993
City rail, Lot M1	Cologne, Germany	1992
City rail, Lot 34	Essen, Germany	1992
Main Sewer, Lot 1	Düsseldorf, Germany	1992

Concerns about safety level of slurry support during excavation appeared for the second time with slurry shield excavations in Holland around the year 2000. The concerns regarded the application of support principles known from diaphragm wall technology. They were triggered by measurements of increased pore water pressure above the hydrostatic level in front of the tunnel face during excavation. The measurements could not be explained by the pressure transfer theories from diaphragm wall technology. The increased pore water pressures were reported by

Bezuijen et al. (2001) at the 2nd Heinenoord tunnel and by Aime et al. (2004) at the Groene Hart tunnel. The measurements of increased pore water pressure were later confirmed by Wendl & Thuro (2011) and Klitzen & Hrdina (2016) at the H 3-4 and H8 projects in Austria, followed by Kaalberg et al. (2014) and Bezuijen et al. (2016) at the N-S line in Amsterdam in the Netherlands. In contrast to the previously referenced projects by Jancsecz & Steiner (1994), the excavations with reported increased pore pressure were conducted in finer soils:

- 2nd Heinenoord Tunnel: d_{10} = 0.14 – 0.2 mm (Broere, 2001)
- H3-4 & H8: d_{10} = 0.3 – 0.7 mm (Köhler et al., 2012)
- Groene Hart: d_{10} = 0.23 mm (Bezuijen, 2002)

It is assumed that the increased pore pressures, which lead to lower face support efficiency, result from the cutting tool interaction with the pressure transfer mechanism at the tunnel face during excavation.

1.2 Problem statement and objectives

The problem statement of this thesis originates from the research proposal of the subproject A6 of SFB 837 submitted by Schoesser & Schanz (2014).

Simultaneous soil excavation and slurry support characterizes the processes at the slurry supported tunnel face during excavation. The cutting tools of different types are fixed at the arms of the cutting wheel. The tools are rotating with the cutting wheel at particular rotation speed. Thrust jacks at the end of the machine push the shield forward and enable the excavation. The passing of cutting tools through a local point at the tunnel face disturbs the pressure transfer mechanism. After each passing of a cutting tool, the pressure transfer mechanism has to form again. The formation of the pressure transfer mechanism is characterized by slurry penetration into the soil. The slurry penetrates up to certain distance depending on the difference between slurry chamber pressure and groundwater pressure. The timespan for the transfer mechanism formation is given by the periodicity of passing of the cutting tools at the local point of the tunnel face.

The chronological superposition of the slurry penetration and the excavation results in a local transient process at the particular point on the tunnel face. The local

disturbation process may cause a reduction of efficiency of the entire slurry face support during excavation. Thereby, the conditions at the slurry supported tunnel face are different than that on the vertical wall of the open trench stabilized by slurry as known from diaphragm wall technology.

The objectives of this thesis are to understand the time-scale of the slurry penetration and the excavation process. A further objective is to characterize the pressure transfer and the resulting tunnel face support efficiency for the particular slurry penetration and excavation depth. Based on the characterization, the tunnel face stability can be assessed. A methodology is to be developed, which would enable us to characterize the efficiency of the pressure transfer for every excavation condition. Furthermore, the measures that can improve the efficiency of the pressure transfer should be suggested.

The last objective is to improve the reliability of the face stability assessment process. On one hand, it is to clarify for which conditions the contemporary design methods, taken from diaphragm wall technology, are applicable without a risk of insufficient face support. On the other hand, it is to specify for which conditions the contemporary methods may deliver unsafe results. In this thesis, an update of the models will eventually be suggested. The decrease in face support safety in comparison to contemporary methods can be seen in the increased pore water pressure during excavation outside of slurry penetrated zone.

1.3 Methodology and structure

In order to fulfil the presented objectives of this thesis, various methodological approaches are pursued. Based on the interpretation of field excavation data of slurry shield machines, statements are made about the tool cutting depth and cutting frequency. Experimental investigations are carried out for understanding of the time-scale of the slurry penetration. The characterization of the pressure transfer efficiency under consideration of cutting process is conducted on the basis of numerical and analytical calculations. For improving the reliability of the face stability assessment, recommendations for a practical design approach are formulated based on the findings of the thesis. The realization of this methodology is described by the following structure of the work.

The literature research starts with the review of the state of the art and practice of the field of tunnel face stability assessment in slurry shield tunnelling. The important steps conducted in the tunnel face stability assessment specifically for slurry shields is the evaluation of pressure transfer from fluid pressure of the slurry to the effective stress in soil skeleton. A further step of the literature research is dedicated to the review of slurry-soil interactions on different scales resulting in the slurry pressure transfer.

The literature research leads to the development of research issues. The possible and eventually required adaptations of the contemporary pressure transfer models for the purposes of slurry shield excavations are discussed in chapter 4. Hypotheses about the pressure transfer during slurry shield excavation resulting from the interaction between cutting tools and pressure transfer mechanism are formulated in this chapter. Two cases of the interaction at the tunnel face are derived in this chapter depending on the comparison between the tool cutting scale and the slurry penetration scale. The demands for the experimental research for the particular case are highlighted here to confirm the established hypothesis.

Field data evaluation focuses in chapter 5 on the characterization of the shield excavation scale. Excavation data obtained from three reference slurry shield projects are assessed here together with the analysis of cuttings wheels.

Experimental research starts in chapter 6. The experimental investigation of the shallow slurry penetration scale (Case A of interaction) is conducted in this chapter and its results are presented and discussed. The results from chapter 6 cannot be directly transferred to the tunnel face without the procedure from chapter 8. In contrast, the deep slurry penetration scale (Case B of interaction) is experimentally investigated in chapter 7. The experimental modelling of interaction of cutting tools with the slurry pressure transfer mechanism is emphasized here for both cases of interaction.

The last block of the thesis starts in chapter 8 and deals with the implementation of the field data evaluation and laboratory experiments into analysis of tunnel face stability. In this chapter, numerical seepage analysis is employed to model the flow in front of the tunnel face in Case A while considering the experimental results for the shallow slurry penetration scale from chapter 6 and the tool cutting scale investigated in chapter 5. In similar way, the implementation is discussed in chapter 9 for the Case B of interaction. The experimental results from chapter 7 are considered. The findings

of the thesis resulted in recommendations for practice, which are summarised in chapter 10. In this chapter, an updated integrated design approach for the minimal support pressure is suggested. The thesis is finalized with a conclusion and an outlook for further research in chapter 11.

2. FACE STABILITY OF SLURRY SHIELD DRIVEN TUNNELS

Chapter 2 is based on the paper: Zizka, Z.; Thewes, M. (2016): Recommendations for Face Support Pressure Calculations for Shield Tunnelling in Soft Ground, published by Deutscher Ausschuss fuer unterirdisches Bauen e. V. German Tunnelling Committee.

Stabilization of the tunnel face is a fundamental aspect of mechanized tunnelling in soft ground. This is reflected by the DAUB Recommendations for selecting and evaluating Tunnel Boring Machines (DAUB, 2010), because it classifies the full face soft ground shield machines based on face support type (Figure 2-1). One of the five systems listed as Shield Machines with Full Face Support represents the slurry support deploying clay (bentonite) suspensions for a supporting medium. The code for slurry type support is SM-V4.

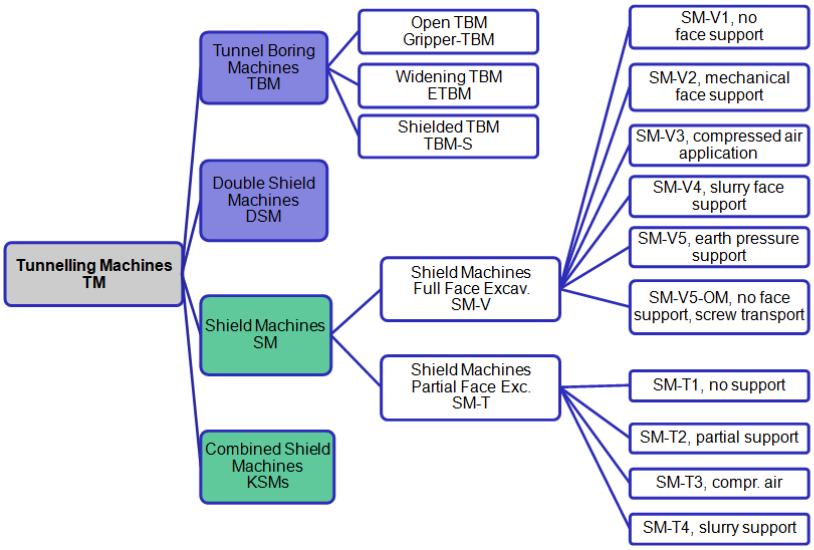

Figure 2-1: Simplified differentiation of tunnelling machines related to their prevalent ground of application according to DAUB (2010)

2.1 Fundamentals of slurry shield tunnelling method

The first application of a machine that can be called a slurry shield was in 1959/60 in the United States. Hydraulic mucking was deployed for the first time on this machine. However, the working chamber of the machine was not pressurized (Maidl et al., 2012). Consequently, Lorenz (1966) obtained a patent for his development of a mechanically excavated tunnel face supported by thixotropic fluid - slurry (Maidl et al., 2012). As Anheuser (1987) points out, this development in slurry shield technology was triggered by the success of clay suspensions (slurries) in diaphragm wall technology to support an open trench.

The Japanese company Mitsubishi constructed the first slurry shield in 1967 (Maidl et al., 2012). Thereby, the Japanese line of development started and was later patented by Yamazaki (1978). The typical characteristics of a Japanese line is that the support pressure is regulated directly by the pumping velocity in the slurry circuit consisting of the slurry feed and discharge pipe. This characteristic distinguishes the Japanese line from the German line. The company Wayss & Freytag started the German line of slurry shields with the first prototype in 1974 (Anheuser, 1987). The prototype introduced an additional working chamber with a compressed air bubble, which was used for support pressure regulation. Nowadays, the German line is predominantly employed throughout the world for excavations of traffic tunnels. The machines belonging to this line are also called Hydro-Shields (Babendererde, 1991) or Mix-Shields (Herrenknecht, 1994). Nevertheless, the internationally acknowledged label “slurry shield” will be used in this thesis also and exclusively for the machines from the German line of development.

There are several projects from history, which can be considered milestones due to extension of the feasible range for the slurry shield tunnelling. The first project to mention is the 4th Elbe Tunnel excavated between 1995 and 2003. The slurry shield machine at this project was equipped with a man-accessible cutting wheel. This feature considerably simplified the replacement of cutting tools under high pressures. Further improvement was achieved at the construction of the Westerscheldt tunnel, which was constructed between 1996 and 2003. Saturation diving (Holzhäuser et al., 2006) was introduced to slurry shield tunnelling during this project, which made tunnel face interventions under very high pressures possible without necessity of man-accessible cutting wheel. Following projects such as the Eurasia tunnel, excavated between 2011

and 2016, benefitted from these developments. Another project to mention is the Wehrhahn-Line tunnel in Düsseldorf, which was completed between 2007 and 2014. This project pushed the boarders in terms of very shallow overburden and many surface constructions. The excavation was conducted with almost zero settlement (Schindler et al., 2016).

2.1.1 Slurry shield construction and application range

The slurry shield technology can be viewed as a combination of a shield in the ground and a separation plant, usually located at the surface. While the shield (Figure 2-2) is responsible for the excavation of the cavity, the plant separates the excavated material from the slurry. Details about separation plants used in tunnelling can be found, for instance, in Maidl et al. (2012) or Paya (2015).

The front area of the shield consists of an excavation chamber (front chamber) and a working chamber (back chamber). The excavation chamber is separated from the working chamber by a submerged wall. An opening is located at the bottom of the submerged wall to enable pressure balance between the chambers. The excavation chamber is completely filled with slurry, while the slurry level in the working chamber is usually adjusted to be slightly above the machine axis. Fresh or regenerated slurry is continuously supplied into the working chamber by a slurry feed pipe. Additionally, the

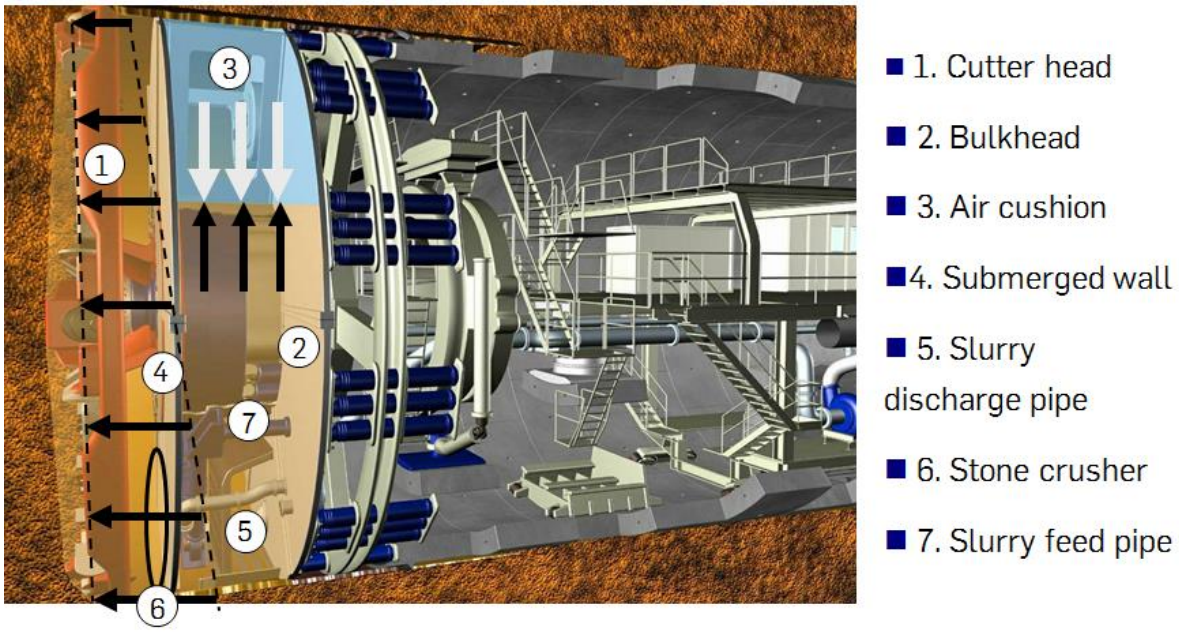

Figure 2-2: Longitudinal cut through Slurry shield machine (Herrenknecht AG)

machine is equipped with a sieve grill and stone crusher located in front of the suction inlet in order to reduce the size of boulders or cobbles for hydraulic transport by the slurry discharge pipe. Through the suction inlet and the discharge pipe, a mixture of excavated soil and suspension is extracted by centrifugal pumps (Babendererde, 1991) to the separation plant at ground level. The slurry in the excavation chamber might be lowered and exchanged by compressed air during stoppages to allow maintenance at the cutting wheel. Excavations with partially lowered slurry in the excavation chamber are possible but very rare.

The front shield area is divided from the back area with atmospheric pressure by a bulkhead. An erector, which manipulates concrete segments and assembles lining rings, is located in the atmospheric pressure area. The thrust cylinders are braced between the bulkhead and the last assembled lining ring. These cylinders are responsible for moving the machine forward during the cutting phase.

As pointed out, slurry shield excavations are usually conducted in non-cohesive soils. The typical application range of slurry shields is shown in area A of Figure 2-3. Grains within this range are small enough to ensure efficient face support by usual slurries but large enough to allow for a simple treating of the excavated material in the separation

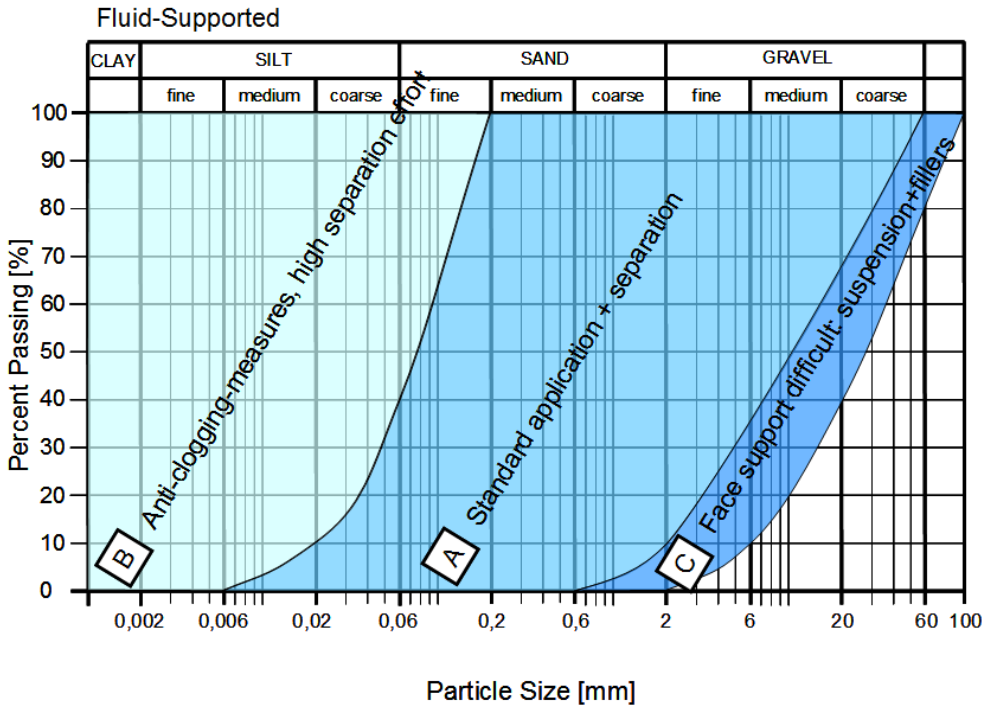

Figure 2-3: Application ranges of shield machine with slurry supported tunnel face (Thewes, 2009)

plant. In zone B, which consists of fine-grained soils and clays, the separation effort becomes more difficult, and clogging of the shield may occur (Thewes, 2009). Zone C consists of very coarse-grained gravels with high permeability. In these soils, the face support mechanism might be inefficient due to deep slurry penetration without stagnation (see chapter 3.3). In this case, fillers should be added to usual slurries to plug the larger pores of the ground (Bayer et al., 2016).

2.1.2 Fundamental requirements for the support medium and pressure

Bentonite slurry is a mixture (suspension) of water and bentonite. Bentonite consists dominantly from a clay mineral montmorillonite. A bentonite suspension has to fulfil two fundamental functions for slurry shield tunnelling. First, it is a hydraulic means of conveying the muck with the use of a pipe system. For this function, it is beneficial to keep the yield point and thus the apparent viscosity of the slurry as low as possible to simplify slurry pumping (Longchamp et al., 2005). Similarly, Anheuser (1987) appoints a high yield point of slurry as an obstacle for pumping and separation. Moreover, the density of the discharged fluid must not exceed a particular design density due to pumping reasons (Wehrmeyer, 2009). Despite treatment of the used slurry in the separation plant, the content of fines and thereby the density still increases successively during excavation.

The second function of the slurry is to stabilize the tunnel face. Two viewpoints are distinguished; the support pressure transfer to soil grains to ensure both global and local micro stability. The slurry´s yield point is the most important parameter of the slurry involved in the analysis for both cases, if the traditional theory (Kilchert & Karstedt, 1984), which was adapted from diaphragm wall technology, is considered (see chapter 3.3). The standardised approaches for determination of slurry properties can be found, for instance, in Triantafyllidis (2004), Longchamp et al. (2005) or DIN 4127 (2013). The slurry properties are discussed in detail in chapter 3.1.2 of this thesis. It is reported in the literature, that saline and brackish water may significantly damage the functionality of slurry (Talmon et al., 2013).

In order to sufficiently support the face, the slurry needs to be pressurized to a particular level, which was determined by the face stability calculation (see chapter 2.4). The required pressure level is achieved and maintained by a compressed-air reservoir (also called an air cushion or air bubble) in the working chamber. The

reservoir acts as an elastic spring element (Babendererde, 1991) and the chamber pressure becomes more or less independent from pressure deviations in the slurry circuit (Krause, 1987). Moreover, the described design allows the volume of slurry in the excavation chamber to fluctuate due to sudden losses of support medium without failure of the tunnel face (Maidl et al., 2012). Nevertheless, some deviations of the support pressure during excavation occur anyway. The “Samson-pressure-unit” has a pressure steering tolerance of +/- 0.05 bar (Babendererde, 1991). An additional source of the deviations might be the device for slurry level regulation in the pressure chamber (Thienert, 2011). To add a certain safety gap to this value, the entire steering tolerance of the support pressure is usually adopted as +/- 0.1 bar (Krause, 1987). Interestingly, the amount of pressure deviation suggested in 1987 is still considered in the design process nowadays without any narrowing (ZTV-ING, 2012).

2.1.3 Cutting tools used in slurry shield tunnelling

The cutting tools are fixed at the cutting wheel and are responsible for removing the soil from the tunnel face. Originally, only scrapers were employed as excavation tools in slurry shield tunnelling, since slurry shields were used primarily for excavations within homogeneous non-cohesive soft soils (Burger, 2006). Nowadays, several types of cutting tools are placed at the cutting wheels to improve the excavation process and to make the shields more adaptable. The following are typical (Maidl et al., 2012) and are shown in Figure 2-4:

- Discs
- Rippers
- Scrapers
- Buckets

Each type of tool fulfils a different function on the cutting wheel. Within soft soil excavations, discs are installed on the cutting wheel to protect other cutting tools from damage, e.g. when the shield encounters some boulders or artificially made structures. Jet-grouted bodies, diaphragm walls or pile walls represent mostly such structures. Therefore, the discs are located slightly in front of other cutters in the excavation direction (Figure 2-4). The offset of the discs in front of the cutting wheel plane is usually 175 mm (Köppl, 2014). The discs are usually located in the middle of the cutting-wheel-arms in order to induce high cutting forces. The chosen rotation direction of the cutting wheel does not influence the interaction between discs and the soil at the tunnel face.

Rippers represent the second type of tool. Rippers may be located in the same position on the cutting wheel as discs and they are interchangeable with discs (except for calibration discs). However, the deployment of rippers is not very frequent in slurry shield tunnelling. The chosen rotation direction of the cutting wheel does not influence the interaction between rippers and tunnel face.

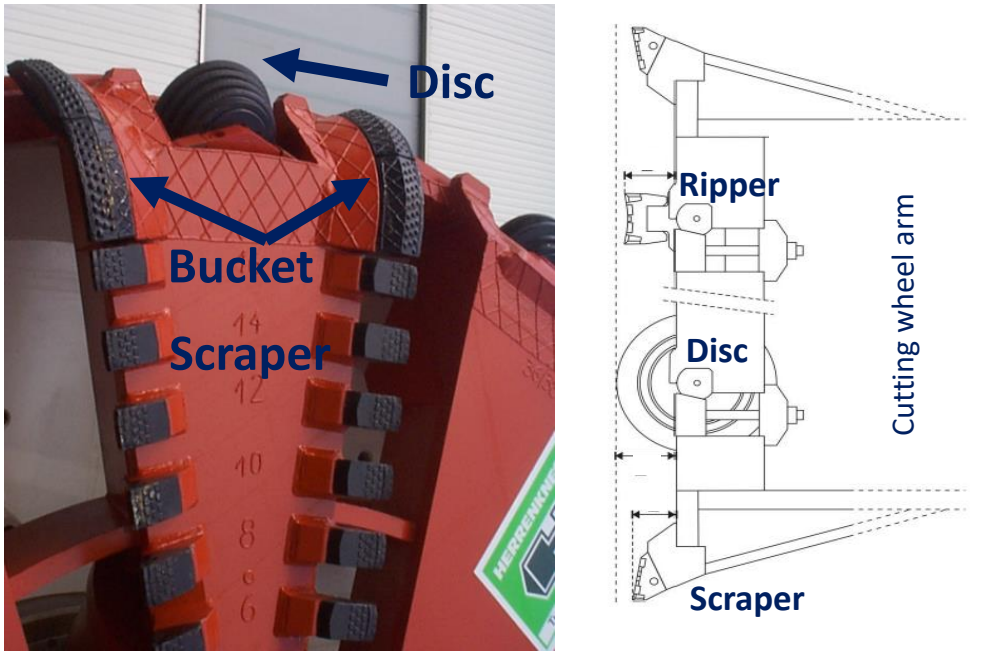

Figure 2-4: Cutting tools at the cutting wheel (adapted from Herrenknecht AG and from Köppl, 2014)

Buckets and scrapers are located slightly behind the discs, considering the excavation direction, and they are responsible for actual soil cutting within soft soil excavations. These tools are usually placed in pairs (tandems) on one cutting wheel arm in order to permit both directions of cutting wheel rotation. The blades of buckets and scrapers are usually located 140 mm in front of the cutting wheel in the longitudinal direction (Köppl, 2014). The tools are placed at the edges of the wheel arms in order to deliver the cut soil to the excavation chamber.

The cutting blades of outlined cutting tools have different widths depending on the tool type (Köppl, 2014):

- Discs: 12 – 25 mm (single ring or two rings type)
- Rippers: 50 – 200 mm
- Scrapers: 100 – 250 mm (narrow & wide type –Maidl et al., 2012)
- Buckets: areal cutting tool, no general size

Due to the blade width and the type of movement, the tools interact differently with the pressure transfer mechanism at the tunnel face as will be discussed in chapter 5 of this thesis.

2.2 Failure modes of the slurry supported tunnel face

The failure modes of the tunnel face are distinguished based on their initial extent. While the local failure mode may start with destabilization of single soil grains, the global failure mode is usually comprised of a soil body with dimensions comparable to the tunnel diameter.

2.2.1 Local failure modes

The local failure mode denotes the possibility of single soil grains falling out of the soil skeleton at the slurry supported vertical wall (Müller-Kirchenbauer, 1972). This wall might be represented by a trench for diaphragm wall, which was the original focus of Müller-Kirchenbauer (1972). Van Rhee & Bezuijen (1992) investigated the influence of seepage on sand slope stability. They suggested also the local single particle mode besides the failure mode described by Müller-Kirchenbauer (1972), which they called local continuum mode. Based on performed experiments, Van Rhee & Bezuijen (1992) concluded that the particular local failure mode depends on flow direction of fluid through the free face. It turns out that the slope stability of soil subjected to inflow, as an analogy to the tunnel face, is governed by the single particle mode. However, as pointed out, Bezuijen & van Rhee (1992) focused on flow of water. Hence, if a different type of liquid is considered, the local continuum mode might be decisive.

Additionally, Xanthakos (1979) described the possibility of grain failure utilizing the peel-off mechanism. Contrary to Müller-Kirchenbauer (1972), he states that only a sufficient yield point of slurry in comparison to grain size (Weiss, 1967) of soil can counter this failure. The influence of the yield point is later discussed in section 3.4.1. A corresponding sketch is also provided in this section.

2.2.2 Global failure modes

The shape of the global failure mode of the tunnel face is on one hand predetermined by encountered ground conditions. On the other hand, the overburden thickness above the cavity is decisive for the failure propagation towards the surface. Cohesive, fine-grained soils tend to cause wide sinkholes in both the longitudinal and transversal directions at the surface involving large amounts of material. In contrast, the non-cohesive, coarse-grained soils generate slim, funnel-like failure bodies (Leca & New, 2007). Leca & New (2007) conducted a wide literature review and realised that an agreement on this issue exists between analytical calculation models and centrifuge experiments.

Two types of failure propagation to the surface are possible. For a deep tunnel with $C_{over}/D > 2.5$ and the corresponding first failure mode, a zone with loosened soil appears close to the cavity. This zone is approx. 1.5-times tunnel diameter high and hence does not reach the surface. For a shallow tunnel with $C_{over}/D < 2.5$ (Figure 2-5), the second failure mode usually occurs (Leca & New, 2007). The second mode consists of a rigid soil body stretching up to the surface (Figure 2-5). These types of face collapses could also be observed in numerical calculations by Vermeer & Ruse (2004).

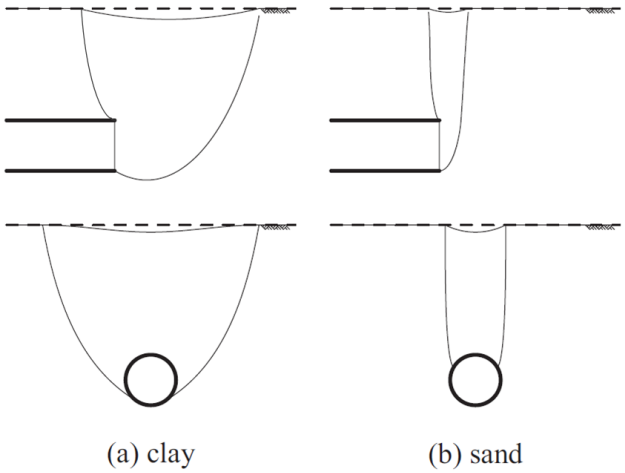

Figure 2-5: Face collapse in cohesive - clay (a) and granular soils – sand (b) and its propagation pattern adapted from Broere (2001), Leca & New (2006) and Fillibeck (2011)

2.3 Local stability assessment

The local face stability is particularly important for slurry shield tunnelling, due to the employment of a liquid support medium. To prevent local failure mode, the slurry

support pressure has to induce a certain support pressure gradient over the soil grain at the tunnel face. Müller-Kirchenbauer (1972) found that the slurry induces a pressure gradient, which depends on its yield point. Thus, a check of local stability may be done indirectly by calculation of the minimally required yield point of the slurry (DIN 4126, 2013). For details about the correlation between slurry yield point and pressure gradient see chapter 3.4.1. Eq. 2-1 defines the minimally required yield point of the slurry based on ground conditions and was developed by Kilchert & Karstedt (1984). DIN 4126 implies that the yield point should be determined for the purposes of this equation by a ball harp or pendulum device after 1 minute of rest time. This is later discussed in section 3.1.2.

$$\frac{\boldsymbol{d_{10}}}{\boldsymbol{2 \cdot \eta_F}} \cdot \frac{\boldsymbol{\gamma_\varphi}}{\boldsymbol{tan(\varphi')}} \cdot \boldsymbol{(1 - n_p)} \cdot \boldsymbol{(\gamma_s - \gamma_{F,fresh})} \cdot \boldsymbol{\gamma_G} \leq \boldsymbol{\tau_F} \qquad \textbf{Eq. 2-1}$$

with

d_{10} Characteristic grain size of the soil (to be obtained from grain distribution curve) [m]
n_p Soil porosity [-]
γ_s Unit weight of soil grains [kN/m³]
γ_G Partial safety factor for permanent load case in GZ1C acc. to DIN 1054 (= 1.00) [-]
$\gamma_{F,fresh}$ Unit weight of fresh slurry [kN/m³]
γ_φ Partial safety coefficient for drained soil within the status GZ1C in load case LF2 acc. to DIN 1054 (= 1.15) [-]
φ' Characteristic drained friction angle of the soil [°]
η_F Safety factor accounting for deviations in the yield point of suspension (= 0.6) [-]
τ_F Yield point of slurry [kPa]

The main weakness of this equation is that it does not consider the flow of slurry induced by slurry excess pressure. This seems satisfactory for the stability calculation of a slurry-supported trench for a diaphragm wall, which is the original application field of DIN 4126 (2014), due to this type of action. However, it is a significant simplification of the slurry supported tunnel face during tunnel excavation.

2.4 Global stability assessment

The aim of the global stability assessment is to determine the minimal required face support pressure, which will prevent the occurrence of global failure. The second aim is to avoid over-excavation (Babendererde, 1991). Thus, the support medium must counteract the earth and groundwater pressures to stabilize the tunnel face. The minimal support pressure calculation focuses solely on the stability criterion, so that

the calculations do not consider any potential ground deformations as design criterion. Hence, this approach is called “the Ultimate Limit State Approach”. Various methods to determine the required support pressure due to the acting earth pressure can be found in literature. All available approaches can be divided into four fundamental groups:

- Analytical methods
- Empirical methods
- Experimental methods
- Numerical methods

In this thesis, only the analytical methods are extensively discussed due to their later application. The analytical calculation methods concerning the ultimate limit state approach are presented in the following chapters. For a thorough description of the other methods the reader is referred to publications by Broere (2001), Kirsch (2009) or Zizka & Thewes (2016). It is necessary to note that slurry pressure in non-cohesive soils cannot be lower than groundwater pressure during excavation.

Analytical methods include limit equilibrium and limit state methods. These methods assume a possible failure mechanism of the tunnel face or a stress distribution in the ground, respectively, and from that determine a support pressure at collapse. The support pressure at collapse is then considered to be the minimal support pressure required. A common feature of most analytical methods is that they are based on one of two most widely used laws of failure in soil mechanics. The first law, the Mohr-Coulomb law of failure, is broadly adopted for frictional or frictional–cohesive materials where the associated flow rule dominates the formulations. The second law, the Tresca law of failure (associated), is mostly applied for purely cohesive materials.

2.4.1 Limit equilibrium solutions

The limit equilibrium methods can be characterised by the required assumption of a kinematical failure mechanism of the tunnel face. The first limit equilibrium failure mechanism was suggested by Horn (1961) and assumes a sliding wedge in front of the tunnel face that is loaded by a rectangular prism stretching up to the terrain surface level (Figure 2-6-b). This sliding wedge mechanism for the investigation of tunnel face stability was introduced to mechanised tunnelling by Anagnostou & Kovari (1994) and Jancsecz & Steiner (1994). The equilibrium condition of the stabilizing and destabilizing

forces is formulated on the sliding wedge. The wedge's weight and the load from the overlaying prism are listed as destabilizing forces. The stabilizing forces are composed of the tunnel face support force and shear resistance forces at the boundary planes of the failure mechanism. Moreover, an assumption of the horizontal earth pressure acting on the vertical triangular planes of the wedge is needed to determine the shear resistance on them. Recently, Anagnostou (2012) suggested a method that eliminates the required assumption of horizontal stresses on the triangular planes. The method originates from the method of slices (Walz & Pulsfort, 1983) and formulates the equilibrium condition on an infinitively slim horizontal slice of the wedge. The equilibrium condition is subsequently integrated over the whole wedge. Hu et al. (2012) generalized the shape of the sliding wedge and of the overlaying prism to allow for a variable width along their vertical axis. Furthermore, the boundaries of the failure mechanism do not necessarily have to have a planar shape as Mohkam & Wong (1989) suggested a failure wedge with inclined slide surface consisting of a logarithmic spiral. The limit equilibrium formulations commonly used in practice will be presented in detail in the section 2.6.

Particularly in German-speaking countries, a limit equilibrium method based on DIN 4085 is used to calculate the component of support force due to the earth pressure. This method assumes a three-dimensional failure body (Figure 2-6-a) suggested by Piaskowski & Kowalewski (1965).

The theoretical works dealing with tunnel face stability were often validated by experimental results using centrifuges or 1-g experimental devices. Among limit equilibrium methods, the formulation by Anagnostou & Kovari (1994) achieved the best accordance with experimental investigation as referred to by Messerli et al. (2010) and Bezuijen & Messemaeckers-van de Graaf (1997) (cited by Broere, 2001). For saturated sand, it has been reported by Plekkenpol et al. (2005) that the formulation of Jancsecz & Steiner (1994) achieved the best correlation with the preformed tests.

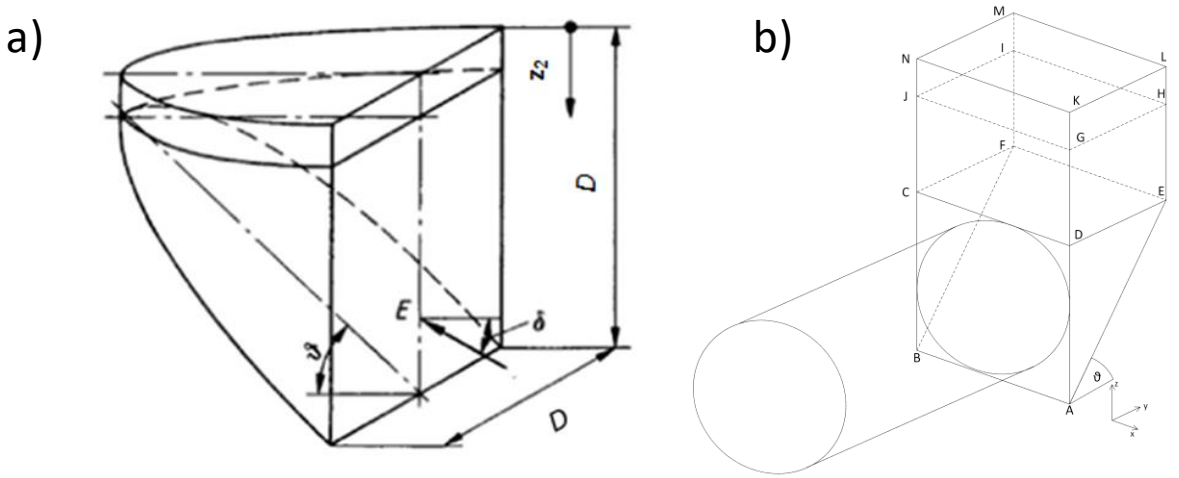

Figure 2-6: Failure mechanism acc. to a) Piaskowski & Kowalewski (1965) and b) Horn (1961) adapted from Zizka & Thewes (2016)

2.4.2 Limit state solutions

Various solutions for the tunnel face stability have been formulated based on bound theorems within the plasticity theory. This group of approaches is often known as “limit state methods”. The solution for the tunnel face stability can be obtained by adopting the upper or the lower bound of the plasticity theory.

The upper bound theorem is also known as the kinematical solution (Kolymbas, 2005) and it is based on plasticity theory, as it assumes a kinematically possible failure mechanism. Adopting the upper bound solution, the tunnel face will collapse as if the work done by the failure mechanism and by external forces acting on it is higher than the work done by internal stresses (Kirsch, 2009). Unfortunately, this approach will give a lower value of support pressure at collapse than what is actually needed in reality. Therefore, the upper bound solution is always taken to be on the unsafe side compared to reality.

The lower bound solution signifies a static approach based on plasticity theory. The lower bound solution of the tunnel face stability is found by determining a statically admissible stress distribution within a soil body that balances the external forces at the boundaries of the body without the yield being exceeded in any point of the soil body (Yu et al., 1998). The lower bound solution always delivers a higher support pressure than at actual tunnel face failure.

In summary, it can be expressed, that if the applied support pressure is higher than the pressure obtained by the lower bound theorem, the tunnel face will not collapse. The

tunnel face will collapse if a lower pressure is applied than what is calculated by the upper bound theorem. The tunnel face may be stable if a tunnel face pressure between upper and lower bound is applied.

Davis et al. (1980) developed both upper and lower bound stability solutions for a tunnel heading through purely cohesive soil assuming undrained conditions. In order to describe the real behaviour of the tunnel, they investigated three different cases that included two simplified cases and one with real three-dimensional tunnel geometry:

1) Plane strain unlined tunnel – approximates infinitely long tunnel
2) The plane strain heading – approximates infinitely wide tunnel
3) Cylindrical tunnel heading – only lower bound solution derived – attempt to describe real conditions

For each case, the authors determined the critical stability ratio, while adopting one of the bound theorems. The critical stability ratio has to be higher than the stability ratio determined for the particular face conditions. The stability ratio is calculated by subtraction of the support pressure (s_{axis}) from the vertical stress ($\sigma_{v,axis}$) at the tunnel axis, then dividing by the undrained shear strength (c_u) of the soil ($Eq.\ 2\text{-}2$). This methodology was originally developed by Broms & Bennermark (1967). The direct subtraction of the vertical stress and horizontal support pressure can be carried out since the coefficient of lateral pressure is equal to 1 here. When the stability ratio achieves the critical ratio, the tunnel collapses. Davis et al (1980) found that the critical stability ratio is variable, since it depends on the ratio between overburden and tunnel diameter. This was confirmed upon the comparison with experiments performed by Mair (1979). Davis et al (1980) concluded that actual collapse pressures can be found "fairly exactly" by adopting the lower bound solution for case 3) – cylindrical tunnel heading. However, these results cannot be completely generalized as the authors recommended to use the suggested approach for tunnels with an overburden/tunnel diameter (C/D) ratio lower than 3.

In contrast to Davis et al. (1980), Broms & Bennermark (1967) found that, based on multiple laboratory experiments, the stability ratio is constant. However, Broms & Bennermark (1967) employed a different experimental set-up, modelling a circular opening in the vertical sheet pile wall (Figure 2-7). They concluded that the purely cohesive soil within a vertical opening is stable, if the stability ratio is lower than 6.

$$N = \frac{\sigma_{v,axis} - s_{axis}}{c_u} \qquad Eq.\,2\text{-}2$$

with

N Existing stability ratio [-]
$\sigma_{v,axis}$ Total vertical stress at the tunnel axis [kPa]
s_{axis} Support pressure ta the tunnel axis [kPa]
c_u Undrained shear strength [kPa]

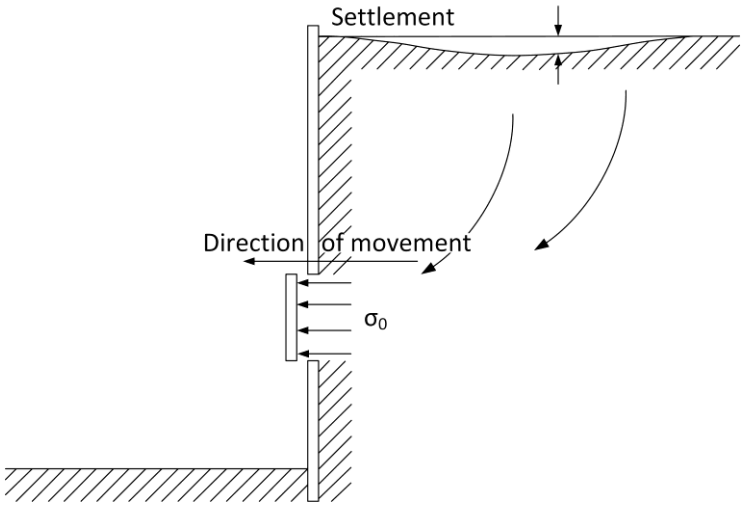

Figure 2-7: Layout of a circular opening in the vertical sheet pile wall (Broms & Bennermark, 1967)

Leca & Dormieux (1990) formulated the upper and lower bound solutions of the face stability for excavation through frictional soils and frictional - cohesive soils by adopting the Mohr-Coulomb failure law and the assumption of drained conditions. Hence, in comparison to previous limit state methods, this one would be applicable for the ground conditions focused on in this thesis. Leca & Dormieux (1990) investigated three possible failure modes of the tunnel face by assuming multiple conical rigid blocks as the failure mechanism. These blocks had an elliptical cross-section at the intersection of the tunnel face. The collapse support pressures were calculated for active failure and blow-out. It should be noted that Leca & Dormieux (1990) were actually investigating the pressure at passive failure of the tunnel face instead of the blow-out pressure of the support medium. Subsequently, the authors compared the theoretically calculated face pressures at collapse with experimentally obtained values by Chambon & Corte (1994). Leca & Dormieux (1990) concluded that there was a close agreement between upper bound solutions and experimental results. Thus, no lower-bound based solutions are recommended to use in frictional soils.

Further improvement of the upper bound solution was suggested recently by Mollon et al. (2010). The new failure mechanism is similar to the original ones by Leca & Dormieux (1990). However, it has a circular cross-section at the intersection of the tunnel face. This calculation approach allows an additionally tension cut-off for the soil failure formulation.

2.4.3 Comparison and evaluation of the models

As summarised by Zizka and Thewes (2016), various methods were developed to investigate the face stability and determine the face support pressure at collapse. The laboratory experiments were used to validate some of the theoretical calculation methods. Some of the developed theoretical models were also applied successfully in practice. The limit equilibrium methods were mostly used for calculations for excavations in non-cohesive soils. However, no real scale in-situ validation of the support pressure at the face collapse is known to the author of this thesis. In literature, references concerning centrifugal testing are available (Mair, 1979 or Chambon & Corte, 1994).

The aim of the analytical face stability calculation within the excavation design process is to define the minimal support pressure, for which the tunnel face will be stable. As in other geotechnical applications with stability investigations, safety factors are to be employed. The safety factors have to be introduced not only due to insufficient accuracy of the particular method but also due to possible locally variable properties of soil. Hence, the calculation method is intended to conduct a quick and transparent calculation. The transparency for the practicing engineer is required to enable clear presentation of the influences on the results. This is fulfilled by the limit equilibrium methods.

In contrast, the application of limit-state-based-methods for non-cohesive soils does not seem to be advantageous. The main disadvantage of the upper-bound-limit-state methods is their difficulty. A non-trivial optimization approach is necessary to find the minimal pressure at the collapse, when the shape of the adopted failure mechanism is realistic. The calculation process requires a certain amount of time. Thereby, the advantage of quick and transparent calculation of analytical models becomes smaller in comparison to the numerical machine-ground interaction analysis. It is worth mentioning that the use of safety coefficients would also be required for the limit state

calculations. Moreover, there is only limited reference concerning the use of limit state methods for the face stability assessment in non-cohesive soils in practice. Furthermore, no analytical stability calculation method can offer the benefit resulting from the application of the numerical analysis of machine-ground interaction. The machine-ground interaction (Zizka & Thewes, 2016) investigates not only the minimal support pressure at the collapse, but also the entire reaction of the ground for different levels of the support pressure.

Based on the discussed requirements and goals of the face stability assessments, it can be concluded that the limit equilibrium methods based on Horn's failure mechanism are the most suitable in non-cohesive soils.

2.5 German safety concept for the face stability analysis

The practical aim of the face stability analysis is not only to define the minimally required support pressure, but also to determine the maximally allowed support pressure. These two pressures are called operational lower and upper limits and are introduced in the German regulation ZTV-ING (2012) and RiL 853 (2011).

The lower support pressure limit has to ensure a minimal support force (S_{ci}), which consists of two components and their respective safety coefficients ($Eq.\ 2\text{-}3$). The first component of the support force ($E_{max,ci}$) has to balance the earth pressure, and is calculated by any method described in section 2.4 adopting drained conditions. In Germany, however, variants of Horn´s failure mechanism are preferred to determine this component. The second component of the support force (W_{ci}) has to balance the groundwater pressure and is determined based on the elevation of the groundwater level above the tunnel crown considering fully saturated conditions.

$$\boldsymbol{S_{ci} = \eta_E \cdot E_{max,ci} + \eta_W \cdot W_{ci}} \qquad Eq.\ 2\text{-}3$$

with

η_E	Safety factor for earth pressure force (= 1.5) [-]
η_W	Safety factor for water pressure force (= 1.05) [-]
S_{ci}	Required support force (circular tunnel face) [kN]
$E_{max,ci}$	Support force due to earth pressure (circular tunnel face) [kN]
W_{ci}	Support force due to groundwater pressure (circular tunnel face) [kN]

The upper support pressure limit is defined as a limiting pressure to avoid a break-up of the overburden or blow-out of the support medium. Therefore, the maximal support pressure has to be smaller than 90 % of the total vertical stress at the tunnel crown. The background of $Eq.\,2\text{-}4$ is explained in Bayer et al. (2016).

Break-up/ blow out safety as defined in ZTV-ING (2012):

$$\mathbf{1} \leq \frac{\mathbf{0.9} \cdot \boldsymbol{\sigma_{v,crown,min}}}{\boldsymbol{s_{crown,max}}} \qquad Eq.\,2\text{-}4$$

with

$\sigma_{v,crown,min}$ Total vertical stress in the tunnel crown considering minimal unit weight of soil [kPa]

$s_{crown,max}$ Maximal allowable pressure in the tunnel crown due to break up safety / blow-out safety [kPa]

This classical limit does not take into account any resistance of the overburden, in contrast with the recently developed approach by Vu et al. (2015). Further studies have been conducted numerically by Chen et al. (2018) to determine the upper limit pressure by evaluation of fracturing tendency. However, the authors obtained fracturing for slurry pressures outside of realistic range.

The operation range of support pressure defined by the two limits is visualized in Figure 2-8. The two limits are generally valid for all tunnel advance phases, i.e. excavation, stoppage, standstill. The limits are further narrowed by support pressure deviations, which have to be taken into account (see section 2.1.1).

Furthermore, it is recommended in ZTV-ING (2012) to consider different unit weights of soil for the calculation of minimal support pressure (lower limit) and of the blow-out (upper limit). The average unit weight, as defined by the by geotechnical consultant,

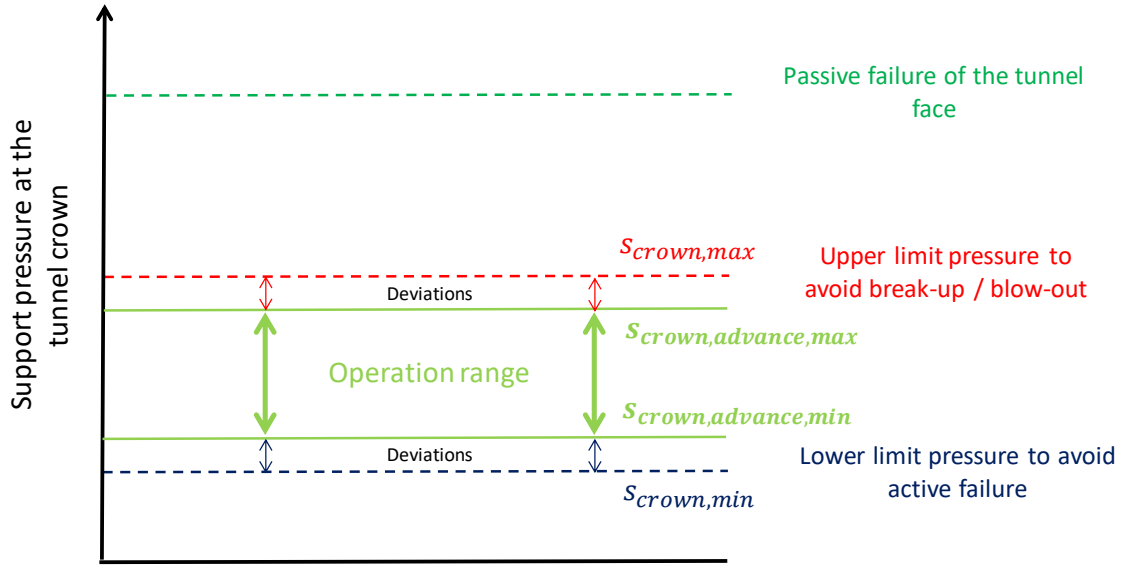

Figure 2-8: Allowable operational pressures at the tunnel crown of a shield machine (Zizka & Thewes, 2016)

should be used for the lower limit and the minimal unit weight for the upper limit. ZTV-ING (2012) additionally prescribes, in the case of compressed-air support, that the support pressure at the lowest point of air contact with the tunnel face must have a minimal safety factor of η = 1.05 compared to the local groundwater pressure.

ZTV-ING (2012) further defines for slurry face support that the efficiency of the slurry support mechanism and the local stability have to be investigated according to DIN 4126. To obtain the local stability, a certain minimal yield point of slurry depending on the characteristic grain size of the soil has to be achieved (section 2.3). To calculate the required pressure for the global stability according to DIN 4126 (2013), while considering the efficiency of the transfer, the required support force due to earth pressure ($E_{max,ci}$) has to be additionally divided by factor η_2 (Table 2-1) depending on the achieved stagnation gradient of slurry. The term stagnation gradient of slurry is

Table 2-1: Coefficient defining the efficiency of the pressure transfer mechanism, Stagnation gradients is explained in detail in section 3.4.1

Stagnation gradient	Pressure transfer coefficient
f_{s0} [kN/m³]	η_2 [-]
higher than 200	1
200 - 100	0.85
100 - 50	0.8
smaller than 50	0.7

extensively discussed in section 3.4.1. Table 2-1 was originally developed for diaphragm walls and considers certain simplification applicable only for diaphragm walls. An update for of Table 2-1 for the purposes of mechanized tunnelling is suggested in chapter 9.

The optimal support pressure for the excavation is located somewhere between the maximal and minimal limit in Figure 2-8. The design of optimal support pressure involves operational considerations, as an unnecessarily high support pressure is detrimental to the excavation progress. Furthermore, it results in issues regarding work safety during compressed air interventions. It may be the case that a higher support pressure does not automatically mean more safety for the excavation due to possible resulting break-ups of the overburden or blow-outs of the support medium. On the other hand, a face pressure above the minimum required level may contribute to a reduction of settlement.

2.6 Practice oriented calculation of minimal support pressure in non-cohesive soils using Horn's failure mechanism

As pointed out in chapter 2.5, the Horn´s failure mechanism (Figure 2-9) is typically used in Germany for calculation of the support force component due to earth pressure. The advantages of using this method are discussed in section 2.4.3. The calculation of the minimal support pressure employing the Horn´s failure mechanism will be presented in this chapter. The method considers effective shear parameters of soils. Therefore, it is particularly suitable for non-cohesive soils.

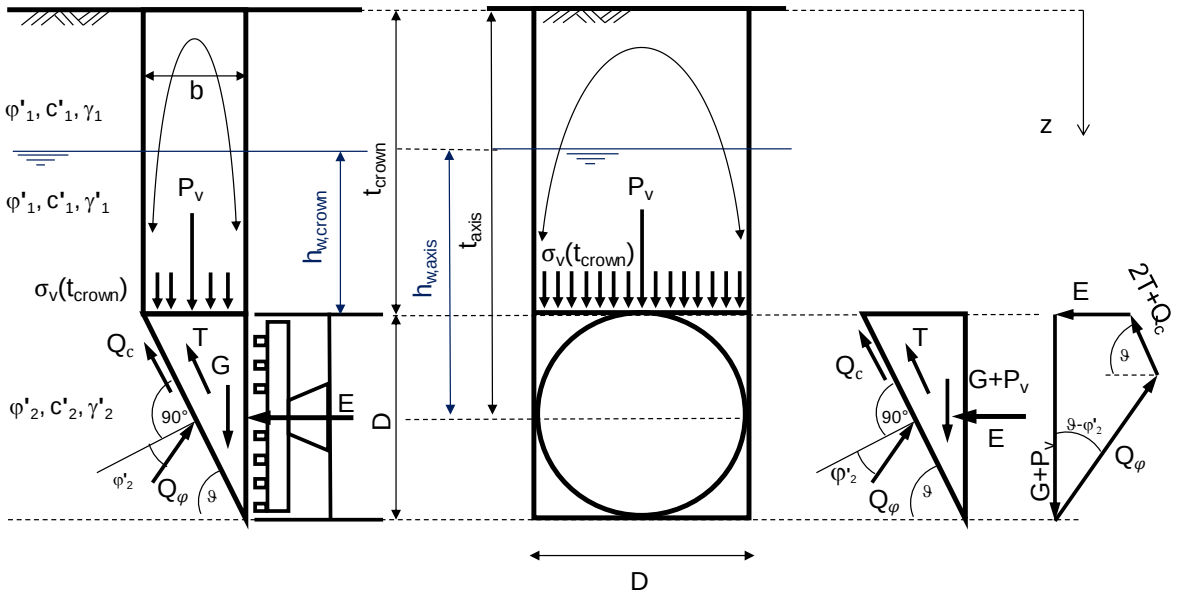

Figure 2-9: Forces acting on the wedge and prism (Zizka & Thewes, 2016)

The method based on Horn´s failure mechanism offers two options for geometrically approximating the tunnel face. The circular tunnel face can be modelled with a square whose edge length is equal to the shield diameter (Jancsecz & Steiner, 1994), as a first option. The second option is to approximate the circular tunnel face with a square of the same cross-sectional area as the circular tunnel face (Anagnostou & Kovári, 1994). Thereby, the front plane of the sliding wedge is defined (Figure 2-9). For simplicity, the formula adopting the edge length to be equal to the diameter will be followed in the upcoming equations.

Once the sliding wedge is assumed, the forces acting on it can be determined (including the support force). The forces must be in a limit equilibrium, meaning that the bearing capacity of the wedge is just fully mobilized. The support force and the mobilized soil shear resistance act as stabilizing forces, while the wedge's own weight and weight of

the overlaying prism cause destabilizing forces. The equilibrium conditions are formulated on the inclined sliding surface (Figure 2-9) in perpendicular and in parallel direction.

By summing two equilibrium conditions, the required support force can be calculated by $Eq.\,2\text{-}5$. The summarized equilibrium condition is expressed dependent on the sliding angle of the wedge (ϑ) as its critical value is not yet known.

$$\boldsymbol{E_{re}(\vartheta) = \frac{(G + P_V) \cdot (sin(\vartheta) - cos(\vartheta) \cdot tan(\varphi'_2)) - 2 \cdot T - c'_2 \cdot \frac{D^2}{sin(\vartheta)}}{sin(\vartheta) \cdot tan(\varphi'_2) + cos(\vartheta)}} \qquad Eq.\,2\text{-}5$$

With

E_{re}	Support force due to the earth pressure [kN]
G	Own weight of wedge [kN]
P_v	Vertical load from the soil prism [kN]
T	Shear force on the vertical slip surface [kN]
ϑ	Sliding angle [°]
φ'_2	Friction angle of soil [°]
c'_2	cohesion of the soil [kPa]
D	Shield diameter [m]
Q	Shear force on inclined surface [kN]

Subsequently, the critical sliding angle (ϑ_{crit}) of the wedge which requires the highest support force ($E_{max,re}$) must be found. Thus, the support force is maximized by varying the sliding angle (Figure 2-10). From this point onward, the determination of variables for $Eq.\,2\text{-}5$ is shown. Assumptions used to determine particular forces vary among

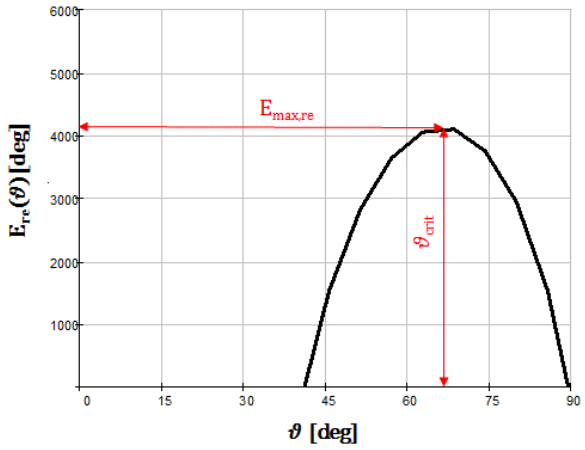

Figure 2-10: Example of the determination of the highest required support force (Emax,re) by variation of the sliding angle (ϑ) (Zizka & Thewes, 2016)

authors. The following pages explain a variety of available options for those calculations.

Two options are available to determine the force P_v acting on the wedge by the prism's weight. P_v can be calculated by multiplying the area on top of the wedge with the vertical effective stress acting on the wedge ($Eq.$ 2-6).

$$\boldsymbol{P_v = A_{silo} \cdot \sigma_v(t_{crown}) = D \cdot \frac{D}{\tan \vartheta_{crit}} \cdot \sigma_v(t_{crown})} \qquad Eq.\ 2\text{-}6$$

with

P_v	Vertical load force from the soil prism on the wedge [kN]
$\sigma_v(t_{crown})$	Vertical surcharge from the prism on the wedge [kPa]
A_{silo}	Cross-sectional area of the silo / of the top of the wedge [m²]

The stress is calculated considering the full weight of the overburden ($Eq.$ 2-7) or accounting for a soil arch above the wedge according to Janssen's silo theory (1895) that leads to a decrease in vertical stress ($Eq.$ 2-8). The criterion used to select between the two approaches is defined by the overburden height. If the overburden height is lower than twice the tunnel diameter, the full weight of the overburden is applied. Janssen´s silo theory may be adopted if the overburden is higher. However, Anagnostou & Kovári (1994) suggest always using Janssen´s equation. The coefficients of the lateral earth pressure at the lateral planes of the silo vary significantly among different authors (Table 2-1). Schmüdderich et al. (2017) performed finite element verification of these coefficients. It turned out that for a deep tunnel, the coefficient should be higher than active earth pressure. So the assumption of K_1 as active earth pressure is safe.

$$\boldsymbol{\sigma_v(z) = \gamma_{1,av} \cdot z + \sigma_s \; for \; t_{crown} \leq 2 \cdot D} \qquad Eq.\ 2\text{-}7$$

with

$\sigma_v(z)$	Vertical stress at the elevation *z* [kPa]
$\gamma_{1,av}$	Average soil unit weight in the overburden area [kN/m³]
z	Vertical coordinate starting from the terrain surface [m]
t_{crown}	Overburden height [m]
σ_s	Surcharge on the surface (traffic load) [kPa]

$$\sigma_v(z) = \frac{\frac{A}{U} \cdot \gamma_{1,av} - c'_1}{K_1 \cdot \tan(\varphi'_1)} \cdot \left(1 - e^{-\frac{U}{A} \cdot K_1 \cdot z \cdot \tan(\varphi_1)}\right) + \sigma_0 \cdot e^{-\frac{U}{A} \cdot K_1 \cdot z \cdot \tan(\varphi'_1)} \quad for\ t_{crown} > 2 \cdot D \qquad Eq.\ 2\text{-}8$$

with

A	Cross-sectional area of the silo / of the top of the wedge [m²]
U	Circumference length of the silo [m]
K_1	Coefficient of lateral earth pressure within the silo (see Table 2-1) [-]

The force G, which describes the wedge's own weight, is defined by $Eq.\ 2\text{-}9$.

$$G = \frac{1}{2} \cdot \frac{D^3}{\tan(\vartheta_{crit})} \cdot \gamma_{2,av} \qquad Eq.\ 2\text{-}9$$

with

G	Own weight of the wedge [kN]
D	Tunnel diameter [m]
$\gamma_{2,av}$	Average soil unit weight in the tunnel face area [kN/m³]

The most contentious point in the limit equilibrium calculation approach is the determination of the shear resistance force on the vertical triangular planes of the wedge. The shear resistance force consists of two components, the friction force and the cohesion force ($Eq.\ 2\text{-}10$).

Table 2-2: Suggested coefficients of the lateral pressure in the silo area (Zizka & Thewes, 2016)

Author	Assumed coefficient of the lateral earth pressure
Terzaghi & Jelinek (1954)	$K_1 = 1.0$
Melix (1987)	$K_1 = 0.8$
Anagnostou & Kovári (1994)	$K_1 = 0.8$
Jancsecz & Steiner (1994)	$K_1 = k_a = \left(\tan\left(45 - \frac{\varphi'_1}{2}\right)\right)^2$
Mayer, Hartwig, Schwab (2003)	$K_1 = 1.0$ if $t_{crown} \leq 5 \cdot d$
Kirsch & Kolymbas (2005)	$K_1 = k_0 = 1 - \sin(\varphi'_1)$
Girmscheid (2008)	$k_a < K_1 < k_p$, $K_1 = 1$ recommended

$$\boldsymbol{T = T_R + T_c} \qquad Eq.\,2\text{-}10$$

with

T	Shear resistance force on the vertical triangular plane of the wedge [kN]
T_R	Shear resistance force due to friction [kN], alternatively $T_{R,1}$ or $T_{R,2}$ see $Eq.\,2\text{-}12$ and $Eq.\,2\text{-}13$
T_c	Shear resistance force due to cohesion [kN]

On one hand, a relative agreement exists about the formulation of the cohesion component since it is independent of the lateral earth pressure acting on the wedge ($Eq.\,2\text{-}11$).

$$\boldsymbol{T_C = \frac{c_2' \cdot D^2}{2 \cdot tan(\vartheta_{crit})}} \qquad Eq.\,2\text{-}11$$

On the other hand, discrepancies are found in the formulation of the shear force component due to friction. Three assumptions must be made as discussed by Broere (2001). The assumptions include:

1) presence of soil arching effects next to the wedge
2) the distribution of the vertical effective stress next to the triangular planes of the wedge
3) the coefficient of the lateral earth pressure acting on the vertical triangular planes of the wedge

For the first assumption (1), the level of vertical stress next to the wedge is usually assumed to be the same as on the top plane of the wedge (see $Eq.\,2\text{-}7$ and $Eq.\,2\text{-}8$). There are two possibilities that exist regarding the distribution of the vertical stress next to the triangular planes of the wedge. This results in two possible equations to calculate shear friction force on the triangular plane. In the first possibility, it is assumed that the same stress is present next to the top level of the wedge as next to the vertical plane of the wedge and simultaneously, at the bottom of the wedge, a stress ($\sigma_{v,bottom}$) is present, which solely corresponds to the weight of the soil located along the vertical plane of the wedge. These assumptions are found in Girmscheid (2008), DIN 4126 (2013) and Anagnostou & Kovári (1994). The corresponding distribution of the vertical stress next to the vertical triangular slip surface can be seen

in Figure 2-11-a). The shear friction force at the triangular side of the wedge is subsequently defined by $Eq.\,2\text{-}12$.

$$\boldsymbol{T_{R,1} = tan(\varphi_2) \cdot K_2 \cdot \left(\frac{D^2 \cdot \sigma_v(t)}{3 \cdot tan(\vartheta_{crit})} + \frac{D^3 \cdot \gamma_2}{6 \cdot tan(\vartheta_{crit})} \right)} \qquad Eq.\,2\text{-}12$$

with

$\sigma_v(t)$	Vertical effective stress in tunnel crown [kPa]
K_2	Coefficient of lateral earth pressure in the wedge area (see Table 2-2) [-]

The second possibility also states that the vertical stress at the top of the wedge is also equal to the stress next to the wedge. However, in this case, the vertical stress linearly increases along the vertical plane according to the unit weight of present soil (Figure 2-11-b). This assumption is found in Kirsch & Kolymbas (2005). The shear friction force is subsequently defined by $Eq.\,2\text{-}13$.

$$\boldsymbol{T_{R,2} = tan(\varphi_2) \cdot K_2 \cdot \left(\frac{D^2 \cdot \sigma_v(t)}{2 \cdot tan(\vartheta_{crit})} + \frac{D^3 \cdot \gamma_2}{6 \cdot tan(\vartheta_{crit})} \right)} \qquad Eq.\,2\text{-}13$$

These particular assumptions for the vertical stress distribution next to the wedge are connected with the coefficients of lateral pressures at the wedge. The coefficients that are outlined in Table 2-3. Zizka & Thewes (2016) suggest to consider the K_2 as proposed by Janczecs & Steiner (1994), due to the consistency of assumptions regarding the stress redistribution during excavation.

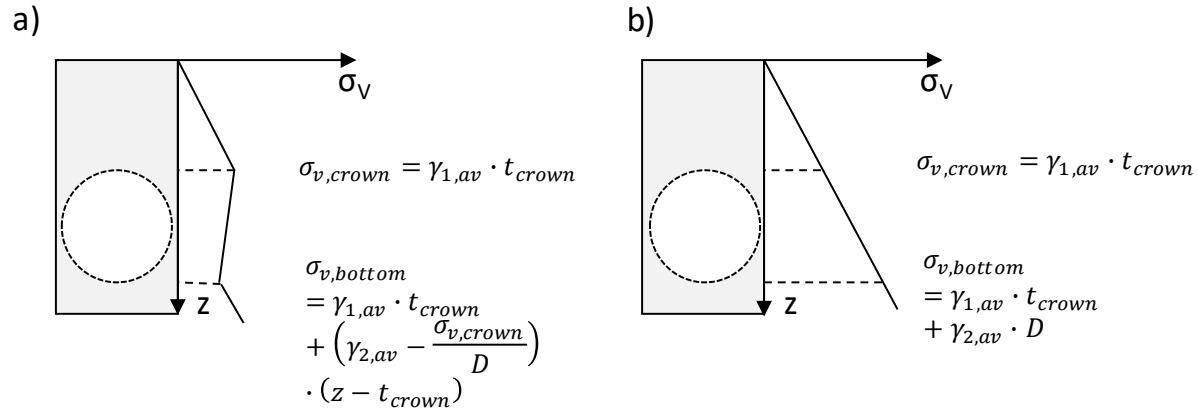

Figure 2-11: Two possible distributions of vertical stress next to vertical triangular plane of the wedge: a) Girmscheid (2008), DIN 4126 (2013) and Anagnostou & Kovari (1994) b) Kirsch & Kolymbas (2005)

In addition to the support force due to earth pressure, the support force due to groundwater pressure must also be determined. The groundwater pressure force is easily found by using $Eq.\,2\text{-}14$, assuming that there is no groundwater flow to the tunnel face.

$$\boldsymbol{W_{re} = \gamma_w \cdot \left(h_{w,crown} + \frac{D}{2}\right) D^2} \qquad Eq.\,2\text{-}14$$

with

$h_{w,crown}$	Groundwater level above the tunnel crown [m]
γ_w	Unit weight of water [kN/m^3]
D	Tunnel diameter [m]
W_{re}	Groundwater pressure force on the rectangular tunnel face area [kN]

Table 2-3: Suggested coefficients for the lateral earth pressure on the triangular vertical planes of the sliding wedge (Zizka & Thewes, 2016)

Author	Assumed coefficient of the lateral earth pressure
Anagnostou & Kovári (1994)	$K_2 = 0.4$
Jancsecz & Steiner (1994)	$K_2 = \frac{k_0 + k_a}{2}$
Mayer, Hartwig, Schwab (2003)	Shear resistance is neglected
Girmscheid (2008)	$k_a \leq K_2 \leq k_p$
Kirsch & Kolymbas (2005), DIN 4126 (2013)	$K_2 = k_0 = 1 - \sin(\varphi_2')$

Consequently, the obtained forces are recalculated from the rectangular wedge face to the circular tunnel face and summed after multiplying with the partial safety coefficients (see $Eq.\,2\text{-}3$ in section 2.5). The required support force due to earth pressure should be further adjusted based on Table 2-1. The minimal required support pressure at the tunnel crown is obtained from the force while assuming the pressure distribution according to the own weight of slurry (Krause, 1986 and Anheuser, 1987). The required minimal support pressure for the tunnel crown can be calculated based on $Eq.\,2\text{-}15$.

$$\boldsymbol{s_{crown,min} = \frac{S_{ci}}{\frac{\pi \cdot D^2}{4}} - \gamma_S \cdot \frac{D}{2}} \qquad Eq.\,2\text{-}15$$

with

γ_S	Unit weight of the support medium [kN/m^3]
$s_{crown,min}$	Support pressure in the tunnel crown [kPa]

2.7 Conclusions about face stability assessment of slurry shield driven tunnels

Slurry shield excavation technology has been successfully applied for many years. It was shown in this chapter that various methods were developed in the past to assess the face stability for both local and global failure modes. The calculation methods for minimal face support pressure were successfully verified by experimental investigation. For the typical application range of slurry shields (drained ground conditions), the calculation process of the minimal support pressure is formalized in ZTV-ING (2012), including recommended safety factors. ZTV-ING (2012) implicitly suggests to use a limit equilibrium method to determine the acting earth pressure at the tunnel face. The application of these relatively simple methods is beneficial due to their transparency, calculation time and objectives of the face stability calculation within mechanized tunnelling. It is worth mentioning that no general stability problems with slurry supported face were reported in practice.

However, when assessing the required minimal face pressure in practice, a significant theoretical shortcoming occurs. The shortcoming can be seen in the very common assumption that the full amount of slurry pressure is efficiently transferred at the tunnel face to counter the water and earth pressure. The assumption regarding the countering of earth pressure is based on a simplified check which defines the minimum required yield point of slurry that results in certain stagnation gradient for the particular ground condition. The simplified check directly investigates the local stability and pressure transfer efficiency (DIN 4126), while adopting principles from diaphragm wall technology.

Hence, the practice-oriented approach determines the minimal support pressure without thorough analysis if the support pressure acts efficiently depending on excavation conditions.

3. SLURRY-SOIL INTERACTION AND THE SLURRY PRESSURE TRANSFER

The importance of slurry pressure transfer in slurry shield tunnelling has already been highlighted by Babendererde (1991). As shown in the previous chapter, practice does not generally place much emphasis on this topic. Babendererde (1991) claimed that the efficiency of slurry face support depends on effectively transferred constant pressure from the support medium to the surface of the tunnel face. Accordingly, the support pressure transfer can be described as a transformation of the hydraulic stress of the slurry into effective stress in the soil skeleton. However, only part of the slurry pressure is subjected to this transformation. When a certain slurry pressure is set up in the working chamber of the machine, it automatically splits up into two components. The first component is equal to the hydrostatic groundwater pressure at a particular point on the tunnel face. The second component, usually called support excess or slurry excess pressure, is defined by $Eq.\ 3\text{-}1$. The second component is the most important for consideration in the pressure transfer analysis, because its success in being transformed efficiently into effective stress in the soil is not always guaranteed. The efficiently transferred pressure counters the earth pressure and avoids tunnel face failure.

$$\Delta \boldsymbol{s_{crown}} = \boldsymbol{s_{crown}} - \boldsymbol{u_{crown}} \qquad Eq.\ 3\text{-}1$$

with

Δs_{crown}	Support (slurry) excess pressure [kPa]
w_{crown}	Hydrostatic water pressure in the tunnel crown [kPa]
u_{crown}	Support pressure at the tunnel crown [kPa]

Three basic elements are involved in the pressure transfer. The suspended bentonite particles, water and porous soil skeleton. Fully saturated conditions are expected in

general, because slurry shield excavations are carried out mostly under groundwater level.

This chapter is dedicated to analysing the interaction between these three components, that is to say, the transfer of slurry excess pressure. The basic properties of the interacting components are first described. The flow of suspensions through porous media can be observed on different scales. Philip & Smiles (1982) defined three possible scales. These scales are the molecular scale, the microscopic or Navier-Stokes scale and the macroscopic or Darcy scale. The molecular scale is not considered in this thesis.

Following this, the strategies for description of flow in soils will be explained with the background of porous media theory. Using these theories, the soil-slurry interaction might be considered as bulk flow (Darcy scale). In contrast, the slurry soil interaction can be observed also on the particle level (microscopic scale). Thus, theoretically possible cases of slurry-soil interaction will be analysed. Finally, the theories developed to calculate the transfer of excess slurry pressure on Darcy´s scale for the purposes of geotechnical engineering will be reviewed. The theories will be compared with the basic theoretical interaction cases at the bulk and particle level.

3.1 Basic properties of interacting materials

In this section, the basic properties of materials involved in slurry soil-interaction will be characterized. Fundamental methods for description of their properties used later in this thesis will be also described.

3.1.1 Definition of non-cohesive soils

Soil is a natural aggregate consisting of mineral grains which can be easily separated (Terzaghi et al., 1996). Unlike in rock, there is no bonding between the minerals in soil grains. These grains are also called the solid phase or skeleton (Prinz & Strauss, 2011). Voids (pores) are located between the grains.

Cohesive and non-cohesive soils are distinguished in DIN 1054 (2006) based on their grain size and plasticity. Coarse grained soils, represented by gravels and sands, are automatically considered as non-cohesive (Table 3-1). The mixed soils are sands and gravels with fraction of fines. They are only considered as non-cohesive soils if the fraction of fines does not have any influence on the soil´s behavior, that is, if the soils are without plastic behavior. Terzaghi et al. (1996) defines the grain size of fines to be smaller than 0.074 mm (conversion from American units). The main objective of this thesis are non-cohesive soils as the main application field of slurry shields.

Figure 3-1: Shapes of soil grains – a) spherical b) flat c) needle-shaped d) rounded e) edged f) sharp-edged (Enzmann, 2000)

Soils may have grains of various shapes and roughness (Figure 3-1). In general, grains of non-cohesive soils are spherical and prismatic (Boley, 2012). This allows their reasonable approximation with sphere in packed bed theories (section 3.2.2) to describe the hydraulic processes in soils.

The hydraulic properties of soils will be discussed in chapter 3.2 on the background of porous media theory. The discussion of mechanical properties of soil including the principle of effective stresses is omitted in this thesis and can be referenced for instance in Terzaghi et al. (1946) or in Mitchell & Soga (2005).

Table 3-1: Soil classification based on grain size

Grain size	Clay	Silt	Sand	Gravel
From [mm]	0	0.002	0.063	2
To [mm]	0.002	0.063	2	63

3.1.2 Basic properties of bentonite slurries

Bentonite slurry (suspension) is a liquid which consists of bentonite particles dispersed in water. As already pointed out in section 2.1.2, the bentonite particles consist of 60 – 80 % montmorillonite mineral. Montmorillonite belongs to a group of three-layer-minerals called smectites. Natural bentonite is characterized into different types based on the presence of sodium or calcium cations in the crystal structure. Natural

bentonites are often artificially processed before delivery to construction site. The typical treatment is the activation of calcium bentonite or the addition of polymers (Praetorius & Schoesser, 2016). Grain density of bentonite is approx. 2.65 g/cm^3 (Product sheet of bentonite B1 – see appendix).

The most characteristic property of bentonite is its high swelling capacity, which results in an ability to bind water in large quantities. Triantafyllidis (2004) reports that the water adsorption ability of bentonite particles also determines the rheological properties of bentonite suspensions, e.g. yield point. Usually, the decisive amount of swelling is completed after 10 hours for typical bentonite slurries (Weiss, 1967). After this time, any ongoing swelling no longer considerably affects the yield point. Wu (1990) mentions that the physical behavior of fluids with a yield point is explained by an internal structure in three dimensions, which needs to be destructed before enabling the movement of the fluid. In literature, two possible views on bentonite suspensions (slurries) are suggested. The first assumes slurry as a suspension of solid particles and a Newtonian fluid, which is water. This approach is used often in chemistry and is comparably advantageous for the evaluation of the interaction of slurry and porous media (e.g. soil) on a microscopic scale. It enables the formulation of all forces that are acting on the particle as well as the assessment of the forces with dominant impact based on grain size of suspended bentonite particles (Herzig, 1970). The grain size distribution of suspended particles in fresh slurry can be seen in Figure 3-2 for reference. However, a loaded slurry from a construction site, which was

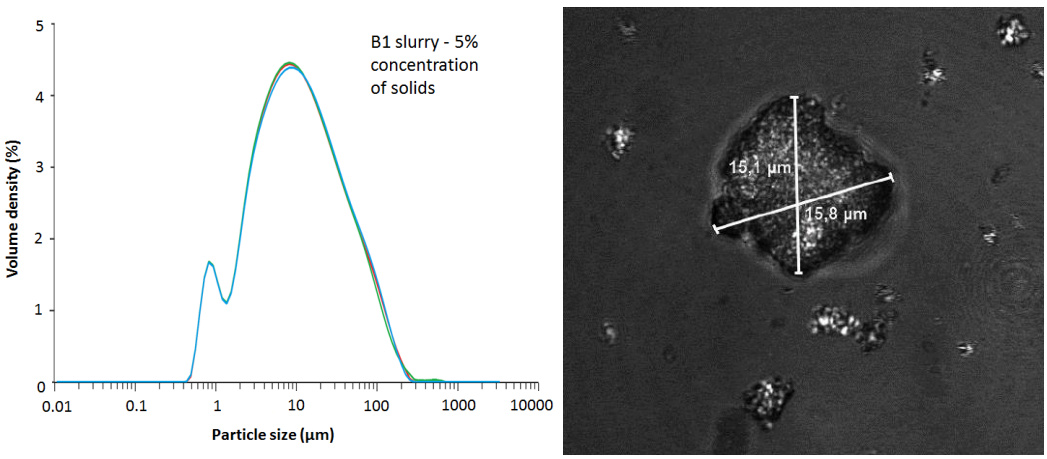

Figure 3-2: Left – Particle size distribution of suspended bentonite particles in B1 - 5% fresh slurry (Malvern report, 2017) determined by the technique of laser diffraction Right - Bentonite particle form B2 - 15% fresh slurry diluted in ratio 1:100 under Lasermicroscope Leica TCS SP8 (Herpers, 2015)

previously cleaned by the second hydrocyclone stage may have a different grain size. Grain distribution curves characterized by D_{50} from 10 µm to 50 µm are reported in literature (Pulsfort & Thienert, 2013).

The second approach considers slurry as homogeneous (bulk flow), but unlike the first approach, it acts as a non-Newtonian fluid. This approach is typical in slurry shield tunneling, diaphragm wall technology and the oil & gas drilling industry. The approach can be also reasonably used for soil-slurry interaction assessment on a macroscopic level. This approach will be employed later within this thesis for characterization and monitoring of slurry properties in experiments (chapters 6 and 7). Therefore, greater attention will be given to the review of particular properties and their determination in lab conditions or on a construction site.

As can be expected, these two points of view differ in variables describing the slurry properties. If the first approach micro level characterization is adopted, the following properties of slurry have to be determined (Herzig et al., 1970):

- Particle diameter
- Particle shape
- Particle size distribution
- Particle concentration in fluid
- Bed porosity
- Diameter of bed pores
- Newtonian properties of the carrier medium (water)

a) b)

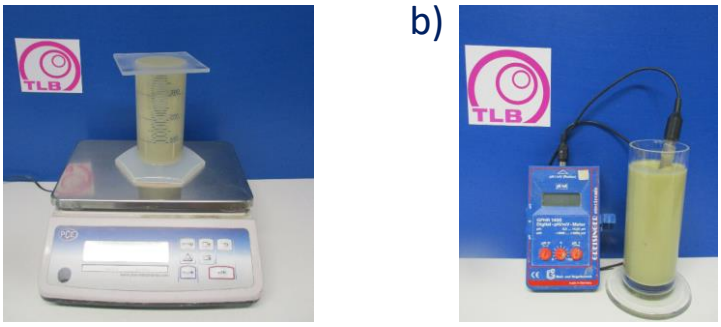

Figure 3-3: Devices required for the determination of physical properties of slurry a) density b) pH, electrical conductivity, temperature

To determine the outlined properties, advanced laboratory devices are usually required, such as laser diffraction analysis, to determine particle size distribution in slurry. These types of characterizations will not be further reviewed here. If the second approach considering slurry as a homogenous fluid is adopted, the physical and rheological properties of slurry need to be determined (Triantafyllidis 2004). Slurry density, pH, electrical conductivity and temperature typically belong to the basic physical properties. Praetorius & Schoesser (2016) note that these properties should also be investigated for the water used for slurry mixing. The devices for measuring the main physical properties of slurry are shown in Figure 3-3. It is important to note that the physical properties can be directly measured, while the rheological parameters can be usually only determined when a rheological model or shear profile is previously adopted.

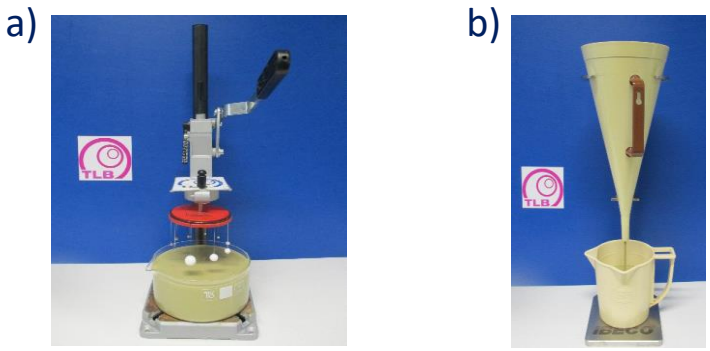

Figure 3-4: Representants of simple devices used for the determination of rheological properties of slurry a) ball harp b) Marsh funnel

Devices for measuring rheological properties may be divided into two groups. The first group includes simple devices, usually located at construction sites. The handling of the devices is formalized in codes DIN 4127 (2014) or API 13B (2014). The devices correlate a measured parameter with a rheological variable from a table or diagram provided in the respective code. On this basis, the ball harp device correlates the number of spheres sunken in slurry during the test with the static yield point of slurry under consideration of a slurry´s density. The particular sphere is characterized by its volume and density (Figure 3-4-a). The table for correlation was developed based on $Eq.\,3\text{-}2$ and is included in DIN 4127 (2014).

$$\boldsymbol{\tau_{f,s} = 0.15 \cdot D_{sp} \cdot (\gamma_{sp} - \gamma_F)} \qquad Eq.\,3\text{-}2$$

with

$\tau_{f,s}$	Static yield point of slurry [Pa]
D_{sp}	Diameter of the sphere [mm]
γ_{sp}	Unit weight of the sphere [kN/m^3]
γ_F	Unit weight of slurry [kN/m^3]

$Eq.\,3\text{-}2$ includes an assumption of a rheological model. This assumption is that the sinking behavior of a sphere into slurry is exclusively governed by the static yield point of that slurry. It is assumed that the sinking process is slow with very low shear rate, so that the obtained yield point can be considered without any viscosity influence. A similar approach is utilized for the pendulum device as defined by DIN 4127 (2014), which accommodates a sphere fixed at the end of a wire. Deflection angle of the pendulum is subsequently correlated with the static yield point of slurry using the same rheological model as the ball harp ($Eq.\,3\text{-}2$). The static yield point determined by these devices was in the past designated as gel strength of slurry (Simons & Ruppert, 1982).

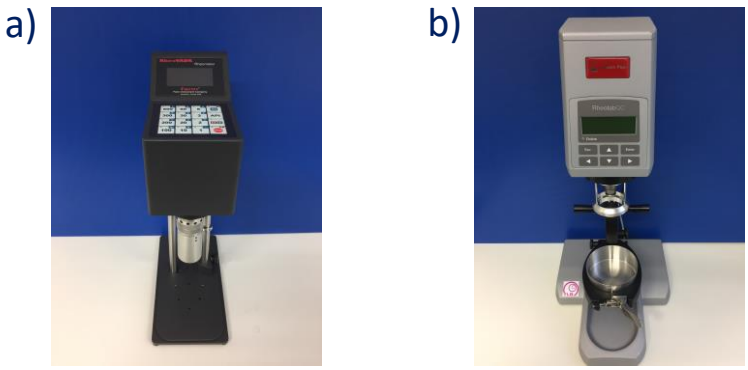

Figure 3-5: a) Standardised direct indicating viscometer after API 13b b) General viscometer

While the ball harp and pendulum device are used to investigate static properties of slurry, the Marsh funnel (Figure 3-4-b) focuses on rheological slurry properties during flow. The Marsh funnel was originally referred to as a funnel viscometer by Marsh (1931). He stated that this device may be used only for comparative measurements of dynamic viscosities. The comparison can be done acc. to Marsh (1931) with water or other fluids, only if their rheological properties have been determined by another viscometer, e.g. by the type developed by Bingham (1911) as Marsh (1931) suggests. In DIN 4127 (2014), however, a procedure for obtaining the absolute dynamic yield point and the dynamic viscosity by Marsh funnel is described. These properties are determined based on the correlation of the timespan required for the outflow of 1.0 and 1.5 liter of slurry from the funnel. The code DIN 4127 (2014) offers a diagram and $Eq.\,3\text{-}3$ for this purposes (note that the number 1000 represents

a shear rate with units s^{-1}). The origin of the diagram, including the adopted rheological model, is not clear to the author of this thesis and thus not explained here. DIN 4127 (2014) only shows the comparison of the dynamic yield point to the previously introduced static yield point by a diagram (Figure 3-6) visualizing the viscous behavior of slurry. In chapters 6 and 7 of this thesis, the Marsh funnel measurement is used only for monitoring the consistency of the properties of used slurries.

$$\boldsymbol{\mu_{dyn,s} = \frac{\tau_{1000} - \tau_{f,dyn}}{1000}} \qquad Eq.\,3\text{-}3$$

With

$\mu_{dyn,s}$	Dynamic viscosity [Pa.s]
τ_{1000}	Shear stress reading from the diagram in DIN 4127 [Pa]
$\tau_{f,dyn}$	Dynamic yield point [Pa]

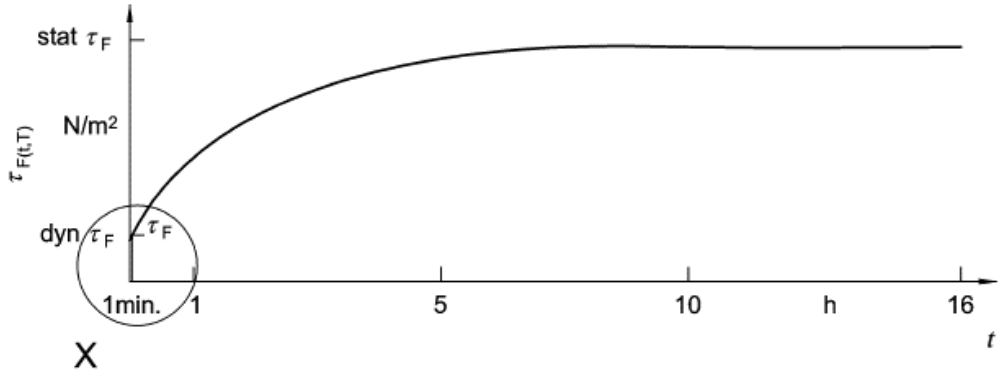

Figure 3-6: Static and dynamic yield point after DIN 4127 (2014) in dependence on time

Ballhoff et al. (2011) recently reported an approach for determining Herschel-Bulkley parameters of a slurry by Marsh funnel. The approach was further studied by Schoesser & Thewes (2015). In contrast, Longchamp et al. (2005) assessed measurements by Marsh funnel as hardly representative of slurry characterization.

The second group of devices for the investigation of the rheological properties of slurry are called viscometers. Bingham (1911) developed one of the first viscometers for determining the rheological properties of clay suspensions. Nowadays, rotational viscometers are mostly used. API 13b (2014) defines the requirements for a standardized direct-indicating viscometer to be employed in the petroleum industry (Figure 3-5-a) and also for operation of the device. The fluid is placed in a gap between two cylinders. The inner cylinder rotates, while the outer cylinder remains static, so

that a certain shear rate, which depends on the rotational velocity of the inner cylinder, is induced in the gap between them. The shear stress is consequently measured for defined shear rates. The following shear profile is required for the determining the viscosities and yield point:

1. Rotation at 1100 RPM
2. Rotation at 600 RPM
3. Rotation at 300 RPM

The first rotation speed is used for destroying the thixotropic structure in the slurry, whereas the shear stresses are logged for the other two rotation speeds (Praetorius & Schoesser, 2016). The shear stresses read from the standardized device are input into the equations $Eq.\,3\text{-}4$, $Eq.\,3\text{-}5$ and $\mathrm{Eq.}\,3\text{-}6$ to calculate the plastic and apparent viscosity, and the Bingham yield point (see API 13b). The units are not perfectly matching in these equations. The numbers 300 and 2 in the equations are supposed to have unit s^{-1}. Note that the Bingham flow rule is hereby adopted and that the equations are applicable only for the standardized direct-indicating viscometer.

$$\boldsymbol{\mu_{Bing} = \frac{\tau_{600} - \tau_{300}}{300}} \qquad Eq.\,3\text{-}4$$

with

τ_{600} Shear stress reading from the viscometer at RPM 600 [Pa]
τ_{300} Shear stress reading from the viscometer at RPM 300 [Pa]
μ_{Bing} Bingham (Plastic) viscosity [Pa.s]

$$\boldsymbol{\tau_{y,B} = \tau_{300} - 300 \cdot \mu_{Bing}} \qquad Eq.\,3\text{-}5$$

with

$\tau_{y,B}$ Bingham yield point [Pa]

$$\boldsymbol{\mu_a = \frac{\tau_{600}}{2}} \qquad \mathrm{Eq.}\,3\text{-}6$$

with

μ_a Apparent viscosity [Pa.s]

In addition to the standardized direct-reading viscometer, a fully variable direct-reading viscometer is also available on the market (Figure 3-5-b). With the help of the

fully variable viscometer, an entire flow curve of slurry at variable shear rates can be determined without previously adopting any flow rule. However, an introduction of a measuring constant may be required to obtain comparable results with the standardized viscometer acc. to API 13b (2014).

The entire flow curve is also called a consistency curve (Luckham & Rossi, 1999). The flow curve is first obtained from the fully variable viscometer and one of the flow rules (explained below) is adopted and the rheological parameters are found using the curve fitting approach to the measured curve (Schoesser & Thewes, 2015). In general, there are four basic flow rules. These are Newtonian, pseudoplastic (Herschel-Bulkley), Bingham plastic, and dilatant (Figure 3-7). Herschel-Bulkley and Bingham plastic flow rules are mostly utilized for bentonite suspension. Dilatant and Newtonian flow rules are provided here for comparison.

Newtonian flow is typical for ideally viscous fluids, such as water. The Bingham plastic flow rule applies to a fluid requiring a particular shear stress to start the flow. This stress is called the yield point of the fluid. After exceeding the yield point, the shear stress change starts to be linearly dependent on shear rate change ($Eq.$ 3-7).

$$\boldsymbol{\tau = \tau_{y,B} + \mu_{Bing} \cdot \dot{\gamma}} \qquad Eq.\ 3\text{-}7$$

with

$\tau_{y,B}$	Bingham yield point [Pa]
μ_{Bing}	Bingham (Plastic) viscosity [Pa.s]
$\dot{\gamma}$	Shear rate [1/s]

In comparison to the Bingham flow rule, the Herschel-Bulkley flow rule is more adaptable in accurately approximating the measured flow curve of slurry. This is due to the parameter *p*, which describes the plastic thinning of slurry at higher shear rates ($Eq.$ 3-8). In other words, the parameter *p* can describe the shear rate-dependent viscosity of the fluid. The introduction of the parameter *p* also enables during curve

fitting for small shear rates to achieve lower yield point of slurry (Schoesser & Thewes, 2015).

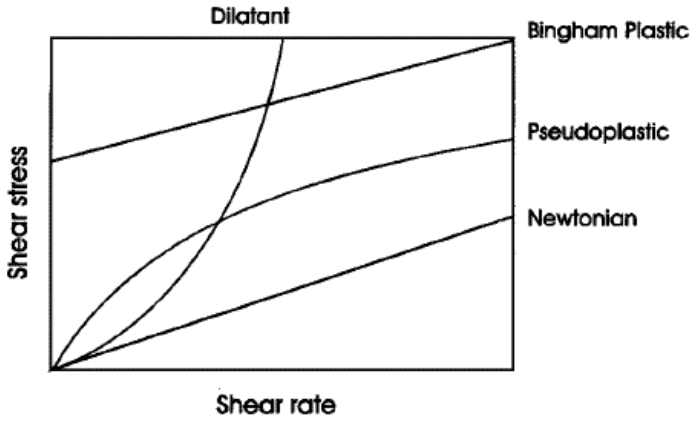

Figure 3-7: Basic consistency curves for different type of flow – Newtonian, pseudoplastic, Bingham plastic, dilatant (Luckham & Rossi, 1999)

$$\boldsymbol{\tau = \tau_{y,HB} + \mu_{HB} \cdot \dot{\gamma}^{p}} \qquad Eq.\,3\text{-}8$$

with

$\tau_{y,HB}$	Herschel-Bulkley yield point [Pa]
μ_{HB}	Herschel-Bulkley Viscosity [Pa.s]
p	Parameter describing shear thinning [-]
$\dot{\gamma}$	Shear rate [1/s]

When reviewing the flow rules, it is necessary to point out that the yield point of a single slurry determined from the curve fitting of a flow curve will be different for the Herschel-Bulkley and the Bingham flow rules. Moreover, the difference in parameters occurring within the Bingham flow rule may be due to the use of either a direct-reading viscometer at defined shear rates or a variable reading viscometer, and the consequential general flow curve approximated by curve fitting. Therefore, it is always necessary to specify the flow rule used to find slurry properties and the method based on which the parameters were determined. In the case of the yield point, the differences may be very significant. Therefore, many researchers state that the yield point of slurry as a material characteristic does not even exist. The determination of rheological properties of slurries is further complicated by the fact that they are time-dependent (Luckham & Rossi, 1999). This behaviour of slurries is referred to in literature as thixotropy, as viscoelasticity or as work softening (Sochi, 2007). When the slurry is in static conditions without flow ($\dot{\gamma}$= 0), the yield point and the viscosity increase with time to a certain value. This can also be seen as a sign that the suspension

is stiffening. Shortly after the flow, a reduced value of the yield point and viscosity is measured. The process is reversible and it is believed that thixotropy is caused by forces of attraction and repulsion between the bentonite particles (Triantafyllidis, 2004).

Attempts to simplify the modelling of rheological properties of Non-Newtonian fluids with a single constant have been reported in literature. A common approach is to find a suitable definition for the effective viscosity for the particular flow process, which will continue to have the dimensions and physical significance of Newtonian viscosity (Sochi, 2010). Nevertheless, the geotechnical engineering field tends to use yield point of slurry as a single variable for characterization of slurry flow in soil as will be shown in section 3.4.

Another relevant testing device used for slurry characterization is the filter press, according to the DIN 4127 (2014) and API 13b (2014) standards. During this test, the slurry is pressurized to 7 bar and the volume of filtrate outflow through filter paper is measured for 7.5 minutes. The volume of filtrate characterizes the stability of slurry. After opening the device, the thickness of the filter cake settled on the paper can also be measured for characterization. Other researchers have employed the filter press to investigate the consolidation behaviour of slurry (section 3.4.2) and to determine its consolidation coefficient (Talmon et al., 2013).

3.2 Characterization of flow processes in soil by the theory of porous media

The aim of this section is to obtain theoretical framework for characterization of flow in soil and later to choose a characterization method, which suits to the objectives of this thesis.

The theory of porous media plays an important role in soil mechanics especially for describing the interaction between the soil skeleton and the liquid filling its pores (de Boer, 1998). The theory is also used in the characterization of flow within a porous medium (Sochi, 2010). Hence, it is also suitable for describing the slurry-soil interaction. Bear (1988) summarized the requirements for a soil to be considered a porous medium:

- Heterogeneous or multiphase matter consisting of a solid matrix and pore space

- Specific surface of the solid matrix is relatively high and the various openings comprising the void space are relatively narrow
- At least some pores between solids are interconnected and evenly distributed, so that any two points within the medium are connected by a free path

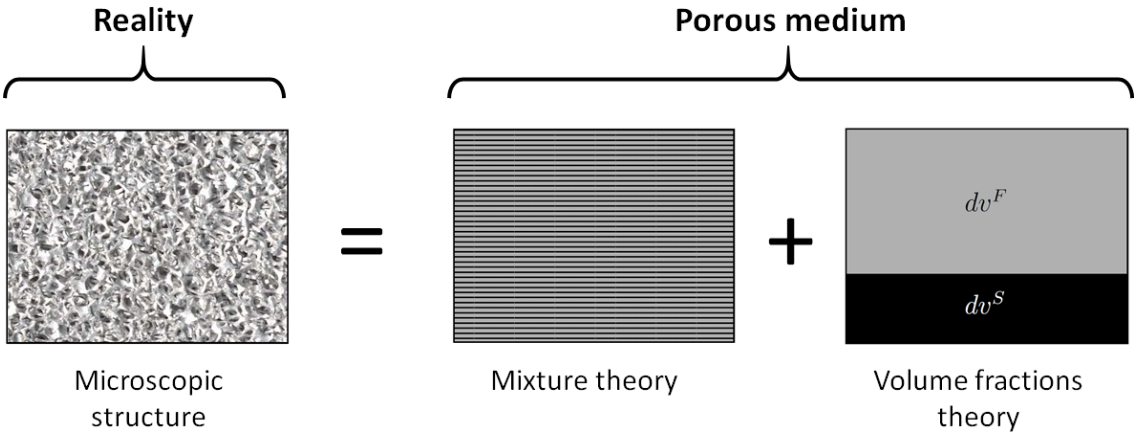

Figure 3-8: Modelling of the porous medium through homogenization of surrogate medium and the concept of volume fractions (Benke, 2003)

The porous media theory distinguishes the macroscopic and microscopic approach while describing the soil. The microscopic approach focus on the structure of single pores including their geometry and avoids using continuum-based description of the medium. However, it is still very difficult to employ the microscopic approach to characterize the porous medium and obtain reasonable results of a macroscopic physical phenomenon (Wu, 1990). Therefore, the macroscopic approach is often used in both theory and applications (Wu, 1990). The macroscopic approach follows two basic principles. These principles are the volume fraction concept and the mixture theory. The volume fraction concept involves distributing the mass of solid and the liquid space based on volume porosity numbers in the representative elementary volume (de Boer, 1998). This approach includes a fundamental assumption that the pores are statistically distributed in the representative volume and only liquids or gases can move in the pores (Figure 3-8). The concept of volume fractions neglects the exact description of pores structure and the localisation of components (Benke, 2003).

The mixture theory assumes that the individual parts of the mixture cover the entire elementary volume and are completely mixed (de Boer, 1998). The individual constituents in the continuum mixture theory have their own degrees of freedom (de Boer, 1998). In the theory of porous media, however, the solid and liquid phase are immiscible, so that the mixture theory combined with the volume fractions theory

offers the best framework for treating the fluid saturated porous media. In this way, the complexities of microscopic pore structure can be avoided by using macroscopic properties for description and characterization of the porous medium (Sochi, 2010). The macroscopic approach leads to the determination of “smeared” properties for the porous media (de Boer, 1998), for instance the porosity, intrinsic permeability (Section 3.2.1) and the macroscopic homogeneity. The macroscopic homogeneity is usually explained as the absence of local variations in macroscopic properties on a scale of representative volume. Hence, the local variations have negligible influence on the macroscopic properties (Sochi, 2010). Furthermore, it is possible to assume that the average areal porosity is equal to the volumetric porosity (Bear, 1988).

The basic aim of the flow description in porous media is to determine the pressure drop during a particular flow length. To describe the flow in porous media, the following theories have been developed (Sochi, 2010):

- Continuum approach
- Capillary bundle approach (sometimes combined with sphere pack models)
- Pore-scale network modelling (Numerical methods)

The continuum and capillary approaches are the macroscopic methods, while the pore-scale network modelling theory is a microscopic method. The microscopic approach is usually a combination of pore-scale network modelling with either the finite volume or finite difference method (Sochi, 2010). In the next two subsections, the basic approaches for describing the flow in porous media (continuum and capillary bundle approaches) will be explained. Newtonian liquid within the pores is here assumed for the sake of simplicity.

3.2.1 Continuum approach of flow characterization in porous media

In the continuum model, all details of pore structures result in bulk properties, and flow physics at the pore level are ignored. The most important model in this group is the Darcy model. Darcy´s model (law) is a basic relationship used in many disciplines for the mathematical description of flow through porous media (Pascal, 1981) and is often used in soil mechanics. Darcy reported in 1856 on the proportionality of the volume of flowing water and the loss of pressure head while performing flow tests in vertical homogeneous sand filters (Bear, 1988). As noted by de Boer (1998), in 1930, Darcy’s law was extended by Nutting for fluids with various viscosity based on

experimental investigation. Darcy´s model ($Eq.\ 3\text{-}9$) adopts continuous liquid motion through rigid porous body. It establishes a dependency of average flow velocity (*v*) on the permeability coefficient of the ground (k_f) and the hydraulic gradient (*i*). The hydraulic gradient is determined by groundwater head loss during flow (Δh) within a particular macroscopic flow distance (ΔL).

$$\boldsymbol{v = \frac{k_f}{n_p} \cdot i = \frac{k_f}{n_p} \cdot \frac{\Delta h}{\Delta L}} \qquad Eq.\ 3\text{-}9$$

with

v	Bulk flow velocity in pores [m/s]
k_f	Coefficient of permeability [m/s]
i	Hydraulic gradient [-]
Δh	Change in hydraulic head [m]
ΔL	Macroscopic flow path [m]
n_p	Porosity [-]

The permeability coefficient can be determined experimentally by measuring the discharge through a cross-sectional area ($Eq.\ 3\text{-}10$), while knowing the pressure gradient. The determination of the permeability coefficient is formalized for soils in DIN 18130-1 (1998). The code also recommends a suitable set-up for conducting the tests.

$$\boldsymbol{Q = v \cdot A; k_f = \frac{Q}{A} \cdot \frac{n_p}{i}} \qquad Eq.\ 3\text{-}10$$

with

Q	Discharge [m^3/s]
A	Cross-sectional area of the flow [m^2]
v	Bulk flow velocity in pores [m/s]
i	Hydraulic gradient [-]
k_f	Coefficient of permeability [m/s]
n_p	Porosity [-]

If the permeability coefficient (k_f) and the viscosity of fluid (μ) are known, the intrinsic permeability (*K*) can be calculated as a fluid-independent constant characterizing a porous medium – soil (Bear 1988). The intrinsic permeability ($Eq.\ 3\text{-}11$) of the medium represents the flow geometry by a square of a length scaling the porous network (Coussy, 2004).

$$\boldsymbol{K = \frac{k_f}{\rho_{fluid}} \cdot \frac{\mu}{g}} \qquad Eq.\ 3\text{-}11$$

with

K	Intrinsic permeability [m^2]
k_f	Coefficient of permeability [m/s]
μ	Dynamic viscosity of fluid [mPa.s]
ρ_{fluid}	Density of fluid [kg/m^3]
g	Gravity acceleration [m/s^2]

The application of Darcy´s law has certain limitations regarding the flow regime and fluid properties (modified from Häfner et al. 2009):

- Only stationary laminar flow can be considered, so that kinetic energy and inertial effects can be neglected (Bear, 1998). Hence, the viscous forces need to dominate (Coussy, 2004). The presence of laminar flow can be assessed based on the calculation of the Reynolds number (Re). In literature, various limits of Reynolds number for laminar flow are referenced: after Herzig et al. (1970) for Re < 10, after Coussy (2004) for Re < 100, after Bear (1988) Re < 1 – 10 (if the Re was calculated adopting an average grain diameter). The Reynolds number can be determined using *Eq.* 3-12. The equation was recommended by Herzig et al. (1970) for suspensions in porous media.
- Sliding effects between the permeating medium and the soil have to be excluded (Klinkenberg effect). Note that this effect is relevant only for gases or gas-liquid-mixtures (Coussy, 2004).
- The flow has to be controlled by the average properties of the soil, so that the size of the flow cross-section is large enough in comparison to the grain size. This assumption is basic for the porous media approach and is also included in DIN 18130-1 (1998), defining the minimal dimensions of the experimental device for soil permeability testing.
- Constant viscosity of the fluid with regard to its shear rate is required, so that the product from flow volume and viscosity remains constant.
- Chemical or physical reaction between fluid and pore structure must be excluded.
- Nearly incompressible fluid is necessary (Bear, 1988).

$$\boldsymbol{Re = \frac{v_m \cdot d_g \cdot \rho_{carrier}}{6 \cdot (1 - n_0) \cdot \mu_{carrier}}} \qquad Eq.\ 3\text{-}12$$

with

Re	Reynolds number [-]
v_m	Suspension approach velocity [m/s] v_m= v $(mean\ interstitial\ velocity) \cdot n_0$

d_g	Grain mean diameter [m]
$\rho_{carrier}$	Density of carrier fluid [kg/m³]
n_0	Initial porosity of the medium [-]
$\mu_{carrier}$	Dynamic viscosity of carrier fluid [kPa.s]

Darcy´s law, including the equations presented above, was originally developed for one-dimensional flow. Bear (1988) states that it is possible to generalize it for three-dimensional flow, as it was theoretically predicted and later also confirmed by numerous experiments.

3.2.2 Capillary bundle approach of flow characterization in porous media

The flow in pores of soil is usually assumed to be laminar and therefore a certain similarity to flow in a tube exists (Zamani & Maini, 2009). Hence, the flow in a capillary tubes can be characterized by Hagen-Poisseuille´s law (Figure 3-9). This law is considered to be the governing law for steady-state flow in all capillary bundle models for porous media (Bear, 1988). The flow through a single tube can be described with $Eq.\,3\text{-}13$ for a Newtonian fluid. From this equation, it is visible that the flow velocity is linearly dependent on pressure gradient.

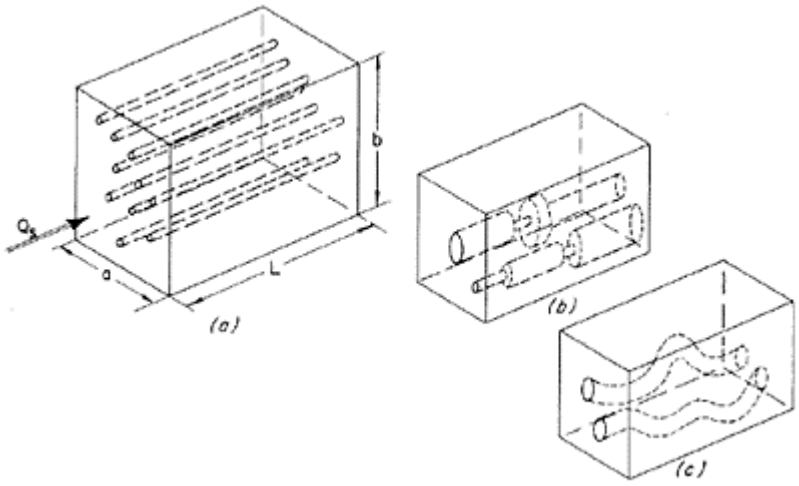

Figure 3-9: Simple capillary tube models (Bear, 1988)

$$\boldsymbol{Q_{f,tube} = \frac{\pi \cdot d_{tube}^4 \cdot \rho_{fluid} \cdot g}{128 \cdot \mu} \cdot \frac{\Delta h}{\Delta L} = v_t \cdot a_{tube}} \qquad Eq.\,3\text{-}13$$

with

$Q_{f,tube}$	Discharge from a tube [m³/s]
d_{tube}	Diameter of a tube [m]
μ	Viscosity [mPa.s]
ρ_{fluid}	Density of fluid [kg/m³]
v_t	Average velocity in tube [m/s]
a_{tube}	Cross-sectional area of tube [m²]

g Gravity acceleration [m/s^2]

The cross-sectional area of the porous medium with side lengths (a) and (b) can then be approximated with the number (N) of tubes (Figure 3-9). The tubes can be either parallel with uniform diameter or parallel with changing diameter to consider bottlenecks or tortuous tangled tubes. In the tortuous angle tubes, it is necessary that the Navier-Stokes equation is applicable (Bear, 1988). Another option is that the tubes are bowed. The specific discharge of porous medium with parallel uniform tubes can be easily characterised by $Eq.\,3\text{-}14$. From the equation, the analogy to Darcy´s law can be observed due to the formulation of the intrinsic permeability (*K*) of the porous medium (Bear, 1988). In contrast to Darcy´s law, the physics of flow is taken into account here.

$$\boldsymbol{q_s = \frac{N \cdot Q_s}{a \cdot b} = \frac{\pi \cdot d_{tube}^4 \cdot \rho_{fluid} \cdot g}{128 \cdot \mu} \cdot \frac{\Delta h}{\Delta L} = \frac{n_p \cdot d_{tube}^4}{32} \cdot \frac{\rho_{fluid} \cdot g}{\mu} \cdot \frac{\Delta h}{\Delta L}; \quad K = \frac{1}{32} n_p \cdot d_{tube}^4} \qquad Eq.\,3\text{-}14$$

with

q_s Discharge [m^3/s/m^2]
Q_s Discharge from a tube [m^3/s]
d_{tube} Diameter of a tube [m]
μ Viscosity [mPa.s]
ρ_{fluid} Density of fluid [kg/m^3]
K Intrinsic permeability [m^2]
n_p Porosity $n_p = N \cdot \pi \cdot d_{tube}^2/4$
1/32 Parameter describing the porous structure
g Gravity acceleration [m/s^2]

The formulation in $Eq.\,3\text{-}14$ for intrinsic permeability enables “parameter 1/32” to be modified for other numbers in order to describe the porous medium more accurately. Nevertheless, a serious shortcoming in the described model is that it assumes that the volumetric porosity only considers pores in the parallel direction to flow, which is not true. Hence, it is usually adapted so that only 1/3 of pores of the medium is placed parallel to the flow direction. Accordingly, the parameter 1/32 is changed to 1/96.

Kozeny proposed an approach characterizing the flow velocity of fluid through porous medium while considering its properties more accurately (Chapuis & Aubertin, 2003). He also assumed the porous medium to be a bundle of parallel tubes with equal length and derived $Eq.\,3\text{-}15$. The equation is called the “Kozeny equation” for the determination of intrinsic permeability of the porous medium. The tubes in the model

could have various cross-sections, from circular to equilateral triangular. The shape of the tube was taken into account by the constant c_0.

$$\boldsymbol{K = \frac{c_0 \cdot n_{vol}{}^3}{M^2}} \qquad Eq.\,3\text{-}15$$

with

K	Intrinsic permeability [m^2]
n_{vol}	Volumetric porosity [m]
M	Specific surface of porous material [m^{-1}], $M = A_s/V_{b,pores}$
A_s	Total interstitial surface area of pores [m^2]
$V_{b,pores}$	Unit bulk volume of pores [m^3]
c_0	Kozeny constant [-]

As referred by Chapuis & Aubertin (2003), Carman experimentally verified the Kozeny equation in 1937 and further developed it. The first development was made by introducing a hydraulic radius and reformulating the specific surface of the porous medium. The specific surface was newly formulated as a surface area of the particle in a packed bed, divided by particle´s volume. The second further development was done by introducing $c_0 = 0.20$. As noted by Bear (1988), it is possible to change the term "specific surface M_s of spheres" to $d_m = 6/M_s$. This delivers the final term for the intrinsic permeability of porous medium known as the Carman-Kozeny equation $Eq.\,3\text{-}16$). The developed equation is valid only for laminar flow.

$$\boldsymbol{K = \frac{d_m^2 \cdot n_{vol}{}^3}{180 \cdot (1 - n_{vol})^2}} \qquad Eq.\,3\text{-}16$$

with

K	Intrinsic permeability [m^2]
n_{vol}	Volumetric porosity [-]
d_m	Mean particle size – diameter of sphere [m]

The Carman-Kozeny equation delivers good results in comparison to other experiments for flow in sand, but is not suitable for flow in clays (Chapuis & Aubertin, 2003). The model is one of the most popular models used in fluid dynamics for flow in porous packed bed (Sochi, 2010). One of the reasons is that the Carman-Kozeny model for Newtonian-fluids enables better estimation of the "real" flow velocity in pores than, for instance, Darcy's model. Hence, the model is considered to be a semi-empirical relation (Sochi, 2010). It is called a semi-empirical model and is classified as a

macroscopic model because it does not consider all the complex features of the void space.

The description of the capillary bundle approach for porous media includes also a certain simplification. The simplification is highlighted in the following example formulated by Civan (2015). If a single pore is assumed to have zero flow velocity at the boundary and the maximum velocity at the pore centre, a certain flow velocity gradient must exist inside the pore. The pores, however, also include enlargements and contractions. Therefore, it is improbable for the flow velocity gradient in the pore to have the parabolic distribution as assumed in the Hagen-Poiseuille law. Nonetheless, the advantage of the model is that it is easy to combine the capillary bundle approach with various other flow rules for liquids. For instance, the Bingham or Herschel-Bulkley type liquid behaviour can be considered (Sochi, 2010).

It is worth mentioning that Lemppenau (2015) conducted an analysis of the penetration depth of bentonite slurry in soil, employing various flow rules for slurry and approximating the pore space of soil using both the Darcy and Blake-Kozeny-Carman models. The analysis saw only a limited success when compared to experimentally determined slurry penetration depths.

3.3 Fundamentals of suspension filtration and flow through porous media

The aim of this section is to introduce basic types of suspension filtration through porous media, as they are distinguished in chemistry. Following this, a particularly relevant case of filtration for slurry shield tunnelling will be discussed further. In contrast to the previous section, which considers interaction between slurry and soil to be a bulk flow, this section focuses on the filtration at the particle level.

3.3.1 General types of suspension filtrations

The goal of filtration is to separate suspended solids from their carrying liquid. The process occurs when slurry, representing the liquid, flows through soil, the filter (porous) medium. The filtration process must be induced by external forces. This external force may be pressure, gravity, or a vacuum or centrifugal force. In the case of tunnel face support, pressure induces the filtration. Hermia (1982) defined four

basic particle retention mechanisms occurring during filtration. The type of filtration mechanism that occurs depends on the comparison between the pore size of the medium and the particle size in the suspension:

- Complete blocking (Figure 3-10-a) is when every retained particle blocks a single pore of the medium, so that the pore entrances are sealed (Grenier et al., 2008).
- Intermediate blocking (Figure 3-10-b) is when a finite probability exists that the particle will block a pore. In this case only a large fraction of the suspended particles seal the entrance pores and the rest is deposited on top of them (Grenier et al., 2008).
- Cake filtration (Figure 3-10-c) is when particles are retained by a so-called cake, which grows over the course of the filtration and increases in resistance
- Standard blocking (Figure 3-10-d) is when particles are retained within the medium and thereby cause narrowing of the pores (also known as deep bed filtration)

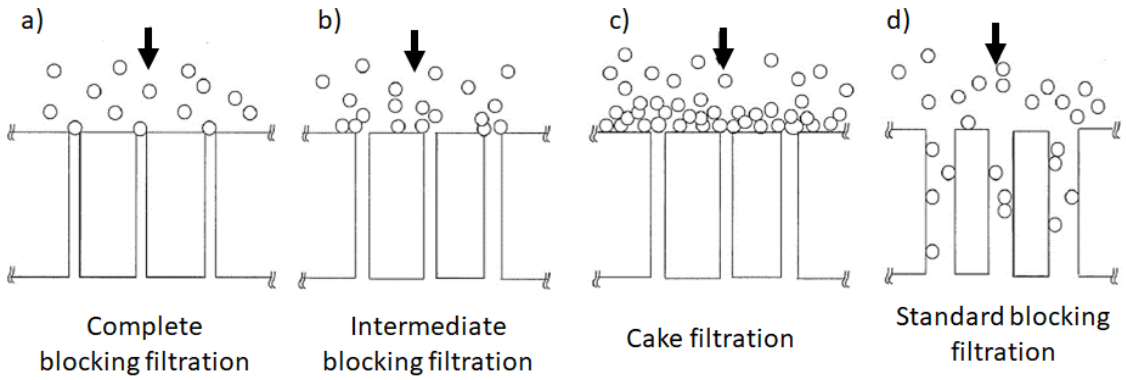

Figure 3-10: Basic filtration models (Tien & Ramarao, 2011)

Tien & Ramarao (2011) point out that deep bed filtration mechanism results from standard blocking, while intermediate or complete blocking is required to initiate the cake filtration. Hence, some authors do not distinguish “filter cake” as a separate type of filtration, but only as a result of one of the other three filtration types.

The blocking mechanisms can be shown in a simplified manner by blocking equation ($Eq.\,3\text{-}17$) for constant filtration pressure. The equation relates the cumulative volume of the filtrate flowing through the filter medium in time with the coefficient q_1. The coefficient might be understood as a blocking speed (Gösele & Alt, 2005).

$$\frac{d^2t}{dV_{filtrate}{}^2} = q_1 \cdot \left(\frac{dt}{dV_{filtrate}}\right)^{q_1} \qquad Eq.\,3\text{-}17$$

with

$V_{filtrate}$	Cumulative volume of the filtrate [m³]
t	Time [s]
q_1	Constant describing the interaction between fluid and porous media [-]

The type of interaction taking place, described above, can be distinguished based on this constant. The typical values of the constant, which depend on the type of interaction, are provided in Table 3-2.

Table 3-2: Coefficient q_1 describing the interaction

Type of filtration	Cake filtration	Intermediate blocking filtration	Standard blocking filtration	Complete blocking filtration
q_1 [-]	0	1	1.5	2

However, it can be generally expected that more than one filtration type is simultaneously present (Gösele & Alt, 2005). Moreover, Tien & Ramarao (2011) point out that the values of the coefficient q_1 are only approximate. The procedure for determining q_1 is not trivial. The determination procedure from experimental data is described by Tien & Ramarao (2011) in detail. The procedure is not utilised in this thesis.

3.3.2 Standard blocking filtration (deep bed filtration)

The standard blocking mechanism is one of four fundamental mechanisms used to describe the interaction between the suspension and the porous media. Based on the size comparison of suspended bentonite particles with the pores of non-cohesive soil, it seems to be the most common form of interaction. Standard blocking filtration represents a framework for describing the deposition of suspended bentonite particles in a porous medium (bed). In this section, the elementary mechanisms of slurry particle clogging within the soil skeleton will be described. Particle transport and deposition (clogging) in porous media are two fundamental processes which occur during standard blocking filtration (Zamani & Maini, 2009).

Several mechanisms are involved in the process of standard blocking filtration. These mechanisms bring suspended particles in contact with retention sites, fix the particles on retention sites (colmatage or clogging) and potentially break away (decolmatage or scouring) previously fixed particles (Herzig et al., 1970). The rates of deposition and of particles breaking away within a porous medium depend on the forces interacting between the filter medium, the carrier fluid and the suspended particles (Sharma & Yortsos, 1987).

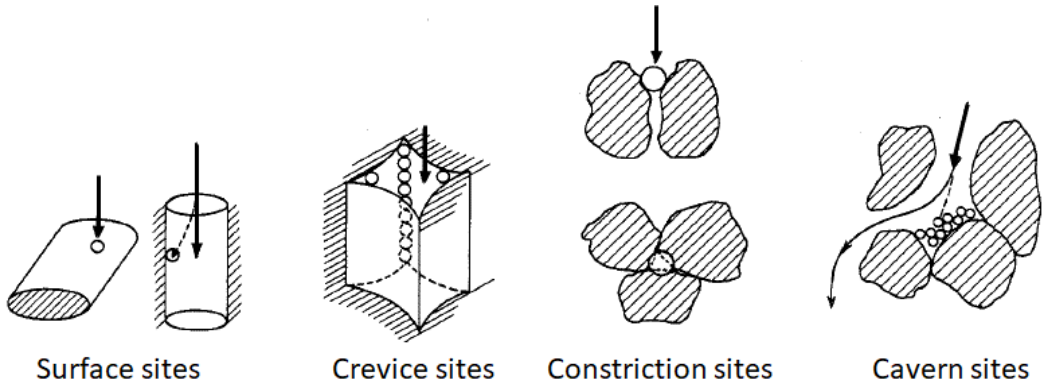

Figure 3-11: Particle retention sites in porous media during deep bed filtration (Herzig et al., 1970)

As previously pointed out, suspended particles are transported to retention sites during filtration. The retention sites in a porous medium in deep bed filtration can be divided in four types. These types are:

- ***Surface sites*** (Figure 3-11-a) – A suspended particle stops and is fixed on the surface of a pore.
- ***Crevice sites*** (Figure 3-11-b) – A suspended particle is wedged between the convex surfaces of two grains. Theoretically, each size of particle can be retained in a crevice. However, a particle needs some kinetic energy to be wedged in the crevice instead being fixed on a face. According to Herzig et al. (1970), wedging is only probable for particles with a maximum size 20-times smaller than the bed grains.
- ***Constriction sites*** (Figure 3-11-c) - If a particular pore is smaller than the suspended particle, the particle can be retained. Geometrically, a spherical particle can be strained in a triangular constriction if it has a maximum diameter 6.5 times smaller than the spherical bed grain. If three uniform spherical particles are involved in straining, they can be a maximum of 10 times smaller, according to Herzig et al. (1970). The straining may also happen due to the successive stoppage of particles in each crevice of the constriction.
- ***Cavern sites*** (Figure 3-11-d)– Particles are retained in pocket areas formed by adjacent grains.

Besides retention sites, Herzig et al. (1970) identify several retention forces. Retention sites can be coupled with particular retention-triggering forces. These forces are:

- ***Axial flow pressure of the fluid*** – The pressure may hold a particle retained at the opening of the constriction.
- ***Friction forces*** – Particles retained in a crevice may be held in place by friction. Axial flow pressure and friction forces together are sometimes considered mechanical stresses acting on the particles (Sharma & Yortsos, 1987).
- ***Surface forces*** – Surface forces are a combination of attractive Van der Waals forces and electrical forces. The electrical forces (Coulomb's forces) between suspended particles and grains may be either attractive or repulsive depending on physiochemical conditions. Van der Waals forces can be neglected for particles larger than 10^{-5} m, hence, for a fraction of suspended bentonite particles. The electrokinetic forces depend on the pH, the ionic strength of the solution and the nature of the particles and ions. The electrokinetic forces may appear both between suspended particles and between particles and grain bed. Ives (1987) points out that suspended clay particles in water and porous bed particles have the same charge. Thus, the electrostatic repulsion might be overcome by Van der Waals´ forces.
  During small particle filtration, particles can flocculate due to electrokinetic forces and can influence the interaction with porous media. In general, surface forces have very small action ranges, so they can only capture particles if they flow very close to the grains.
- ***Chemical forces*** – These forces are relevant for colloidal particles with theoretically possible chemical bonding. Colloidal particle deposition can cause a change in the morphology of pores and influence the porosity of the porous medium. The change in pore structure induces local pressure gradients (Zamani & Maini, 2009). Additionally, colloidal forces, as a type of compound forces, can be considered as separate group. These forces are London–van der Waals forces, electrical double layer forces, solvation forces, hydrophobic forces and steric forces. They are considered to be compound since they are both described by the Derjaguin–Landau–Verwey–Overbeek (DLVO) theory. This theory offers a framework for the prediction of total interparticle interaction (Liang et al., 2007).

The existence of retention forces causes the grains of porous medium to capture the suspended clay particles. These processes displayed in Figure 3-12 are (Herzig et al., 1970):

- ***Sedimentation*** - This process is induced by gravitational force if it is larger than the flow force. Sedimentation plays an important role if the density of particles is significantly higher than the density of the carrier fluid (Zamani & Maini,

2009). The efficiency of a single collector can be described by $Eq.\,3\text{-}18$ using the gravitational sedimentation parameter.

$$N_G = \frac{2 \cdot g \cdot {D_p}^2 \cdot (\rho_s - \rho_{carrier})}{9 \cdot \mu_{carrier} \cdot v_{ch}} \qquad Eq.\,3\text{-}18$$

with

N_G	Gravitational parameter [-]
ρ_s	Particle density [g/cm³]
v_{ch}	Characteristic velocity [m/s]
D_p	Radius of suspended particles [m]
$\mu_{carrier}$	Viscosity of carrier fluid [mPa.s]
g	Gravitational acceleration [m/s²]
$\rho_{carrier}$	Density of carrier fluid [g/cm³]

- ***Inertia*** – Due to the different densities of the particles and fluid, the particles cannot maintain the same trajectories as the fluid and might deviate from the streamlines. The deviation may bring the particles into contact with the grains. The inertial forces become more significant in comparison to gravity forces as the flow velocities of suspended particles increase and the grain size of the porous media decreases. However, Zamani & Maini (2009) say that inertial collection efficiency is lower for higher flow rates of liquids. The inertial effect can be characterized by the Stokes number ($Eq.\,3\text{-}19$). According to Zamani & Maini (2009), the Stokes number quantifies the inertial force in the motion equation.

$$N_{St} = \frac{2 \cdot \rho_s \cdot v_m \cdot {D_p}^2}{9 \cdot \mu \cdot d_g} \qquad Eq.\,3\text{-}19$$

with

N_{St}	Stokes number [-]
ρ_s	Particle density [g/cm³]
v_m	Suspension approach velocity [m/s] $v_m = v\ (mean\ interstitial\ velocity) \cdot n_0$
D_p	Radius of suspended particles [m]
μ	Viscosity of carrier fluid [mPa.s]
d_g	Radius of bed grain [m]

- ***Hydrodynamic effects*** – Due to the flow field resulting from non-spherical pore geometry, the particles conduct random drifting motions across streamlines. This type of movement increases the probability of collision with bed grains (Zamani & Maini, 2009).

- ***Direct interception*** – Direct collisions with grains occur in the pore tortuosities, due to the size of the particles. The fraction of suspended particles which come into contact with grains is proportional to $\left(\frac{particle\ diameter}{constriction\ radius}\right)^2$ (Figure 3-12). A collision happens when a particle flows in a streamline at a distance closer to the grain than the radius of the particle.
- ***Diffusion by Brownian motion*** – The suspended particles may reach areas outside of the flow of the suspension due to diffusion. They may be subsequently fixed at these areas. Brownian motion is usually the dominant factor for the deposition of very small particles in the absence of electrostatic forces (Zamani & Maini, 2009). Brownian motion may usually be neglected for the bulk flow of bentonite slurry through a porous medium, because the viscous drag of fluid restricts this movement for particles larger than 1 µm (Ives, 1970).

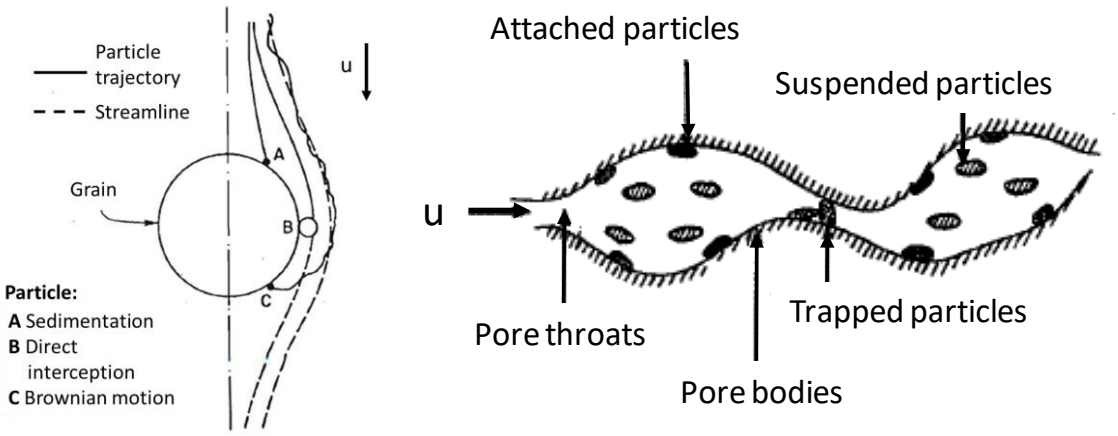

Figure 3-12: Left - Three dominant capturing processes of suspended particles, grain = collector (modified from McDowel-Boyeret al., 1986), Right – particles within a porous medium (Sharma & Yortsos, 1987)

The process of capturing particles is reversible in some cases. The process in which particles separate from grains is called decolmatage, as previously noted. Herzig et al. (1970) distinguish two decolmatage processes:

- ***Spontaneous decolmatage*** – This occurs when the pressure or flow rate spontaneously changes the flow close to the retained particles. Another scenario might be that a flowing particle collides with the retained one.
- ***Provoked decolmatage*** – Provoked decolmatage results from outer impulses, when the flow rate or pressure is changed in the entire porous medium.

Generally, the ratio between the diameter of the suspended particle and the diameter of the bed grain is important for the retention of “large” particles. In contrast, the specific surface of porous beds plays the most important role in the retention of “small” particles. According to Herzig et al. (1970), the previously described interaction mechanism within deep bed filtration can be classified depending on the size of suspended particles. This means that for a certain particle size, the prevailing retention sites, capture mechanisms and governing forces can be defined (Table 3-3). The ratio between bed grain and particle size defines the manner in which the retained particles change the free passage and facilitate the retention of other particles. Consequently, permeability reduction of porous media through which a suspension is flowing, may happen due to the following processes (Sharma & Yortsos, 1987):

- ***Particles larger than pore throat*** – These particles are captured in the pore throat and thereby abruptly reduce the area allowed for suspension flow.
- ***Particles considerably smaller than pore throat size*** – These particles are uniformly captured over pore bodies and throats. Hence, permeability is reduced successively during ongoing flow through the porous medium.

Table 3-3: Types of standard blocking filtration (Herzig et al., 1970), compare with Fig. 3-2

Type of standard blocking filtration	Particle size [µm]	Retention sites	Retention forces	Capture mechanism	Spontaneous decolmatage	Provoked decolmatage
Mechanical	> 30	constrictions, crevices, caverns	Friction, fluid pressure	Sedimentation, direct interception	improbable	flow direction reversal
Physiochemical	1 - 3	surface sites	Van der Waals and elektrokinetic forces	Direct interception	possible	increase in flow rate
Colloidal	< 0.1	surface sites	Van der Waals forces, elektrokinetic forces and chemical bonding	Direct interception, diffusion	possible	increase in flow rate

In the past, a number of theoretical models have been developed for the characterization of particle deposition within various sizes of porous media. Models which consider deep bed filtration to be the governing interaction mechanism are reviewed in Shirato et al. (1978) and Zamani & Maine (2009). Two important

representations of models for standard blocking filtration are discussed here. Iwasaki et al. (1937) derived an equation for particle deposition in sandy porous media ($Eq.\,3\text{-}20$) for constant pressure conditions. The equation introduces a constant filter coefficient (λ). The equation includes certain simplifying assumptions. These assumptions are (Ives, 1970):

- The suspension is homogeneous, non-flocculating and flows at a constant rate.
- The porous medium is isotropic and uniform.
- The porous medium is initially clean and thus does not contain any deposited particles.
- Every layer of the filter is equally efficient.
- The suspension entering and leaving the porous medium is uniformly dispersed.

$$-\frac{\boldsymbol{\partial C_{partcile}}}{\boldsymbol{\partial y}} = \boldsymbol{\lambda \cdot C_{particle}} \qquad Eq.\,3\text{-}20$$

with

$C_{partcile}$	Particle concentration [-]
y	Distance from the inlet face of the porous media
λ	Filter coefficient (a measure of the efficiency of clarification of the suspension)

In comparison to Iwasaki, Ives (1970) presented a more general equation for the filtration coefficient of sand. The equation accounts for variations of the filtration coefficient during ongoing filtration due to successive particle deposition ($Eq.\,3\text{-}21$). The aim of the equation is to highlight the importance of pore geometry and interstitial velocity (Ives, 1970). It considers the increase of the specific surface of the filter due to localized coatings of grains by deposited particles in the first term in brackets. The second term in brackets of $Eq.\,3\text{-}21$ stands for the diminution of the specific surface in the filter since the particles are accumulated in the side spaces of pores. The third term indicates that interatrial velocity increases when pore cross-sections are narrowed by deposited particles. Ives (1970) expects that further particle deposition is not possible when the limiting velocity is reached, so that a specific deposit reaches the saturation value.

$$\boldsymbol{\lambda = \lambda_0 \cdot \left(1 + \frac{b_{grains} \cdot \sigma}{n_0}\right)^{n_1} \cdot \left(1 - \frac{\sigma_{spec}}{n_0}\right)^{n_2} \cdot \left(1 - \frac{\sigma_{spec}}{\sigma_{u,spec}}\right)^{n_3}} \qquad Eq.\,3\text{-}21$$

with

b_{grains}	Geometric constant related to packing of the filter grains [-]

$\sigma_{u,spec}$	Ultimate saturation value of the specific deposit [-]
λ	Filter coefficient (a measure of the efficiency of clarification of the suspension) [-]
σ_{spec}	Specific deposit [-]
λ_0	Initial value of the filter coefficient at t = 0 s [-]
n_1, n_2, n_3	Empirical exponents
n_0	Initial porosity (clean bed)

As noted by Arwanitaki (2009), the model formulations developed in chemistry have not yet been used for practical purposes in geotechnical engineering practice, due to their complexity and sometimes ambiguous output. The complexity can easily be seen in the non-existence of a closed analytical solution. However, they offer a good framework for the analysis of slurry-soil interaction for the purposes of geotechnical engineering. The interpretation of the experiential results in chapter 6 and 7 of this thesis is inspired by this framework.

3.4 Theories of support pressure transfer at the tunnel face

The support pressure transfer theories describing the interaction between bentonite slurry and the soil skeleton will be presented in this section. In contrast to the previous sections, this section focus exclusively on approaches used in geotechnical engineering or on approaches, which have been developed for the purpose of geotechnical engineering. The theories discussed in this section are divided in groups depending on factors which are taken into account while assessing the pressure transfer. These groups of theories are as follow:

- Theories not considering time factor
- Theories considering time factor
- Theories considering time factor and the interaction with cutting tools on the level of entire tunnel face

The theories for pressure transfer used in geotechnical engineering will be also later coupled with the fundamental theories from the previous sections to obtain deeper understanding of the processes. The approach also offers clues about processes at the micro-level for the later evaluation of the macroscopic experiments.

3.4.1 Theories not considering time factor

The representatives of this first group originate from diaphragm wall technology. They do not take into account any time-dependent processes or any interaction between the pressure transfer mechanism and the cutting tools of a shield machine.

Morgenstern & Amir-Tahmasseb (1965) conducted one of the first attempts to analyse the interaction between slurry and soil for the purposes of open trench stabilization. The authors pointed out that at the time of publishing their paper, several mechanisms like hydrostatic pressure, arching of the soil and electro-osmotic forces were discussed as the main mechanisms responsible for the slurry support of non-cohesive open trenches. They concluded based on an analysis of a case study that the yield strength of slurry is not the factor that directly contributes to the stability of the trench. According to the authors, the role of yield strength can be seen in the increased carrying capacity of the slurry for cuttings produced during the excavation. The floating cuttings in the slurry subsequently increase the slurry´s bulk density, which increases the trench stability by increasing hydraulic pressure. Thus, the hydrostatic pressure induced by the self-weight of slurry is the mechanism enabling the support of the trench. The authors also stated that the presence of suspended bentonite particles in the slurry is essential for the formation of an impervious membrane at the interface of the slurry and non-cohesive soil. However, the authors did not establish any connection between the rheological properties of slurry and its penetration behaviour. Their theory expects that all of the slurry excess pressure is transferred at the soil skeleton.

Weiss (1967) performed laboratory experiments dealing with stabilization of non-cohesive soils by bentonite slurry. In his experiments, he visualized the penetration behaviour of slurry in the pores of soil and suggested that the penetration depth can be calculated from the equivalent pore diameter and the yield point of slurry. In his research, Weiss (1967) observed the formation of filter cake in soils with low permeability coefficients, and slurry penetration inside the skeleton for coarse soils with high permeability coefficients. He concluded that the yield point has considerable influence on trench stability, and hence on the pressure transfer. He summarizes the stability condition as three partial conditions:

- The first condition requires a certain yield point of slurry to achieve the equilibrium of forces on a single soil grain ($Eq.\,3\text{-}22$).

- The second condition is that the slurry pressure exceeds the groundwater pressure.
- The third condition requires the slurry excess pressure to counter the earth pressure.

From the pressure transfer point of view, only the first condition is important. This condition results from the assumption that yield strength should retain the movement of soil grains.

$$\boldsymbol{\tau_{f,0} \geq \frac{2}{3 \cdot \pi} \cdot d_{25} \cdot (\gamma_s - \gamma_F)} \qquad Eq.\ 3\text{-}22$$

with

$\tau_{f,0}$	Yield point immediately after mixing the slurry [Pa]
d_{25}	Characteristic grain size of soil (25% passage) [mm]
γ_s	Unit weight of soil grains [kN/m³]
γ_F	Unit weight of slurry [kN/m³]

Further research on the stability of slurry-stabilized trenches was conducted by Müller-Kirchenbauer (1972). Müller-Kirchenbauer performed both, experiments and theoretical analysis. He stated that penetration of slurry in the pores of soil influences the slurry pressure transfer on the soil skeleton. The penetration behaviour of slurry is determined by the grain size distribution of soil and the stagnation gradient of slurry. Müller-Kirchenbauer (1972) distinguishes two cases of slurry-soil interaction. The first is the formation of a filter cake at the soil's surface and the second is slurry penetration inside soil´s pores without any aggregation of slurry particles at the surface. In case of slurry penetration, the shear resistance of the pore channel wall is activated. The shear resistance is in equilibrium with the excess hydraulic head of the slurry in the trench at the end of the penetration process. The final penetration depth is described by a stagnation gradient, which can easily be determined from an experiment using to *Eq.* 3-23.

$$\boldsymbol{l_{max} = \frac{\Delta s}{f_{s0}}} \qquad Eq.\ 3\text{-}23$$

with

l_{max}	Final penetration distance of slurry in soil [m]
Δs	Excess hydraulic head of the slurry [kPa]
$f_{s0,MC}$	Stagnation gradient of slurry in soil [kN/m³]

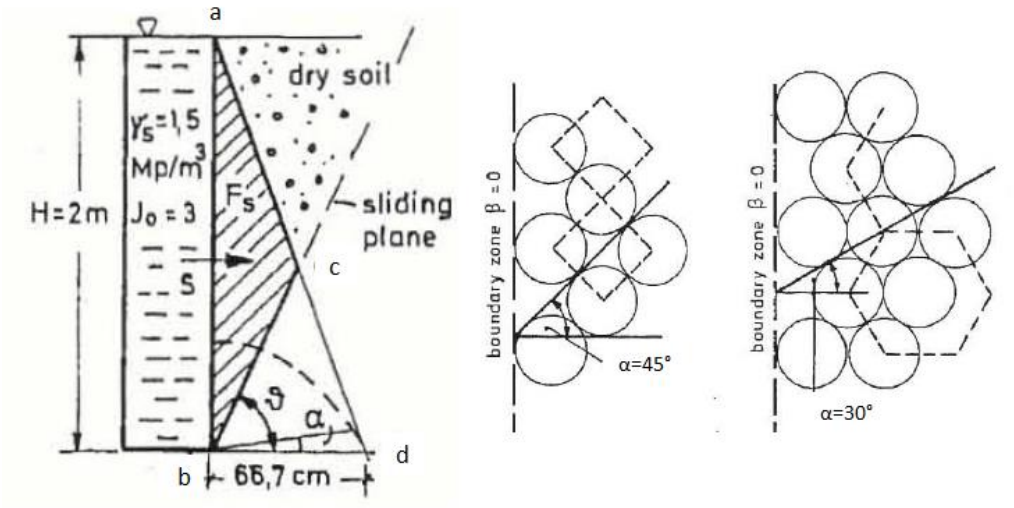

Figure 3-13: Left - Sketch of slurry supported open trench with slurry penetrated area (abd) and the slurry penetrated area which is stabilizing the trench (abc) Right – Mechanism of the single grain sliding out of the wall for α = 30° and 45° (Müller-Kirchenbauer, 1972)

Based on the stagnation gradient, Müller-Kirchenbauer (1972) calculated the force induced by slurry pressure, which is supporting the trench. While calculating the force, he only considers the stabilization effect of slurry, which stagnated inside the soil wedge. The soil wedge to be stabilized is assumed to be two-dimensional (plain strain conditions assumed) and is visualized in Figure 3-13. The supporting force is calculated using $Eq.3\text{-}24$. Thereby, he considers that the entire slurry excess pressure is transferred at the soil skeleton anyway. The same approach was applied by Anagnostou & Kovári (1994), when they evaluated pressure transfer on three-dimensional soil wedge.

$$\boldsymbol{F_{slurry} = A_{FS} \cdot f_{s0} \cdot \gamma_F} \qquad Eq.3\text{-}24$$

with

F_{slurry}	Retaining force due to slurry pressure [kN]
A_{FS}	Area of the slurry penetrated soil inside the wedge [m²]
γ_F	Unit weight of slurry [kN/m³]
f_{s0}	Stagnation gradient of slurry in soil [kN/m³]

Müller-Kirchenbauer (1972) also offers an equation for predicting the stagnation gradient based on the equivalent pore diameter of the soil and the yield point of slurry ($Eq.3\text{-}25$).

$$f_{s0,MC} = C \cdot \frac{2 \cdot \tau_{f,0}}{R_{pore}} \cdot \frac{1}{\gamma_F} \qquad Eq.\,3\text{-}25$$

with

C	A constant [-]
R_{pore}	Equivalent pore radius [m]
$\tau_{f,0}$	Yield point immediately after mixing the slurry [N/m^2]
γ_F	Unit weight of slurry [kN/m^3]
$f_{s0,MC}$	Stagnation gradient of slurry in soil acc. to Müller-Kirchenbauer [kN/m^3]

In addition to the global pressure transfer, Müller-Kirchenbauer (1972) also points out the necessity of the stabilization of single grains as a precondition for the successful conduction of slurry pressure transfer. In contrast to Weiss (1967), he considers a different, theoretically possible movement direction for grains sliding out of the skeleton. The direction is defined by the inclination of the tangency plane between two grains (Figure 3-13). The inclination may have an angle between 30 and 45 degrees. Subsequently, the minimal yield point of the slurry can be calculated ($Eq.\,3\text{-}26$). He confirmed the validity of the procedure using an experimental set-up.

$$\tau_{f,0} \geq \frac{2 \cdot sin(\alpha_{incl} - \beta)}{3 \cdot \pi} \cdot d_{20} \cdot (\gamma_s - \gamma_F) \qquad Eq.\,3\text{-}26$$

with

$\tau_{f,0}$	Yield point immediately after mixing the slurry [Pa]
d_{20}	Characteristic grain size of soil (20 % passage) [mm]
γ_s	Unit weight of soil grains [kN/m^3]
α_{incl}	Inclination of tangency plane between two grains (30-45 degrees)
β	Inclination of the soil plane to the vertical line [degrees]
γ_F	Unit weight of slurry [kN/m^3]

Kilchert & Karstedt (1984) presented the next development in slurry pressure transfer investigation. The authors identify three pressure transfer mechanisms and corresponding ways of pressure transfer. The authors specify the necessary properties of slurry to enable the pressure transfer:

- Yield point
- Certain penetration behaviour of the slurry in the soil
- Self-weight of slurry
- Stability of the slurry against separation into solid particles and water

The authors reference Müller-Kirchenbauer (1977) regarding his hypothesis, stating that an interrelation exists between the type of support pressure transfer and the penetration behaviour of the slurry. The three types of pressure transfers are discussed in Table 3-4 and visualized in Figure 3-14. By introducing these three types of pressure transfer, the "classical theory" for slurry-soil interaction in diaphragm wall technology was completed.

Table 3-4: Pressure transfer mechanisms and their characteristics (adapted from Kilchert & Karstedt, 1984)

Characteristics	Type I Completely formed filter cake	Type II Pure slurry penetration	Type III Incompletely formed filter cake reduced penetration
Penetration Depth	No penetration in void space	Deep, predictable	Intermediate, not predictable
Pressure transfer principle	Slurry plugs pore entrances, thin membrane with reduced permeability converts hydraulic pressure into the normal effective stress	Shear stresses transferred from the fluid on the walls of pores	Transfer simultaneously over both fundamental mechanisms
Pressure gradient	Very high over the thickness of the filter cake	Low, constant over the penetration depth	Constant over the penetration depth, however, two inclinations are observable. 1) filter cake area 2) penetration area
Pressure transfer mechanism constitution	Settling of slurry particles at the interface of slurry and soil	Slurry particles are in direct contact with pore walls	Additional aggregates are present in the filter cake, slurry particles penetrate into soil pores
Typical soil type	Fine, $d_{10} < 0{,}2\ mm$	Coarse	Intermediate / coarse, slurry with floating aggregates
Permeability coefficient	2.2 – 4*10^{-10} m/s for soil with 10^{-4} m/s (Arwanitaki, 2009)	Not investigated	Not investigated

Recently, it was additionally suggested by Koenig & Schroeder (2015) to distinguish the Type IIIb of pressure transfer. The mechanism is almost completely the same as the mechanism Type III. The only difference is that soil particles floating in the slurry may penetrate the soil pores again and clog them.

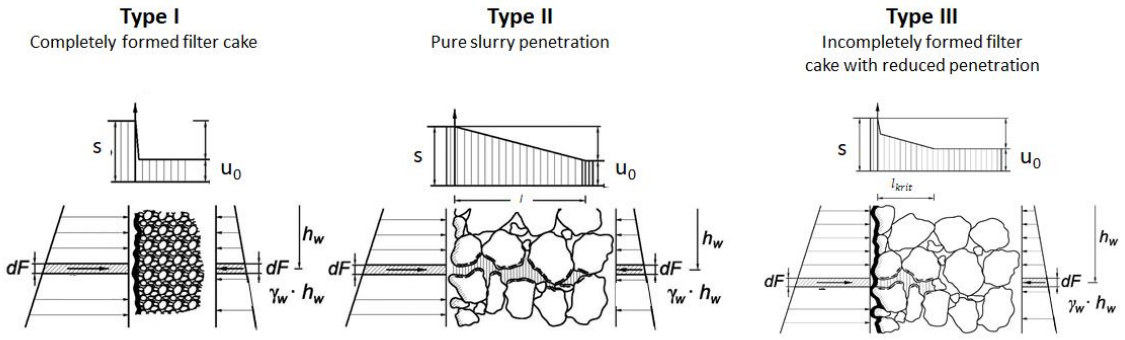

Figure 3-14: Visualization of slurry pressure transfer models (modified from Thienert, 2011)

In case of pure slurry penetration, Type II, the penetration depth depends on the yield point of the slurry, the characteristic grain size of the soil (d_{10}) and the excess slurry pressure. The penetration distance is directly proportional to the slurry excess pressure. The factor of proportionality between these two variables is called the stagnation gradient (Kilchert & Karstedt, 1984). The stagnation gradient corresponds to stagnation gradient originally introduced by Müller-Kirchenbauer (1972) in *Eq.* 3-23. As Kilchert & Karstedt (1984) state, the dependency of the pressure (stagnation) gradient ($Eq.$ 3-27) on the characteristic grain size (d_{10}) and the yield point of slurry was derived from experiments conducted by Weiss (1967), Müller-Kirchenbauer (1977) and Simons & Ruppert (1982). Thienert (2011), however, supposes that the static shear stresses due to the yield point of slurry are not solely responsible for the transfer during ongoing penetration. He remarks that transferred shear stresses also depend on the plastic viscosity of the slurry.

$$\boldsymbol{f_{s0,KK} = \frac{a \cdot \tau_{f,s}}{d_{10}} \rightarrow l_{max,calc} = \frac{\Delta s}{f_{s0,KK}}} \qquad Eq.\ 3\text{-}27$$

with

$f_{s0,KK}$	Slurry stagnation gradient acc. to Kilchert & Karstedt [kN/m²/m]
a	Empirical factor from the experiments; 2 or 3.5 [-]
d_{10}	Characteristic grain size of soil (10 % passage in sieve analysis) [mm]
$\tau_{f,s}$	Static yield point of slurry [Pa]
Δs	Slurry excess pressure [kPa]
$l_{max,calc}$	Slurry penetration depth [m]

As mentioned in $Eq.\,3\text{-}27$, two possible values exist for the empirical fitting factor (a). If the value a =2 is chosen, the evaluation of the referenced experiments considers the standard deviation of the results. If a = 3.5 is taken, it corresponds with the evaluation of referenced experimental results considering average values. Simons & Ruppert (1982) state that the coefficient might be between 2.5 and 4. Another doubt exists regarding the yield point of slurry to be used in $Eq.\,3\text{-}27$. Despite his statement of viscous pressure transfer during penetration, Thienert (2011) suggests, in accordance with Weiss, to consider the yield point of the slurry after 1 minute of thixotropic solidification. This implies the use of a ball harp or pendulum device for the determination (compare section 3.1.2). This is supported by the argument by Koenig & Schroeder (2015) who noted that all described classical theories expect static pressure transfer governed exclusively by the yield point of slurry. However, the research of Koenig & Schroeder (2015) dealt with diaphragm walls, in contrast to the work of Thienert (2011). Hence, the input of the yield point of the slurry obtained by the ball harp (section 3.1.2) in $Eq.\,3\text{-}27$ has purely empirical meaning not distinguishing between slurry application for a diaphragm wall or a slurry shield.

According to Kilchert & Karstedt (1984), the precondition for the global pressure transfer is also the local stability of single grains. However, Kilchert & Karstedt (1984) are analysing the local stability in different way than Weiss (1967) or Müller-Kirchenbauer (1972). The local stability according to Kilchert & Karstedt (1984) is automatically fulfilled for Type I pressure transfer (Table 3-4). For Type II, the local stability of grains is provided by the minimal required yield point of the slurry, which ensures a certain slurry pressure gradient over the grains. The required gradient for the local stability can be calculated using $Eq.\,3\text{-}28$. The equation is based on the calculation of the slope stability of non-cohesive soil (Terzaghi & Jelinek, 1954). The pressure gradient represents a stabilizing effect which can be compared to flow pressure induced by liquid flowing into the slope.

$$\boldsymbol{f_{s0,req} = (1 - n_p) \cdot (\gamma_s - \gamma_F) \cdot \left(\frac{sin(\beta)}{tan(\varphi')} - cos(\beta) \right)} \qquad Eq.\,3\text{-}28$$

with

$f_{s0,req}$	Required pressure gradient [kN/m^2/m]
n_p	Porosity of soil [-]
γ_s	Unit weight of soil grains [kN/m^3]

γ_F Unit weight of slurry [kN/m³]
β Inclination of trench wall, usually $\beta = 90\ deg$ [deg]
φ' Friction angle of soil [deg]

The pressure gradient offered by the slurry ($Eq.\ 3\text{-}27$) according has to be according to Kilchert & Karstedt (1984) at least two-times higher than the required pressure gradient ($Eq.\ 3\text{-}28$). The factor 2 is here a purely empirical factor for the purposes of local stability calculations. If the equation $Eq.\ 3\text{-}27$ and $Eq.\ 3\text{-}28$ are put together while considering the factor, the minimal yield point of slurry can be derived ($Eq.$ 2-1). Acc. to Jancsecz & Steiner (1994) this approach for local stability is not exact for soils without uniform grain size distribution, because it does not include forces and moments on single particles.

Krause (1987) suggests that the support of soil by cutting wheel and by shield circumference tip should be considered as additional safety margins for the tunnel face. He identifies three cases of slurry excess pressure transfer (Figure 3-15) at the tunnel face dependent on the grain size of soil. The cases partially correspond to the types discussed in Table 3-4. Type I (Table 3-4) pressure transfer acts the same at the slurry-supported tunnel face as it does at the diaphragm wall (Figure 3-15-a). For Type II pressure transfer, Krause (1987) suggests that the main difference between diaphragm walls and slurry shields is the additional formation of a filter cake at the slurry supported tunnel face (Figure 3-15-b). He also assumes this behaviour in coarse-grained soil. However, he does not explicitly discuss the source of different behaviour in comparison to the diaphragm walls. He designates the case (Figure 3-15-c), in which shear stresses induced by slurry in a soil skeleton are very low, to be the boundary case

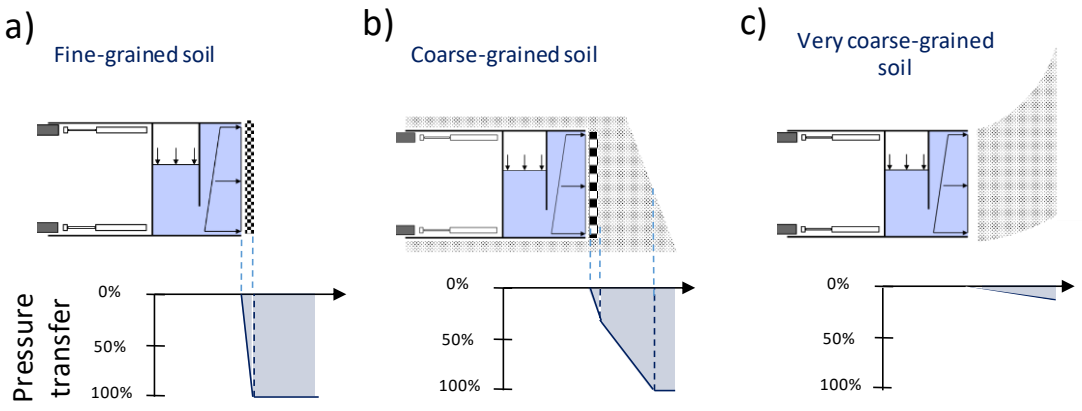

Figure 3-15: Pressure transfer mechanism and pressure drops in dependence on grain size of soil (modified from Krause, 1987)

with insufficient pressure transfer. Krause (1987) expects, in accordance with previous investigations for diaphragm walls, that the entire slurry excess pressure is transferred to the soil skeleton (Figure 3-15). However, the full transfer occurs after the formation of the pressure transfer mechanism, which he considers as a time-dependent process (section 3.4.2). It is worth mentioning that Krause (1987) does not distinguish in terms of efficiency, in comparison to Müller-Kirchenbauer (1972), whether the transfer occurs inside or outside of the sliding wedge to support.

Despite his suggestion that both filter cake and the penetration zone simultaneously exist at the tunnel face, Krause (1987) later only goes into detail about the penetration zone. He explains that the slurry penetration distance is determined by the shear stress transferred from the fluid on the walls of the soil's pore channel ($Eq.\,3\text{-}29$). After evaluation of his experiments, Krause (1987) suggested introducing the factor "b" for the calculation of slurry penetration depth. The factor can vary between 5 and 15. He agreed with Kilchert & Karstedt (1984) about considering the influence of characteristic grain size, but used the gel strength of slurry instead. As gel strength of slurry, he considers the yield point determined by rotational viscometer. Krause (1987) further investigated which gel strength should be employed, regarding the thixotropic behaviour of slurry. First, he assumed the gel strength of a slurry already stagnated in the ground to be higher than the gel strength of a penetrating slurry. Consequently, he expected the penetration depth to be smaller by repeated penetration. In order to test the assumption, Krause (1987) performed a single control test. In the test, he conducted the slurry penetration. After stagnation, he removed the first 4 cm of the penetrated soil and repeated the slurry penetration. The procedure and test results are visualized in Figure 3-16. He reports negligible differences without any clear trend regarding the penetration depth change due to changed gel strength during re-penetration. However, he does not provide any time-sequence for conducting the re-penetration. Despite its different goal, the investigation can be seen as the first attempt to investigate the re-penetration behaviour of slurry (see section 4.1).

$$\boldsymbol{l_{Krause} = \frac{\Delta s \cdot d_{10} \cdot b_{Krause}}{\tau_{G'}}} \qquad Eq.\,3\text{-}29$$

with

Δs	Slurry excess pressure [kPa]
l_{Krause}	Slurry penetration distance [m]
b_{Krause}	Empirical factor by Krause, = 5 - 10 [-]

d_{10} Characteristic grain size of soil (10 % passage in sieve analysis) [mm]
$\tau_{G'}$ Gel strength of slurry (see section 3.1.2) [kPa]

An interesting point of his work is the comparison of slurry penetration experiments in two different spatially oriented set-ups. In the first set-up the slurry penetrated the soil horizontally, while in the second, the slurry penetrated vertically. Krause (1987) concludes that both set-ups delivered comparable results, however, conducting experiments with horizontal set-ups was much more complicated.

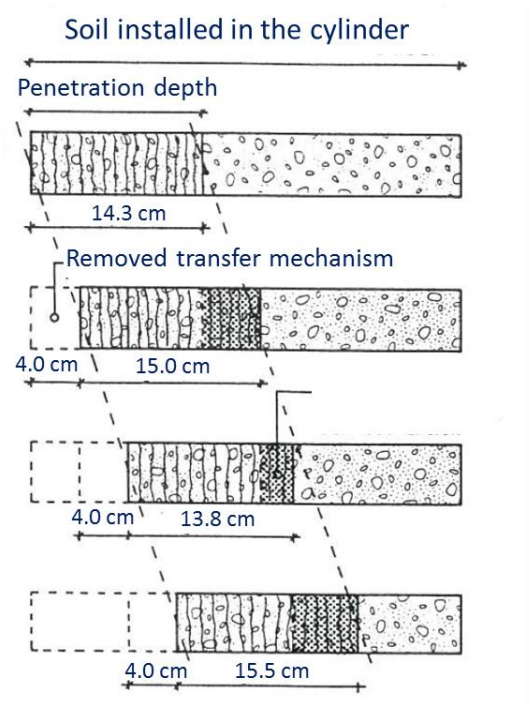

- Slurry concentration 5 %
- Slurry exces pressure 0.2 bar
- Soil d_{10}=0.48 mm

Figure 3-16: Pressure transfer mechanism and pressure drops in dependence on grain size of soil (adapted from Krause, 1986)

Pulsfort & Thienert (2013) investigated the role of loaded slurry with fine particles in support pressure transfer. Along with Kilchert & Karstedt (1984), they suggested that a Type III pressure transfer activates (Table 3-4) in this case. Pulsfort & Thienert (2013) developed an experimental methodology to assess the pressure gradient of the hybrid model (Type III). In the experiments, they investigated the penetration depth of loaded slurry in soils. They called the obtained penetration depth the critical penetration depth ($Eq.$ 3-30).

$$\boldsymbol{l_{krit} = \frac{1}{141} exp\left(186 \cdot k_{f,w}\right) \cdot \left(\frac{d_{15}}{D_{85}} - 6.46\right)} \qquad Eq.\ 3\text{-}30$$

with

l_{krit}	Critical penetration distance [m]
$k_{f,w}$	Permeability coefficient of soil for water [m/s]
d_{15}	Grain size of soil (15% passing in sieve analysis) [mm]
D_{85}	Grain size of particles suspended in slurry (85% passing) [mm]

While combing the experimental methodology with the calculation of the theoretical pressure gradient, they determined the partial contributions of pressure transfer by filter cake and by shear stresses on the soil´s pore walls. The contribution of shear stress to the entire pressure transfer is described by $Eq.\,3\text{-}31$. They concluded that taking the loading of slurry into consideration significantly benefits the increase in pressure gradient and therefore also improves the local stability for the Type III model.

$$\Delta \boldsymbol{s_{shear}} = \frac{\boldsymbol{l_{krit}}}{\boldsymbol{l_{max,calc}}} \cdot \Delta \boldsymbol{s} \qquad Eq.\,3\text{-}31$$

with

Δs_{shear}	Pressure partially transferred over the shear stresses between slurry and pore walls of soil [kN/m^3]
l_{krit}	Critical penetration distance [m]
$l_{max,calc}$	Penetration depth acc. to *Eq. 3-27* [m]
Δs	Slurry excess pressure [kPa]

It is worth mentioning that the expectation of Pulsfort & Thienert (2013) for hybrid mechanism in shield tunnelling was already previously in-situ confirmed by Arwanitaki (2009) for diaphragm walls. She discovered that the filter cake (Type I in Table 3-4) at the construction sites of diaphragm walls additionally contains the particles of the subsoil up to a certain size. The maximum size of the particles was determined by the carrying capacity of slurry characterized by its yield strength.

Recently, Min et al. (2013) experimentally investigated “filter cake formation” in highly permeable sand during tunnelling (Figure 3-17 and Table 3-5). They confirmed the three types of pressure transfer mechanism from Table 3-4. Additionally, Min et al. (2013) suggested a methodology to predict which of the three types occurs. The methodology is based on the comparison between the average pore sizes of soil (D_0) with the size of soil particles suspended in slurry (D_{85}). D_0 can be determined from $Eq.\,3\text{-}32$, based on the permeability coefficient of soil and the porosity of soil. The authors do not provide any notice regarding the amount of transferred slurry excess pressure.

$$d_{\text{pores}} = \sqrt{\frac{k_{f,w}}{31 \cdot 1.5 \cdot n_p}} \qquad Eq.\ 3\text{-}32$$

with

d_{pores}	Average pore size of soil [m]
$k_{f,w}$	Permeability coefficient of soil [m/s]
n_p	Porosity [-]

Table 3-5: Type of slurry soil interaction depending on particle size comparison (Min et al., 2013)

D_{85}/d_{pores}	Corresponding type of slurry soil interaction
> 1	Filter cake (Type I)
0.5 < x < 1	Filter cake with infiltrated zone (Type II)
< 0.5	No filter cake (Type III)

Figure 3-17: Experimental visualization of theoretically possible cases of slurry soil interaction (Min et al., 2013), Type I: filter cake – all grains of slurry are lodged on the surface of soil, Type II: filter cake with an infiltrated zone - some grains of slurry are penetrated into the soil, Type III: infiltrated zone without filter cakes - all grains of the slurry are penetrated into the soil

3.4.2 Theories considering time factor

As pointed out in the previous section, Krause (1987) emphasized the significance of considering the time-factor in the analysis of support pressure transfer for the first time. He stated that the pressure transfer mechanism is damaged each time a cutting tool passes through a local point. After passing, the mechanism has to be renewed before the slurry pressure can be transferred again. He decided to investigate time-dependent slurry penetration behaviour over a 60-minute timespan without a closer analysis of the cutting processes at the tunnel face. He conducted numerous experiments with varying slurry types, slurry excess pressures and soils. Krause (1987)

concluded that the time-dependent behaviour can be approximated within two bounds of "comparative" penetration depth ($Eq.\,3\text{-}33$, $Eq.\,3\text{-}34$ *and* $Eq.\,3\text{-}35$). As mentioned before two phases of flow are not considered by Krause in these equations. Furthermore, it is necessary to point out that the flow in front of the tunnel face during excavation was not part of his investigation.

$$\boldsymbol{l_E(t) = l_{E,comp} \cdot l_E(t = 60min)} \qquad Eq.\,3\text{-}33$$

with

$l_E(t)$	Time dependent slurry penetration distance [m]
$l_{E,comp}$	Comparative penetration distance – upper or lower bounds [%]
$l_E(t = 60min)$	Slurry penetration distance at 60 minutes [minutes]

$$\boldsymbol{l_{E,comp} = \frac{100 \cdot t_{min}}{1 + t_{min}}} \textbf{ for the upper bound} \qquad Eq.\,3\text{-}34$$

$$\boldsymbol{l_{E,comp} = \frac{100 \cdot t_{min}}{3 + t_{min}}} \textbf{ for the lower bound} \qquad Eq.\,3\text{-}35$$

with

$l_{E,comp}$	Comparative penetration distance – upper or lower bound [%]
t_{min}	Timespan since the penetration start [minutes]

Krause (1987) distinguishes two phases during the penetration process. The first phase is characterized by fast flow, while the flow velocity in the second phase slows down significantly and asymptotically approaches zero velocity. Krause (1987) assigns the reduced slurry flow velocity in the second phase to the formed pressure transfer mechanism. The major shortcoming of this approach is the principal unsuitability for those types of interactions, in which the penetration is finished earlier than within the timespan of 60 minutes after the start of penetration.

Anagnostou & Kovári (1994) developed a theoretical model determining the time-dependent slurry penetration depth specifically for slurry shield tunnelling. The authors consider only Type II slurry-soil interaction (Table 3-4). Their model is based on the theory of immiscible fluids and assumes one-dimensional flow in front of the tunnel face. The time-dependent slurry penetration distance is dependent on the permeability coefficient of soil and the ratio between slurry and water viscosity. The

theory developed by Anagnostou & Kovári (1994) delivers the following behaviour of slurry during penetration:

- slurry excess pressure decreases linearly over the penetrated area
- infiltration velocity of slurry decreases with increasing penetration distance
- pressure (stagnation) gradient decreases gradually with increasing penetration distance

The time-dependent penetration depth of slurry after Anagnostou & Kovari (1994) is described by $Eq.\,3\text{-}36$. The equation needs to be solved iteratively by inputting penetration depth up to the maximal penetration depths and calculating the corresponding timespans.

$$\boldsymbol{t = \frac{n_p \cdot \mu_{dyn,s} \cdot \gamma_w \cdot \Delta p}{k_{f,w} \cdot \mu_w \cdot f_{s0}^2} \cdot \left[-\frac{l}{l_{max}} - ln\left(1 - l \cdot \frac{l}{l_{max}}\right)\right]} \qquad Eq.\,3\text{-}36$$

with

t	Timespan since slurry penetration start [s]
n_p	Porosity of soil
$\mu_{dyn,s}$	Dynamic viscosity of slurry [Pa.s]
γ_w	Unit weight of water [kN/m^3]
Δp	Slurry excess pressure [kPa]
l	Penetration distance at timespan t [m]
l_{max}	Maximum penetration distance of slurry [m]
$k_{f,w}$	Permeability coefficient of soil for water [m/s]
μ_w	Dynamic viscosity of water [Pa.s]
f_{s0}	Slurry stagnation gradient [kN/m^3]

The theory suggested by Anagnostou & Kovári (1994) implies that the slurry excess pressure is always entirely transferred to the soil skeleton at every stage of penetration. This causes a changing pressure (stagnation) gradient depending linearly on the penetration depth. Hence, it is only decisive for the efficiency if the pressure transfer occurs inside the soil wedge to be stabilized (Figure 3-13), or outside it. Only the transfer inside the wedge can be considered as efficiently supporting the tunnel face. Time-dependency of the pressure transfer can be seen in the statement that at the start of the penetration the entire slurry excess pressure is transferred inside the wedge. The authors mean the wedge from Figure 2-9. With ongoing time, the slurry penetrates further into the soil and may even leave the area of the wedge. If the slurry leaves the wedge area, the efficient pressure transfer is reduced. To evaluate eventual

flowing out of slurry, the forward movement of the shield has to be considered. The forward movement of the shield increases the pressure (stagnation) gradient acc. to $Eq.\,3\text{-}37$. Hence, the increased advance rate of the shield may have a positive influence on the pressure transfer.

$$\boldsymbol{f_s = f_{s0} + n_p \cdot \gamma_w \cdot \frac{\mu_{dyn,s}}{\mu_w} \cdot \frac{v_{TBM}}{k_{f,w}}} \qquad Eq.\,3\text{-}37$$

with

n_p	Porosity of soil [-]
$\mu_{dyn,s}$	Dynamic viscosity of slurry [Pa.s]
γ_w	Unit weight of water [kN/m^3]
$k_{f,w}$	Permeability coefficient of soil [m/s]
μ_w	Dynamic viscosity of water [Pa.s]
v_{TBM}	Advance rate of the shield [m/s]
f_s	Slurry stagnation gradient considering AR of shield [kN/m^2/m]
f_{s0}	Slurry stagnation gradient [kN/m^2/m]

Talmon et al. (2013) published a work that does not explicitly focus on slurry face support, but also deals with time-dependent slurry penetration and consequent stagnation. The authors have specified four processes responsible for the stagnation of slurry in ground and hence, responsible for the support pressure transfer:

1) Hydraulic resistance of pore water flow within the body of surrounding soil (the influence of this process is negligible in their test cell)
2) Hydraulic resistance of non-consolidated slurry invading in the granular soil
3) Dewatering properties of the consolidated slurry in the filter cake
4) Mechanical filtration of suspended solids

Talmon et al. (2013) distinguish two phases of slurry penetration, as Krause (1987) did. They call the first phase a viscous mud spurt, since in this phase the slurry is penetrating the soil very fast. In the following second phase, slurry consolidation is ongoing and the filter cake forms according to the authors. Thus, the flow slows down. Their experimental investigation focused on the transition between mud spurt and slurry consolidation, and the corresponding time-scale. They expect that during the transition, slurry behaviour changes from undrained to drained. The authors see the pressure transfer as a competition of mud spurt and filter cake formation in general. They establish a theory, which predicts whether mud spurt or filter cake formation will be dominant. They derive the decision about the dominant effect from the Peclet

number (*Pe*). They consider the Peclet number to be higher than 10, if the slurry behaves undrained (with mud spurt). To support this statement, they refer to the book by Winterwerp & van Kesteren (2002). The authors consider the Peclet number to be a ratio of the timescale of changes in flow velocity within a soil´s pores to the timescale required for slurry consolidation. Hence, they can obtain the Peclet number from pore velocity, Terzaghi´s consolidation coefficient of slurry and hydraulic pore diameter ($Eq.\,3\text{-}38$).

$$\boldsymbol{Pe} = \frac{\boldsymbol{v_{slurry} \cdot d_{hyd}}}{\boldsymbol{c_v}} \qquad Eq.\,3\text{-}38$$

with

Pe	Peclet number [-]
d_{hyd}	Hydraulic pore diameter
c_v	Terzaghi´s consolidation coefficient of slurry to be obtained from filter press test [m²/s]
v_{slurry}	Velocity of slurry in pores [m/s]

The equation can be rewritten assuming Herschel-Bulkley fluid (section 3.1.2) behaviour in the pores of the soil, as shown by the authors. Hence, the Peclet number can be obtained based on a comparison between actual penetration and the final penetration depth of the slurry ($Eq.\,3\text{-}39$).

$$\boldsymbol{Pe} = \frac{\boldsymbol{d_{hyd}^2}}{\boldsymbol{8 \cdot c_v}} \cdot \left(\frac{\boldsymbol{\tau_{y,HB}}}{\boldsymbol{\mu_{HB}}}\right)^{\frac{\boldsymbol{1}}{\boldsymbol{p}}} \cdot \left(\frac{\boldsymbol{l_{max}}}{\boldsymbol{l}} - \boldsymbol{1}\right)^{\frac{\boldsymbol{1}}{\boldsymbol{p}}} \cdot \boldsymbol{cos(\theta)} \qquad Eq.\,3\text{-}39$$

with

Pe	Peclet number [-]
d_{hyd}	Hydraulic pore diameter
c_v	Terzaghi´s consolidation coefficient of slurry to be obtained from filter press test [m²/s]
$\tau_{y,HB}$	Yield point of slurry (Herschel-Bulkley) [Pa]
μ_{HB}	Viscosity of slurry (Herschel-Bulkley) [Pa.s]
p	Parameter describing shear thinning in Herschel-Bulkley flow rule [-]
l_{max}	Maximum penetration depth of slurry [m]
l	Penetration depth [m]
θ	Inclination of model tubes in comparison to bulk flow direction [48 deg]

However, their determination of the Peclet number contains some simplifications. First, they assume a soil to be a bundle of straight tubes. They then assume the flowing slurry as a Newtonian fluid, and determine its shear rate. Later, however, while

calculating the shear stress exerted on the pore wall by the flowing slurry, they consider the slurry as a Herschel-Bulkley type fluid.

Talmon et al. (2013) subsequently compared their theory with laboratory measurements, and concluded that the duration of the majority of experiments was significantly shorter than the time-scale required for the mud spurt termination. However, they still consider the theory to be reasonable for describing the penetration behaviour of slurry. The authors considered a relationship to calculate the pressure transfer depending on slurry penetration depth and slurry velocity in pores ($Eq.\,3\text{-}40$). The relationship states that the entire slurry excess pressure will be transferred at the end slurry penetration.

$$\frac{\boldsymbol{ds}}{\boldsymbol{dx}} = \boldsymbol{6.2}\,\frac{\boldsymbol{\tau_{y,HB}} + \boldsymbol{\mu_{HB}} \cdot \left(\dfrac{\boldsymbol{8 \cdot v_{slurry}}}{\dfrac{\boldsymbol{2}}{\boldsymbol{3}} \cdot \dfrac{\boldsymbol{n_p}}{\boldsymbol{1 - n_p}} \cdot \boldsymbol{d_{15}}} \right)^{\boldsymbol{p}}}{\dfrac{\boldsymbol{2}}{\boldsymbol{3}} \cdot \dfrac{\boldsymbol{n_p}}{\boldsymbol{1 - n_p}} \cdot \boldsymbol{d_{15}}} \qquad Eq.\,3\text{-}40$$

with

ds	Slurry excess pressure transfer [kPa]
dx	Time-dependent slurry penetration depth [m]
$\tau_{y,HB}$	Yield point of slurry adopting Herschel-Bulkley flow rule [Pa]
μ_{HB}	Viscosity of slurry (Herschel-Bulkley) [Pa.s]
p	Consistency index (Herschel-Bulkley) [-]
n_p	Porosity of soil [m]
d_{15}	Grain size of soil corresponding to 15 % falling [m]
v_{slurry}	Velocity of slurry in pores [m/s]

3.4.3 Theories considering time factor and the interaction with cutting tools globalized over the entire tunnel face

The theories characterizing support pressure transfer with regard to the interaction of the transfer mechanism with cutting tools were exclusively developed for the purposes of slurry shield excavations.

Bezuijen et al. (2001) formulated a theory which explains the groundwater head increase due to adjacent slurry shield excavations and determines the amount of slurry pressure transferred on the soil skeleton. The theory states that rotating cutting tools very frequently damage the pressure transfer mechanism, so that there is only a short timespan between each subsequent pass of the cutting tools. During the timespan, the

transfer mechanism has no time to form. Thus, no filter cake forms during excavation, and the pressure is transferred due to the flow of water into the soil skeleton (the flow pressure) without a pressure drop over the filter cake. The theory was developed based on a measurement of pore pressure in front of the tunnel face at the 2nd Heinenoord tunnel (Figure 3-18). The distribution of the pore pressure head is described by $Eq.\,3\text{-}41$. The equation was developed by solving steady state groundwater flow in three dimensions.

$$\boldsymbol{\phi(x) = \phi \cdot \left(\sqrt{1 + \left(\frac{x}{R}\right)^2} - \frac{x}{R} \right)} \qquad Eq.\,3\text{-}41$$

with

$\phi(x)$	Pore pressure head in dependence on the distance to the tunnel face [m]
ϕ	Pore pressure head in the excavation chamber [m]
x	Distance from the tunnel face [m]
R	Excavation radius [m]

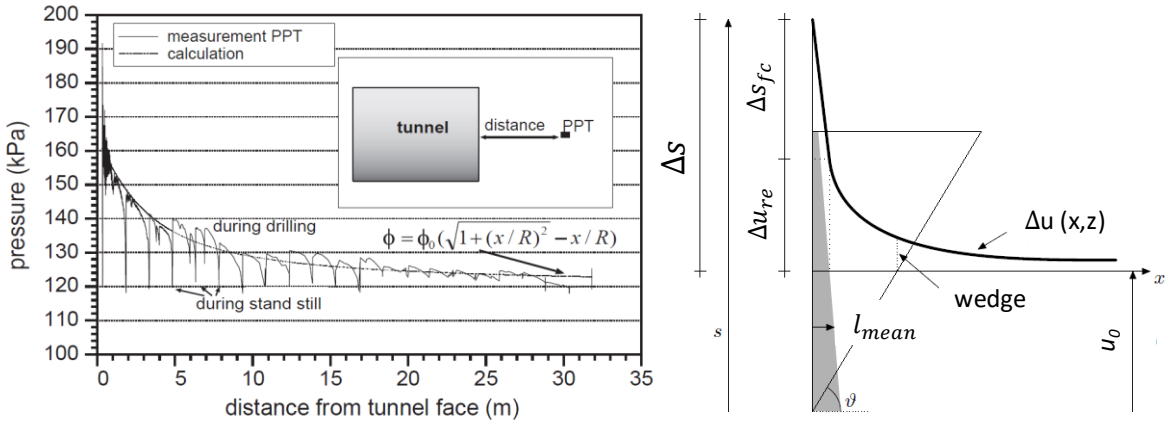

Figure 3-18 Left - Measurement of pore pressure heads in front of the shield and derived approximation of the excess pressure head distribution (Bezuijen et al. 2001), Right – pressure drop over the mean filter cake (Δs_{fc}) and resulting pore pressure head distribution (Δu(x,z)) acc. Broere & van Tol (2000)

The pressure transferred acc. to Bezuijen´s et al. theory (2001) is determined from a pressure gradient in front of the tunnel face. The gradient within this theory exclusively depends on the excavation radius and slurry excess pressure in the excavation chamber ($Eq.\,3\text{-}42$). Thus, the rheology of the employed slurry and the revolution per minute of the cutting wheel or penetration rate of the machine do not play any role here.

$$\boldsymbol{i_B = \phi \cdot \frac{1}{R}} \qquad Eq.\,3\text{-}42$$

with

i_B	Average hydraulic gradient at the tunnel face acc. to Bezuijen et al. (2001) [-]
ϕ	Slurry excess pressure in the excavation chamber [m]
R	Excavation radius – D/2 [m]

The transferred slurry pressure ($Eq.\,3\text{-}43$) is calculated as a difference between the pore pressure head in the excavation chamber and the pore pressure head at the distance from the tunnel face, which corresponds to the length of the sliding wedge at the tunnel axis. $Eq.\,3\text{-}41$ is used here to determine the pore pressure head at the intersection of the sliding wedge and the tunnel axis.

$$\boldsymbol{\Delta s_B = \left(\phi - \phi(l_{wedge})\right) \cdot \gamma_W} \qquad Eq.\,3\text{-}43$$

with

Δs_B	Support excess pressure transferred [kPa]
l_{wedge}	Length of the sliding wedge at the tunnel axis [m]
$\phi(l_{wedge})$	Slurry excess pressure at the distance corresponding to l_{wedge} [m]
γ_w	Unit weight of water [kN/m^3]

Kaalberg et al. (2014) developed $Eq.\,3\text{-}44$ to consider a certain pressure drop over the formed pressure transfer mechanism, filter cake or penetration zone at the tunnel face during excavation. For this purpose, they introduced parameter α ($Eq.\,3\text{-}44$).

$$\boldsymbol{\phi_0 = \phi \cdot \alpha} \qquad Eq.\,3\text{-}44$$

with

ϕ_0	Excess pore pressure at the interface between pressure transfer mechanism and pure soil [m]
ϕ	Slurry excess pressure in the excavation chamber [m]
α	Parameter for consideration of pressure transfer mechanism formation [-]

According to Bezuijen et al. (2016), the parameter α can either be less than or equal to 1. If this parameter is equal to 1, it denotes the absence of the formation of a pressure transfer mechanism during excavation, and the original equation ($Eq.\,3\text{-}41$) is obtained again. This additionally emphasizes that the globally observed penetration velocity of

slurry at the tunnel face is smaller than the advance rate of the shield (Bezuijen et al., 2016). Thus, the support pressure is transferred only due to flow pressure of slurry penetrating the soil. This is according to the authors, because no plastering occurs at the tunnel face (no plastering phase as described by Talmon et al, 2013). In contrast, if the parameter α decreases below 1, formation of the pressure transfer mechanism is possible. This enables the slurry penetration velocity to be higher than the excavation velocity of the shield. However, the higher velocity can only be observed at the start of the excavation, because after some excavation cycles the slurry penetration velocity becomes equal to the excavation velocity due to the yield point and viscosity of slurry (Bezuijen et al., 2016). The assumption of equal slurry penetration and excavation velocities enables the calculation of the parameter α ($Eq.\,3\text{-}45$). According to the authors, $Eq.\,3\text{-}45$ is valid only if $\alpha \leq 1$.

$$\boldsymbol{\alpha = \frac{n \cdot R \cdot v_{TBM}}{\phi \cdot k_{f,w}}} \qquad Eq.\,3\text{-}45$$

with

n	Porosity of soil [-]
ϕ	Slurry excess pressure in the excavation chamber [m]
$k_{f,w}$	Permeability of soil for water [m/s]
v_{TBM}	Advance rate of the shield [m/s]
R	Excavation radius of the shield [m]
α	Parameter for consideration of pressure transfer mechanism formation [-]

The inputting of $Eq.\,3\text{-}45$ into $Eq.\,3\text{-}44$ has an interesting implication. It delivers that the pore pressure at the interface between slurry penetrated zone and soil becomes independent from slurry excess pressure in the excavation chamber.

Broere & van Tol (2000) developed a different theory with the same aim to explain the increased groundwater heads during slurry shield excavations. In contrast to Bezuijen et al. (2001), it considers incomplete formation of the pressure transfer mechanism due to disturbance of the mechanism by cutting tools. The theory, however, does not distinguish calculation procedures for slurry penetration and filter cake formation. This theory homogenizes the formation state of the pressure transfer mechanism over the entire tunnel face, and adopts an existence of a “mean” filter cake. Hence, the slurry excess pressure drops only partly over the mean filter cake, and the rest transforms in the excess pore water pressure in front of the tunnel face (Figure 3-18-right). The

authors used for calculation of pore pressure heads in ground the storage theory of semi-confined aquifer. They concluded that the support pressure required to stabilize the tunnel face has to be increased, not as a consequence of the reduced slurry pressure transfer on the soil grains, but as a consequence of the excess pore water pressure to be counterbalanced.

In the calculation procedure, the theory of a mean filter cake uses a relationship experimentally obtained by Krause (1987) for the time-dependent slurry penetration distance (l_{mean}) in $Eq.\,3\text{-}46$. In contrast to Krause (1987), Broere & van Tol (2000) consider the parameter "b" in $Eq.\,3\text{-}46$ as the timespan, during which 50 % (l_E^* = 50 %) of the slurry penetration is reached.

$$\boldsymbol{l_{mean} = \frac{t_{min}}{b + t_{min}} \cdot l_{max,calc}} \qquad Eq.\,3\text{-}46$$

with

l_{mean}	Mean slurry penetration depth achieved during excavation [m]
b	The timespan during which 50% of upper penetration bound by Krause (1987) is reached, b = 1 min [min]
t_{min}	The timespan between subsequent removal of the filter cake [min]
$l_{max,calc}$	Slurry penetration depth acc. to *Eq. 3.27* with a =3.5 [m]

It is necessary to note that Broere & van Tol (2000) used the equation for maximal penetration depth of slurry ($Eq.\,3\text{-}27$), according to Kilchert & Karstedt (1984) in Krause´s equation ($Eq.\,3\text{-}33$) for the calculation of time-dependent penetration depth, as opposed to the 60-minute penetration depth that Krause (1987) proposed. Broere & van Tol (2000) subsequently linearized the dependence between the penetration distance of slurry and the pressure drop (Δs_{fc}) over the transfer mechanism ($Eq.\,3\text{-}47$).

$$\boldsymbol{\Delta s_{fc} = l_{mean} \cdot \frac{3.5 \cdot \tau_{f,s}}{d_{10}}} \qquad Eq.\,3\text{-}47$$

with

Δs_{fc}	Pressure transfer over the mean filter cake [kPa]
$\tau_{f,s}$	Yield point of slurry [kPa]
l_{mean}	Mean slurry penetration depth achieved during excavation [m]
d_{10}	Characteristic grain size of soil [m]

In linearizing, they state that, in contrast to Anagnostou & Kovári (1994), the pressure (stagnation) gradient remains constant during penetration and the transferred pressure depends only on the penetration distance. By adopting this approach and considering the pressure (stagnation) gradient as a solely static variable, they are neglecting the flow force which occurs during formation of the pressure transfer. The remaining part of the slurry excess pressure at the end of the mean pressure transfer mechanism is consequently causing the groundwater flow (Δu_{re}).

The model by Broere & van Tol (2000) assumes stationary groundwater flow in semi-confined aquifer. Therefore, according to the authors, the model is only valid for cases in which the equilibrium state can be achieved immediately after the start of the excavation. Broere & van Tol (2001) extended the theory for transient groundwater flow. Thus, the model enabled the calculation of transient formation and dissipation of the excess pore pressure. However, the fundamental characteristic of the model regarding the pressure transfer described by $Eq.\,3\text{-}47$ remained unchanged.

The theories of Bezuijen et al. (2016) and Broere & van Tol (2001) were compared by Xu & Bezuijen (2018). The authors showed that despite of different background of flow calculation, they deliver similar results.

3.5 Conclusion about state of the art of the slurry-soil interaction and the slurry pressure transfer

The volume of pore space of non-cohesive soils can be described on the macroscopic level by porosity. From the grain distribution curve of soil, information regarding their pore geometry can be obtained. However, no direct link exists between macroscopic porosity and the size of pores derived from a soil distribution curve. This brings up the first issue in slurry-soil interaction analysis. The second issue is the characterization of bentonite slurry properties during interaction. Characterization of physical properties of slurries is clear and unambiguous, while the determination of their rheological properties requires adopting a certain flow rule. Moreover, consideration of the slurry flow history is necessary (thixotropic behaviour).

The review of flow processes characterization in soil based on the theory of porous media showed that considering the physics on the pore scale is still complicated. It turned out to be reasonable to use “smeared” characterization, for instance, to employ

Darcy´s law. The permeability coefficient can, after certain adaptation, substantially characterize the pressure drop of slurry during flow within a porous media. The benefit offered by the Carman-Kozeny equation cannot be fully utilized for slurry-soil interaction due to the impossibility of exact consideration of a soil´s pore structure from its macroscopic properties. Consequently, due to inexact knowledge of the flow rate of slurry in pores, the shear stress between slurry and soil cannot be determined satisfactorily. An additional problem of handling the slurry-soil interaction as a bulk flow in porous media is that this approach does not take into account any change in the structure of the pores during the interaction. This change can be captured by approaches developed in chemistry for characterization of filtration processes. For the interaction of non-cohesive soils with slurry, it seems that complete blocking and filter cake filtrations are not likely (filter cake as defined in section 3.3). At the particle level, some pores of non-cohesive soils are always larger than some suspended slurry particles. Hence, intermediate filtration and deep bed filtration seem more probable. However, both basic filtration mechanisms may lead to the filter cake formation in later stages, when soil pores are modified by settled slurry particles. This highlights the necessity of considering the time factor within the interaction assessment. Additionally, the review showed that the size of the suspended particles further plays an important role in deep bed filtration. More abrupt change of a soil´s permeability coefficient is expected for larger suspended particles within comparably smaller pores. The review shows also that there is always some retention of suspended slurry particles during flow through the porous media. Numerous theories for pressure drop during suspension flow in porous media exist based on particle and bed grain interaction analysis. These theories require many experimentally determined constants. The determination of the constants is not trivial. Thus, they are not used in geotechnical engineering.

Two basic interaction mechanisms between slurry and soils are usually assumed in geotechnical engineering. The calculation of slurry excess pressure transfer is conducted with respect to these mechanisms. These models are the slurry filter cake model and the slurry penetration model (as considered in section 3.4), for which non-cohesive soils correspond with intermediate filtration and with deep bed filtration model (as considered in section 3.3), respectively. The two basic geotechnical models assume that the slurry excess pressure is immediately transferred in its entirety within the slurry penetrated area. Methods exist to describe the time-dependent penetration

behaviour of slurry. However, the methods do not sufficiently characterize various pressure transfer mechanisms during different formation stages of the mechanism. Finally, models considering the interaction of pressure transfer mechanism with cutting tools can be found in literature, however, these models adopt the interaction with tools in a homogenized way for the whole tunnel face. Thus, they are not able to take into account different local formation stages of the pressure transfer mechanism during excavation, which are believed to be of relevance for the entire process. Furthermore, the methods do not provide a direct link between excavation settings of the machine and between soil and slurry properties and the pressure transfer.

Krause (1987), Broere & von Tol (2000), Bezuijen et al. (2001) on one side and Anagnostou & Kovári (1994) and Kilchert & Karstedt (1984) on the other have noted essential discrepancies between theories on support pressure transfer during excavation. Three questions result from the discrepancies:

- Does the pressure (stagnation) gradient change during the slurry penetration process?
- What might be the source of the eventually reduced amount of transferred slurry excess pressure?
- Are there any dependencies on the excavation process?

4. THEORETICAL CONSIDERATIONS CONCERNING THE ADAPTATIONS OF PRESSURE TRANSFER MODELS

The formation of the pressure transfer mechanism is a successive process requiring a certain timespan as demonstrated in section 3.4.2. During excavation, however, the soil on the face including the pressure transfer mechanism is periodically disturbed by the passing cutting tools (section 2.1.3). The necessity for formation of the pressure transfer mechanism to stabilize the tunnel face can be demonstrated in an example from practice referenced by Anheuser (1989) and also Jancsecz & Steiner (1994). According to the authors, stability problems with a slurry supported tunnel face were reported during excavations through ground with water-saturated sand or gravel lenses. The problems occurred when the surrounding ground was less permeable than the saturated lenses. These lenses could not be supported by slurry. The reason for not stabilizing these lenses is obviously impossible formation of the pressure transfer mechanism. The impossibility of formation was caused due to the impossibility of water outflow from the lenses into less permeable surrounding ground, which would enable slurry infiltration at the tunnel face. This very well-known example from practice has interesting implications:

- Flow of liquid in front of the tunnel face is necessary for the establishment of the pressure transfer mechanism. When a formed pressure transfer mechanism is damaged by cutting tools, the flow is also required for the re-establishment.
- Due to continuous damage and re-establishment of the pressure transfer mechanism, the slurry shield can be considered an additional source of liquid causing flow in the ground

The flow of liquid in front of the tunnel face will inevitably cause increased pore water pressure. Bezuijen et al. (2001) reported that the increased pore pressures are observable only during excavation stage and not during ring building stage

(section 3.4.3). Hence, the measurements confirm that a considerable flow appears only when the pressure transfer mechanism is disturbed by cutting tools and has to rebuild. Furthermore, Broere & van Tol (2001) expect that a larger amount of support fluid enters the soil only just after the pressure transfer mechanism is removed. Due to the lack of disturbance of the pressure transfer mechanism in diaphragm wall technology (section 3.4.1) and assumption of its full development, increased pore pressures are not expected in these models. Hereby, the decisive influence of the cutting process on the increased pore pressures in soil is displayed.

The frequency of damage depends on the actual revolutions per minute (RPM) of the cutting wheel and on the arrangement of cutting tools (See chapter 5). When a cutting tool has passed through a particular point (Figure 4-1), the pressure transfer mechanism is partly or even completely damaged, and has to be formed again. The amount of damage depends on the penetration depth of the slurry compared to the tool cutting depth per passing. Hence, the movement of a cutting tool within a concentric cutting track causes an instantaneously heterogeneous “formation state” of the transfer mechanism within the track (Figure 4-1). The whole process results in a heterogeneous “formation state” of the pressure transfer mechanism over the entire face in every moment during excavation due to offset of cutting tools in different tracks.

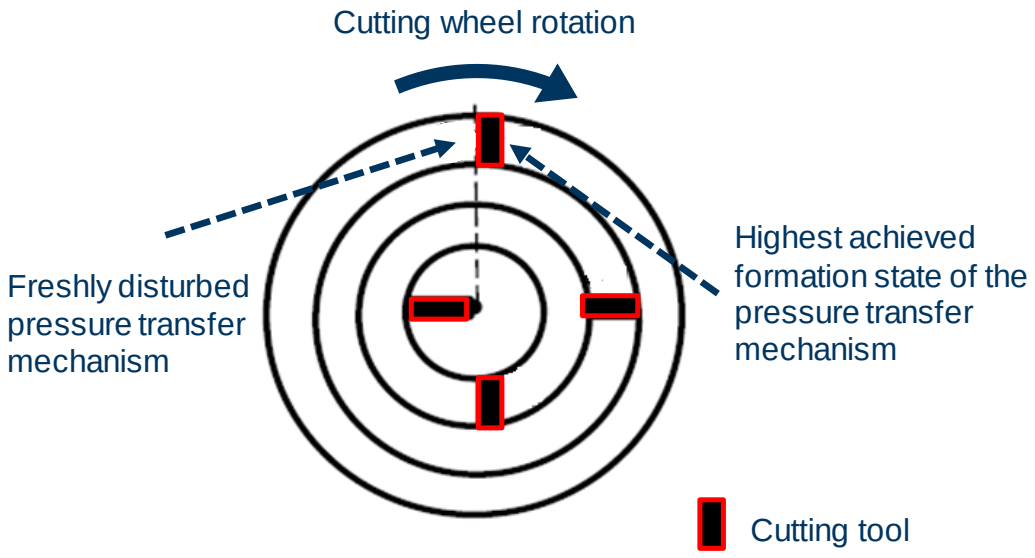

Figure 4-1: Disturbances of the pressure transfer mechanism by cutting tools (Schoesser & Schanz, 2014)

Generally, two cases may be obtained, which predetermine the heterogeneity of the formation state and influence the pressure transfer. Case A and Case B are derived from the comparison of slurry penetration scale and tool penetration scale (Figure 4-2). Similar considerations have been presented by Wehrmeyer (2000) regarding the cutting process while analysing muck composition for the purposes of excavation control. Both boundary cases A and B are discussed in detail in the following sections.

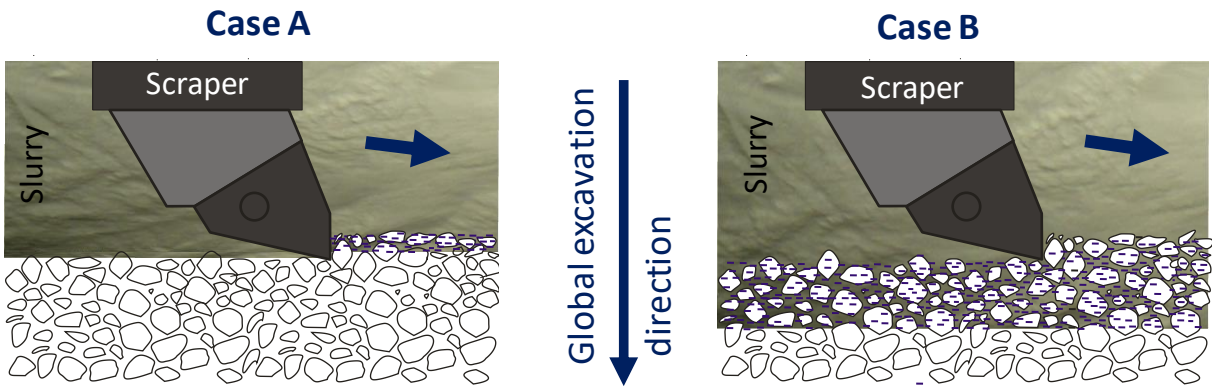

Figure 4-2: Two theoretically possible cases at the slurry supported tunnel face – Case A and Case B (Zizka et al., 2017)

4.1 Case A - Tool penetration deeper than pressure transfer mechanism

In Case A, the cutting depth of a single tool is deeper than the depth of slurry penetrated soil, when observed locally. In contrast, it seems that the average primary slurry penetration velocity is lower than the advance rate of the shield, when observed globally. The average penetration velocity is considered for the timespan of one excavation cycle. Case A results in a periodic removal of the entire pressure transfer mechanism with every pass of the cutting tool. Due to the entire removal of the pressure transfer mechanism, abrupt changes in the reaction occur when a tool passes. This causes transient local pressure gradients, which are highest at a particular point on the tunnel face just before a cutting tool passes through this point, because the pressure transfer mechanism achieves here its highest formation state (Figure 4-1). When a tool passes, the gradient causes flow of slurry and decreases. The abrupt change of the conditions at the particular point when a tool passes results in a more heterogeneous pressure transfer mechanism, relative to Case B.

The heterogeneous state of formation of the mechanism within the tunnel face implies that the slurry excess pressure is being transferred during excavation according to one of the three following modes depending on the actual formation state of the pressure transfer mechanism (compare with mechanisms responsible for slurry stagnation referenced by Talmon et al. (2013) in section 3.4.2). The modes of slurry excess pressure transfer are:

- ***Flow pressure*** – in areas where the soil including pressure transfer mechanism is freshly cut, comparable to pressure transfer suggested by Bezuijen et al. (2001)
- ***Pressure drop over the partially formed pressure transfer mechanism and flow pressure*** – in areas where the pressure transfer mechanism is still forming and has not yet been completely formed, comparable to pressure transfer suggested by Broere & van Tol (2000)
- ***Pressure drop over the fully formed pressure transfer mechanism*** – in areas where the mechanism is almost completely developed, corresponds to the transfer suggested by Kilchert & Karstedt (1984)

By all three modes, the entire slurry excess pressure is completely transferred on the soil skeleton, but in different grades of efficiency, to stabilize the tunnel face. As pointed out by Anagnostou & Kovári (1994), the slurry excess pressure transfer is only efficient for face support if it occurs within the stabilized soil wedge (section 2.4.1). On one hand, it can be expected that the slurry excess pressure would be transferred by flow within the largest distance (Figure 4-3), so it is likely to be the least efficient mode of transfer. On the other hand, if the pressure transfer mechanism is completely formed, the efficiency would be the highest. The efficiency of all three modes of the pressure transfer can be characterized by resistance against flow of slurry. In the case of flow pressure mode, the resistance is the lowest because the pore space of soil is not yet modified by interaction with slurry (section 3.3.1). After the full formation of pressure transfer mechanism, the resistance is considerably increased due to modified pore space. Thus, the flow becomes negligible.

In section 3.2, frameworks for description of flow processes in porous media, including the resistance against flow, are reviewed. It turns out that the most reasonable is to use the Darcy´s law, because there is no need to assess the slurry soil interaction on the micro level (section 3.5). In the case of Darcy´s law, the resistance against slurry flow is expressible by a single variable. Moreover, this single variable (permeability coefficient) is directly determinable from experiments.

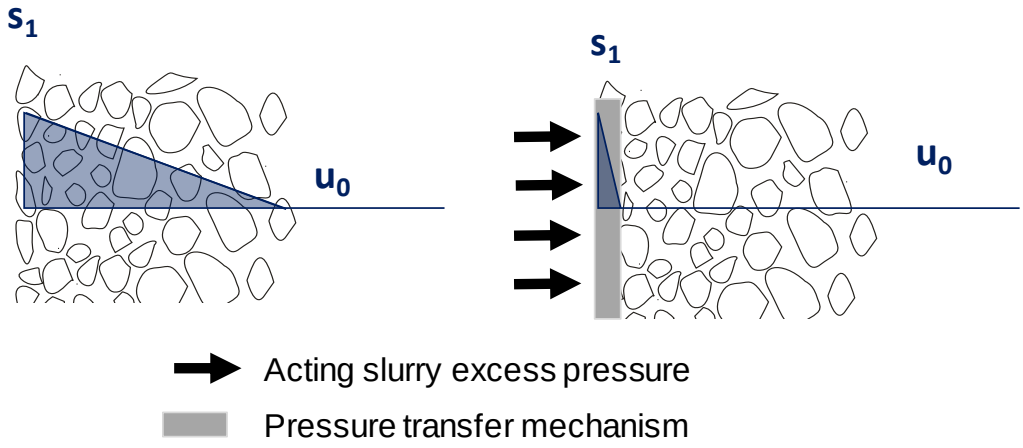

Figure 4-3: Two boundary ways of pressure transfer causing different pressure drop – Left by flow pressure and right by formed pressure transfer mechanism, s_1 = slurry pressure in the excavation chamber and u_0 = far field hydrostatic pore pressure

Based on the discussion in section 3.2.1, however, Darcy's law seems not to be applicable for the characterization of slurry and soil interaction without certain adaptation. The main reason is the expected time-dependent and nonlinear relationship between intrinsic permeability (K) and the permeability coefficient (k_f) ($Eq.3\text{-}11$). While the time-dependency may result from successive changes of the soil´s pore space by slurry particles, the non-linearity can be caused by the flow-rate dependent viscosity of bentonite slurries, as referenced e.g. in Longchamp et al. (2005). Note that the density change of the fluid during the interaction process will have a negligible influence non-linearity in ($Eq.3\text{-}11$), since the difference of density between water and fresh slurry density is only approx. 3 % (Zizka et al., 2017).

Nevertheless, the coefficient of permeability (k_f) can be directly determined time-dependently from experiments as an instantaneous relationship between pressure gradient and discharge ($Eq.4\text{-}1$) within very small time-steps. The porosity of soil is assumed to be constant in $Eq.4\text{-}1$. Hence, the entire change of hydraulic resistance of soil during interaction with slurry is expressed by the permeability coefficient and its development.

$$k_f(t) = \frac{Q(t)}{A_{cyl}} \cdot n_p \cdot \frac{\Delta L}{\Delta h(t)} \qquad Eq.\,4\text{-}1$$

with

$Q(t)$	Time dependant discharge [m³/s]
A_{cyl}	Cross-sectional area of the flow [m²]
ΔL	Macroscopic flow path [m]
$k_f(t)$	Time-dependent coefficient of permeability [m/s]
$\Delta h(t)$	Measured time-dependent pressure difference in the set-up [m]
n_p	Porosity [-]

The spatial distribution of the permeability coefficient at the tunnel face depends on the comparison between slurry and the tool penetration scale (section 6.4). Due to expected comparably shallow slurry penetration depth in Case A, it is not essential for the face stability assessment to evaluate pressure transfer along the slurry penetration depth. The slurry penetration depth will be always smaller than the dimensions of the soils wedge that is to be stabilized. Hence, the permeability coefficient development of the transfer mechanism can be used as a single variable for characterization. The

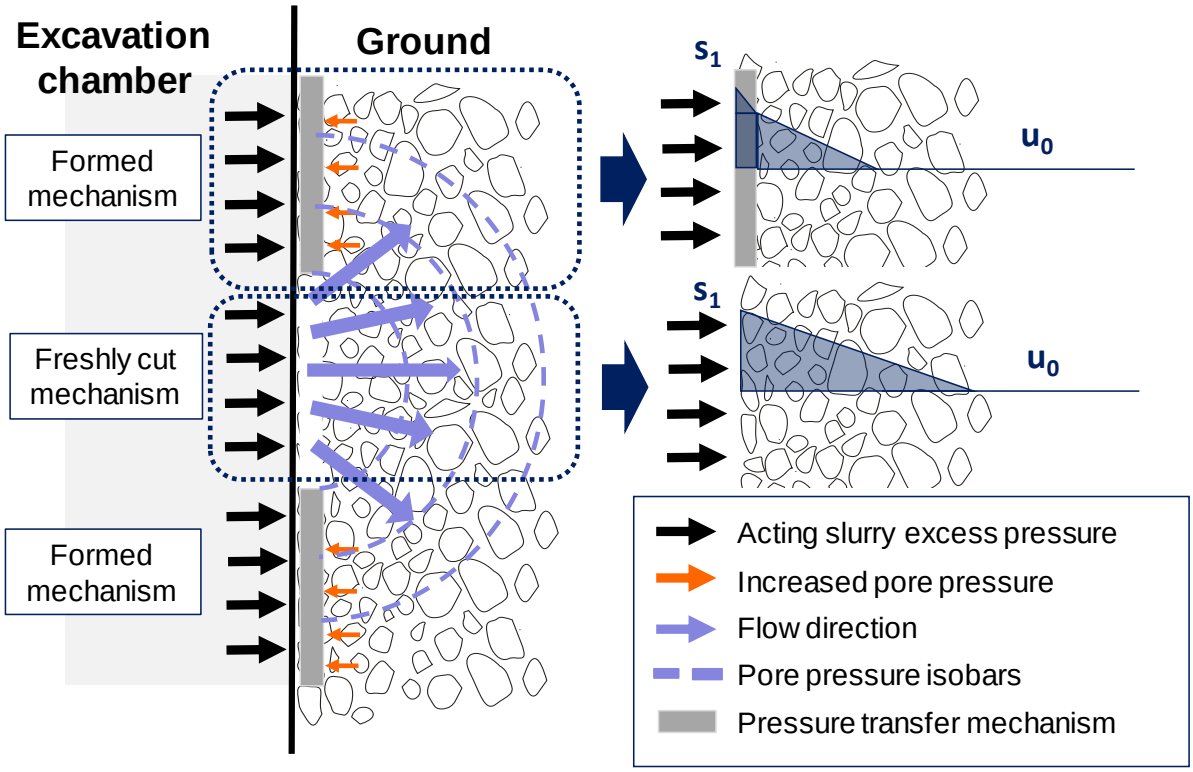

Figure 4-4: Mutual influence of adjacent cutting tracks and consequent reduction of the efficiency of the pressure transfer mechanism. s_1 = slurry pressure in excavation chamber and u_0 = far field hydrostatic pore pressure

development of permeability coefficient will be investigated experimentally in chapter 6 of this thesis.

It is expected that mutual influencing of concentric cutting tracks is a significant factor for the face stability in Case A of pressure transfer (Figure 4-4). It is expected that the areas with the flow mode of transfer will influence the adjacent areas with formed pressure transfer mechanism. The flow will increase pore pressure behind the pressure transfer mechanism in these areas. This will decrease the efficiency of the pressure transfer for areas with formed pressure transfer mechanism. It seems impossible to investigate this influence experimentally in the lab. Hence, the mutual influence has to be numerically simulated.

The simulation will be conducted in chapter 8. For the purpose of the simulation heterogeneous pressure transfer model (HPT model) is introduced and implemented in numerical seepage analysis. This model will enable to consider not only the all the described modes of the pressure transfer simultaneously, but will make possible take into account the mutual influence of concentric cutting tracks. Furthermore, the evaluation of the numerical model will be used to check the adopted pressure gradient in the experiments for investigation of the time-dependent permeability coefficient.

4.2 Case B - Tool penetration shallower than pressure transfer mechanism

In Case B, the cutting depth of a single tool is shallower than the depth of slurry penetrated soil, when observed locally (Figure 4-2). In contrast, it seems that the average primary slurry penetration velocity is faster than the advance rate of the shield, when observed globally. Case B results in a partial removal of the pressure transfer mechanism with every pass of the cutting tool. Due to the only partial removal of the pressure transfer mechanism, the occurring change in the reactions is comparably less abrupt than in Case A. Thus, lower grade of heterogenity of the pressure transfer mechanism can be observed within a cutting track and consequently on the entire tunnel face. It can be derived that the pressure transfer will take place by pressure drop over the partially or fully formed pressure transfer mechanism and never by a sole flow pressure. It can be here again expected that the entire slurry excess pressure will be transferred, as the equilibrium condition requires. Considering the

efficiency of the pressure transfer, it is equally important as in Case A that the transfer occurs within the soil wedge.

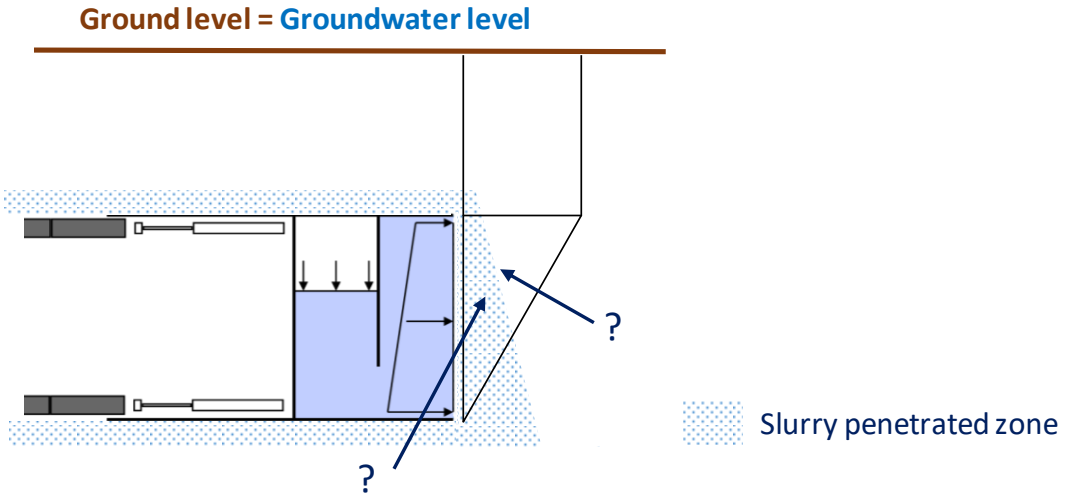

Figure 4-5: Fundamental question of the Case B pressure transfer: Occurs the transfer mostly inside or outside of slurry penetrated zone?

The fundamental question in Case B of pressure transfer is the ratio of pressure transferred inside and outside of slurry penetrated zone (Figure 4-5). Classic theories expect (see chapter 3) that the transfer occurs entirely within the slurry penetrated zone for Type II pressure transfer. The gradient of slurry pressure within this zone is believed to be constant. Note that, because of the definition of Case B, Type I pressure transfer is irrelevant in this case. However, the classic theories do not consider the origin of the pressure transfer zone establishment during excavation and its consequences for the pressure transfer.

The first insight (section 3.4.2), was suggested by Anagnostou & Kovári (1994), although they did not include a thorough discussion concerning establishment of this zone. They propose that the infiltration of slurry takes place simultaneously with the removal of ground during excavation leading to a “quasi-steady state” after some excavation cycles (Figure 4-6). The quasi steady-state requires that global average slurry penetration velocity becomes equal to advance rate of the machine. This is also assumed by Bezuijen et al. (2016). According to Anagnostou & Kovári (1994), the quasi-steady state is reached either from point (a) or point (b) in Figure 4-6. From point (a), when the average **slurry flow velocity is first lower than the advance rate**, the penetration distance will be gradually reduced and point (a) will move on the curve **towards the left and up**. In contrast, when the average infiltration velocity at some

particular time is **higher than the advance rate (b)**, the **penetration distance will increase over the course of ti**me and, consequently, the **average infiltration velocity will decrease**.

Due to the definition of Case B, however, the average primary slurry penetration needs to first be faster than the excavation, because otherwise Case A would appear. The requirement results in deeper slurry penetration than tool penetration during one cycle. Hence, the point (b) from Figure 4-6 would be relevant for the Case B. However, maximal slurry penetration (l_{max}) has to be assumed at the same time, when excavation starts. This penetration depth corresponds to the slurry penetration depth of Type II pressure transfer expected in diaphragm wall technology (section 3.4.1). Thus, this slurry penetration depth cannot be further increased physically in order to decrease the flow velocity of slurry. Consequently, a question appears how the quasi-steady state could be achieved in Case B.

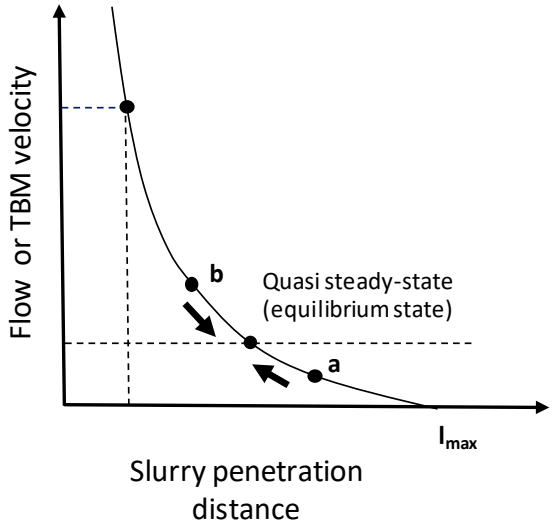

Figure 4-6: Relationship between slurry penetration distance and slurry flow velocity, excavation advance rate is equal to the slurry flow velocity at quasi-steady state (Anagnostou & Kovari, 1994)

It is necessary to introduce the slurry re-penetration concept. Re-penetration is the process in which slurry penetrates the pore space of soil that already contain slurry fluid (including particles) from the previous excavation cycle. Due to the already present slurry particles in the skeleton, it is expected that re-penetration results in a shallower depth compared to primary penetration. The re-penetration concept is the only concept that can justify why the thickness of slurry penetrated zone decreases simultaneously with average penetration velocity during excavation (Figure 4-6) and

why the equilibrium state (quasi steady state) appears. This happens during excavation despite the fact that, during primary penetration, the average slurry flow's velocity is faster than the advance rate of the machine.

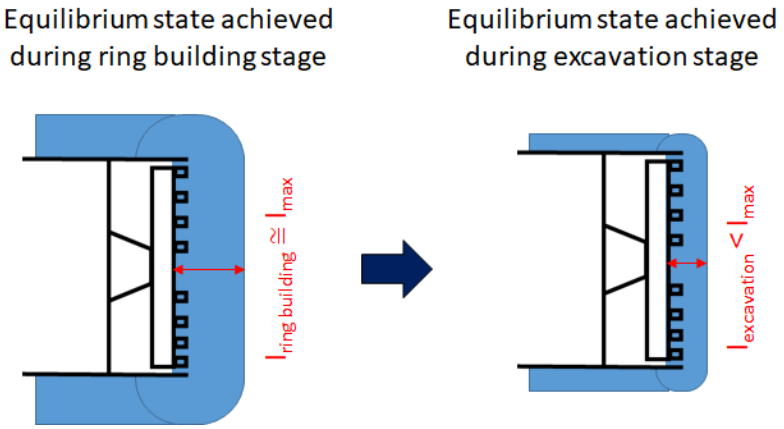

Figure 4-7: Two boundary cases observable: Equilibrium state without excavation (Left) and equilibrium state during excavation (Right)

When introducing the re-penetration concept, it is necessary to have a closer look at the initial state of the pressure transfer mechanism before excavation starts. The initial state can be described by a pressure gradient (slurry pressure drop), which is measurable as an excess pore pressure distribution. In general, three options theoretically are possible (Figure 4-8). While options 1) and 2) are expectable and also suggested by other authors (Müller-Kirchenbauer, 1972 and Krause, 1986), option 3) seems unrealistic due to the impossibility of a correlation with any basic filtration mechanism in section 3.3.1. Therefore, only options 1) and 2) will be further discussed in regard to the process of achieving an equilibrium state during excavation when starting from the approximately final slurry penetration depth achieved during the ring-building stage.

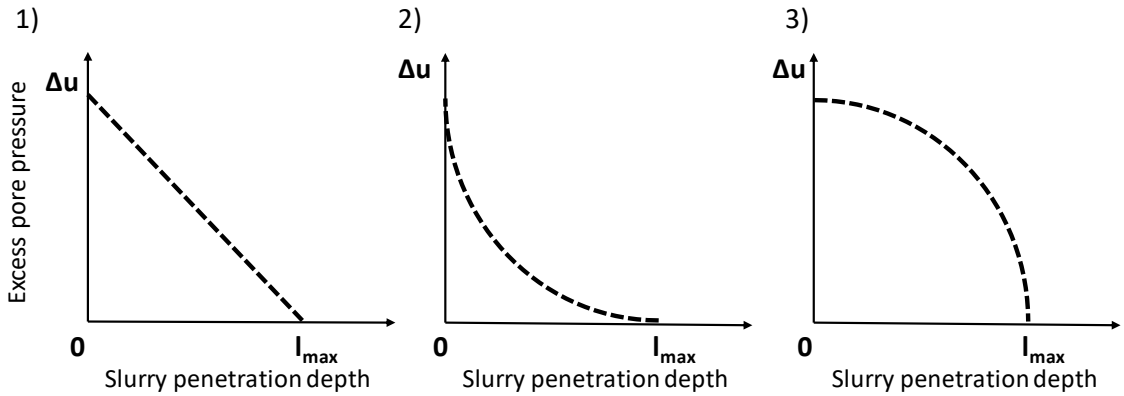

Figure 4-8: Theoretically possible drops of pore pressure within slurry penetrated zone

The mechanism for Case B-1, assuming linear distribution of pore pressure 1), is shown in Figure 4-9. Note that the rotating cutting wheel is adopted in the figure. Thickness of the slurry penetrated zone at the start of the excavation (at the end of the ring building phase) corresponds to the slurry penetration depth during primary penetration. When the excavation starts, the thickness of this zone decreases with every cutting cycle, because the slurry is at first unable to re-penetrate the same thickness as the tools are removing. With ongoing reduction of thickness of slurry penetrated zone, the ratio between slurry penetrated distance and tool cutting distance within one excavation cycle is successively increasing. When the ratio becomes 1, the equilibrium state during excavation is achieved. The equilibrium state corresponds to the quasi steady-state by Anagnostou & Kovári (1994).

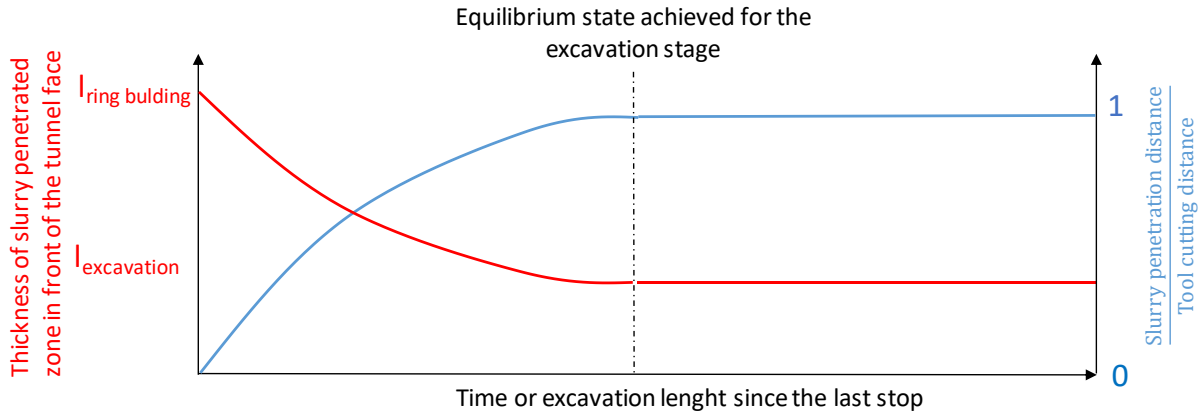

Figure 4-9: Case B-1 for reaching equilibrium state of the pressure transfer mechanism during excavation, considering the option 1) from Fig. 4-8

A different mechanism appears when the distribution of pore pressure within slurry penetrated zone corresponds to the option 2) from Figure 4-8. The mechanism for Case B-2 is shown in Figure 4-10. Note that the rotating cutting wheel is adopted. The thickness of the slurry penetrated zone at the start of the excavation corresponds again to the slurry penetration depth during primary penetration. However, when the excavation starts, the thickness of slurry penetrated zone starts to temporarily increase. The temporary increase is connected with slurry penetration depth larger than the tool cutting depth within one cycle. This is possible due to the higher pressure gradient close to the soil´s surface from the primary penetration. When this area is continuously disturbed by the cutting tools, deeper slurry penetration appears. However, after some excavation cycles, the thickness of slurry penetrated zone decreases and achieves the equilibrium state during excavation. This happens due to

the “reconstruction” of slurry penetrated zoned under impact of cutting tools. It is also necessary to point out that the slurry and soil interaction in Case B-2 cannot probably be viewed as a bulk flow of liquid through pores. The equilibrium state again corresponds to the quasi steady-state by Anagnostou & Kovári (1994).

The distribution of stresses inside and outside of slurry penetrated zone will be investigated in chapter 7. First, the focus will be given to pore pressure and effective stress distribution during primary slurry penetration. Consequently, the framework for a simulation of the re-penetration case in the lab will be presented and the stress distribution during re-penetration will be investigated. The numerical simulation of mutual influence of cutting tracks seems to be unnecessary in Case B, so the experimental result will be directly implemented in face stability assessment in chapter 9. For better face stability assessment, it is necessary to determine the self-bearing capacity of the soil wedge if only a reduced pressure transfer occurs inside the slurry penetrated zone.

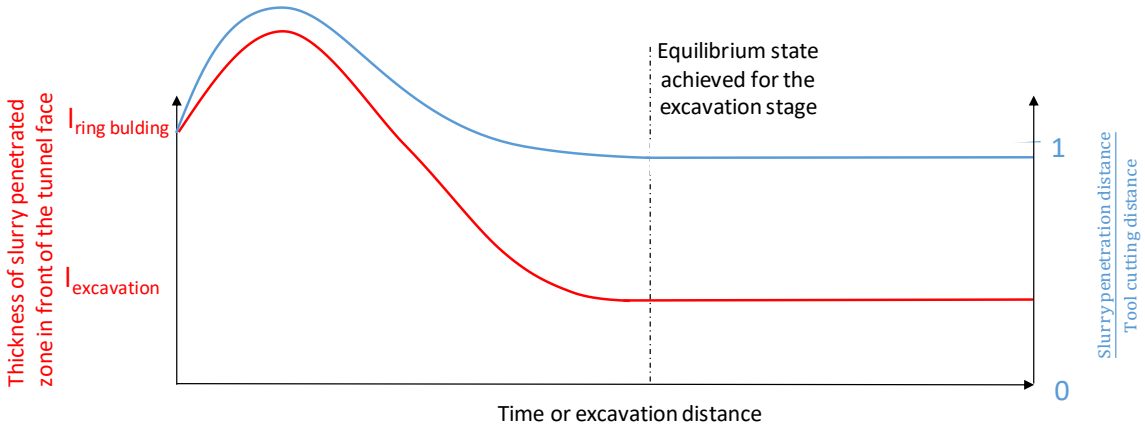

Figure 4-10: Case B-2 for reaching equilibrium state of the pressure transfer mechanism during excavation, considering option 2) from Fig. 4-8

5. ANALYSIS OF EXCAVATION SCALE

Chapter 5 is based on the paper: Thewes, M., Schoesser, B., Zizka, Z. (2016): Transient Face Support in Slurry Shield Tunnelling Due to Different Time Scales for Excavation Sequence of Cutting Tools and Penetration Time of Support Fluid. Proceedings of the ITA World Tunnel Congress 2016, San Francisco.

The interaction mechanisms of various cutting tools with soft soil on the tunnel face are different as already indicated in section 2.1.3. Within this chapter, the particular interaction types are analysed in detail. In literature, theoretical models can be found describing the cutting process (Köppl 2014, Rostami & Ozdemir 1993). The evaluation of the cutting process reported in literature focuses mostly on the interaction between cutting tools and the soil on the tunnel face as the wear prediction is the main focus of these models. The tool interaction with filter cake (Type I) or penetration zone (Type II) is usually not discussed.

The cutting mechanism of the disc in soft soil is shown in Figure 5-1. A cutting disc pushes a groove into the tunnel face while passing through a particular point. The groove is created by pushing and compacting of the soil. The soil is pushed in an axial and tangential direction to the disc penetration direction (Köppl, Thuro, Thewes 2015). Hence, it may be derived, that a disc is also not damaging the filter cake or slurry penetration zone. The type of disc action may lead only to compaction of the filter cake or of the penetration zone. A second type of tools is represented by rippers. The employment of rippers is not frequent in slurry shield tunnelling and therefore they are not considered here in detail. Buckets and scrapers, the last types of tools, are located slightly behind the discs on the cutting wheel in the longitudinal direction parallel to the machine axis. These tools are placed on one cutting-wheel-arm in pairs (tandems) to permit both rotation directions of the cutting wheel. Therefore, one tool of the tandem is always actively cutting and the second is passively moving without

significant cutting. In contrary to the disc cutters, the active scrapers and buckets are displacing the soil from the tunnel face (Figure 5-1), so that they are responsible for actual soil cutting within soft soil excavations (Köhler et al., 2011). The displaced soil is consequently collected by the cutting wheel arm and fed into the excavation chamber. Köppl (2014) expects that the cutting mechanisms of buckets is similar to the scrapers. The cutting process of an active scraper is illustrated in Figure 5-1 for non-cohesive soils. It may be assumed based on the cutting action of active scrapers and buckets, that they are damaging the pressure transfer mechanism. Thereby, they have much more significant influence on the slurry and ground interaction than disc tools (Thewes et al., 2016). Thus, only these tools will be considered in analysis of the excavation scale.

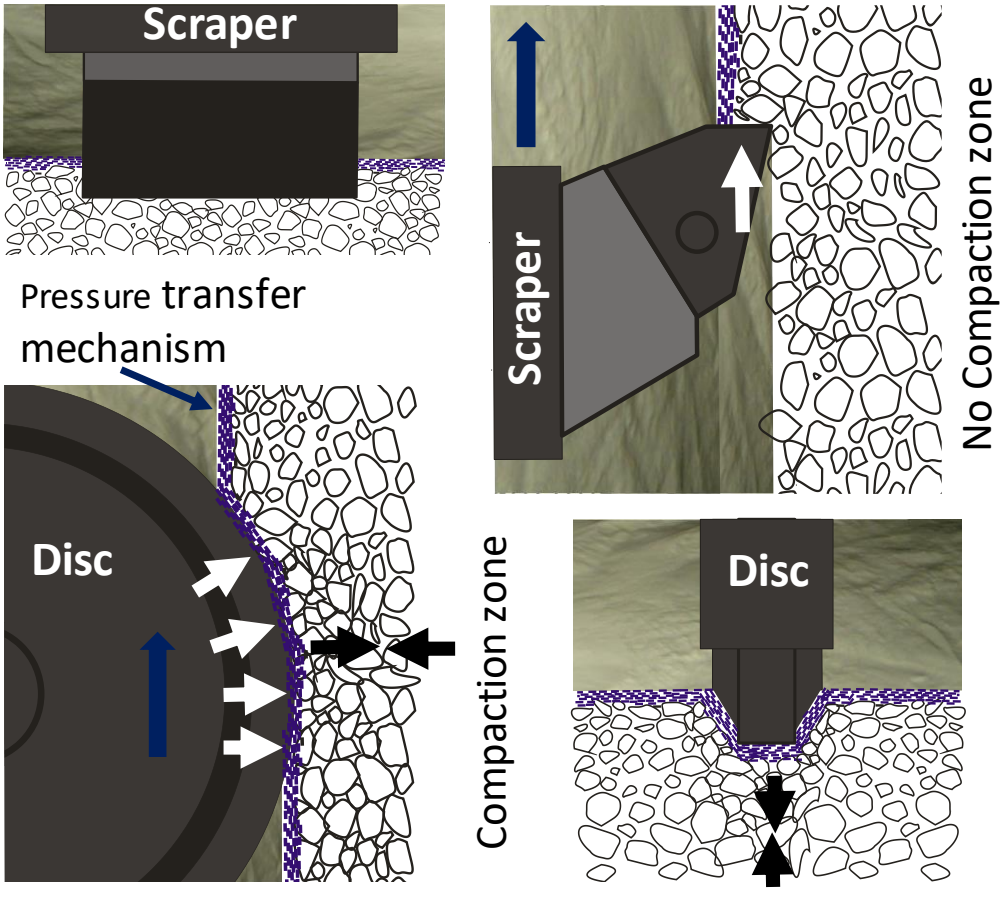

Figure 5-1: Interaction between cutting tools and a pressure transfer mechanism. The way of interaction is valid for both Type I and II from Table 3-4

Three reference slurry shield tunnelling projects (Table 5-1) are used here to characterize the excavation scale at the tunnel face. The projects were chosen with the

intention of having a similar excavation diameter and being conducted in similar ground conditions. The chosen projects were constructed during the two last decades.

Table 5-1: Outline of reference slurry shield projects used to determine the excavation scale

Project name	Shield diameter [m]	Ground type
P1	9.8	Sand / Clay
P2	9.8	Sand / Clay
P3	9.5	Sand / Gravel

5.1 Analysis of tool layout on cutting wheels

The cutting wheels of reference slurry shields are analysed based on the number of tools disturbing pressure transfer mechanism in one concentric cutting track. The analysis of cutting wheels demonstrates that each wheel can be divided in zones using this methodology (Figure 5-2). These zones can be recognized as homogeneous cutting zones due to the equal penetration depth of each tool passing and due to equal timespan between subsequent tool passing through one particular point within the zone. The particular zones are indicated with numbers in Figure 5-2.

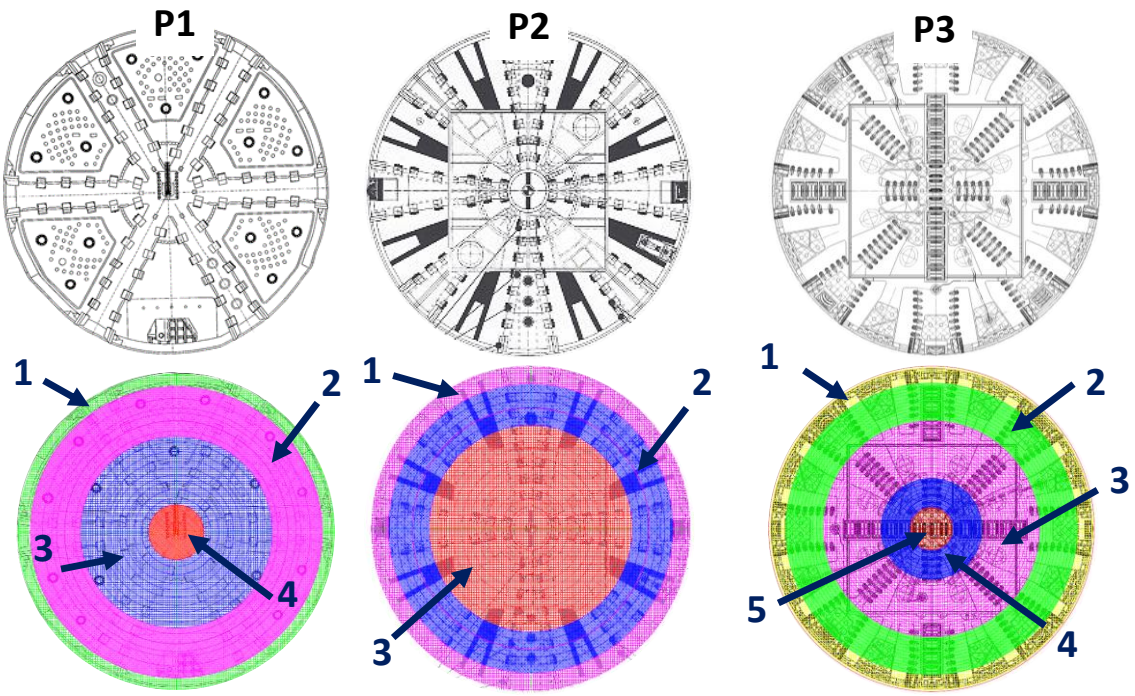

Figure 5-2: Cutting wheels of reference projects P1, P2 and P3 (up), division into homogeneous cutting zones including numbers of zones (down) (Zizka et al., 2018)

The resulting number of tools within one track is outlined in Table 5-2. The overlapping of tool tracks was determined only within one zone on the cutting wheel of the P1

shield machine. Furthermore, only disc cutters were found on the P3 wheel in zone 5. Therefore, no soil cutting is expected here and number 0 characterizes this zone in Table 5-2. A clear construction principle was found that the number of tools within one track depends on the distance to the centre of the cutting wheel. The highest number of tools is placed close to the circumference of the cutting wheel and decreases with the direction towards the cutting wheel centre.

Table 5-2: Division of cutting wheels into homogeneous zones, * denotes 2 active tools if their overlapping is taken into account

Number of the cutting zone	Amount of active tools within one track		
	P1	P2	P3
1	6	8	8
2	1 (2)*	4	4
3	2	2	2
4	1	/	1
5	No existence		0

The division of the wheels into zones and the number of tools (tandems) within one track obtained in this section will be used in the following analysis of penetration and time scale within excavation cycle.

5.2 Tool penetration and timespans between tool passes

A characterization of the excavation scale requires a coupling of timespan between tool passing and tool penetration. This can be done by an analysis of excavation data that are logged by every shield machine during tunnel advance. The revolution of cutting wheel per minute (*RPM*) and penetration of the cutting wheel per revolution (*PR*) belong to these data. While the RPM is logged directly, the penetration per revolution (*PR*) is calculated automatically from the RPM and the measured advance rate of the machine (*AR*) using $Eq.\,5\text{-}1$.

$$\boldsymbol{PR = \frac{AR}{RPM}} \qquad Eq.\,5\text{-}1$$

with

AR Advance rate of the machine [mm/min]

RPM Revolutions per minute of the cutting wheel [revolution/min]

PR Penetration of cutting wheel per revolution [mm/revolution]

RPM and PR are recorded as actual values or as average values per ring. For the later purpose of excavation scale characterization, it is more reasonable to take the average values into account to avoid infrequent peaks. However, neither PR nor RPM are conclusive for the determination of the excavation scale. The data have to be adapted to the basis of a single tool. For the adaptation, the three-dimensional movement of the single cutting tool fixed at the cutting wheel has to be considered. The cutting tool excavates the soil while the wheel is moving forward and rotating simultaneously. When these two basic moves are superimposed, a space helix arises (Figure 5-3). Every cutting tool located on the cutting wheel follows its own helix. Thus, every tool located within a particular cutting track cuts only a certain part of the whole wheel penetration (p_{wheel}) during one-wheel rotation. The size of the part depends on the number of tools in the cutting track ($Eq.\,5\text{-}2$).

$$\boldsymbol{p_{tool} = \frac{PR}{n_{tool}}} \qquad Eq.\,5\text{-}2$$

with

p_{tool}	Actual penetration of a single cutting tool per passing through a particular point
p_{wheel}	Penetration of cutting wheel per revolution
n_{tool}	Amount tool tandems within one track (offset in tandem locations between adjacent cutting tracks is neglected)

On a similar basis, the timespans between subsequent tool passes within one cutting track can be derived. These timespans define the period during which the pressure transfer mechanism may form without being disturbed by cutting tools. The timespan depends on the RPM of the cutting wheel and the amount of the tools within one cutting track ($Eq.\,5\text{-}3$).

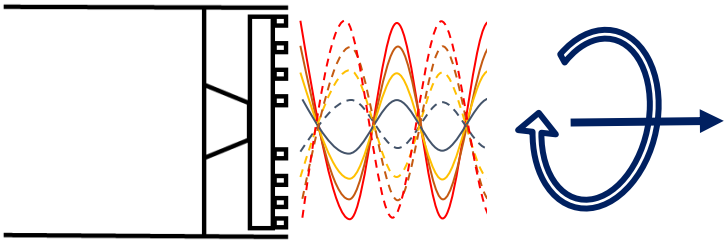

Figure 5-3: Every cutting tool traces a three-dimensional helix when the machine excavates a tunnel (Thewes et al., 2016)

$$t_{tool} = \frac{1}{RPM \cdot n_{tool}} \qquad Eq.\,5\text{-}3$$

with

t_{tool} Average timespan between subsequent passing of cutting tools
RPM Revolutions per minute of the cutting wheel
n_{tool} Amount tool tandems within one track

The raw excavation data (PR & RPM) from the reference projects were adapted according to described methodology and are visualized in Figure 5-4. The raw data were adapted for each homogeneous cutting zone of the particular shield machine separately. The same trend regarding the excavation sequence was observed among all three investigated projects. Obviously, the penetration of one tool per pass increases with increasing timespan between passes. Furthermore, linear trend lines are provided for each homogeneous cutting zone on each cutting wheel. The linear trend lines show within every particular assessed project equal inclination and are only slightly offset.

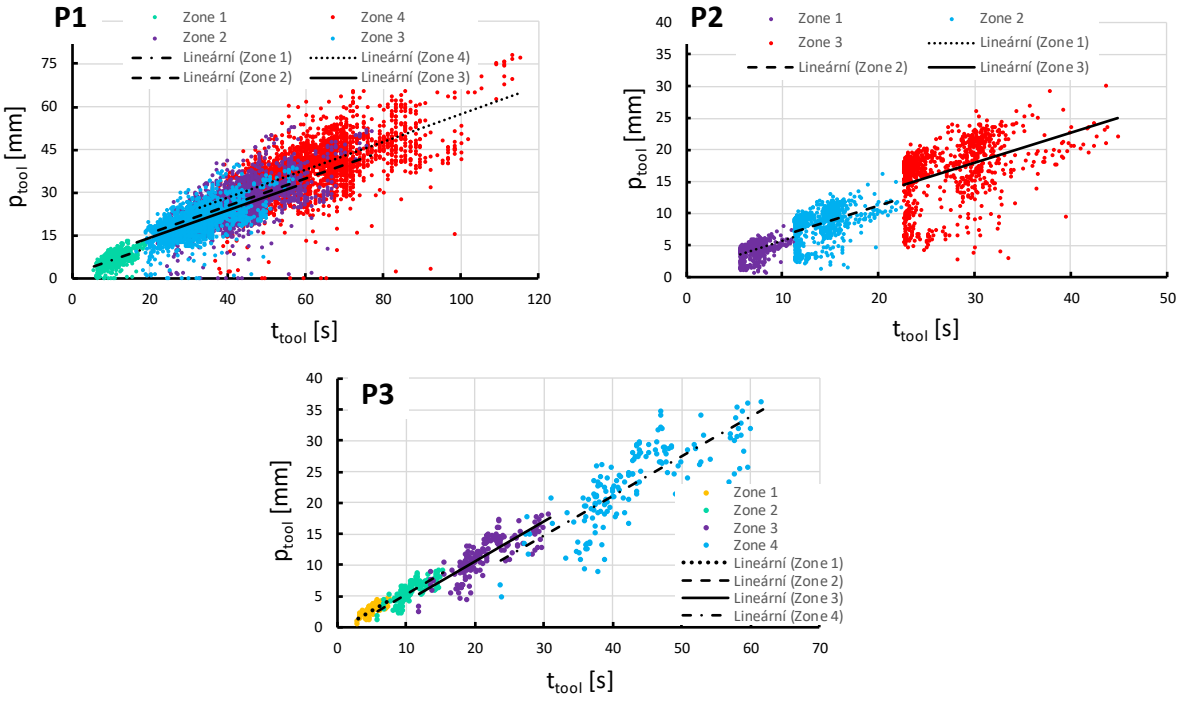

Figure 5-4: Coupling of penetration of one cutting tool with timespan between subsequent tools passing (different scale of the diagrams) (Thewes et al., 2016)

The trend lines are visualizing the coupling between a particular timespan and the typical penetration depth of a cutting tool. If the maximal and the minimal RPM logged during excavation of the reference shield machines are taken, the minimal and maximal timespans between tool passing can be calculated using $Eq.\,5\text{-}3$. According to the equations defining linear trend lines for each homogeneous cutting zone, the respective typical penetration depths of the single tools can be obtained. Hereby, the bounds for the excavation scale of reference projects could be defined (Table 5-3). Note that the minimal RPM is coupled with maximal PR and vice versa.

Table 5-3: Resulting excavation scales, *no scrapers disturbing the pressure transfer mechanism are located in this zone

Case study	Homoge-neous zone	Timespan between subsequent tool passing [s]		Typical tool penetration per passing [mm]		RPM [-]		PR [mm/rev]		AR [mm/min]	
		Max	Min	Max	Min	Min	Max	Max	Min	Min	Max
Project P1	Zone 1	18.9	6.3	12.9	5.3	0.6	1.6	69.3	31.6	41.6	50.5
	Zone 2	75.5	25	51.5	21						
	Zone 3	56.6	18.8	38.6	15.8						
	Zone 4	113.2	37.5	77.3	31.6						
Project P2	Zone 1	11.3	5.6	7.6	4.3	0.67	1.3	61	34.2	40.7	45.6
	Zone 2	22.5	11.3	15.2	8.6						
	Zone 3	45	22.5	30.5	17.1						
Project P3	Zone 1	7.8	3.4	3.8	1.4	0.96	2.2	30.2	11.1	29	24.4
	Zone 2	15.6	6.8	7.6	2.8						
	Zone 3	31.3	13.6	15.1	5.5						
	Zone 4	62.5	27.3	30.2	11.1						
	Zone 5	Infinity*		0	0						

6. EXPERIMENTAL INVESTIGATIONS: CASE A – SHALLOW SLURRY PENETRATION SCALE

Chapter 6 is based on the paper: Zizka, Z., Schoesser, B., Thewes, M. (2017): Excavation cycle dependent changes of hydraulic properties of granular soil at the tunnel face during slurry shield excavations", in: 9th International Symposium on Geotechnical Aspects of Underground Construction in Soft Ground, Sao Paulo.

Chapter 6 is dedicated to the analysis of the slurry penetration scale for Case A of interaction. First, the experimental set-up and the methodology of the experimental investigation will be introduced. The results will be presented in the following section and the whole chapter is finalized with the preliminary check regarding the relevance for the Case A. In other words, the experimentally determined slurry penetration scale will be superimposed with tool penetration as discussed in chapter 4. The aim of this chapter is to determine the time-dependent permeability coefficient of soil during slurry penetration in laboratory conditions. The transfer of the results to the tunnel face conditions will be conducted in chapter 8. Further aim of this chapter is to assess the influence of back-pressure on the development of the permeability coefficient.

6.1 Experimental set-up & methodology

The experimental device aims to investigate Case A slurry-soil interaction for local flow gradients at the tunnel face. These gradients appear in Case A at the tunnel face, when the entire pressure transfer mechanism is suddenly cut by a passing tool. Hence, the hydraulic changes of soil due to the interaction with slurry occur only within very small

distance in front of the tunnel face in a limited area of the tunnel face close to a cutting tool. A first approximation for the investigation assuming equal action of the same slurry excess pressure at the tunnel face and in the experiment was considered here. The suitability of this assumption will be checked in chapter 8 by numerical simulation.

In literature, set-ups for investigation of transient slurry penetration are referenced (Krause, 1986, Talmon et al., 2013 and Xu et al., 2017). In the referenced set-ups with different geometry, the slurry is injected from the top of the soil cylinder, while simultaneously supplying the top of the cylinder with compressed air (Figure 6-1). This construction of the set-up leads to generation and overestimation of excess pore pressures in soil sample, due to combination of two conditions. The first condition is characterized by the presence of fluid in the bottom drain line in comparison to presence of a gas in the supply line, which causes significantly higher flow resistance at the outflow while allowing large volume of gas enter the set-up at the inflow. The second condition is the flow stream narrowing at the outflow from all pores of the soil sample into the bottom drain-pipe. The narrowing condition brings comparably larger hydraulic resistance of the sample against flow, which may be even larger in some cases than hydraulic resistance of pore water flow within the body of surrounding soil due to much smaller cross-sectional flow area. The combination of the two conditions influences the development of the permeability coefficient due to slow dissipation of the excess pore pressure in the sample. To enable experimental modelling of local pressure gradients at the tunnel face, a different construction was chosen here.

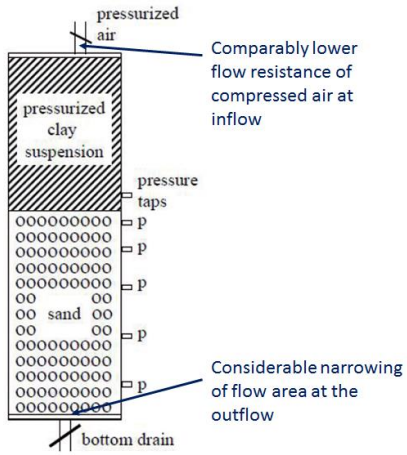

Figure 6-1: Experimental set-up for the investigation of transient slurry penetration (Talmon et al., 2013 - comments added)

Furthermore, experiments to illustrate the influence of hydraulic boundary conditions are described and conducted in chapter 7.

The developed experimental set-up was designed based on the device described in DIN 18130-1 (1998) for the investigation of water permeability of soils and can be designated as a column test. The experimental set-up is visualized in Figure 6-2 and extensively described in the appendix. The set-up consists of a slurry cylinder, a soil cylinder with 20 cm inside diameter and a reservoir with free surface for the discharged fluid from the soil cylinder. The reservoir is located on a scale. Alternatively, the outflow from the soil cylinder occurs into a pressurized water cylinder with adjusted back-pressure (the set-up is visualized in the appendix), which is located also on a scale. The scale is in both cases connected to a computer for continuous data logging during the experiment. Pore pressure sensors continuously monitor pressures in the slurry and soil cylinder. The data were logged every 0.25 s.

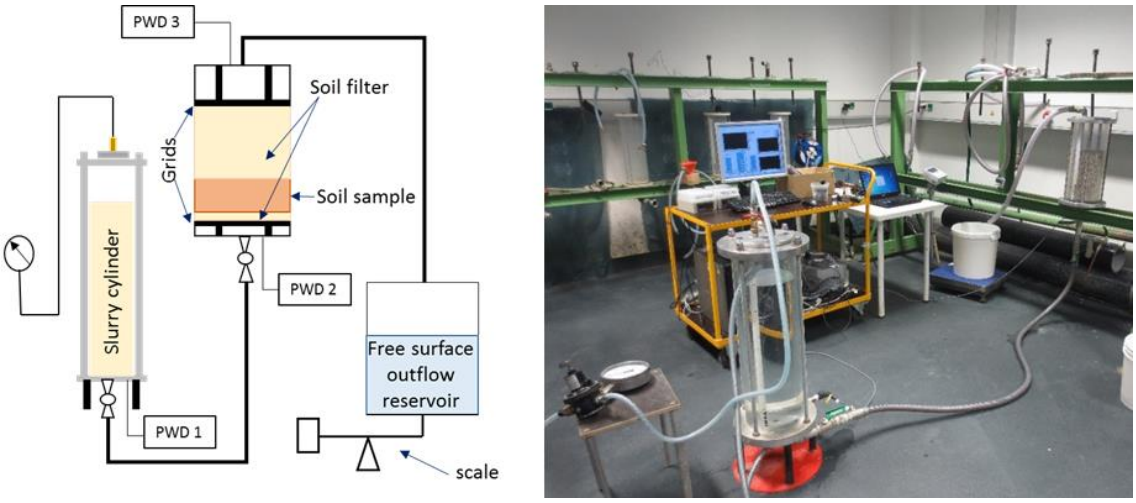

Figure 6-2: Experimental set-up for the investigation of the Case A (Zizka et al., 2017)

In the developed set-up (Figure 6-2), two soil filters and two stiff plastic grids stabilize the soil sample, which is compacted to a prescribed ratio (porosity n ≈ 0.4) and has thickness of 10 cm. The requirements for the soil filters were adopted based on DIN 18130-1 (1998) taking into account the requirements for filters by Terzaghi & Jelinek (1954). Thus, the filters have a significantly higher permeability coefficient and therefore do not influence the flow significantly. The thickness of the bottom filter was reduced to 2.5 cm to minimize its influence on the slurry penetration behaviour. Contrary to the bottom filter, the thickness of the upper filter was adopted to 17.5 cm. Furthermore, the aim of the bottom grid is to ensure uniform distribution of slurry in

the cylinder before entering the soil pores. The details about the used filters and grids can be found in the appendix. Hence, the permeability coefficient of the 10 cm thick soil sample is obtained by the presented device.

First, the experimental set-up is completely saturated with water (incl. also outflow pipe). Before the experiment starts, the injection pressure is adjusted, and the slurry is pumped under limited flow rate regulated by a valve in the soil cylinder up to the bottom interface between the filter soil and the soil sample. The experiment starts immediately after the dissipation of eventually occurring excess pressure from the previous procedure. It means that after the start of the experiment, slurry enters the soil cylinder with overpressure and first has to establish excess pressure there. The author assumes that this is the most realistic way to physically simulate slurry penetration at the tunnel face. 15 minutes were chosen as a limiting time span for the experiment duration.

The original intention was to assess the time-dependent slurry penetration depth in the soil sample visually. However, this turned out to be difficult due to very shallow penetration depths (section 6.3). Therefore, only the final penetration depth was determined directly visually during disassembling of the set-up and subsequently, the time-dependent penetration was obtained based on scaling of the final penetration by the time-dependent volume discharge of the fluid from the experiment measured by the scale ($Eq.\,6\text{-}1$).

$$\boldsymbol{l(t) = l_{max} \cdot \frac{V(t)}{V_{max}}} \qquad Eq.\,6\text{-}1$$

with

$l(t)$ Time-dependent slurry penetration depth (m)
l_{max} Final penetration depth (m)
$V(t)$ Volume of discharged fluid at time t (m^3)
V_{max} Volume of the discharged fluid at the end of experiment (m^3)

If the slurry penetration depth were to only be defined by the volume of discharged water and the porosity of compacted soil, an inaccuracy will be included. This inaccuracy was mentioned by Krause (1987). He stated that using this approach, the filtrated water, i.e., the amount of slurry from which the slurry particles were filtered out, would unrealistically increase the slurry penetration depth. Thus, using the

combined approach of visual determination and outflow scaling, as described above, improves the accuracy of the results.

6.2 Experimental programme and materials

The experimental program (Table 6-1) was designed with the aim of investigating the Case A interaction, which expects a shallow slurry penetration depth for local pressure gradients. Two slurry concentrations, two soil fractions and three levels of injection pressure were chosen. The chosen injection pressures correspond to a realistic range of slurry excess pressure at a real slurry shield. Additionally, the influence of back-pressure was tested. The back pressure was adopted in a way that pressured difference was the same as in the basic experiments. The experimental program resulted in eleven combinations. Three experimental runs for each combination were carried out in order to guarantee the reproducibility of the results (two runs with back-pressure). The reason for performing less experimental runs with back-pressure is discussed in section 6.3.2. 30 experiments were performed in total. Medium and coarse uniformly graded sands with relatively small characteristic grain size (d_{10}) were chosen for the investigation (Table 6-2). The installation and compaction of the soils in the cylinder were controlled to obtain highly similar porosities among all investigated samples.

Table 6-1: Experimental program for the investigation of the Case A

Slurry	Soil [mm]	Injection pressure [bar]	No. Experiment (repetitions)	No. of combina-tion
B1, 5.5%	0.25-0.50	0.2	1a, 1b, 1c	1
B1, 6%	0.25-0.50	0.3 0.5 0.7	2a, 2b, 2c 3a,3b, 3c 4a, 4b, 4c	2 3 4
B1, 5.5%	0.50-1.00	0.2	5a, 5b, 5c	5
B1, 6%	0.50-1.00	0.3 0.5 0.7	6a, 6b, 6c 7a, 7b, 7c 8a, 8b, 8c	6 7 8
B1, 6%	0.25-0.50	0.3 - BP 0.5 - BP 0.7 - BP	9a, 9b 10a, 10b 11a, 11b	9 10 11

Table 6-2: Properties of soils used in the investigation (see appendix for grain distribution curve)

Soil fraction [mm]	0.25 – 0.50	0.50 – 1.00
Density [g/cm^3]	1.569	1.572
d_{10} [mm]	0.27	0.54
Porosity [-]	0.408	0.407
Compaction ratio [-]	0.597	0.597
Water permeability coefficient – steady state [m/s]	$4*10^{-4}$	$2*10^{-3}$
Intrinsic permeability [m^2]	$6.1*10^{-11}$	$3.1*10^{-10}$

Another requirement for obtaining reproducible results involving bentonite slurry is the monitoring of its physical and rheological properties. Before every experiment, the slurry was tested according to DIN 4127 (2013). The testing procedures and their relevancy are discussed in 3.1.2. The determined average values are outlined in Table 6-3. As can be seen, two types of slurry have been used. However, Table 6-3 shows that the tested properties of the two types were very similar. This is due to different batches delivered by the supplier, which were used in the experimental series. Hence, the experimental combinations with these two slurries can be considered as comparable.

Table 6-3: Slurry properties used in the investigation (see appendix for the product sheet of B1 bentonite and the testing protocols)

Slurry	B1 6 %	B1 5.5 %
Density [g/cm^3]	1.036	1.032
Yield point (ball harp) [Pa]	57	59
pH [-]	9.6	9.7
Marsh time - t_{M1000}; t_{M1500} [s]	51; 105	69; 111
Apparent viscosity [mPa.s]	19.1	Not tested
Plastic viscosity [mPa.s]	2.9	
Yield point (Bingham) [Pa]	15.55	

The resulting pressure drops over the soil samples are important factors for the evaluation of the slurry penetration experiments. The obtained average pressure drops are shown in Table 6-4. It is expected that the pressure loss over the grids and filter is negligible, due to the considerations of the characteristics defined by DIN 18130-1

(1998). Thus, it is expected that the pressure drop during the whole experiment from Table 6-4 is influenced dominantly by the soil sample.

Table 6-4: Resulting pressure drop over the soil sample (10 cm long)

Pressure drops over the soil sample [bar]	**1** - 0.25-0.5 mm, 0.2 bar, 0.41, B1 5.5%	**2** - 0.25-0.5 mm, 0.3 bar, 0.41, B1 6%	**3** - 0.25-0.5 mm, 0.5 bar, 0.41, B1 6%	**4** - 0.25-0.5 mm, 0.7 bar, 0.41, B1 6%	**5** - 0.5-1.0 mm, 0.2 bar, 0.41, B1 5.5%	**6** - 0.5-1.0 mm, 0.3 bar, 0.41, B1 6%
	0.08	0.15	0.35	0.55	0.08	0.15

6.3 Results and Interpretation

The obtained experimental results for the shallow slurry penetration scale will be presented and discussed in this section. It is distinguished between experiments with and without back pressure.

6.3.1 Experiments without back-pressure

As the first point, the time-dependent slurry penetration depth was evaluated. A clue about the formation state of the pressure transfer mechanism can be obtained from the inclination of the time-dependent slurry penetration curve as discussed in section 3.4.2. This suggest that hydraulic properties of the slurry penetrated soil area can also be deduced from the development of the slurry penetration curve.

The curves in Figure 6-3 show the development of the slurry penetration depth obtained as an average from three runs for the particular combination of parameters. Note that the lines describing the slurry penetration in soil 0.5-1.0 mm with pressures 0.5 bar and 0.7 bar are not shown, because the slurry did not stagnate within the soil sample so the time-dependent penetration depth cannot be determined by using $Eq.\,6\text{-}1$. It can be seen that each slurry penetration curve can be characterized by a fast increase of the depth at the start of the penetration (also called mud spurt in Talmon et al., 2013). During the mud spurt phase, the relationship between time and penetration depth is roughly linear. After this fast increase, the slurry penetration depth changes only insignificantly during the second part of the curve. According to Talmon et al. (2013) slurry consolidates at this stage. The strong difference of slurry behaviour at different penetration stages is an important aspect for the further

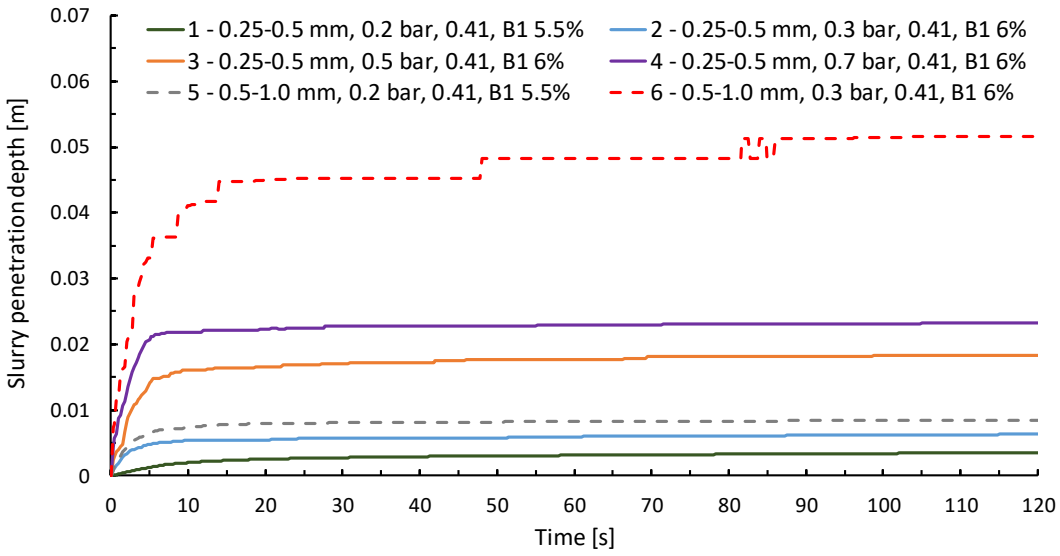

Figure 6-3: Time-dependent slurry penetration – each line resents an average from three experimental runs

comparison of tool cutting and slurry penetration scale. It can be also observed that the grain size of soil has much higher influence on the penetration behaviour than the injection pressure. The characteristic grain size (d_{10}) of the 0.50 – 1.00 mm soil is two-times higher than of the used finer soil (Table 6-2). Hence, the penetration depth should increase for the coarser soil acc. to $Eq.\,3\text{-}27$ also approx. by factor 2 for the same injection pressure (pressure drop).

This is only true for the very small injection pressure of 0.2 bar (pressure drop 0.08 bar – measured by pore pressure sensors in the soil cylinder), when the penetration depth increases from 0.35 cm for the finer soil to 0.85 cm for the coarser soil within the 120 s time span. For injection pressure 0.3 bar (pressure drop 0.15 bar), the increase in slurry penetration depth between the two soils is larger than factor 5. Hence, the penetration depth dependence on the injection pressure (pressure drop) could be obtained for both soil types as is predicted by the theories discussed in section 3.4. However, the penetration depth does not depend linearly on the injection pressure (Figure 6-4). For both investigated soils, non-linear dependence on the pressure drop (injection pressure) was obtained. Note that it is assumed that the pressure drop over the sample is approximately equal to the pressure drop over the slurry penetrated zone at the final penetration stage. Moreover, even the dependencies show a different trend. While the slurry penetration depth in finer soil (0.25 – 0.5 mm) seems to converge to some particular value for the increasing pressure drop, the penetration depth diverges for the coarser soil with increasing pressure drop (injection pressure). As can be seen from Figure 6-4, DIN 4126 (2013) could not predict the slurry penetration depth properly. It is believed that the retained slurry in pore space of finer soil (0.25 – 0.5 mm) changed the pore geometry significantly. Or it may also be that the slurry particles influenced primarily by mechanical forces (larger than 30 µm) are retained within the soils. Hence the empirical macroscopic correlation between yield point of slurry and characteristic

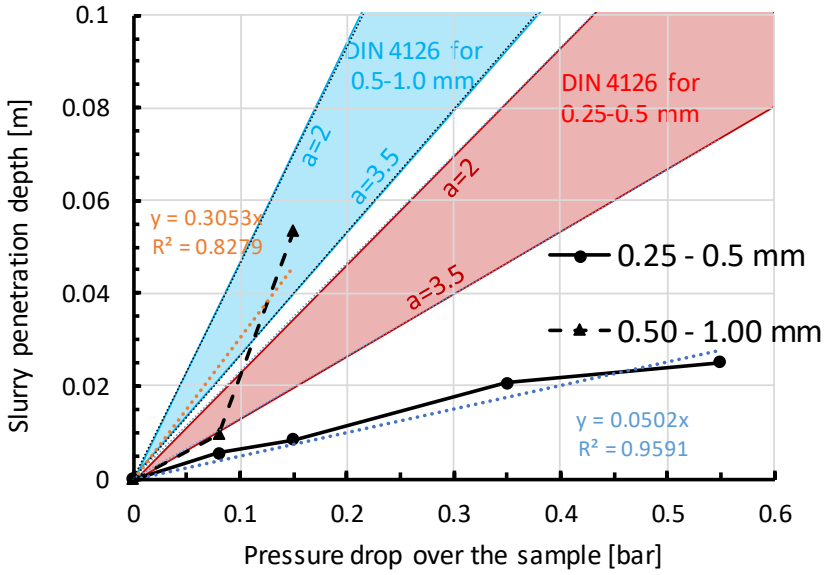

Figure 6-4: Dependence of the average slurry penetration depth on the average pressure drop over the sample for slurry B1 6% (DIN 4126 uses Eq. 3-27 with a = 2 or 3.5)

grain size is questionable. This would mean that this slurry and soil combination should be investigated on the micro level to predict the penetration depth (section 3.3.2).

Consequently, it was aimed to compare the time-dependent slurry penetration depth for the combinations relevant for the Case A with contemporary prediction theories. Two theories were chosen for the comparison: after Krause (1987) and after Anagnostou & Kovári (1994). These theories are described in section 3.4.2. Figure 6-5 is visualizing the comparison of the measurements with the theory acc. to Krause (1987) utilizing the upper and lower bound. For the purpose of comparison, the experimentally obtained penetration depths were recalculated to the so called "comparative penetration depth ($l_{E,comp}$)" using $Eq.3\text{-}33$ while assuming that l_E(t=60min) is equal to the experimentally determined final penetration depth. The calculation of the comparative slurry penetration depth is also beneficial for comparison of the slurry penetration process for slurry-soil combinations with very different absolute final penetration depth.

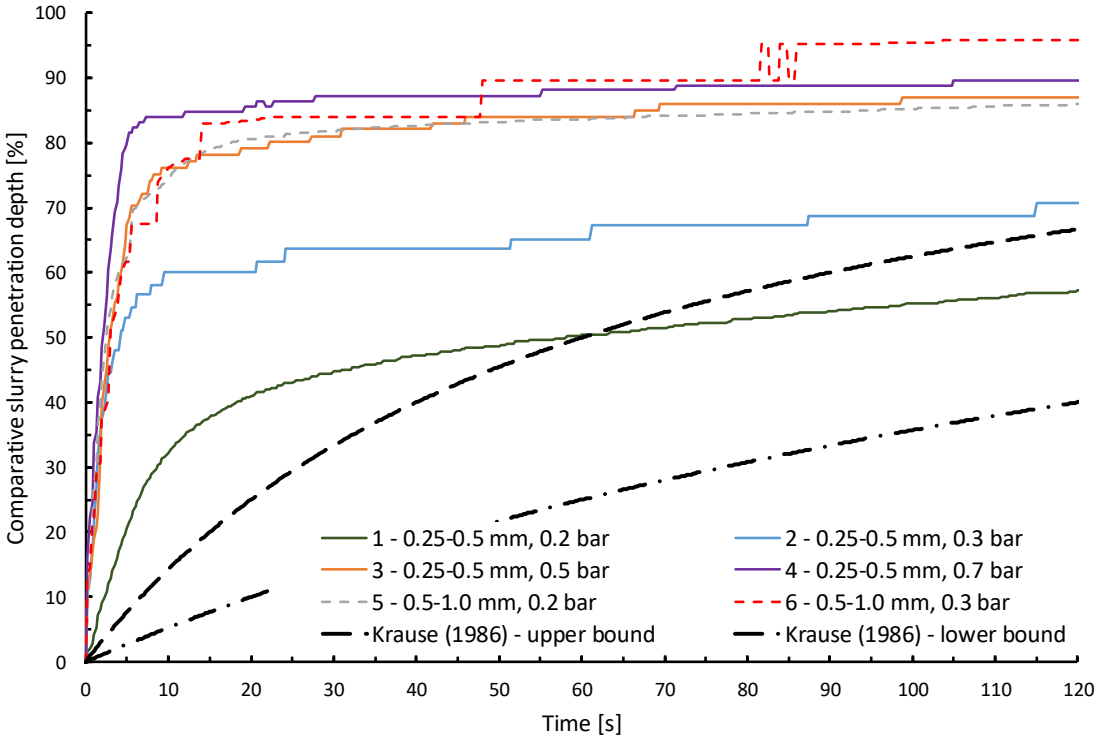

Figure 6-5: Comparative slurry penetration depth determined using the methodology by Krause (1987) obtained from the experimental results and compared with bounds acc. to Krause (1987)

It turns out that the penetration bounds suggested by Krause (1987) cannot sufficiently approximate the slurry penetration behaviour for relevant Case A combinations within

the short time scale. Nevertheless, it can be observed using this methodology that certain soil and slurry combinations show very similar penetration behaviour. This is particularly noticeable for all combinations with 0.5–1.00 mm soils and for combinations with 0.5 and 0.7 bar and 0.25-0.5 mm soil. From these mentioned combinations, the combinations with soil 0.25 – 0.5 mm and low injection pressures are diverging. Thus, it can be concluded that the low injection pressures were not able to sufficiently overcome the resistance against slurry provided by the pore space of the finer soil sample. It can be also expected that the change in pore geometry due to retention of slurry particles for finer soil fraction (0.25-0.5 mm) depends on the amount of the injection pressure. For the coarser soil (0.5-1 mm), it is impossible to notice the role of the injection pressure. Hence, it can be concluded that the retained slurry particles did not significantly influence the pore geometry for the coarser soil.

Furthermore, the results for time dependent slurry penetration were compared with the theory according to Anagnostou & Kovári (1994). The comparison is shown in Figure 6-6. Note that the theory requires input of the final penetration depth of slurry ($Eq.3\text{-}36$). It turns out that the theory proposed by Anagnostou & Kovári (1994) expected a much steeper increase in penetration depth for the experimental combinations. This was observable through a comparison of all experimental

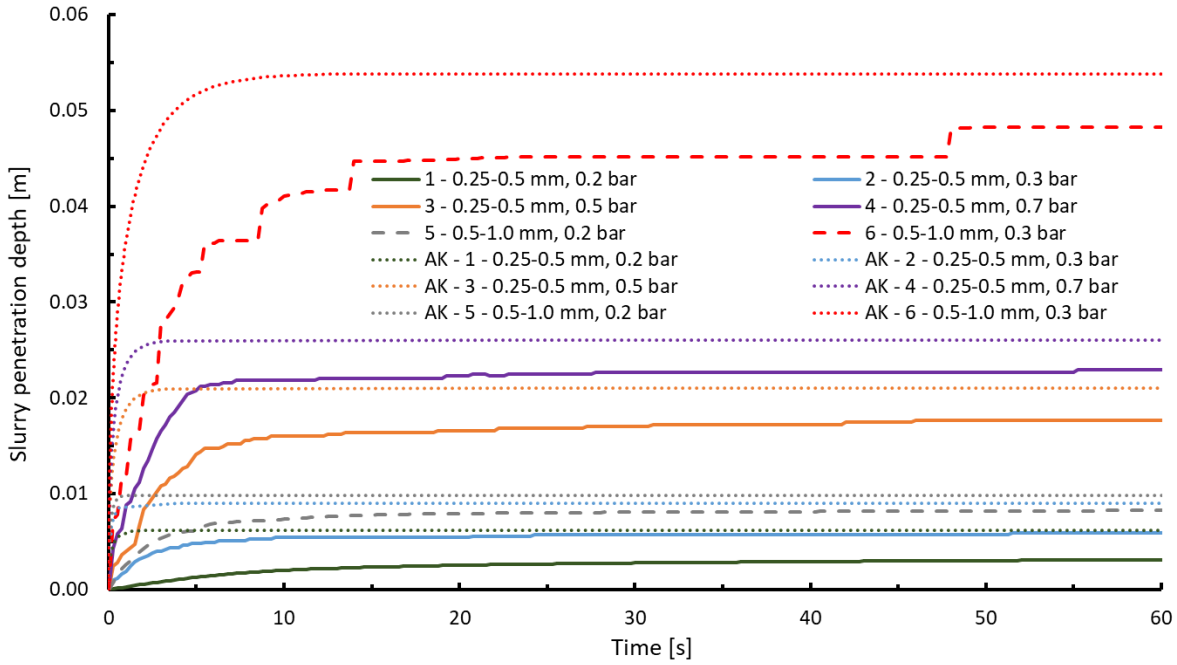

Figure 6-6: Comparison of the experimentally obtained and the calculated slurry penetration depth acc. to Anagnostou & Kovari (1994), AK denotes the calculated penetration depth

combinations. The reason for this might be the underestimation of the resistance of the pore space against the slurry flow by the theory. This underestimation results from the consideration of slurry-soil interaction as a bulk flow of immiscible fluid inside the pore space. Thus, the changes of the pore space during interaction are not taken into account.

However, as it will be shown further in this section; the hydraulic properties of the pressure transfer mechanism are not always dependent on the instantaneous penetration behaviour described by the inclination of the slurry penetration curve. The hydraulic properties can only be evaluated when the permeability coefficient of the pressure transfer mechanism is determined. The determination is here conducted based on methodology described in section 4.1 of this thesis using $Eq.\,4\text{-}1$. Outflow from the set-up ($Q(t)$) and pressure drop over the sample were measured ($\Delta h(t)$) continuously to provide the input to the equation, while the length (ΔL) was considered constant as the length of the soil sample (10 cm). Thus, the permeability coefficient of the 10 cm thick soil sample is obtained by the presented device. The approach is reasonable for later utilisation of the results in numerical seepage models in chapter 8. Figure 6-7 shows the developments of permeability coefficients for various soil-slurry-injection pressure combinations. Every development in Figure 6-7 can be divided, similarly as the slurry penetration curve, into two branches.

The first branch is characterized by a very steep fluctuating decrease in the permeability coefficient and is called the descending branch. The second branch is characterized by an insignificant decrease in the permeability coefficient. In the second branch, the permeability coefficient development becomes nearly horizontal in the diagram with a logarithmic scale of the vertical axis and converges against a constant value. Note that the developments are evaluated within the timespan 120 s, which corresponds to the maximal time-scale from chapter 5. The distinction between the two branches is shown in Figure 6-7 for all combinations. The timespans required for reaching the second (stagnating) branch after the slurry penetration start are also summarized for all investigated combinations in Figure 6-8.

The transition point between the two branches in Figure 6-7 and Figure 6-8 can be considered the approximate threshold between the forming and the formed pressure transfer mechanism, in relation to its hydraulic properties. As can be seen from Figure 6-7 and Figure 6-8, the second branch is achieved sooner for higher injection pressures for the finer soil (0.25–0.5 mm). The higher injection pressures further deliver a lower permeability coefficient achieved at the second branch of the development within the evaluated timescale. This is particularly visible for the experiments with 0.7 & 0.5 bar injection pressure. The faster decrease might be explained by higher flow velocity during mud spurt. It is worth noting that the coarser soil (0.50 – 1.00 mm) behaved differently and that a longer timespan was required for higher injection pressure to reach the stagnation branch. The different behaviour of coarser soil during slurry injection was already highlighted in Figure 6-4. When focusing on the slurry soil interaction on the micro-level, theory (section 3.3.2) states that the development of the permeability coefficient during filtration should be dependent on the comparison between slurry particle size and the pore size. Hence, the finer soils fraction should for

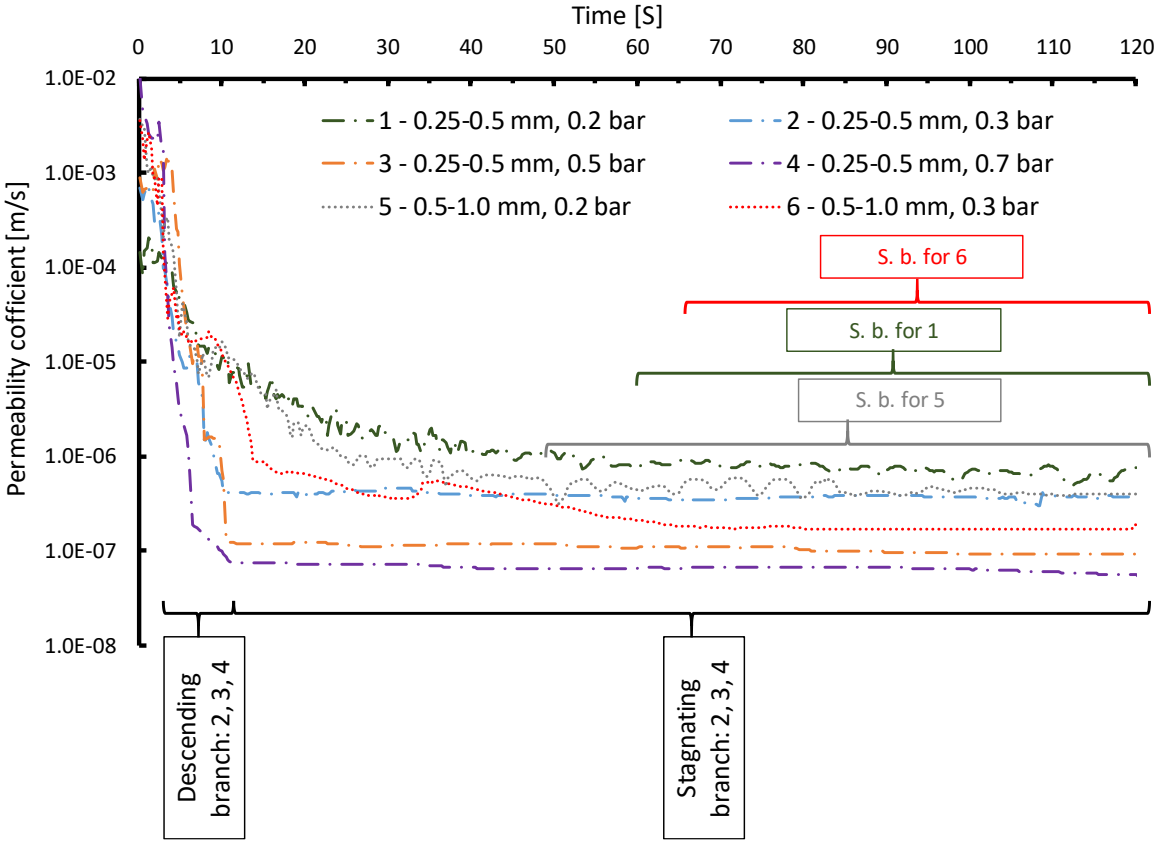

Figure 6-7: Permeability coefficient development (Zizka et al., 2018) and stagnation branches (S. b.) for the combinations

the same slurry deliver more abrupt decrease of permeability. This behaviour is only partially observable in Figure 6-7 for higher injection pressure within the finer soil. Thus, it may be concluded that there is a certain threshold of injection pressure required to speed up the changes of pore space due to the slurry particles retention. This could be related to the hydrodynamic capturing processes as outlined in section 3.3.2.

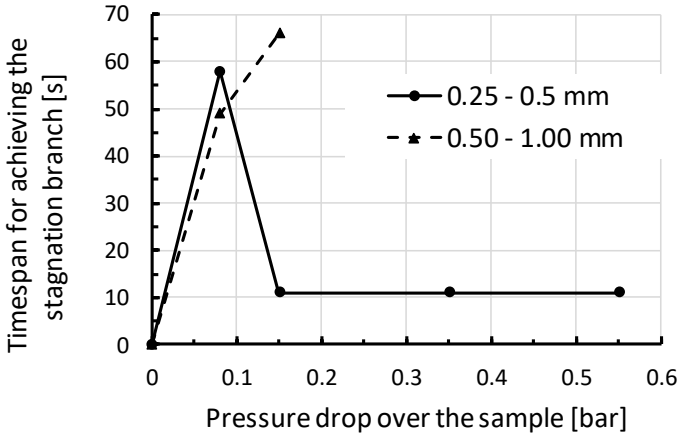

Figure 6-8: Timespan required for slurry to achieve the stagnation branch

As was expected in section 4.1, it was only possible to apply Darcy´s law for the evaluation of the slurry soil interaction while considering very short time steps (0.25 s), due to time-dependency of the flow. It turns out that the level of time-dependency of flow decreases in the later stages of the experiments (the stagnating branch). Nevertheless, the instantaneous permeability coefficient should be considered for the purposes of the assessment of slurry soil interaction at the tunnel face. Furthermore, it turns out that the permeability coefficient development for slurry also depends, in contrast to water, on the injection pressure, in addition to the slurry and soil characteristics.

6.3.2 Experiments with back-pressure

The second aim of the investigation within this chapter was to check the dependency of slurry penetration behaviour on the back-pressure. For this purpose, the time-dependent penetration depth between experiments with and with-out back-pressure will be compared. This will be followed by the comparison of permeability coefficient developments.

The comparison of the time-dependent penetration depth shows that the two series of experiments are slightly deviating. However, the deviation becomes negligible for the higher injection pressures (Figure 6-9). This would indicate a difficult steering of the prescribed difference between the injection and back-pressure when the injection excess pressure is low. In Figure 6-10, the developments of permeability coefficients are compared. It is possible to observe here, that a reduction of soil´s permeability coefficient during penetration of slurry was more significant in experiments with back-pressure. However, this can be explained by higher hydraulic resistance of the set-up with the back-pressure, which was 0.2 m in comparison to 0.1 m for the set-up without back pressure. Note that the hydraulic head loss was calculated for water using the usual pipe flow calculation methodology (Freeman, 2014 and Albert & Schneider, 2014). The highest difference between the two series of experiments could again be observed for experiments with 0.3 bar of slurry excess pressure. It is necessary to note that for the experiments with back-pressure, another type of outflow scale has to be used. This scale had a lower degree of accuracy due to necessary weighing of higher loads caused by the outflow cylinder with the back-pressure.

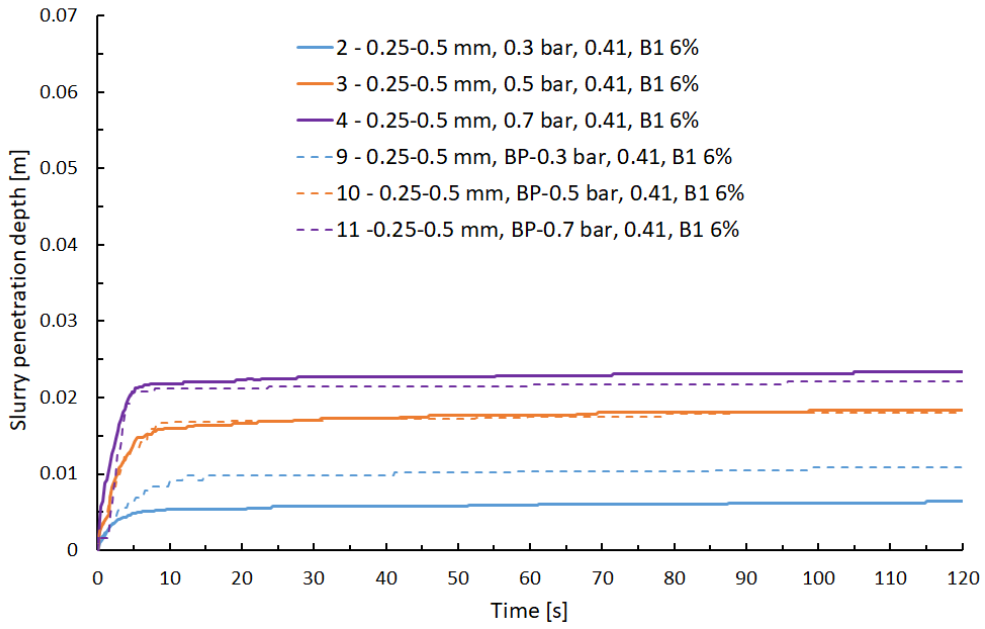

Figure 6-9: Comparison of slurry penetration depth with and without back-pressure – each line represents an average from experimental runs (BP stands for back-pressure)

It could be concluded, that the back-pressure seems to have negligible influence on the results for higher injection excess pressures, however, it is difficult to assess the influence of back-pressure on slurry penetration behaviour in these small-scale experiments with comparably shallow slurry penetration depth. Therefore, the influence will be revisited in Chapter 7, using the experimental set-up for the investigation of Case B interaction with deep slurry penetration.

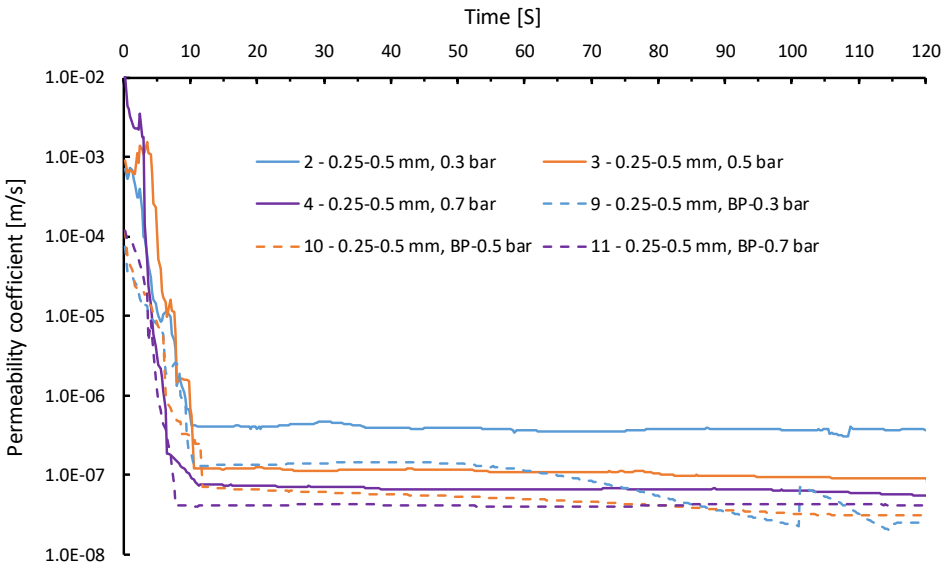

Figure 6-10: Comparison of permeability coefficient development with and without back-pressure

6.4 Comparison of tool cutting with slurry penetration scale for the Case A

The obtained excavation scales from chapter 5 will be compared in this section with slurry penetration scales determined experimentally using the methodology described in this chapter. The aim of the comparison is to make a preliminary decision, which combinations of slurry and tool penetration scale are likely to deliver Case A of the interaction (see chapter 4). At this time the relationship between the pressure gradient in the experiment and at the tunnel face is not yet known. This will be investigated in chapter 8.

The comparison is conducted in Figure 6-11, Figure 6-12 and Figure 6-13, for the respective reference projects. The slurry penetration scale is again displayed as the time-dependent penetration depth. The tool penetration scale is displayed by skew lines for each homogeneous cutting zone of each reference slurry shield. The points at the ends of the skew lines represent bounds of the tool cutting scale. Additionally, two vertical lines at the bounds create a circumference of each homogeneous cutting zone.

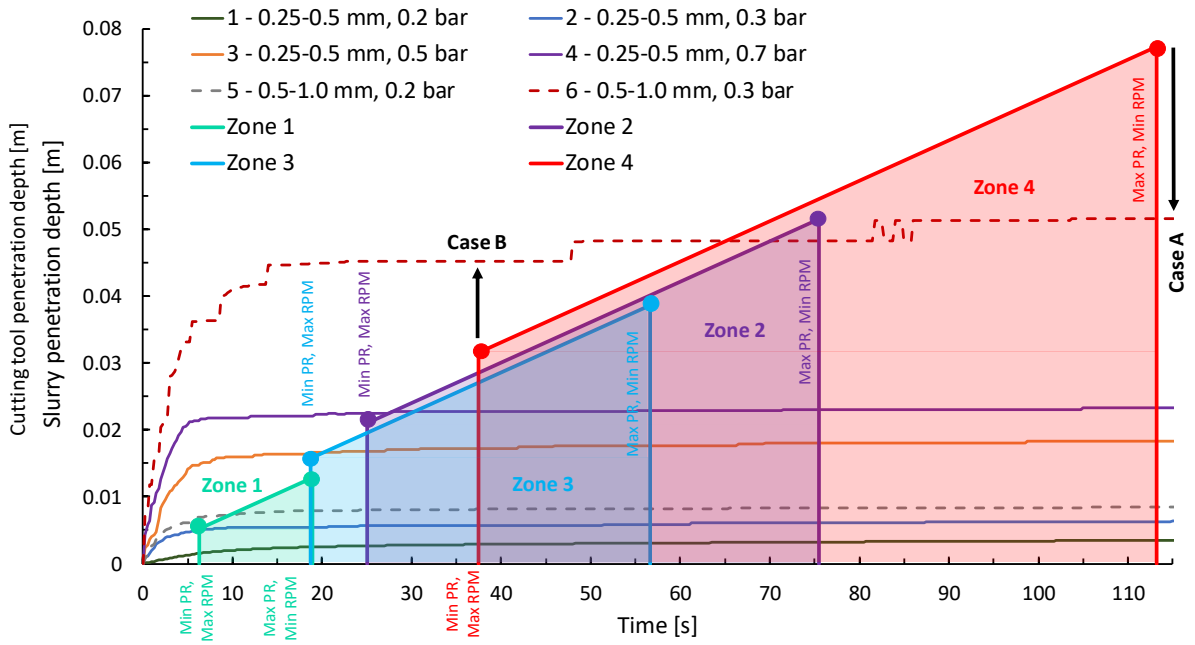

Figure 6-11: Project P 1 - Comparison of the time dependent penetration distance of slurry in experiments with cutting tool penetration depths and the timespans between tool passing in respective cutting zones of the reference project (Zizka et al., 2018)

The skew lines are representing various combinations resulting from the minimal and maximal RPM and the corresponding PRs. If the slurry penetration line crosses any of the boundary lines of a homogeneous zone, the Case A of interaction occurs for this homogeneous cutting zone. That means that every tool rotating in this zone removes the entire pressure transfer mechanism. Further, it is important to compare the location of slurry penetration line with regard to the bound points. If the slurry penetration line is located below a bound point, Case A occurs for the particular bound of the excavation scale.

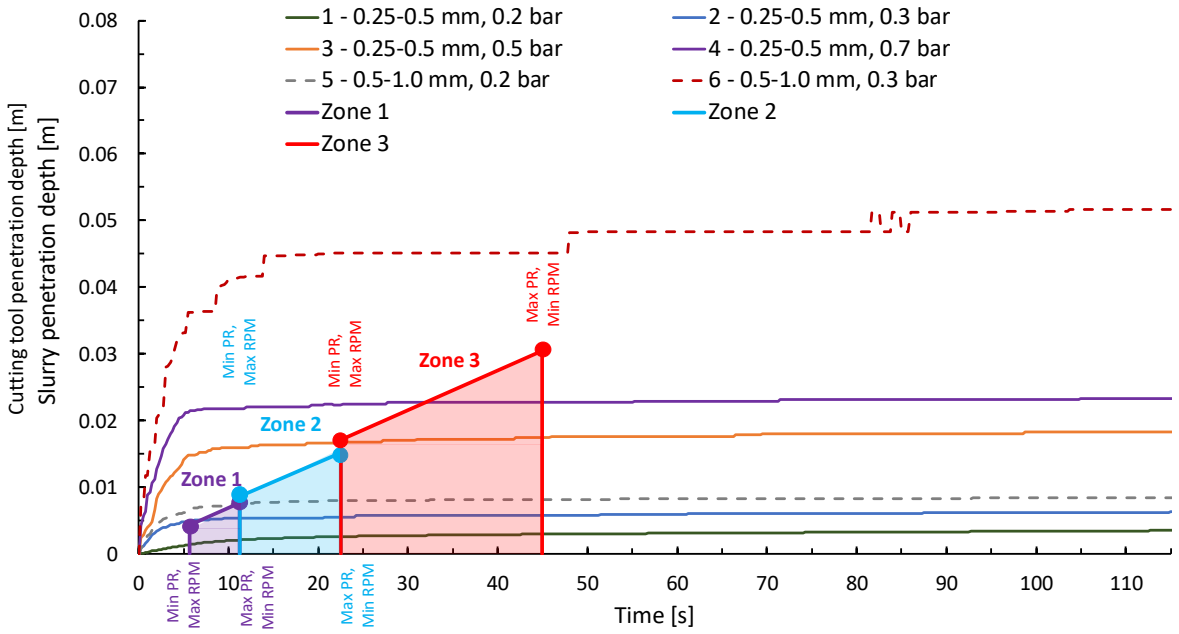

Figure 6-12: Project P2 - Comparison of the time dependent penetration distance of slurry in experiments with cutting tool penetration depths and the timespans between tool passing in respective cutting zones of the reference project (Zizka et al., 2018)

It could be confirmed in Figure 6-11, Figure 6-12 and Figure 6-13 that the cutting process is much slower than the slurry penetration during its initial phase (mud spurt). The cutting scale becomes comparable with slurry penetration scale, when the stagnation of slurry starts and its instantaneous penetration velocity decreases. Therefore, the occurrence of Case A depends rather on the cutting depth of tools than on the frequency of cutting. During the detailed analysis of the particular cutting scales, it turned out that the reference project P1 has the widest excavation scale. The widest excavation scale denotes large timespans between passing of cutting tools connected with comparably deep penetration of cutting tools (Figure 6-11).

Reference project P2 delivered the shortest excavation scale (Figure 6-12), however, the cutting depth of tools was still deeper in the most of homogeneous cutting zones than in the project P3. In comparison to project P2, the excavation scale of project P3 is slightly wider (Figure 6-13). The Zone 1 experiences only a very shallow cutting depth, so that only one slurry-soil combination with the lowest injection pressure could deliver Case A of interaction in this zone. As mentioned in chapter 5, the project P3 has 5 homogeneous cutting zones in total. However, Zone 5 is not shown in in Figure 6-13 due to non-present scrapers disturbing the pressure transfer mechanism in this zone. That means that the pressure transfer mechanism is always formed in this zone and is never disturbed.

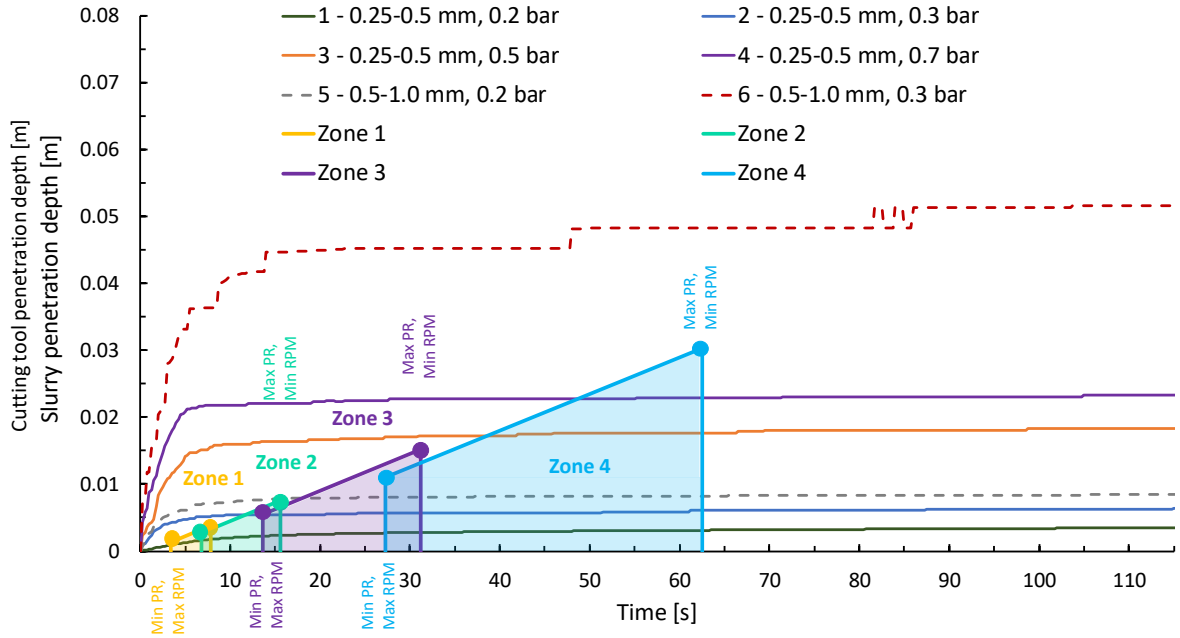

Figure 6-13: Project P3 - Comparison of the time dependent penetration distance of slurry in experiments with cutting tool penetration depths and the timespans between tool passing in respective cutting zones of the reference project (Zizka et al., 2018)

In general, it could be observed that Case A appears more often in cutting zones closer to the tunnel axis, while the appearance of Case A at the circumference is less frequent. The areas with Case A on the particular tunnel face of all reference projects were summed up and put in relation with the area of the entire tunnel in Figure 6-14. Two bounds of excavation scale from Table 5-3 were distinguished. It can be concluded that larger parts of the tunnel face belong to Case A for lower slurry injection pressures. Hence, Case A occurs for the soil 0.25 – 0.5 mm and injection pressure 0.2 bar regardless of the excavation scale at the entire tunnel face for every reference project.

With increasing injection pressure, the occurrence of Case A decreases, especially for the bound with minimal PR combined with maximal RPM. As previously explained, the low cutting depth caused by frequent passing of the cutting tools plays the responsible role.

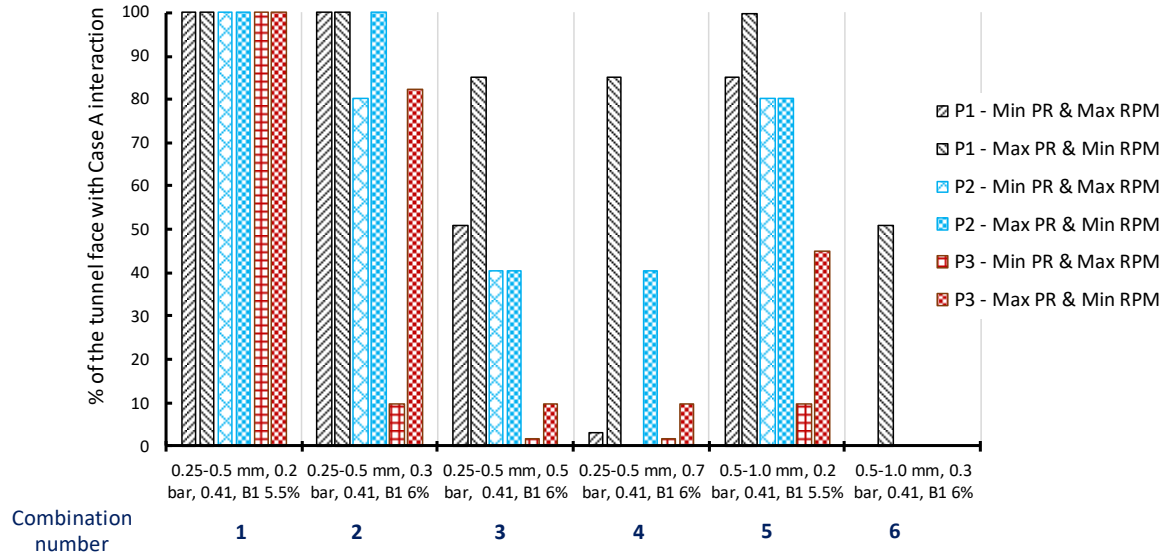

Figure 6-14: Percentage of the area of the tunnel face with the Case A interaction (Zizka et al., 2018)

Developments of the permeability coefficient are superimposed in Figure 6-15 with excavation scale from the reference project P1. The permeability coefficient development in respective cutting zones at the tunnel face can be evaluated based on Figure 6-15. The permeability coefficient lines show the coefficient development within a cutting track. The crossings between the development lines and zone borders illustrate the minimal permeability coefficients achievable for the pressure transfer mechanism in the respective zone. Additionally, the homogeneous cutting zones are shown in the diagram with borders for the two bounds of the excavation scale. It can be clearly observed that the two visualised excavation bounds significantly influence the extent of the second branch of permeability coefficient development within the homogeneous cutting zones.

6.5 Summary of experimental investigation for the Case A

The new experimental set-up to analyse slurry and soil interaction was introduced in this chapter. For the operation of the set-up, a methodology was developed to investigate a very shallow time-dependent slurry penetration depth and how to assess

development of permeability coefficient during slurry penetration. While using the developed methodology, it was found that both slurry penetration depth development and permeability coefficient development can be divided into two branches. Within the tests, the influence of back-pressure could not be conclusively assessed, due to the very shallow penetration scale of slurry.

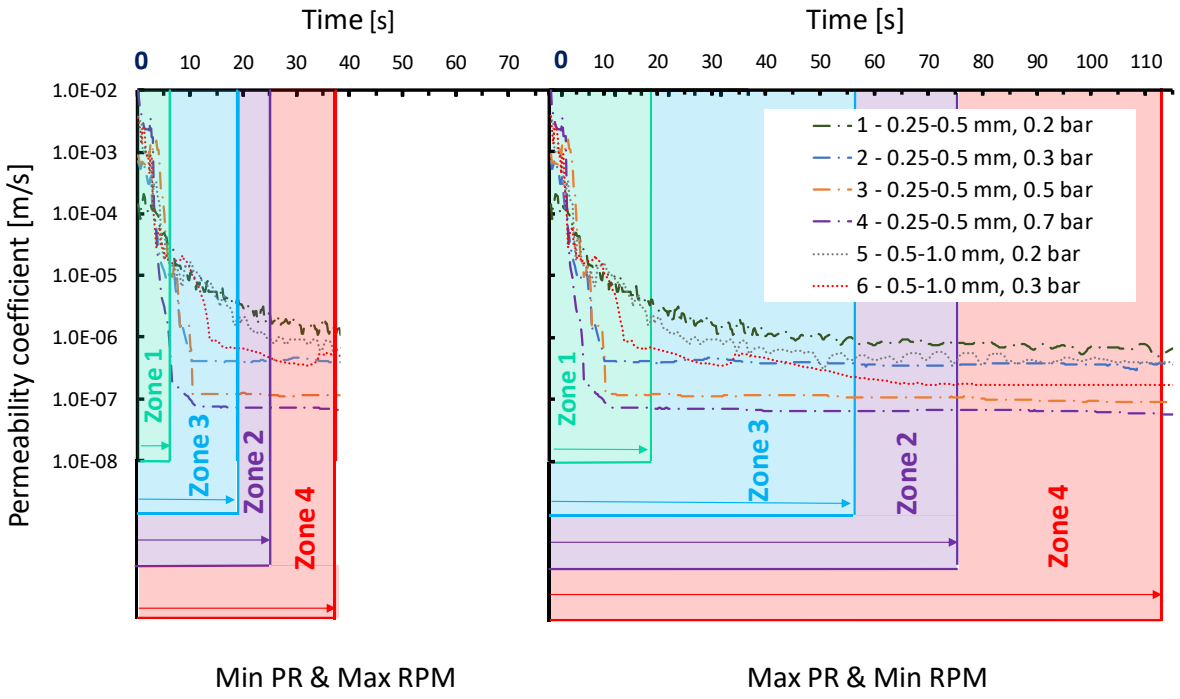

Figure 6-15: Permeability coefficient development and its minimal achievable values in respective homogeneous cutting zones of Project P1. The horizontal dashed lines signify the extent of the permeability development in respective zone in dependence on chosen PR and RPM (Zizka et al., 2018)

A comparison of tool penetration scale and slurry penetration scale showed that the occurrence of Case A depends on the cutting depth of tools, rather than on the frequency of cutting. Generally, the occurrence of a Case A interaction is more expectable in cutting zones closer to the tunnel axis, while the appearance of Case A at the circumference is less frequent. However, it is necessary to point out that the relationship for coupling of slurry excess pressure in the real excavation chamber of the shield with pressure drop in the experiment is not yet known. This will be clarified in chapter 8 based on numerical calculation considering interaction of adjacent cutting tracks.

The experimental program used in this chapter has certain limitations. The program focused on investigations using two type of uniformly graded sands from the standard

application range of slurry shield (Figure 2-3). However, the increased pore pressure during excavation were observed especially in similar soils, as pointed out in the introduction of this thesis. In the future, the experiments should be conducted with even finer or non-uniformly grained sand and with slurry with lower concentrations of solids.

7. EXPERIMENTAL INVESTIGATIONS: CASE B – DEEP SLURRY PENETRATION SCALE

Chapter 7 is dedicated to the analysis of the deep slurry penetration scale for Case B of the interaction with cutting tools (Figure 4-2). First, experimental set-ups, methodology and program of the experimental investigation will be presented. The obtained experimental results for the deep penetration scale are discussed in section 7.3. It will be distinguished between penetration scale for primary slurry penetration (section 7.3.1), for slurry re-penetration (section 7.3.2) and for the slurry re-penetration with soil cutting (section 7.3.3). While the investigation of slurry penetration and re-penetration are conducted in column tests, the investigation dealing with re-penetration with soil cutting are performed using the RUB tunnelling device.

The general aim of this chapter is to determine the amount of pressure transfer inside and outside of the slurry penetrated zone as stated in chapter 4. The pressure transfer will be assessed by measuring the drop of injection pressure (pore pressure) and the increase of effective stress inside the soil samples. A further aim is to evaluate the influence of boundary flow conditions in the experimental set-up on the obtained pressure transfer. This question remained open from the investigations in chapter 6, because it was difficult to assess the influence of boundary flow conditions due to shallow slurry penetration scale. The results of experimental investigation obtained in this chapter will be later utilised in chapter 9.

7.1 Experimental set-up & methodology

7.1.1 Primary penetration of slurry

While considering the definition of the Case B interaction, a new experimental set-up was developed, which allows for characterization of comparably deeper slurry penetration than the set-up used in chapter 6. The experimental set-up is visualized in Figure 7-1 (detailed sketch is also provided in the appendix). The set-up can be designated as column test and consists of a slurry cylinder, a soil cylinder (internal diameter 40 cm) and a reservoir with free surface for the discharged fluid from the soil cylinder. Alternatively, the reservoir for the discharged fluid can be pressurized to induce back-pressure in the set-up. The version of the set-up with back pressure is sketched in the appendix. The reservoir is in both cases located on a scale. The scale is connected to a computer for continuous data logging during the experiment. One pore pressure sensor (PWD) continuously monitors pressures in the slurry cylinder and 7 other sensors are placed in the soil cylinder. Two total stress sensors are located at two measurements levels in the middle of the soil cylinder (Figure 7-2). Data from both sensor types are transferred to the computer. The data are logged every 0.25 s. In the developed set-up, two stiff plastic grids stabilize the soil sample, which is compacted to a prescribed ratio (porosity). The effective surcharge stress induced by the grids on the soil sample is adjustable by screws and can be controlled. A further aim of the grids during slurry penetration is to ensure uniform distribution of slurry before entering the soil sample at the bottom and uniform outflow of displaced water at the top. The

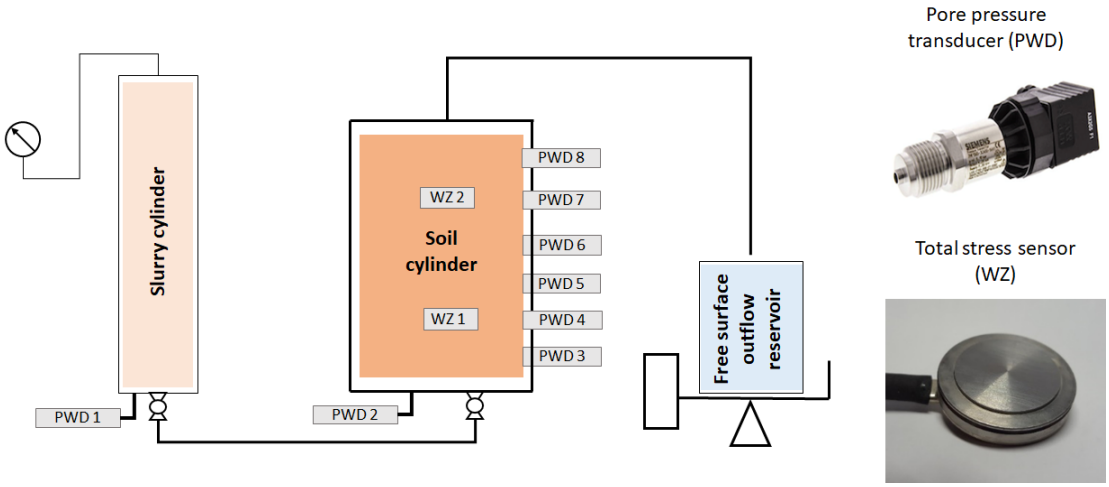

Figure 7-1: Experimental set-up for the investigation of Case B interaction – column test

boundary between the bottom grid and the cylinder circumference is sealed. The chosen layout of sensors enables to track the reaction of soil during slurry penetration inside and outside of the slurry penetrated zone. The vertical location of the sensors is shown in Figure 7-2. On one hand, the location of the sensors makes the tracking possible for only a certain number of combinations of slurry concentration, injection pressure and soil, due to particular target penetration depth. On the other hand, the soil cylinder offers a desirable level of adaptability for investigation purposes in this chapter dealing with change of boundary flow conditions. The outflow pipe diameter can be adjusted and the back-pressure can be induced in the set-up. The slurry inflow pipe diameter was kept constant at 2.3 cm. The changing of the outflow-pipe-diameter is used to demonstrate the influence of hydraulic boundary conditions on the time-dependent measured variables as expected in section 6.2. The same discussion with regard to the design of the experimental set-up from section 6.1 could be repeated here. To characterize the changes of hydraulic flow conditions more properly, the hydraulic resistances of each set-up version were calculated. Note that the flow of water was assumed for the calculation purposes. The resulting hydraulic resistance is based on usual pipe flow calculation (Freimann, 2014 and Albert & Schneider, 2014) and is expressed as hydraulic head loss in Table 7-1.

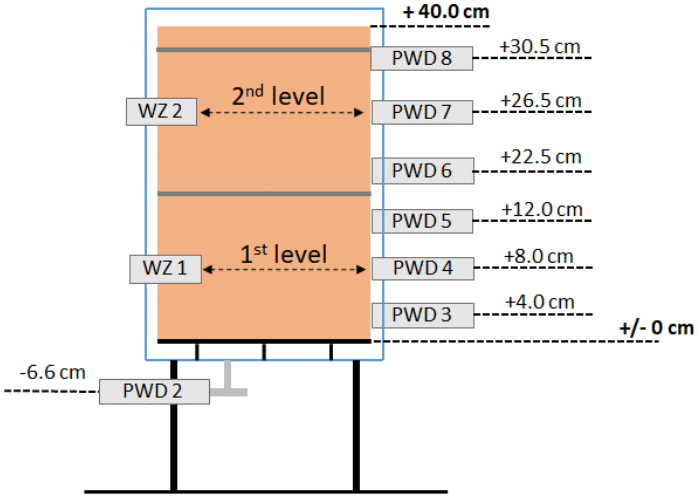

Figure 7-2: Location of sensors in the set-up (column test) and designation of the measurement levels

The experiment starts with the adjustment of the injection pressure in the slurry cylinder and a full saturation of the soil sample with water. The effective stress in the soil sample is adjusted by screws (for details see appendix). The goal is to induce a

similar initial effective stress at both measuring levels (Figure 7-2). The starting conditions in the experiments were varied in terms of initial location of slurry:

1) Slurry is present in the slurry cylinder while the pipe connecting the slurry cylinder with soil cylinder is filled with water.
2) Slurry is present in the slurry cylinder and pumped under limited flow rate, regulated by a valve in the soil cylinder, up to the bottom interface between the grid and the soil sample (coordinate +/- 0 cm in Figure 7-2).

Table 7-1: Hydraulic head loss in set-up for water flow (see section 7.2.1 for the detailed explanation of the experimental combinations)

Experimental combination	I - basic	II – reduced outflow diameter	III – back-pressure	IV – basic
Hydraulic head loss [m]	0.3	0.9	0.4	0.3

On one hand, the first option is favourable due to slurry entering the pore space of soil first under dynamic flow condition. On the other hand, the soil is subjected to water flow first before coming into contact with slurry. The water flow could considerably influence the measured pore pressure and total stress. The second option reduces the possibility of unwanted influences due to “pure” water flow from the start of the experiment. However, slurry enters the soil pores being first in static condition, which is disadvantageous, due to possible thixotropic solidification. Thus, both options are investigated in this chapter.

The penetration experiment begins with the opening of the valve and takes 30 minutes to complete. The 30-minute timespan was determined to be sufficient based on preliminary experiments. It is worth mentioning that the primary slurry penetration does not properly represent the processes of the Case B interaction at the tunnel face. However, the process has to be understood before conducting the tests with slurry re-penetration. More details about the set-up and the step-by-step description of the methodology are provided in the appendix.

7.1.2 Re-penetration of slurry

The same set-up (column test) as in the previous section 7.1.1 was used for the investigation of slurry re-penetration (Figure 7-1 and Figure 7-2). However, a different methodology for the conducting of the experiment was employed. The greatest

challenge of the laboratory modelling of the re-penetration is to achieve the same conditions that are present at the tunnel face during excavation. Either the depth of the primary penetration or the timespan at which the re-penetration starts must be chosen for the experiment. Moreover, in order to keep the process realistic, the timespan for the duration of re-penetration must be determined. It was concluded in section 4.2 that the slurry in Case B reaches between the tool passages a particular penetration depth, which corresponds exactly to the cutting depth of the excavation tool at single passing ($p_{tool} = l_r$). This was designated on the global level as a requirement for the equilibrium state during excavation (Figure 7-3) because of the movement of the slurry penetration front that follows the movement of the shield. If the slurry would achieve a smaller penetration depth, no penetration of the suspension would occur after some cutting cycles. If, in contrast, the depth of penetration during the re-penetration would be greater in comparison to the cutting depth, an infinitely high penetration depth of the slurry would occur after some cutting cycles. Hence, the slurry re-penetration depth needs to correspond to cutting depth of a single tool per passing and needs to be achieved during the timespan between two subsequent tool passes. These variables for the definition of the excavation scale are taken from chapter 5. The determination of the primary penetration depth (l_p), before the re-penetration starts, needs to be conducted parametrically. The re-penetration will be started at different timespans, from the beginning of the primary penetration until the previously formulated spatial and time condition for equilibrium state during excavation are fulfilled ($p_{tool} = l_r$).

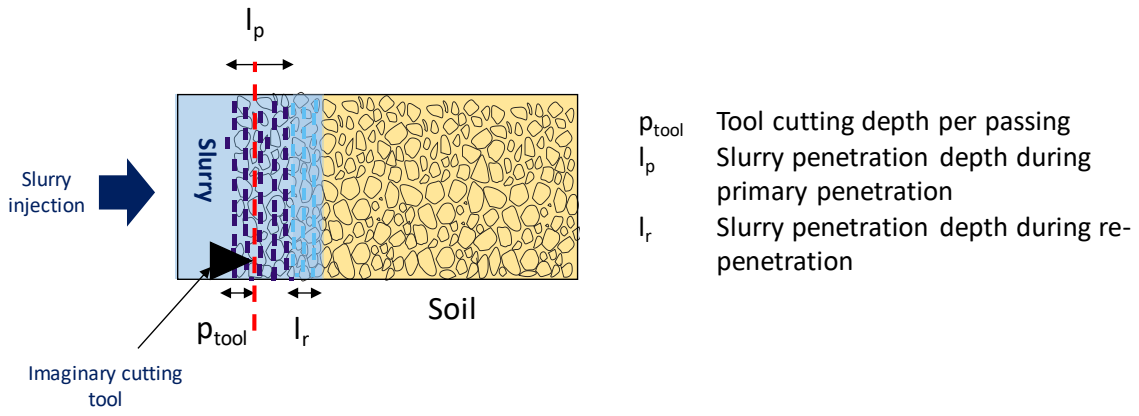

Figure 7-3: Principle of slurry re-penetration including the cutting tool

However, no cutting mechanism is present in the developed column experimental set-up, so the re-penetration has to be simulated as pressure-controlled steps (Figure 7-4). The principle of this method is to increase the slurry pressure at the start of the re-penetration (s_2) in a way that the pore pressure in the soil at the adopted tool cutting depth (p_{tool}) becomes exactly the same as the slurry pressure during the previous primary penetration (s_1) in the chamber. The timespan for starting the re-penetration has to be parametrically determined here, as described above, in order to fulfil the boundary conditions for realistic re-penetration depth.

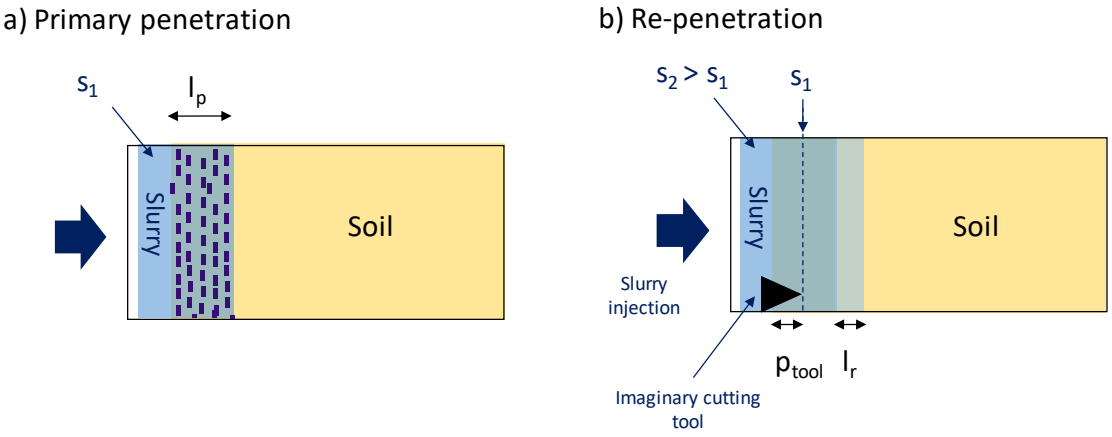

Figure 7-4: Principle of the pressure-steered re-penetration experiment – movement of injection pressure p_1 further in soil, the moving distance corresponds to the tool excavation depth

However, the described approach for pressure-controlled re-penetration also has certain disadvantages. It is principally assumed that concentration of slurry particles at the end of primary penetration stage is evenly distributed inside the slurry penetrated zone. A further requirement is that the even distribution also remains during re-penetration, so the slurry moves inside the soil pores as a “bulk fluid”. In reality, it is expected that the requirements can only be fulfilled for certain coarse soils. Hence, the investigation of the primary slurry penetration has to deliver a clue, if the fulfilment of the requirements can be expected for the investigated soils. A further disadvantage of the pressure controlled re-penetration is that the amount of total stress in the system is increased beyond the level during the primary penetration and thereby beyond the support excess pressure.

Nevertheless, the benefits of the developed methodology for modelling of the re-penetration prevail. The main benefit is the realistic time-scheduling of the experiment

in comparison to the conditions at the tunnel face that avoids any unwanted slurry solidification in the soil skeleton.

7.1.3 Re-penetration of slurry with soil cutting – RUB Tunnelling device

The RUB tunnelling device (Küpferle et al., 2016) was used for the investigation in this section. The employment of the RUB tunnelling device shall eliminate the physical simplification introduced by the pressure-controlled slurry re-penetration (section 7.1.2). The original version of the tunnelling device was adapted by introduction of slurry face support system (Küpferle et al., 2018) as is presented in Figure 7-5. Detailed drawing of the set-up is provided in the appendix. A lathe was used to place the set-up. A simplified cutting wheel is fixed at the end of a shaft (Figure 7-5-b and Figure 7-5-c) inside the soil cylinder and is propelled by the lathe. Cylindrical steel pins represent simplified cutting tools placed at the star-shaped cutting wheel. A single pin is always located within one cutting track. Hence, single homogeneous cutting zone is here presented. It is expected that the pins disturb the pressure transfer mechanism (slurry penetrated zone) in a similar fashion as scrapers (Chapter 5). The fixing of the shaft to the lathe enables it to move forward and rotate the cutting wheel while simultaneously creating the desired helix-movement of the cutting tools (Section 5.2). The length of used pins depended on the experimental run approx. 1 – 1.6 cm long. Thus, it has to be assured that the slurry penetration is deeper than 1 – 1.6 cm at the start of the excavation in order obtain Case B of the interaction.

Before excavation begins, the soil cylinder is filled with water-saturated and compacted soil. The free area between lid and tunnel face represents a slurry chamber and is therefore filled with slurry (Figure 7-5). The slurry chamber and the centre of the cutting wheel are fed by two separate slurry pipes. After closing, sealing and fixing the soil cylinder on the lathe, a defined pressure is applied to the entire cylinder using the slurry feed pipes. The pressure is monitored by a pore pressure sensor in both the soil cylinder and slurry cylinders. After a defined period of time, the drainage port is opened. The slurry starts to penetrate into the soil and the support mechanisms begin to build up. Note that the starting condition for slurry penetration is slightly different than in the column tests. The formation of the pressure transfer mechanism can be verified by the measured constant pore pressure in the slurry chamber and decreasing pore pressure in the soil outside of the slurry penetrated zone.

Consequently, when the pressure transfer mechanism is entirely built-up, the machine is started, and the cutting process begins. As pointed out before, a desired PR and RPM can be adjusted within a limited range. During excavation, the outflow from the soil cylinder and pore pressures are measured and logged every 0.25 s. Note that the drainage remains open during excavation.

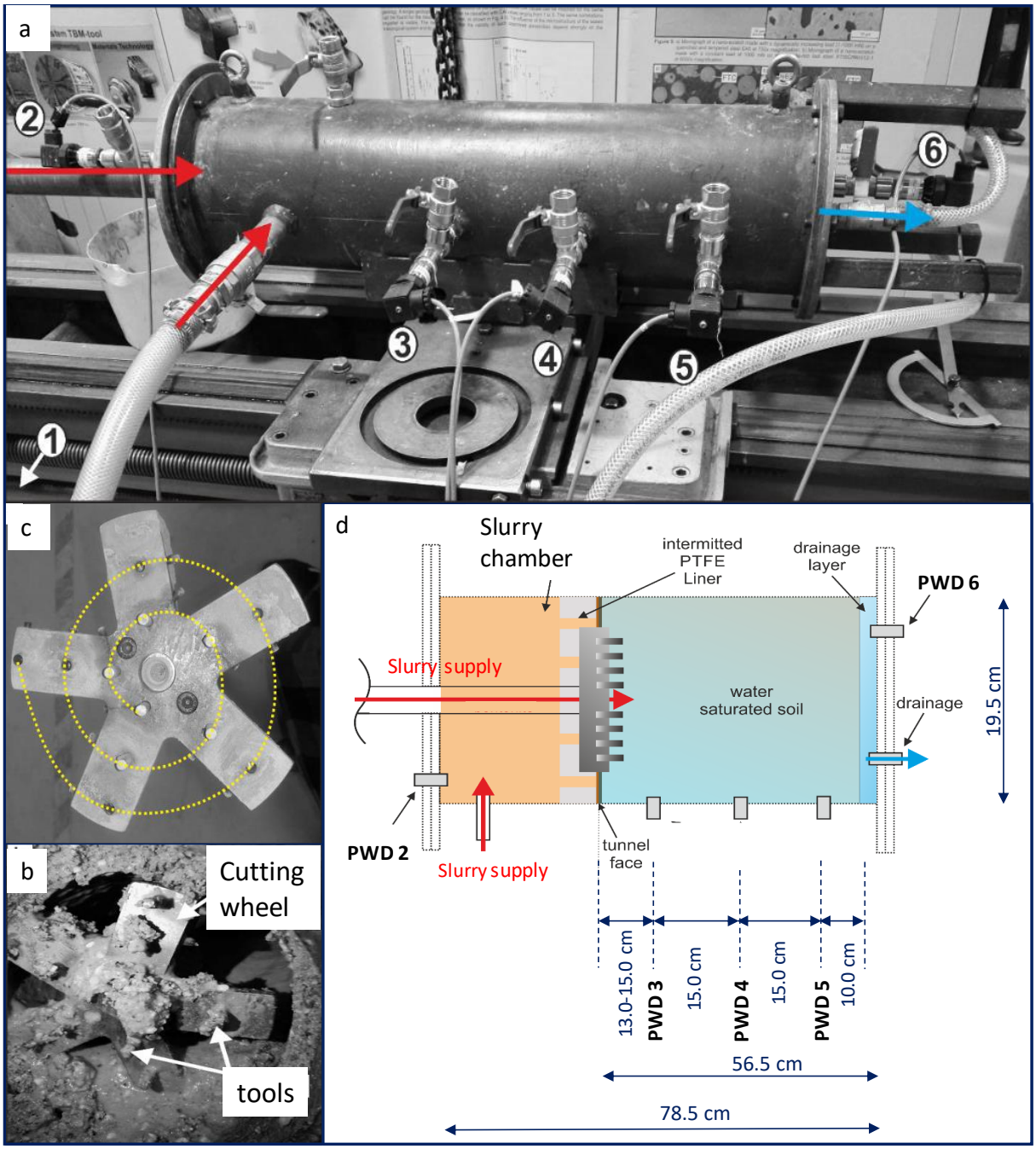

Figure 7-5: Experimental device with introduced soil cutting process – RUB tunneling device (Küpferle et al., 2018)

7.2 Experimental programme and materials

Three experimental series were conducted to investigate Case B of the interaction, as pointed out at the start of this chapter. The experimental programs and characterization of used materials will be presented in next sections.

7.2.1 Primary penetration and re-penetration

The experimental program (Table 7-2) was designed with the aim of investigating the Case B interaction, which expects a comparably deeper slurry penetration. Simultaneously, the slurry has to stagnate before the second measuring level in the experimental device (Figure 7-2). Another requirement is that relatively high injection pressures representing the slurry excess pressures are used. This is due to easier tracking of soil reaction during slurry penetration. Hence, one slurry concentration, two soil fractions and several levels of injection pressure were chosen based on preliminary tests. The chosen injection pressures correspond to a realistic range of slurry excess pressures at a real slurry shield. First, the main focus of the investigation was to assess the influence of flow boundary condition on the soil reaction during the slurry penetration test (experiments I-IV). Hence, the starting condition, internal

Table 7-2: Experimental program for investigating the primary slurry penetration in Case B of interaction, *hydraulic head difference between the outflow level of the soil cylinder and the fluid level in the outflow reservoir is approx. 0.07 bar, therefore back-pressure was 0.57 bar instead of 0.5 bar

Slurry	Initial slurry front location	Soil [mm]	Injection pressure [bar]	Back-pressure [bar]	Internal diameter of the outflow pipe [cm]	No. Experiment (repetitions)
B1, 6%	Slurry cylinder	1.00-2.00	0.2	0	2.3	Ia, Ib, Ic
			0.5	0	0.9	IIa, IIb, IIc
			1	0.57*	2.3	IIIa, IIIb, IIIc
B1, 6%	Soil sample	1.00-2.00	0.5	0	2.3	IVa, IVb, IVc
			0.3	0	2.3	Va, Vb, Vc
			0.7	0	2.3	VIa, VIb, VIc
B1, 6%	Soil sample	0.063-4.00	0.3	0	2.3	VIIa, VIIb, VIIc
			0.9	0	2.3	VIIIa, VIIIb, VIIIc

diameter of outflow pipe and the back-pressure were varied. The back-pressure was introduced in the way that pressure drop over the set-up remained the same as in the experiments without back pressure. The experimental runs with back-pressure are labelled later in the thesis with "BP-0.5 bar". Furthermore, focus was given to investigate the influence of injection pressure (experiments IV – VI). The tests VII-VIII were conducted to investigate the influence of soil grading on the penetration behaviour. The experimental program resulted in eight combinations. In general, three experimental runs for each combination were carried out in order to guarantee the reproducibility of the results. 24 experiments were performed in total.

A coarse, uniformly graded sand of fraction 1-2 mm with relatively high characteristic grain size (d_{10}) was chosen for the investigation basis (Table 7-3). Note that the soil fraction 0.063-4 mm was principally investigated with RUB tunneling device, therefore it is characterized in section 7.2.2.

Table 7-3: Properties of soils used in the slurry penetration and re-penetration investigation (grain distribution curve is provided in the appendix)

Soil fraction [mm]	1.00 - 2.00
Density [g/cm^3]	1.57 (1.59)
d_{10} [mm]	1.15
Porosity [-]	0.41
Compaction ratio [-]	0.63 (0.72)
Water permeability coefficient [m/s]	(5-11)*10^{-3}

The installation and compaction of the soils in the cylinder were controlled to obtain highly similar porosities among all investigated samples. Another requirement for obtaining reproducible results of experiments involving bentonite slurry is the monitoring of its physical and rheological properties. Before every experiment, the slurry was tested according to DIN 4127 (2014). The methods used are described in section 3.1.2. The resulting average values of slurry characteristics are outlined in Table 7-4.

Table 7-4: Slurry properties used in the slurry penetration investigation (product sheet and testing protocols are provided in the appendix), the value in parentheses denotes an extreme

Parameter	Slurry - penetration	Slurry – re-penetration
	B1 - 6 %	B1 – 6 %
Density [g/cm^3]	1.031 - 1.036	1.035-1.043
Yield point (ball harp) [Pa]	58-59(69)	58
pH [-]	9.4 - 9.9	9.2-9.3
Marsh time [s]	t_{M1000} = 49-52 (63) t_{M1500} = 95-105 (133)	t_{M1000} = 66-71 t_{M1500} = 146-176
Apparent viscosity [mPa.s]	19.1	Not tested
Plastic viscosity [mPa.s]	2.9	
Yield point (Bingham) [Pa]	15.55	

The resulting pressure drops over the soil samples are important factors for the evaluation of the slurry penetration experiments. The average pressure drops are shown in Table 7-5 and put in reference to injection pressures.

Table 7-5: Resulting pressure drop over the soil sample

Pressure drops over the soil sample [bar]	**I,II, III, IV** - 1-2 mm, 0.5 bar	**V** - 1-2 mm, 0.3 bar	**VI** - 1-2 mm, 0.7 bar	**VII** - 0.063-4 mm, 0.3 bar	**VIII** - 0.063-4 mm, 0.9 bar
	0.4	0.2	0.6	0.2	0.8

The next step was represented by the investigation of pressure-controlled slurry re-penetration. For this purpose, the same materials as for primary slurry penetration were tested. Based on evaluation of the excavation scale in section 5, it was aimed to simulate two possible conditions at the tunnel face. Within the first condition, an imaginary cutting tool is passing every 60 s at a local point of the tunnel face and simultaneously cuts an imaginary p_{tool}=40 mm deep part of the slurry penetrated zone (Figure 7-4). Note that the location of pore pressure sensors (PWD) in the set-up is specially designed for this combination. The chosen imaginary cutting depth is both realistic and simultaneously relatively high, so that the pressure difference measurement between 4 cm distance is not dominated by measuring inaccuracy. The chosen combination corresponds to the excavation scale in homogeneous cutting Zone 4 of the reference project P1 (section 5.2). As described in the methodology of re-

penetration experiment without soil cutting (section 7.1.2), timespan for starting the slurry re-penetration after inducing the primary penetration was varied to find a combination fulfilling the formulated requirement for the realistic re-penetration. The necessary increase in injection pressure during re-penetration was also determined based on preliminary experiments. In the second investigated condition, a cutting tool was characterized by passing at every 100 s and imaginary cutting 40 mm of soil. The combination corresponds again to the homogeneous cutting Zone 4 of the reference project P1. It was omitted on the experimental modelling of shallower cutting depths from other reference projects due to their problematic tracking with sensors. The experimental program is shown in Table 7-6. It resulted in six combinations. In general, three experimental runs for each combination were carried out in order to guarantee the reproducibility of the results. 18 experiments were planned in total.

Table 7-6: Experimental program for investigating the slurry re-penetration in Case B of interaction

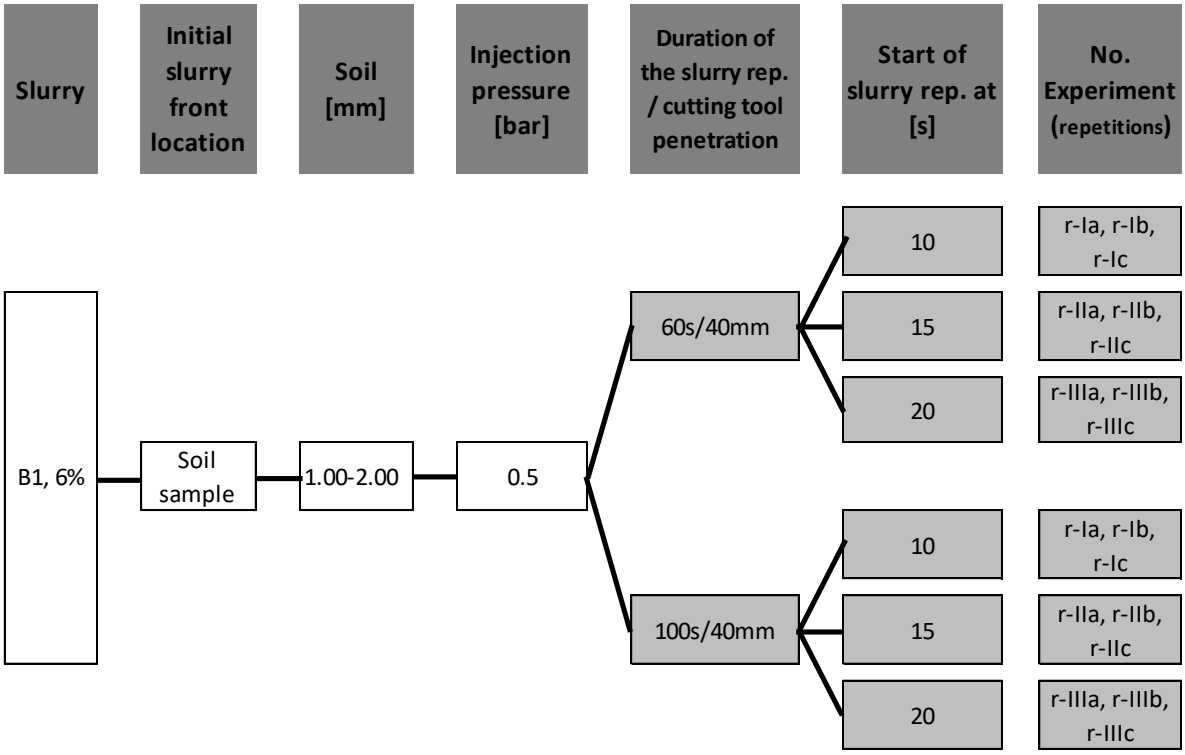

7.2.2 Re-penetration with soil cutting – RUB Tunnelling device

The experimental program was designed also with the aim of investigating of Case B interaction. Hence, the slurry penetration depth during primary penetration was higher than the tool cutting depth per passing. Two soils have been used for the investigation (Table 7-7). The coarse and uniformly graded sand (1-2 mm) was supplemented by a well-graded soil sample with diversified particle size (0.063-4 mm). The respective soil samples were coupled with suitable slurry chamber pressures, which were additionally also varied. Note that the slurry chamber pressure is not directly comparable with slurry injection pressures from the previous section. But the particular pressure drop induced by chamber pressure corresponds to the pressure drop in the set-up induced by the injection pressure from section 7.2.1. The slurry concentration was unchanged in comparison to the other experimental series. The properties of the slurry used in this series are shown in Table 7-8. The properties were monitored for each experimental run. The diameter of the outflow pipe was in this experimental series not changed. It turned out later during the experiments that the chosen diameter was sufficient. It could be checked based on the lack of formation of excess pore pressure in front of the drainage during excavation.

Table 7-7: Properties of soils used in the slurry re-penetration with soil cutting investigation, grain size distribution curves are provided in the appendix

Soil fraction [mm]	1.00 - 2.00	0.063 - 4.00
Density [g/cm^3]	1.57 - 1.59	1.59 - 1.67
d_{10} [mm]	1.15	0.07
Porosity [-]	0.4	0.37 - 0.4
Water permeability coefficient [m/s]	(5-11)*10^{-3}	6.41*10^{-4}

An important aspect of this experimental series is represented by the soil cutting process. Due to the experimental scale, it was not possible to induce a realistic tool cutting depth per pass. On the other hand, the used lathe did not allow for RPMs realistic for shield machines. Hence, following parameters characterizing the cutting process were adopted:

- RPM = 71
- PR = 0.1 mm/rev
- AR = 7.1 mm/min

Table 7-8: Slurry properties used in the slurry re-penetration with cutting investigation (product sheet and testing protocols are provided in the appendix)

Parameter	Slurry - re-penetration with cutting
	B1 - 6 %
Density [g/cm^3]	1.038 – 1.040
Yield point (ball harp) [Pa]	47
pH [-]	10.6 – 10.8
Marsh time [s]	t_{M1000} = 49-59 t_{M1500} = 111-124

It resulted in a pass of a cutting tool through a particular point at the tunnel face each 0.85 s and a tool penetration per passing 0.1 mm. The excavation speed (AR) was also smaller in comparison to a real-scale shield (Table 5-3). This excavation scale influence is considered in the evaluation of the experiments.

The experimental program resulted in four combinations. In general, three experimental runs for each combination were carried out in order to check the reproducibility of the results. Hence, 12 experiments were performed in total within this series (Table 7-9).

Table 7-9: Experimental program for investigating the slurry re-penetration with consideration of soil cutting in Case B of interaction

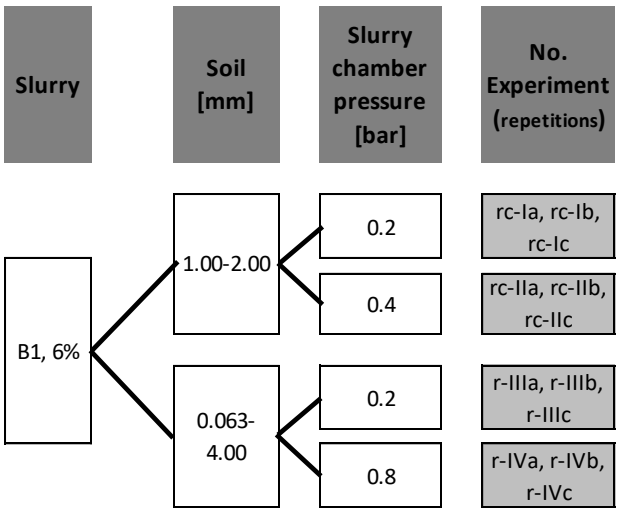

7.3 Results and Interpretation

7.3.1 Primary penetration of slurry within the column test

In this section the obtained results from experiments with varying boundary flow conditions are first presented and discussed (combinations I-IV). After that, this section is focused on the influence of varied slurry injection pressure (combinations IV-VI). Finally, the remaining combinations VII-VIII (influence of soil grading) are discussed.

Influence of the boundary flow condition

Following the methodology for Case A characterization, the time-dependent slurry penetration depth was evaluated first. It was focused on the influence of varying boundary flow conditions in the set-up, as slurry back-pressure, reduced diameter of the outflow from the set-up and location of slurry front at the experiment start. The time-dependent penetration depths are visualized in Figure 7-6-left. The results are shown as averages for the entire experimental combination. It could be shown that the different flow boundary conditions have the influence on the slurry penetration depth. The experimental combinations I, II, III were conducted with equal batch of slurry. For combination IV, a different batch was used delivering slightly different rheological properties for the same concentration of solids (see appendix for details). For the purpose of more exact comparison of all four combinations and further analysis, the comparative slurry penetration depth is shown in Figure 7-6-right. Comparative penetration depth is determined from the actual penetration depth while assuming

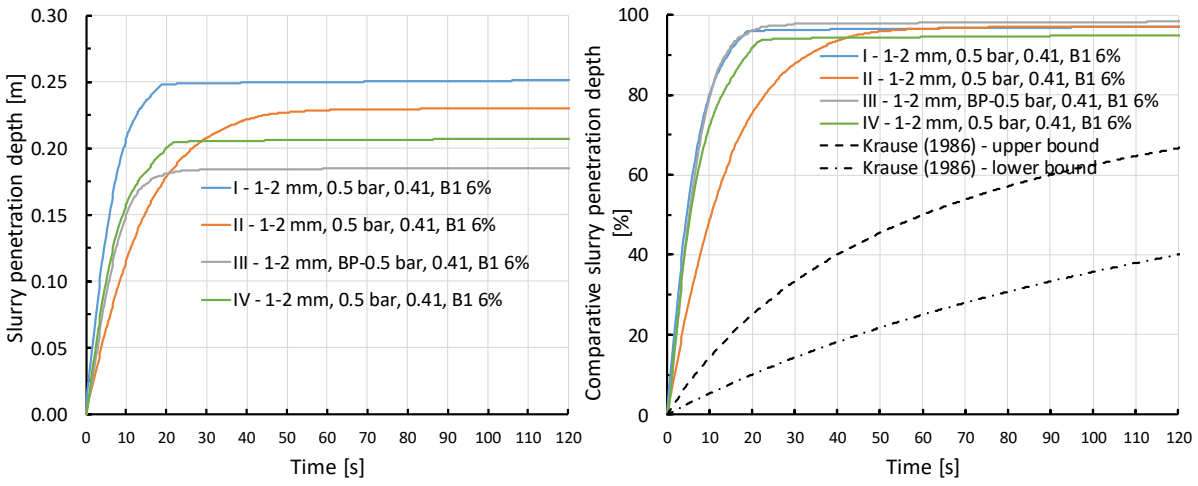

Figure 7-6: Time-dependent slurry penetration for different boundary flow conditions –absolute penetration depth left and comparative penetration depth right

that 100 % corresponds to the final penetration of each combination ($Eq.\,3\text{-}33$). Both diagrams show that the reduction of the outflow diameter (combination II) has the most significant influence on the development of the penetration depth. However, the final penetration depth does not change significantly due to the outflow diameter reduction. The introduction of the back-pressure (combination III) did not influence the time-dependent development of the penetration, but it reduced the absolute penetration depth. This may be caused by increased hydraulic resistance of the set-up due to the introduction of the outflow cylinder with back-pressure. The hydraulic resistance of the set-up for water is shown in Table 7-1. Combination IV differentiates from the basis combination I by generally lower penetration depth. This can be caused by different batch of bentonite as pointed out before. However, the obtained comparative penetration depth in Figure 7-6-right was almost identical for these two combinations. Interestingly, the methodology suggested by Krause (1987) to calculate the time-dependent penetration depth from the final one could not even get close to the measured penetration depth development for both bounds ($Eq.\,3\text{-}34$ and $Eq.\,3\text{-}35$).

The influence of varied boundary flow conditions was further studied through a visualisation of pore water pressures and effective stresses. The pore pressures and effective stresses are evaluated as differences between their static level before the experiment starts and their actual level during the experiment at the particular time and sensor. On one hand, this method of evaluation has certain advantages such as the exclusion of the factor of gravity at different elevations and the minimization of measurement error in comparison to “absolute amount” measurements. On the other hand, the approach for determining the differences in effective stress is sensitive to influences resulting from effective stress path in the set-up. For instance, if the initial effective stress would be higher than slurry injection pressure, no increase of the effective stress would be observed during the experiment. Hence, the initial effective stress is an important factor in the experiments. Simultaneously, the initial effective stress cannot be too low, because it would induce stress redistribution in the set-up during the experiment leading to the obtaining of low change in effective stress. Thus, the initial stress was kept constant on reasonable level approximately 20 kPa within all experiments determined by trial and error approach. The trial and error approach aimed to determine the initial effective stress for which the pore pressure drop during

the experiment would correspond to the effective stress change. Average results from three experiments within a combination are shown in following diagrams.

The differences in pore pressures and effective stresses are first visualized at two levels (PWD 4 corresponding to WZ 1; PWD 7 corresponding to WZ 2). The location of the sensors in the set-up can be taken from Figure 7-2. The reaction of soil at the 1st measurement level located closer to the injection point is shown in Figure 7-7. The 1st measurement level is from approx. 5 s ahead (10 s for combination II) located inside slurry penetrated zone. This fact is decisive for the reaction of soil measured at this level. For the characterization of soil´s reaction, four consecutive stages could be distinguished for all experimental combinations. These stages can be generalized for the slurry penetrated zone in experimental combination I-IV as:

1) Increase in effective stress due to flow pressure
2) Decrease in effective stress due to excess pore pressure formation and reaching the peak
3) Increase in effective stress caused by the dissipation of excess pore pressures
4) Branches reach constant effective stress and excess pore pressure

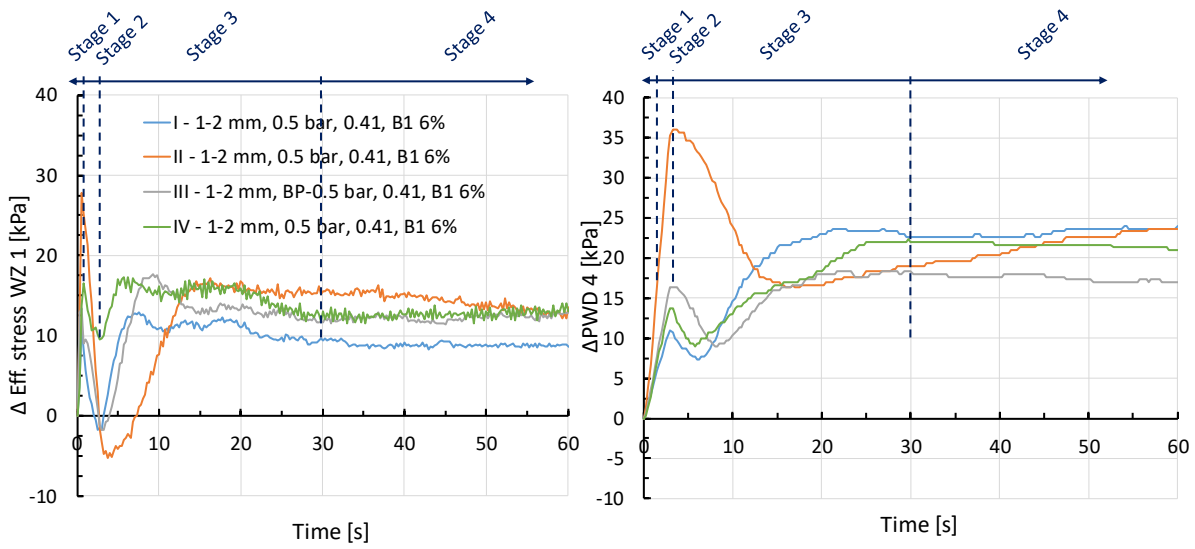

Figure 7-7: Time-dependent slurry penetration at different boundary conditions of flow – 1st measurement level, stages are marked specifically for combination IV

As the next focus, the development for effective stress and excess pore pressure will be evaluated at the 2nd measurement level where PWD 7 and WZ 2 are located. The 2nd level (Figure 7-2) is located further from the slurry injection point. Hence, the 2nd level is not achieved by the slurry penetration front (compare the location to Figure

7-6). The development of effective stress and pore pressure can be seen Figure 7-8 for experimental combinations I-IV. Also for the zone not penetrated by slurry, four consecutive stages characterizing the reaction of soil could be identified:

1) Increase in effective stress is comparably lower here than for the measuring level closer to the injection point.
2) Decrease in effective stress simultaneously with the formation of excess pore pressure. Excess pore pressure is also comparably lower at this measurement level.
3) Increase in effective stress with ongoing dissipation of pore excess pressure
4) Reaching the constant increased values of effective stress and zero excess pore pressure. The constant value of effective stress increase is comparably higher here.

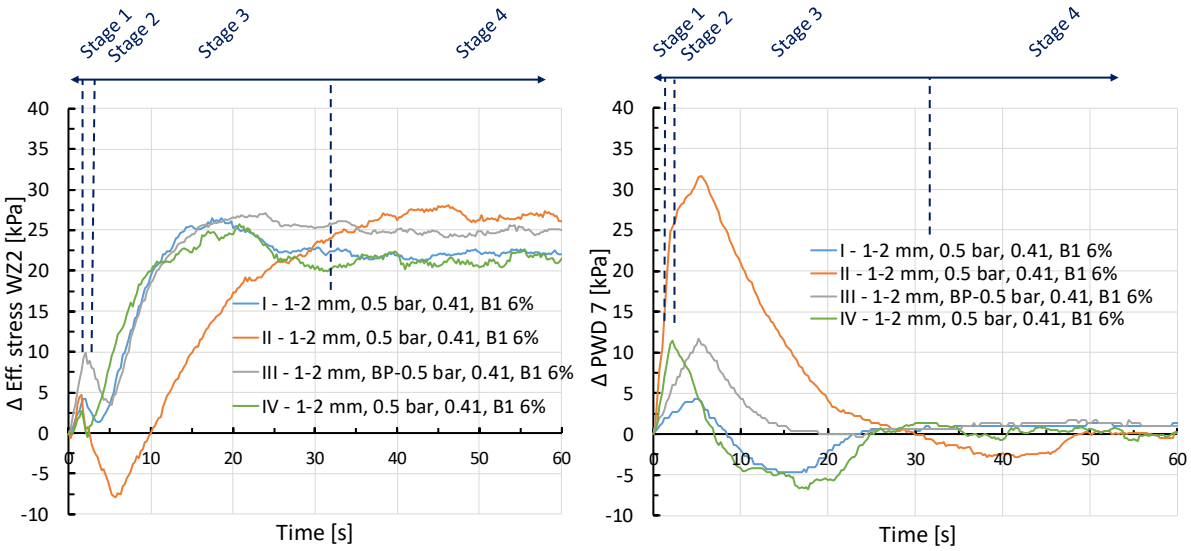

Figure 7-8: Time-dependent slurry penetration at different boundary conditions of flow – 2nd measurement level, stages are marked specifically for combination IV

Through a comparison of the defined stages between the experimental combinations with different flow boundary conditions, the influence of these flow condition on the soil´s reaction can be assessed. Experimental combination I is taken here as the reference.

At the 1st time-stage of the first measurement level, combinations I and III are showing similar size of the effective stress peak, while combinations II and IV are reaching higher peak values. It is caused by higher flow pressure, resulting in a higher change in effective stress in these combinations. Higher flow pressure can be explained by higher set-up resistance for flow in combination II and by higher flow resistance against slurry

in combination IV. Note that in combinations I, II, and III the soil skeleton is first entered by water. This is in contrast to combination IV, in which slurry immediately enters the soil skeleton. At the 2nd measurement level, combination II showed the highest increase in effective stress. However, the increase was comparable with combination III, while obtaining a much lower increase for combinations II and IV.

Subsequently, the 2nd time-stage is characterized by comparably much higher excess pore pressure peaks in combination II at both measurements levels while the other combinations delivered similar size of the peaks. Different situation occurs for the effective stress in this stage. The drop in effective stress at the 1st measurement level is significantly lower for the combination IV. It could mean that at this stage the effective stress is not only caused by flow pressure, but rather by viscous stagnation forces of slurry. This expectation could be supported by the same inclination of slurry penetration lines in Figure 7-6 during this 2nd time-stage. At the 2nd measurement level this effect is not observable, because the slurry penetration front did not reach this level. In contrast, the drop in the effective stress for combination II is even more significant. It results in an effective stress that is even lower than the value at the start of the experiment.

The 3rd stage is characterized by successive increases in effective stress due to slurry stagnation. The highest effective stress increase is reached during this stage. At this time, the effective stress is still partially induced by flow pressure, but also by stagnation. This is justified by combination IV, which reaches its peak the fastest due to immediate contact between the slurry and the soil skeleton. The peak is observable at both measurements' levels. It can be observed that the 3rd time-stage is considerably delayed for combination II, due to the slow dissipation of excess pore pressure. The slow dissipation in combination II is explained by the reduced outflow pipe diameter. The development of the monitored variables in other three combinations is very similar at this stage.

During the 4th and final time-stage, the excess pore pressure inside the slurry penetrated zone and the effective stresses, both outside and inside the penetrated zone, reach the stationary values. The excess pore pressure outside of the slurry penetrated zone converges to zero. During this stage the slurry excess pressure is transferred only by stagnation forces resulting from slurry properties. It can be

observed that the stationary value of the transferred effective stress is slightly lower than the peak value during the 3rd time-stage.

Consequently, the excess pore pressure distributions were evaluated for the experimental combinations I-IV at defined time-stages. For this purpose, four timespans from the beginning of penetration were chosen: 3s, 10s, 40s and 60s. The objective was to characterize the pore pressure development in the set-up properly. The early penetration stages (Figure 7-9-left) are characterized by pore pressure increase throughout the entire set-up. This is particularly observable for combination II with reduced outflow diameter. In this combination, the pore pressure also remains increased throughout the whole set-up for the timespan t=10 s, while the pressure for the other combinations has already dropped by then. When the combinations are compared with regard to the location of slurry penetration zone at the start of the experiment, lower pore pressures drops are observed for combinations I and II at the early penetration stage. However, the difference to the combination IV is already negligible at t=10 s. During the early stages of the penetration the influence of the back-pressure can be seen in the clearest way, when decreasing the drop of the distribution also at the time t=10 s in comparison to combination I. Consequently, when the pore pressure distributions in later slurry penetration stages are compared (Figure 7-9- right), it is concluded that the role of set-up is already almost negligible at

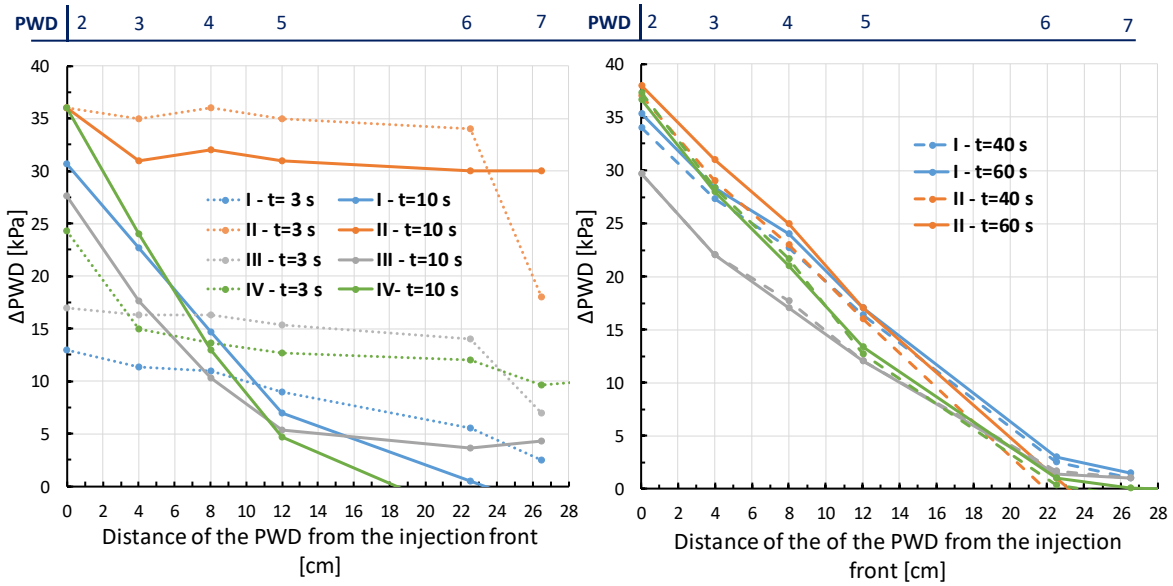

Figure 7-9: Distribution of pore pressures in the set-up depending on boundary flow condition, Left: at 3s and 10 s, Right at 40s and 60s since experiment start

this stage. The pore pressure distributions at these stages are approximately linear for all combinations. Thus, the investigation of the pore pressure distribution confirmed that in later penetration stages (t=40s, 60 s) the increased pore pressure is measurable only inside the slurry penetrated zone.

In terms of further use of the particular boundary flow conditions of the experiments, it was decided to continue with boundary conditions employed in combination IV. The following reasons can be outlined for this decision:

- Back-pressure has negligible influence
- Reduced outflow diameter exaggerates the influence of the set-up over the slurry / soil combination
- When the slurry front is located at the soil edge, it is beneficial for the slurry re-penetration investigation due to easier determination of the moment when slurry enters the soil. The knowledge of the moment is important for steering of the re-penetration
- When the slurry front is located at the soil edge, it is beneficial also for improving constant pressure boundary condition in the experiment. Not a significant influence on the slurry penetration depth was observed

Influence of the injection pressure

In this section, it was focused on the investigation of the injection pressure influence on the reaction of the soil during penetration (combinations IV-VI). For this investigation, the same flow boundary conditions as in combination IV were used.

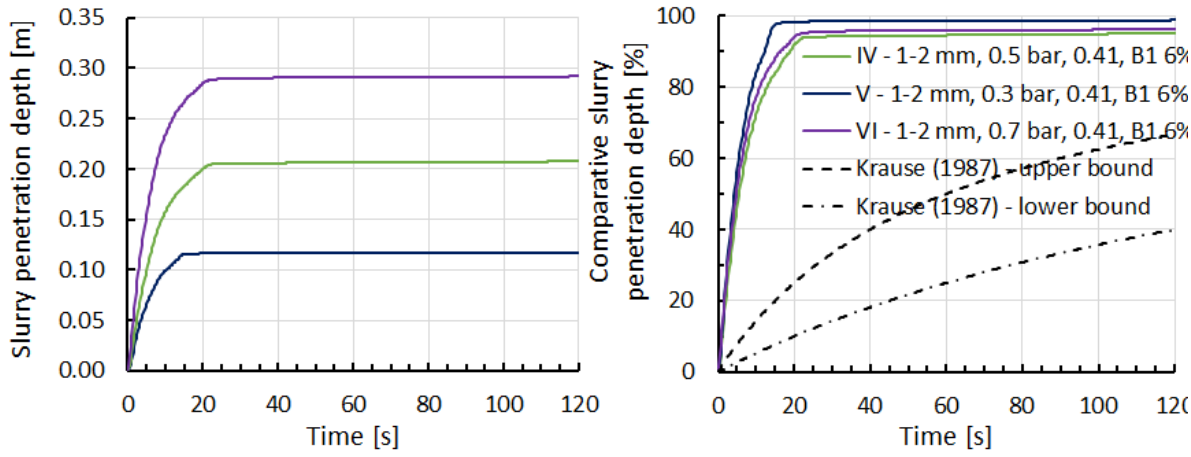

Figure 7-10: Time-dependent slurry penetration for different injection pressures –absolute penetration depth left and comparative penetration depth right (% of the final penetration depth)

Figure 7-10 is showing the time-dependent slurry penetration depth for different injection pressures. As was expected, higher injection pressure caused a deeper slurry penetration. Interestingly, the diagram with comparative penetration depth (calculated as in the previous cases) is showing very similar lines for the all injection pressures (compare with Figure 6-3 with soil fraction 0.25-0.5 mm). The timespan for reaching the stagnation is slightly lower for the injection pressure 0.3 bar in combination V. In contrast, these timespans are equal for injection pressures 0.5 and 0.7 bar in combinations IV and VI respectively.

To study the dependence of penetration depth on the injection pressure in detail, the diagram in Figure 7-11 was plotted. Note that the point showing the zero slurry penetration for the zero pressure was added based on logical derivation. The diagram shows the relationship between the slurry penetration depth and the pressure drop over the soil sample. It turned out that the slurry penetration depth is linearly dependent on the pressure drop. Thus, the relationship in Figure 7-11 is showing a different trend than in Figure 6-4. The linear relationship in Figure 7-11 is indicating that the methodology for pressure controlled re-penetration as described in section 7.1.2 can be used for this slurry-soil combination without significant deviations from realistic re-penetration at the tunnel face with soil cutting. Moreover, Figure 7-11 shows that the interaction between slurry and soil in this combination does not have to be assessed on the micro-level. The linear dependence between pressure drop and penetration logically means that the retention of slurry particles in the pore space does

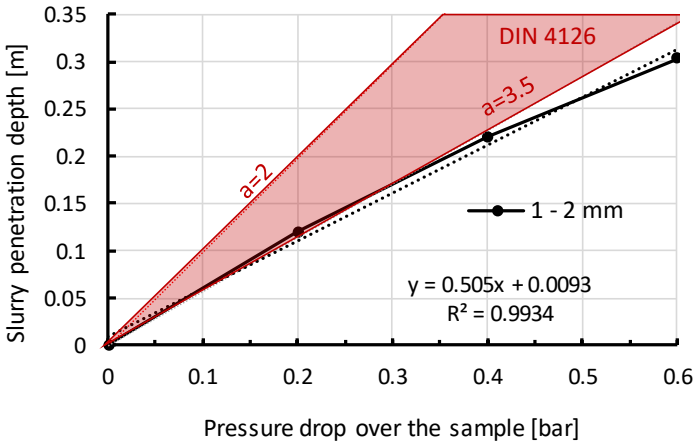

Figure 7-11: Relationship between slurry penetration depth and pressure drop in the experiment for soil 1-2 mm, porosity 0.41 and slurry B1 6% (DIN 4126 uses Eq. 3-27 with a = 2 or 3.5)

not cause significant change in the pore space geometry. This can be confirmed also by Figure 7-10 showing no dependence of the comparative slurry penetration depth development on the injection pressure.

Further, the influence of varied injection pressure was studied through visualisation of pore water pressure and effective stress developments in the set-up. The same visualisation methodology was employed here as it was previously in this section. The differences in pore pressures and effective stresses are first visualized at two levels (PWD 4 corresponding to WZ 1; PWD 7 corresponding to WZ 2). The location of the sensors in the set-up can be taken from Figure 7-2. Inside the slurry penetrated zone (Figure 7-12), the reaction of soil can be again divided into the same four stages as during the investigation of boundary flow conditions:

1) The effective stress peak due to flow pressure is comparable for combinations IV and VI while it is significantly smaller for combination V
2) Drop of effective stress due to excess pore pressure is for combination VI the smallest due to very short duration of this stage for combination VI formation. The pore pressure peak does not exist in combination V for this stage.
3) In this stage is the influence of injection pressure visible the most, when the effective stress increases due to flowing slurry and simultaneous excess pore pressure dissipates
4) Reaching of branches with constant effective stress and excess pore pressure is characterized by the most significant effective stress drop in combination VI.

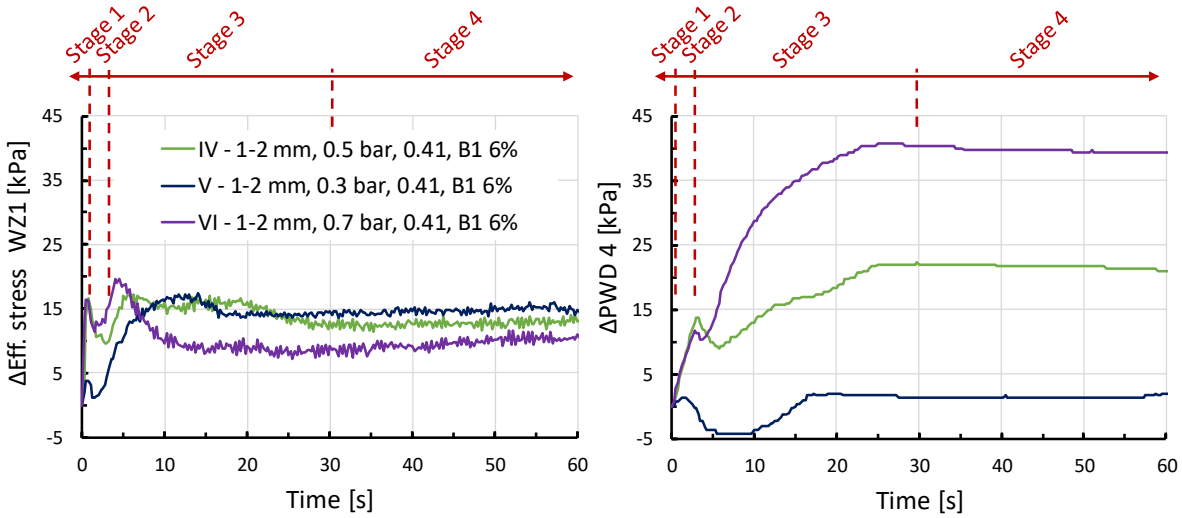

Figure 7-12: Time-dependent reaction of soil at different injection pressures – 1st measurement level, stages are marked specifically for combination IV

This is due to a higher increase in pore pressure inside the slurry penetrated zone

As the next focus, the development for effective stress and excess pore pressure will be evaluated at the 2nd level, where PWD 7 and WZ 2 are located outside of slurry penetrated zone in general (Figure 7-13). Note that this measurement level is achieved by slurry in combination VI at the end of the penetration process. The influence of injection pressure on the soil´s reaction outside of the slurry penetrated zone is summarized again in following four stages:

1) Increase of effective stress is generally lower here and is comparable for combinations IV and VI. In combination V, no peak could be identified.
2) Drop in effective stress simultaneously with the formation of excess pore pressure. Pore pressure peak is the highest for combination IV, which is difficult to explain. Excess pore pressure is also comparably lower at this measurement level.
3) Increase in effective stress with ongoing dissipation of pore excess pressure. The increase is also connected with increasing slurry penetrated are with pressure transfer. The influence of the injection pressure is the most significant at this stage
4) Reaching the constant increased values of effective stress and zero excess pore pressure for combination IV and V. Increased pore pressure is measurable here for combination VI due to deeper slurry penetration. The constant value of effective stress increase is comparably higher here than inside the slurry penetrated zone.

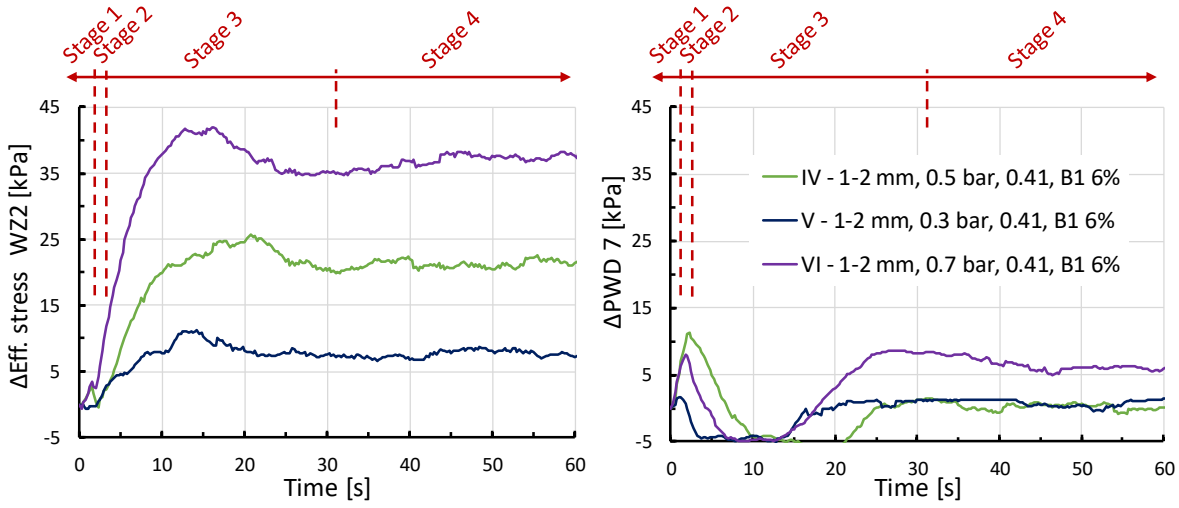

Figure 7-13: Time-dependent reaction of soil at different injection pressures – 2nd measurement level, stages are marked specifically for combination IV

As the last step the pore pressure distribution at various timespans from the beginning of penetration will be evaluated. This is shown for timespan t=3s, t=10s, t=40s and t=60s in Figure 7-14. The distributions are scaled by the injection pressure in general. The only deviation to the scaling can be noticed for the timespan t=3s for combinations IV and VI, when the distributions are comparable. The encountered deviation from the trend cannot be reasonably explained. The regular scaling is observable also for the later stages of the slurry penetration in Figure 7-14-right. For all combinations, approx. linear pore pressure distribution inside the slurry-penetrated zone could be measured. The inclination is steeper at t=10 s than at the end of the penetration process. From the distributions, the stagnation gradients of slurry can be calculated. The gradients will be compared for the investigated combinations in chapter 9.

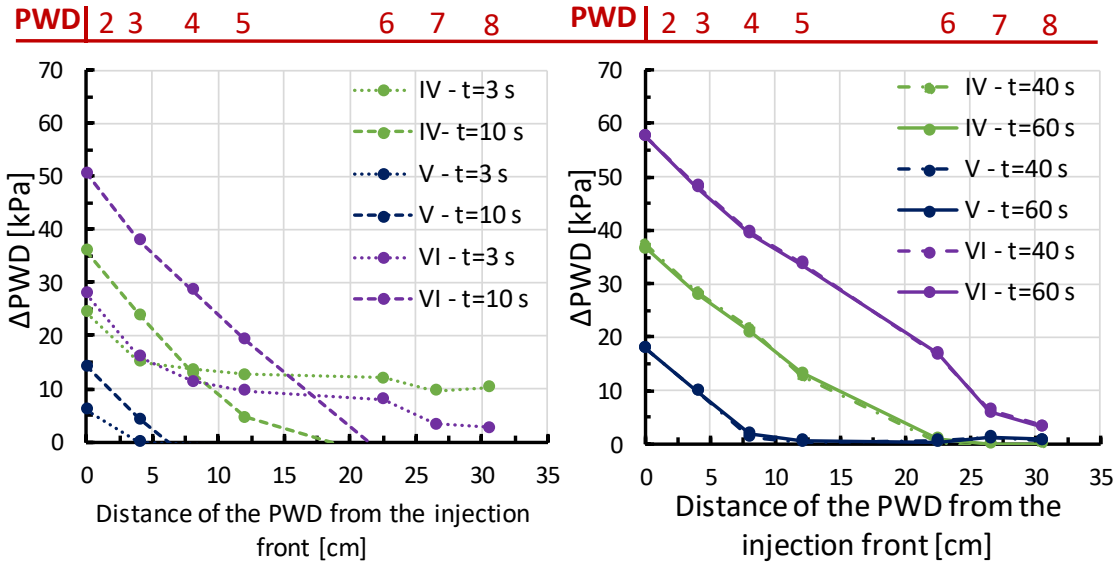

Figure 7-14: Distribution of pore pressures in soil at different stages of slurry penetration depending on the injection pressure

Influence of well-graded soil sample

As pointed out previously, these experiments were primarily conducted to visualize the penetration behaviour specifically for soil used in RUB tunnelling device (section 7.3.3). To test the primary slurry penetration depth for soil fraction 0.063-4 mm, additional tests were conducted using the set-up from Figure 7-1. The final slurry penetration depths depending on pressure drop and also pore pressure distribution in the soil sample are shown in Figure 7-15. The timescale up to 120 s is shown here due to the fact that the slurry penetration process takes longer in this finer soil. It is worth mentioning that the retained slurry particles in the pore space caused here change in

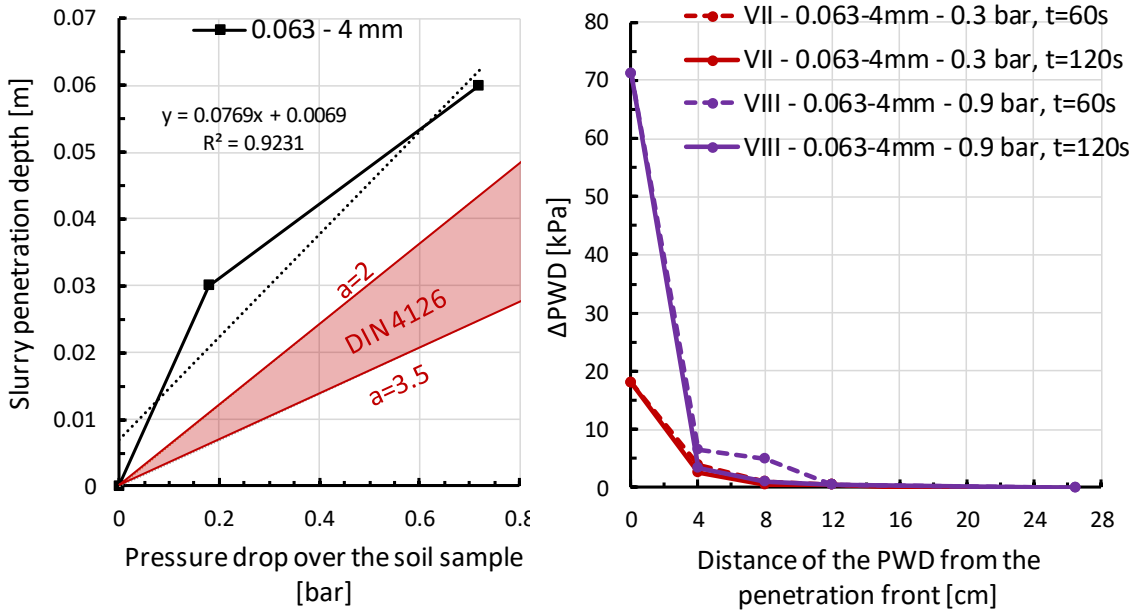

Figure 7-15: Slurry penetration depth vs. Pressure drop –left, distribution of the pore pressure inside the soil sample, note that combination VII corresponds to rc-III and combination VIII to rc-IV respectively

the geometry of the pore space, as in soil fraction 0.25-0.5 mm (section 6.3.1). It resulted in a non-linear dependence of pressure drop (defined by injection pressure) on penetration depth. Furthermore, Figure 7-15 also shows non-linear pore pressure distribution inside the slurry penetrated zone. Together with non-linear penetration depth dependence in this soil, it signifies a different slurry-soil-interaction mechanism than for the previously investigated soil with fraction 1-2 mm.

7.3.2 Re-penetration of slurry within the column test

The demand for the investigation of re-penetration of slurry was highlighted in chapter 4. The conditions at the tunnel face were simulated using the described methodology in section 7.1.2. The re-penetration of slurry was simulated for two excavation scales:

1) 40 mm cutting depth & 60 s timespan between tool passing
2) 40 mm cutting depth & 100 s timespan between tool passing

The two excavation scales will be evaluated separately. It was first assessed for the first excavation scale 40 mm & 60 s, which is a combination from the experimental program in Table 7-6 that fulfils the required condition for realistic re-penetration at the tunnel face. The time-dependent slurry penetration depth is shown in Figure 7-16. It is worth mentioning that the re-penetration depth was evaluated again using the methodology described in section 6.1. The slurry penetration development is visualized from the start of the experiment. The re-penetration starts at varying time-spans since the start of the experiment as defined in the experimental program (Table 7-6). It is observable in Figure 7-16-right that only the combination r-II - 15s+60s fulfilled the requirement for the re-penetration depth 4 cm within 60 s between imaginary passes of subsequent cutting tools.

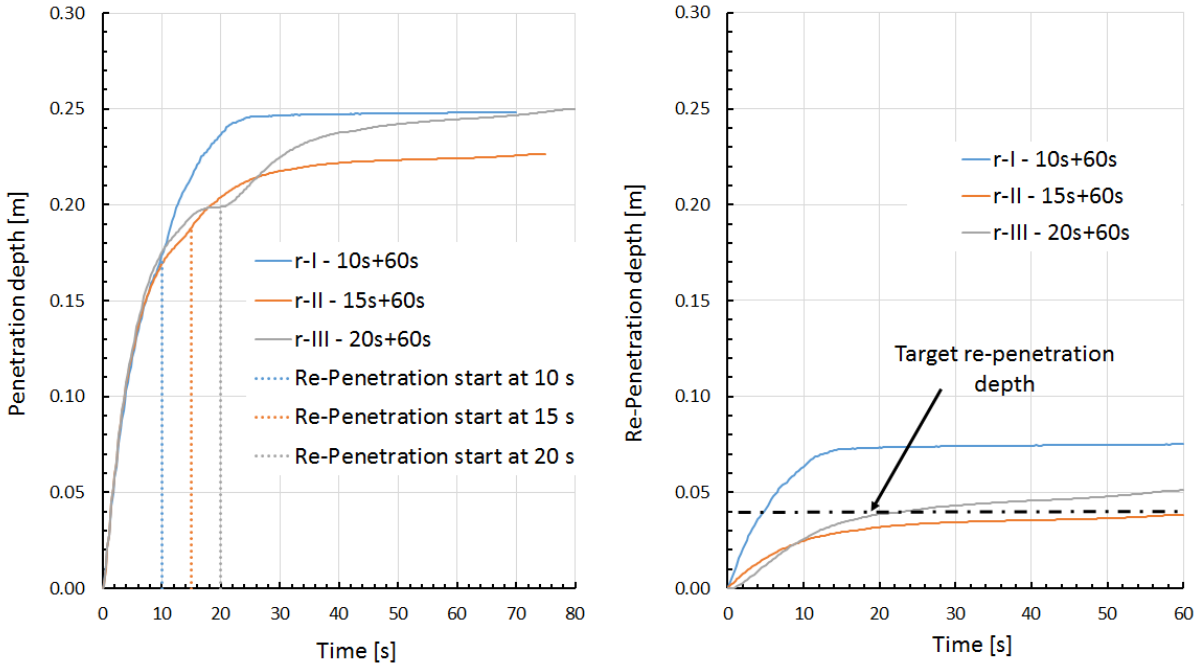

Figure 7-16: Time-dependent slurry penetration - left, time-dependent slurry re-penetration – right for the excavation scale 40 mm + 60s

A further requirement for the realistic simulation of the re-penetration is that the slurry pressure level during primary penetration at the interface between slurry and soil moves 4 cm deeper into the soil. Note that the 4 cm corresponds to the adopted cutting depth. The requirement can be confirmed by checking the sensors PWD 2 and PWD 3 during the experiment, because the PWD 3 is located 4 cm in soil and the PWD 2 is located in slurry. Thus, the PWD 2 is showing approx. the slurry pressure at soil-slurry interface. The pressures are compared in Figure 7-17. As in other sections of this thesis, the average values from each experimental combination are compared. It could be confirmed that the pressure condition was fulfilled for all combinations. Hence, the combination r-II – 15s+60s can be considered for the excavation scale 40 mm & 60 s as realistically modelling the conditions at the tunnel face during excavation.

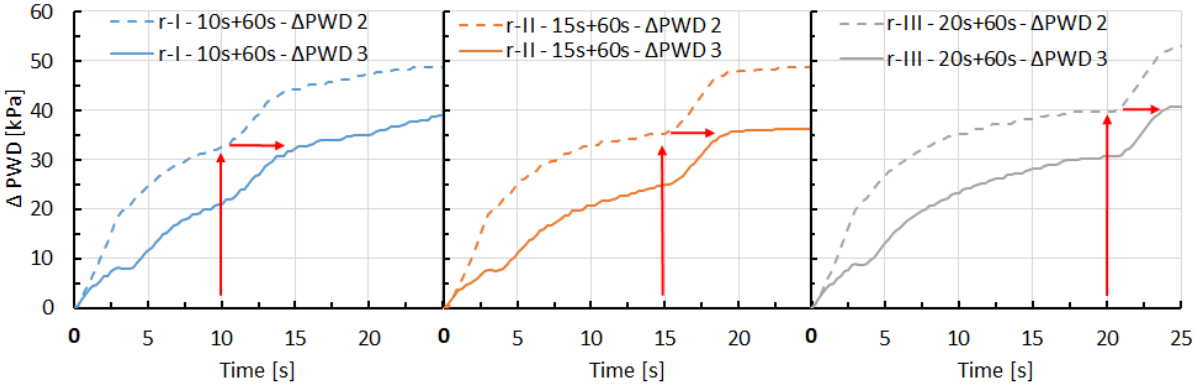

Figure 7-17: Comparison of PWD 2 and PWD 3 for the excavation scale 40 mm + 60s

Further, the influence of re-penetration on soil´s reaction was studied by visualisation of changes in pore water pressure and effective stress during the transient process. The same visualisation methodology was here employed as previously in this chapter. The differences in pore pressures and effective stresses are first visualized at two measurement levels (PWD 4 corresponding to WZ 1 and PWD 7 corresponding to WZ 2). The location of the sensors in the set-up can be taken from Figure 7-2. The measurements at the 1st level inside the slurry penetrated zone are shown in Figure 7-18. Until the beginning of re-penetration, the reaction of soil corresponds to the previously discussed behaviour. Subsequently, the reaction of soil during re-penetration can be divided into three stages:

1) Immediate increase in effective stress due to increases in injection pressure to simulate re-penetration. Pore pressure does not yet react at this stage.
2) Decrease in effective stress due to formation of pore pressure resulting from injection pressure increase

3) Reaching of the increased stationary values of effective stress and pore pressure

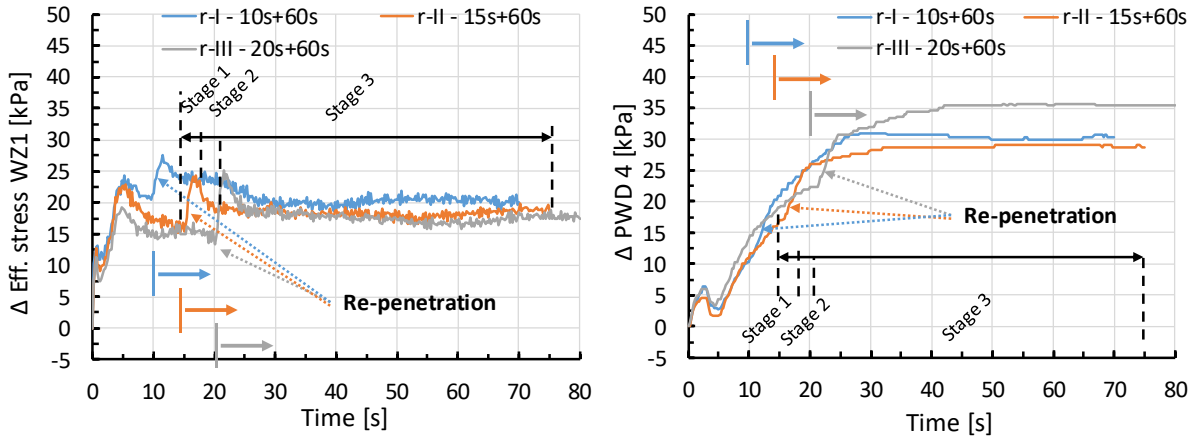

Figure 7-18: Reaction of soil at the 1st measurement level during re-penetration with excavation scale 40mm + 60s, stages are marked specifically for combination r-II

Distinguishable between the three combinations is the different effective stress value when the re-penetration starts. The measurements at the 2nd level outside the slurry penetrated zone are shown in Figure 7-19. Until the start of the re-penetration, the reaction of soil again corresponds to the previously discussed behaviour. Subsequently, the reaction of soil during re-penetration can be divided into one (two) stages:

1) Effective stress increases and remains unchanged (combinations r-I and r-II). Pore pressures are not influenced by the re-penetration. The respective diagram shows only the change of pore pressure caused by leaving and reaching the hydrostatic state again.
2) This stage is only observable in combination r-I and is characterized by a slight decrease in effective stress. The stage occurs only for combination r-I due to early start of the re-penetration. It can be seen from Figure 7-16 that the first decrease of slurry flow velocity occurs during re-penetration. That is in contrast to other two combinations.

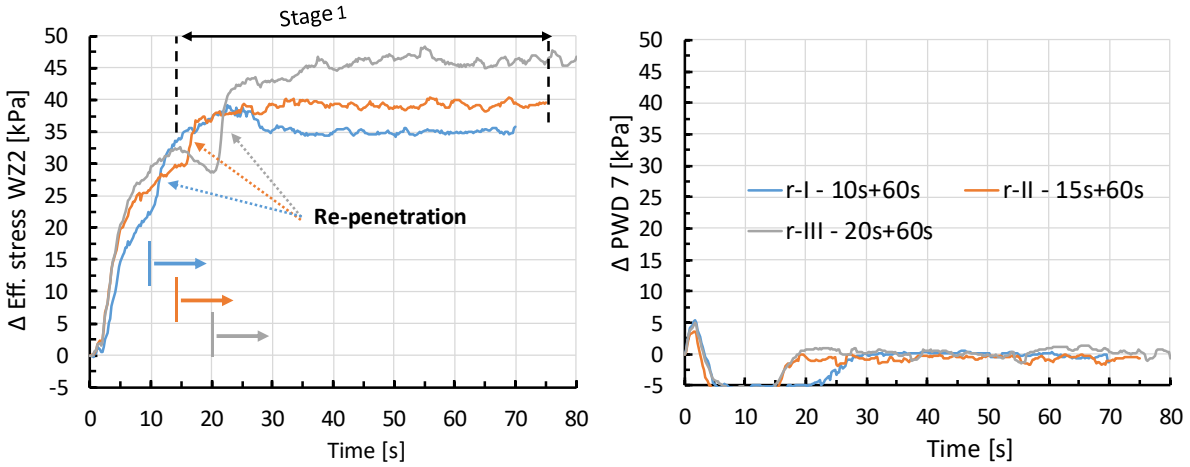

Figure 7-19: Reaction of soil at the 2nd measurement level during re-penetration with excavation scale 40mm + 60s, stages are marked specifically for combination r-II

As the last point, the distributions of pore pressure inside the set-up were investigated. The pore pressure distribution is visualised at timespans 3s, 10s, 40s and 60s starting from the beginning of the re-penetration. The distributions are shown in Figure 7-20. The pore pressures at early stage t=3s are not showing linear distribution, while at 10s the distribution has already become linear. The distribution remains linear until 60s, which denotes the end of excavation cycle. Between 10s and 60s the lines are only slightly shifted to the right. Note that the distance 0 cm means the distance from the

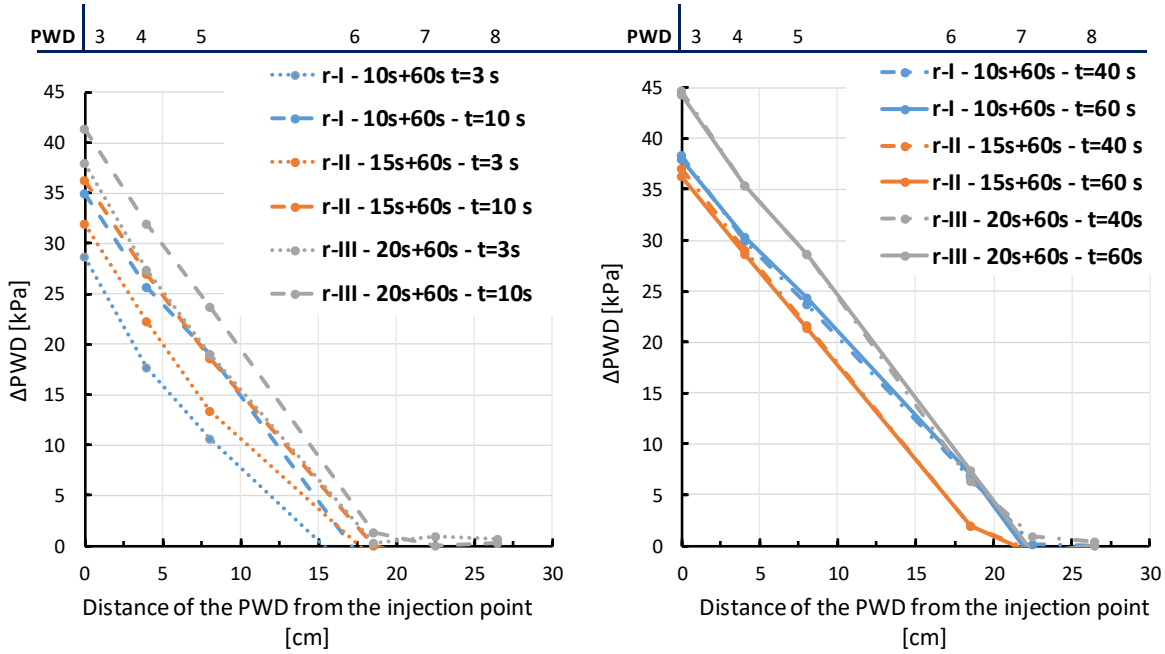

Figure 7-20: Distribution of pore pressures during re-penetration with excavation scale 40mm + 60s, timespans are given from the start of the re-penetration

point of imaginary cutting depth. No further significant difference could be observed between the combinations.

The second excavation scale, with cutting depth 40 mm and timespan between subsequent cutting tools equal to 100 s, was evaluated in the same manner. Due to the previously presented results in this section, the experimental combination r-IV – 20s+100s was not investigated since it would exceed the 4cm re-penetration depth at 100 s, as could be concluded from Figure 7-16 since the re-penetration depth exceeded 4 cm already at 60 s. It could be shown by evaluation of the time-dependent slurry penetration depth in Figure 7-21 that only the combination r-V – 30s+100s fulfilled the required re-penetration depth 4 cm. With respect to the moving injection pressure during the switch to the re-penetration, it can be seen Figure 7-21 that too high pressure for the re-penetration was used in combination r-VI – 40s+100s. Hence, the combination r-V – 30s+100s can be considered for the excavation scale 40 mm & 100 s as realistically modelling the conditions at the tunnel face during excavation.

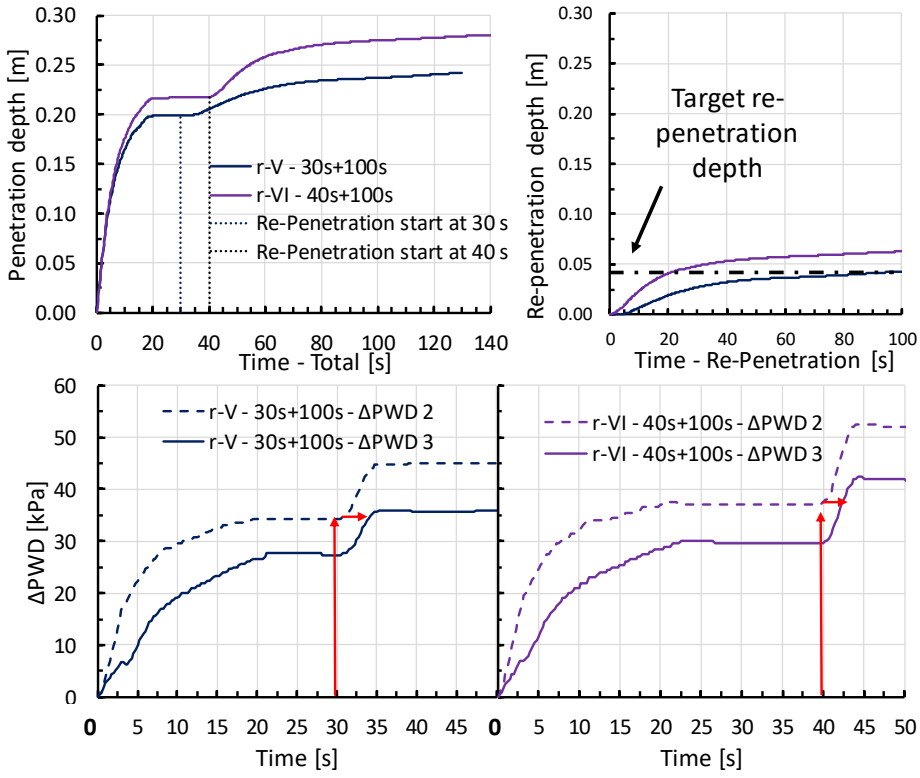

Figure 7-21: Time dependent penetration depth and Comparison of PWD 2 and PWD 3 for the excavation scale 40 mm + 100s

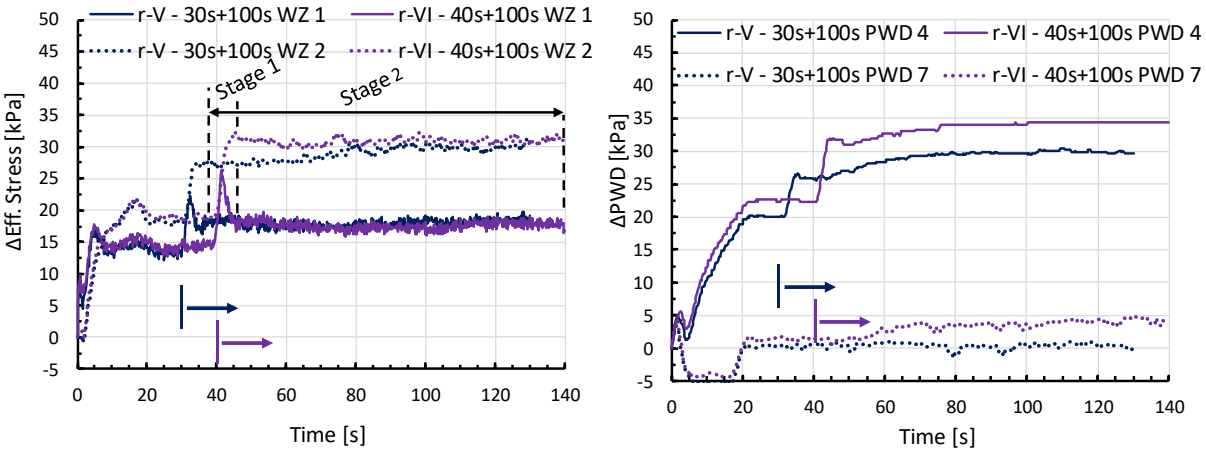

Figure 7-22: Reaction of soil at the 1st and 2nd measurement level during re-penetration with excavation scale 40mm + 100s, stages are marked specifically for combination r-IV and WZ 1

Further, the reaction of soil was evaluated again by measuring the effective stress and pore water pressures inside and outside of the slurry penetrated zone. The results of the measurements are shown in Figure 7-22. The trends shown by evaluation of effective stresses and pore water pressure for the previous combinations in this section could be confirmed here. The higher increase in effective stress at stage 1) in the combination r-VI is caused by a higher increase in injection pressure during re-penetration. The distributions of the pore pressure were also evaluated. This is shown in Figure 7-23 and it has also confirmed the trend observed for the previous excavation scale.

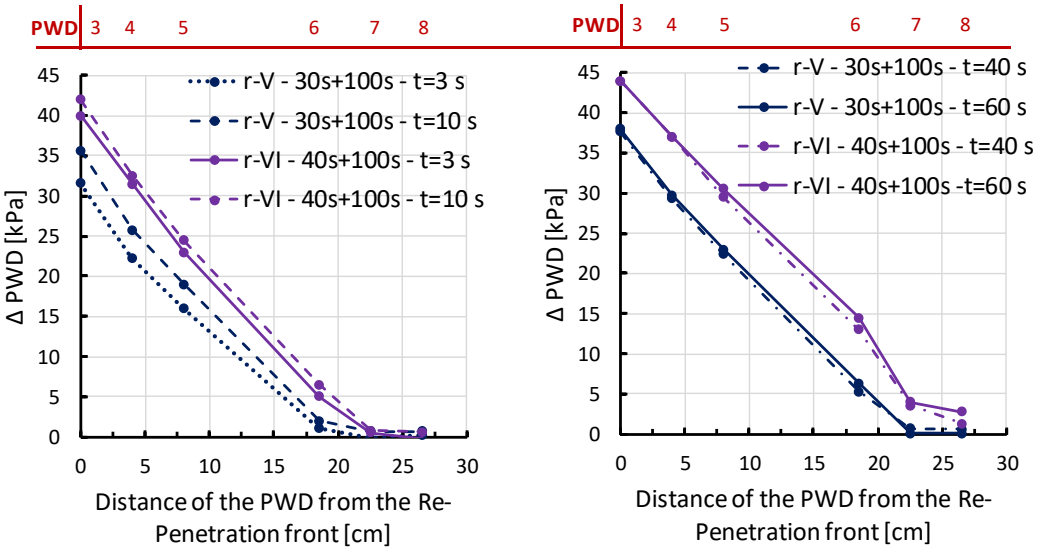

Figure 7-23: Distribution of pore pressures during re-penetration with excavation scale 40mm + 60s, timespans are given from the start of the re-penetration

7.3.3 Re-penetration with soil cutting – RUB Tunnelling device

The RUB tunnelling device was employed to investigate the reaction of soil during slurry re-penetration with soil cutting. As mentioned in section 7.2.2, two soil fractions (1-2 mm and 0.063-4 mm) were tested with the tunnelling device. For both soil fractions, it was necessary to confirm that the depth of the primary slurry penetration is larger than the length of pins at the cutting wheel. The primary slurry penetration depths for the soil fractions were already investigated in section 7.3.1. The pressure drops 0.4 bar (combination IV) and 0.2 bar (combination V) delivered for the soil fraction 1-2 mm penetration depths of 20-25 cm and 9-14 cm respectively. The pressure drops 0.2 bar (combination VII) and 0.8 bar (combination VIII) delivered for soil fraction 0.063-4mm slurry penetration depth 3 cm and 6 cm. While considering the length of the pins (11- 16 mm), it could be concluded that Case B is relevant for the interaction. For the soil fraction 1-2 mm, linear pore pressure distribution inside the slurry penetrated zone was determined for all investigated combinations during primary penetration, while the distribution was non-linear for fraction 0.063-4 mm (section 7.3.1).

The excavation with RUB tunnelling device starts after the establishment of the pressure transfer mechanism, when the approximately final slurry penetration depth is achieved. Since it is not possible to visually check the slurry penetration before the start of excavation, the distribution of the pore pressure inside the device after the primary slurry penetration was evaluated. Assuming linear distribution of the pore pressure inside the penetrated zone as was determined in section 7.3.1, it turned out that the slurry penetration in soil fraction 1-2 mm is approx. 14 cm for chamber pressure 0.2 bar and 25 cm for the pressure 0.4 bar, respectively. Hence the results fit well with the primary slurry penetration obtained for respective pressure drops in section 7.3.1. No pore pressure outside of slurry chamber could be measured for the soil fraction 0.063-4 mm due to shallow slurry penetration. Hence, the primary penetration depths, 3 cm and 6 cm respectively, obtained in the column test in section 7.3.1 are here taken for the interpretation of the tests using RUB tunnelling device.

As the first point, the pore pressure development in the RUB tunnelling device during excavation will be evaluated. The pore pressure distributions during excavation in soil 1–2 mm are shown in Figure 7-24. The figure shows average distributions for the two amounts of slurry pressure in the chamber, additionally the pore pressure distribution curves acc. to Bezuijen et al. (2001) calculated by $Eq.\,3\text{-}41$ are drawn. Note that the curve acc. to Bezuijen et al. (2001) expects ideal three-dimensional flow field in front of the tunnel face, which is probably not completely achieved in the RUB tunnelling device. The experimentally obtained pore pressure distributions show here approx. linear distribution depending on the distance from the rotating cutting tools. This could be confirmed for both chamber pressures. Further, it could be observed that the pore pressure starts to increase when the cutting tools arrive to the distance approx. 12 cm for chamber pressure 0.2 bar and to approx. 22 cm for chamber pressure 0.4 bar, respectively. Note that the measurements in the RUB tunnelling device due to excavation conditions are comparably less exact than in the column tests. Nevertheless, the mentioned distances correspond well with the previously obtained slurry penetration distances for the primary penetration. Thus, it could be concluded for soil fraction 1-2 mm that increased pore pressures can be observed only inside the slurry penetrated zone also during excavation. The result corresponds to the re-penetration test in the column from section 7.3.2. The only discrepancy in terms of linearity of pore pressure distribution noticed during the experiment with the RUB tunnelling device was observed directly after the start of the excavation. It can be seen in Figure 7-24 that pore pressure inside the slurry penetrated zone at the PWD 3

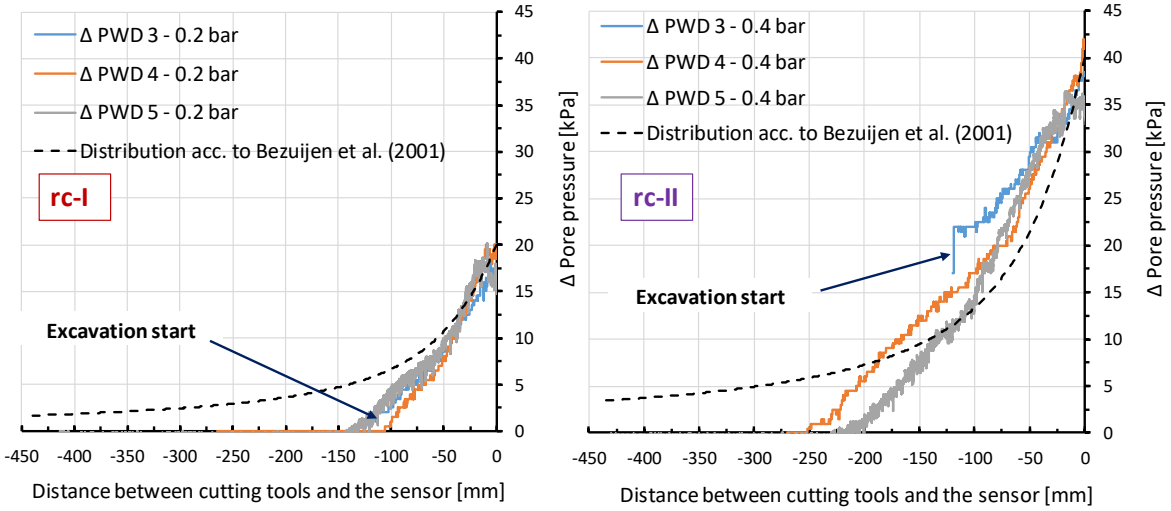

Figure 7-24: Excess pore pressure depending on the location cutting wheel in relation to the particular sensor – Left for rc-I and right for rc-II

increased immediately after the excavation start for both chamber pressures. Interestingly, the distribution at PWD 3 consequently converged again to the linear distribution. The behaviour was observable in all experiments with soil fraction 1-2 mm within the referenced combinations. However, the phenomenon is more visible for higher chamber pressures. The phenomenon can easily be explained by the sudden offsetting of the interface between slurry and soil. Before excavation starts, the interface is located at the edge of the cutting wheel. When excavation starts, the interface is moved to the foremost tip of these pins due to the rotating pins. At the end of excavation, while dismantling the set-up, it could be visually confirmed for both combinations that slurry was present in front of the cutting wheel. That excludes any transition to Case A of the interaction.

The pore pressure distributions during excavation for the soil fraction 0.063-4 mm and respective combination rc-III and rc-IV with chamber pressures 0.2 and 0.8 bar are shown in Figure 7-25. Within these combinations, it is possible to observe a sudden peak in pore pressure in the whole set-up directly at the start of the excavation. The observation inventible confirms that the increased pore pressures are possible for this soil fraction also outside the slurry penetrated zone. Consequently, the peaks dissipate after a few seconds (note that the cutting wheel moves forward constant speed 7.1 mm/min). Interestingly, the peaks achieve a pore pressure amount which approx. corresponds to the distribution acc. to Bezuijen et al. (2001) at the respective distances. The fit is particularly visible for chamber pressure 0.8 bar. The sudden pore

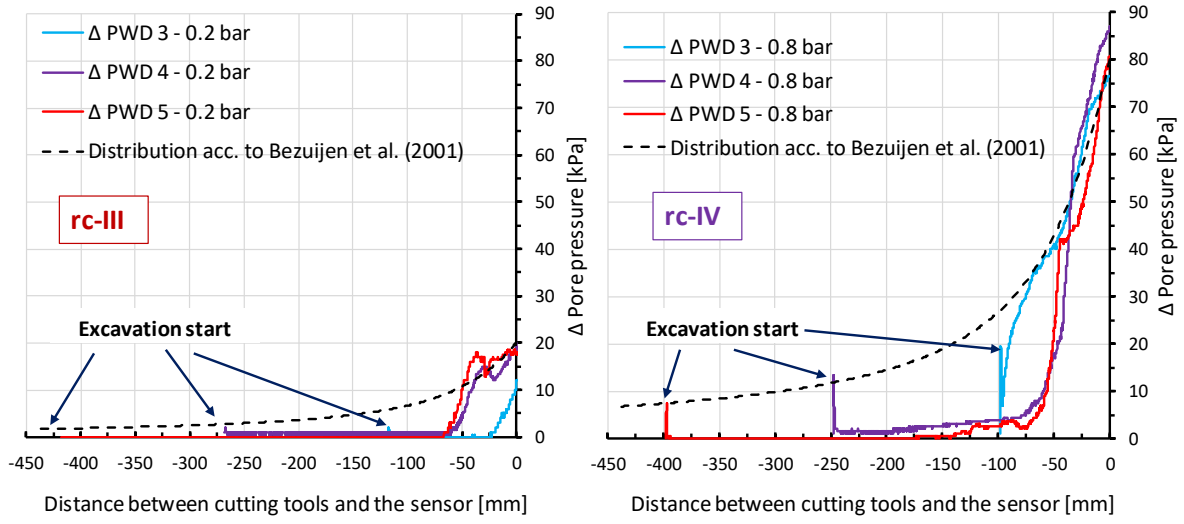

Figure 7-25: Excess pore pressure depending on the location cutting wheel in relation to the particular sensor – Left for rc-III and right for rc-IV

pressure increase at the excavation start can only be reasoned by the disturbance of the pressure transfer mechanism, while the later dissipation can be connected to a transformation of the pressure transfer mechanism forced by the distribution by cutting tools (pins). In later excavation stages, the measured pore pressure starts to increase, when the cutting wheel arrives to a certain distance from the sensor. The distance, when the pore pressure starts to increase, is different between the two combinations in Figure 7-25. As could be expected, the distance is higher for the higher chamber pressure. In combination rc-IV, the pore pressure at the sensor PWD 3 starts to increase at a larger distance to the cutting wheel than the remaining sensors. This might imply that the transformation of the pressure transfer mechanism is still occurring, while the cutting wheel is passing the PWD 3. When the sensors PWD 4 and 5 were later passed, much steeper pore pressure increase occurred, indicating the finished transformation. Interestingly, the steeper increase of pore pressure at PWD 4 and 5 occurs approximately at the distance from the cutting tools, which is comparable with the primary slurry penetration distance. The gradual increase in pore pressure is visible for higher chamber pressure at larger distances from the cutting tools. For the lower chamber pressure 0.2 bar, the gradual increase is not visible. The described changes in pore pressure distribution for combination rc-IV indicate that a larger amount of increased pore pressure occurs outside of the slurry penetrated zone at the start of the excavation due to water flow (PWD 3). After a certain excavation distance, the amount of pore pressure increase outside of the slurry penetrated zone is lower (PWD 4 and PWD 5), which results in steeper observable pore pressure increase during cutting wheel approach. Moreover, it can be assumed that the slurry penetration depth in front of the cutting tools is not changing and that only the pressure drop inside the pressure transfer mechanism transforms. The transformation results in measurably increased pore pressure that is also outside of the slurry penetrated zone. The expectation of unchanging slurry penetration depth can be derived from steady observable two branches of pore pressure distribution with different inclination (gradual vs steep pore pressure increase).

It is necessary to note that no similar phenomenon is observable for the combination with lower chamber pressure. This may be reasoned that lower chamber pressure cannot induce the transformation of the pressure transfer mechanism. At the end of excavation, it could be again visually confirmed for both combinations that slurry was

present in front of the cutting wheel. That excludes any transition to the Case A interaction.

Further insight into the processes at the tunnel face of the tunnelling device may be provided by the measured outflow from the system. Figure 7-26 shows the volume of outflow from the experimental set-up measured during excavation in soil fraction 1-2 mm. Average outflows including linear trend-lines are illustrated here for both chamber pressures. Additionally, two lines show the theoretically excavated pore volume of the soil sample. For the determination of excavated pore volume, the average porosity of soil from the all experimental runs and the cross-sectional area of the set-up were considered for the first line and for the second line, only the tunnel face area was considered. The modes of slurry penetrated zone expansion during excavation are closely explained in Figure 7-27.

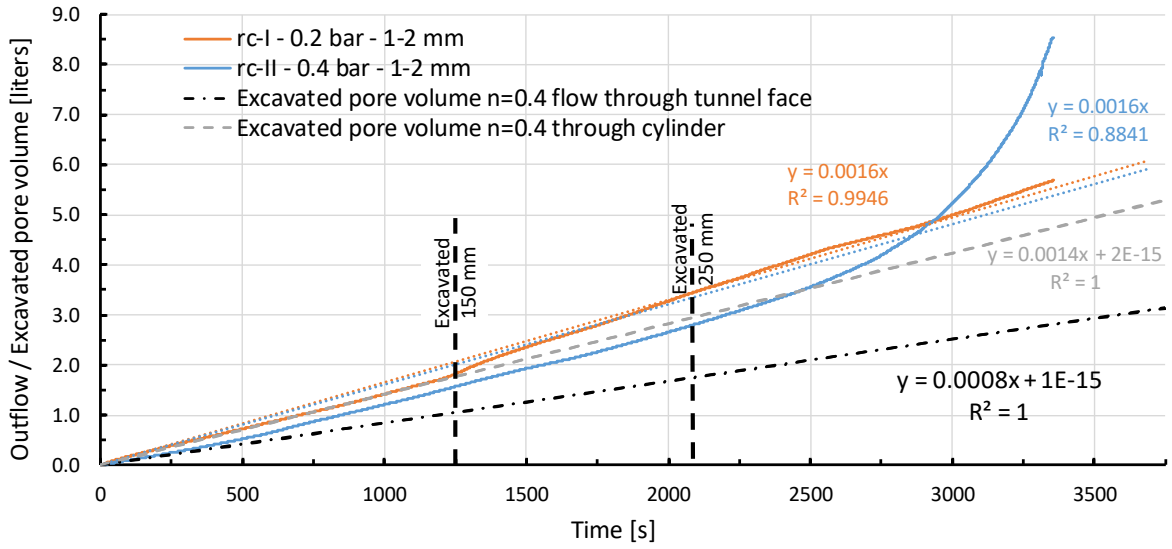

Figure 7-26: Outflow curves during the excavation in 1-2 mm soil fraction with B1 6% slurry obtained for combinations rc-I and rc-II

At the start of the experiment, both outflow lines are linear. It means that the outflow corresponds to linear increase of excavation distance. It indicates that no changes are occurring in the pressure transfer mechanism. However, a change in the inclination of the outflow line occurs for the combination rc-I – 0.2 bar approx. at time 1250 s from the excavation start. At this time, the distance is excavated, which was previously penetrated by the slurry before the start of the excavation. It is necessary to say that the change of the line inclination is rather small, and it might be also caused by inhomogeneity of the soil sample. The outflow line further continues with slightly

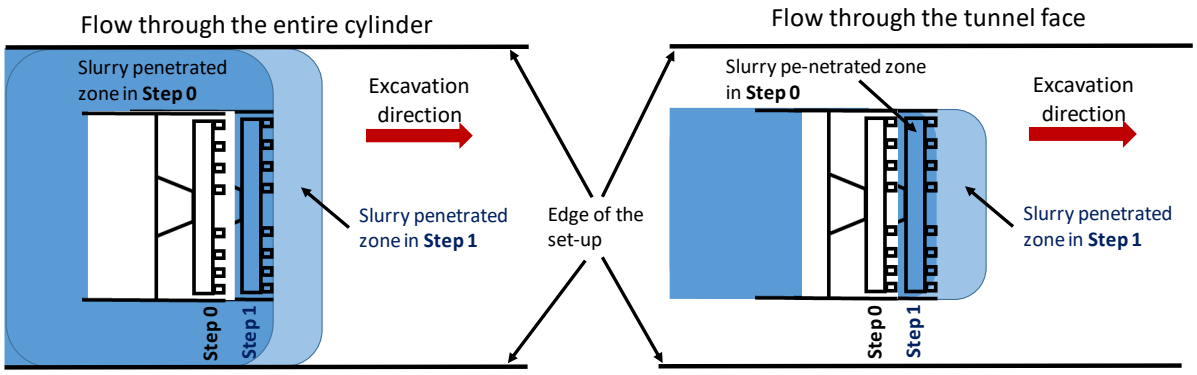

Figure 7-27: Longitudinal section of the RUB tunnelling device showing two modes of slurry penetrated zone expansion during the experiment

changed inclination until the end of the excavation. Further change in linearity appears at the rc-II – 0.4 bar outflow line at approx. 2100 s since the excavation start. At this time, the line starts to diverge from the linear volume increase dependent on the excavation distance. Interestingly, the previously penetrated zone is at this time just completely excavated. On one hand, the non-linear increase of the outflow may also be caused by the slurry penetration front approaching the end of the set-up. On the other hand, the slurry was noticed in the outflow first at 2400 s from the excavation start. From this time until the end of the experiment, the outflow curve for combination rc-II- 0.4 bar became significantly non-linear. This denotes that the pore pressure increase measured by the sensor PWD 5 in Figure 7-24 was extensively compensated by increased slurry flow volume. Different outflow curves could be determined for the soil fraction 0.063- 4 mm. The outflow curves of two different chamber pressures are shown together with excavated pore volumes in Figure 7-28. In contrast to the soil fraction 1-2 mm, here the non-linearities in outflow curves concentrate at this stage, shortly after start of the excavation. In this early stage, the outflow is non-proportionally higher than the excavation advance. After certain excavation time, however, the linear relationship between outflow and excavation advance is established. The linear parts of the outflow curves have in the later stages very similar inclination. The point at which the linear part of the outflow is reached is denoted as the equilibrium state during excavation. The two tested levels of chamber pressure require different timespans to reach the linear part of outflow curve. The timespans are approx. 200 s for combination rc-III – 0.2 bar and 400 s for the combination rc-IV – 0.8 bar. The increased outflow in the early excavation stage can confirm the transformation of the pressure transfer mechanism, which was predicted

based on pore pressure measurements. The timespans 200 and 400 s correspond to 25 mm and 50 mm of excavation distance. Note that this distance is similar to the primary slurry penetration depth in the column test for the respective pressure level.

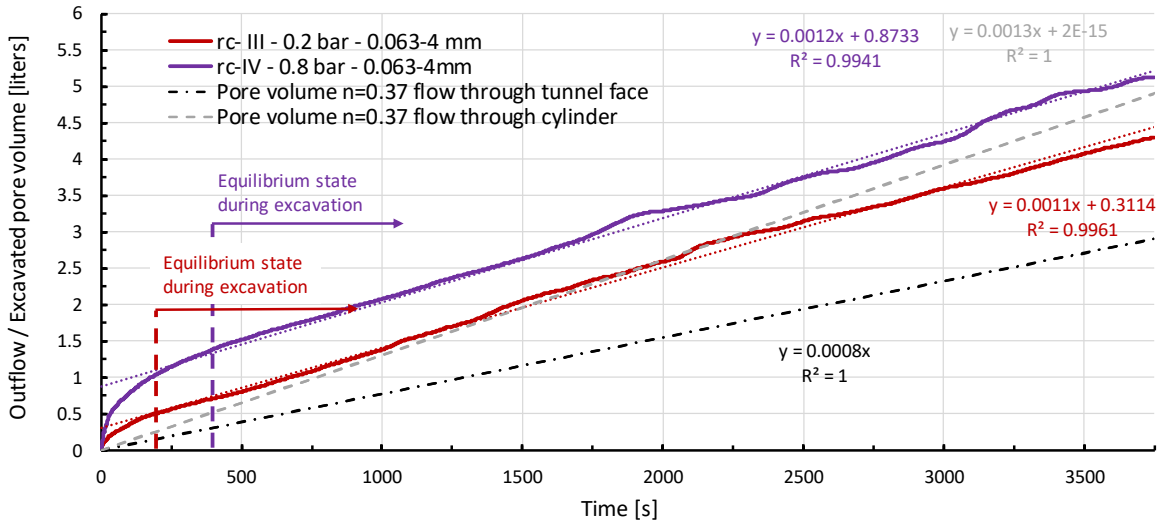

Figure 7-28: Outflow curves during the excavation in 0.063-4 mm soil fraction with B1 6% slurry obtained for combinations rc-III and rc-IV

While considering the pore pressure measurements together with outflow curves, the development of the pressure transfer mechanism for soil fraction 0.063-4 mm can be reconstructed. The developments are shown in Figure 7-29. Figure 7-29-a is visualizing the non-linear pore pressure distribution at the end of primary slurry penetration. The main characteristic of this stage is the lack of increased pore pressure outside the slurry penetrated zone. Figure 7-29-b represents an early excavation stage short after the start of excavation. The stage can be characterized by the lowest pore pressure drop over slurry penetrated zone. In this stage, the highest pore pressure outside of slurry penetrated zone can be observed. This stage is transient and occurs only until the equilibrium stage is achieved. The phase before reaching the equilibrium stage is connected with considerably higher outflow from the set-up. The equilibrium stage during excavation is shown in Figure 7-29-c. The stage shows comparably higher pressure drop over the slurry penetrated zone with still some pore pressure outside the slurry penetrated zone. The stage occurs continuously until the end of the excavation. It is expected that the described stages are strongly influenced by the excavation scale of the RUB tunnelling device. In contrast, no such transient phenomenon was noticed for the 1-2 mm soil fraction.

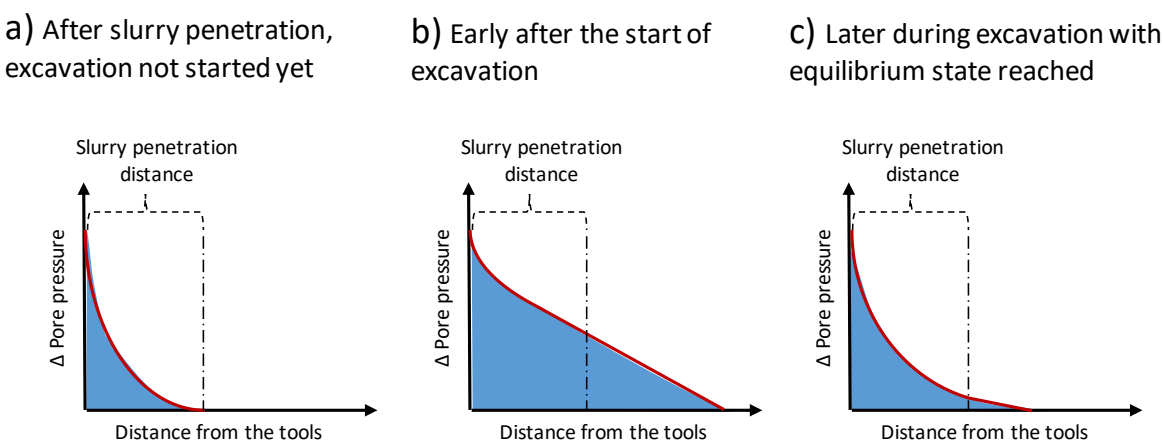

Figure 7-29: Development of the pressure transfer mechanism in terms of expected pore pressure distribution in front of cutting tools for soil fraction 0.063-4 mm during different excavation stages

7.4 Summary of experimental investigation for the Case B

A new experimental column set-up to analyse soil reaction for the deep slurry penetration scale was introduced in this chapter. The set-up enables measurement of the reaction in terms of effective stress and pore pressure increase. The experiments dealing both with slurry penetration and re-penetration were conducted using the set-up. For the operation of the set-up, a methodology was developed to realistically simulate the conditions at the tunnel face. The methodology was called as pressure-controlled re-penetration.

The slurry penetration test shown that the time-dependent reaction of soil can be strongly influenced by the set-up, if the boundary flow conditions are not designed properly. Moreover, it could be confirmed that the back-pressure has negligible influence on the slurry penetration behaviour, concluding that the differences in the measured variables are probably caused by increased hydraulic resistance of the set-up. The investigation of the re-penetration behaviour with the column tests consequently showed fundamentally different behaviour in comparison to primary penetration. The main difference can be seen in non-increased pore pressure outside of the slurry penetrated zone during the entire re-penetration. This result strongly influences subsequent fluctuations of transferred effective stress during the re-penetration in contrast to primary penetration.

Further tests dealing with slurry re-penetration were conducted using the RUB tunnelling device. Due to the mechanical limitations of the RUB-Tunnelling device, a different excavation scale has to be employed than in the column tests. The excavation scale was characterized by very low PR and high RPM. Nevertheless, the result from column test could be confirmed for soil fraction 1-2 mm; no increased pore pressure appears outside of slurry penetrated zone. Furthermore, approximately linear distribution of the pore pressure inside the slurry penetrated zone could be observed. Additionally, well-graded soil sample with diversified particle size 0.063-4 mm was tested with RUB tunnelling device. During primary penetration tests (column), this soil fraction showed a non-linear distribution of pore pressure inside the slurry penetrated zone. Hence, the soil was not suitable for tests with pressure-controlled slurry re-penetration inside the column test. The investigation with the RUB tunnelling device determined the existence of increased pore pressure outside of slurry penetrated zone and ongoing transformation of the pressure transfer mechanism after the start of the excavation for this soil.

The differences between the column test and the RUB tunnelling device can be explained for the soil fraction 1-2 mm by the insufficient cutting depth per pass in the RUB tunnelling device. The penetration rate of the RUB tunnelling device is 0.1 mm/rev. Thus, the cutting depth per passing is comparably lower than the grain size and could not induce “dynamic slurry penetration process”. In contrast, it is believed that the re-penetration for the soil fraction 0.063 – 4 mm was modelled more properly in the RUB tunnelling device. It can be derived from the obtained results that show considerable influence of the cutting process.

The experimental program employed in this chapter has certain limitations. The program focused primarily on investigations using the uniformly graded coarse sand from the standard application range of slurry shield (Figure 2-3). The soil fraction shows the linear distribution of pore pressure inside the slurry penetrated zone. The obtained results can be generalized for all soils with such a distribution. Additionally, well graded sand was investigated. This soil showed a non-linear distribution of pore pressure inside the slurry penetrated zone. Hence, the obtained results for this soil can be generalized for all soils with such a distribution. In the future, the experiments can additionally be conducted with well graded sand and with slurry with lower concentrations of solids to confirm the expected generalization of the results.

8. CASE A – PRESSURE TRANSFER ANALYSIS AND THE IMPLEMENTATION INTO TUNNEL FACE STABILITY ASSESSMENT

In chapter 4, the theoretical considerations of the adaptation of pressure transfer model due to transient conditions during excavation were discussed. Section 4.1 consequently specified the requirements for the pressure transfer analysis in Case A of the interaction. In this chapter, the numerical pressure transfer analysis for the Case A interaction will be conducted using the implemented heterogeneous pressure transfer model (HPT model) suggested by Zizka et al. (2015). As input for the analysis, the experimentally obtained data from chapter 6 will be used and the assumption of the pressure gradient in the experiments will be proven by the numerical analysis. Consequently, the transferred slurry excess pressure during excavation will be determined and the tunnel face stability analysis for the transferred pressure will be evaluated. The stability analysis will be carried out with the practice-oriented calculation method described in section 2.6. This chapter can be considered as a suggestion for the adaptation of the contemporary calculation models for Case A of the interaction.

8.1 Methodology and the numerical models used in the pressure transfer analysis

A finite element seepage analysis (Bathe, 2014) is employed to evaluate the slurry pressure transfer. The seepage analysis enables implementation of the heterogeneous pressure transfer (HPT) model derived in the section 4.1. The seepage analysis can calculate a spatial distribution of hydraulic heads in front of the tunnel face during

excavation, while considering mutual influence of adjacent cutting tracks. From these heads, hydraulic gradients can be determined and consequently using $Eq.8\text{-}1$ the transferred pressure is calculated.

$$\Delta \boldsymbol{s_{av}} = \boldsymbol{i_{av}} \cdot \boldsymbol{\gamma_w} \cdot \boldsymbol{l_t} \qquad Eq.8\text{-}1$$

with

Δs_{av}	Slurry excess pressure transferred [kPa]
i_{av}	Average hydraulic gradient at the tunnel face [-]
l_t	Distance of the pressure transfer [m]
γ_w	Unit weight of water [kN/m^3], for the sake of simplicity adopted = 10 kN/m^3

The employment of a simple groundwater flow analysis is possible since the formation of the pressure transfer mechanism itself is not investigated here, and only the slurry pressure transfer is modelled. That means that the formation process of the pressure transfer must be known for the modelling purposes. Therefore, experimental determination of the pressure transfer mechanism formation (slurry penetration scale) was conducted in chapter 6 for Case A. The formation of the pressure transfer mechanism is characterized by the permeability coefficient in the model. Furthermore, the periodicity of the pressure transfer mechanism removal has to be adopted for the modelling purposes. Corresponding analysis of the excavation scale was performed in chapter 5. In this chapter these two scales are superimposed and the heterogeneous pressure transfer (HPT) model is established.

To implement the heterogeneous pressure transfer model into seepage analysis, the tunnel face has to be segmented radially and circumferentially (Figure 8-2). The radial segments are representing the concentric cutting tracks. Consequently, each cutting track is segmented circumferentially representing the stages of pressure transfer formation. Hence, the permeability coefficient of the forming pressure transfer mechanism can be assigned to these segments based on their instantaneous position in relation to cutting tools within the cutting track and the timespan since the transfer mechanism was disturbed by the last passing cutting tool.

8.1.1 Model for the parametric investigation of the tunnel face segmentation

As the first step, the influence of the tunnel face segmentation was investigated. A simplified model was developed for this purpose. The stationary seepage analysis

(Analysis Reference manual MIDAS GTS, 2010) was justifiable for this initial investigation. Hence, only an instantaneous moment during excavation is modelled here. Several further assumptions were conducted in the investigation:

- The cutting wheel has a simplified layout of the cutting tools with one tool per cutting track (Figure 8-2).
- The pressure transfer mechanism fully forms between subsequent passes of the cutting tool and is always completely removed by every tool pass.
- The permeability coefficient and thickness of the fully formed pressure transfer were adopted as referenced by Arwanitaki (2009): k_{16} = 3*10^{-10}m/s and thickness 1 cm. Note that this assumption diverges from the other pressure transfer model in this chapter (own experimentally determined results for permeability coefficient are first used in next sections).
- The permeability coefficient of the freshly cut pressure transfer mechanism corresponds to the permeability coefficient of soil (assumed k_1 = 10^{-4}m/s).
- The reduction (between k_1 and k_{16}) of the permeability coefficient during formation of the transfer mechanism follows the power-law curve with 16 steps (Figure 8-1).

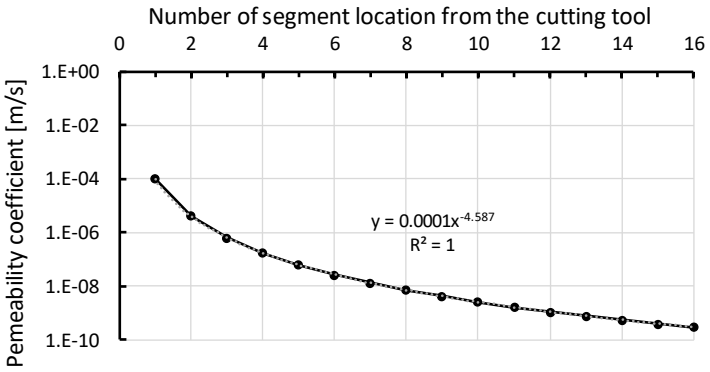

Figure 8-1: Assumed permeability coefficient development

- The bentonite slurry has a slightly higher unit weight than water in reality. This difference is neglected in the performed calculations.
- Slurry excess pressure of 100 kPa is assumed (10 m of water column).

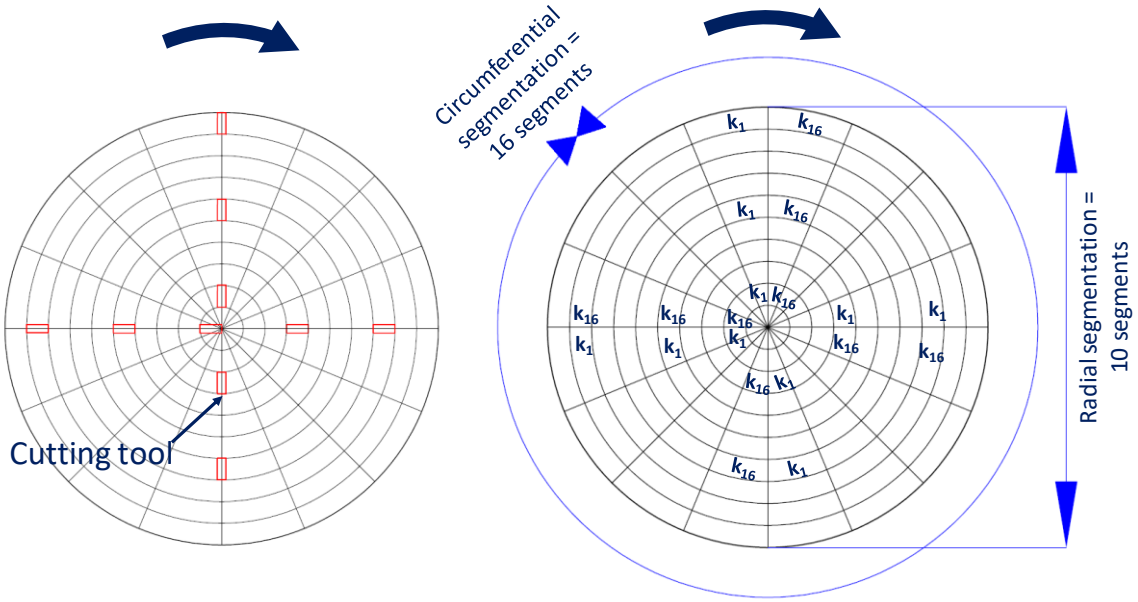

Figure 8-2: Left – simplified layout of the cutting tools (Calculation case C1), Right – segmentation of the tunnel face including the location of the fully formed (k16) and freshly cut (k1) pressure transfer mechanism. Note that the location of these boundary states depends on the cutting tool layout revolution direction of the cutting wheel

The investigated segmentations of the tunnel face are summarized in Table 8-1. The first segmentation (C1) assumes the formation of the pressure transfer mechanism in 16 steps within 10 cutting tracks resulting in 160 segments on the tunnel face (Figure 8-2). This segmentation was complemented by three other segmentation layouts (Figure 8-3). Theoretically, the densest segmentation would deliver the best results. However, it is valid only for the circumferential direction, since the segmentation in the radial direction is limited by the finite width of a real cutting tool, which is approx. 0.25 m for a machine with 10 m diameter (based on the reference projects from chapter 5). Thus, the second segmentation layout (C2) is characterised by 16 segments

Table 8-1: Investigated segmentations of the tunnel face

Calculation Case	Adopted segmentation		
	Resulting amount of the segments	Amount of the radial segments	Amount of the circumferential segments
C1	160	10	16
C2	320	20	16
C3	320	10	32
C4	624	20	32

in circumference and 20 concentric cutting tracks. Thereby, the layout resulted in 320 segments and a cutting track width of 0.25 m. Further segmentation layout took over from the original its radial segmentation; however, the circumferential segmentation amounted to 32 segments resulting in 320 segments in total (C3). Finally, the fourth layout (C4) combined the finest segmentation both in radial and circumferential direction reaching 624 areas in total (note, that the most inner cutting track was divided only to 16 segments due to meshing reasons).

Total dimensions of the model are 300x300x90 m (Figure 8-4). The assumed dimensions assure that the flow in the model is not influenced by the boundary conditions of the model. Tunnel length was 150 m and the tunnel diameter is 10 m. The overburden is 30 m and the groundwater level is assumed to be at the surface of the model. Therefore, a total hydraulic head of 90 m is assigned to boundaries of the model while adopting the zero point of the coordinate system at the left bottom corner of the model. It is worth mentioning that the total head is the sum of the pore pressure head and the elevation from the origin of the coordinate system. Therefore, the total head is constant all over the model for the hydrostatic distribution of the pore pressure. The tunnel lining was assumed to be impermeable. In total, two types of mesh were used in the model, the first to model the pressure transfer mechanism and the second for the soil. The transfer mechanism mesh (Figure 8-4) was modelled as a 1 cm thick layer on the tunnel face, divided in aforementioned segments (depending on calculation case) with varying permeability. Hence, the thickness of the pressure transfer mechanism during its formation was not varied. The slurry excess pressure was introduced by means of increased total head on the cavity-side surface of the

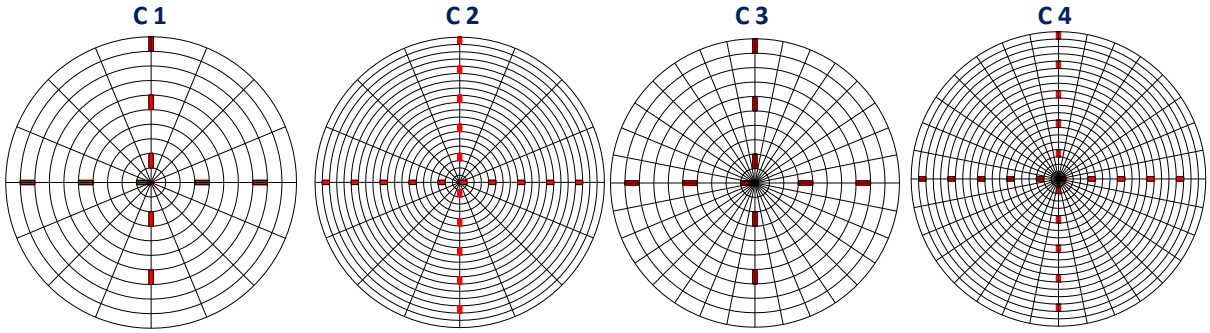

Figure 8-3: Investigated variants of the tunnel face segmentation

pressure-transfer-mechanism-mesh. The calculation was conducted using MIDAS-GTS software (Analysis Reference MIDAS GTS, 2010).

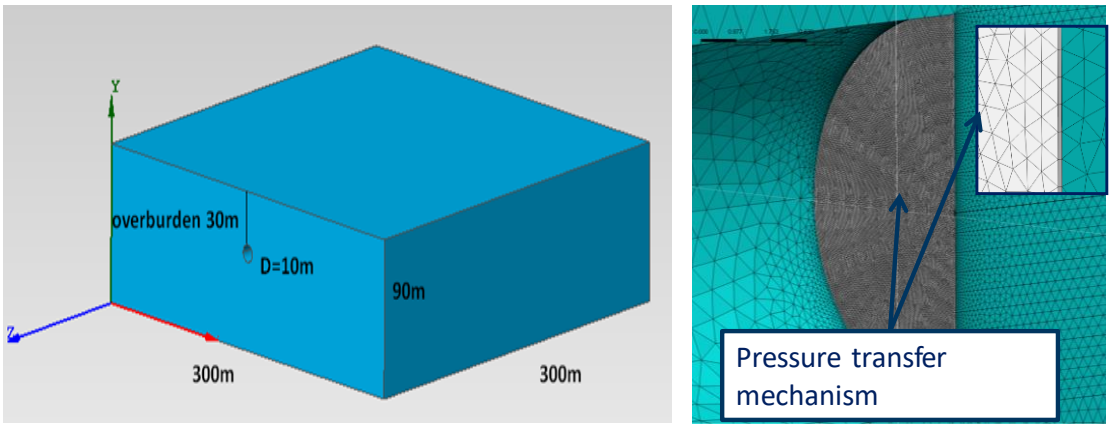

Figure 8-4: Left – dimensions of the numerical model, right – detail of the used FE mesh

The evaluation of the pressure transfer was conducted in a simplified manner for the purposes of investigation of the segmentation influence. This was possible due to the aim of the investigation to compare the pressure transfer for different segmentations without necessarily determining the absolute value of the transferred pressure. It was adopted to evaluate the transferred pressure within 1 m in front of every tunnel face segment (Figure 8-5). Consequently, the average transferred pressure for the entire tunnel face was calculated using $Eq.\,8\text{-}2$.

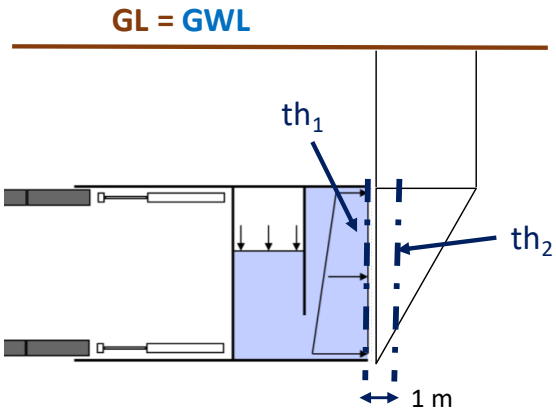

Figure 8-5: Simplified evaluation of the transferred slurry excess pressure

$$\Delta s_{av} = \frac{\sum(th_1 - th_{2,i}) \cdot \gamma_w \cdot a_i}{\sum a_i} \qquad Eq.\,8\text{-}2$$

with

Δs_{av}	Average slurry excess pressure transferred [kPa]
th_1	Total hydraulic head in the excavation chamber [m]

$th_{2,i}$ Total hydraulic head in the middle of the particular tunnel face segment projected to the end of the adopted efficient pressure transfer zone[m]
a_i Area of the particular tunnel face segment [m^2]
γ_w Unit weight of water [kN/m^3]

8.1.2 Model for evaluation of the pressure transfer and simplified cutting wheel

The main difference of the model for evaluation of the pressure transfer was the employment of transient seepage analysis (Manie & Kikstra, 2016) with software DIANA. This enables the modelling of not only the quasi-stationary state during excavation, but also the start and the end of excavation properly. As the input for the transient analysis, the experimentally obtained developments of permeability coefficients from chapter 6 were used. Hence, each segment of the tunnel face did not get assigned the particular permeability coefficient, but its development within time based on the experimental result. The assigning was again conducted in relation to segment location to the cutting tools in the tracks. Since the methodology of adapted Darcy´s law was used for evaluation of the experiments, the results for the permeability coefficient development could be directly inputted here in the numerical seepage model with adapted Darcy´s law (Zizka et al., 2017). It is necessary to check only if the pressure gradient at the tunnel face corresponds to the gradient in the experimental set-up. The same soil as in the experiments was considered here to surround the tunnel (Table 6-2).

During the development of this model, the results from the parametric study dealing with tunnel face segmentation were considered regarding the segmentation of the tunnel face (section 8.2.1). Thus, the segmentation with 10 radial and 16 circumferential segments was used, including the same simplified cutting wheel. Boundary conditions of the used model remained the same as in the previous section.

$Eq.\,8\text{-}2$ was employed again for the calculation of the pressure transfer from the distribution of the total heads. However, the pressure head $th_{2,i}$ was always determined on the inclined surface of the imaginary Horn´s sliding wedge. In other words, the middle point of each segment at the tunnel face was horizontally projected on the inclined sliding surface, where $th_{2,i}$ was found. This approach is more exact, because it determines the amount of slurry excess pressure which was transferred within the sliding wedge (Figure 8-6). As pointed out in chapter 4, this amount is only

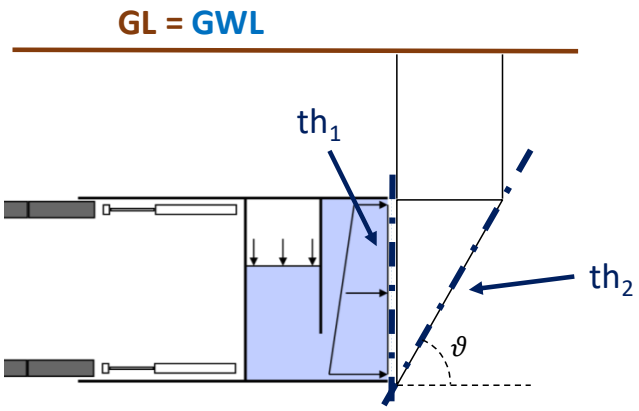

Figure 8-6: Evaluation of the transferred slurry excess pressure

decisive for the stabilization of the tunnel face. The dimensions of the wedge were determined using the calculation approach of Horn (Section 2.6). The influence of the flow on the overlying prism and on the force at the triangular plane of the wedge are neglected. In the calculation, following tunnel geometry and soil properties were considered:

- Non-cohesive soil fraction 0.25 – 0.5 mm (Table 6-2)
- Shear properties: parametrized φ'= 30° and 35°, c´= 0 kPa (assumed)
- Unit weight: γ/γ´ = 19/11 kN/m^3 (assumed)
- Overburden: 10 m
- Tunnel diameter: 10 m

The results of the face stability calculation according to the methodology from section 2.6 are shown in Table 8-2. The inclination angle of the sliding wedge defining its dimensions was also determined.

Table 8-2: Determination of the operational limit pressures for the adopted scenario

Friction angle [°]	Sliding angle ϑ [°]	Lower Limit pressure [kPa]	Upper limit pressure [kPa]	Operation range incl. Deviations		Average acting earth pressure at the tunnel face [kPa]
				Min [kPa]	Max [kPa]	
φ_1 = 30°	66.3	152	189	162	179	37
φ_2 = 35°	68.3	142	189	152	179	30

Consequently, the numerical seepage calculation was performed using DIANA 9.6 software (Manie & Kikstra, 2016) as a non-linear transient analysis employing regular Newton iteration method. The calculation time step was 0.5 s. Total dimensions of the model were changed in comparison to the previous section to 300 m x 300 m x 70 m, because the overburden was reduced to 10 m. All investigated calculation cases with the model for evaluation of the pressure transfer and simplified cutting wheel are summarized in Table 8-3. The experimental combination for the pressure transfer mechanisms denotes the number of the experimental combination from chapter 6 used for permeability coefficient development.

Table 8-3: Cases investigated with the model for evaluation of the pressure transfer

Calculation Case	RPM [-]	PR [mm/rev]	AR [mm/min]	Experimental combination for pressure transfer mechanism formation	Slurry excess pressure in the excavation chamber [bar]	Hydraulic head at the tunnel face [m]
S 1a	1.875	25	46.9	**1** - 0.25-0.5 mm, 0.2 bar, 0.41, B1 5.5%	0.08	70.8
S 1b					0.2	72
S 2a				**2** - 0.25-0.5 mm, 0.3 bar, 0.41, B1 6%	0.15	71.5
S 2b					0.3	73
S 3a				**3** - 0.25-0.5 mm, 0.5 bar, 0.41, B1 6%	0.35	73.5
S 3b					0.5	75
S 4a				**4** - 0.25-0.5 mm, 0.7 bar, 0.41, B1 6%	0.55	75.5
S 4b					0.7	77
S 5				Multi-permeability model	0.7	77

The adopted excavation setting of the machine (PR & RPM) was chosen in the way that the pressure transfer mechanism is cut by every passing of the cutting tools. One rotation of the cutting wheel takes 32 seconds. This means that each tool passes one segment of the tunnel face within 2 seconds. The first chosen slurry excess pressure in the chamber in each calculation case corresponds to the pressure drop in the experimental set-up for the particular experimental combination (see Table 6-4). The second adopted slurry excess pressures might be chosen arbitrarily; however, the values chosen correspond to the injection pressures in the experimental set-up of the particular combination. The calculations with the second excess pressures were conducted to investigate the influence of the amount of slurry excess pressure at the pressure drop over the pressure transfer mechanism at the tunnel face. Knowledge of the influence is necessary for later iteration between pressure drop in the experiment and at the tunnel face to achieve their equality. For that purpose, the calculation case

S 5 is also included in Table 8-3. This Case S 5 serves for later demonstration of the practice-oriented approach for the determination of the transferred slurry excess pressure.

The starting point of each calculation scenario is always the shield stoppage (Figure 8-7). At this point, the pressure transfer mechanism is completely formed at the entire tunnel face. Subsequently, the excavation starts, and the cutting wheel conducts three rotations. When the excavation stops, the pressure transfer mechanism formation is further modelled.

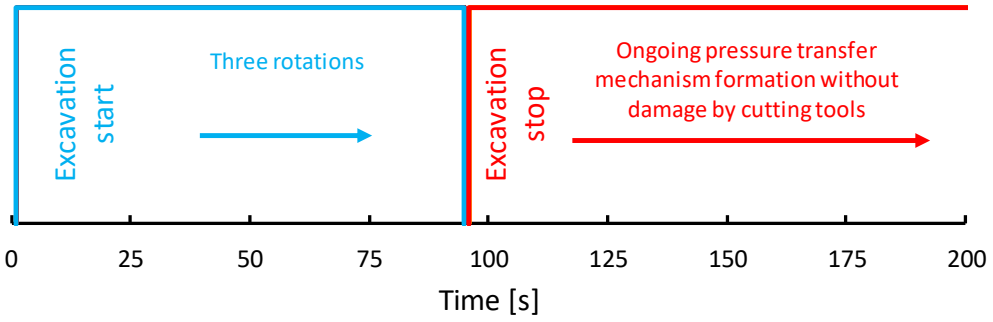

Figure 8-7: Calculation scenario – model for evaluation of pressure transfer with simplified cutting wheel

8.1.3 Model for evaluation of the pressure transfer and realistic cutting wheel

The same methodology was used in this section as in the previous one. The only difference was the introduction of real cutting wheels from the reference projects from chapter 5 and consideration of real RPM and PR. The approximation of the real cutting wheels of projects P1 and P2 is shown in Figure 8-8. The reference project P3 is not considered here due to the lower chance for occurrence of a Case A transfer at the tunnel face as concluded in section 6.4 based on excavation data. The approximation aimed to keep equal the extent of homogeneous cutting zones, the amount of active cutting tools within cutting track of the particular zone and the angular offset between cutting tools in adjacent cutting tracks. As pointed out in section 2.1.3, cutting tools are usually placed in tandems on cutting wheel arms. For the modelling purposes, only the active cutting tool from the tandem is modelled here. This is satisfactory due to the same reasons as discussed in section 5.1. Furthermore, the full overlapping of cutting tools is considered in the homogeneous zone 2 of P1 project as a simplification. Thus, two cutting tools per track are modelled in this zone.

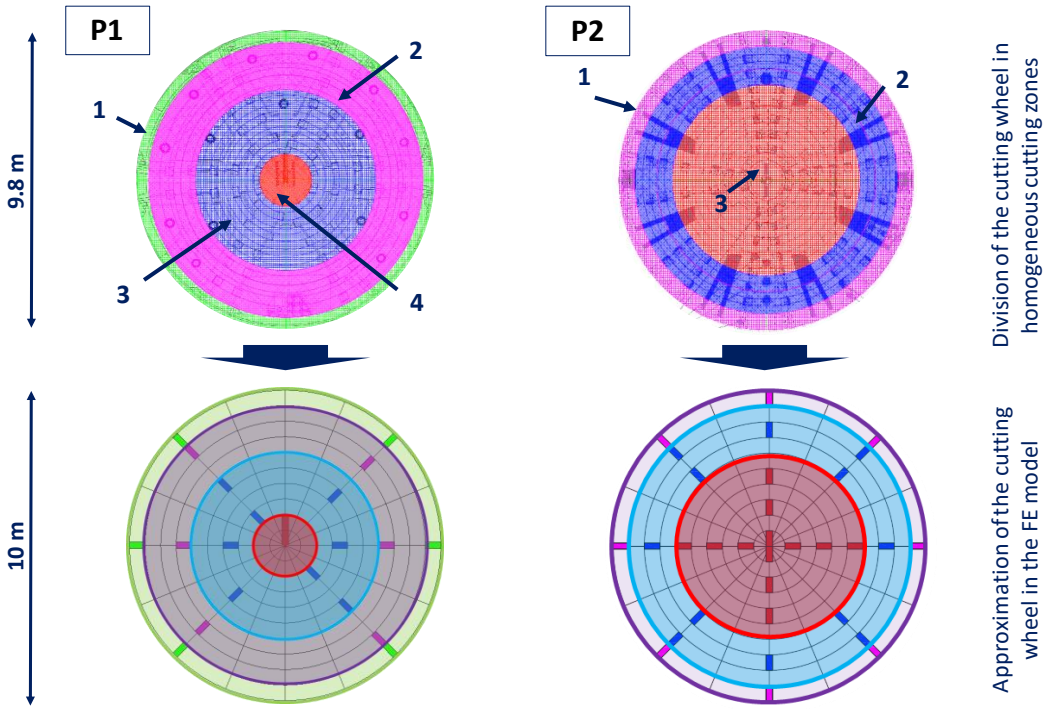

Figure 8-8: Approximation of the cutting wheel from reference projects P1 and P2 for the calculation purposes

Table 8-4: Cases investigated with the model considering real cutting wheels

Calculation Case	RPM [-]	PR [mm/rev]	AR [mm/min]	Experimental combination for pressure transfer mechanism formation	Slurry excess pressure in the excavation chamber [kPa]	Hydraulic head at the tunnel face [m]
R1a - Ref P1	0.682	62	42.3	**2** - 0.25-0.5 mm, 0.3 bar, 0.41, B1 6%	15	71.5
R1b - Ref P1					30	73
R1c - Ref P1					70	77
R2a - Ref P2	0.682	59.8	40.8	**2** - 0.25-0.5 mm, 0.3 bar, 0.41, B1 6%	15	71.5
R2b - Ref P2					30	73
R2c - Ref P2					70	77

The calculation cases conducted with the model considering realistic cutting wheels are summarized in Table 8-4. In order to obtain comparable results, the RPM was chosen for both reference projects the same. Based on the chosen RPM the corresponding tool cutting depth in homogeneous cutting zones could be obtained using the coupling determined in chapter 5. Thus, the PR of the machines and the resulting AR could be calculated. The RPM was chosen in the way that the delivered PR secures that the pressure transfer mechanism is cut by every tool passing in each homogeneous cutting zone of both reference projects. The chosen RPM is such that the cutting wheel rotates in 88s. The first chosen slurry excess pressure corresponds again to the pressure drop in the experimental set-up for the particular combination. The second adopted slurry excess pressure corresponds to the injection pressures in the experimental set-up of the particular combination (could be also chosen arbitrarily). This calculation procedure was chosen due to the same reason as in the previous section.

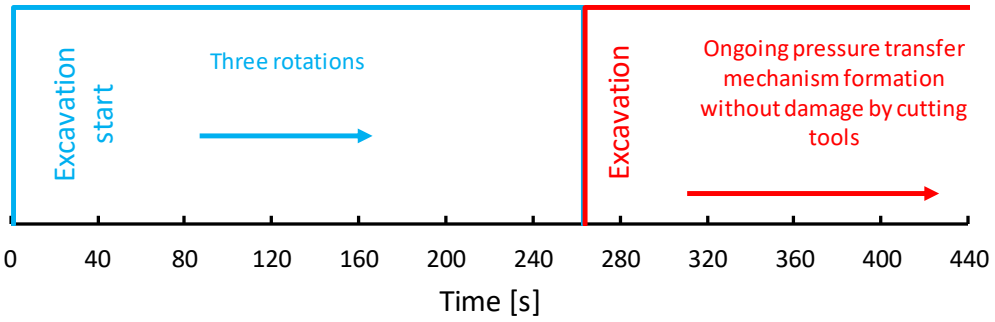

Figure 8-9: Calculation scenario – model considering realistic cutting wheels

The starting point of each calculation scenario is again the shield stoppage (Figure 8-9). At this point, the pressure transfer mechanism is formed at the entire tunnel face. Subsequently, the excavation starts, and the cutting wheel conducts again three rotations. When the excavation stops, the pressure transfer mechanism formation is further modelled.

8.2 Results and interpretation for the pressure transfer analysis

The results of the calculations using the HPT model will be presented separately in the same sections as the models were previously introduced.

8.2.1 Parametric study for investigation of the segmentation of the tunnel face

The parametric study was conducted with the simplified steady-state analysis. The study aimed to investigate the influence of segmentation at the tunnel face (Section 8.1.1). The results outlined in Table 8-5 and visualized in Figure 8-10 showed that the segmentation is of a certain influence. Figure 8-10 shows the total hydraulic heads at the interface between pressure transfer mechanism and soil. Note that total head 100 m denotes no pressure drop over the pressure transfer mechanism and total head 90 m denotes entire pressure drop.

Table 8-5: Cases investigated with the model considering real cutting wheels

Calculation case (Segmentation of the tunnel face)	Support excess pressure in the excavation chamber [kPa]	Support excess pressure transferred [kPa]
C1 (16 circ, 10 rad)	100	52.1
C2 (16 circ, 20 rad)	100	47.2
C3 (32 circ, 10 rad)	100	55.8
C4 (32 circ, 20 rad)	100	51.2

Two effects can be observed here. The first one is that more segments in radial direction reduce the pressure transfer, and in contrast, the modelling of more segments in circumferential direction increase the pressure transfer. This behaviour can be assigned to the mutual influences of adjacent segments. Therefore, adopting the segmentation from case C2 may lead to an underestimation, and adopting the segmentation from case C3 to an overestimation of the pressure transferred compared to finer segmentation. Furthermore, the Table 8-5 shows that the obtained pressure

transfers correlate for models with 160 areas (C1) and 624 areas (C4), in which the segments on the tunnel face are approx. square shaped. As pointed out in section 8.1.1, the segmentation in calculation Case C4 can be expected to deliver the most accurate results. The amount of transferred pressure obtained for case C1 deviates only slightly from C4. The Case C1 significantly reduces the time consumption for both modelling and calculation in comparison to C4. Thus, the tunnel face segmentation from C1 will be used in further calculations.

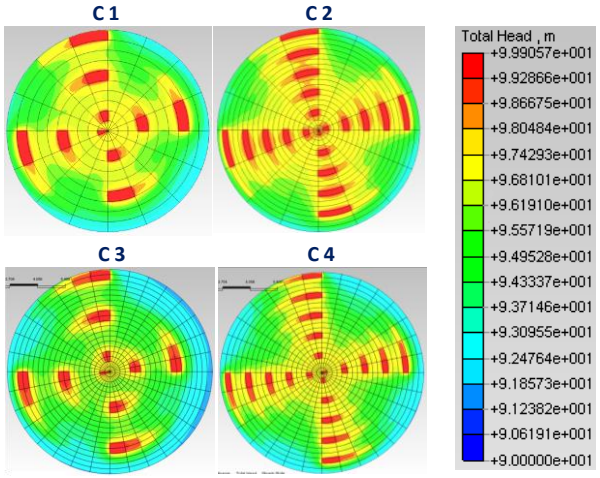

Figure 8-10: Total hydraulic heads in front of the pressure transfer mechanism (clockwise rotation of the wheels), (Zizka et al., 2015)

8.2.2 Investigation considering experimental results for slurry penetration and a simplified cutting wheel

The main aim of this chapter was to investigate the pressure transfer during excavation (Section 8.1.2). The results of this investigation for the cutting wheel with a single homogeneous cutting zone will be presented in this section. The pressure transfer was evaluated at the time 45 s or 77 s, respectively, from the start of the excavation. The corresponding position of the cutting at this time is shown in Figure 8-11.

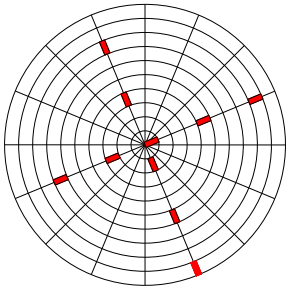

Figure 8-11: Position of the cutting wheel at 45 s and 77 s since excavation start (the cutting wheel rotates clockwise)

First, excess pore pressures in front of the tunnel face at the tunnel axis level were evaluated. In order to make the distributions comparable between calculation cases, the excess pressures were scaled by the respective slurry excess pressure in the excavation chamber. In Figure 8-12–left, the particular curves are visualizing the distribution in dependency on time since the excavation start for the calculation case S 3a. While the dashed lines are showing the distributions from start of the excavation until reaching of the "equilibrium" state during excavation, the solid lines are displaying the equilibrium-state during excavation (t = 45 s) and the successive decrease in the excess pore pressure after the excavation stops. The successive decrease is observable due to the ongoing formation of the pressure transfer mechanism. This behaviour was observed by Bezuijen at al. (2001) at the 2nd Heinenord Tunnel during stoppages for ring building. The excess pore pressure in soil is less than 1 kPa at the time 125 s, hence approx. 30 s after the excavation stop. At this time, the distribution of excess pore pressure corresponds to the stationary state referred by the classic theories from diaphragm wall technology (Kilchert & Karstedt, 1984). As pointed out in section 3.4.1, the classic theories expect no increased pore water pressure outside of the pressure transfer mechanism. Furthermore, it turned out from the FE analysis that the excess pressure distribution is unchanging after 31 s from the excavation start until the excavation stops. The timespan corresponds approx. to the period required for one cutting wheel revolution. This is also valid for cases S2, S3 and S4. In contrast, the distribution of excess pore pressure first becomes stable after 65 s of excavation for calculation cases S1 due to very low chamber excess pressure. In Figure 8-12-right, the

distribution of excess pore pressures for all calculation cases at the equilibrium-state is shown. It turned out that the scaled distribution depends only on experimental combination used for the modelling of permeability coefficient development of the pressure transfer mechanism and not on the absolute amount of slurry excess pressure in the excavation chamber. Further, it can be observed that different amounts of pressure drop occurred over the pressure transfer mechanism. It can be determined on the vertical axis as the difference between 100 % and the point at which the curve moves from the vertical axis. The range for the pressure drop spans from 27.1 % for case S3 to 42.5 % for case S1.

The approximation of excess pore pressure by Bezuijen et al. (2001) based on in-situ measurements during excavation is also shown in this figure. This curve is located above the distributions obtained in this calculation example. It indicates that a higher formation state of the pressure transfer mechanism was applied in the presented calculation example during excavation than during the measurement at the 2nd Heinennord Tunnel. The obtained calculation results could be better approximated by the theory of Kaalberg et al. 2014 and Bezuijen et al. (2016) using $Eq.\,3\text{-}44$. The range determined before for the drop over the transfer mechanism could stand for

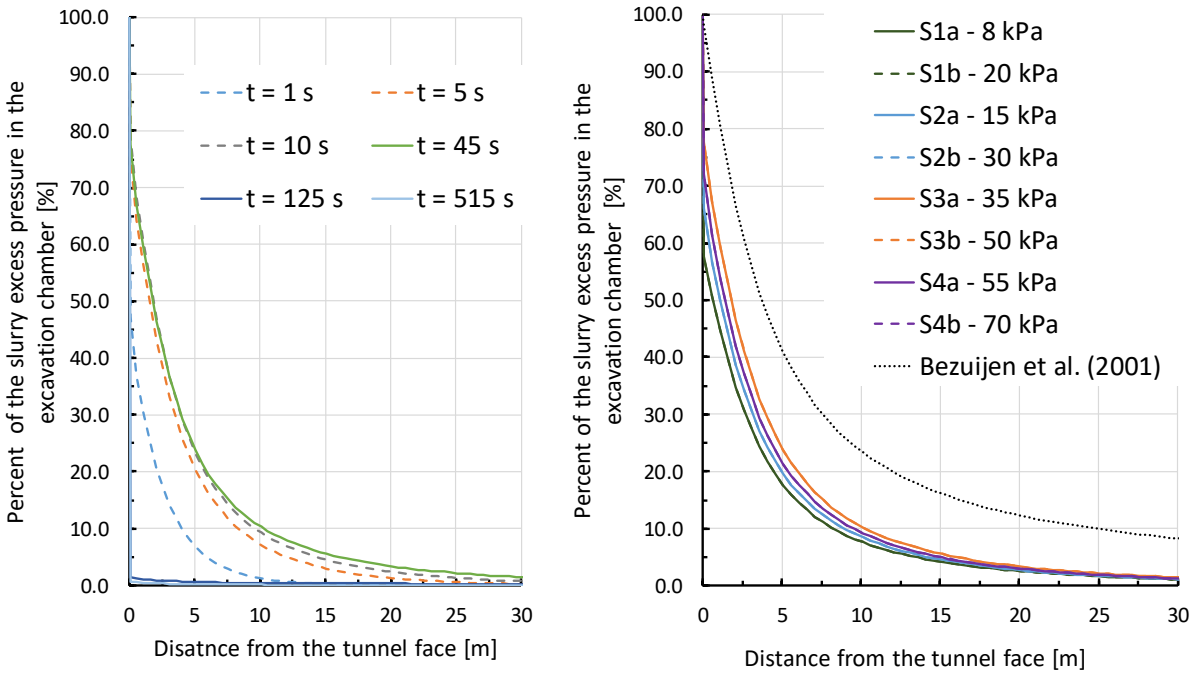

Figure 8-12: Distribution of excess pore pressures in front of the tunnel face during excavation, Left – calculation case S 3a, Right – all cases at time 45 s or 77 s since the start of the excavation

parameter α in $Eq.\,3\text{-}44$, when divided by 100. However, Bezuijen et al. (2016) state, that α can be smaller than 1 only for the case, when slurry penetration is faster in average than excavation (this would correspond to Case B).

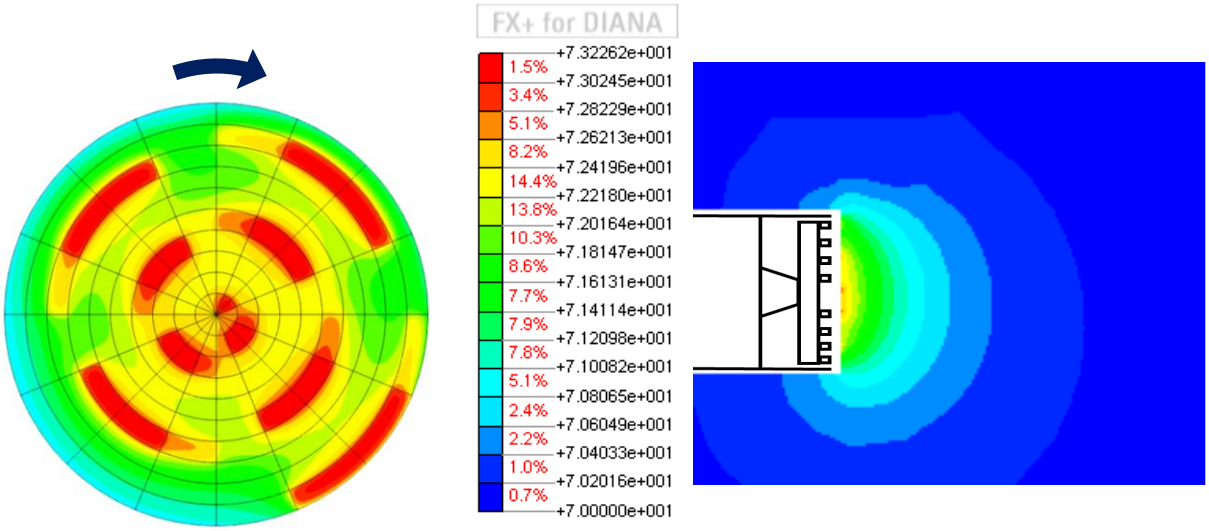

Figure 8-13: Total head distribution [m] obtained by the numerical model for the calculation case S3a at 45s since the excavation start, Left – interface between pressure transfer mechanism and soil, Right – zoomed-in longitudinal section through the model at the tunnel axis

Second, the influence of slurry shield excavation on the hydraulic heads in ground was evaluated. This is done exemplary in Figure 8-13 for the calculation case S3a. The distribution of the hydraulic head at the interface between pressure transfer mechanism and soil (left) and the longitudinal section of through the model at the tunnel axis (right) are shown. Note that a total head of 73.5 m denotes no pressure drop over the pressure transfer mechanism and total head 70 m denotes an entire pressure drop. It can be seen that the slurry shield creates “a bubble shape” in front of the tunnel face with increased pore water pressure. Further, it is observable that the highest hydraulic heads are located next to the just passed cutting tools. The hydraulic heads decrease with increasing distance from the just passed cutting tool (Figure 8-13-left). The observed decrease in heads means that the pressure transfer mechanism is more efficient and that higher slurry pressure drop occurs. It may be seen that the distance from the passing cutting tool is not solely decisive, but also that the adjacent cutting tracks are mutually influencing.

Consequently, the focus was given to the evaluation of the slurry pressure transfer within the sliding wedge. The results are presented in Table 8-6. It can be seen that

different amounts of slurry excess pressure were transferred for calculation cases with different pressure transfer mechanisms formation, for different wedge dimensions (depending on the friction angle of soil) and for different slurry excess pressure in the excavation chamber. If the efficiency of the pressure transfer mechanism is evaluated, it has to be focused at the columns with scaled transferred pressure (% of pressure transferred). It can be seen that the efficiencies are not significantly diverging. The efficiency of the pressure transfer mechanism does not depend on the amount of slurry excess pressure, but only on the particular permeability coefficient development in respective calculation case. It turned out that permeability development from experimental combination 1 (case S 1 in Table 8-6) delivered the most efficient pressure transfer mechanism. The least efficient pressure transfer mechanism (the lowest pressure transfer) was obtained for the calculation case S3 with permeability development from experiment 3. This can be explained based on the formation of the pressure transfer mechanism, which starts immediately for low gradients. For high gradients, the formation is also fast due to comparably fast flow velocity. For the middle gradients (experimental combination 3 and S3), the formation cannot start immediately due to the combination of comparably high gradient and comparably slower flow velocity. Another explanation can be used for the highest efficiency in case S1. As shown in Figure 4-4, the adjacent cutting tracks are mutually influencing. The

Table 8-6: Results of the pressure transfer calculation with simplified cutting wheel, number of calculation case indicates the adopted permeability development determined in chapter 6

Calculation case	Support excess pressure in the excavation chamber [kPa]	Soil with φ'=30°, ϑ =66,3°		Soil with φ'=35°, ϑ =68,3°	
		Average pressure transferred over the entire tunnel face [kPa]	% - of the applied excess pressure transferred	Average pressure transferred over the entire tunnel face [kPa]	% - of the applied excess pressure transferred
S 1-a	8	5.97	74.63	5.88	73.45
S 1-b	20	14.93	74.63	14.69	73.45
S 2-a	15	10.76	71.71	10.56	70.42
S 2-b	30	21.51	71.71	21.12	70.42
S 3-a	35	22.57	64.47	22.01	62.88
S 3-b	50	32.24	64.47	31.44	62.88
S 4-a	55	38.03	69.15	37.27	67.76
S 4-b	70	48.41	69.15	47.43	67.76

very low slurry excess pressure in the case S1 in combination with permeability coefficient development may cause that the mutual influence of the tracks is limited, which leads to increase of pressure transfer efficiency.

The last investigation point in this section was focused on the pressure drops over the pressure transfer mechanism in the calculation cases. The pressure drop was evaluated for the highest achieved formation state at the tunnel face just before the cutting tool passed through the particular point. As previously stated in chapter 6, this pressure creates the initial pressure gradient which is responsible for the slurry penetration into the soil. The pressure drop was evaluated for the middle point of each cutting track at the time 45 s since the excavation start. It can be seen from Figure 8-14 that the pressure drop is increasing with increasing distance from the tunnel axis. This is explainable by the flow conditions in front of the tunnel face. While the flow close to the center of the tunnel face occurs mainly in the parallel direction to the excavation, the flow at the circumference combines tangential and parallel direction. This inevitably leads to larger pressure gradients (drops) at the circumference.

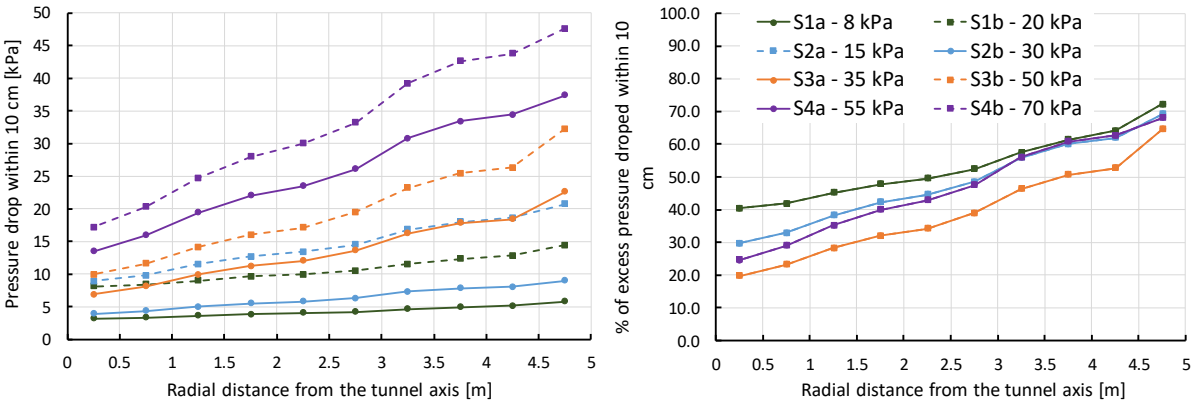

Figure 8-14: Pressure drop over 10 cm of the pressure transfer mechanism depending on the radial distance from tunnel axis, Left – absolute pressure drop, Right – drop as a percentage of the applied slurry excess pressure

As was expected, the higher slurry excess pressure in the excavation chamber induced higher pressure drop over the pressure transfer mechanism (Figure 8-14–left). However, as can be seen when comparing Figure 8-14-left with Table 6-4, the pressure drop at the tunnel face is always lower than the pressure drop in the experiments for the same slurry excess pressure. Figure 8-14-right shows that the percentage of slurry excess pressure dropped over the transfer mechanism does not depend on the absolute value of the slurry excess pressure. These results corresponds to the previous

statement regarding the pressure transfer inside the wedge. In contrast, the percentage is strongly influenced by the formation of the pressure transfer mechanism, specifically by the decrease of its permeability coefficient, which was experimentally determined in chapter 6.

The described behavior is taken into account in the calculation case S5. It is adopted in this case that the excavation occurs through conditions characterized by Table 8-2. Hence support pressure 170 kPa is adjusted for the excavation resulting in 70 kPa of slurry excess pressure in the chamber. In the calculation case S5, the pressure transfer of this 70 kPa is investigated. The basic question of this calculation is, which developments of permeability coefficient should be assigned to which cutting tracks to obtain the same pressure drop at the tunnel face as in the experiment. To predict the drops, the percentages of the drop obtained in Figure 8-14-right can be taken and multiplied with the excess pressure in the chamber. The assigning should be consequently done in the way that the average drop over the area with particular permeability coefficient development corresponds to the drop in the experiment. So it is done in Figure 8-15. The tunnel face was divided into two zones. The average expected pressure drop over the each zone was calculated and compared with pressure drop obtained in available experiments. The extension of each zone was varied until the best fit of pressure drops was achieved. It turned out that the best fit for 70 kPa excess pressure in the chamber would deliver experimental combinations 2 and 3 with a pressure drop of 0.35 bar (combination 3) in Zone 1 and 0.15 bar in Zone 2

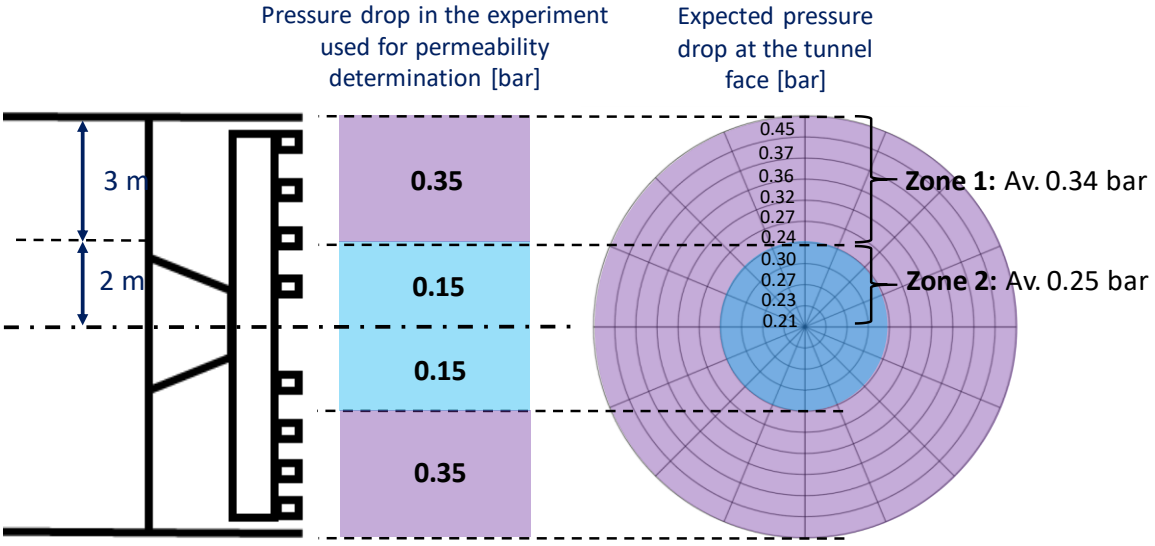

Figure 8-15: Assigning of permeability coefficient developments to cutting tracks for calculation – scenario S5 (multi-zone model)

(combination 2). The comparison between predicted and calculated pressure drop for this two-zone model is shown in Figure 8-16.

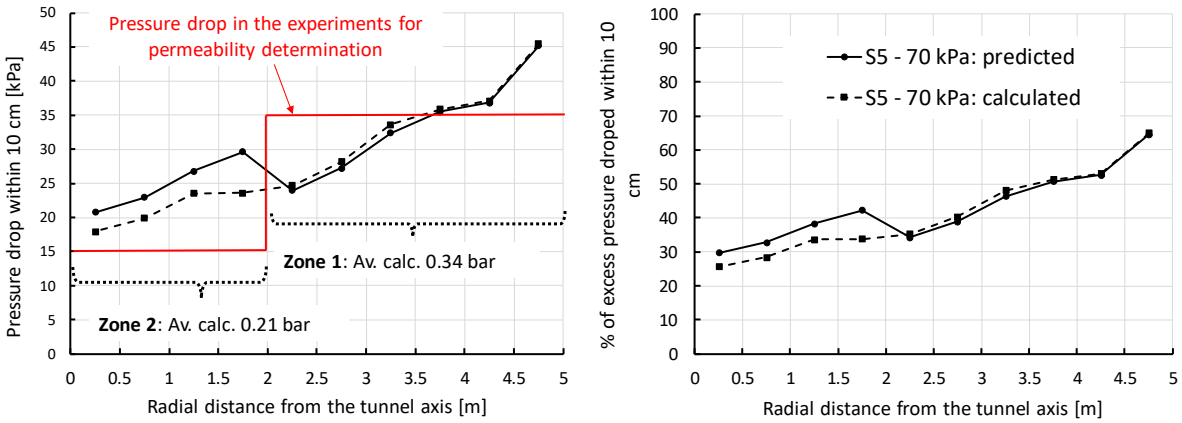

Figure 8-16: Comparison between predicted pressure drop and subsequently for calculation scenario S5, pressure drop from assigned experimental combination is also shown

Based on the comparison, it turns out that the described prediction methodology can also be used for multi-zone tunnel face. Only decent differences between predicted and calculated pressure drop over 10 cm could be observed close to the border between the zones. The pressure transfer analysis is conducted in section 8.3 for this model together with face stability analysis.

8.2.3 Investigation considering experimental results for slurry penetration and a realistic cutting wheel

After clarifying the pressure transfer for the simplified cutting wheel, the investigation was focused on a realistic cutting wheel, including various homogeneous cutting zones as determined in chapter 5. The pressure transfer was evaluated at the time 123.75 s from the start of the excavation (after one and half rotation). The position of the two cutting wheels at this time is shown in Figure 8-17.

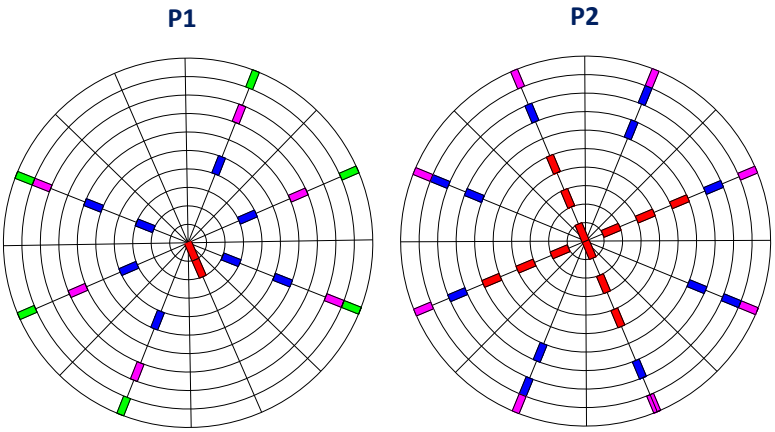

Figure 8-17: Orientation of the cutting wheel of reference projects at 123.75 s since excavation start

Following the evaluation scheme from the previous section, excess pore pressures in front of the tunnel face at the tunnel axis level were first evaluated. These are evaluated and compared for both reference projects in Figure 8-19. It could also be confirmed for the model with various homogeneous cutting zones that the scaled distribution of pore pressures does not depend on the absolute amount of slurry excess pressure in the chamber. However, a difference was noticed between the two reference projects. The difference can be summarized by the pressure drop at the tunnel face over the pressure transfer mechanism. The slurry excess pressure drops at the tunnel face by 39.2 % for project P1 in comparison to 28.1 % for project P2. The calculated drop is again larger in comparison to the curve by Bezuijen et al. (2001) due to achieved higher formation degree of the pressure transfer. The difference between two reference shields can be seen also from Figure 8-18. The distribution of the

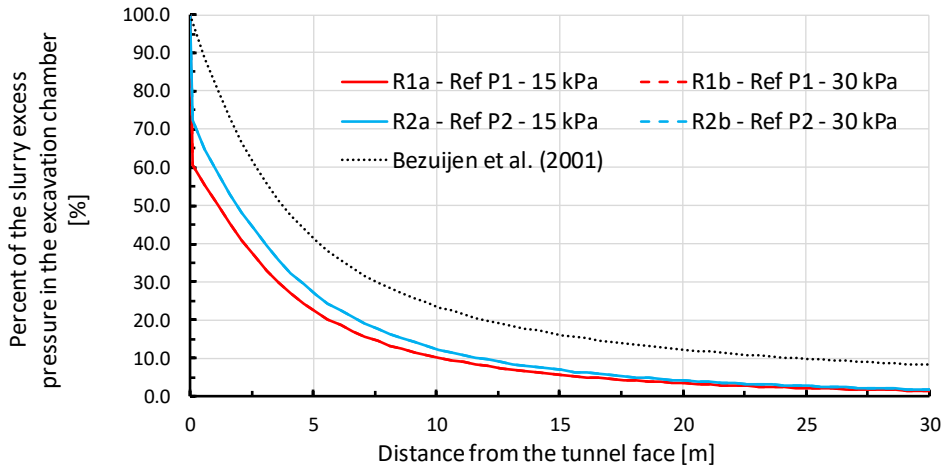

Figure 8-18: Scaled distribution of excess pore pressure in front of the tunnel face during excavation for two reference slurry shield from Projects P1 and P2

hydraulic heads at the interface between pressure transfer mechanism and soil is shown in the figure. Note that total head 73.0 m denotes no pressure drop over the pressure transfer mechanism and total head 70 m denotes entire pressure drop. The difference between projects is caused by different cutting tool layouts and different amount of cutting tools within tracks. In general, less cutting tools are placed at the wheel of P1 reference shield. In Figure 8-18, it can be also observed that green areas are present in larger extent. This signifies higher pressure drop over the pressure transfer mechanism.

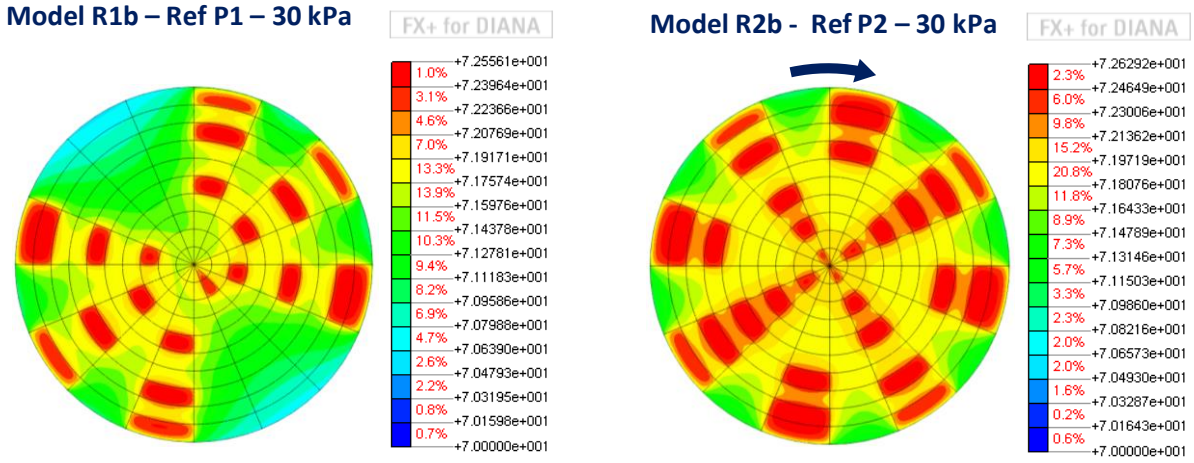

Figure 8-19: Total head distribution obtained by the numerical model for the calculation case R1b – Ref P1 – 30 kPa (left) and case R2b – Ref P2 – 30 kPa at 129.75 s since the excavation start

Consequently, the focus was given to the evaluation of the slurry pressure transfer within the soil wedge. The results are presented in Table 8-7. It can be concluded that despite keeping the same RPM, better support pressure transfer was obtained for reference project P1. The difference is approximately 8 % and can again be assigned to the distribution of the cutting tools as previously stated. It was shown again, as in the previous section that the absolute amount of support excess pressure does not influence the percentage of pressure transferred. If the efficiencies of the pressure transfer are compared for the two investigated soils, it turns out that the pressure transfer decreases for the soil with φ'=35° by 1.4 % for project P1 and by 1.6 % for project P2 respectively.

As the last investigation point in this section, the pressure drops over the pressure transfer mechanism in the calculation cases were evaluated. The pressure drop was evaluated for the highest achieved formation state at the tunnel face just before the

Table 8-7: Results of the pressure transfer calculation with realistic cutting wheels

Calculation case	Support excess pressure in the excavation chamber [kPa]	Soil with φ'=30°, ϑ=66.3°		Soil with φ'=35°, ϑ=68.3°	
		Average pressure transfered over the entire tunnel face [kPa]	% - of the applied excess pressure transfered	Average pressure transfered over the entire tunnel face [kPa]	% - of the applied excess pressure transfered
R1a - Ref P1	15	10.2	67.73	10.0	66.39
R1b - Ref P1	30	20.3	67.73	19.9	66.39
R2a - Ref P2	15	9.0	60.23	8.8	58.60
R2b - Ref P2	30	18.1	60.23	17.6	58.60

cutting tool passed through the particular point. As stated previously, this pressure creates the initial pressure gradient, which is responsible for the slurry penetration into the soil. The pressure drop was evaluated for the middle of each cutting track at the time 123.75 s since the excavation start. It can be observed in Figure 8-20 that a different amount of cutting tools within a track has an influence on the distribution of pressure drop. Therefore, the amount of the pressure drop does not increase quite as steeply towards the circumference for the realistic cutting wheels as at the simplified cutting wheel (Figure 8-14). This is particularly visible for the reference project P1. At this reference cutting wheel the drop even decreases between radial distance 1.25 – 1.75 m and dramatically between 2.75 - 3.25 m from the tunnel axis. The decrease happens in lower extent also at P2 cutting wheel between radial distances 2.25 - 2.75 m. When the two realistic cutting wheels are compared (Figure 8-20-right), it can be concluded that the distributions are locally quite different, but the global trend is still the same. The local discrepancies are caused either by amount of cutting tools present in the adjacent cutting tracks or angular offset of cutting tools between the adjacent cutting tracks. Interestingly, the pressure drop at the circumference of project P1 does not increase that significantly in comparison to the adjacent cutting track with less tools. The situation is different for the reference project P2. While the circumferential cutting track at project P1 has 6 tools and the adjacent track 2 tools, 8 tools are located in the circumferential track of project P2 neighboring a track with 4 tools. The discrepancies in general, especially higher pressure drops for project P1, can also satisfy the differences in transferred slurry excess pressure summarized in Table 8-7.

Figure 8-20-left also shows the pressure drop measured in the experiments for the permeability development determination in chapter 6. When comparing the measured drop with the calculated one at the tunnel face, it can be concluded that slurry excess chamber pressure 15 kPa again delivered significantly lower drop. The average calculated pressure drops at the tunnel face for 30 kPa excess chamber pressure were 13.8 kPa for project P1 and 11.4 kPa for project P2. Hence, the slurry excess pressure delivered very similar average pressure drop as measured in the experiment.

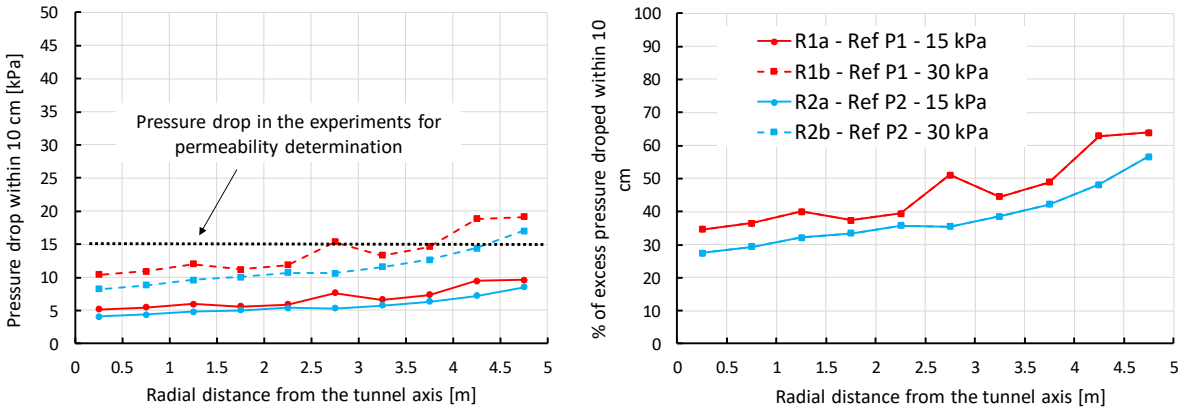

Figure 8-20: Pressure drop over 10 cm of the pressure transfer mechanism depending on the radial distance from tunnel axis, Left – absolute pressure drop, Right – drop as a percentage of the applied slurry excess pressure, Note: two points are provided for the project Ref P1 at the distance 4.75 m due to two distances between tools in this track

In the next section 8.3, when investigating the face stability, the excavation occurs through conditions characterized by Tab. 8-2. Hence, the support pressure 170 kPa is adjusted for the excavation resulting in 70 kPa of slurry excess pressure in the chamber due to the adopted location of groundwater level. In the scenarios R1c – Ref P1 and R2c – Ref P2, the pressure transfer of this 70 kPa should be investigated. On one hand, using the findings presented previously in this section, no additional FEM calculation is necessary. On the other hand, the pressure drop induced by the excess pressure 70 kPa has to be compared with pressure drop measured in the experiment before the face stability investigation. To predict the pressure drop for 70 kPa, the same methodology is used as in section 8.2.2 for S5 calculation case. Thus, the percentage of the pressure drop for the particular reference project from Figure 8-20-right is multiplied by 70 kPa. The resulting pressure drops are shown in Figure 8-21. It turns out that the average pressure drop for calculation case R1c was 32 kPa and 27 kPa for R2c. Hence, the pressure drop in the experiment was smaller. However, as turned out

in the parametric study, the difference will cause not significant in accuracy for the analysis of the pressure transfer.

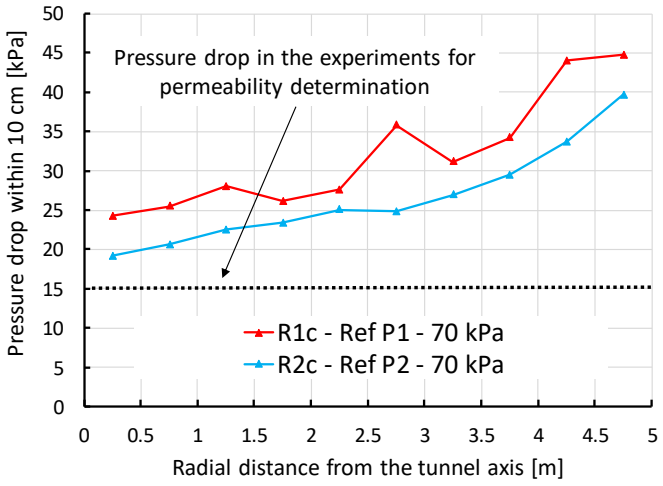

Figure 8-21: Pressure drop over 10 cm of the pressure transfer mechanism depending on the radial distance from tunnel axis compared with pressure drop measured in the

8.2.4 Comparison of the calculated pressure transfer with other theories

In this section, the results of pressure transfer calculation will be compared with other available theories discussed in section 3.4 of this thesis. The amount of slurry excess pressure transferred according to various models is shown in Table 8-8. The comparison is conducted for the applied slurry excess pressure of 70 kPa in the chamber. In case of the developed HPT models, the average pressure transfer over the entire tunnel face is considered. The results for the HPT models were taken from section 8.2.3 and 8.3.

Table 8-8: Comparison of transferred slurry excess pressure, *average, **only over the pressure transfer mechanism

Calculation Case	Applied slurry excess pressure [kPa]	Transferred pressure [kPa]					
		HPT model*	DIN 4126 (2013)	Anagnostou & Kovari (1994)	Broere & van Tol (2001)**	Bezuijen et al. (2001)	Bezuijen et al. (2016)
S5	70	45.2	70.0	70.0	24.3	22.5	43.5
R1c - Ref P1	70	46.5	70.0	70.0	29.6	22.5	46.1
R2c - Ref P2	70	42.0	70.0	70.0	18.8	22.5	46.9

The comparison showed that highest pressure would be transferred according to DIN 4126 (2013) and the stationary theory by Anagnostou & Kovári (1994). These theories delivered full amount of the transfer due to geometric condition of slurry

stagnation inside the sliding wedge (section 2.6). Moreover, the stagnation gradient predicted by DIN 4126 was between 430-752 kN/m^3, which is far beyond 200 kN/m^3 required by DIN 4126 to adopt full pressure transfer. Note that the stationary theory by Anagnostou & Kovári (1994) is originating from DIN 4126. The lowest pressure transfer was predicted acc. to the theory presented by Bezuijen et al. (2001). The theory considers only the shield geometry and the slurry excess pressure. Therefore, the same amount of transferred pressure was calculated for all cases. The theory is based on groundwater flow. The theory by Broere & van Tol (2001) expects partial pressure drop over the slurry penetrated zone during excavation and the rest of slurry excess pressure causing groundwater flow in semi-confined aquifer. It turns out that their approach for calculation of pressure drop shows the same trend as HPT model for the investigated calculation cases. The theory by Bezuijen et al. (2016) did not reflect well the trend obtained by HPT model.

The next point was focused on comparison in terms of percentual pressure drop over the pressure transfer mechanism. The comparison is shown in Table 8-9. Both DIN 4126 (2013) and Anagnostou & Kovári (1994) consider here the entire pressure drop over the pressure transfer mechanism. This indicates that no increased pore pressure should be observable outside of the pressure transfer mechanism during excavation. In contrast, the pressure drop predicted by Bezuijen et al. (2001) is 0%, because they do not consider any existence of pressure transfer mechanism during excavation. A similar pressure drop over the pressure transfer mechanism was predicted by Brore & van Tol (2001) as by the HPT model. Their theory reflects well the trend resulting from the calculations using HPT model. The trend is quite well described by Bezuijen et al. (2016). However, Bezuijen et al. (2016) state that theory should not be applicable for a case with entirely cut pressure transfer mechanism.

Table 8-9: Comparison of pressure drop over the pressure transfer mechanism

Cauculation Case	Pressure drop over the pressure transfer mechanism [%]					
	HPT model	DIN 4126 (2013)*	Anagnostou & Kovari (1994)	Broere & van Tol (2001)	Bezuijen et al. (2001)**	Bezuijen et al. (2016)
S5	30	100	100	35	0	44
R1c - Ref P1	39	100	100	42	0	50
R2c - Ref P2	28	100	100	27	0	51

Finally, it is worth mentioning that previously in this section, the pressure transfers delivered by HPT model for excavation stage were compared. During stoppage or downtime, the HPT model delivers complete pressure transfer over the pressure transfer mechanism with no increased pore pressure existence outside of the mechanism for all calculation cases.

8.3 Face stability assessment for Case A

In this section, the tunnel face stability is investigated while considering the efficiently transferred slurry excess pressure from the previous section. Consequently, additional notes to the face stability in the Case A interaction are provided.

8.3.1 Face stability assessment for excavation with simplified and with realistic cutting wheels

In this section, a tunnel face stability analysis is conducted for the excavation characterized in section 8.1.2. The required face support pressures from Table 8-2 are considered here again. As discussed before, no additional FEM calculation for cases R1c and R2c were conducted, so that the slurry excess pressure was multiplied by the efficiency of the pressure transfer for the particular project determined in Table 8-7.

The comparison between the support pressure transferred and the acting earth pressure is conducted for investigation with a simplified cutting wheel (S5) and investigation with realistic cutting wheel (R1c and R2c) in Table 8-10. Note that RPM for calculation case S5 is 1.875, while for the remaining cases it is 0.682.

Table 8-10 shows that the slurry excess pressure 70 kPa delivered a stable tunnel face for all cases. However, the safety level required by ZTV-ING (2012) for the transferred pressure was not achieved for the most of cases. It is worth mentioning that the applied slurry excess pressure includes also safety gap 10 kPa due to possible pressure deviations. That increases the transferred pressures.

Table 8-10: Comparison between pressure transferred and the acting earth pressure

Calculation case	Support excess pressure in the excavation chamber [kPa]	Average pressure transferred over the entire tunnel face [kPa]		Average earth pressure acting at the tunnel face [kPa]		Resulting safety factor for the earth pressure [-]		Required safety factor for the earth pressure acc. to ZTV-ING (2012) [-]
		Soil with φ'=30°, c=0kPa	Soil with φ'=35°, c=0kPa	Soil with φ'=30°, c=0kPa	Soil with φ'=35°, c=0kPa	Soil with φ'=30°, c=0kPa	Soil with φ'=35°, c=0kPa	
S5	70	46	45	37	30	**1.26**	**1.53**	1.5
R1c - Ref P1	70	47	46	37	30	**1.30**	**1.58**	
R2c - Ref P2	70	42	41	37	30	**1.16**	**1.39**	

8.3.2 Additional notes to the face stability in Case A

To analyse the slurry excess pressure transfer for a wider range of soil conditions, the diagram in Figure 8-22 was plotted. The excavation conditions from Table 8-2 were generalized here for different soil friction angles of non-cohesive soils. The required average support excess pressure without any safety factor was calculated. Note that it was assumed that hydraulic properties of the soils remain constant independent of the friction angle. For each soil friction angle, sliding angle of the wedge according to Horn (section 2.6) was determined. Subsequently, the pressure transfer inside the particular wedge was calculated for the three cutting wheels. The transferred pressure is consequently compared with the acting earth pressure in Figure 8-22. It can be seen that cases R1c – Ref P1 and S5 would always deliver a stable tunnel face. In contrast,

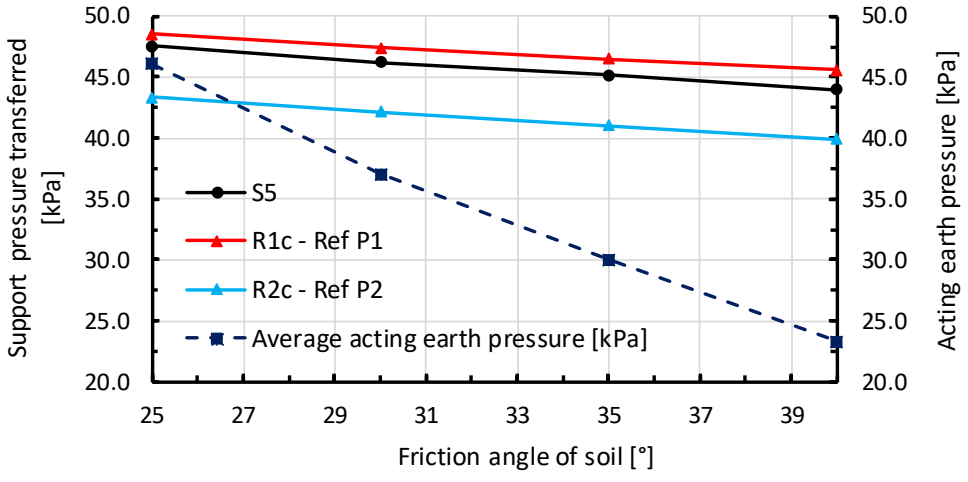

Figure 8-22: Comparison of transferred slurry pressure with acting earth pressure depending on friction angle of soil

problems with face stability might occur for case R2c – Ref P2 during excavation through soil with lower friction angle than 27°.

To analyse the slurry excess pressure transfer in more detail, Figure 8-23 was plotted for the ground condition from Table 8-2 considering soil friction angle φ'=35° and c´=0 kPa. This figure shows the pressure transfer in relation to the vertical and horizontal distance from the tunnel axis. Note that 100 % would mean the entire transfer of the slurry excess pressure. The comparison of calculation cases shows that a similar amount of transferred pressure could be expected close to the tunnel crown (+5 m). At this elevation, the sliding wedge has the largest length, so the pressure transfer is not so sensitive here for the formation of the mechanism. In contrast, the sliding wedge is much slimmer at the tunnel bottom (-5 m) making the formation of the pressure transfer important. The investigated cases delivered very different results here in terms of slurry excess pressure transfer. Case S5 deviates considerably from the other two cases. Note that in S5, the amount of cutting tools within one track does not increase with increasing distance from the tunnel axis. Hence, it could be here observed, that despite the slim wedge at the tunnel bottom, the pressure transfer is higher here than at the tunnel axis. It correlates with the investigation conducted for determination of the pressure drops in front of the tunnel face (see Figure 8-14). For the two other investigated cases, the amount of cutting tools increases with increasing distance from the tunnel axis. It can be observed in Figure 8-23 that this effect is dominant for the decrease of the transferred slurry pressure at the tunnel bottom. When the transferred pressure is compared between cases at the tunnel axis elevation

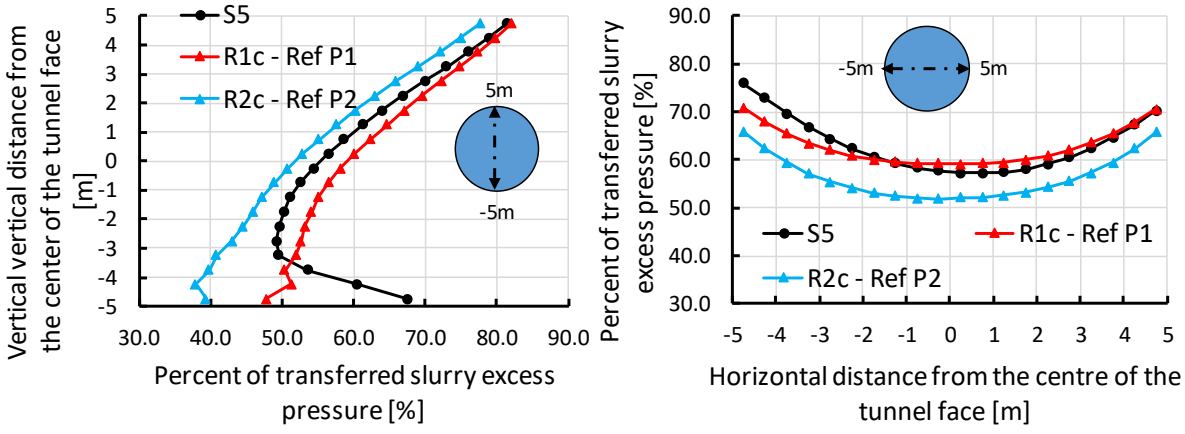

Figure 8-23: Pressure transfer depending on the location at the tunnel face – along the vertical axis (left) and along the horizontal axis (right)

along the horizontal direction, no significant differences can be determined. The pressure transfer distribution increases here from the tunnel axis to the tunnel circumference. The small difference between investigated cases is caused by the sufficient dimension of the wedge at the tunnel axis. Nevertheless, only approximately 55 % of the slurry excess pressure is transferred at the tunnel axis. The distributions from Figure 8-23 show that a zone of reduced pressure transfer appears close to the tunnel axis. If the amount of cutting tools within one track decreases with the distance to the centre, the zone with reduced pressure transfer extends further to the tunnel bottom (R1c and R2c).

The existence of a zone with reduced pressure transfer close to the axis seems to be less problematic for smaller tunnel diameters (e.g. 7 m), but it could represent a more considerable problem for large tunnel diameters. In case of large tunnel diameters, it is expected that the zone with reduced pressure transfer will be larger.

9. CASE B – IMPLEMENTATION OF THE EXPERIMENTAL RESULTS INTO ANALYTICAL FACE STABILITY ASSESSMENT

In chapter 4, the theoretical considerations of the adaptation of pressure transfer model were discussed. Section 4.2 consequently specified questions regarding the face support within Case B of interaction. The aim of this chapter is to utilize the experimental results obtained in chapter 7 for answering the questions from chapter 4.2. A further aim is to suggest an engineering model to assess a self-bearing capacity of the soil wedge for cases, when slurry excess pressure is transferred first outside of the wedge.

This chapter employs a different approach than chapter 8 to characterize the conditions at the tunnel face during excavation. No additional numerical model considering interaction between cutting track is here presented. The approach, why no additional cutting track interaction model is necessary here, is discussed later within this chapter. Implications for the entire tunnel face support and stability are discussed based on experimental results from chapter 7. Since the chapter is dedicated to Case B of the interaction, the results of re-penetration from column tests and RUB tunnelling device are mainly considered.

First, the conditions at the tunnel face during excavation and Case B of the interaction are discussed. Further, a resulting adaptation of the face stability calculation model is discussed and an engineering model to improve reliability of face stability calculation is finally suggested.

9.1 Conditions at the tunnel face during excavation and resulting model adaptation

9.1.1 Slurry penetration depth

In chapter 4, expectations regarding the slurry penetration depth during excavation were formulated. It was suggested that the slurry penetration during excavation depends on the distribution of pore pressure in slurry penetrated zone (stagnation gradient of slurry) during primary penetration. For the soil fraction 1- 2 mm, it was determined in chapter 7, that the distribution of pore pressure was almost perfectly linear regardless of slurry injection pressure (Figure 7-14). Thus, it could be expected that the slurry penetration depth during excavation will be reduced in comparison to primary penetration.

The experimentally determined slurry penetration depth within the column test is shown for soil fraction 1-2 mm in Figure 9-1. The slurry penetration depth was determined using the methodology from section 7.1.2. In Figure 9-1, the fluctuations of slurry penetration depths for two excavation scales are shown. The two particular excavation scales are reaching a different total slurry penetration depth during an excavation cycle. For the excavation scale 30s+100s adopting a tool passing every 100 s and the cutting depth 40 mm, the maximal reached penetration depth is almost equal to the maximal primary slurry penetration depth. This can be explained with the soil cutting at the moment, when the maximal primary slurry penetration is almost

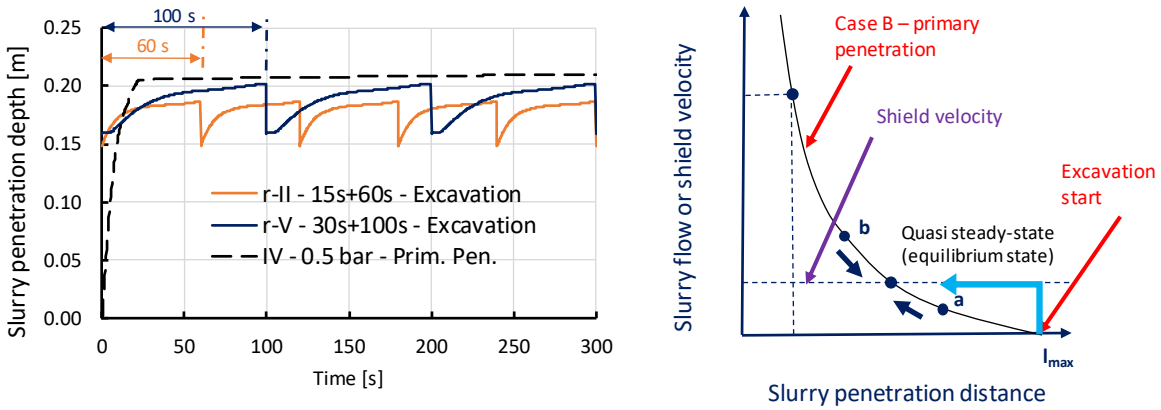

Figure 9-1: Slurry penetration depth during excavation in soil fraction 1-2 mm for two excavation scales compared with primary penetration depth (left) and schema for reaching the penetration depth during excavation according to Anagnostou & Kovari (1994) (right)

reached. The reduced slurry penetration depth is shown for the faster excavation scale adopting a tool passing within every 60 s.

Fig. 9-1-right shows a sketch by Anagnostou & Kovári (1994), which describes how an equilibrium during excavation automatically adjusts at the tunnel face. The equilibrium signifies that the slurry penetration depth corresponds to the cutting depth during excavation cycle. The shortcoming of this sketch for Case B of the interaction has been already discussed in chapter 4. Based on the results from chapter 7, it could be confirmed that the equilibrium point can be reached by slurry penetrating in average faster during primary slurry penetration than a shield excavation only due to re-penetration. The decrease of average slurry penetration velocity due to re-penetration can be easily derived from Figure 9-1-left.

Broere & van Tol (2000) also expect a reduced slurry penetration depth during excavation. Their calculation approach suggested in $Eq.\,3\text{-}47$ would also deliver different slurry penetration depths for soil fraction 1-2 mm for the two investigated excavation scales. The average penetration depth within a cycle in front of the tunnel face would be 0.12 m for the scale with tool passing every 60 s and 0.14 m for the tool passing every 100 s. Hence, the approach reflects the influence of the excavation scale properly in comparison to the experimental results. But it predicts slightly lower slurry penetration depth. The approach by Broere & van Tol (2000) does not consider eventual differences in the cutting depth of tools per passing. Moreover, the approach expects that the slurry excess pressure, which did not drop over the slurry penetrated zone transforms in groundwater flow. This was not observed for soil fraction 1-2 mm due to the increased stagnation gradient during penetration process (see section 9.1.2).

Bezuijen et al. (2001) and Bezuijen et al. (2016) do not focus on the prediction of slurry penetration depth during excavation in detail. As pointed out in section 3.4.3, Bezuijen et al. (2016) assume that the slurry penetration front moves together with the slurry shield. It means that the slurry adopts the velocity of movement from the shield. It corresponds to the equilibrium state from Figure 9-1.

The column experiments from chapter 7 in this thesis for the investigation of the re-penetration were conducted while physically simulating a passing of a single cutting tool. Thus, no interaction between cutting tracks was considered in the column

experiments. It could be expected that the interaction would cause a sort of smearing effect, but the overall mechanics of moving of slurry penetration front will be preserved. The argument can be supported by the statement that zones immediately after cutting and zones with longer times since cutting do not differentiate dramatically in terms of their hydraulic properties (see section 7.3, specially the diagrams with pore pressure distributions). The expectation shown in Figure 4-9 for reduction of slurry penetration distance during excavation could be confirmed.

The previously discussed reduction of the penetration depth during excavation determined in column test could not be confirmed by observations in the RUB tunnelling device. The slurry penetration depth cannot be determined directly inside the device and had to be predicted based on pore pressure distribution. The result is explainable due to excavation scale adopted in the RUB tunnelling device as discussed in section 7.4. Moreover, from the global pore pressure distribution, a local slurry penetration depth cannot be determined with a high accuracy.

The slurry penetration depth in soil fraction 0.063-4 mm is not discussed here, because it could only be evaluated based on pore pressure distribution within the RUB tunnelling device. Hence, it is assessed within the next section together with the stagnation gradient.

9.1.2 Stagnation gradient development

The stagnation gradient of slurry is defined according to *Eq.* 3-23 as slurry excess (pore) pressure drop divided by slurry penetration distance. Thus, the gradient is expressed by inclination of an imaginary line placed between excess slurry pressure in chamber and a point with zero excess pressure in the ground. It is assumed that the slurry penetrates up to the point with zero excess pressure. As could be expected from the development of the penetration depth (Figure 9-1), not only the depth during re-penetration is changing in soil 1-2 mm, but also the stagnation gradient is changing. To determine the stagnation gradients more properly, the measured excess pore pressure has to be evaluated as was shown in Figure 7-14, Figure 7-20 and Figure 7-23. It turns out that the pore pressure distributions for soil 1-2 mm are almost linear. Thus, using the linear regression based on least square method, the stagnation gradient for the particular experimental combination and adopted time can be determined. The average obtained pore pressure distribution and stagnation gradients are shown in

Figure 9-2. In Figure 9-2-left, the pore pressures are shown here as scaled percentages of the pore pressure at the injection point to improve the comparison. Additionally, a stagnation gradient calculated using $Eq.3\text{-}27$ acc. to DIN 4126 (2013) is also shown here. The calculated gradient distinguishes an assumption for the empirical factor "a" as discussed in $Eq.3\text{-}27$. It can be seen that the calculation adopting a=2 is significantly underestimating the measured gradients, while the formula from DIN 4126 (2013) with a=3.5 is approximating the final stagnation gradients very well. Generally, it can be seen that the stagnation gradients obtained for the re-penetration are slightly higher than for the primary penetration. This could be expected due to lower penetration depth as discussed in the previous section. Figure 9-3 shows the development of the stagnation gradient between passes of subsequent cutting tools. Note that the gradients are observed locally here. Fundamentally different gradients were determined for early stages of penetration and re-penetration. While the stagnation gradient for re-penetration at 3s is comparable with later stages, the gradient for primary penetration is much lower. The measured time-dependent stagnation gradient first shows increase after the start of the re-penetration and then successive decrease until the end of the excavation cycle. The different development might have a fundamental influence on the face stability. Hence, it is fundamentally necessary to consider re-penetration when experimentally modelling the Case B interaction.

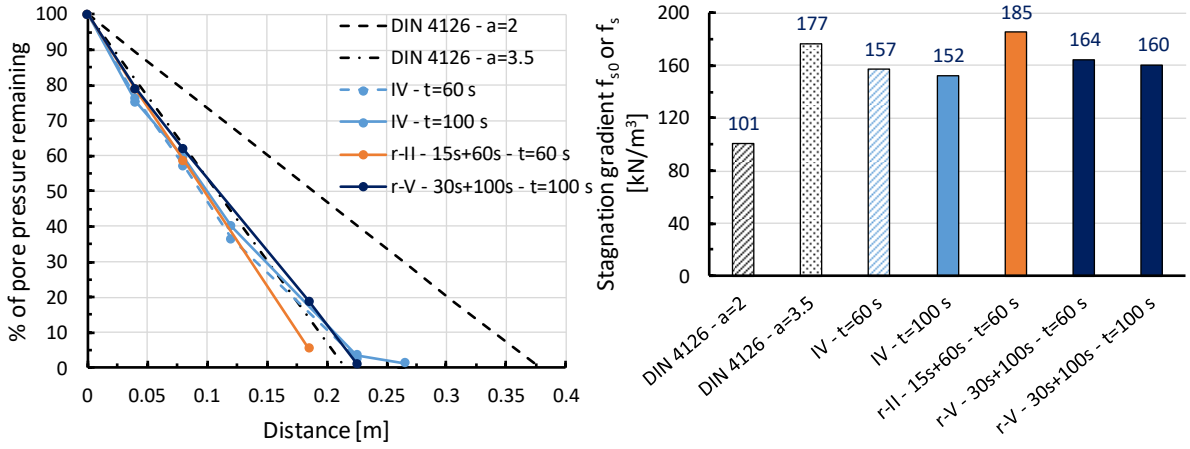

Figure 9-2: Pore pressure distribution in comparative presentation (left) and achieved stagnation gradients (right) for soil with grain fraction 1-2 mm

Anagnostou & Kovári (1994) suggested an approach to calculate the stagnation gradient while considering the influences of excavation. The theory is described in section 3.4.2. Using $Eq.\,3\text{-}37$, the stagnation gradient during excavation was calculated for two excavation scales from the final gradient measured in combination IV at t=60s (primary penetration). The comparison of the calculated gradients with measured during primary penetration and re-penetration is shown in Figure 9-3. The comparison shows that the theory by Anagnostou & Kovári (1994) shows only a very limited increase in the stagnation gradient due to excavation, which is lower in comparison to corresponding settings of the re-penetration experiments. In contrast, Broere & van Tol (2001) consider the equal stagnation gradient (f_{s0}) both for static case and excavation as pointed out in section 3.4.3. In their theory, the gradient calculation adopts the approach included in DIN 4126 (2013) while considering a=3.5. Thereby, Broere & van Tol (2000) do not reflect the obtained experimental results correctly.

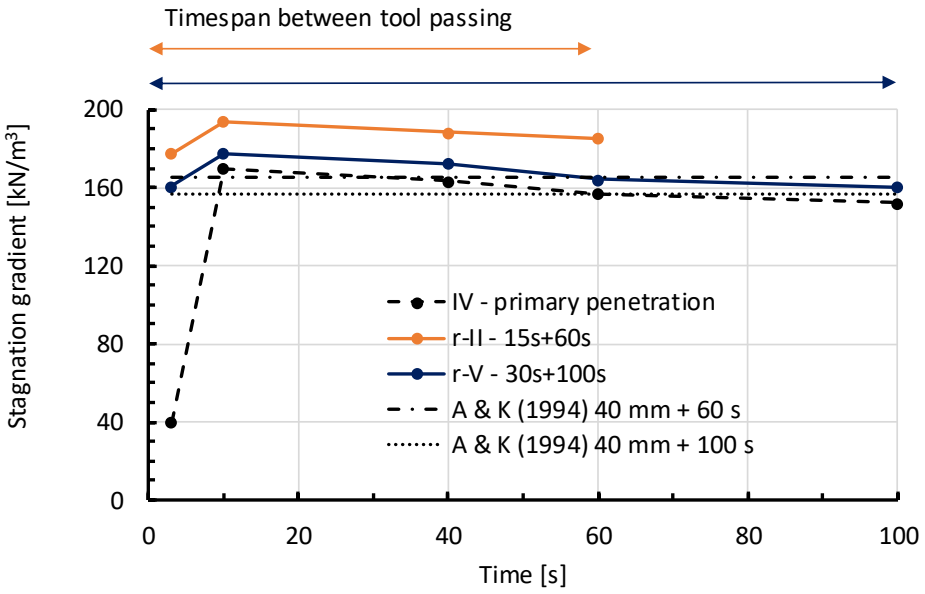

Figure 9-3: Stagnation gradients measured during slurry penetration compared with transient stagnation gradients predicted by Anagnostou and Kovari (1994)

To evaluate the efficiency of the entire face support, the interaction between cutting tracks has to be considered. This can be done by considering a weighted average stagnation gradient. Note that this approach is possible only for the re-penetration, since the changes in the gradient are not so dramatic in comparison to primary penetration. Hence, the flow in one track should not influence the flow in the adjacent track. The influence is expectable only for the primary penetration (high difference between gradient at 3s and 10s) and is also considered in the assessment for the Case A. It is also assumed that the gradient does not depend on the distance to the tunnel

axis in contrast to Case A. This assumption is justified also by considerably reduced flow processes in comparison to Case A of the interaction. The stagnation gradients calculated as weighted averages are shown in Table 9-1. The gradients are compared to primary penetration at t=100s, which is considered here as a steady state gradient. It could be shown that the stagnation gradient during excavation will be higher in combination r-II by 24% and in in combination r-V by 9% than in the static situation. In comparison to Anagnostou & Kovári (1994), the major influence here is not represented by global movement of the machine, but rather by local cutting and flow processes.

Table 9-1: Stagnation gradient – weighted average within a cutting track

Experimental combination	Weighted average of stagnation gradient [kN/m^3]	% of IV at t=100s
r-II - 15s+60s	189	124
r-V - 30s+100s	166	109

A different situation appears when the stagnation gradient during excavation is evaluated for soil fraction 0.063-4 mm. The soil fraction 0.063-4 mm was characterized with non-linear pore pressure distribution inside the slurry penetrated zone. Using the same methodology as for soil fraction 1-2 mm based on linear regression, the stagnation gradient was determined. The stagnation gradient is shown together with pore pressure distribution in Figure 9-4. It can be seen that DIN 4126 delivered comparably higher stagnation gradient than measured in the column test for combination VIII under static condition at 120 s since the experiment start. The theory for calculation of the stagnation gradient during excavation acc. to Anagnostou & Kovári (1994) again showed an increase of this gradient as for soil 1-2mm. This theory does not take into account the reformation of the pressure transfer mechanism as observed in the RUB tunnelling device for soil fraction 0.063-4 mm. To characterize the pore pressure distribution from the RUB tunnelling device, the curves were approximated. Note that only the curves of PWD 4 and 5 are considered for the approximation here due to terminated pressure transfer reformation. The approximation of pore pressure distribution was divided into two branches. Linear approximation was considered for the area of 6 cm in front of the cutting tools, which approximately corresponds to the extent of slurry penetrated zone during static

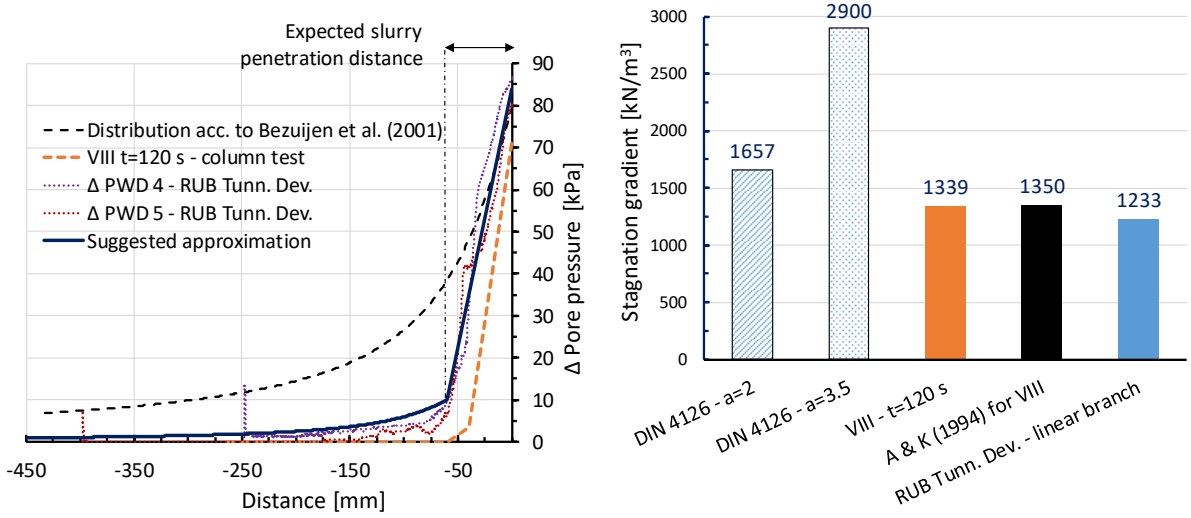

Figure 9-4: Pore pressure distribution in comparative presentation (left) and achieved stagnation gradients (right) for soil with grain fraction 0.063-4 mm

primary penetration. From the distance 6 cm onwards, the distribution was approximated by the theory by Bezuijen et al. (2016). Thus the measured pore pressure at the distance of 6 cm was considered as ϕ_0 from $Eq.3\text{-}44$. Subsequently, the pore pressure was input as ϕ to $Eq.3\text{-}41$ to calculate the non-linear part of the pore pressure distribution. It is possible to see from Figure 9-4 that the division into two branches fits the measured results well. Based on the approximation, it was also possible to calculate the parameter "α" ($Eq.3\text{-}44$) as introduced by Kaalberg et al. (2014) and Bezuijen et al. (2016) and also the stagnation gradient of the linear branch. The parameter alpha amounted to 0.125, which denotes that 12.5 % of slurry excess pressure resulted in increased groundwater pressure. The comparison of the approximated stagnation gradient from the RUB tunnelling device with the measured in column test shows that during excavation, a lower stagnation gradient was obtained than during static conditions due to existence of increased pore pressure also outside of the slurry penetrated zone. Hence, a fundamentally different behaviour was obtained here than for the soil fraction 1-2 mm. Based on the pore pressure development obtained for the soil fraction 0.063-4 mm, the expected slurry penetration distance assumed in Figure 4-10 can be revisited. It is expected that the slurry penetration distance during excavation does not change in the device and only the amount of flow through the tunnel face is changing. The obtained experimental results were obtained with the RUB tunnelling device, hence, they reflect a simplified assessment for the whole tunnel face.

9.1.3 Development of effective stress

In section 7.3.2, development of effective stress was investigated during the re-penetration within the column test. The effective stress development was investigated inside and outside of slurry penetrated zone. During the experiment, the original effective stress level was increased by slurry injection. The simulated stress path is, however, not close to realistic conditions at the tunnel face. The slurry excess pressure during excavation is usually lower in practice than the original effective stress at the rest, because the support pressure is designed based on active three-dimensional earth pressure. So it leads usually to a release of the effective stress while the shield is approaching the observed location. The stress release occurs to an extent which is allowed by the slurry excess pressure. When the horizontal effective stress is equal to the transferred support excess pressure, equilibrium is found. The described stress path would be almost impossible to simulate in the laboratory conditions. Hence, the face support is considered as a mechanism causing an effective stress increase in the ground and in the column test. The difficulties connected with the employed approach of physical modelling of effective stress during slurry penetration are already discussed in chapter 7. Hence, the focus is given to its development to characterize the acting of support pressure properly rather than on absolute value of the measured effective stress. The developments of the effective stress are shown in Figure 9-5 for soil 1-2 mm. The developments show certain pressure drops and peaks when a tool is passing. As pointed out in section 7.1.2, the re-penetration within the column test was modelled using the pressure-controlled methodology. This brings additional stress to

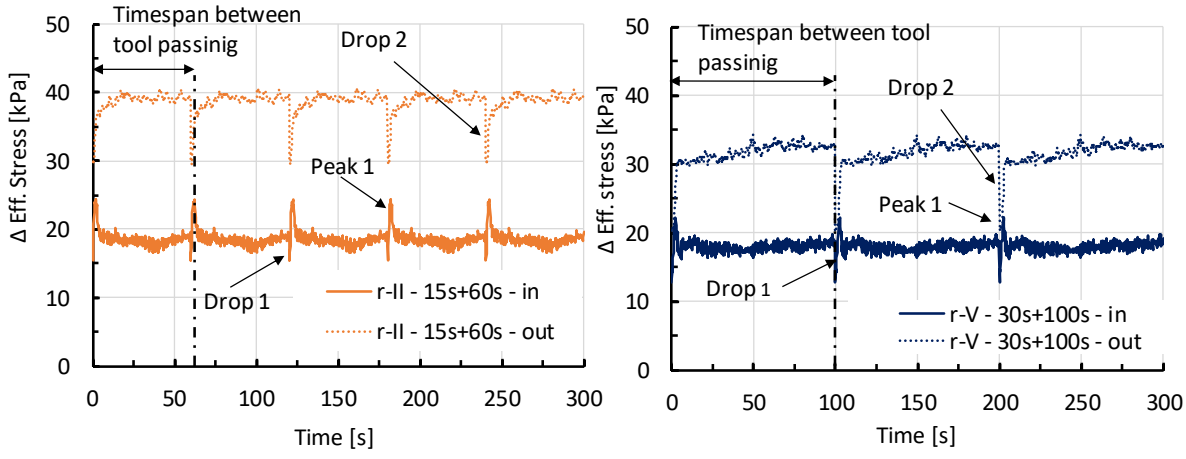

Figure 9-5: Development of effective stress outside (out) and inside (in) the slurry penetrated zone for soil fraction 1-2 mm

the system in comparison to primary penetration. Thus, the drops 1 and 2 from Figure 9-5 are the starting effective stress levels before the re-penetration pressure is activated. In reality, the drops/increases of the stress in the system will not occur. Hence, it is possible to expect the developments of effective stress levels outside of slurry penetrated zone as constant. In contrast, the peak 1 inside the slurry penetrated zone is realistic. The peak is caused by higher amount of effective stress measured at the sensor's location, when the soil is cut by a passing cutting tool. The higher amount of effective stress is later reduced within the ongoing re-penetration slurry process by simultaneously increasing pore pressure.

When the change of effective stress is observed on the global tunnel face level, it can be concluded that the effective stress state outside of the slurry penetrated zone is not changed by passing of the cutting tool. It means that the full slurry support acts at the place during entire excavation cycle. Inside the slurry penetrated zone, effective stress peaks are connected with a tool pass. These peaks are temporarily increasing the efficiency of the support. This behaviour could be also determined by calculation of the pressure gradients in the previous section.

The development of effective stress could not be investigated within the RUB tunnelling device, therefore, the development is not discussed here for soil fraction 0.063-4 mm.

9.2 Resulting adaptation of the face stability calculation model

The discussion of the experimental results from chapter 7 in terms of their relevance for support pressure transfer in Case B interaction was conducted within the previous section. The transfer of slurry excess pressure within the sliding wedge is the fundamental requirement for the face stability, as pointed out in chapter 4. It was concluded for Case B that a relation exists between pore pressure distribution within the slurry penetrated zone during primary penetration and the distribution during excavation.

It was shown for soil fraction 1-2 mm with linear pore pressure distribution under static tunnel face condition that no increased pore pressure occurs during excavation outside of slurry penetrated zone. Furthermore, the slurry penetrated zone is not increased, but might decrease depending on the excavation scale. Depending on excavation scale,

it could be also shown that the stagnation gradient of slurry slightly increases during excavation, when the slurry penetrated zone decreases. Hence, the support pressure transfer becomes more efficient under transient conditions during excavation than during static conditions due to shallower slurry penetration. Nevertheless, the support pressure must also be designed for static conditions for the case of possible standstills or ring building stage. Therefore, support pressure transfer acc. to the static model presented by Angnostou & Kovári (1994) and incorporated in DIN 4126 (2013), using a=3.5, represents a safe design approach also for the excavation stage (a=2 can be adopted to further increase the safety). The area to be considered with efficient slurry excess pressure transfer is shown in Figure 9-6-a. Hence, to obtain the efficiently acting support force, the slurry stagnation gradient is to be multiplied with the marked-red-area content in Figure 9-6-a. Furthermore, the stagnation gradient and also slurry penetration depth under static conditions could be predicted well by this model adopting a=3.5. As it was also discussed in the previous section, it can be expected in Case B based on the experimental results that adjacent cutting tracks do not influence each other in considerable manner. Thus, it is concluded for soil fraction 1-2 mm, and other soils with linear pore pressure distribution, that no adaptation of contemporary pressure transfer model is necessary due to consideration of passing cutting tools at the face. To specify the recommendation of stagnation gradient provided by DIN 4126 (2013) for the purposes of slurry shield excavation, the diagram in Figure 9-7 was developed.

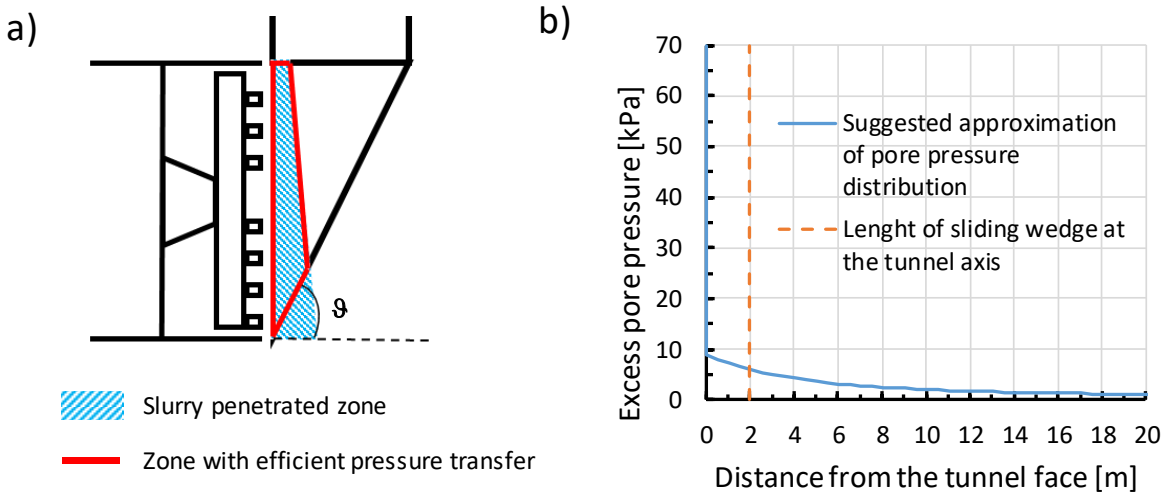

Figure 9-6: a) Determination of zone with efficient pressure transfer for soil with linear pore pressure distribution within slurry penetrated zone, b) Determination of average increased pore pressure at the sliding surface of the wedge

The diagram shows recommended minimal stagnation gradients of slurry to avoid decrease of efficiently transferred slurry excess pressure due to the deep slurry penetration. The diagram considers shield diameter (D), slurry excess pressure in the excavation chamber (Δs_{crown}) and also the dimensions of the sliding wedge expressed by the sliding angle (ϑ). The diagram was developed taking into account the unit weight of loaded slurry 12 kN/m^3. The assumption is in comparison to the unit weight of fresh slurry on the safe side for the purposes of the diagram. The minimal recommended stagnation gradient was calculated to assure a maximal decrease of efficient slurry excess pressure transfer lower than 5 kPa in average over the entire tunnel face. This threshold was chosen as it represents the minimal accuracy of slurry pressure steering in the chamber. Therefore, no higher accuracy for the determination of the efficient transfer of slurry excess pressure is necessary. Consequently, if the excavation is conducted with the minimal recommended stagnation gradient, the deepest slurry penetration is achieved, for which no increase of slurry excess pressure is necessary due to too deep slurry penetration.

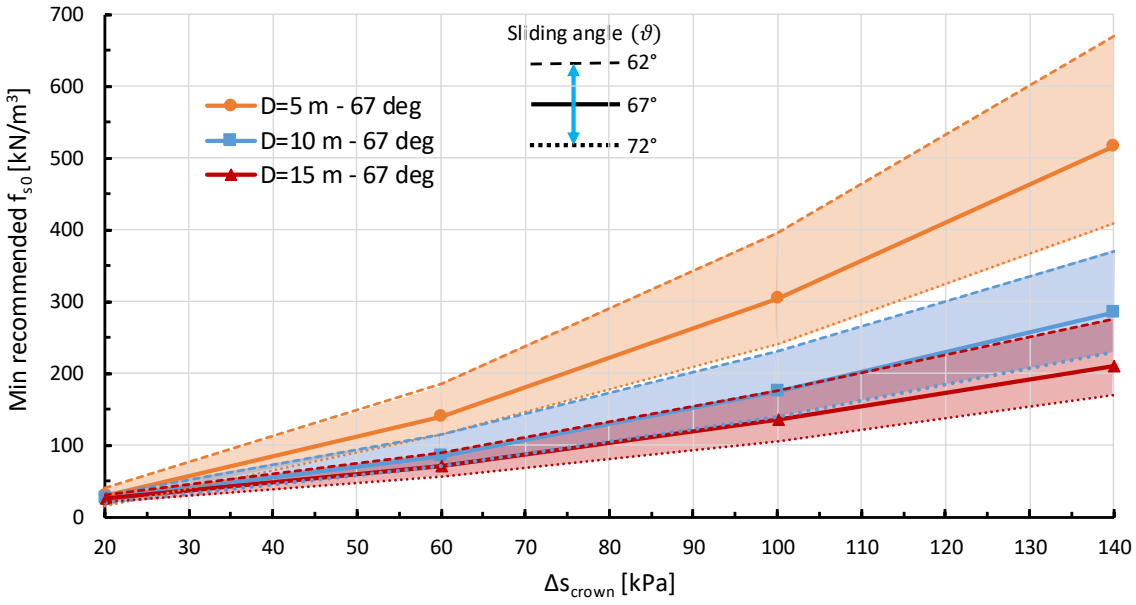

Figure 9-7: Minimal recommended stagnation gradient of slurry $f_{s0,min}$ to avoid a loss of efficient face support due to deep slurry penetration

In contrast it was demonstrated in the previous section for soil fraction 0.063-4 mm with non-linear pore pressure distribution under static condition that increased pore pressure during excavation also occurs outside of slurry penetrated zone. The distribution of remaining pore pressure outside of the expected slurry penetrated zone was approximated using the approach suggested by Bezuijen et al. (2001) and Bezuijen

et al. (2016) while inputting the remaining pressure as ϕ in $Eq.3\text{-}41$. The approximation by $Eq.3\text{-}41$ offers an approach for scaling-up the result obtained at the RUB tunnelling machine for a real size shield machine by changing the diameter in the equation. The up-scaled pore pressure distribution is shown in Figure 9-6-b. Slurry excess pressure in the chamber 70 kPa is assumed. The parameter for consideration of pressure transfer mechanism formation α= 0.125, which was previously determined by the RUB tunnelling device, is adopted. Other excavation conditions were considered as in section 8.1.2 (incl. the dimensions of the wedge $\vartheta = 68.3°$). The pore pressure distribution acc. to Bezuijen et al. (2016) delivered 6 kPa excess pore pressure at the intersection of tunnel axis and sliding surface of the wedge. The theory by Bezuijen et al. (2016) scales-up the excess pore pressure distribution based on the diameter of the shield machine. In the methodology for scaling-up used here, the influence of excavation velocity was not considered. The resulting pore pressure decrease within 2 m distance is smaller for the real machine than would be measured in the RUB tunnelling device at an equal distance. The scaled-up distribution of pore pressure also shows that the particular sliding angle of the wedge will not have significant influence on the pore pressure level at the intersection. Hence, the distribution delivered in average 64 kPa (91%) of efficiently transferred slurry excess pressure to support the wedge (9% was not efficiently transferred). Safe face support was achieved for this transferred amount of excess pressure due to the assumed safety factor 1.5 as prescribed by ZTV-ING (2012) for active earth pressure in the calculation of the minimal required face support pressure.

It is worth mentioning that the calculation here for the soil fraction 0.063-4 mm was demonstrated based on one example and shown non-linear behaviour. Thus, it should not be generalized without further confirmation. The efficiency of the pressure transfer would probably be increased with increased slurry excess pressure.

9.3 Additional check of the self-bearing capacity of the wedge

Uncertainties remained after the experimental investigation in chapter 7. The uncertainties are connected with the soil grain size fraction 0.063-4 mm. This soil fraction strongly shows non-linear distribution of pore pressure inside the slurry penetrated zone at the end of the primary penetration. The uncertainties appeared

during the test with RUB tunnelling device and can be assessed as not fully understood transformation of the pressure transfer mechanism during excavation.

The transformation of the pressure transfer leads to a phenomenon that the increased pore pressure can be observed in this type of soils also outside of slurry penetrated zone despite the occurrence of the Case B interaction at the tunnel face. When the excess pore pressure distribution is scaled-up for a real machine, excess pore pressure can be noticed at the intersection of tunnel axis and the sliding wedge surface. The efficiency of pressure transfer is reduced in that case. Küpferle et al. (2018) determined an increase of cohesion inside the slurry penetrated zone for soil fraction 0.063-4 mm by 28 kPa while its friction angle remained approximately the same.

In this section, the required increase of cohesion to achieve self-bearing of the wedge will be investigated. The self-bearing capacity of the wedge may compensate the lower efficiency of slurry excess pressure transfer within the wedge. However, the transfer outside of the wedge is still necessary to obtain a stable tunnel face.

9.3.1 Parametric study

In this section, the minimally required drained cohesion of the soil will be determined, for which the wedge will be stable without any face support. For the calculation, the model after Horn (1964) as described in section 2.6 is used. Note that no safety factors are adopted here. The calculation is conducted in excess pressures, hence the groundwater head and the required support pressure due to groundwater are not considered here. However, the calculations are conducted with submerged unit weight of soil assuming that the excavation is performed under groundwater table. No surcharge from the overburden on the wedge is considered. The starting calculation case of the parametric study adopted tunnel diameter 10 m, friction angle 35° and submerged unit weight of soil 9 kN/m^3. These parameters were consequently varied within the study. The required minimal cohesion of soil for stable wedge is consequently shown in Figure 9-8.

The required cohesion increases with decreasing soil friction angle, increasing shield diameter and increasing submerged unit weight of soil in the tunnel face area. In all calculation cases, it turns out that the minimal cohesion is significantly lower than 28 kPa. Hence, it is concluded that the increase of slurry penetration depth inside the

wedge by decreasing the slurry concentration might have considerable stabilization effect for the wedge. The stabilization effect might compensate the decrease of slurry excess pressure transfer inside the wedge.

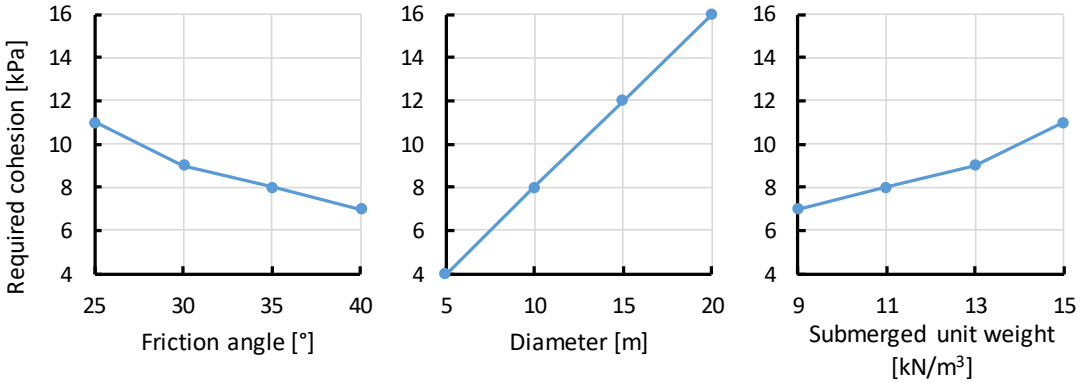

Figure 9-8: Results of the parametric study – minimally required cohesion of soil to achieve self-bearing of the wedge

The result delivers interesting implication that in case of very deep slurry penetration with low stagnation gradient, there is still some additional safety due to the quite low cohesion increase inside the slurry penetrated zone. It is worth emphasizing that the surcharge from the overburden has to be countered by the transferred slurry excess pressure outside of the wedge.

9.3.2 Limitations of the additional check

The limitation of the described additional check is the required deep slurry penetration which needs to reach the distance from the tunnel face to the sliding surface of the wedge to increase cohesion in this area. The desired slurry penetration can be acc. DIN 4126 (2013) adjusted by changing the slurry concentration. Simultaneously, it is assumed that the distribution of slurry particles will be constant along the penetrated distance.

10. RECOMMENDATIONS FOR PRACTICE

In chapter 4 of this thesis, theoretically possible interactions between slurry, soil and cutting tools were defined. Case A and Case B were derived based on the comparison between tool cutting depth and slurry penetration depth between tool passes.

In this chapter, the efficiency of the particular interaction case will first be evaluated in terms of face stability. Further, an approach will be shown how to design the required face support for excavation while considering particular interaction case. For this purpose, an integrated design approach considering slurry and soil properties, cutting wheel design and excavation setting will be introduced. Critical scenarios in terms of face support for the particular interaction case are also discussed in this chapter.

10.1 Efficiency of the pressure transfer mechanism and measures to its increase

The efficiency was defined as excess pore pressure drop (slurry excess pressure drop) within the wedge. The pressure drop corresponds to the transferred effective stress. The efficiencies of the particular pressure transfer mechanism are sketched in Figure 10-1. The visualised efficiencies were determined based on calculations and laboratory tests in chapter 8 for Case A, and in chapter 9 for Case B.

It is clearly visible from Figure 10-1 that the lowest efficiency was obtained for Case A of the interaction. Thereby, it deviates most severely from the currently employed calculation approach included DIN 4126 (2013). Case A delivers unsafe results in comparison to the code. As shown in chapter 8, the efficiency of the Case A interaction further depends on the RPM of the machine, slurry excess pressure and the cutting tool layout at the cutting wheel. While higher RPM and larger amount of cutting tools in a cutting track decrease the efficiency, the amount of slurry pressure might either

decrease or increase the efficiency. The influence of slurry excess pressure in the chamber is discussed in detail in chapter 8. In Case A of the interaction, the stagnation gradient of slurry does not correspond with the pore pressure gradient.

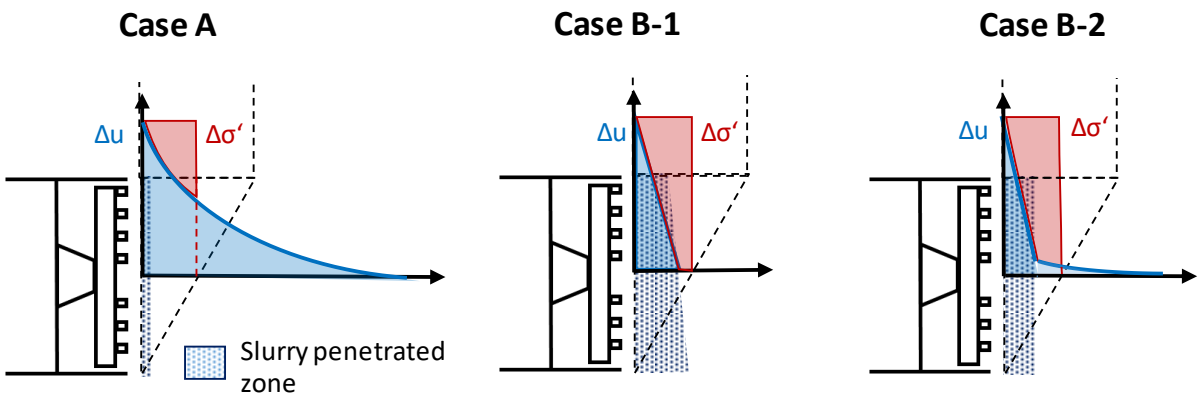

Figure 10-1: Efficiency of the pressure transfer mechanisms for different interaction at the tunnel face during excavation stage, illustrated for the elevation at the tunnel axis

The increased pore pressure in front of the slurry penetrated zone is caused by a rush primary penetration of slurry through zones where the cutting tools just passed and damaged the pressure transfer mechanism. The mechanism predicted in Figure 4-4 could be confirmed in chapter 8 by FE calculation. The procedure, how to determine the efficiency is discussed in section 10.2. It is worth mentioning that its determination for Case A is very time-consuming.

Case B-1, in contrast, delivered the highest efficiency of the pressure transfer. It turns out that the efficiency is slightly higher during excavation than predicted by DIN 4126 (2013) for static conditions. The increase in efficiency depends on the excavation scale. Increases in cutting depth per passing and frequency of passing of cutting tools improve the efficiency during excavation. The efficiency depends not only on the ratio between static yield point of slurry and characteristic grain size of soil, but also on other factors taken into account in Figure 9-7.

Case B-2 showed slightly decreased efficiency compared to Case B-1. The decrease is caused by reformation of the pressure transfer mechanism during excavation and subsequent increase of pore water pressure in front of the slurry penetrated zone. It was concluded based on up-scaling of results from the RUB tunnelling device that the zone with increased pore water will exceed the area of the sliding wedge. Compared to Case B- 1, the efficiency of Case B-2 is more complicated to predict. Nevertheless,

the efficiency is better than in Case A. The amount of the efficiently transferred pressure can be easily increased in Case B-2 by slurry excess pressure increase.

In general, it should be aimed to obtain Case B at the tunnel face during excavation. However, a very deep slurry penetration has to be avoided and the minimal stagnation gradient from Figure 9-7 should be achieved. It can be concluded that higher slurry concentration is not always better for the pressure transfer efficiency, because it may result in Case A of the interaction. It should be mentioned that the results discussed here were obtained for a fresh slurry. It is important to keep in mind that the loaded slurry will have a reduced penetration depth in soil as was shown by Pulsfort & Thienert (2013).

Additional critical scenarios may occur for the pressure transfer efficiency due to particular circumstance. The first circumstance is an excavation through semi-confined aquifer. This situation was already studied by Broere & van Tol (2000) and Broere (2001). The situation can be characterized as excavation through permeable soil layer with limited dimensions in vertical direction, because the permeable soil is covered and underlain by impermeable layer. In this case, due to limited flow directions in front of the tunnel face, the efficiency of the pressure transfer mechanism will be lowered. The efficiency will be considerably decreased, especially for Case A of interaction. A similar problem due to limited flow field in front of the tunnel face can be encountered during excavations between artificial structures. This is represented for instance by excavation bordered on both right and left side by diaphragm or pile walls. Other critical situation for the slurry face support can be caused by contaminants entering slurry destroying its rheological properties as discussed by Maidl et al. (2012).

Another situation would appear during excavation with heterogeneous tunnel face with Case A of interaction at the bottom half of the tunnel face and Case B at the rest. The situation is visualized in Figure 10-2-left. The presence of the coarse soil with higher permeability and Case B of interaction will benefit the dissipation of increased pressure from the finer soil. Hence, it will increase the efficiency of pressure transfer in comparison to the whole tunnel face with Case A interaction.

Finally, some questions in terms of slurry face support efficiency could not be clarified within this thesis. The questions are centred on an excavation scenario with simultaneous presence of Case A and B at the tunnel face. The scenario can occur due

to presence of different homogeneous cutting zones at the tunnel face (Figure 10-2-right). It is expected that the presence of Case A will also decrease the efficiency of pressure transfer for the area with Case B. The expectation was not yet proven by the FE seepage analysis. The system behaviour is different in comparison to the heterogeneous tunnel face due to presence of materials with equal permeability. Hence, it can be adopted that the distribution of increased pore pressure will be dominated by the presence of Case A at the part of the tunnel face.

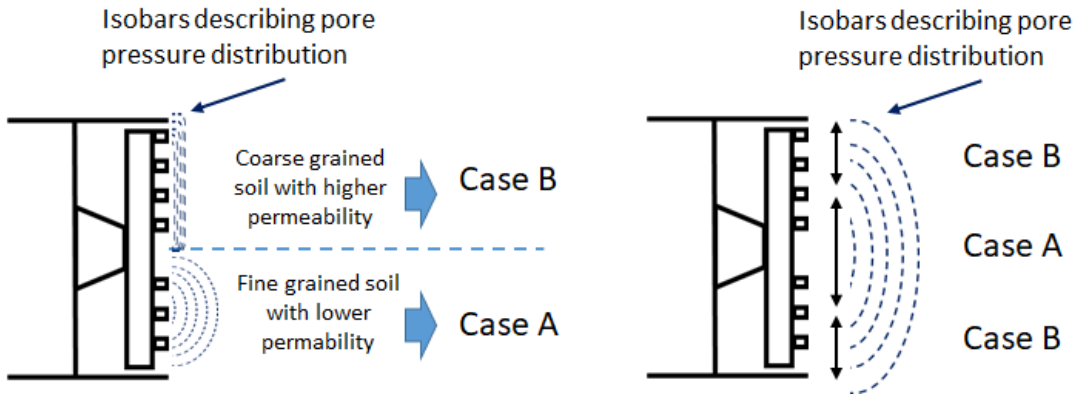

Figure 10-2: Left - Heterogeneous tunnel face, Right - Homogeneous tunnel face with simultaneous presence of Case A and B at the tunnel face within homogenous soil conditions

10.2 Integrated design approach for the required face support pressure

The integrated approach combines the relevant information for the design of the minimal support pressure under consideration of transient slurry-soil-tool interaction. The approach employs both experimental investigation and calculations. The calculations are conducted either analytically or numerically. Two scenarios are discussed in following sections.

10.2.1 Scenario with fixed parameters

In this scenario, it is assumed that next to the soil conditions, also cutting wheel design, excavation setting (PR & RPM) and slurry properties are defined and these cannot be changed. In the first stage of the analysis, it has to be investigated which type of interaction is relevant for the tunnel face. The procedure is shown in Figure 10-3. It starts with the calculation of the minimal excavation pressure required for stabilization of the tunnel face in point (1). All relevant safety factors (section 2.5) are here considered and the calculation is conducted as described in section 2.6 of this thesis. After the determination of the slurry excess pressure (2), experimental investigation in the lab have to be conducted (3). In this investigation, in-situ similar soil has to be used in combination with the defined slurry type and concentration. The test is to be conducted with 25% of slurry excess pressure. The reason for performing this test only

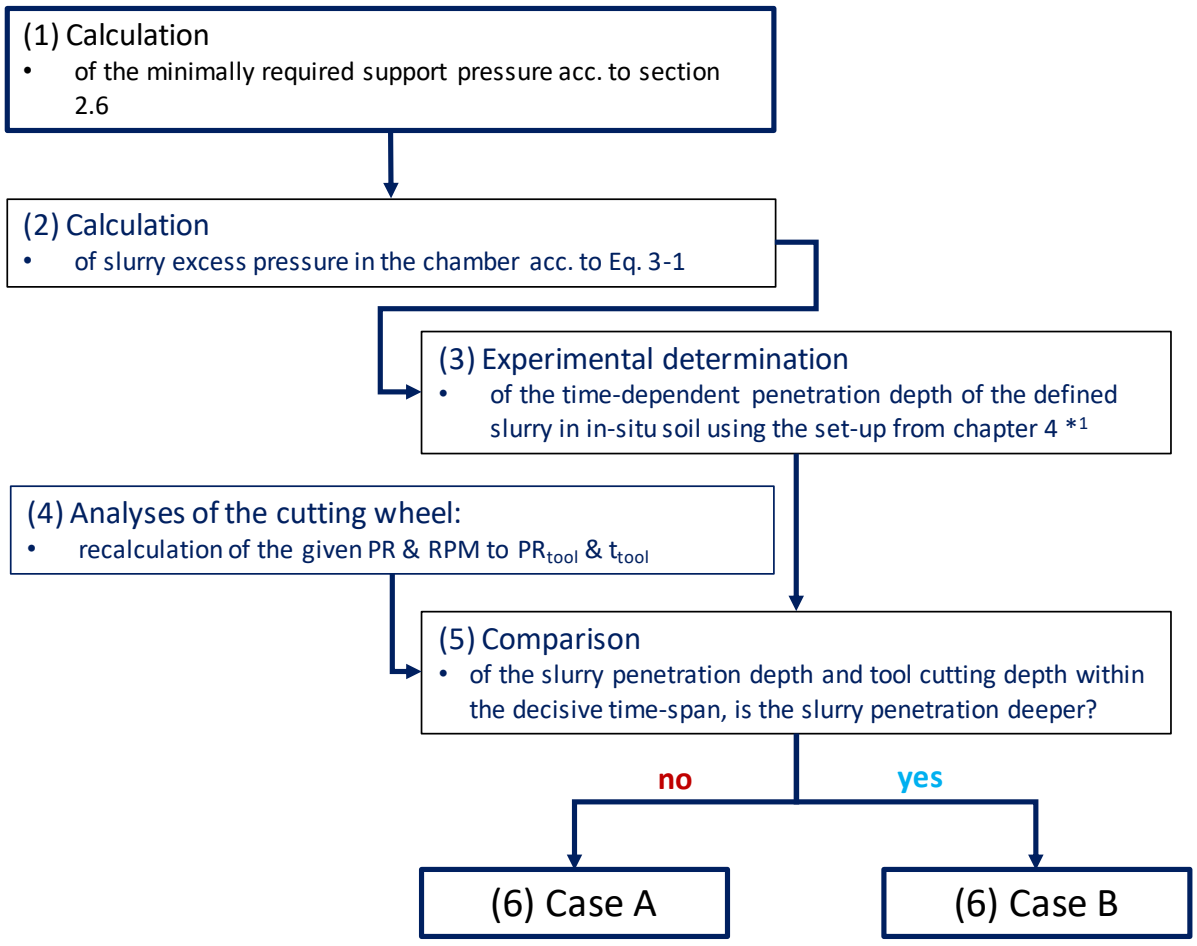

*1 the pressure drop in the experiment should correspond to 25% of excess chamber pressure based on Fig. 8-15 & 8-20

Figure 10-3: Flow chart to analyse the presence of Case A or B of interaction at the tunnel face

with 25% of excess pressure is to exclude the appearance of Case A interaction at the entire tunnel face. The exclusion has to be reliable due to comparably less efficient pressure transfer in Case A of interaction as shown in the previous section. It was shown in chapter 8 that a pressure drop of approx. 25 % of slurry excess pressure may appear in Case A close to the tunnel axis. The obtained slurry penetration depth is consequently to compare with the tool cutting depth per passing in each homogenous cutting zone (5). The determination of the cutting depth is shown in chapter 5. If Case A can be excluded, the procedure from Figure 10-5 is to follow. Otherwise the procedure continues acc. to Figure 10-4.

The analysis of Case A of the interaction at the tunnel face starts with experimental determination of the time-dependent permeability coefficient for defined slurry in in-situ soil in point (7) in Figure 10-4. The experiment is to be conducted in a set-up described in chapter 6 with pressure drop corresponding to 64-80 % of the slurry excess pressure from the point (2) in Figure 10-3. This is due to two reasons. The first reason is that pressure drop at the tunnel face corresponds in Case A approx. to 40-50 % of the chamber excess pressure. The second reason is that the chamber excess pressure will have to be increased due to lower efficiency to approx. 160 % of the originally determined pressure in point (2). Hence, 64-80 % of the original excess pressure from point (2) represents approx. 40-50 % from the increased excess pressure. Consequently, the transient FE seepage analysis is conducted (8) with the experimentally determined permeability coefficients, cutting wheel geometry and excavation setting while considering 160 % of the excess pressure from point (2) at the tunnel face. The pressure transfer within the sliding wedge is determined based on the transient seepage analysis as shown in chapter 8 (9). Further, it is compared, if the efficiently transferred pressure is higher than the minimally required (10). If the transferred pressure is higher, the excavation can proceed with 160 % of the excess pressure from point (2). Otherwise, the slurry excess pressure have to be further increased. However, it is not necessary to conduct either the experimental or the seepage calculation again. It is sufficiently exact to multiply the previously determined efficiency from the seepage analysis with the further increased slurry excess pressure to obtain updated efficiently transferred pressure. During execution of the characterization procedure of Case A in Figure 10-4, it can be found that in some homogeneous cutting zones at the tunnel face, Case B becomes relevant. This situation was not investigated within this thesis and remains open.

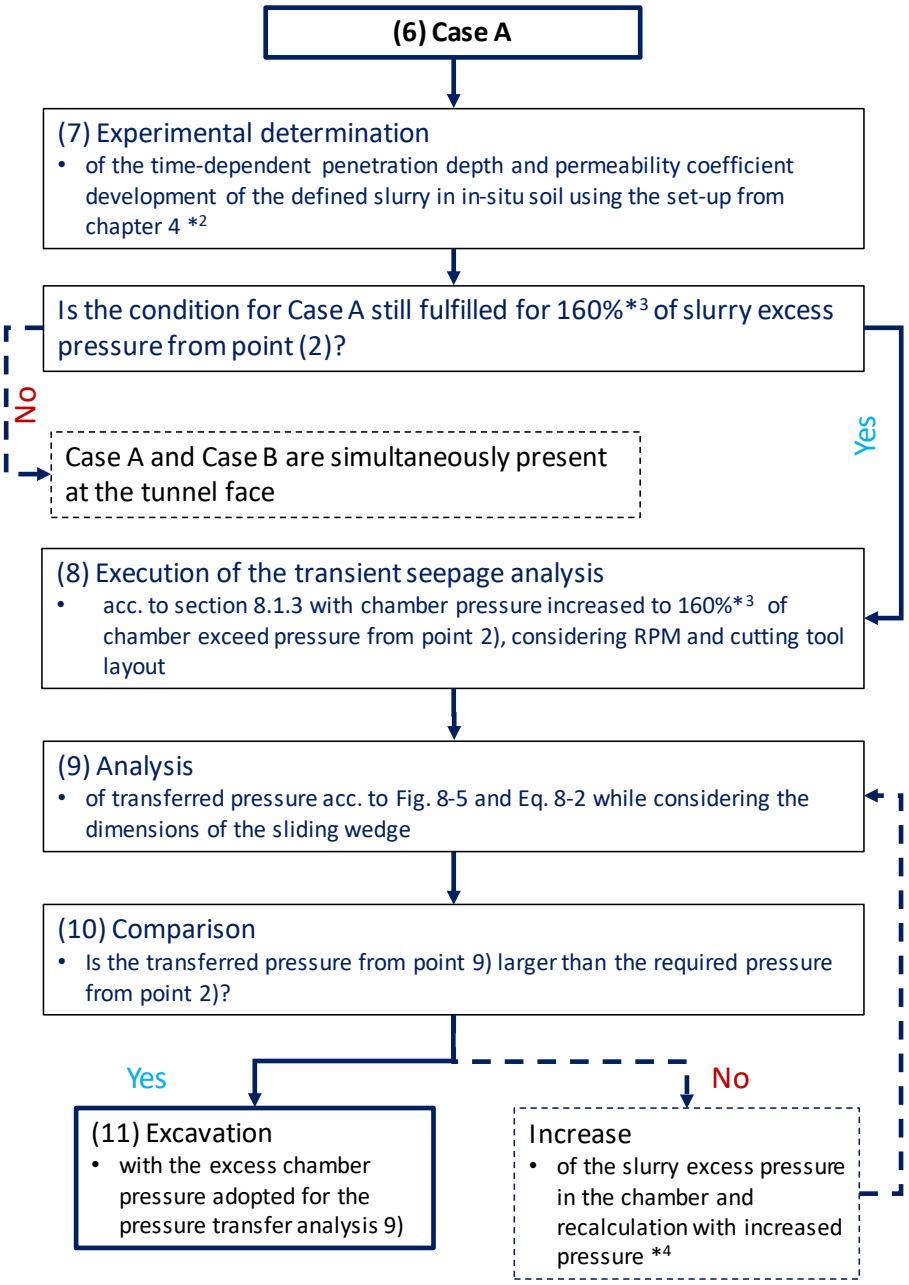

*2 the pressure drop in the experiment should correspond to 64-80% of excess chamber pressure previously design in point 2). It is here already expected that the chamber pressure will be later increased to 160% of the pressure 2). Fig. 8-19 shows that drop ranges approx. 40-50% of the chamber pressure

*3 increase to 160% because only approx. 60 % of the applied slurry excess pressure is efficiently transferred acc. to Tab. 8-6

*4 Note, it is not necessary conduct the seepage analysis again for the slightly increased slurry excess pressure based on results from chapter 8, when the obtained pressure drops at the face still correspond to the drop used in the permeability test

Figure 10-4: Flow chart to determine the minimal support pressure in Case A of interaction

If the flow-chart in Figure 10-3 delivers Case B of interaction, the work flow described in Figure 10-5 must be followed. First the slurry penetration experiment is to conduct (7) with pressure drop corresponding to 100 % of the slurry excess pressure from point

(2). The set-up for deep slurry penetration scale from chapter 7 is used here to investigate the pore pressure distribution inside the slurry penetrate zone. Note that only the primary penetration test is to be executed. If the linear distribution is obtained, the stagnation gradient of slurry is calculated and the efficiently transferred pressure acc. to Figure 9-7 is determined (9). If the efficiently transferred pressure is lower than the slurry excess pressure from point (2) by less than 5 kPa, the excavation can be conducted with the excess pressure slurry excess pressure from point (2). Otherwise, two options are available. Choosing the first option, slurry excess pressure from point (2) is increased and the efficiently transferred pressure is recalculated. The increase is conducted until the previously formulated condition for the efficiently transferred pressure is fulfilled. The second option is to determine the additional bearing capacity of the wedge (section 9.3). To make the second option possible, the slurry penetration depth from the experiment has to be at least equal to the dimension of the sliding wedge at the tunnel axis. The increase of cohesion of slurry penetrated soil is measured using a triaxial test. The additional bearing capacity is calculated with the determined increased cohesion from the triaxial test. Consequently, the required efficiently transferred pressure is recalculated for the wedge area under consideration of the increased cohesions. The required pressure is compared with the transferred pressure from point (9). If the transferred pressure is higher, the excavation can process with the excess pressure from point (2) without additional increase.

In contrast, if the test from point (7) determines the non-linear pore pressure distribution inside the slurry penetrated zone, the RUB tunnelling device must be used for detailed investigation. The experiment is conducted with 100% of excess pressure from point (2). The aim of the experiment is to determine the reformation of the pressure transfer mechanism during excavation and the amount of the remaining excess pore pressure at the end of slurry penetrated zone (section 9.2). The distribution of the remaining excess pore pressure is further up-scaled adopting the excavation diameter of the real machine and using the methodology by Bezuijen et al. (2016) described by combination of $Eq.3\text{-}44$ and $Eq.3\text{-}41$. Consequently, the excess pore water pressure at the intersection of the tunnel axis with inclined sliding surface can be determined. The excess pressure for excavation from point (2) is finally increased by the amount of the excess pore pressure determined at the intersection.

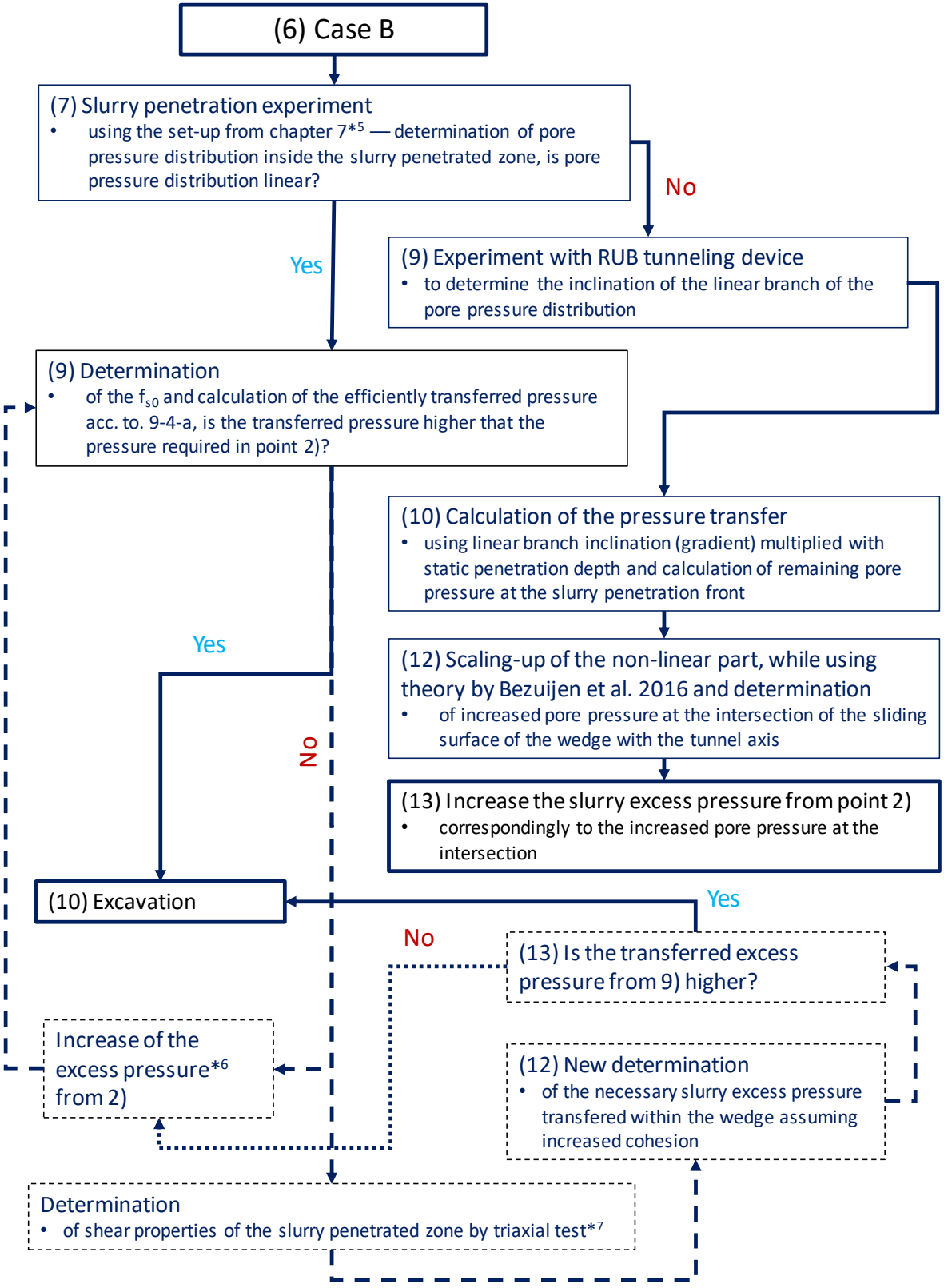

*5 Pressure drop in set-up corresponds to 100% of slurry excess pressure
*6 In case of linear pore pressure distribution, the support pressure increase improves the efficiency only insignificantly
*7 Enough deep slurry penetration to reach the sliding surface is at the tunnel axis is necessary

Figure 10-5: Flow chart to determine minimal support pressure for Case B of interaction

10.2.2 Scenario without fixed parameters

In this scenario, it is assumed that soil conditions and cutting wheel design are fixed. Other settings like slurry concentration and excavation settings can be adjusted. As extensively pointed out in section 10.1, it should be generally aimed to obtain Case B of interaction at the tunnel face due to comparably higher efficiency of the pressure transfer. As shown in Figure 10-2, the comparison between slurry penetration depth and tool penetration depth should be conducted for slurry penetration depth obtained for 25% of the slurry excess pressure in the chamber to guarantee the Case B at the entire tunnel face. The following measures can be applied to obtain Case B at the tunnel face are:

- Decrease the yield point or slurry – note, that the criterion for the local stability of the tunnel face after DIN 4126 (2013) still have to be fulfilled, furthermore, minimally recommended slurry stagnation gradient to avoid efficiency decrease (Figure 9-7) is to be achieved
- Increase RPM and simultaneously decrease PR to keep the advance speed constant
- Increase slurry excess pressure to obtain deeper slurry penetration – note that this measure is efficient only in coarse soils

After the experimental confirmation of the Case B with adjusted parameters, the design of the minimally required pressure follows Figure 10-5.

A further scenario can also be assumed with not yet specified slurry shield design. In this scenario, the cutting wheel and the excavation design is still to be conducted. Based on the grain size distribution at the whole tunnel alignment, it should be evaluated, if the Case A interaction is likely to occur. Consequently, if it turns out from the assessment that Case A is inevitable regardless of slurry concentration decrease, increase of RPM or slurry excess pressure increase, layout of cutting tools is to be adjusted. The adjustment should focus on reduction of cutting tools per track. The reduction of the cutting tools, in comparison to the ordinary design, is especially important for the area at the circumference of the cutting wheel.

11. CONCLUSION & OUTLOOK

Stability of the slurry supported tunnel face considering transient support mechanism during excavation in non-cohesive soils was investigated within this thesis. The aim of the thesis was to clarify whether the application of the slurry pressure transfer methods originally from the diaphragm wall technology delivers a stable tunnel face under transient conditions during slurry shield excavations. A further aim was to determine the excavation conditions, for which contemporary calculation methods should be updated. The aims of the thesis were closely connected with the superimposing of tool and slurry penetration scales.

Slurry shield excavation technology was described in chapter 2. The chapter focused further on the review of the state of the art and practice of the face stability assessment. It turns out that several methods are employed nowadays to determine the earth pressure acting at the tunnel face. The limit equilibrium approach based on Horn's failure mechanism became the most popular in practice due to its transparency and simultaneous sufficient accuracy reflecting the aim of the analytical calculations. It was concluded that the contemporary face stability assessment for slurry shield excavations neglects the slurry soil-interaction to a large extent. The check for local stability is usually the only check conducted in detail.

The third chapter is dedicated to the detailed investigation of slurry soil interaction and the resulting transfer of slurry fluid pressure to effective stress in soil. The characteristics of the interacting materials were outlined at the beginning of the chapter. Consequently, the theoretical background of slurry soil interaction was characterized as flow in porous media. Assumption of this theory allowed for a more detailed description based on fundamental models for suspension filtration in porous media. At the end of the chapter, the contemporary models used to determine the slurry pressure transfer within geotechnical engineering were reviewed. The coupling of the methods from geotechnical engineering and the fundamental filtration models delivered better understanding of the processes. Several discrepancies were

determined resulting from application of the methods from the geotechnical engineering. The discrepancies further highlighted the demand for research in this thesis.

The methodology for consideration of transient processes at the slurry supported tunnel face was introduced in chapter 4. It was suggested that the decisive factor is the comparison between slurry penetration depth and tool cutting depth. Two particular cases were defined. Case A reflects deeper cutting depth than slurry penetration depth, while Case B represents shallower cutting depth than slurry penetration depth. Subsequently, hypothesis were provided for these boundary cases, which were clarified experimentally or numerically in the following chapters of the thesis. It was concluded that different characterization approaches are necessary for the respective cases.

In chapter 5, analysis of the excavation scale was conducted to obtain the basis for the further comparison with slurry penetration scale. It was concluded based on reference projects that every cutting wheel can be divided in several homogeneous cutting zones. Within each cutting zone, the cutting depth of each passing tools and the timespan between passes are constant. Statistical evaluation of the excavation data delivered typical relationship between the cutting depth of a tool and the timespan between each subsequent pass of the cutting tool.

Consequently, the shallow slurry penetration scale was investigated in chapter 6. A new framework for characterization of the slurry penetration scale for Case A was developed, including the theoretical background. Time-dependent permeability of soil for slurry and time dependent slurry penetration depth were evaluated. These variables represented the input for numerical analysis in chapter 8. Based on the comparisons of slurry penetration scale with tool excavation scale, it was concluded that the presence of Case A of the interaction is more frequent in cutting zones close to the tunnel axis.

In chapter 7, deep slurry penetration scale for Case B of the interaction was investigated. The focus of the investigation was given to the distribution and development of pore pressure and effective stress inside and outside of slurry penetrated zone. It was distinguished between primary slurry penetration and slurry re-penetration. During the investigation of primary slurry penetration, the role of the

experimental set-up was evaluated. It was concluded that a certain outflow diameter is necessary to avoid the influence of the experimental set-up on the dissipation of excess pore pressure. Pressure steered re-penetration methodology for the column test experiments was developed to simulate the conditions at the real tunnel face during exaction. The methodology enables consideration of the entire excavation scale of the machine. However, the application of the methodology is suitable only for soils with linear pore pressure distribution inside the slurry penetrated zone. Therefore, the column tests were supplemented by the tests using RUB tunnelling device. The conducted experiments in chapter 7 have shown diametrically different reactions of soil for slurry injection during primary penetration in comparison to the re-penetration in terms of pore pressure and effective stress development.

Pressure transfer and face stability analysis for Case A of the interaction were evaluated in chapter 8. An FE transient seepage model was developed to consider the transient interaction between adjacent cutting tracks at the tunnel face. The experimental results from chapter 6 and excavation scales from chapter 5 were used here as the input. It was shown that Case A of the interaction significantly reduces the amount of efficiently transferred slurry excess pressure. This turned out to be the major shortcoming of the contemporary models. It was concluded that the safety margin used nowadays in face stability calculation can compensate the reduced transfer and avoids the tunnel face failure. However, the excavations are not conducted with the expected level of safety.

In chapter 9, the experimental results from chapter 7 for the Case B of interaction were implemented in face stability analysis. The implementation was conducted based on the experimental determination of slurry stagnation gradient. It was distinguished between linear and non-linear distribution of pore pressure within the slurry penetrated zone. For the linear distribution, a diagram was developed which defines the minimally required slurry stagnation gradient without necessary increase of slurry excess pressure due to deep slurry penetration. For the non-linear distribution, a procedure was shown, how to scale up the pore pressure distribution from RUB tunnelling device for the real tunnel face and consequently determine the efficient pressure transfer. Further, it turns out that a minimal increase of cohesion within the slurry penetrated zone due to presence of slurry particles can stabilize the sliding wedge while the slurry excess pressure is transferred first outside of the wedge. It was

concluded that for Case B with linear pore pressure distribution, no update of contemporary models is necessary. In contrast, the non-linear distribution may slightly reduce the adopted amount of the efficient pressure transfer.

In chapter 10, the knowledge obtained within this thesis is transformed into recommendation for practice. The recommendation states that Case A of the interaction should be avoided at the tunnel face. To achieve this, certain measures in terms of excavation steering and slurry design are suggested. Hence, it is recommended to conduct excavation with Case B of the interaction. However, slurry penetration depth of slurry should be limited, because of eventual reduction of efficient slurry pressure transfer inside the wedge. Chapter 10 suggests an integrated approach for the design of minimal slurry pressure to stabilize the tunnel face. The integrated approach considers excavation settings of the shield, cutting wheel design, slurry properties and soils conditions. The approach is presented in terms of flow charts.

It could be shown in this thesis that the slurry penetration at the tunnel face is influenced during excavation by the soil cutting process and the discrepancies from the contemporary theories summarized in chapter 3 could be clarified. Some questions, however, could not have been partially or completely answered by the thesis. Slurry shield excavation with simultaneous presence of Case A and B at the tunnel face represents one of these questions. A numerical seepage model should be developed to assess the interaction between the zones with Case A and Case B of interaction. As an input to this model, experimental results from this thesis can be used. Further, more detailed experimental investigation in terms of excavation scale variation should be conducted for Case B with non-linear pore pressure distribution inside the slurry penetrated zone. It is expected that these types of soils can be often encountered on the construction sites. The approach suggested in this thesis for the transfer of the laboratory results into field should be further verified for this case. This can be done only by in-situ monitoring of pore pressure during excavation. Moreover, the possible transition between Case A and Case B during excavations was also not investigated in this thesis. It may theoretically happen that Case B of the interaction can be predicted before the start of the excavation. However, the slurry penetration depth may decrease during the excavation and the Case A appears.

In the future, it is also advised to conduct the investigations outlined in this thesis with loaded slurries. As the slurry is typically loaded by fines during the most of its life cycle at the construction site. The loading of slurry with fines can significantly influence its penetration behaviour.

REFERENCES

Aime, R.; Aristaghes, P.; Autuori, P.; Minec, S. (2004): 15 m diameter tunnelling under Netherlands Polders. Singapore. In Proc. WTC Singapore - Underground Space for Sustainable Urban Development, pp. 1–8.

Albert, A.; Schneider, K. (2014): Bautabellen für Ingenieure. Mit Berechnungshinweisen und Beispielen. 21. Aufl. Köln: Bundesanzeiger Verl.

API 13b, 2014: Recommended Practice for Field Testing Oil-Based Drilling Fluids, American petroleum institute

Anagnostou, G. (2012): The contribution of horizontal arching to tunnel face stability. In Geotechnik 35 (1), pp. 34–44. DOI: 10.1002/gete.201100024.

Anagnostou, G.; Kovári, K. (1994): The face stability of slurry-shield-driven tunnels. In Tunnelling and Underground Space Technology 9 (2), pp. 164–174. DOI: 10.1016/0148-9062(94)90438-3.

Anagnostou, G.; Kovári, K. (1996): Face stability conditions with earth-pressure-balanced shields. In Tunnelling and Underground Space Technology 11 (2), pp. 165–173. DOI: 10.1016/0886-7798(96)00017-X.

Anheuser, L. (1987): Tunnelvortriebsanlagen mit flüssigkeitsgestützter Ortsbrust. In Bautechnik 64 (11), pp. 361–370.

Anheuser, L. (1989): Beispiele zur Bewältigung schwieriger Vortriebsphasen bei Schilden mit flüssigkeitsgestützter Ortsbrust. In Forschung + Praxis, STUVA Tagung 32, pp. 43–47.

Arwanitaki, A. (2009): Über das Kontaktverhalten einer Zweiphasen Schlitzwand und nichtbindigen Böden. Doctoral Thesis. Ruhr-Universitaet, Bochum.

Babendererde, S. (1991): Tunnelling Machines in Soft Ground: a Comparison of Slurry and EPB Shield Systems. In Tunnelling and Underground Space Technology 6 (2), pp. 169–174.

Balhoff, M. T.; Lake, L. W.; Bommer, P. M.; Lewis, R. E.; Weber, M. J.; Calderin, J. M. (2011): Rheological and yield stress measurements of non-Newtonian fluids using a Marsh Funnel. In Journal of Petroleum Science and Engineering 77 (3-4), pp. 393–402. DOI: 10.1016/j.petrol.2011.04.008.

Bathe, K.-J. (2014): Finite element procedures. 2nd Edition. ISBN: 978-0-9790049-5-7

Bayer, L.; Diete, P.; Fahlbusch, D.; Thewes, M.; Schoesser, B.; Seeger, J. et al. (2016): Suspension mit erhöhter Dichte anstelle von Ballastierungen beim Hydroschildvortrieb der U-Bahnlinie U5 in Berlin. In Taschenbuch für den Tunnelbau, pp. 39–79.

Bear, J. (1988): Dynamics of fluids in porous media. Estados Unidos: Dover Publications. ISBN: 978-0-4866567-5-5.

Benke, S. (2003): Modellierung thermomechanischer Prozesse in porösen Medien. Doctoral thesis. Rheinisch-Westfälische Technische Hochschule, Aachen.

Bezuijen, A. (2002): Consolidation of grout - element tests. In Technical report 403050/3, Geo Delft.

Bezuijen, A.; Messemaeckers-van de Graaf, C. A. (1997): Stabiliteit van het graaffront bij vloeistofondersteuning. In Technical Report 33, Boren Tunnels, en Leidingen.

Bezuijen, A.; Pruiksma, J. P.; van Meerten, H. H. (2001): Pore Pressures in front of tunnel, measurements, calculations and consequences for stability of tunnel face. In Modern Tunneling Science and Technology: Proceedings of the International Symposium, Kyoto, Japan. pp. 27–33.

Bezuijen, A.; Steeneken, S. P.; Ruigrok, J. A. T. (2016): Monitoring pressures and analysing pressures around a TBM. In Book of abstracts and e-Proceedings of the 13th international conference Underground Construction, Prague, Czech Republic, pp. 1–8.

Bingham, E. C. (1916): An investigation of the laws of plastic flow. In BULL. NATL. BUR. STAND. 13 (2), pp. 309. DOI: 10.6028/bulletin.304.

Boer, R. de (1998): Theory of Porous Media — Past and Present. In Z. angew. Math. Mech. 78 (7), pp. 441–466. DOI: 10.1002/(SICI)1521-4001(199807)78:7.

Boley, C. (2012): Handbuch Geotechnik. Grundlagen - Anwendungen - Praxiserfahrungen. Wiesbaden: Vieweg+Teubner Verlag (Praxis).

Broer, R. de; Bluhm, J. (2004): Eine Theorie fürs grobe und feine. In Essener Unikate 23.

Broere, W. (2001): Tunnel face stability & new CPT applications. PhD Thesis. Technical University, Delft.

Broere, W.; van Tol, A. F. (2000): Influence of infiltration and groundwater flow on tunnel stability. In Geotechnical Aspects of Underground Construction in Soft Ground, Tokyo, Japan. pp. 339–344.

Broere, W.; van Tol, A. F. (2001): Time-dependent infiltration and groundwater flow in face stab. In T. Adachi, K. Tateyama & M. Kimura (eds.) Modern Tunneling Science and Technology, Kyoto, Japan, pp. 629–634.

Broms, B. B.; Bennermark, H. (1967): Stability of clay at vertical openings. In Journal of the geotechnical engineering division, ASCE (193), pp. 71–94.

Burger, W. (2006): Schneidräder für Lockergestein: Prinzipien und Auslegungsaspekte. In Tunnel (2), pp. 8–19.

Chambon, P.; Corté, J. (1994): Shallow Tunnels in Cohesionless Soil: Stability of the tunnel face. In Journal of Geotechnical Engineering 7 (120), pp. 1148–1165.

Chapuis, R.; Aubertin, M. (2003): Predicting the coefficient of permeability of soils using the Kozeny-Carman equation. EMP-RT-2003-03: Ecole Pytechnique de Montreal.

Chen, T.; Pang, T.; Zhao, Y.; Zhang, D.; Fang, Q. (2018): Numerical simulation of slurry fracturing during shield tunnelling. In Tunnelling and Underground Space Technology 74, pp. 153–166. DOI: 10.1016/j.tust.2018.01.021.

Civan, F. (2015): Reservoir Formation Damage. San Diego, CA, USA: Elsevier Science.

Coussy, O. (op. 2004): Poromechanics. Chichester: John Wiley & Sons.

Davis, E. H.; Gunn, M. J.; Mair, R. J.; Seneviratine, H. N. (1980): The stability of shallow tunnels and underground openings in cohesive material. In Geotechnique 30 (4), pp. 397–416.

Deutscher Ausschuss für unterirdisches Bauen e. V. (DAUB), Köln: Empfehlungen zur Auswahl von Tunnelvortriebsmaschinen (Stand 10/2010). Available online at http://www.daub-ita.de/fileadmin/documents/daub/gtcrec1/gtcrec11.pdf.

DIN 1054: 2010-12: Baugrund – Sicherheitsnachweise im Erd- und Grundbau – Ergänzende Regelungen zu DIN EN 1997-1.

DIN 4085: 2017-08: Baugrund - Berechnung des Erddrucks.

DIN 18130-1: 1998-05: Bestimmung des Wasserdurchlässigkeitsbeiwerts Teil 1 : Laborversuche.

DIN 4127: 2014-02: Erd- und Grundbau – Schlitzwandtone für stützende Flüssigkeiten – Anforderungen, Prüfverfahren, Lieferung, Güteüberwachung.

DIN 4126: 2013-09: Nachweis der Standsicherheit von Schlitzwänden.

Enzmann, F. H. (2000): Modellierung von Porenraumgeometrien und Transport in korngestützten porösen Medien. Doctoral Thesis. Johannes-Gutenberg-Universität, Mainz.

Fillibeck, J. (2011): Oberflächensetzungen beim Tunnelvortrieb im Lockergestein - Prognose, Messung und Beeinflussung. Habilitationsschrift. Technische Universität, Munich.

Freimenn, R. (2014): Hydraulik für Bauingenieure. 3. Auflage. CARL HANSER VERLAG GMBH.

Garnier, J.; Gaudin, C.; Springman, S. M.; Culligan, P. J.; Goodings, D.; Konig, D. et al. (2007): Catalogue of scaling laws and similitude questions in geotechnical centrifuge modelling. In International Journal of Physical Modelling in Geotechnics 7 (3), pp. 1–23. DOI: 10.1680/ijpmg.2007.070301.

Girmscheid, G. (2008): Baubetrieb und Bauverfahren im Tunnelbau. Berlin: Ernst & Sohn.

Goldscheider, M. (2013): Gültigkeitsgrenzen des statischen Kollapstheorems der Plastomechanik für Reibungsböden. In geotechnik 36 (4), pp. 243–263. DOI: 10.1002/gete.201300007.

Gösele, W.; Alt, Ch.(2005): Filtration. In: Ullmann's Encyclopedia of Industrial Chemistry 2005. Available online at http://dx.doi.org/10.1002/14356007.b02_10.

Grenier, A.; Meireles, M.; Aimar, P.; Carvin, P. (2008): Analysing flux decline in dead-end filtration. In Chemical Engineering Research and Design 86 (11), pp. 1281–1293. DOI: 10.1016/j.cherd.2008.06.005.

Grombach, P. (2000): Handbuch der Wasserversorgungstechnik. 3., völlig überarb. Aufl. München, Wien: Oldenbourg-Industrieverl.

Häfner, F.; Wagner, S.; Freese, C. (2009): Durchlässigkeitsmessung. Bestimmung der absoluten Durchlässigkeit poröser Stoffe mit Flüssigkeit und Gas. In Institut für Bohrtechnik, Technische Universität Bergakademie Freiberg.

Hermia, J. (1982): Constant Pressure Blocking Filtration Laws-Application to Power-Law Non-Newtonian Fluids 60, pp. 183–187.

Herpers, K. (2015): Bestimmung des Bentonitgehalts im kohäsionslosen Lockergestein nach dem Eindringvorgang von Bentonitsuspension. Projektarbeit. Ruhr-Universität, Bochum.

Herrenknecht, M. (1994): Die Entwicklung der Mixschilde. In Tiefbau (11), pp. 674–685.

Herrenknecht AG: Longitudinal cut through Slurry shield machine. Available online at https://www.herrenknecht.com/en/home.html, checked on 2011.

Herzig, J. P.; Leclerc D. M.; Goff, P. L. (1970): Flow of suspensions through porous media - Application to deep filtration. New differential equation for clogged beds is derived. In Industrial and engineering chemistry 62 (5), pp. 8–35.

Holzhäuser, F.; Hunt, S. W.; Mayer, C. (2006): Global experience with soft ground and weak rock tunneling under very high groundwater heads. In North American Tunneling Chicago, IL.

Horn; M. (1961): Horizontaler Erddruck auf senkerchte Abschlussflaechen von Tunnelrohren. Referate zum Thema: "Unterirdische Bauwerke". In Landeskonferenz der Ungarischen Tiefbauindustrie - Deutsche Übersetzung von STUVA E.V., pp. 7–16.

Hu, X.; Zhang, Z.; Kieffer, S. (2012): A real-life stability model for a large shield-driven tunnel in heterogeneous soft soils. In Front. Struct. Civ. Eng. DOI: 10.1007/s11709-012-0149-7.

Ives, K. J. (1970): Rapid filtration. In Water Research 4 (3), pp. 201–223. DOI: 10.1016/0043-1354(70)90068-0.

Ives, K. J. (1987): Filtration of Clay Suspensions Through Sand. In Clay Minerals 22 (1), pp. 49–61. DOI: 10.1180/claymin.1987.022.1.05.

Iwasaki, T.; Slade, J. J.; Stanley, W. E. (1937): Some notes on sand filtration [with discussion]. In Journal of American Water Works Association, 29 (10), pp. 1591–1602.

Jacob, Erich (1975): Der Bentonitschild, Technologie und erste Anwendung in Deutschland. In Forschung + Praxis, STUVA Tagung 19, pp. 30–38.

Jancsecz, S.; Steiner, W. (1994): Face support for a large Mix-Shield in heterogeneous ground conditions: Springer US. In Papers presented at the seventh international symposium, 'Tunnelling'94', pp. 1–19.

Janssen, H. A. (1895): Versuche über Getreidedruck in Silozellen. In Zeitschrift des Vereins deutscher Ingenieure 35 (Band XXXIX), pp. 1045–1049.

Kaalberg, F.; Ruigrok, J.; Nijs, R. de (2014): TBM face stability & excess pore pressures in close proximity of piled bridge foundations controlled with 3D FEM. In Chungsik Yoo, Seong-Wan Park, Bumjoo Kim, Hoki Ban (Eds.): Geotechnical Aspects of Underground Construction in Soft Ground: CRC Press, pp. 555–560.

Kilchert, M.; Karstedt, J. (1984): Band 2 Standsicherheitsberechnung von Schlitzwaenden nach DIN 4126. Wiesbaden Berlin: Bauverlag GmbH (Beuth-Kommentare).

Kirsch, A. (2009): On the face stability of shallow tunnels in sand. Doctoral Thesis, Innsbruck University, Innsbruck.

Kirsch, A.; Kolymbas, D. (2005): Theoretische Untersuchung zur Ortsbruststabilität. In Bautechnik 82 (7), pp. 449–456. DOI: 10.1002/bate.200590151.

Klitzen, J.; Herdina, J. (2016): Hydroshield drive with a diameter of 13 m in the Lower Inn Valley - Project design and experience from construction of contract H3-4 / Hydroschildvortrieb mit 13 m Durchmesser im Unterinntal - Projektplanung und Erfahrungen im Baulos H3-4. In Geomechanik Tunnelbau 9 (5), pp. 534–546. DOI: 10.1002/geot.201600036.

Koenig, D.; Schroeder, T. (2015): Zusammensetzung des Filterkuchens an Schlitzwandlamellen mit kurzer und langer Standzeit. In Bauingenieur 90 (2).

Köhler, M.; Maidl, U.; Martak, L. (2011): Abrasiveness and tool wear in shield tunnelling in soil / Abrasivität und Werkzeugverschleiß beim Schildvortrieb im Lockergestein. In Geomechanik Tunnelbau 4 (1), pp. 36–54. DOI: 10.1002/geot.201100002.

Kolymbas, D. (op. 2008): Tunnelling and tunnel mechanics. A rational approach to tunneling. Berlin: Springer.

Köppl, F. (2014): Abbauwerkzeugverschleiß und empirische Verschleißprognose beim Vortrieb mit Hydroschild TVM in Lockergesteinen. Doctoral Thesis. Technische Universität, Munich.

Köppl, F.; Thuro, K.; Thewes, M. (2015): Factors with an influence on the wear to excavation tools in hydroshield tunnelling in soft ground / Einflussfaktoren auf den Verschleiß der Abbauwerkzeuge beim Vortrieb mit Hydroschild-TVM in Lockergesteinen. In Geomechanik Tunnelbau 8 (3), pp. 248–257. DOI: 10.1002/geot.201500003.

Köppl, F.; Thuro, K.; Thewes, M. (2015): Suggestion of an empirical prognosis model for cutting tool wear of Hydroshield TBM. In Tunnelling and Underground Space Technology 49, pp. 287–294. DOI: 10.1016/j.tust.2015.04.017.

Krause, T. (1987): Schildvortrieb flüssigkeitsgestuetzte Ortsbrust. Dissertation. Technische Universität, Braunschweig.

Küpferle, J.; Röttger, A.; Theisen, W.; Alber, M. (2016): The RUB Tunneling Device – A newly developed test method to analyze and determine the wear of excavation tools in soils. In Tunnelling and Underground Space Technology 59, pp. 1–6. DOI: 10.1016/j.tust.2016.06.006.

Küpferle, J.; Zizka, Z.; Schoesser, B.; Röttger, A.; Alber, M.; Thewes, M.; Theisen, W. (2018): Influence of the slurry-stabilized tunnel face on shield TBM tool wear regarding the soil mechanical changes – Experimental evidence of changes in the tribological system. In Tunnelling and Underground Space Technology 74, pp. 206–216. DOI: 10.1016/j.tust.2018.01.011.

Leca, E.; Dormieux, L. (1990): Upper and lower bound solutions for the face stability of shallow circular tunnels in frictional material. In Geotechnique 40 (4), pp. 581–606.

Leca, E.; New, B. (2007): Settlements induced by tunneling in Soft Ground. ITA/AITES Report Presented by the WG "Research". In Tunnelling and Underground Space Technology 22 (2), pp. 119–149. DOI: 10.1016/j.tust.2006.11.001.

Lemppenau, B. (2015): Theoretische Analyse der experimentell ermittelten Eindringvorgänge von Bentonitsuspensionen in kohäsionslose Lockergesteine unter Berücksichtigung der Theorie poröser Medien. MSc thesis. Ruhr-Universität, Bochum.

Li, Y.; Emeriault, F.; Kastner, R.; Zhang, Z. X. (2009): Stability analysis of large slurry shield-driven tunnel in soft clay. In Tunnelling and Underground Space Technology 24 (4), pp. 472–481. DOI: 10.1016/j.tust.2008.10.007.

Liang, Y.; Hilal, N.; Langston, P.; Starov, V. (2007): Interaction forces between colloidal particles in liquid: theory and experiment. In Advances in Colloid and Interface Science 134-135, pp. 151–166. DOI: 10.1016/j.cis.2007.04.003.

Longchamp, P.; et al. (2005): Slurry for use in slurry shield TBM. In AFTES Recommendations (1), pp. 1–20.

Lorenz, H. (1966): Process for producing excavations in water-bearing ground on 1966. Patent no. US3260054 A.

Luckham, P. F.; Rossi, S. (1999): The colloidal and rheological properties of bentonite suspensions. In Advances in Colloid and Interface Science 82 (1-3), pp. 43–92. DOI: 10.1016/S0001-8686(99)00005-6.

Maidl, B.; Herrenknecht, M.; Maidl, U.; Wehrmeyer, G. (2012): Mechanised shield tunnelling. 2nd ed. Berlin: Ernst & Sohn.

Maidl, B.; Herrenknecht, M.; Anheuser, L. (1994): Maschineller Tunnelbau im Schildvortrieb. 1. Auflage. Berlin: Ernst & Sohn.

Mair, R. J. (1979): Centrifugal modelling of tunnel construction in soft clay. PhD Thesis. University of Cambridge, Cambridge.

Malvern Instruments limited (2015): Mastersizer 3000 - Smarter particle sizing. Product sheet with method description.

Manie, J.; Kikstra W. (2016): Manual DIANA 9.6. Delft

Marsh, H. N. (1931): Properties and Treatment of Rotary Mud. In American institute of mining and metalurgical engineers.

Mayer, P. M.; Hartwig, U.; Schwab, C. (2003): Standsicherheitsuntersuchungen der Ortsbrust mittels Bruchkörpermodell und FEM. In Bautechnik (80), pp. 452–467.

McDowell-Boyer, L. M.; Hunt, J. R.; Sitar, N. (22): Particle transport through porous media. In Water Resour. Res. 22 (13), pp. 1901–1921.

Melix, P. (1987): Modellversuche und Berechnungen zur Standsicherheit oberflächennaher Tunnel. Institut für Bodenmechanik und Felsmechanik der Universität Fridericiana, Karlsruhe.

Messerli, J.; Pimentel, E.; Anagnostou, G. (2010): Experimental study into tunnel face collapse in sand. In Springman, Laue, Seward (Eds.): Physical Modelling in Geotechnics, vol. 1, pp. 575–580.

MIDAS GTS (2010): Analysis reference manual.

Min, F.; Zhu, W.; Han, X. (2013): Filter cake formation for slurry shield tunneling in highly permeable sand. In Tunnelling and Underground Space Technology 38, pp. 423–430. DOI: 10.1016/j.tust.2013.07.024.

Mitchell, J. K.; Soga, K. (2005): Fundamentals of soil behavior, 3rd ed. Hoboken, NJ: Wiley.

Mohkam, M.; Wong, Y. W. (1989): Three dimensional stability analysis of the tunnel face under fluid pressure. In G. Swoboda, editor, Numerical Methods in Geomechanics, pp. 2271–2278.

Mollon, G.; Dias, D.; Soubra, A.-H. (2010): Face Stability Analysis of Circular Tunnels Driven by a Pressurized Shield. In J. Geotech. Geoenviron. Eng. 136 (1), pp. 215–229. DOI: 10.1061/(ASCE)GT.1943-5606.0000194.

Morgenstern, N.; Amir-Tahmasseb, I. (1965): The stability of a slurry trench in cohesionless soils. In Géotechnique 15 (4), pp. 387–395. DOI: 10.1680/geot.1965.15.4.387.

Müller-Kirchenbauer, H. (1972): Stability of slurry trenches. In Proceedings of 5th European Conference on Soil Mechanics and Foundation Engineering, Madrid, pp. 543-553.

Müller-Kirchenbauer, H. (1977): Zur Standsicherheit von Schlitzwänden in geschichteten Baugrund. Veröffentlichung des Grundbauinstitus der Technicschen Universität Berlin, Heft 1, pp 72-88.

Pascal, H. (1981): Non-steady flow through porous media in the presence of a threshold gradient. In Acta Mechanica 39 (3-4), pp. 207–224. DOI: 10.1007/BF01170343.

Paya Silvestre, S. (2015): Elektrokoagulation zur Trennung von gebrauchten Bentonitsupensionen im Tunnelbau. Doctoral Thesis. Ruhr-Universität, Bochum.

Philip, J. R.; Smiles D. E. (1982): Macroscopic Analysis of the behavior of colloidal suspensions. In Advances in Colioid and Interface Science, 17, pp. 83–103.

Piaskowki, A.; Kowalewski, Z. (1965): Application of thixotropic clay suspensions for stability of vertical sides of deep trenches without strutting. In Proc. Of 6th Int. Conf. on Soil Mech. And Found. Eng, Montreal.

Plekkenpol, J. W.; van der Schrier, J. S.; Hergarden, H. J. A. M. (2005): Shield tunnelling in saturated sand - face support pressure and soil deformations. In Tunnelling. A Decade of Progress. GeoDelft 1995-2005.

Praetorius, S.; Schoesser, B. (2016): Bentonithandbuch. Ringspaltschmierung für den Rohrvortrieb. Berlin: Ernst & Sohn, a Wiley brand (Bauingenieur-Praxis).

Prinz, H.; Strauss, R. (2011): Ingenieurgeologie. 5. Auflage. Heidlberg: Spektrum Akademischer Verlag.

Pulsfort, M.; Thienert, C. (2013): Neue Erkentnisse zur Stützdruckübertragung beim Tunnelvortrieb mit Flüssigkeitsgestützter Ortsbrust. Gütersloh: Bauverl. (Forschung + Praxis Vorträge der STUVA-Tagung, 2013).

Richtlinie 853 (RIL) Deutsche Bahn AG, 2013: Eisenbahntunnel planen, bauen und instandhalten.

Rostami, J.; Ozdemir, L. (1993): A new model for performance prediction of hard rock TBMs. Proceedings of the Rapid Excavation and Tunneling Conference, Boston, 13-17 June 1993, pp. 793-793.

Rubarth, W. (1998): Separating solids from suspension. In Tunnels & Tunnelling International 31 (4), pp. 45–47.

Ruse, N. M.; Vermeer, P. A. (Eds.) (2004): Räumliche Betrachtung der Standsicherheit der Ortsbrust beim Tunnelvortrieb. Zugl.: Stuttgart, Univ., Doctoral thesis., 2004. Stuttgart: IGS (Mitteilung / Institut für Geotechnik Stuttgart, 51).

Schindler, S.; Hegemann, F.; Koch, S.; Koenig, M.; Mark, P. (2016): Radar interferometry based settlement monitoring in tunnelling: Visualisation and accuracy analysis, In Visualisation in engineering 4:7, pp. 1-16.

Schmuedderich, Ch.; Barciaga, T.; Qarmout, M.; Lavasan, A.; König, D.; Schnaz, T. (July 10th 2017): Three dimensional analysis of tunnel face stability using FEM. SFB Workshop: Stability Analysis in Geotechnical Problems. Bochum, July 10th 2017.

Schoesser, B.; Schanz, T. (2014): A6 Lokal instationäre Suspensionsstützung bei Flüssigkeitsschilden. SFB 837 - Finanzierungsantrag 2014-2018. Ruhr-Univeristät, Bochum, pp. 129–148.

Schoesser, B.; Thewes, M. (2015): Marsh Funnel testing for rheology analysis of bentonite slurries for Slurry Shields. In ITA WTC 2015 Congress and 41st General Assembly in Dubrovnik, Croatia.

Schoesser, B.; Thewes, M. (2015): Rheology testing for bentonite suspensions – do we tap the full potential out of Marsh funnel tests? In Tunnels & Tunnelling International. DOI: 10.13140/RG.2.1.1207.4003.

Sharma, M. M.; Yortsos, Y. C. (1987): Transport of particulate suspensions in porous media: Model formulation. In AIChE Journal 33 (10), pp. 1636–1644.

Shirato, M.; Aragaki, T.; Iritani, E. (1978): Blocking filtration laws for filtration of power-law non-newtonian fluids. In Journal of Chemical Engineering of Japan, pp. 162–164.

Simons, H.; Ruppert, F. (1982): Entwicklung geeigneter Verfahren zum Messen der physikalischen Eigenschaften von Bentonitsuspensionen auf Baustellen. Mitteilung des Lehrstuhls für Grundbau und Bodenmechanik. Technische Universität, Braunschweig.

Sochi, T. (2007): Pore scale modeling of Non-Newtonian flow. PhD Thesis, Imperial College, London. Department of Earth Science and Engineering.

Sochi, T. (2010): Non-Newtonian flow in porous media. In Polymer 51 (22), pp. 5007–5023. DOI: 10.1016/j.polymer.2010.07.047.

Talmon, A. M.; Mastbergen, D. R; Huisman, M. (2013): Invasion of pressurized clay suspensions into granular soil. In Journal of Porous Media 16 (4), pp. 351–365.

Tang, X.-W.; Liu, W.; Albers, B.; Savidis, S. (2014): Upper bound analysis of tunnel face stability in layered soils. In Acta Geotech. 9 (4), pp. 661–671. DOI: 10.1007/s11440-013-0256-1.

Terzaghi, K.; Jelinek, R. (1954): Theoretische Bodenmechanik. Springer-Verlag, Berlin Heidelberg.

Terzaghi, K.; Peck, R. B.; Mesri, G. (1996): Soil mechanics in engineering practice. 3rd ed. New York: Wiley.

Thewes, M. (2009): Bentonite slurry shield machines: Steate-of-the-Art and Important Aspects for Application. Invited lecture at the workshop "Operacion y mantenimiento de escudos: Presente y futuro. Barcelona.

Thewes; M. (1999): Adhäsion von Tonböden beim Tunnelvortrieb mit Flüssigkeitsschilden. Doctoral thesis, Bergische Universität, Wuppertal.

Thewes, M.; Schoesser, B.; Zizka, Z. (2016): Transient face support in slurry shield tunnelling due to different time scales for penetration time of support fluid and for excavation sequence of cutting tools., In: ITA-AITES World Tunnel Congress; International Tunnelling and Underground Space Association; Society for Mining, Metallurgy, and Exploration. San Francisco, California

Thienert, C. (2011): Zementfreie Mörtel für die Ringspaltverpressung beim Schildvortrieb mit flüssigkeitsgestützter Ortsbrust. Doctoral thesis. Bergische Universität, Wuppertal.

Tien, C.; Ramarao, B. V. (2011): Revisiting the laws of filtration. An assessment of their use in identifying particle retention mechanisms in filtration. In Journal of Membrane Science 383 (1-2), pp. 17–25. DOI: 10.1016/j.memsci.2011.07.019.

Triantafyllidis, T. (2004): Planung und Bauausführung im Spezialtiefbau: Teil 1: Schlitzwand- und Dicht: John Wiley & Sons.

van Rhee, C.; Bezuijen, A. (1992): Influence of seepage on stability of sandy slope. In Journal of Geotechnical Engineering 118 (8), pp. 1236–1240.

Vermeer, P. A.; Ruse, N.; Marcher, T. (2002): Tunnel Heading Stability in Drained Ground. In FELSBAU 20 (6), pp. 8–18.

Vu, M. N.; Broere, W.; Bosch, J. (2015): The impact of shallow cover on stability when tunnelling in soft soils. In Tunnelling and Underground Space Technology 50, pp. 507–515. DOI: 10.1016/j.tust.2015.09.005.

Walz, B.; Pulsfort, M. (1983): Ermittlung der rechnerischen Standsicherheit suspensionsgestützter Erdwände aus der Grundlage eines prismatischen Bruchkörpermodells. In Tiefbau Ingenieurbau Straßenbau 25, pp. 4–7.

Wehrmeyer, G. (2000): Zur Kontrolle der geförderten Aushubmassen beim Tunnelvortrieb nit Flüssigkeitsschilden. Doctoral Thesis. Ruhr-Universität, Bochum.

Wehrmeyer, G. (2009): Muck slurry pumping circuits for TBMs. In: Mechanised Tunneling with segmental lining, pp. 92–106.

Weiss, F. (1967): Die Standfestigkeit flüssigkeitsgestützter Erdwände. München: Ernst & Sohn (Bauingenieur-Praxis, 70).

Wendl, K.; Thuro, K. (2011): Auswirkung von Hydroschildvortrieben auf den Grundwasserkörper am Beispiel von zwei Vortrieben in Tirol. Berlin. In 18. Tagung für Ingenieurgeologie und Forum „Junge Ingenieurgeologen“, pp. 1–7.

Winterwerp, J. C.; van Kesteren, W. G. M. (Eds.) (op. 2004): Introduction to the physics of cohesive sediment in the marine environment. Amsterdam: Elsevier (Developments in sedimentology, 56).

Wu, Y.-S. (1990): Theoretical Studies of Non-Newtonian and Newtonian Fluid Flow through Porous Media. PhD thesis, University of California, Berkeley.

Xanthakos, P. P. (1979): Slurry walls: McGraw-Hill Book Company.

Xu, T.; Bezuijen, A. (2018): Analytical methods in predicting excess pore water pressure in front of slurry shield in saturated sandy ground. In Tunnelling and Underground Space Technology 73, pp. 203–211. DOI: 10.1016/j.tust.2017.12.011.

Xu, T.; Dias, T.; Bezuijen, A. (2017): Slurry infiltration ahead of slurry TBM's in saturated sand: laboratory tests and consequences for practice. In 9th International Symposium on Geotechnical Aspects of Underground Construction in Soft Ground, 2017. Sao Paulo, Brazil.

Yamazaki, H. (1978): Method of driving and forming a tunnel with hydraulic boring machine. App. no. US 05/738,271. Patent no. US4072021 A.

Yu, H. S.; Salgado, R.; Sloan, S. W.; Kim, J. M. (1998): Limit analysis versus limit equilibrium for slope stability. In J. of Geotech. and Geoenv. Eng. 124 (1), pp. 1–11.

Zamani, A.; Maini, B. (2009): Flow of dispersed particles through porous media — Deep bed filtration. In Journal of Petroleum Science and Engineering 69 (1-2), pp. 71–88. DOI: 10.1016/j.petrol.2009.06.016.

Zizka, Z.; Schoesser, B.; Thewes, M. (2017): Excavation cycle dependent changes of hydraulic properties of granular soil at the tunnel face during slurry shield excavations. In 9th Symposium on Geotechnical Aspects of Underground Constructions in Soft Ground. Sao Paulo, Brazil.

Zizka, Z.; Schoesser, B.; Thewes, M.; Popovic, I. (2107): Excess pore pressures in front of the tunnel face during slurry shield excavations due to different time scales for excavation sequence of cutting tools and penetration time of support fluid. In ECCOMAS Thematic Conference EURO:TUN 2017, Innsbruck.

Zizka, Z.; Schoesser, B.; Thewes, M.; Schanz, T. (2018): Slurry Shield Tunneling. New Methodology for Simplified Prediction of Increased Pore Pressures Resulting from Slurry Infiltration at the Tunnel Face Under Cyclic Excavation Processes. In Int J Civ Eng 15 (4), p. 387. DOI: 10.1007/s40999-018-0303-2.

Zizka, Z.; Thewes, M. (2016): Recommendations for Face Support Pressure Calculations for Shield Tunnelling in Soft Ground. Deutscher Ausschuss für unterirdisches Bauen e. V. (DAUB) - German Tunnelling Committee. Available online at http://www.daub-ita.de/fileadmin/documents/daub/gtcrec1/gtcrec10.pdf.

Zizka, Z.; Thewes, M.; Popovic, I. (2015): Analysis of slurry pressure transfer on the tunnel face during excavation. SEE Tunnel - Promoting tunnelling in South East European Region; 41st General Assembly and World Tunnel Congress of International Tunnelling and Underground Space Association ITA-AITES, Dubrovnik, Croatia.

ZTV-ING - Bundesanstalt für Straßenwesen (2012): ZTV-ING - Zusätzliche Technische Vertragsbedingungen und Richtlinien für Ingenieurbauten Teil 5 Tunnelbau.

LIST OF FIGURES

Figure 2-1: Simplified differentiation of tunnelling machines related to their prevalent ground of application according to DAUB (2010) 7

Figure 2-2: Longitudinal cut through Slurry shield machine (Herrenknecht AG) 9

Figure 2-3: Application ranges of shield machine with slurry supported tunnel face (Thewes, 2009) 10

Figure 2-4: Cutting tools at the cutting wheel (adapted from Herrenknecht AG and from Köppl, 2014) 13

Figure 2-5: Face collapse in cohesive - clay (a) and granular soils – sand (b) and its propagation pattern adapted from Broere (2001), Leca & New (2006) and Fillibeck (2011) 15

Figure 2-6: Failure mechanism acc. to a) Piaskowski & Kowalewski (1965) and b) Horn (1961) adapted from Zizka & Thewes (2016) 19

Figure 2-7: Layout of a circular opening in the vertical sheet pile wall (Broms & Bennermark, 1967) 21

Figure 2-8: Allowable operational pressures at the tunnel crown of a shield machine (Zizka & Thewes, 2016) 25

Figure 2-9: Forces acting on the wedge and prism (Zizka & Thewes, 2016) 27

Figure 2-10: Example of the determination of the highest required support force (Emax,re) by variation of the sliding angle (ϑ) (Zizka & Thewes, 2016) 28

Figure 2-11: Two possible distributions of vertical stress next to vertical triangular plane of the wedge: a) Girmscheid (2008), DIN 4126 (2013) and Anagnostou & Kovari (1994) b) Kirsch & Kolymbas (2005) 32

Figure 3-1: Shapes of soil grains – a) spherical b) flat c) needle-shaped d) rounded e) edged f) sharp-edged (Enzmann, 2000) 38

Figure 3-2: Left – Particle size distribution of suspended bentonite particles in B1 - 5% fresh slurry (Malvern report, 2017) determined by the technique of laser diffraction Right -

Bentonite particle form B2 - 15% fresh slurry diluted in ratio 1:100 under Lasermicroscope Leica TCS SP8 (Herpers, 2015) 39

Figure 3-3: Devices required for the determination of physical properties of slurry a) density b) pH, electrical conductivity, temperature 40

Figure 3-4: Representants of simple devices used for the determination of rheological properties of slurry a) ball harp b) Marsh funnel 41

Figure 3-5: a) Standardised direct indicating viscometer after API 13b b) General viscometer..... 42

Figure 3-6: Static and dynamic yield point after DIN 4127 (2014) in dependence on time..... 43

Figure 3-7: Basic consistency curves for different type of flow – Newtonian, pseudoplastic, Bingham plastic, dilatant (Luckham & Rossi, 1999)..... 46

Figure 3-8: Modelling of the porous medium through homogenization of surrogate medium and the concept of volume fractions (Benke, 2003) 48

Figure 3-9: Simple capillary tube models (Bear, 1988) 52

Figure 3-10: Basic filtration models (Tien & Ramarao, 2011) 56

Figure 3-11: Particle retention sites in porous media during deep bed filtration (Herzig et al., 1970) 58

Figure 3-12: Left - Three dominant capturing processes of suspended particles, grain = collector (modified from McDowel-Boyeret al., 1986), Right – particles within a porous medium (Sharma & Yortsos, 1987)..... 61

Figure 3-13: Left - Sketch of slurry supported open trench with slurry penetrated area (abd) and the slurry penetrated area which is stabilizing the trench (abc) Right – Mechanism of the single grain sliding out of the wall for α = 30° and 45° (Müller-Kirchenbauer, 1972). 67

Figure 3-14: Visualization of slurry pressure transfer models (modified from Thienert, 2011) 70

Figure 3-15: Pressure transfer mechanism and pressure drops in dependence on grain size of soil (modified from Krause, 1987)..... 72

Figure 3-16: Pressure transfer mechanism and pressure drops in dependence on grain size of soil (adapted from Krause, 1986)..... 74

Figure 3-17: Experimental visualization of theoretically possible cases of slurry soil interaction (Min et al., 2013), Type I: filter cake – all grains of slurry are lodged on the surface of soil, Type II: filter cake with an infiltrated zone - some grains of slurry are penetrated into

the soil, Type III: infiltrated zone without filter cakes - all grains of the slurry are penetrated into the soil 76

Figure 3-18 Left - Measurement of pore pressure heads in front of the shield and derived approximation of the excess pressure head distribution (Bezuijen et al. 2001), Right – pressure drop over the mean filter cake (Δs_{fc}) and resulting pore pressure head distribution ($\Delta u(x,z)$) acc. Broere & van Tol (2000) 82

Figure 4-1: Disturbances of the pressure transfer mechanism by cutting tools (Schoesser & Schanz, 2014) 90

Figure 4-2: Two theoretically possible cases at the slurry supported tunnel face – Case A and Case B (Zizka et al., 2017) 91

Figure 4-3: Two boundary ways of pressure transfer causing different pressure drop – Left by flow pressure and right by formed pressure transfer mechanism, s_1 = slurry pressure in the excavation chamber and u_0 = far field hydrostatic pore pressure 93

Figure 4-4: Mutual influence of adjacent cutting tracks and consequent reduction of the efficiency of the pressure transfer mechanism. s_1 = slurry pressure in excavation chamber and u_0 = far field hydrostatic pore pressure 94

Figure 4-5: Fundamental question of the Case B pressure transfer: Occurs the transfer mostly inside or outside of slurry penetrated zone? 96

Figure 4-6: Relationship between slurry penetration distance and slurry flow velocity, excavation advance rate is equal to the slurry flow velocity at quasi-steady state (Anagnostou & Kovari, 1994) 97

Figure 4-7: Two boundary cases observable: Equilibrium state without excavation (Left) and equilibrium state during excavation (Right) 98

Figure 4-8: Theoretically possible drops of pore pressure within slurry penetrated zone 98

Figure 4-9: Case B-1 for reaching equilibrium state of the pressure transfer mechanism during excavation, considering the option 1) from Fig. 4-8 99

Figure 4-10: Case B-2 for reaching equilibrium state of the pressure transfer mechanism during excavation, considering option 2) from Fig. 4-8 100

Figure 5-1: Interaction between cutting tools and a pressure transfer mechanism. The way of interaction is valid for both Type I and II from Table 3-4 102

Figure 5-2: Cutting wheels of reference projects P1, P2 and P3 (up), division into homogeneous cutting zones including numbers of zones (down) (Zizka et al., 2018) 103

Figure 5-3: Every cutting tool traces a three-dimensional helix when the machine excavates a tunnel (Thewes et al., 2016) 105

Figure 5-4: Coupling of penetration of one cutting tool with timespan between subsequent tools passing (different scale of the diagrams) (Thewes et al., 2016) 106

Figure 6-1: Experimental set-up for the investigation of transient slurry penetration (Talmon et al., 2013 - comments added) 110

Figure 6-2: Experimental set-up for the investigation of the Case A (Zizka et al., 2017) 111

Figure 6-3: Time-dependent slurry penetration – each line resents an average from three experimental runs 116

Figure 6-4: Dependence of the average slurry penetration depth on the average pressure drop over the sample for slurry B1 6% (DIN 4126 uses Eq. 3-27 with a = 2 or 3.5) 117

Figure 6-5: Comparative slurry penetration depth determined using the methodology by Krause (1987) obtained from the experimental results and compared with bounds acc. to Krause (1987) 118

Figure 6-6: Comparison of the experimentally obtained and the calculated slurry penetration depth acc. to Anagnostou & Kovari (1994), AK denotes the calculated penetration depth 119

Figure 6-7: Permeability coefficient development (Zizka et al., 2018) and stagnation branches (S. b.) for the combinations 121

Figure 6-8: Timespan required for slurry to achieve the stagnation branch 122

Figure 6-9: Comparison of slurry penetration depth with and without back-pressure – each line represents an average from experimental runs (BP stands for back-pressure) 123

Figure 6-10: Comparison of permeability coefficient development with and without back-pressure124

Figure 6-11: Project P 1 - Comparison of the time dependent penetration distance of slurry in experiments with cutting tool penetration depths and the timespans between tool passing in respective cutting zones of the reference project (Zizka et al., 2018) 125

Figure 6-12: Project P2 - Comparison of the time dependent penetration distance of slurry in experiments with cutting tool penetration depths and the timespans between tool passing in respective cutting zones of the reference project (Zizka et al., 2018) 126

Figure 6-13: Project P3 - Comparison of the time dependent penetration distance of slurry in experiments with cutting tool penetration depths and the timespans between tool passing in respective cutting zones of the reference project (Zizka et al., 2018) 127

Figure 6-14: Percentage of the area of the tunnel face with the Case A interaction (Zizka et al., 2018) 128

Figure 6-15: Permeability coefficient development and its minimal achievable values in respective homogeneous cutting zones of Project P1. The horizontal dashed lines signify the extent of the permeability development in respective zone in dependence on chosen PR and RPM (Zizka et al., 2018) 129

Figure 7-1: Experimental set-up for the investigation of Case B interaction – column test 132

Figure 7-2: Location of sensors in the set-up (column test) and designation of the measurement levels 133

Figure 7-3: Principle of slurry re-penetration including the cutting tool 135

Figure 7-4: Principle of the pressure-steered re-penetration experiment – movement of injection pressure p_1 further in soil, the moving distance corresponds to the tool excavation depth..... 136

Figure 7-5: Experimental device with introduced soil cutting process – RUB tunneling device (Küpferle et al., 2018) 138

Figure 7-6: Time-dependent slurry penetration for different boundary flow conditions –absolute penetration depth left and comparative penetration depth right..... 145

Figure 7-7: Time-dependent slurry penetration at different boundary conditions of flow – 1st measurement level, stages are marked specifically for combination IV..... 147

Figure 7-8: Time-dependent slurry penetration at different boundary conditions of flow – 2nd measurement level, stages are marked specifically for combination IV..... 148

Figure 7-9: Distribution of pore pressures in the set-up depending on boundary flow condition, Left: at 3s and 10 s, Right at 40s and 60s since experiment start..... 150

Figure 7-10: Time-dependent slurry penetration for different injection pressures –absolute penetration depth left and comparative penetration depth right (% of the final penetration depth) 151

Figure 7-11: Relationship between slurry penetration depth and pressure drop in the experiment for soil 1-2 mm, porosity 0.41 and slurry B1 6% (DIN 4126 uses Eq. 3-27 with a = 2 or 3.5) 152

Figure 7-12: Time-dependent reaction of soil at different injection pressures – 1st measurement level, stages are marked specifically for combination IV 153

Figure 7-13: Time-dependent reaction of soil at different injection pressures – 2nd measurement level, stages are marked specifically for combination IV 154

Figure 7-14: Distribution of pore pressures in soil at different stages of slurry penetration depending on the injection pressure 155

Figure 7-15: Slurry penetration depth vs. Pressure drop –left, distribution of the pore pressure inside the soil sample, note that combination VII corresponds to rc-III and combination VIII to rc-IV respectively 156

Figure 7-16: Time-dependent slurry penetration - left, time-dependent slurry re-penetration – right for the excavation scale 40 mm + 60s 157

Figure 7-17: Comparison of PWD 2 and PWD 3 for the excavation scale 40 mm + 60s 158

Figure 7-18: Reaction of soil at the 1st measurement level during re-penetration with excavation scale 40mm + 60s, stages are marked specifically for combination r-II 159

Figure 7-19: Reaction of soil at the 2nd measurement level during re-penetration with excavation scale 40mm + 60s, stages are marked specifically for combination r-II 160

Figure 7-20: Distribution of pore pressures during re-penetration with excavation scale 40mm + 60s, timespans are given from the start of the re-penetration 160

Figure 7-21: Time dependent penetration depth and Comparison of PWD 2 and PWD 3 for the excavation scale 40 mm + 100s 161

Figure 7-22: Reaction of soil at the 1st and 2nd measurement level during re-penetration with excavation scale 40mm + 100s, stages are marked specifically for combination r-IV and WZ 1 162

Figure 7-23: Distribution of pore pressures during re-penetration with excavation scale 40mm + 60s, timespans are given from the start of the re-penetration 162

Figure 7-24: Excess pore pressure depending on the location cutting wheel in relation to the particular sensor – Left for rc-I and right for rc-II 164

Figure 7-25: Excess pore pressure depending on the location cutting wheel in relation to the particular sensor – Left for rc-III and right for rc-IV 165

Figure 7-26: Outflow curves during the excavation in 1-2 mm soil fraction with B1 6% slurry obtained for combinations rc-I and rc-II 167

Figure 7-27: Longitudinal section of the RUB tunnelling device showing two modes of slurry penetrated zone expansion during the experiment 168

Figure 7-28: Outflow curves during the excavation in 0.063-4 mm soil fraction with B1 6% slurry obtained for combinations rc-III and rc-IV 169

Figure 7-29: Development of the pressure transfer mechanism in terms of expected pore pressure distribution in front of cutting tools for soil fraction 0.063-4 mm during different excavation stages 170

Figure 8-1: Assumed permeability coefficient development 175

Figure 8-2: Left – simplified layout of the cutting tools (Calculation case C1), Right – segmentation of the tunnel face including the location of the fully formed (k16) and freshly cut (k1) pressure transfer mechanism. Note that the location of these boundary states depends on the cutting tool layout revolution direction of the cutting wheel 176

Figure 8-3: Investigated variants of the tunnel face segmentation 177

Figure 8-4: Left – dimensions of the numerical model, right – detail of the used FE mesh 178

Figure 8-5: Simplified evaluation of the transferred slurry excess pressure 178

Figure 8-6: Evaluation of the transferred slurry excess pressure 180

Figure 8-7: Calculation scenario – model for evaluation of pressure transfer with simplified cutting wheel 182

Figure 8-8: Approximation of the cutting wheel from reference projects P1 and P2 for the calculation purposes 183

Figure 8-9: Calculation scenario – model considering realistic cutting wheels 184

Figure 8-10: Total hydraulic heads in front of the pressure transfer mechanism (clockwise rotation of the wheels), (Zizka et al., 2015) 186

Figure 8-11: Position of the cutting wheel at 45 s and 77 s since excavation start (the cutting wheel rotates clockwise) 186

Figure 8-12: Distribution of excess pore pressures in front of the tunnel face during excavation, Left – calculation case S 3a, Right – all cases at time 45 s or 77 s since the start of the excavation 188

Figure 8-13: Total head distribution [m] obtained by the numerical model for the calculation case S3a at 45s since the excavation start, Left – interface between pressure transfer mechanism and soil, Right – zoomed-in longitudinal section through the model at the tunnel axis 189

Figure 8-14: Pressure drop over 10 cm of the pressure transfer mechanism depending on the radial distance from tunnel axis, Left – absolute pressure drop, Right – drop as a percentage of the applied slurry excess pressure 191

Figure 8-15: Assigning of permeability coefficient developments to cutting tracks for calculation – scenario S5 (multi-zone model) 192

Figure 8-16: Comparison between predicted pressure drop and subsequently for calculation scenario S5, pressure drop from assigned experimental combination is also shown 193

Figure 8-17: Orientation of the cutting wheel of reference projects at 123.75 s since excavation start 194

Figure 8-18: Scaled distribution of excess pore pressure in front of the tunnel face during excavation for two reference slurry shield from Projects P1 and P2 194

Figure 8-19: Total head distribution obtained by the numerical model for the calculation case R1b – Ref P1 – 30 kPa (left) and case R2b – Ref P2 – 30 kPa at 129.75 s since the excavation start 195

Figure 8-20: Pressure drop over 10 cm of the pressure transfer mechanism depending on the radial distance from tunnel axis, Left – absolute pressure drop, Right – drop as a percentage of the applied slurry excess pressure, Note: two points are provided for the project Ref P1 at the distance 4.75 m due to two distances between tools in this track 197

Figure 8-21: Pressure drop over 10 cm of the pressure transfer mechanism depending on the radial distance from tunnel axis compared with pressure drop measured in the permeability determination experiment 198

Figure 8-22: Comparison of transferred slurry pressure with acting earth pressure depending on friction angle of soil 201

Figure 8-23: Pressure transfer depending on the location at the tunnel face – along the vertical axis (left) and along the horizontal axis (right) 202

Figure 9-1: Slurry penetration depth during excavation in soil fraction 1-2 mm for two excavation scales compared with primary penetration depth (left) and schema for reaching the penetration depth during excavation according to Anagnostou & Kovari (1994) (right) 206

Figure 9-2: Pore pressure distribution in comparative presentation (left) and achieved stagnation gradients (right) for soil with grain fraction 1-2 mm 209

Figure 9-3: Stagnation gradients measured during slurry penetration compared with transient stagnation gradients predicted by Anagnostou and Kovari (1994) 210

Figure 9-4: Pore pressure distribution in comparative presentation (left) and achieved stagnation gradients (right) for soil with grain fraction 0.063-4 mm 212

Figure 9-5: Development of effective stress outside (out) and inside (in) the slurry penetrated zone for soil fraction 1-2 mm 213

Figure 9-6: a) Determination of zone with efficient pressure transfer for soil with linear pore pressure distribution within slurry penetrated zone, b) Determination of average increased pore pressure at the sliding surface of the wedge 215

Figure 9-7: Minimal recommended stagnation gradient of slurry $f_{s0,min}$ to avoid a loss of efficient face support due to deep slurry penetration 216

Figure 9-8: Results of the parametric study – minimally required cohesion of soil to achieve self-bearing of the wedge 219

Figure 10-1: Efficiency of the pressure transfer mechanisms for different interaction at the tunnel face during excavation stage, illustrated for the elevation at the tunnel axis 222

Figure 10-2: Left - Heterogeneous tunnel face, Right - Homogeneous tunnel face with simultaneous presence of Case A and B at the tunnel face within homogenous soil conditions ... 224

Figure 10-3: Flow chart to analyse the presence of Case A or B of interaction at the tunnel face 225

Figure 10-4: Flow chart to determine the minimal support pressure in Case A of interaction 227

Figure 10-5: Flow chart to determine minimal support pressure for Case B of interaction 229

LIST OF TABLES

Table 1-1: Projects used to review the functionality of slurry face support by Jancsecz & Steiner (1994) 2

Table 2-1: Coefficient defining the efficiency of the pressure transfer mechanism, Stagnation gradients is explained in detail in section 3.4.1..... 25

Table 2-2: Suggested coefficients of the lateral pressure in the silo area (Zizka & Thewes, 2016)..... 30

Table 2-3: Suggested coefficients for the lateral earth pressure on the triangular vertical planes of the sliding wedge (Zizka & Thewes, 2016)..... 33

Table 3-1: Soil classification based on grain size..... 38

Table 3-2: Coefficient q_1 describing the interaction..... 57

Table 3-3: Types of standard blocking filtration (Herzig et al., 1970), compare with Fig. 3-2 62

Table 3-4: Pressure transfer mechanism and their characteristics (adapted from Kilchert & Karstedt, 1984)..... 69

Table 3-5: Type of slurry soil interaction depending on particle size comparison (Min et al., 2013)... 76

Table 5-1: Outline of reference slurry shield projects used to determine the excavation scale 103

Table 5-2: Division of cutting wheels into homogeneous zones, * denotes 2 active tools if their overlapping is taken into account 104

Table 5-3: Resulting excavation scales, *no scrapers disturbing the pressure transfer mechanism are located in this zone..... 107

Table 6-1: Experimental program for the investigation of the Case A..... 113

Table 6-2: Properties of soils used in the investigation (see appendix for grain distribution curve) . 114

Table 6-3: Slurry properties used in the investigation (see appendix for the product sheet of B1 bentonite and the testing protocols) 114

Table 6-4: Resulting pressure drop over the soil sample (10 cm long) 115

Table 7-1: Hydraulic head loss in set-up for water flow (see section 7.2.1 for the detailed explanation of the experimental combinations) 134

Table 7-2: Experimental program for investigating the primary slurry penetration in Case B of interaction, *hydraulic head difference between the outflow level of the soil cylinder and the fluid level in the outflow reservoir is approx. 0.07 bar, therefore back-pressure was 0.57 bar instead of 0.5 bar 139

Table 7-3: Properties of soils used in the slurry penetration and re-penetration investigation (grain distribution curve is provided in the appendix) 140

Table 7-5: Resulting pressure drop over the soil sample 141

Table 7-4: Slurry properties used in the slurry penetration investigation (product sheet and testing protocols are provided in the appendix), the value in parentheses denotes an extreme 141

Table 7-6: Experimental program for investigating the slurry re-penetration in Case B of interaction 142

Table 7-7: Properties of soils used in the slurry re-penetration with soil cutting investigation, grain size distribution curves are provided in the appendix 143

Table 7-8: Slurry properties used in the slurry re-penetration with cutting investigation (product sheet and testing protocols are provided in the appendix) 144

Table 7-9: Experimental program for investigating the slurry re-penetration with consideration of soil cutting in Case B of interaction 144

Table 8-1: Investigated segmentations of the tunnel face 176

Table 8-2: Determination of the operational limit pressures for the adopted scenario 180

Table 8-3: Cases investigated with the model for evaluation of the pressure transfer 181

Table 8-4: Cases investigated with the model considering real cutting wheels 184

Table 8-5: Cases investigated with the model considering real cutting wheels 185

Table 8-6: Results of the pressure transfer calculation with simplified cutting wheel, number of calculation case indicates the adopted permeability development determined in chapter 6 190

Table 8-7: Results of the pressure transfer calculation with realistic cutting wheels 196

Table 8-8: Comparison of transferred slurry excess pressure, *average, **only over the pressure transfer mechanism 198

Table 8-9: Comparison of pressure drop over the pressure transfer mechanism 199

Table 8-10: Comparison between pressure transferred and the acting earth pressure 201

Table 9-1: Stagnation gradient – weighted average within a cutting track 211

LIST OF SYMBOLS

Latin Alphabet

a	[-]	Empirical factor from the experiments; 2 or 3.5
a_i	[m^2]	Area of the particular tunnel face segment [m^2]
a_{pores}	[m^2]	Total interstitial surface area of pores
a_{tube}	[m^2]	Cross-sectional area of a single tube
A	[m^2]	Cross-sectional area of the flow
A_{FS}	[m^2]	Area of the slurry penetrated soil inside the wedge
A_{silo}	[m^2]	Cross-sectional area of the silo / of the top of the wedge
AR	[mm/min]	Advance rate of the machine
b	[min]	the timespan during which 50% of upper penetration bound by Krause (1987) is reached, b = 1 min
b_{grains}	[-]	Geometric constant related to packing of the filter grains
b_{Krause}	[-]	Empirical factor by Krause, b = 5 - 10
c_0	[-]	Kozeny constant
c'	[kPa, kN/m^2]	Drained cohesion
c_1'	[kPa, kN/m^2]	Drained average cohesion within the silo area
c_2'	[kPa, kN/m^2]	Drained average cohesion within the wedge area
c_u	[kPa, kN/m^2]	Undrained shear strength
c_v	[m^2/s]	Terzaghi´s consolidation coefficient of slurry to be obtained from filter press test

C	[-]	A constant
C_{over}	[m]	Overburden
$C_{partciles}$	[%]	Particle concentration
d_{10}	[m]	Characteristic grain size of the soil approximated (to be obtained from grain distribution curve)
d_{15}	[m]	Grain size of soil (15% passing in sieve analysis)
d_{20}	[m]	Grain size of soil (20% passing in sieve analysis)
d_{25}	[m]	Grain size of soil (25% passing in sieve analysis)
d_g	[m]	Radius of bed grain
d_g	[m]	Grain mean diameter
d_{hyd}	[m]	Hydraulic pore diameter of the soil
$d_{l,i}$	[m]	Lower limit of grain size class from the sieve analysis
d_m	[m]	Mean particle size – diameter of sphere
d_{pores}	[m]	Average pore size of soil
d_{tube}	[m]	Diameter of a tube
$d_{u,i}$	[m]	Upper limit of a grain size class from the sieve analysis
d_w	[m]	Characteristic grain size calculated from grain distribution curve
ds	[kPa, kN/m^2]	Differential of slurry excess pressure transfer
dx	[m]	Differential of time-dependent slurry penetration depth
D	[m]	shield diameter
D_{85}	[m]	Grain size of particles suspended in slurry (85% passing)
D_c	[-]	Compaction ratio
D_p	[m]	Radius of suspended particles

D_r	[-]	Relative density
D_{sp}	[m]	Diameter of the sphere
e	[-]	Void ratio
e_{max}	[-]	Void ratio of the soil in its loosest state
e_{min}	[-]	Void ratio in the densest state
$E_{max,ci}$	[kN]	Support force due to earth pressure (circular tunnel face)
$E_{max,re}$	[kN]	Support force due to earth pressure (rectangular tunnel face)
E_{re}	[kN]	Support force due to the earth pressure
E_w	[kN]	Support force due to the groundwater pressure
f_s	[kN/m^3]	Stagnation gradient of slurry during excavation acc. to Anagnostou & Kovari (1994)
f_{s0}	[kN/m^3]	Stagnation gradient of slurry
$f_{s0,KK}$	[kN/m^3]	Slurry stagnation gradient acc. to Kilchert & Karstedt
$f_{s0,MC}$	[kN/m^3]	Stagnation gradient of slurry in soil acc. Müller-Kirchenbauer (1974)
$f_{s0,req}$	[kN/m^3]	Required stagnation gradient
F_{slurry}	[kN]	Retaining force due to slurry pressure
g	[m/s^2]	Gravity acceleration
G	[kN]	own weight of wedge
Δh	[m]	Excess hydraulic head/Change in hydraulic head
$\Delta h(t)$	[m]	Measured time-dependent pressure drop in the set-up
$h_{w,crown}$	[m]	Groundwater level above the tunnel crown
i	[-]	Hydraulic gradient
i_{av}	[-]	Average hydraulic gradient at the tunnel face

i_B	[-]	Average hydraulic gradient at the tunnel face acc. to Bezuijen et al. (2001)
k_0	[-]	Lateral earth pressure coefficient at rest
k_1	[-]	Coefficient of lateral earth pressure within the silo
k_2	[-]	Coefficient of lateral earth pressure within the wedge
k_a	[-]	Active lateral earth pressure coefficient
k_f	[m/s]	Coefficient of permeability
$k_f(t)$	[m/s]	Time-dependent coefficient of permeability
$k_{f,s}$	[m/s]	Coefficient of permeability for slurry
$k_{f,w}$	[m/s]	Coefficient of permeability for water
k_p	[-]	Passive lateral earth pressure coefficient
K	[m]	Intrinsic permeability
l	[m]	Penetration distance at timespan t
$l_E(t)$	[m]	Time dependent slurry penetration distance
$l_E(t = 60min)$	[m]	Slurry penetration depth at 60 minutes
$l_{excavation}$	[m]	Slurry penetration distance during excavation
$l_{E,comp}$	[%]	Comparative penetration distance – upper or lower boarded
l_{crit}	[m]	Critical slurry penetration distance
l_{Krause}	[m]	Slurry penetration distance acc. to Krause (1987)
l_{max}	[m]	Maximum (Final) penetration depth of slurry
$l_{max,calc}$	[m]	Penetration depth acc. to Eq. 3-27
l_{mean}	[m]	Mean slurry penetration depth achieved during excavation
l_p	[m]	Slurry penetration depth during primary penetration before the re-penetration starts

l_r	[m]	Slurry penetration depth during re-penetration
$l_{ring\ building}$	[m]	Slurry penetration depth during ring building stage
l_{wedge}	[m]	Length of the sliding wedge at the tunnel axis
ΔL	[m]	Macroscopic flow path
l_t	[m]	Distance of the pressure transfer
m_s	[kg]	Mass of solids
M	[m^{-1}]	Specific surface of porous material
M_s	[m^{-1}]	Specific surface of spheres
n_0	[-]	Initial porosity (clean bed)
n_1, n_2, n_3	[-]	Empirical exponents
n_{max}	[-]	Porosity of the soil in its loosest state
n_{min}	[-]	Porosity in the densest state
n_p	[-]	Porosity
n_{tool}	[-]	Amount tool tandems within one track
n_{vol}	[-]	Volumetric porosity
N	[-]	Existing stability ratio
N_G	[-]	Gravitational parameter
N_{St}	[-]	Stokes number
p	[-]	Parameter describing shear thinning in Herschel-Bulkley flow rule
p_{tool}	[m]	Actual penetration of a single cutting tool per passing through a particular point
P_v	[kN]	vertical load from the soil prism
Pe	[-]	Peclet number

PR	[min/rev]	Penetration rate – penetration of cutting wheel per revolution
q_1	[-]	Constant describing the interaction between suspension and porous media
Q	[kN]	Shear force on inclined surface
Q_f	[m³/s]	Discharge
$Q_f(t)$	[m³/s]	Time dependant discharge
$Q_{f,tube}$	[m³/s]	Discharge from a tube
R	[m]	Excavation radius
R_{pore}	[m]	Equivalent pore radius
Re	[-]	Reynolds number
RPM	[-]	Revolutions per minute of the cutting wheel
s	[kPa, kN/m²]	Slurry pressure
s_1	[kPa, kN/m²]	slurry pressure in excavation chamber
s_2	[kPa, kN/m²]	Slurry pressure
s_{axis}	[kPa, kN/m²]	Support pressure at the tunnel axis
Δs_B	[kPa, kN/m²]	Support excess pressure transferred acc. to Bezuijen et al. (2001)
s_{crown}	[kPa, kN/m²]	Support pressure at the tunnel crown
$s_{crown,max}$	[kPa, kN/m²]	Maximal allowable pressure in the tunnel crown due to break up safety / blow-out safety
$s_{crown,min}$	[kPa, kN/m²]	Minimal support pressure in the tunnel crown
Δs	[kPa, kN/m²]	Slurry excess pressure
Δs_{av}	[kPa, kN/m²]	Average slurry excess pressure transferred
Δs_{crown}	[kPa, kN/m²]	Support (slurry) excess pressure at the tunnel crown
Δs_{fc}	[kPa, kN/m²]	Pressure transfer over the mean filter cake

Δs_{shear}	[kPa, kN/m²]	Pressure transferred over the shear stresses between slurry and pore walls of soil
S_{ci}	[kN]	Required support force (circular tunnel face)
t	[s]	Time
th_1	[m]	Total hydraulic head in the excavation chamber
$th_{2,i}$	[m]	Total hydraulic head in the middle of the particular tunnel face segment projected to the distance of 1 m in front of the tunnel face
t_{tool}	[s]	The timespan between subsequent removal of the filter cake
t_{min}	[minutes]	Timespan since the penetration start
T	[kN]	Shear resistance force on the vertical triangular plane of the wedge
T_c	[kN]	Shear resistance force due to cohesion
T_R	[kN]	Shear resistance force due to friction
u_0	[kPa, kN/m²]	Hydrostatic water pressure
u_{crown}	[kPa, kN/m²]	Hydrostatic water pressure in the tunnel crown
Δu	[kPa, kN/m²]	Excess pore pressure / Pore pressure change
Δu_{re}	[kPa, kN/m²]	Excess pore pressure as the remaining part of slurry excess pressure
U	[m]	Circumference length of the silo
v	[m/s]	Bulk flow velocity in pores
v_{ch}	[m/s]	Characteristic velocity
v_{cr}	[m/s]	Critical velocity
v_m	[m/s]	Suspension approach velocity v_m= v $(mean\ interstitial\ velocity) \cdot n_0$
v_{slurry}	[m/s]	Velocity of slurry in pores
v_{TBM}	[m/s]	AR of the shield
v_{tube}	[m/s]	Average velocity in tube

$V_{b,pores}$	[m³]	Unit bulk volume of pores
$V_{filtrate}$	[m³]	Cumulative volume of the filtrate
$V_{filtrate}(t)$	[m³]	Volume of discharged fluid at time t
V_{max}	[m³]	Volume of the discharged fluid at the end of experiment
V_s	[m³]	Volume of solid constituent
W_{ci}	[kN]	Support force due to groundwater pressure (circular tunnel face)
W_{re}	[kN]	Groundwater pressure force (rectangular tunnel face area)
$x_{sieve,i}$	[%]	Sieve fall
z	[m]	Distance from the inlet face of the porous media
z		Vertical coordinate starting from the terrain surface [m]

Greek alphabet

α	[-]	Parameter for consideration of pressure transfer mechanism formation
α_{incl}	[°]	Inclination of tangency plane between two grains (30-45 degrees)
β	[°]	Inclination of trench wall, usually $\beta = 90\ deg$ for vertical trench
θ	[48 deg]	Inclination of model tubes in comparison to bulk flow direction
γ	[kN/m³]	unit weight of soil
$\dot{\gamma}$	[1/s]	Shear rate
$\gamma_{1,av}$	[kN/m³]	Average soil unit weight in the overburden area
$\gamma_{2,av}$	[kN/m³]	Average soil unit weight in the tunnel face area
γ_2	[kN/m³]	Unit weight of soil within the wedge area
$\gamma_{F,fresh}$	[kN/m³]	Unit weight of fresh slurry

$\gamma_{F,loaded}$	[kN/m³]	Unit weight of loaded slurry
γ_F	[kN/m³]	Unit weight of slurry
γ_G	[-]	Partial safety factor for permanent load case in GZ1C acc. to DIN 1054
γ_{Supp}	[kN/m³]	Unit weight of the support medium
γ_s	[kN/m³]	Unit weight of soil grains
γ_{sp}	[kN/m³]	Unit weight of the sphere
γ_w	[kN/m³]	Unit weight of water, for the sake of simplicity adopted = 10 kN/m³
γ_φ	[-]	Partial safety coefficient for drained soil within the status GZ1C in load case LF2 acc. to DIN 1054 (= 1.15)
η_2	[-]	Pressure transfer coefficient
η_E	[-]	Safety factor for earth pressure force (= 1.5)
η_F	[-]	Safety factor accounting for deviations in the yield point of suspension (= 0.6)
η_W	[-]	Safety factor for water pressure force (= 1.05)
ϑ	[°]	Sliding angle
ϑ_{crit}	[°]	Critical sliding angle
λ	[-]	Filter coefficient (a measure of the efficiency of clarification of the suspension)
λ_0	[-]	Initial value of the filter coefficient at t = 0 s
μ	[mPa.s, cp]	Viscosity
μ_a	[mPa.s, cp]	Apparent viscosity
μ_{Bing}	[mPa.s, cp]	Bingham (Plastic) viscosity
$\mu_{carrier}$	[mPa.s, cp]	Viscosity of carrier fluid
$\mu_{dyn,s}$	[mPa.s, cp]	Dynamic viscosity of slurry
μ_{HB}	[mPa.s, cp]	Viscosity of slurry (Herschel-Bulkley)

$\mu_{stat,s}$	[mPa.s, cp]	Static viscosity of slurry
μ_w	[mPa.s, cp]	Dynamic viscosity of water
ρ_{bulk}	[g/cm^3]	Bulk density of soil
$\rho_{carrier}$	[g/cm^3]	Density of carrier fluid
$\rho_{d,max}$	[g/cm^3]	Dry density in the densest state of soil
$\rho_{d,min}$	[g/cm^3]	Dry density in its loosest state of soil
ρ_d	[g/cm^3]	Dry density of soil
ρ_{fluid}	[g/cm^3]	Density of fluid
ρ_s	[g/cm^3]	Grain density (density of solid constituents)
σ_s	[kPa, kN/m^2]	Surcharge on the surface (traffic load)
σ_{spec}	[-]	Specific deposit
$\sigma_{u,spec}$	[-]	Ultimate saturation value of the specific deposit
$\sigma_{v,axis}$	[kPa, kN/m^2]	Total vertical stress at the tunnel axis
$\sigma_{v,crown,min}$	[kPa, kN/m^2]	Total vertical stress in the tunnel crown considering minimal unit weight of soil
$\sigma_v(t_{crown})$	[kPa, kN/m^2]	Vertical surcharge from the prism on the wedge
$\sigma_v(z)$	[kPa, kN/m^2]	Vertical stress at the elevation *z*
τ	[Pa, N/m^2]	Shear stress
τ_{1000}	[Pa, N/m^2]	Shear stress reading from the viscometer at RPM 1000
τ_{300}	[Pa, N/m^2]	Shear stress reading from the viscometer at RPM 300
τ_{600}	[Pa, N/m^2]	Shear stress reading from the viscometer at RPM 600
$\tau_{G'}$	[Pa, N/m^2]	Gel strength of slurry
$\tau_{f,0}$	[Pa, N/m^2]	Yield point immediately after mixing the slurry

$\tau_{f,dyn}$	[Pa, N/m^2]	Dynamic yield point of slurry
$\tau_{f,s}$	[Pa, N/m^2]	Static yield point of slurry
τ_f	[Pa, N/m^2]	Yield point of slurry
$\tau_{y,B}$	[Pa, N/m^2]	Bingham yield point of slurry
$\tau_{y,HB}$	[Pa, N/m^2]	Herschel-Bulkley yield point of slurry
φ'	[°]	Characteristic drained friction angle of the soil
φ'_1	[°]	Characteristic drained friction angle of the soil within silo
φ'_2	[°]	Characteristic drained friction angle of the soil within wedge
ϕ	[m]	Slurry excess pressure head in the excavation chamber
$\phi(x)$	[m]	Pore pressure head in dependence on the distance to the tunnel face
ϕ_0	[m]	Excess pore pressure head at the interface between pressure transfer mechanism and soil

LIST OF ABBREVIATIONS

Approx.	Approximately
AR	Advance rate
DFG	Deutsche Forschungsgemenischaft (German research foundation)
DIN	Deutsche Institut für Normung e. V.
Eff.	Effective
FE	Finite elements
GL	Ground level
GWL	Groundwater level
HPT	Heterogeneous pressure transfer
Max	Maximum
Min	Minimum
No.	Number
P1	Excavation reference project P1
P2	Excavation reference project P2
P3	Excavation reference project P3

PR	Penetration rate
PTFE	Polytetrafluoroethylene
PWD	Pore pressure sensor
Rep.	Re-penetration
Ril	Richtlinie / DB Netz, Deutsche Bahn Gruppe
RPM	Revolutions per minute
RUB	Ruhr-University Bochum
SFB	Sonderforschungsbereich (Collaborative research centre)
TBM	Tunnel boring machine (here considered equivalent to a soft-soil shield machine)
Vs.	Versus
WZ	Total stress sensor
ZTV-ING	Zusätzliche Technische Vertragsbedingungen und Richtlinien für Ingenieurbauten

CURRICULUM VITAE

Personal Information

Name:	Zdenek Zizka
Title:	Ing.
Date and Place of Birth:	25 October 1986, Pelhrimov (Czechoslovakia)
Nationality:	Czech
E-mail:	zdenek.zizka@gmail.com

Professional Experience

Since 08/2018	Tunnel designer METROPROJEKT Praha a.s., Prague (Czech Republic)
08/2012 – 06/2018	Research Assistant Institute for Tunnelling and Construction Management, Ruhr-Universität Bochum (Germany)
04/2017 – 06/2018	Tunnelling consultant Freelance Bochum (Germany)
03/2012 – 09/2016	Tunnelling Engineer Maidl Tunnelconsultants GmbH & Co. KG, Duisburg & Munich (Germany)

Education

10/2011 – 01/2012	Civil Engineering M.Sc., Ruhr-Universität Bochum (Germany) – study visit
10/2010 – 06/2012	Geotechnical Engineering Ing., Czech Technical University, Prague (Czech Republic) – Master degree
10/2008 – 02/2009	Civil Engineering B.Sc., Technische Universität Dresden (Germany), Herbert-Quandt Scholarship for study visit
10/2006 – 06/2010	Civil Engineering Bc., Czech Technical University, Prague (Czech Republic) – Bachelor degree
09/1998 – 06/2006	Christian Doppler Gymnasium (High school), Prague (Czech Republic)

APPENDIX

In this section, the detailed testing procedures and the protocols of the experiments conducted in the frame of this study are attached as well as all relevant diagrams and additional information, to which it was addressed in the main chapters.

A. APPENDIX

A.1 Parameter sheets of products used in testing 2
A.1.1 Grain distribution curves of soils 2
A.1.2 Product sheet of Bentonite B1 3
A.1.3 Properties of slurries – Case A 4
A.1.4 Properties of slurries – Case B 6
A.2 Case A tests 9
A.2.1 Setup and testing procedure 9
A.2.2 Testing protocols 12
A.2.3 Diagrams 23
A.3 Case B – column tests 30
A.3.1 Set-up and testing procedure 30
A.3.2 Testing protocols 35
A.3.3 Diagrams 48
A.4 Case B – RUB tunnelling device 71
A.4.1 Setup and testing procedure 71
A.4.2 Testing protocols 74
A.4.3 **Diagrams** 78

A.1 Parameter sheets of products used in testing

A.1.1 Grain distribution curves of soils

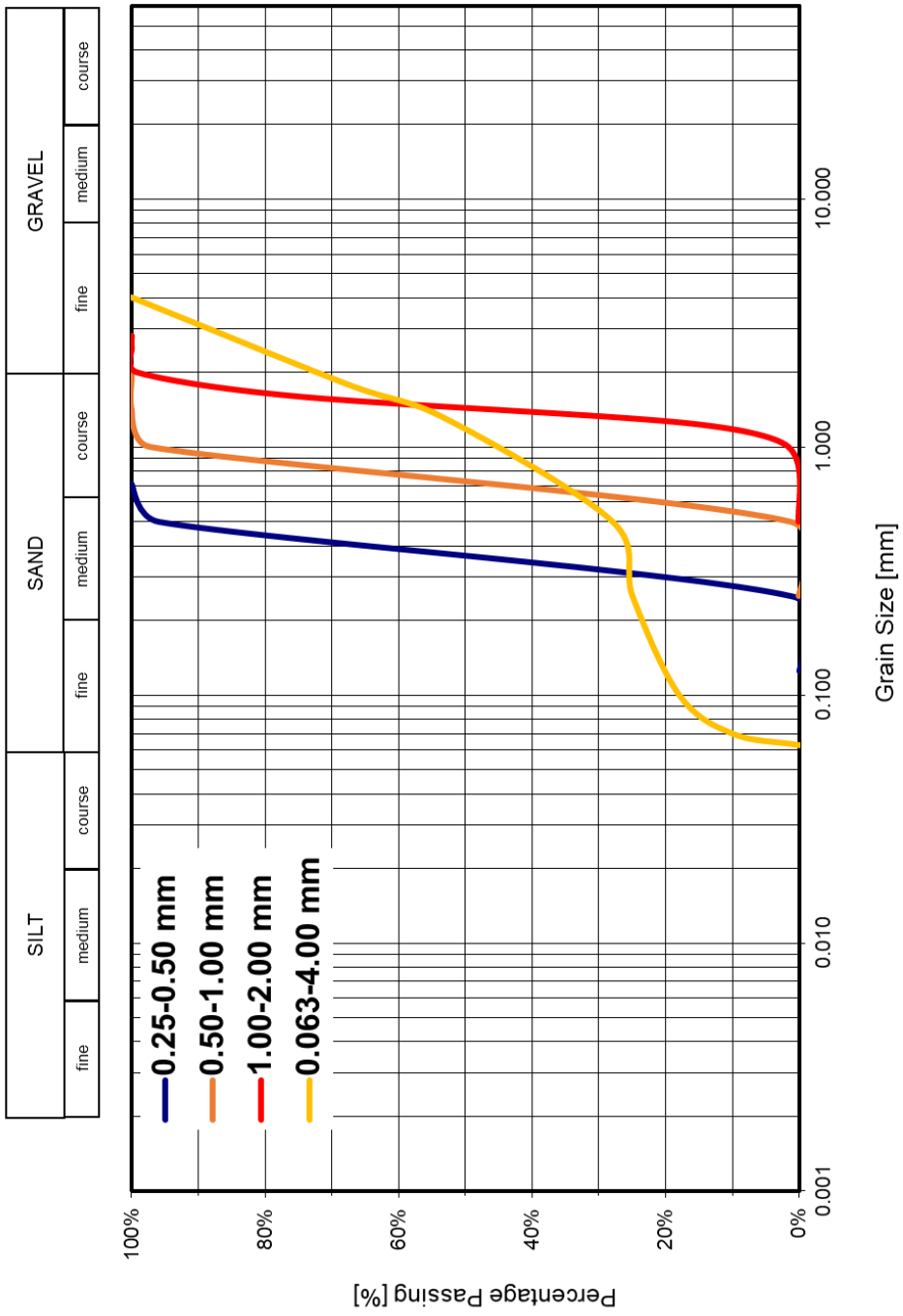

A.1.2 Product sheet of Bentonite B1

S&B Industrial Minerals GmbH

IBECO®

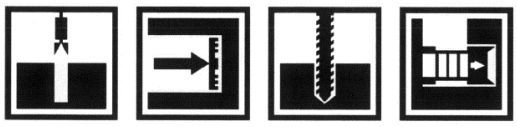

Aktiv-Bentonit IBECO B1

Beschreibung	Description	Description
Natriumbentonit	Sodium bentonite	Bentonite sodique
Anwendung	**Application**	**Application**
• Schlitzwand • Schildvortrieb • Stützflüssigkeit bei Bohrarbeiten • Rohrvortrieb	• Diaphragm walling • Tunnel boring works • Supporting slurry for drilling works • Pipe jacking	• Parois moulées • Bouclier à pression de boue • Boues support pour travail de forage • Foncage du tuyaux

	Technische Durchschnittswerte	Technical values (average)	Valeur techniques (moyenne)		
w	Wassergehalt DIN 18121	Water content	Teneur d'eau	10 ± 2	%
ρ_s	Korndichte DIN 18124	Specific density	Poids spécifique	2,65	g/cm³
ρ'_s	Dichte im Anlieferungszustand DIN 4127,3.7	Specific density as received	Poids spécifique livré	2,30 ± 0,06	g/cm³
	Schüttdichte	Bulk density	Densité apparente tassée	800 ± 50	g/l
	Mahlfeinheit d_w auf Sieb 0,063mm DIN 53734	Dry screen residue on sieve 0,063 mm	Refus au tamis (voie sèche) 0,063 mm	20 ± 5	%

	Suspensions-kennwerte	Rheological Properties	Caractéristiques Rhéologiques		Tongehalt in kg/m³ Dosage of bentonite in kg/m³ Concentration de bentonite en kg/m³			
					30	40	50	60
ρ_F	Suspensionsdichte	Slurry density	Densité de gel	t/m³	1,015	1,022	1,028	1,034
f	Filtratwasserabgabe	Filtrate volume	Volume de filtrat	ml	14	12	11	10
f	Filtratwasser EN 1538	Filtrate EN 1538	Vol. de filtrat EN 1538	ml	< 30			
τ_F	Fließgrenze (Kugel) DIN 4126	Liquid limit (ball)	Rigidité (billes)	N/m²	< 5,8	12	30	58
τ_F	Fließgrenze (Pendel) DIN 4127	Liquid limit (pendulum)	Rigidité (pendule)	N/m²	6	16	32,5	59
	Marsh-Zeit EN 1538	Marsh viscosity	Viscosité marsh	s/l	31	35	40	50
	Scheinbare Viskosität API RP 13B	Apparent viscosity API RP 13B	Viscosité apparente	mPas	5,5	8	11	16
	Plastische Viskosität API RP 13B	Plastic viscosity API RP 13B	Viscosité plastiquee	mPas	3	3,5	4	4
	Bingham Fließgrenze API RP 13B	Bingham Liquid limit API RP 13B	Bingham Rigidité API RP 13B	Pa	5	8	11	17

Anmerkung	Remark	Remarque
Nach DIN 4127 Punkt 5 können die Fließgrenzwerte um ± 35 % und die Filtratwasserwerte um ± 30 % von den angegebenen Werten abweichen.	According to DIN 4127 item 5 there is an allowed tolerance from the given values of ± 35 % for the static shear strength and of ± 30 % for the filtrate.	La norme DIN 4127 § 5 admet des écarts de ± 35 % pour la rigidité et de ± 30 % pour le filtrat.
Lieferform	**Delivery**	**Livraison**
• Lose per Silo-Lkw • In Säcken, auf Paletten, geschrumpft • In Big Bags	• Bulk per road tanker • In bags on pallets, shrink wrapped • In big bags	• Vrac en camion-silo • En sacs sur palette filmée • En big bags
Da wir auf die Verwendung unseres Produktes keinen Einfluss nehmen können, beschränkt sich unsere Haftung auf diese Produktinformation.	The values listed are indicative and are not to be construed as rigid specifications.	Les renseignements contenus dans cette fiche technique sont fournis à titre indicatif et ne peuvent engager notre responsabilité.

S&B Industrial Minerals GmbH
- Geschäftsbereich IBECO -
Ruhrorter Straße 72 • D – 68219 Mannheim • Tel.+49 6 21 / 8 04 27-0 • Fax +49 6 21 / 8 04 27-50

AMAN/HSPE 0606

A.1.3 Properties of slurries – Case A

Experiment name		1a	1b	1c	2a	2b	2c
Date		14.07.2017	14.07.2017	14.07.2017	05.07.2016	13.07.2016	20.07.2016
Slurry		B1-5.5%	B1-5.5%	B1-5.5%	B1-6%	B1-6%	B1-6%
Density [g/cm³]		1.0308	1.0308	1.0308	1.0341	1.0342	1.0338
Yield point (ball harp) [N/m²]		58.56	58.56	58.56	54.98	58.54	58.53
Marsh time [s]	tm1000	68	68	68	50	48	50
	tm1500	179	179	179	99	95	105
	delta tm	111	111	111	49	47	55
pH [-]		9.81	9.81	9.81	9.85	9.45	9.4
Dynamic viscosity [N/m²]		8.1	8.1	8.1	4.9	5.2	6.1

Experiment name		3a	3b	3c	4a	4b	4c
Date		05.07.2016	14.07.2016	20.07.2016	13.07.2016	15.07.2016	20.07.2016
Slurry		B1-6%	B1-6%	B1-6%	B1-6%	B1-6%	B1-6%
Density [g/cm³]		1.0341	1.0355	1.0338	1.0342	1.0349	1.0338
Yield point (ball harp) [N/m²]		54.98	58.52	58.53	58.54	47.9	58.53
Marsh time [s]	tm1000	50	48	50	48	54	50
	tm1500	99	99	105	95	106	105
	delta tm	49	51	55	47	52	55
pH [-]		9.85	9.42	9.4	9.45	9.4	9.4
Dynamic viscosity [N/m²]		4.9	6.1	6.1	5.2	5	6.1

Experiment name		5a	5b	5c	6a	6b	6c
Date		06.09.2017	05.09.2017	05.09.2017	09.02.2016	11.05.2016	16.06.2016
Slurry		B1-5.5%	B1-5.5%	B1-5.5%	B1-6%	B1-6%	B1-6%
Density [g/cm³]		1.0339	1.0344	1.0344	1.04	1.0356	1.0376
Yield point (ball harp) [N/m²]		58.53	58.53	58.53	47.92	58.51	58.5
Marsh time [s]	tm1000	64	73	73	54	54	52
	tm1500	168	188	188	114	124	104
	delta tm	104	115	115	60	70	52
pH [-]		9.52	9.47	9.47	10.32	9.89	9.85
Dynamic viscosity [N/m²]		8.7	10	10	6	7	5.2

Experiment name		7a	7b	7c	8a	8b	8c
Date		16.06.2016	09.02.2016	13.05.2016	29.06.2016	13.05.2016	17.02.2016
Slurry		B1-6%	B1-6%	B1-6%	B1-6%	B1-6%	B1-6%
Density [g/cm³]		1.0376	1.04	1.0353	1.0393	1.0353	1.033
Yield point (ball harp) [N/m²]		58.5	47.92	54.98	58.48	54.98	58.54
Marsh time [s]	tm1000	52	54	51	51	51	55
	tm1500	104	114	102	109	102	116
	delta tm	52	60	51	58	51	61
pH [-]		9.85	10.32	9.83	9.32	9.83	10.3
Dynamic viscosity [N/m²]		5.2	6	5	6	5	5.9

Experiment name		9a	9b	9c	10a	10b	11a
Date		24.08.2016	25.08.2016	26.08.2016	31.08.2016	08.09.2016	01.09.2016
Slurry		B1-6%	B1-6%	B1-6%	B1-6%	B1-6%	B1-6%
Density [g/cm³]		1.0331	1.0348	1.033	1.0341	1.0347	1.0359
Yield point (ball harp) [N/m²]		58.54	58.52	58.54	58.79	58.52	58.51
Marsh time [s]	tm1000	49	50	50	50	50	53
	tm1500	105	98	104	97	100	99
	delta tm	56	48	54	47	50	46
pH [-]		9.4	9.85	9.4	9.9	9.74	9.86
Dynamic viscosity [N/m²]		6.2	4.7	5.8	4.6	5	3.1

Experiment name		11b	12a	12b
Date		09.09.2016	02.09.2016	09.09.2016
Slurry		B1-6%	B1-6%	B1-6%
Density [g/cm³]		1.0356	1.0351	1.0356
Yield point (ball harp) [N/m²]		58.51	58.52	58.51
Marsh time [s]	tm1000	51	49	51
	tm1500	100	101	100
	delta tm	49	52	49
pH [-]		9.81	9.88	9.81
Dynamic viscosity [N/m²]		4.4	5.9	4.4

A.1.4 Properties of slurries – Case B

Experiment name		Ia	Ib	Ic	IIa	IIb	IIc
Date		19.07.2016	21.07.2016	26.07.2016	14.09.2016	10.04.2018	10.04.2018
Slurry		B1-6%	B1-6%	B1-6%	B1-6%	B1-6%	B1-6%
Density [g/cm³]		1.0338	1.0341	1.034	1.0358	1.036	1.036
Yield point (ball harp) [N/m²]		58.5	58.5	58.5	58.5	57.74	57.74
Marsh time [s]	tm1000	50	50	51	48	66	66
	tm1500	105	96	101	86	155	155
	delta tm	55	46	50	38	89	89
pH [-]		9.4	9.43	9.89	9.86	10.7	10.7
Dynamic viscosity [N/m²]		5.5	4.5	5	2.5	7	7

Experiment name		IIIa	IIIb	IIIc	IVa	IVb	IVc
Date		30.08.2016	01.09.2016	12.09.2016	24.11.2017	27.11.2017	27.11.2017
Slurry		B1-6%	B1-6%	B1-6%	B1-6%	B1-6%	B1-6%
Density [g/cm³]		1.0332	1.0359	1.0312	1.036	1.035	1.035
Yield point (ball harp) [N/m²]		69.04	58.5	58.6	57.74	57.75	57.75
Marsh time [s]	tm1000	63	53	50	66	74	74
	tm1500	133	99	97	149	185	185
	delta tm	70	47	47	83	111	111
pH [-]		9.81	9.86	9.87	9.29	9.28	9.28
Dynamic viscosity [N/m²]		5	4	4.5	5.5	7	7

Experiment name		Va	Vb	Vc	VIa	VIb	VIc
Date		10.01.2018	10.01.2018	16.01.2018	16.01.2018	16.01.2018	23.01.2018
Slurry		B1-6%	B1-6%	B1-6%	B1-6%	B1-6%	B1-6%
Density [g/cm³]		1.036	1.036	1.044	1.044	1.044	1.038
Yield point (ball harp) [N/m²]		57.74	57.74	57.67	57.67	57.67	57.72
Marsh time [s]	tm1000	64	64	62	62	62	58
	tm1500	144	144	132	132	132	119
	delta tm	80	80	70	70	70	61
pH [-]		9.16	9.16	9.03	9.03	9.03	8.75
Dynamic viscosity [N/m²]		5	5	4	4	4	5

Experiment name		VIIa	VIIb	VIIIa	VIIIb
Date		04.05.2017	04.05.2017	10.05.2017	10.05.2017
Slurry		B1-6%	B1-6%	B1-6%	B1-6%
Density [g/cm³]		1.039	1.039	1.038	1.038
Yield point (ball harp) [N/m²]		47.87	47.87	47.87	47.87
Marsh time [s]	tm1000	53	53	54	54
	tm1500	118	118	116	116
	delta tm	66	66	63	63
pH [-]		10.81	10.81	10.76	10.76
Dynamic viscosity [N/m²]		6.5	6.5	6	6

Experiment name		r - Ia	r - Ib	r- Ic	r- IIa	r - IIb	r - IIc
Date		29.11.2017	29.11.2017	04.12.2017	18.12.2017	18.12.2017	18.12.2017
Slurry		B1 - 6%	B1 - 6%	B1 - 6%	B1 - 6%	B1 - 6%	B1 - 6%
Density [g/cm³]		1.041	1.041	1.043	1.039	1.039	1.039
Yield point (ball harp) [N/m²]		57.69	57.69	57.4	57.71	57.71	57.71
Marsh time [s]	tm1000	70	70	68	67	67	67
	tm1500	174	174	176	176	176	176
	delta tm	104	104	108	109	109	109
pH [-]		9.26	9.26	9.28	9.35	9.35	9.35
Dynamic viscosity [N/m²]		7.8	7.8	8.1	8.1	8.1	8.1

Experiment name		r - IIIa	r - IIIb	r - IIIc	r - Va	r - Vb	r - Vc
Date		13.12.2017	13.12.2017	13.12.2017	23.01.2018	23.01.2018	24.01.2018
Slurry		B1 - 6%	B1 - 6%	B1 - 6%	B1 - 6%	B1 - 6%	B1 - 6%
Density [g/cm³]		1.04	1.04	1.04	1.038	1.038	1.048
Yield point (ball harp) [N/m²]		57.7	57.7	57.7	57.72	57.72	57.63
Marsh time [s]	tm1000	66	66	66	58	58	58
	tm1500	174	174	174	119	119	120
	delta tm	108	108	108	61	61	62
pH [-]		9.3	9.3	9.3	8.75	8.75	8.99
Dynamic viscosity [N/m²]		8	8	8	5	5	5.2

Experiment name		r - VIa	r - VIb	r - VIc
Date		24.01.2018	24.01.2018	30.01.2018
Slurry		B1 - 6%	B1 - 6%	B1 - 6%
Density [g/cm³]		1.048	1.048	1.045
Yield point (ball harp) [N/m²]		57.63	57.63	57.66
Marsh time [s]	tm1000	58	58	59
	tm1500	120	120	127
	delta tm	62	62	68
pH [-]		8.99	8.99	9.35
Dynamic viscosity [N/m²]		5.2	5.2	4.3

Experiment name		rc - Ia	rc - Ib	rc - Ic	rc - IIa	rc - IIb	rc - IIc
Date		22.03.2017	23.03.2017	30.03.2017	08.02.2017	21.02.2017	02.03.2017
Slurry		B1 - 6%	B1 - 6%	B1 - 6%	B1 - 6%	B1 - 6%	B1 - 6%
Density [g/cm³]		1.038	1.0387	1.039	1.0397	1.038	1.038
Yield point (ball harp) [N/m²]		47.88	47.87	47.87	47.89	47.878	47.878
Marsh time [s]	tm1000	49	53	59	50	49	48
	tm1500	116	118	120	124	111	116
	delta tm	67	65	61	74	62	68
pH [-]		10.51	10.81	10.8	10.56	10.49	10.51
Dynamic viscosity [N/m²]		7	6.5	4.5	8.1	7	8

Experiment name		rc - IIIa	rc - IIIb	rc - IIIc	rc - IVa	rc - IVb	rc - IVc
Date		21.02.2018	21.02.2018	06.06.2018	19.02.2018	20.02.2018	20.02.2018
Slurry		B1 - 6%	B1 - 6%	B1 - 6%	B1 - 6%	B1 - 6%	B1 - 6%
Density [g/cm³]		1.031	1.031	1.032	1.035	1.031	1.031
Yield point (ball harp) [N/m²]		57,78	57,78	58.55	48.34	57,78	57,78
Marsh time [s]	tm1000	90	90	114	82	96	96
	tm1500	not determinable	not determinable	not determinable	not determinable	not determinable	not determinable
	delta tm	not determinable	not determinable	not determinable	not determinable	not determinable	not determinable
pH [-]		10.61	10.61	10.4	10.69	10.75	10.75
Dynamic viscosity [N/m²]		not determinable	not determinable	not determinable	not determinable	not determinable	not determinable

A.2 Case A tests

Tests for the investigation of slurry-soil interaction for a shallow slurry penetration were introduced in chapter 6.

A.2.1 Setup and testing procedure

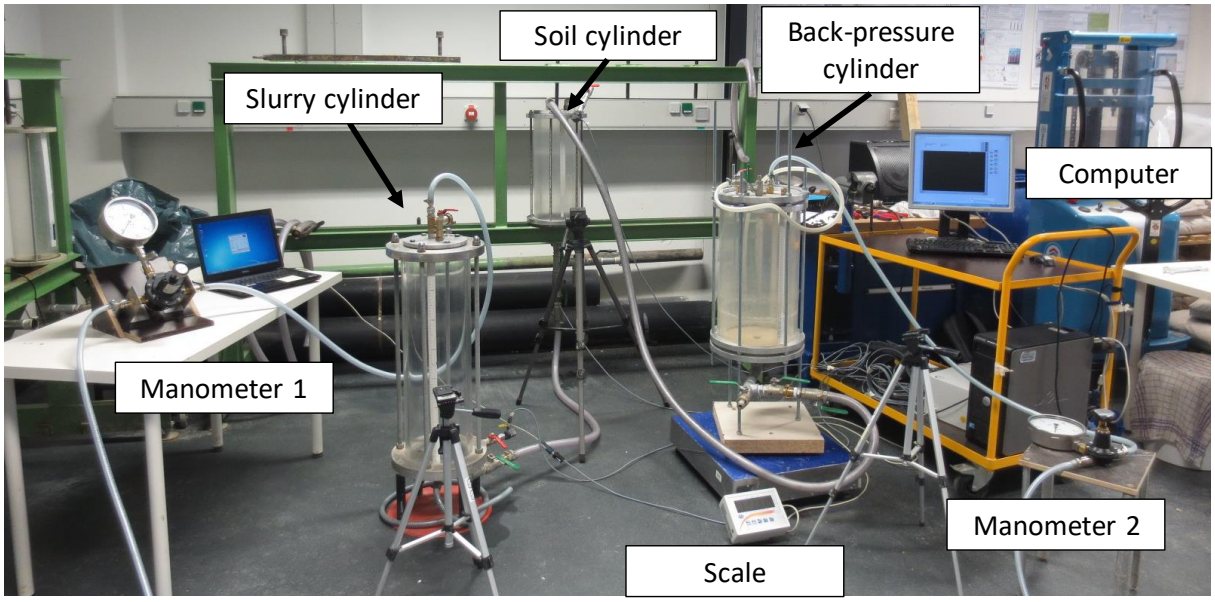

Figure A-2-1: Photo of set-up for the testing of shallow slurry penetration – Case A (Variant with back-pressure)

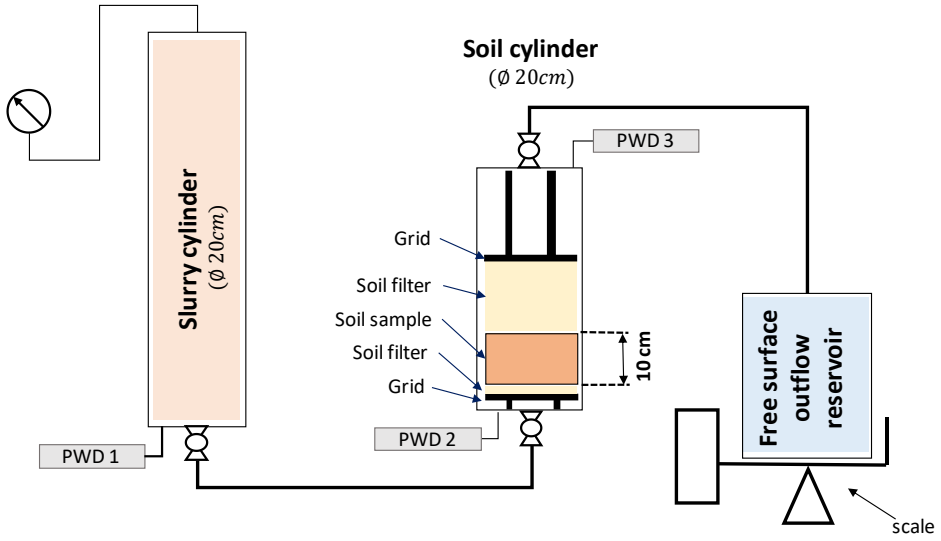

Figure A-2-2: Schema of set-up for the testing of shallow slurry penetration – Case A

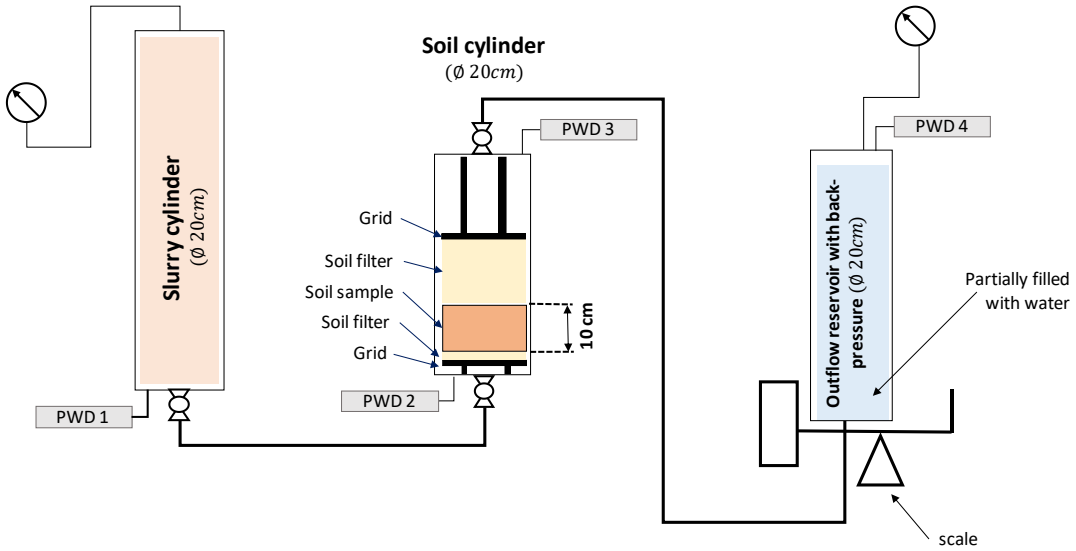

Figure A-2-3: Schema of set-up for the testing of shallow slurry penetration – Case A with the back-pressure

Equipment

- 1 slurry cylinder
- 1 soil cylinder
- 1 bucket/outflow cylinder
- 2 grids (the grids are similar to those visualized in Figure A-3-5)
- 2 pipes
- 1-2 computer connected scales*
- 1 stopwatch
- 1 computer
- 2 video cameras + tripods
- 1 -2 manometers for pressure steering*
- 3-4 pore water pressure sensors (PWD)* connected to the computer

*depends on variant with/without back-pressure

Preparation

1. Slurry mixing 24 hour before the experiment
2. Check of slurry properties the day before the test starts
3. Installation of bottom grid at bottom of soil cylinder

4. Installation of bottom filter soil and compaction to the prescribed porosity
5. Installation of soil sample and compaction to the prescribed porosity
6. Installation of bottom filter soil and compaction to the prescribed porosity
7. Connecting all pipes between cylinders
8. Water saturation of the cylinder for 45-60 minutes
9. Water permeability test
10. Slow pumping of slurry up to the interface between filter soil and investigated soil sample

Procedure

11. Opening valve and starting of slurry penetration
12. Recording of the outflow from the set-up by scale and monitoring of pore water pressure in the set-up every 0.25 s, recording the slurry levels in the cylinder by camera
13. End of the experiment after minimally 15 minutes
14. Visual determination of the maximal slurry penetration depth during dismantling

A.2.2 Testing protocols

Date:	14.07.2017	14.07.2017	14.07.2017
Experiment No:	**1a**	**1b**	**1c**
Installation of the test soil			
Grain size of the test soil [mm]	0.25-0.50	0.25-0.50	0.25-0.50
Grain size of the filter bottom [mm]	2-4	2-4	2-4
Grain size of the filter top [mm]	2-4	2-4	2-4
Weight of the installed test soil [kg]	4.94	4.94	4.94
Weight of the installed filter bottom [kg]	1.16	1.45	1.31
Weight of the installed filter top [kg]	8.45	8.53	8.36
Height of the installed test soil [m]	0.100	0.100	0.100
Height of the installed filter bottom [m]	0.025	0.025	0.025
Height of the installed filter top [m]	0.175	0.175	0.175
Slurry properties			
Type of bentonite	B1	B1	B1
Concentration [%]	5.5	5.5	5.5
Date of mixing	13.07.2017	13.07.2017	13.07.2017
pH-value [-]	9.81	9.81	9.81
Density of the slurry [g/cm³]	1.031	1.031	1.031
Marsh-time tM,1000 [s]	68	68	68
Marsh-time tM,1500 [s]	179	179	179
Ball harp number	9	9	9
(stat.) Yield point [N/m²]	58.56	58.56	58.56
Water permeability test			
Injection pressure [bar]	0.2	0.2	0.2
Back presure [bar]	0	0	0
Filling level in the slurry cylinder at the start [cm]	60.5	60.2	59.5
Filling level in the slurry cylinder at the end [cm]	9.4	12.5	12.5
Time of experiment [s]	178	203	169
Outflow [kg]	15.93	14.85	14.65
Slurry permeability test			
Injection pressure [bar]	0.2	0.2	0.2
Back pressure [bar]	0	0	0
Filling level in the slurry cylinder at the start [cm]	52.5	52.7	49
Filling level in the slurry cylinder at the end [cm]	48	48.7	44.6
Slurry at top test soil [s]	not reached	not reached	not reached
Slurry at top filter [s]	not reached	not reached	not reached
Time of experiment [s]	1140	1080	960
Outflow [kg]	1.396	1.229	1.26
Penetration depth [cm]	0.8	0.5	0.6

Date:	05.07.2016	13.07.2016	20.07.2016
Experiment No:	**2a**	**2b**	**2c**
Installation of the test soil			
Grain size of the test soil [mm]	0.25-0.50	0.25-0.50	0.25-0.50
Grain size of the filter bottom [mm]	2-4	2-4	2-4
Grain size of the filter top [mm]	2-4	2-4	2-4
Weight of the installed test soil [kg]	4.94	4.94	4.94
Weight of the installed filter bottom [kg]	1.35	1.5	1.59
Weight of the installed filter top [kg]	8.34	8.32	8.6
Height of the installed test soil [m]	0.100	0.1	0.1
Height of the installed filter bottom [m]	0.025	0.025	0.025
Height of the installed filter top [m]	0.175	0.175	0.175
Slurry properties			
Type of bentonite	B1	B1	B1
Concentration [%]	6	6	6
Date of mixing	04.07.2016	12.07.2016	19.07.2016
pH-value [-]	9.85	9.45	9.4
Density of the slurry [g/cm³]	1.034	1.034	1.034
Marsh-time tM,1000 [s]	50	48	50
Marsh-time tM,1500 [s]	99	95	105
Ball harp number	8/9/9	9	9
(stat.) Yield point [N/m²]	54.98	58.54	58.53
Water permeability test			
Injection pressure [bar]	0.3	0.3	0.3
Back pressure [bar]	0	0	0
Filling level in the slurry cylinder at the start [cm]	59.1	55.7	58
Filling level in the slurry cylinder at the end [cm]	7.5	5.9	9.6
Time of experiment [s]	119	111	114
Outflow [kg]	16.07	15.54	15.14
Slurry permeability test			
Injection pressure [bar]	0.3	0.3	0.3
Back pressure [bar]	0	0	0
Filling level in the slurry cylinder at the start [cm]	50.8	47	40.7
Filling level in the slurry cylinder at the end [cm]	45.9	41.8	36
Slurry at top test soil [s]	not reached	not reached	not reached
Slurry at top filter [s]	not reached	not reached	not reached
Time of experiment [s]	1200	1200	1200
Outflow [kg]	0.28	0.31	0.34
Penetration depth [cm]	1.5	1.2	1.4

Date:	13.07.2016	15.07.2016	20.07.2016
Experiment No:	**4a**	**4b**	**4c**
Installation of the test soil			
Grain size of the test soil [mm]	0.25-0.50	0.25-0.50	0.25-0.50
Grain size of the filter bottom [mm]	2-4	2-4	2-4
Grain size of the filter top [mm]	2-4	2-4	2-4
Weight of the installed test soil [kg]	4.94	4.94	4.94
Weight of the installed filter bottom [kg]	1.49	1.26	1.54
Weight of the installed filter top [kg]	8.58	8.62	8.63
Height of the installed test soil [m]	0.100	0.1	0.1
Height of the installed filter bottom [m]	0.025	0.025	0.025
Height of the installed filter top [m]	0.175	0.175	0.175
Slurry properties			
Type of bentonite	B1	B1	B1
Concentration [%]	6	6	6
Date of mixing	12.07.2016	14.07.2016	19.07.2016
pH-value [-]	9.45	9.4	9.4
Density of the slurry [g/cm³]	1.034	1.035	1.034
Marsh-time tM,1000 [s]	48	54	50
Marsh-time tM,1500 [s]	95	106	105
Ball harp number	9	8	9
(stat.) Yield point [N/m²]	58.54	47.9	58.53
Water permeability test			
Injection pressure [bar]	0.7	0.7	0.7
Back pressure [bar]	0	0	0
Filling level in the slurry cylinder at the start [cm]	60	62.5	59.9
Filling level in the slurry cylinder at the end [cm]	6	0.5	7.5
Time of experiment [s]	86	60	85
Outflow [kg]	16.77	19.67	16.29
Slurry permeability test			
Injection pressure [bar]	0.7	0.7	0.7
Back pressure [bar]	0	0	0
Filling level in the slurry cylinder at the start [cm]	53.5	45	44
Filling level in the slurry cylinder at the end [cm]	49.9	34.6	39.5
Slurry at top test soil [s]	not reached	not reached	not reached
Slurry at top filter [s]	not reached	not reached	not reached
Time of experiment [s]	1200	1200	1200
Outflow [kg]	0.67	0.61	0.19
Penetration depth [cm]	2.5	2.7	2.5

Date:	06.09.2017	05.09.2017	05.09.2017
Experiment No:	**5a**	**5b**	**5c**
Installation of the test soil			
Grain size of the test soil [mm]	0.5-1.0	0.5-1.0	0.5-1.0
Grain size of the filter bottom [mm]	5.6-8	5.6-8	5.6-8
Grain size of the filter top [mm]	5.6-8	5.6-8	5.6-8
Weight of the installed test soil [kg]	4.94	4.94	4.94
Weight of the installed filter bottom [kg]	1.06	1.24	1.19
Weight of the installed filter top [kg]	8.59	8.67	9.52
Height of the installed test soil [m]	0.100	0.1	0.1
Height of the installed filter bottom [m]	0.025	0.025	0.025
Height of the installed filter top [m]	0.175	0.175	0.175
Slurry properties			
Type of bentonite	B1	B1	B1
Concentration [%]	5.5	5.5	5.5
Date of mixing	05,09,2017	04.09.2017	04.09.2017
pH-value [-]	9.52	9.47	9.47
Density of the slurry [g/cm³]	1.034	1.033	1.033
Marsh-time tM,1000 [s]	64	72	72
Marsh-time tM,1500 [s]	168	187	187
Ball harp number	9	9	9
(stat.) Yield point [N/m²]	58.53	58.53	58.525
Water permeability test			
Injection pressure [bar]	0.2	0.2	0.2
Back pressure [bar]	0	0	0
Filling level in the slurry cylinder at the start [cm]	59.5	58.5	59.9
Filling level in the slurry cylinder at the end [cm]	6	13	7.5
Time of experiment [s]	95	102	105
Outflow [kg]	16.712	14.241	16.454
Slurry permeability test			
Injection pressure [bar]	0.2	0.2	0.2
Back pressure [bar]	0	0	0
Filling level in the slurry cylinder at the start [cm]	39.2	52.8	50.4
Filling level in the slurry cylinder at the end [cm]	34.5	48	45.5
Slurry at top test soil [s]	not reached	not reached	not reached
Slurry at top filter [s]	not reached	not reached	not reached
Time of experiment [s]	900	1200	1200
Outflow [kg]	0.218	0.334	0.336
Penetration depth [cm]	0.8	1.2	1

Date:	09.02.2016	08.06.2016	16.06.2016
Experiment No:	**6a**	**6b**	**6c**
Installation of the test soil			
Grain size of the test soil [mm]	0.5-1.0	0.5-1.0	0.5-1.0
Grain size of the filter bottom [mm]	8.0-16.0	5.6-8	5.6-8
Grain size of the filter top [mm]	8.0-16.0	5.6-8	5.6-8
Weight of the installed test soil [kg]	5.2	4.94	4.94
Weight of the installed filter bottom [kg]	1.33	1.59	1.59
Weight of the installed filter top [kg]	7.55	8.46	8.60
Height of the installed test soil [m]	0.100	0.100	0.100
Height of the installed filter bottom [m]	0.025	0.025	0.025
Height of the installed filter top [m]	0.155	0.175	0.175
Slurry properties			
Type of bentonite	B1	B1	B1
Concentration [%]	6	6	6
Date of mixing	08.02.2016	07.06.2016	15.06.2016
pH-value [-]	10.32	9.84	9.85
Density of the slurry [g/cm³]	1.037	1.039	1.038
Marsh-time tM,1000 [s]	54	51	52
Marsh-time tM,1500 [s]	114	114	104
Ball harp number	8	9	9
(stat.) Yield point [N/m²]	47.92	58.49	58.5
Water permeability test			
Injection pressure [bar]	0.3	0.3	0.3
Back pressure [bar]	0	0	0
Filling level in the slurry cylinder at the start [cm]		61.1	58.4
Filling level in the slurry cylinder at the end [cm]		6.8	6
Time of experiment [s]		36	92
Outflow [kg]		16.94	16.33
Slurry permeability test			
Injection pressure [bar]	0.3	0.3	0.3
Back pressure [bar]	0	0	0
Filling level in the slurry cylinder at the start [cm]	22.2	40.4	35
Filling level in the slurry cylinder at the end [cm]	19	34	29.6
Slurry at top test soil [s]	6	not reached	not reached
Slurry at top filter [s]	540	not reached	not reached
Time of experiment [s]	2700	1260	1415
Outflow [kg]	0.93	0.26	0.42
Penetration depth [cm]	>10	7.5	3.2

Date:	16.06.2016	09.02.2016	08.06.2016
Experiment No:	**7a**	**7b**	**7c**
Installation of the test soil			
Grain size of the test soil [mm]	0.5-1.0	0.5-1.0	0.5-1.0
Grain size of the filter bottom [mm]	5,6-8	8,0-16,0	5,6-8
Grain size of the filter top [mm]	5,6-8	8,0-16,0	5,6-8
Weight of the installed test soil [kg]	4.94	5.2	4.94
Weight of the installed filter bottom [kg]	1.59	1.33	1.66
Weight of the installed filter top [kg]	8.6	7.55	8.43
Height of the installed test soil [m]	0.100	0.100	0.100
Height of the installed filter bottom [m]	0.025	0.025	0.025
Height of the installed filter top [m]	0.175	0.155	0.175
Slurry properties			
Type of bentonite	B1	B1	B1
Concentration [%]	6	6	6
Date of mixing	15.06.2016	08.02.2016	07.06.2016
pH-value [-]	9.85	10.32	9.84
Density of the slurry [g/cm³]	1.038	1.037	1.039
Marsh-time tM,1000 [s]	52	54	51
Marsh-time tM,1500 [s]	104	114	114
Ball harp number	9	8	9
(stat.) Yield point [N/m²]	58.5	47.92	58.49
Water permeability test			
Injection pressure [bar]	0.5	0.5	0.5
Back pressure [bar]	0	0	0
Filling level in the slurry cylinder at the start [cm]	56.9		59.7
Filling level in the slurry cylinder at the end [cm]	5.5		4.6
Time of experiment [s]	52		55
Outflow [kg]	16.1		17.05
Slurry permeability test			
Injection pressure [bar]	0.5	0.5	0.5
Back pressure [bar]	0	0	0
Filling level in the slurry cylinder at the start [cm]	49.1	46.2	41.3
Filling level in the slurry cylinder at the end [cm]	38.1	41.9	29.6
Slurry at top test soil [s]	6	10	6
Slurry at top filter [s]	not reached	14	not reached
Time of experiment [s]	1320	1200	1560
Outflow [kg]	1.73	1.23	1.69
Penetration depth [cm]	>10	>10	>10

Date:	29.06.2016	08.06.2016	17.02.2016
Experiment No:	**8a**	**8b**	**8c**
Installation of the test soil			
Grain size of the test soil [mm]	0.5-1.0	0.5-1.0	0.5-1.0
Grain size of the filter bottom [mm]	5,6-8	5,6-8	8,0-16,0
Grain size of the filter top [mm]	5,6-8	5,6-8	8,0-16,0
Weight of the installed test soil [kg]	4.94	4.94	5.2
Weight of the installed filter bottom [kg]	1.63	1.61	1.33
Weight of the installed filter top [kg]	8.32	8.63	7.55
Height of the installed test soil [m]	0.100	0.100	0.100
Height of the installed filter bottom [m]	0.025	0.025	0.025
Height of the installed filter top [m]	0.175	0.175	0.155
Slurry properties			
Type of bentonite	B1	B1	B1
Concentration [%]	6	6	6
Date of mixing	28.06.2016	07.06.2016	16,02.2016
pH-value [-]	9.32	9.84	not measured
Density of the slurry [g/cm³]	1.039	1.039	1.033
Marsh-time tM,1000 [s]	51	51	55
Marsh-time tM,1500 [s]	109	114	116
Ball harp number	9	9	9
(stat.) Yield point [N/m²]	58.48	58.49	58.54
Water permeability test			
Injection pressure [bar]	0.7	0.7	0.7
Back pressure [bar]	0	0	0
Filling level in the slurry cylinder at the start [cm]	58.2	58.7	
Filling level in the slurry cylinder at the end [cm]	6	6.2	
Time of experiment [s]	76	17	
Outflow [kg]	16.29	16.47	
Slurry permeability test			
Injection pressure [bar]	0.7	0.7	0.7
Back pressure [bar]	0	0	0
Filling level in the slurry cylinder at the start [cm]	44.7	43.6	12.9
Filling level in the slurry cylinder at the end [cm]	25.7	23.3	7.3
Slurry at top test soil [s]	5	3	15
Slurry at top filter [s]	7	not reached	not reached
Time of experiment [s]	1320	1200	900
Outflow [kg]	4.34	4.57	1.52
Penetration depth [cm]	>10	>10	>10

Date:	24.08.2016	25.08.2016	26.08.2016
Experiment No:	**9a**	**9b**	**9c**
Installation of the test soil			
Grain size of the test soil [mm]	0.5-1.0	0.5-1.0	0.5-1.0
Grain size of the filter bottom [mm]	5,6-8	5,6-8	5,6-8
Grain size of the filter top [mm]	5,6-8	5,6-8	5,6-8
Weight of the installed test soil [kg]	4.94	4.94	4.94
Weight of the installed filter bottom [kg]	1.22	1.36	1.40
Weight of the installed filter top [kg]	8.96	8.81	8.76
Height of the installed test soil [m]	0.100	0.100	0.100
Height of the installed filter bottom [m]	0.025	0.025	0.025
Height of the installed filter top [m]	0.175	0.175	0.155
Slurry properties			
Type of bentonite	B1	B1	B1
Concentration [%]	6	6	6
Date of mixing	23.08.2016	24.08.2016	25.08.2016
pH-value [-]	9.4	9.85	9.4
Density of the slurry [g/cm³]	1.033	1.035	1.033
Marsh-time tM,1000 [s]	49	50	50
Marsh-time tM,1500 [s]	105	98	104
Ball harp number	9	9	9
(stat.) Yield point [N/m²]	58.54	58.52	58.54
Water permeability test			
Injection pressure [bar]	1	1	1
Back pressure [bar]	0.57	0.57	0.57
Filling level in the slurry cylinder at the start [cm]	60	59.3	60
Filling level in the slurry cylinder at the end [cm]	3.6	4.2	3.4
Filling level in the bp-cylinder at the start [cm]	14	14	14
Filling level in the bp-cylinder at the end [cm]	42.8	45	44.1
Time of experiment [s]	110	89	90
Outflow [kg]	16.2	17.05	17.2
Slurry permeability test			
Injection pressure [bar]	1	1	1
Back pressure [bar]	0.57	0.57	0.57
Filling level in the slurry cylinder at the start [cm]	48	47.5	49.6
Filling level in the bp-cylinder at the start [cm]	32.5	38	40
Filling level in the bp-cylinder at the end [cm]	14	14	14
Filling level in the slurry cylinder at the end [cm]	19.9	18.5	18.7
Slurry at top test soil [s]	2	2	2
Slurry at top filter [s]	not reached	not reached	not reached
Time of experiment [s]	1140	1200	1200
Outflow [kg]	1.35	1.6	1.65
Penetration depth [cm]	>10	>10	>10

Date:	31.08.2016	08.09.2016
Experiment No:	**10a**	**10b**
Installation of the test soil		
Grain size of the test soil [mm]	0,25-0,50	0,25-0,50
Grain size of the filter bottom [mm]	2-4	2-4
Grain size of the filter top [mm]	2-4	2-4
Weight of the installed test soil [kg]	4.94	4.94
Weight of the installed filter bottom [kg]	1.34	1.25
Weight of the installed filter top [kg]	8.71	8.48
Height of the installed test soil [m]	0.100	0.100
Height of the installed filter bottom [m]	0.025	0.025
Height of the installed filter top [m]	0.175	0.175
Slurry properties		
Type of bentonite	B1	B1
Concentration [%]	6	6
Date of mixing	30.08.2016	07.09.2016
pH-value [-]	9.9	9.74
Density of the slurry [g/cm³]	1.034	1.035
Marsh-time tM,1000 [s]	50	50
Marsh-time tM,1500 [s]	97	100
Ball harp number	9	9
(stat.) Yield point [N/m²]	58.79	58.52
Water permeability test		
Injection pressure [bar]	0.8	0.8
Back pressure [bar]	0.57	0.57
Filling level in the slurry cylinder at the start [cm]	60.3	64.3
Filling level in the slurry cylinder at the end [cm]	7	12.8
Filling level in the bp-cylinder at the start [cm]	14	14
Filling level in the bp-cylinder at the end [cm]	27.01	40.5
Time of experiment [s]	90	107
Outflow [kg]	16.35	15.55
Slurry permeability test		
Injection pressure [bar]	1	1
Back pressure [bar]	0.57	0.57
Filling level in the slurry cylinder at the start [cm]	51	56.6
Filling level in the bp-cylinder at the start [cm]	45.6	507
Filling level in the bp-cylinder at the end [cm]	14	14
Filling level in the slurry cylinder at the end [cm]	16.8	16.9
Slurry at top test soil [s]	not reached	not reached
Slurry at top filter [s]	not reached	not reached
Time of experiment [s]	1200	1200
Outflow [kg]	0.35	0.55
Penetration depth [cm]	1.2	1.2

Date:	01.09.2016	09.09.2016
Experiment No:	**11a**	**11b**
Installation of the test soil		
Grain size of the test soil [mm]	0,25-0,50	0,25-0,50
Grain size of the filter bottom [mm]	2-4	2-4
Grain size of the filter top [mm]	2-4	2-4
Weight of the installed test soil [kg]	4.94	4.94
Weight of the installed filter bottom [kg]	1.52	1.31
Weight of the installed filter top [kg]	8.39	8.69
Height of the installed test soil [m]	0.100	0.100
Height of the installed filter bottom [m]	0.025	0.025
Height of the installed filter top [m]	0.175	0.175
Slurry properties		
Type of bentonite	B1	B1
Concentration [%]	6	6
Date of mixing	31.08.2016	08.09.2016
pH-value [-]	9.86	9.81
Density of the slurry [g/cm³]	1.036	1.036
Marsh-time tM,1000 [s]	53	51
Marsh-time tM,1500 [s]	99	100
Ball harp number	9	9
(stat.) Yield point [N/m²]	58.51	58.51
Water permeability test		
Injection pressure [bar]	1	1
Back pressure [bar]	0.57	0.57
Filling level in the slurry cylinder at the start [cm]	62.2	61.1
Filling level in the slurry cylinder at the end [cm]	10	9.6
Filling level in the bp-cylinder at the start [cm]	14	14
Filling level in the bp-cylinder at the end [cm]	41.3	40.5
Time of experiment [s]	101	99
Outflow [kg]	15.9	15.6
Slurry permeability test		
Injection pressure [bar]	1	1
Back pressure [bar]	0.57	0.57
Filling level in the slurry cylinder at the start [cm]	57.4	57
Filling level in the bp-cylinder at the start [cm]	52.5	50.8
Filling level in the bp-cylinder at the end [cm]	14	14
Filling level in the slurry cylinder at the end [cm]	16.25	16.3
Slurry at top test soil [s]	not reached	not reached
Slurry at top filter [s]	not reached	not reached
Time of experiment [s]	1200	1200
Outflow [kg]	0.3	0.4
Penetration depth [cm]	2	2

Date:	02.09.2016	09.09.2016
Experiment No:	**12a**	**12b**
Installation of the test soil		
Grain size of the test soil [mm]	0,25-0,50	0,25-0,50
Grain size of the filter bottom [mm]	2-4	2-4
Grain size of the filter top [mm]	2-4	2-4
Weight of the installed test soil [kg]	4.94	4.94
Weight of the installed filter bottom [kg]	1.32	1.31
Weight of the installed filter top [kg]	8.6	8.56
Height of the installed test soil [m]	0.100	0.100
Height of the installed filter bottom [m]	0.025	0.025
Height of the installed filter top [m]	0.175	0.175
Slurry properties		
Type of bentonite	B1	B1
Concentration [%]	6	6
Date of mixing	01.09.2016	08.09.2016
pH-value [-]	9.88	9.81
Density of the slurry [g/cm³]	1.035	1.036
Marsh-time tM,1000 [s]	49	51
Marsh-time tM,1500 [s]	101	100
Ball harp number	9	9
(stat.) Yield point [N/m²]	58.52	58.51
Water permeability test		
Injection pressure [bar]	1.2	1.2
Back pressure [bar]	0.57	0.57
Filling level in the slurry cylinder at the start [cm]	64	62
Filling level in the slurry cylinder at the end [cm]	9.8	6
Filling level in the bp-cylinder at the start [cm]	14	14
Filling level in the bp-cylinder at the end [cm]	39.1	44
Time of experiment [s]	87	88
Outflow [kg]	15.05	17.1
Slurry permeability test		
Injection pressure [bar]	1.2	1.2
Back pressure [bar]	0.57	0.57
Filling level in the slurry cylinder at the start [cm]	50.5	48.8
Filling level in the bp-cylinder at the start [cm]	44.5	42.3
Filling level in the bp-cylinder at the end [cm]	14	14
Filling level in the slurry cylinder at the end [cm]	16.6	17.1
Slurry at top test soil [s]	not reached	not reached
Slurry at top filter [s]	not reached	not reached
Time of experiment [s]	1200	1200
Outflow [kg]	0.3	0.75
Penetration depth [cm]	2	2.4

A.2.3 Diagrams

A.2.3.1 Time-dependent slurry penetration

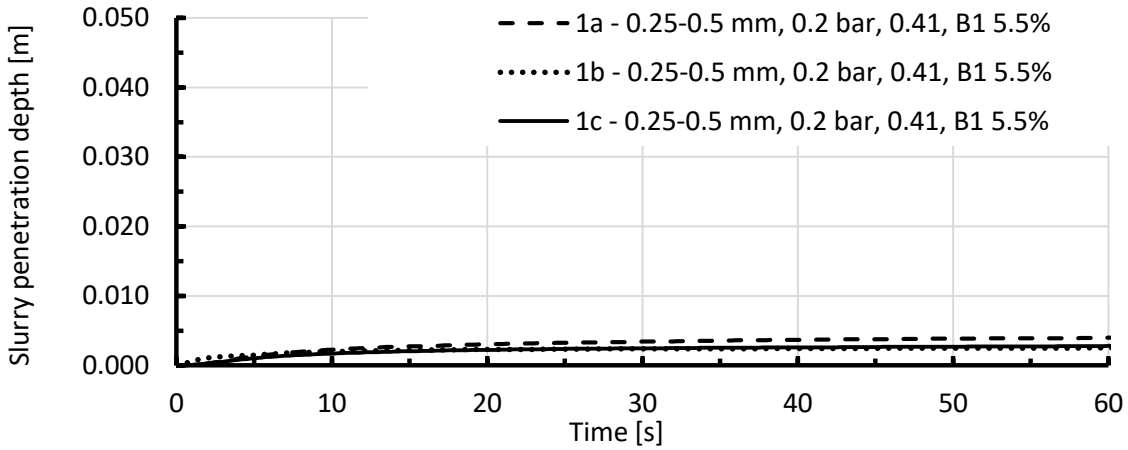

Figure A-2-4: Slurry penetration depth in combination 1

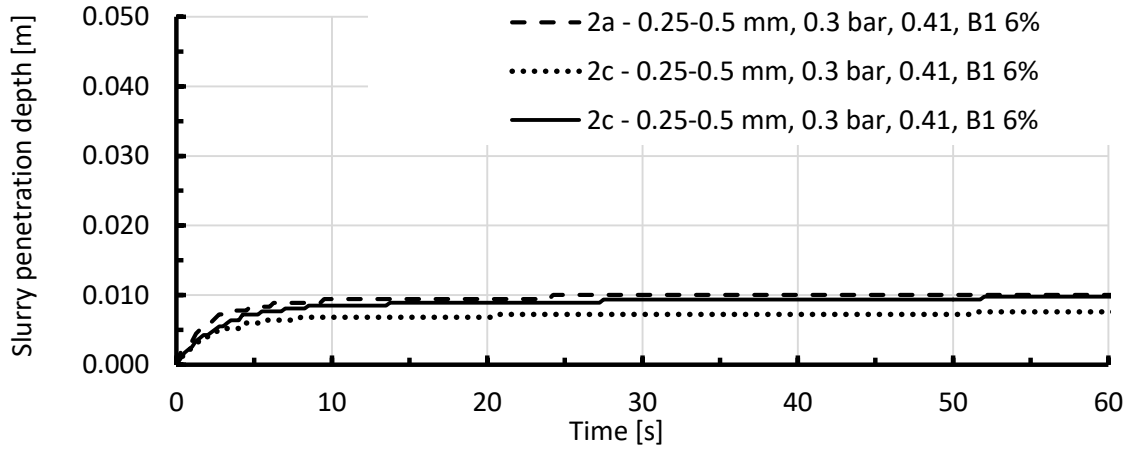

Figure A-2-5: Slurry penetration depth in combination 2

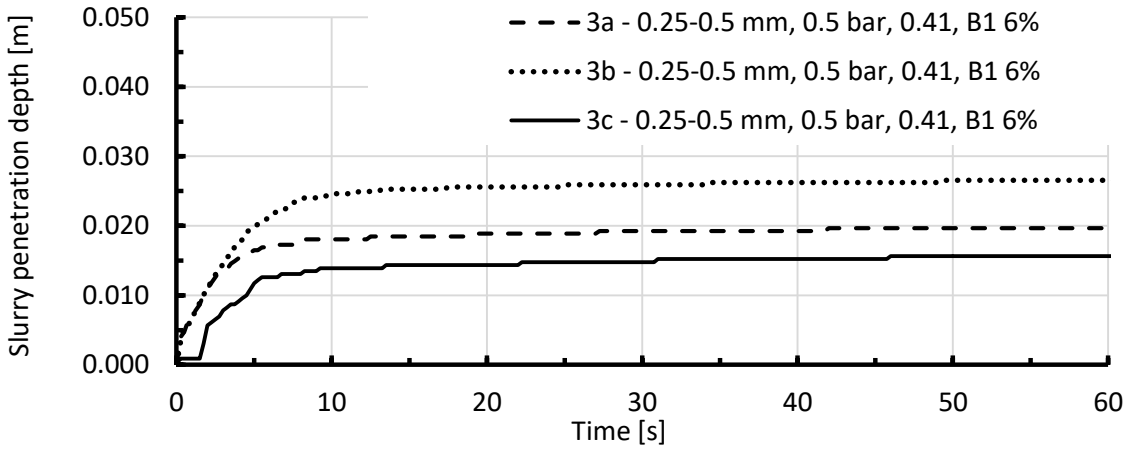

Figure A-2-6: Slurry penetration depth in combination 3

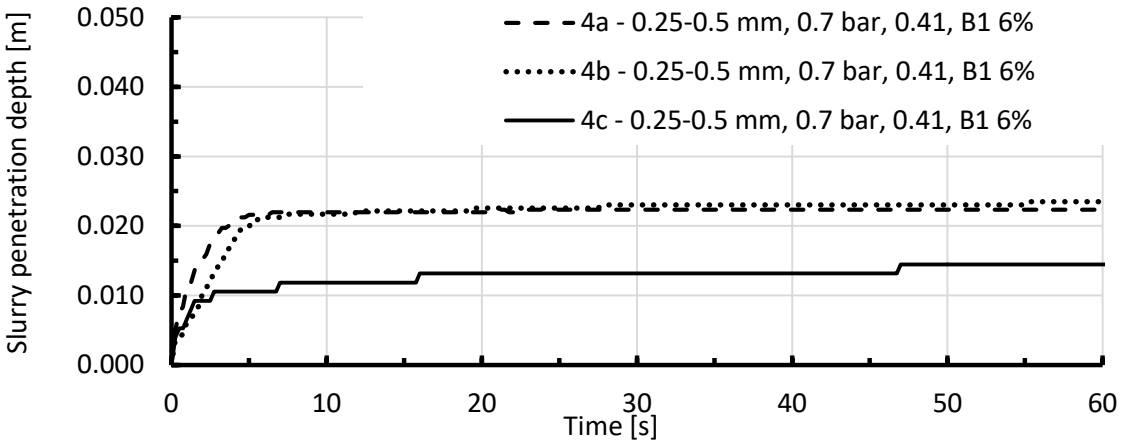

Figure A-2-7: Slurry penetration depth in combination 4

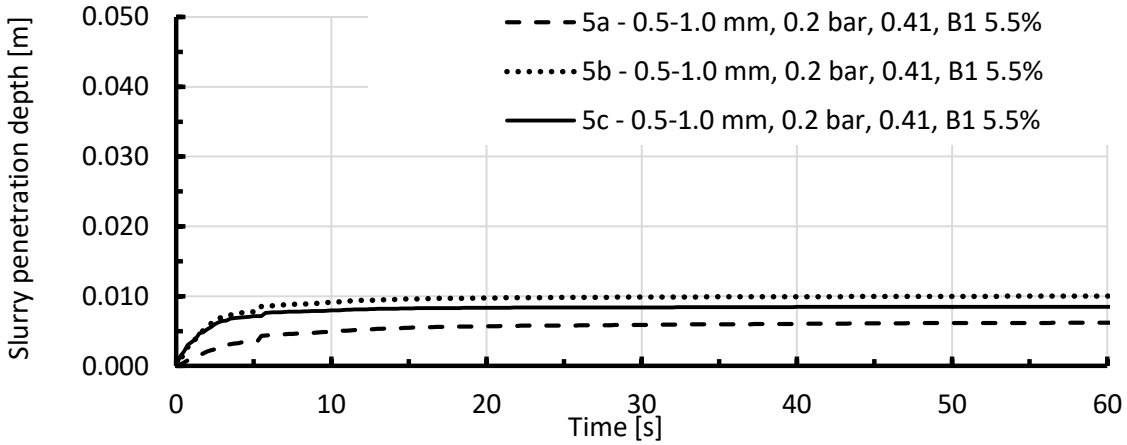

Figure A-2-8: Slurry penetration depth in combination 5

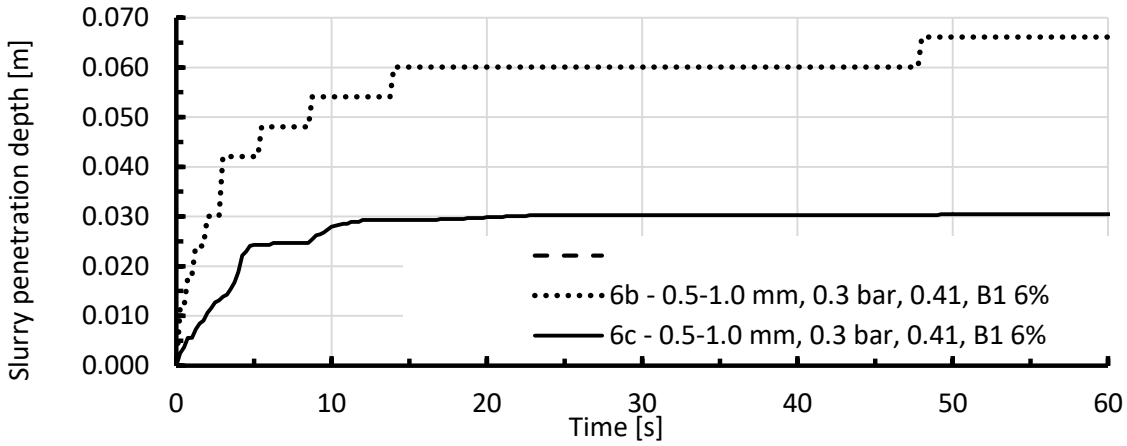

Figure A-2-9: Slurry penetration depth in combination 6

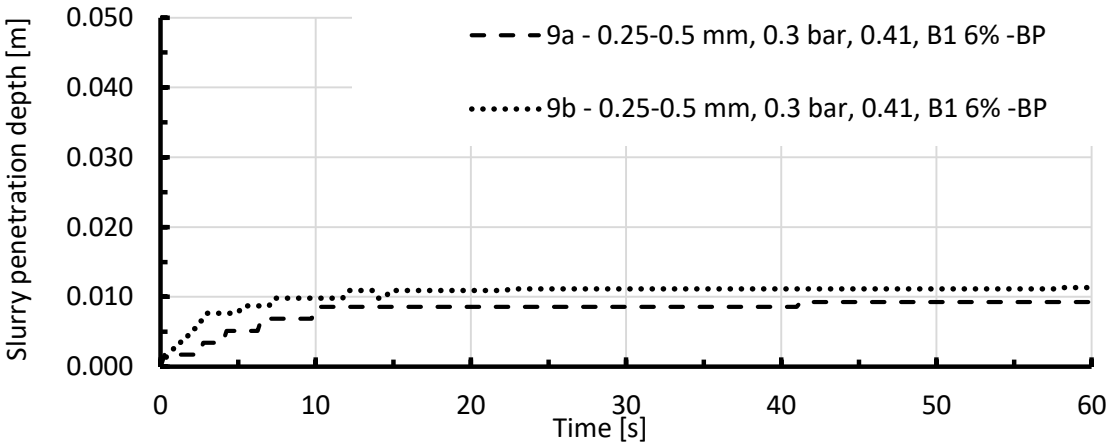

Figure A-2-10: Slurry penetration depth in combination 9

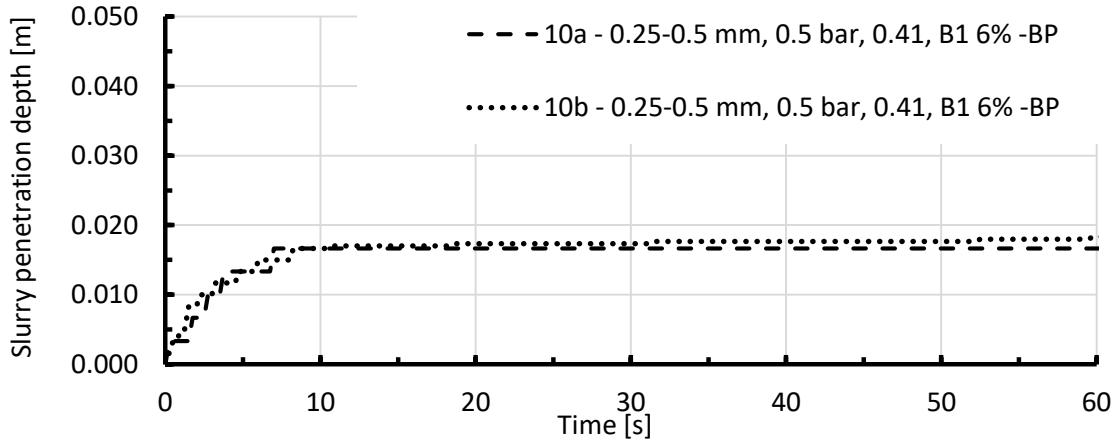

Figure A-2-11: Slurry penetration depth in combination 10

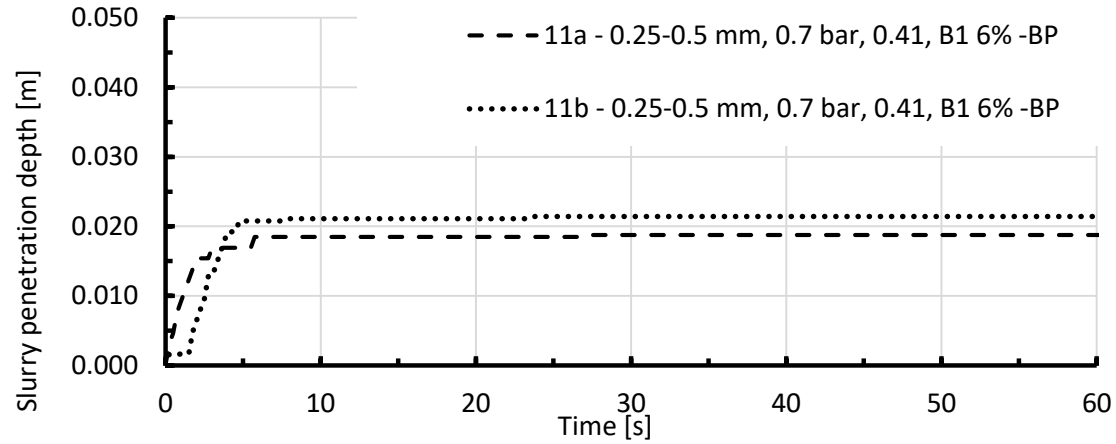

Figure A-2-12: Slurry penetration depth in combination 11

A.2.3.2 Time-dependent development of permeability coefficient of soil for slurry

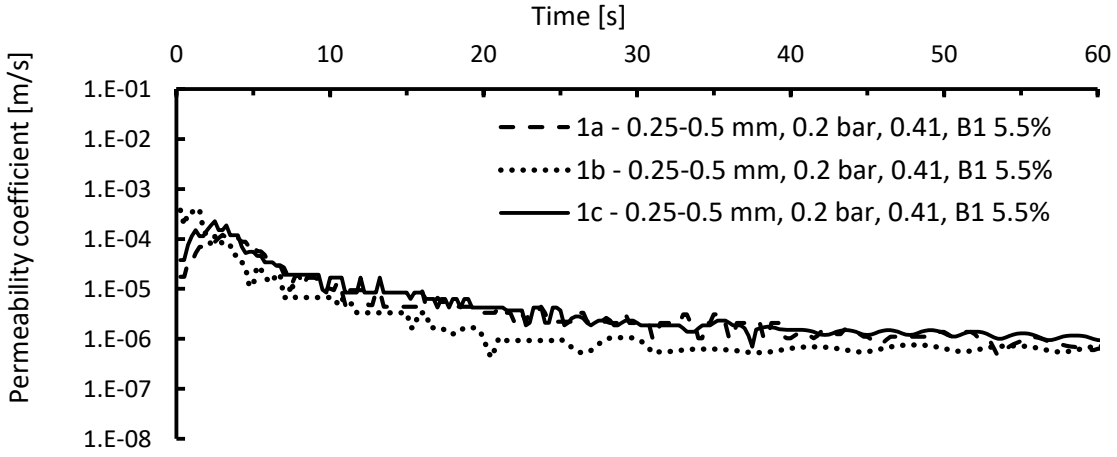

Figure A-2-13: Permeability coefficient development in combination 1

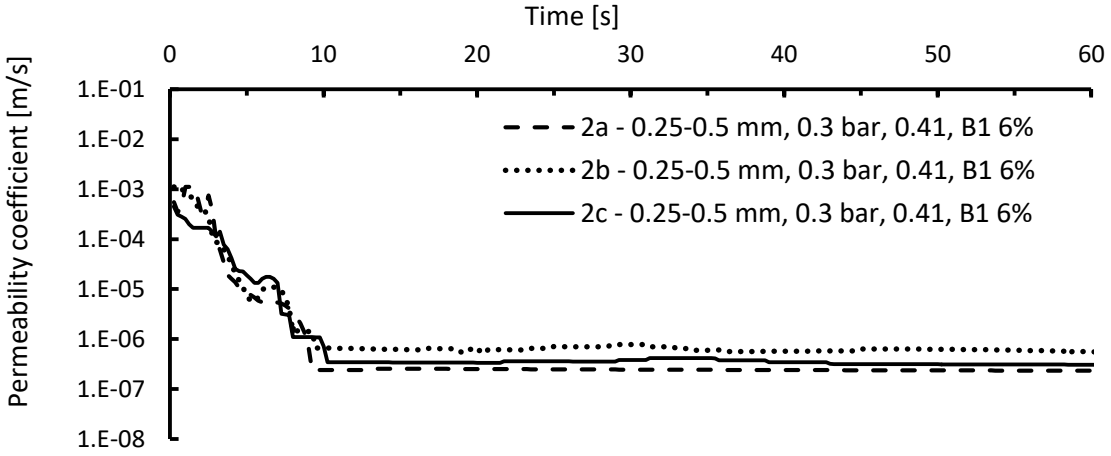

Figure A-2-14: Permeability coefficient development in combination 2

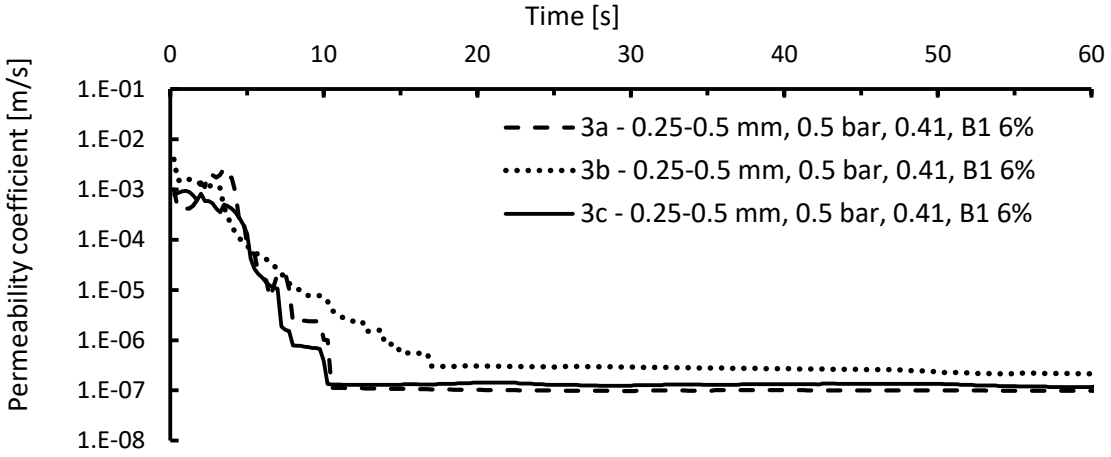

Figure A-2-15: Permeability coefficient development in combination 3

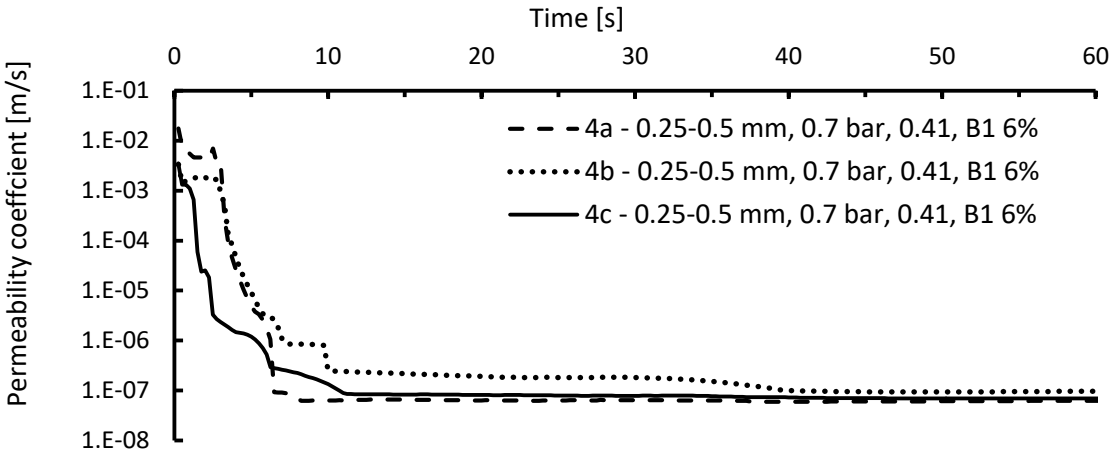

Figure A-2-16: Permeability coefficient development in combination 4

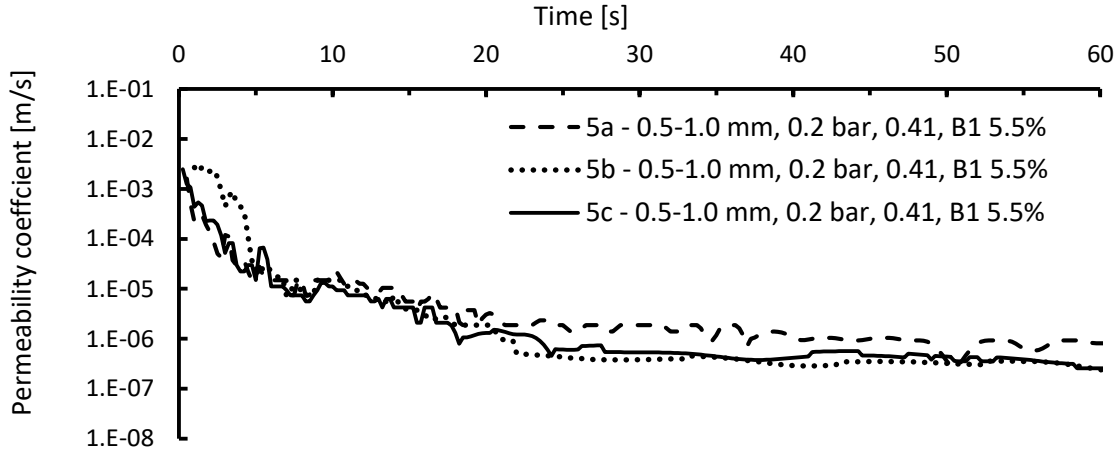

Figure A-2-17: Permeability coefficient development in combination 5

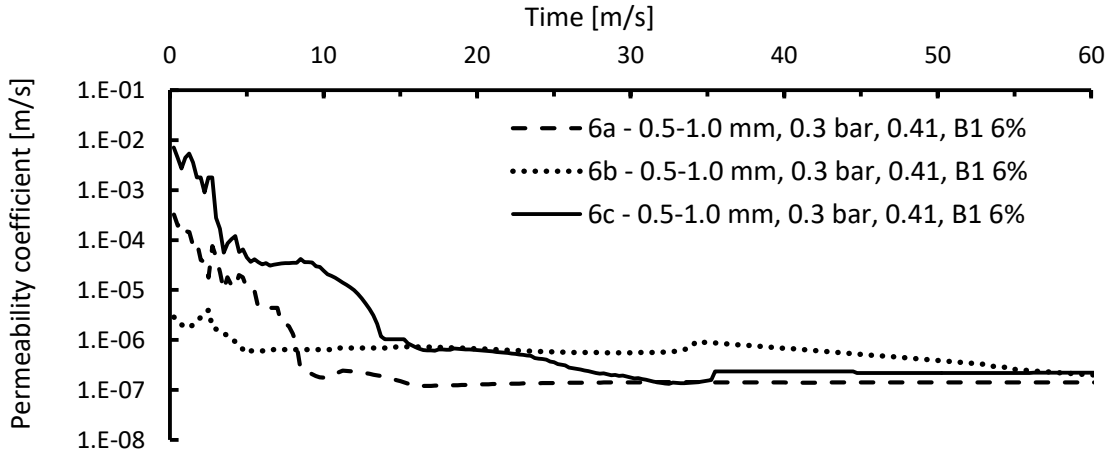

Figure A-2-18: Permeability coefficient development in combination 6

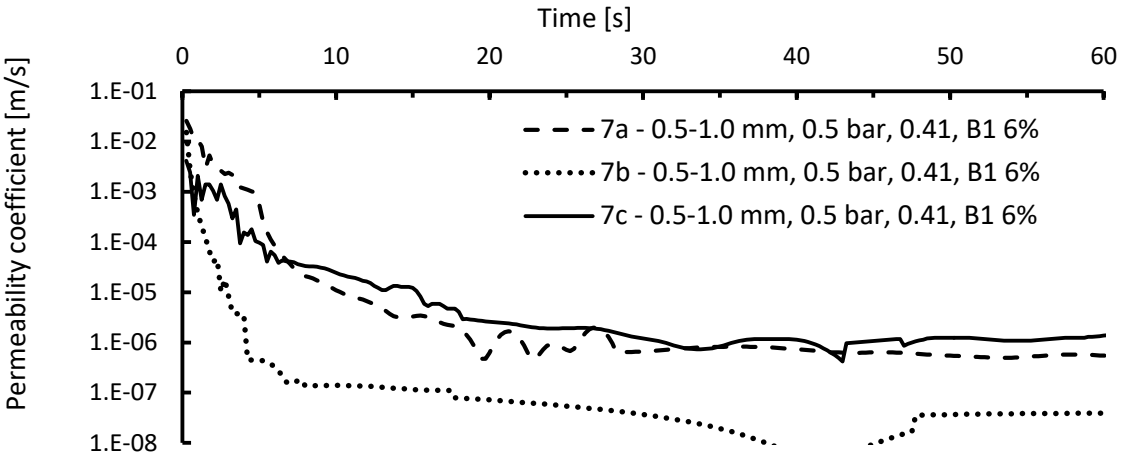

Figure A-2-19: Permeability coefficient development in combination 7

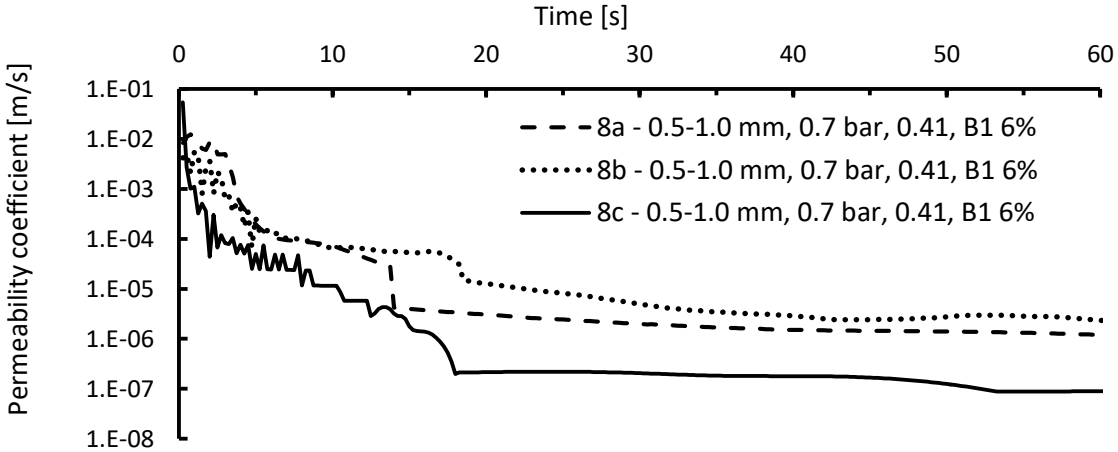

Figure A-2-20: Permeability coefficient development in combination 8

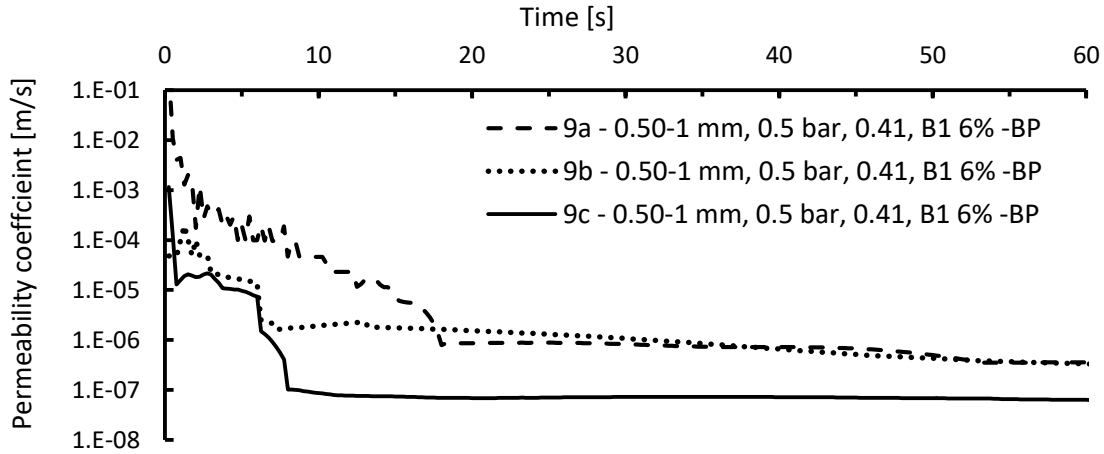

Figure A-2-21: Permeability coefficient development in combination 9

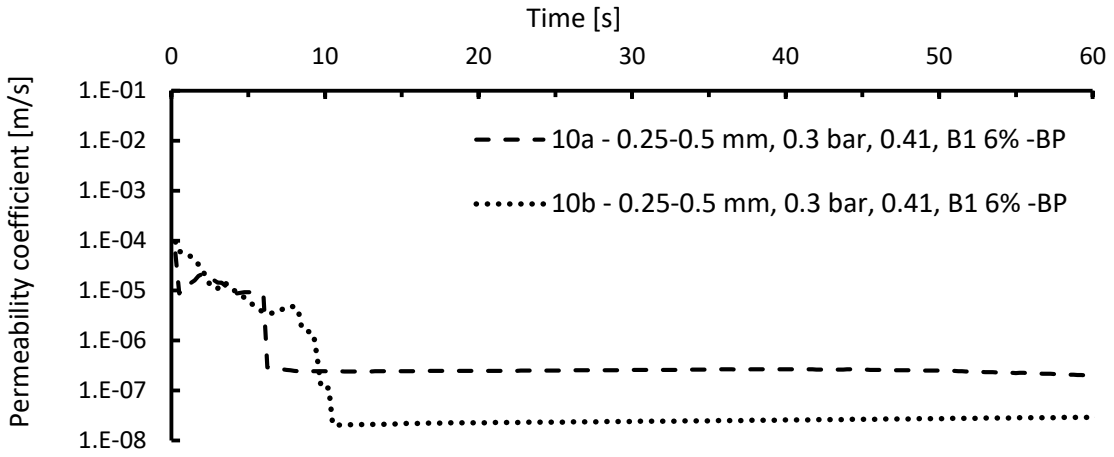

Figure A-2-22: Permeability coefficient development in combination 10

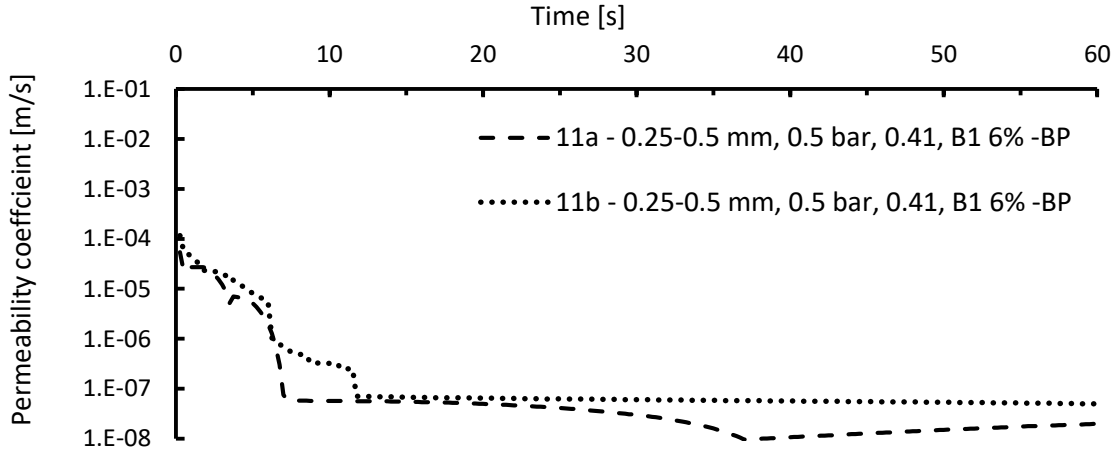

Figure A-2-23: Permeability coefficient development in combination 11

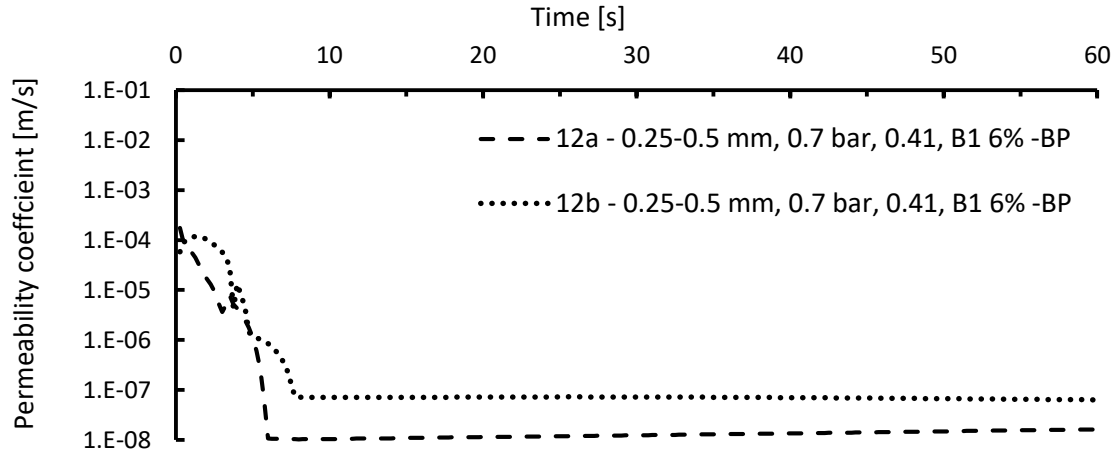

Figure A-2-24: Permeability coefficient development in combination 12

A.3 Case B – column tests

Tests for the investigation of slurry-soil interaction for a deep slurry penetration (Case B) were introduced in chapter 7.

A.3.1 Set-up and testing procedure

A.3.1.1 Set-up

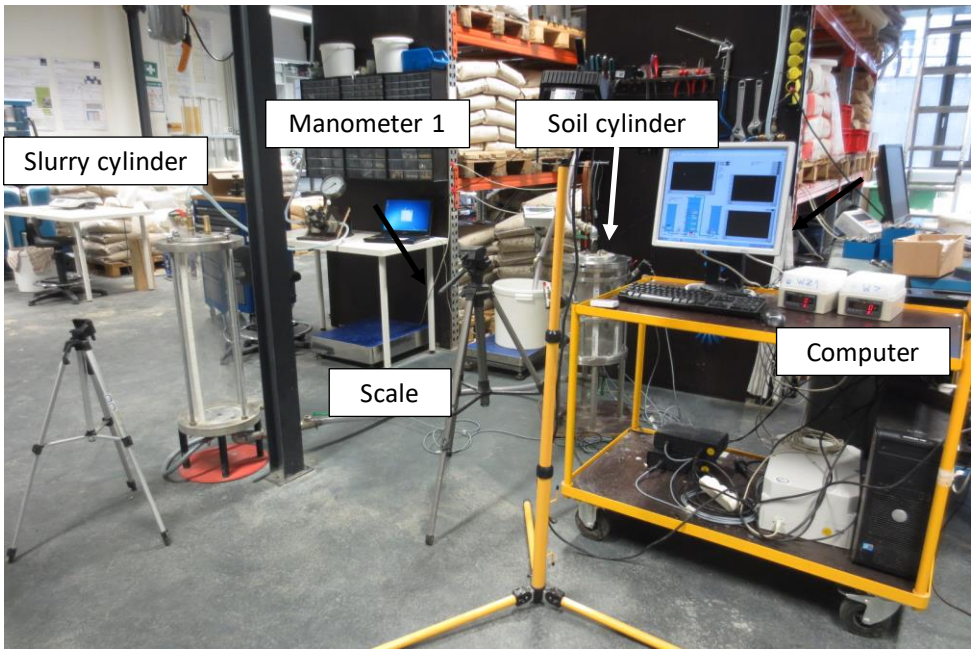

Figure A-3-1: Photo of set-up for the testing of deep slurry penetration – Case B

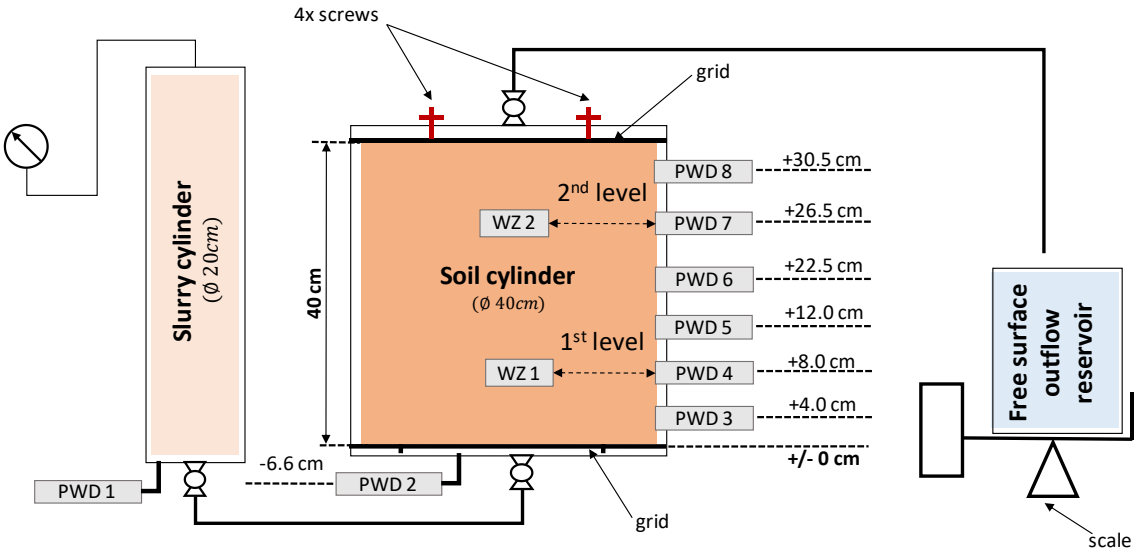

Figure A-3-2: Schema of set-up for the testing of deep slurry penetration – Case B

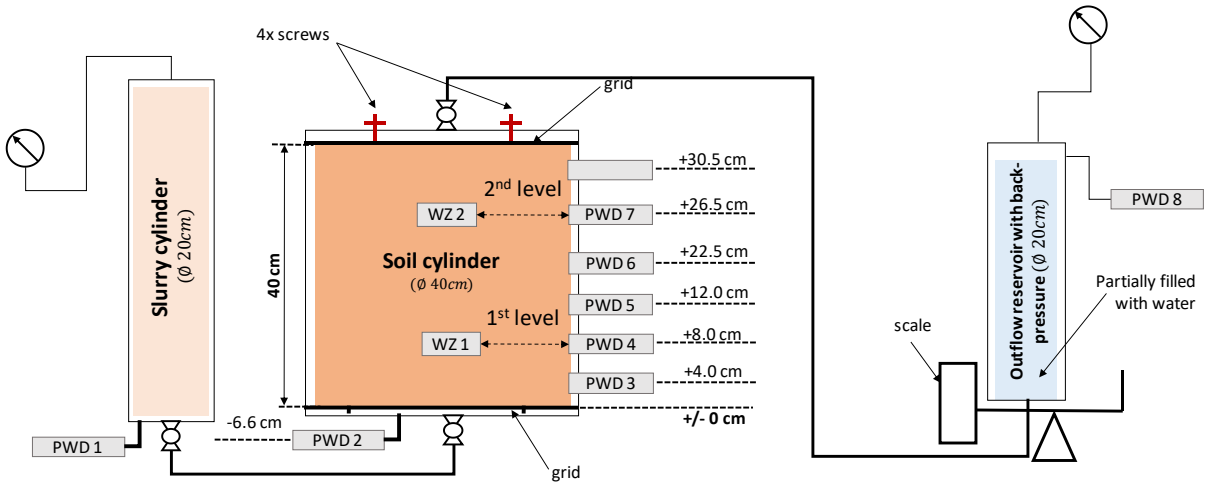

Figure A-3-3: Schema of set-up for the testing of deep slurry penetration – Case B with back-pressure

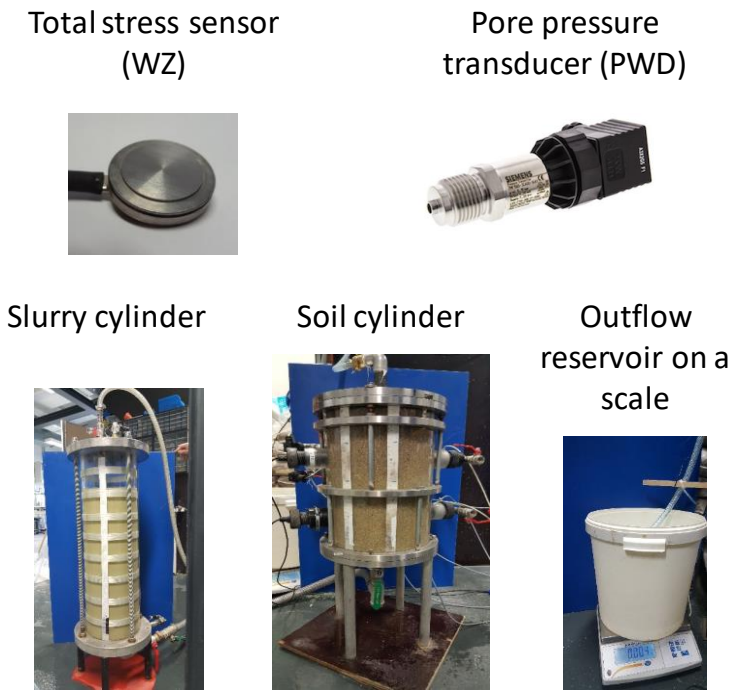

Figure A-3-4: Detailed view on the components of set-up for the testing of deep slurry penetration – Case B

The plastic grid and the wired mesh fixing the soil sample at the bottom of the cylinder

The plastic grid and the wired mesh fixing the soil sample at the top of the cylinder

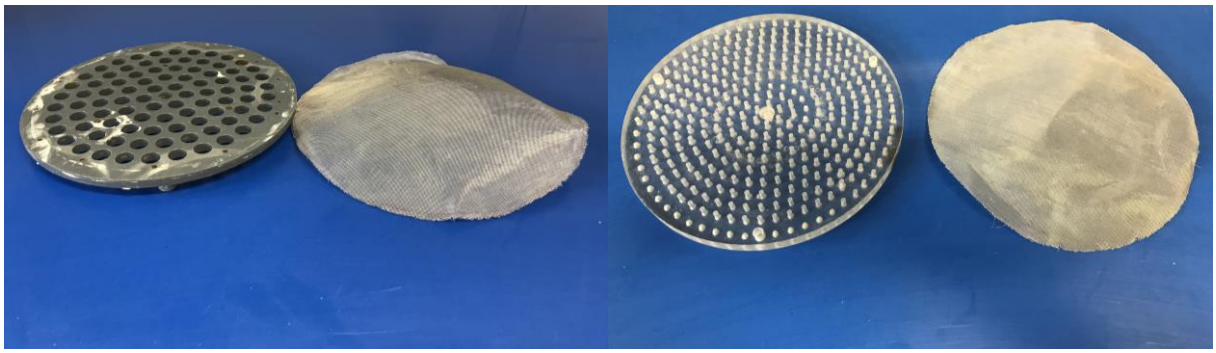

Figure A-3-5: Stabilization of the soil sample in the soil cylinder

Screws pushing on the plastic grid

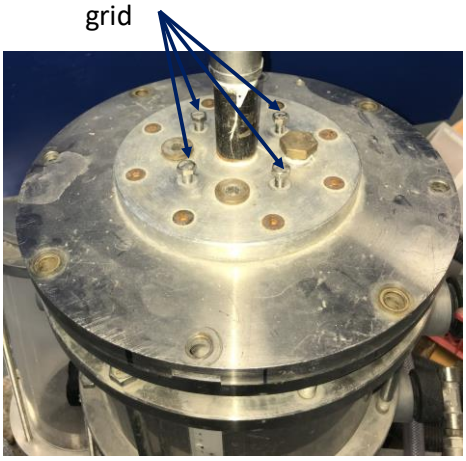

Figure A-3-6: Location of the screws at the cover of the soil cylinder

Equipment

- 1 slurry cylinder
- 1 soil cylinder
- 1 bucket/outflow cylinder*
- 2 grids
- 2 pipes
- 4 effective stress regulating screws
- 1-2 computer connected scales*
- 2 stopwatches
- 1 computer
- 2 video cameras + tripods
- 1 -2 manometers for pressure steering*
- 8 pore water pressure sensors (PWD)* connected to the computer
- 2 total stress sensors (WZ)

*depends on variant with/without back-pressure

Preparation

1. Slurry mixing 24 hour before the experiment
2. Check of slurry properties the day before the test starts
3. Installation of bottom grid at bottom of soil cylinder
4. Installation of soil sample and compaction to the prescribed porosity
5. Installation of the top grid
6. Connecting all pipes between cylinders
7. Water saturation of the cylinder for minimally 30 minutes
8. Adjusting the desired level of effective stress by screws
9. Water permeability test
10. Slow pumping of slurry up to the interface between the bottom grid and investigated soil sample (this point can be disregarded, if the methodology considers the slurry only in the slurry cylinder at the start of the test)

A.3.1.2 Primary penetration of slurry

Procedure

11. Opening valve and starting of slurry primary penetration
12. Recording of the outflow from the set-up by scale and monitoring of pore water pressure in the set-up every 0.25 s, recording the slurry levels in the cylinder by camera
13. End of the experiment after minimally 20 minutes
14. Visual determination of the maximal slurry penetration depth during dismantling

A.3.1.3 Re-penetration of slurry

Procedure

11. Opening valve and starting of slurry primary penetration
12. Recording of the outflow from the set-up by scale and monitoring of pore water pressure in the set-up every 0.25 s, recording the slurry levels in the cylinder by camera
13. The primary slurry penetration takes a defined time
14. Increase of injection pressure by the manometer to desired value
15. Re-penetration during the desired timespan
16. Visual determination of the total maximal slurry penetration depth

A.3.2 Testing protocols

Experiment No.:	Ia	Ib	Ic
Date of experiment:	19.07.2016	21.07.2016	26.07.2016
Soil properties			
Grain size of the soil [mm]	1-2	1-2	1-2
Number of installed layers	4	4	4
Height of layers [cm]	10	10	10
Actual weight of soil sample [kg]	35.22	35.22	35.22
Height of the soil sample [cm]	39.1	39.1	39.1
Density of the sample [g/cm³]	1.57	1.57	1.57
Actual bulk density ρ [g/cm³]	1.57	1.57	1.57
Porosity n: $n = 1 – \rho_d/\rho$ [–]	0.41	0.41	0.41
max ρ_d = mass of the closest compact soil [g/cm³]	1.65	1.65	1.65
min ρ_d = mass of the least compact soil [g/cm³]	1.43	1.43	1.43
Actual compactness of the ground D [–]	0.63	0.63	0.63
Water permeability test			
Pressure in s-cylinder (pressure gauge) [bar]	0.5	0.5	0.5
Back-Pressure [bar]	0	0	0
Height of the water in the s-cylinder before start[cm]	51	62.5	58.3
Height of the water in the s-cylinder at the end [cm]	3.5	6.5	4.3
Duration of the experiment [s]	18	21	19
Slurry properties			
Type of bentonite	B1	B1	B1
Concentration [%]	6	6	6
Date of mixing	18.07.2016	20.07.2016	25.07.2016
pH-value [-]	9.4	9.43	9.89
Density [g/cm³]	1.034	1.03	1.034
Yield point with ball harp [N/m²]	49.67	58.5	58.5
Marsh-time tM_{1000} [s]	105	50	51
Marsh-time tM_{1500} [s]	55	96	101
Slurry penetration test			
Pressure in s-cylinder (pressure gauge) [bar]	0.5	0.5	0.5
Back-Pressure [bar]	0	0	0
Height of the slurry in the s-cylinder before start [cm]	60.5	62.5	65.3
Pressure of the first load cell (WZ1) before start [kPa]	22	13	20
Pressure of the second load cell (WZ2) before start [kPa]	33	27	32
Height of the slurry in the s-cylinder at the end [cm]	35.2	36.7	39.9
Pressure of the first load cell (WZ1) at the end [kPa]	24	23	35
Pressure of the second load cell (WZ2) at the end [kPa]	39	46	37
Slurry penetration depth [cm]	26	27	26
Duration of the experiment [s]	1800	1830	1920
Filtrate volume [kg]	7.66	8.02	7.63

Experiment No.:	IIa	IIb	IIc
Date of experiment:	14.09.2016	10.04.2018	10.04.2018
Soil properties			
Grain size of the soil [mm]	1-2	1-2	1-2
Number of installed layers	4	4	4
Height of layers [cm]	10	10	10
Actual weight of soil sample [kg]	35.22	35.22	35.22
Height of the soil sample [cm]	39.1	39.1	39.1
Density of the sample [g/cm³]	1.57	1.57	1.57
Actual bulk density ρ [g/cm³]	1.57	1.57	1.57
Porosity n: $n = 1 - \rho_d/\rho$ [–]	0.41	0.41	0.41
max ρ_d = mass of the closest compact soil [g/cm³]	1.65	1.65	1.65
min ρ_d = mass of the least compact soil [g/cm³]	1.43	1.43	1.43
Actual compactness of the ground D [–]	0.63	0.63	0.63
Water permeability test			
Pressure in s-cylinder (pressure gauge) [bar]	0.5	0.5	0.5
Back-Pressure [bar]	0	0	0
Height of the water in the s-cylinder before start[cm]	64	61.6	61.5
Height of the water in the s-cylinder at the end [cm]	4.5	3.3	6.5
Duration of the experiment [s]	63	15	14
Slurry properties			
Type of bentonite	B1	B1	B1
Concentration [%]	6	6	6
Date of mixing	13.09.2016	09.04.2018	09.04.2018
pH-value [-]	9.86	10.7	10.7
Density [g/cm³]	1.036	1.036	1.036
Yield point with ball harp [N/m²]	58.5	57.74	57.74
Marsh-time tM_{1000} [s]	48	66	66
Marsh-time tM_{1500} [s]	86	155	155
Slurry penetration test			
Pressure in s-cylinder (pressure gauge) [bar]	0.5	0.5	0.5
Back-Pressure [bar]	0	0	0
Height of the slurry in the s-cylinder before start [cm]	61	61.5	57.9
Pressure of the first load cell (WZ1) before start [kPa]	15	23	18
Pressure of the second load cell (WZ2) before start [kPa]	33	20	22
Height of the slurry in the s-cylinder at the end [cm]	40	40	26.6
Pressure of the first load cell (WZ1) at the end [kPa]	53	67	59
Pressure of the second load cell (WZ2) at the end [kPa]	45	48	48
Slurry penetration depth [cm]	28	22.5	22.5
Duration of the experiment [s]	1830	1260	1260
Filtrate volume [kg]	8.13	6.39	6.05

Experiment No.:	IIIa	IIIb	IIIc
Date of experiment:	30.08.2016	01.09.2016	12.09.2016
Soil properties			
Grain size of the soil [mm]	1-2	1-2	1-2
Number of installed layers	4	4	4
Height of layers [cm]	10	10	10
Actual weight of soil sample [kg]	35.22	35.22	35.22
Height of the soil sample [cm]	39.1	39.1	39.1
Density of the sample [g/cm³]	1.57	1.57	1.57
Actual bulk density ρ [g/cm³]	1.57	1.57	1.57
Porosity n: $n = 1 - \rho_d/\rho$ [–]	0.41	0.41	0.41
max ρ_d = mass of the closest compact soil [g/cm³]	1.65	1.65	1.65
min ρ_d = mass of the least compact soil [g/cm³]	1.43	1.43	1.43
Actual compactness of the ground D [–]	0.63	0.63	0.63
Water permeability test			
Pressure in s-cylinder (pressure gauge) [bar]	1	1	1
Back-Pressure [bar]	0.57	0.57	0.57
Height of the water in the s-cylinder before start[cm]	58.5	60	60.2
Height of the water in the s-cylinder at the end [cm]	4.2	4.5	2.5
Duration of the experiment [s]	26	26	26
Slurry properties			
Type of bentonite	B1	B1	B1
Concentration [%]	6	6	6
Date of mixing	29.08.2016	31.08.2016	11.09.2016
pH-value [-]	9.81	9.86	9.87
Density [g/cm³]	1.1033	1.036	1.031
Yield point with ball harp [N/m²]	69.04	58.5	58.6
Marsh-time tM_{1000} [s]	63.33	53	50
Marsh-time tM_{1500} [s]	133	99	97
Slurry penetration test			
Pressure in s-cylinder (pressure gauge) [bar]	1	1	1
Back-Pressure [bar]	0.57	0.57	0.57
Height of the slurry in the s-cylinder before start [cm]	67.6	66	65.8
Pressure of the first load cell (WZ1) before start [kPa]	75	70	61
Pressure of the second load cell (WZ2) before start [kPa]	73	72	59
Height of the slurry in the s-cylinder at the end [cm]	49.8	45	43
Pressure of the first load cell (WZ1) at the end [kPa]	106	80	38
Pressure of the second load cell (WZ2) at the end [kPa]	95	88	52
Slurry penetration depth [cm]	15	19	23
Duration of the experiment [s]	1830	1830	1830
Filtrate volume [kg]	5.45	6.40	7.35

Experiment No.:	IVa	IVb	IVc
Date of experiment:	24.11.2017	27.11.2017	27.11.2017
Soil properties			
Grain size of the soil [mm]	1-2	1-2	1-2
Number of installed layers	4	4	4
Height of layers [cm]	10	10	10
Actual weight of soil sample [kg]	35.22	35.22	35.22
Height of the soil sample [cm]	39.1	39.1	39.1
Density of the sample [g/cm³]	1.57	1.57	1.57
Actual bulk density ρ [g/cm³]	1.57	1.57	1.57
Porosity n: $n = 1 - \rho_d/\rho$ [–]	0.41	0.41	0.41
max ρ_d = mass of the closest compact soil [g/cm³]	1.65	1.65	1.65
min ρ_d = mass of the least compact soil [g/cm³]	1.43	1.43	1.43
Actual compactness of the ground D [–]	0.63	0.63	0.63
Water permeability test			
Pressure in s-cylinder (pressure gauge) [bar]	0.5	0.5	0.5
Back-Pressure [bar]	0	0	0
Height of the water in the s-cylinder before start[cm]	58.3	64	68
Height of the water in the s-cylinder at the end [cm]	8.2	8.6	9.6
Duration of the experiment [s]	19	24	30
Slurry properties			
Type of bentonite	B1	B1	B1
Concentration [%]	6	6	6
Date of mixing	23.11.2017	26.11.2017	26.11.2017
pH-value [-]	9.29	9.28	9.28
Density [g/cm³]	1.036	1.035	1.035
Yield point with ball harp [N/m²]	57.74	57.75	57.75
Marsh-time tM_{1000} [s]	66	74	74
Marsh-time tM_{1500} [s]	149	111	111
Slurry penetration test			
Pressure in s-cylinder (pressure gauge) [bar]	0.5	0.5	0.5
Back-Pressure [bar]	0	0	0
Height of the slurry in the s-cylinder before start [cm]	58.3	61.4	59.9
Pressure of the first load cell (WZ1) before start [kPa]	24	13	30
Pressure of the second load cell (WZ2) before start [kPa]	20	11	21
Height of the slurry in the s-cylinder at the end [cm]	41.3	43.3	42.9
Pressure of the first load cell (WZ1) at the end [kPa]	58	47	73
Pressure of the second load cell (WZ2) at the end [kPa]	46	31	39
Slurry penetration depth [cm]	22	22	21.5
Duration of the experiment [s]	1320	1200	1800
Filtrate volume [kg]	4.91	7.11	6.87

Experiment No.:	Va	Vb	Vc
Date of experiment:	10.01.2018	10.01.2018	16.01.2018
Soil properties			
Grain size of the soil [mm]	1-2	1-2	1-2
Number of installed layers	4	4	4
Height of layers [cm]	10	10	10
Actual weight of soil sample [kg]	35.22	35.22	35.22
Height of the soil sample [cm]	39.1	39.1	39.1
Density of the sample [g/cm³]	1.57	1.57	1.57
Actual bulk density ρ [g/cm³]	1.57	1.57	1.57
Porosity n: $n = 1 - \rho_d/\rho$ [–]	0.41	0.41	0.41
max ρ_d = mass of the closest compact soil [g/cm³]	1.65	1.65	1.65
min ρ_d = mass of the least compact soil [g/cm³]	1.43	1.43	1.43
Actual compactness of the ground D [–]	0.63	0.63	0.63
Water permeability test			
Pressure in s-cylinder (pressure gauge) [bar]	0,3	0,3	0,3
Back-Pressure [bar]	0	0	0
Height of the water in the s-cylinder before start[cm]	58,5	66	64.1
Height of the water in the s-cylinder at the end [cm]	2,3	9.7	18
Duration of the experiment [s]	23	24	19
Slurry properties			
Type of bentonite	B1	B1	B1
Concentration [%]	6	6	6
Date of mixing	09.01.2018	09.01.2018	15.01.2018
pH-value [-]	9,16	9,16	9.03
Density [g/cm³]	1.036	1.036	1.044
Yield point with ball harp [N/m²]	57,74	57,74	58.442
Marsh-time tM_{1000} [s]	64	64	62
Marsh-time tM_{1500} [s]	144	144	132
Slurry penetration test			
Pressure in s-cylinder (pressure gauge) [bar]	0.3	0.3	0.3
Back-Pressure [bar]	0	0	0
Height of the slurry in the s-cylinder before start [cm]	60,3	50	50
Pressure of the first load cell (WZ1) before start [kPa]	20	29	16
Pressure of the second load cell (WZ2) before start [kPa]	23	29	16
Height of the slurry in the s-cylinder at the end [cm]	50,2	42.5	42.5
Pressure of the first load cell (WZ1) at the end [kPa]	46	51	35
Pressure of the second load cell (WZ2) at the end [kPa]	37	32	25
Slurry penetration depth [cm]	15	11	9.5
Duration of the experiment [s]	1200	1260	1200
Filtrate volume [kg]	4.43	4.01	3.86

Experiment No.:	VIa	VIb	VIc
Date of experiment:	16.01.2018	16.01.2018	23.01.2018
Soil properties			
Grain size of the soil [mm]	1-2	1-2	1-2
Number of installed layers	4	4	4
Height of layers [cm]	10	10	10
Actual weight of soil sample [kg]	35.22	35.22	35.22
Height of the soil sample [cm]	39.1	39.1	39.1
Density of the sample [g/cm³]	1.57	1.57	1.57
Actual bulk density ρ [g/cm³]	1.57	1.57	1.57
Porosity n: $n = 1 - \rho_d/\rho$ [–]	0.41	0.41	0.41
max ρ_d = mass of the closest compact soil [g/cm³]	1.65	1.65	1.65
min ρ_d = mass of the least compact soil [g/cm³]	1.43	1.43	1.43
Actual compactness of the ground D [–]	0.63	0.63	0.63
Water permeability test			
Pressure in s-cylinder (pressure gauge) [bar]	0,3	0.7	0.7
Back-Pressure [bar]	0	0	0
Height of the water in the s-cylinder before start[cm]	62.1	66	64
Height of the water in the s-cylinder at the end [cm]	11	10	10.2
Duration of the experiment [s]	21	15	13
Slurry properties			
Type of bentonite	B1	B1	B1
Concentration [%]	6	6	6
Date of mixing	15.01.2018	15.01.2018	22.01.2018
pH-value [-]	9.03	9.03	8.75
Density [g/cm³]	1.044	1.044	1.038
Yield point with ball harp [N/m²]	58.442	58.442	58.494
Marsh-time tM_{1000} [s]	62	62	58
Marsh-time tM_{1500} [s]	132	132	119
Slurry penetration test			
Pressure in s-cylinder (pressure gauge) [bar]	0.7	0.7	0.7
Back-Pressure [bar]	0	0	0
Height of the slurry in the s-cylinder before start [cm]	52.4	60.7	54.5
Pressure of the first load cell (WZ1) before start [kPa]	24	20	21
Pressure of the second load cell (WZ2) before start [kPa]	23	21	19
Height of the slurry in the s-cylinder at the end [cm]	26.5	36.8	30.8
Pressure of the first load cell (WZ1) at the end [kPa]	70	76	70
Pressure of the second load cell (WZ2) at the end [kPa]	57	63	68
Slurry penetration depth [cm]	30.5	30	30.5
Duration of the experiment [s]	1200	1200	1200
Filtrate volume [kg]	9.48	9.05	8.54

Experiment No.:	VIIa	VIIb
Date of experiment:	10.05.2017	10.05.2017
Soil properties		
Grain size of the soil [mm]	0,063-4,0	0,063-4,0
Number of installed layers	4	4
Height of layers [cm]	0.1	0.1
Actual weight of soil sample [kg]	37.78	37.78
Height of the soil sample [cm]	39.5	39.5
Density of the sample [g/cm³]	1.623	1.623
Actual bulk density ρ [g/cm³]	1.744	1.744
Porosity n: $n = 1 - \rho_d/\rho$ [–]	0.387	0.387
max ρ_d = mass of the closest compact soil [g/cm³]		
min ρ_d = mass of the least compact soil [g/cm³]		
Actual compactness of the ground D [–]		
Water permeability test		
Pressure in s-cylinder (pressure gauge) [bar]	0.3	0.3
Back-Pressure [bar]	0	0
Height of the water in the s-cylinder before start[cm]	60.7	60.7
Height of the water in the s-cylinder at the end [cm]	2.8	2.8
Duration of the experiment [s]	133	133
Slurry properties		
Type of bentonite	B1	B1
Concentration [%]	6	6
Date of mixing	09.05.2017	09.05.2017
pH-value [-]	10.76	10.76
Density [g/cm³]	1.038	1.038
Yield point with ball harp [N/m²]	47.875	47.875
Marsh-time tM_{1000} [s]	54	54
Marsh-time tM_{1500} [s]	116	116
Slurry penetration test		
Pressure in s-cylinder (pressure gauge) [bar]	0.3	0.3
Back-Pressure [bar]	0	0
Height of the slurry in the s-cylinder before start [cm]	56.5	56.6
Pressure of the first load cell (WZ1) before start [kPa]	35	31
Pressure of the second load cell (WZ2) before start [kPa]	30	25
Height of the slurry in the s-cylinder at the end [cm]	52.2	53
Pressure of the first load cell (WZ1) at the end [kPa]	26	24
Pressure of the second load cell (WZ2) at the end [kPa]	13	15
Slurry penetration depth [cm]	3	3.6
Duration of the experiment [s]	1320	1320
Filtrate volume [kg]	1.20	1.02

Experiment No.:	VIIIa	VIIIb
Date of experiment:	04.05.2017	04.05.2017
Soil properties		
Grain size of the soil [mm]	0,063-4,0	0,063-4,0
Number of installed layers	4	4
Height of layers [cm]	0.1	0.1
Actual weight of soil sample [kg]	37.78	37.78
Height of the soil sample [cm]	39.5	39.5
Density of the sample [g/cm³]	1.623	1.623
Actual bulk density ρ [g/cm³]	1.744	1.744
Porosity n: $n = 1 - \rho_d/\rho$ [–]	0.387	0.387
max ρ_d = mass of the closest compact soil [g/cm³]		
min ρ_d = mass of the least compact soil [g/cm³]		
Actual compactness of the ground D [–]		
Water permeability test		
Pressure in s-cylinder (pressure gauge) [bar]	0.9	0.9
Back-Pressure [bar]	0	0
Height of the water in the s-cylinder before start[cm]	60.5	60.5
Height of the water in the s-cylinder at the end [cm]	4.9	4.9
Duration of the experiment [s]	96	96
Slurry properties		
Type of bentonite	B1	B1
Concentration [%]	6	6
Date of mixing	03.05.2017	03.05.2017
pH-value [-]	10.81	10.81
Density [g/cm³]	1.039	1.039
Yield point with ball harp [N/m²]	47.873	47.873
Marsh-time tM_{1000} [s]	53	53
Marsh-time tM_{1500} [s]	118	118
Slurry penetration test		
Pressure in s-cylinder (pressure gauge) [bar]	0.9	0.9
Back-Pressure [bar]	0	0
Height of the slurry in the s-cylinder before start [cm]	56	56
Pressure of the first load cell (WZ1) before start [kPa]	12	12
Pressure of the second load cell (WZ2) before start [kPa]	9	9
Height of the slurry in the s-cylinder at the end [cm]	48.1	48.1
Pressure of the first load cell (WZ1) at the end [kPa]	75	75
Pressure of the second load cell (WZ2) at the end [kPa]	63	63
Slurry penetration depth [cm]	6.2	6.5
Duration of the experiment [s]	1320	1320
Filtrate volume [kg]	2.17	2.31

Experiment No.:	r-Ia	r-Ib	r-Ic
Date of experiment:	29.11.2017	29.11.2017	04.12.2017
Soil properties			
Grain size of the soil [mm]	1-2	1-2	1-2
Number of installed layers	4	4	4
Height of layers [cm]	10	10	10
Actual weight of soil sample [kg]	35.22	35.22	35.22
Height of the soil sample [cm]	39.1	39.1	39.1
Density of the sample [g/cm³]	1.57	1.57	1.57
Actual bulk density ρ [g/cm³]	1.57	1.57	1.57
Porosity n: $n = 1 - \rho_d/\rho$ [–]	0.41	0.41	0.41
max ρ_d = mass of the closest compact soil [g/cm³]	1.65	1.65	1.65
min ρ_d = mass of the least compact soil [g/cm³]	1.43	1.43	1.43
Actual compactness of the ground D [–]	0.63	0.63	0.63
Water permeability test			
Pressure in s-cylinder (pressure gauge) [bar]	0.5	0.5	0.5
Back-Pressure [bar]	0	0	0
Height of the water in the s-cylinder before start[cm]	63.8	63.4	55.7
Height of the water in the s-cylinder at the end [cm]	4.6	7.3	15.9
Duration of the experiment [s]	19	18	14
Slurry properties			
Type of bentonite	B1	B1	B1
Concentration [%]	6	6	6
Date of mixing	28.11.2017	28.11.2017	03.12.2017
pH-value [-]	9.26	9.26	9.28
Density [g/cm³]	1.041	1.041	1.043
Yield point with ball harp [N/m²]	57.69	57.69	57.69
Marsh-time tM_{1000} [s]	70	70	68
Marsh-time tM_{1500} [s]	174	174	176
Re-penetration test			
Pressure in s-cylinder (pressure gauge) [bar]	0.5	0.5	0.5
Back-Pressure [bar]	0	0	0
Pressure at start of re-penetration [bar]	0.6	0.6	0.6
Time of primary penetration [sec]	10	10	10
Time of re-penetration [sec]	60	60	60
Height of the slurry in the s-cylinder before start[cm]	60.4	55.3	56.8
Pressure of the first load cell (WZ1) before start [kPa]	23	24	20
Pressure of the second load cell (WZ2) before start [kPa]	28	29	28
Height of the slurry in the s-cylinder at the end [cm]	42.7	36.1	37.7
Pressure of the first load cell (WZ1) at the end [kPa]	55	53	56
Pressure of the second load cell (WZ2) at the end [kPa]	51	58	61
Slurry penetration depth [cm]	24	24.5	26
Duration of the experiment [s]	70	70	70
Filtrate water volume [kg]	6.98	7.61	7.53

Experiment No.:	r-IIa	r-IIb	r-IIc
Date of experiment:	18.12.2017	18.12.2017	18.12.2017
Soil properties			
Grain size of the soil [mm]	1-2	1-2	1-2
Number of installed layers	4	4	4
Height of layers [cm]	10	10	10
Actual weight of soil sample [kg]	35.22	35.22	35.22
Height of the soil sample [cm]	39.1	39.1	39.1
Density of the sample [g/cm³]	1.57	1.57	1.57
Actual bulk density ρ [g/cm^3]	1.57	1.57	1.57
Porosity n: $n = 1 - \rho_d/\rho$ [–]	0.41	0.41	0.41
max ρ_d = mass of the closest compact soil [g/cm^3]	1.65	1.65	1.65
min ρ_d = mass of the least compact soil [g/cm^3]	1.43	1.43	1.43
Actual compactness of the ground D [–]	0.63	0.63	0.63
Water permeability test			
Pressure in s-cylinder (pressure gauge) [bar]	0.5	0.5	0.5
Back-Pressure [bar]	0	0	0
Height of the water in the s-cylinder before start[cm]	58.5	62	62.3
Height of the water in the s-cylinder at the end [cm]	12	8.7	7.3
Duration of the experiment [s]	14	17	17
Slurry properties			
Type of bentonite	B1	B1	B1
Concentration [%]	6	6	6
Date of mixing	17.12.2017	17.12.2017	17.12.2017
pH-value [-]	9.35	9.35	9.35
Density [g/cm^3]	1.039	1.039	1.039
Yield point with ball harp [N/m²]	57.71	57.71	57.71
Marsh-time tM_{1000} [s]	67	67	67
Marsh-time tM_{1500} [s]	176	176	176
Re-penetration test			
Pressure in s-cylinder (pressure gauge) [bar]	0.5	0.5	0.5
Back-Pressure [bar]	0	0	0
Pressure at start of re-penetration [bar]	0.6	0.6	0.6
Time of primary penetration [sec]	15	15	15
Time of re-penetration [sec]	60	60	60
Height of the slurry in the s-cylinder before start[cm]	56.5	58	55.5
Pressure of the first load cell (WZ1) before start [kPa]	21	21	22
Pressure of the second load cell (WZ2) before start [kPa]	22	22	23
Height of the slurry in the s-cylinder at the end [cm]	40.2	42.1	44
Pressure of the first load cell (WZ1) at the end [kPa]	55	67	58
Pressure of the second load cell (WZ2) at the end [kPa]	60	62	54
Slurry penetration depth [cm]	22.5	23	22.5
Duration of the experiment [s]	75	75	75
Filtrate water volume [kg]	6.30	6.52	6.57

Experiment No.:	r-IIIa	r-IIIb	r-IIIc
Date of experiment:	13.12.2017	13.12.2017	13.12.2017
Soil properties			
Grain size of the soil [mm]	1-2	1-2	1-2
Number of installed layers	4	4	4
Height of layers [cm]	10	10	10
Actual weight of soil sample [kg]	35.22	35.22	35.22
Height of the soil sample [cm]	39.1	39.1	39.1
Density of the sample [g/cm³]	1.57	1.57	1.57
Actual bulk density ρ [g/cm^3]	1.57	1.57	1.57
Porosity n: $n = 1 - \rho_d/\rho$ [–]	0.41	0.41	0.41
max ρ_d = mass of the closest compact soil [g/cm^3]	1.65	1.65	1.65
min ρ_d = mass of the least compact soil [g/cm^3]	1.43	1.43	1.43
Actual compactness of the ground D [–]	0.63	0.63	0.63
Water permeability test			
Pressure in s-cylinder (pressure gauge) [bar]	0.5	0.5	0.5
Back-Pressure [bar]	0	0	0
Height of the water in the s-cylinder before start[cm]	63.3	59.2	63
Height of the water in the s-cylinder at the end [cm]	11.5	8.5	9.1
Duration of the experiment [s]	16	15	16
Slurry properties			
Type of bentonite	B1	B1	B1
Concentration [%]	6	6	6
Date of mixing	12.12.2017	12.12.2017	12.12.2017
pH-value [-]	9.3	9.3	9.3
Density [g/cm^3]	1.039	1.039	1.039
Yield point with ball harp [N/m²]	57.7	57.7	57.7
Marsh-time tM_{1000} [s]	66	66	66
Marsh-time tM_{1500} [s]	174	174	174
Re-penetration test			
Pressure in s-cylinder (pressure gauge) [bar]	0.5	0.5	0.5
Back-Pressure [bar]	0	0	0
Pressure at start of re-penetration [bar]	0.6	0.6	0.6
Time of primary penetration [sec]	20	20	20
Time of re-penetration [sec]	60	60	60
Height of the slurry in the s-cylinder before start[cm]	53.9	54	55.8
Pressure of the first load cell (WZ1) before start [kPa]	21	22	18
Pressure of the second load cell (WZ2) before start [kPa]	24	25	22
Height of the slurry in the s-cylinder at the end [cm]	33.4	34.9	37
Pressure of the first load cell (WZ1) at the end [kPa]	60	65	73
Pressure of the second load cell (WZ2) at the end [kPa]	70	58	73
Slurry penetration depth [cm]	25	25	25
Duration of the experiment [s]	80	80	80
Filtrate water volume [kg]	7.55	7.40	7.40

Experiment No.:	r-Va	r-Vb	r-Vc
Date of experiment:	23.01.2018	23.01.2018	24.01.2018
Soil properties			
Grain size of the soil [mm]	1-2	1-2	1-2
Number of installed layers	4	4	4
Height of layers [cm]	10	10	10
Actual weight of soil sample [kg]	35.22	35.22	35.22
Height of the soil sample [cm]	39.1	39.1	39.1
Density of the sample [g/cm³]	1.57	1.57	1.57
Actual bulk density ρ [g/cm³]	1.57	1.57	1.57
Porosity n: $n = 1 - \rho_d/\rho$ [–]	0.41	0.41	0.41
max ρ_d = mass of the closest compact soil [g/cm³]	1.65	1.65	1.65
min ρ_d = mass of the least compact soil [g/cm³]	1.43	1.43	1.43
Actual compactness of the ground D [–]	0.63	0.63	0.63
Water permeability test			
Pressure in s-cylinder (pressure gauge) [bar]	0.5	0.5	0.5
Back-Pressure [bar]	0	0	0
Height of the water in the s-cylinder before start[cm]	64.3	66.2	64
Height of the water in the s-cylinder at the end [cm]	11.5	10.5	75
Duration of the experiment [s]	16	18	19
Slurry properties			
Type of bentonite	B1	B1	B1
Concentration [%]	6	6	6
Date of mixing	22.01.2018	22.01.2018	23.01.2018
pH-value [-]	8.75	8.75	8.99
Density [g/cm³]	1.038	1.038	1.048
Yield point with ball harp [N/m²]	58.494	58.494	
Marsh-time tM_{1000} [s]	58	58	58
Marsh-time tM_{1500} [s]	119	119	120
Re-penetration test			
Pressure in s-cylinder (pressure gauge) [bar]	0.5	0.5	0.5
Back-Pressure [bar]	0	0	0
Pressure at start of re-penetration [bar]	0.6	0.6	0.6
Time of primary penetration [sec]	30	30	30
Time of re-penetration [sec]	100	100	100
Height of the slurry in the s-cylinder before start[cm]	57	44	59
Pressure of the first load cell (WZ1) before start [kPa]	21	21	20
Pressure of the second load cell (WZ2) before start [kPa]	23	23	23
Height of the slurry in the s-cylinder at the end [cm]	38.5	27	40
Pressure of the first load cell (WZ1) at the end [kPa]	62	57	68
Pressure of the second load cell (WZ2) at the end [kPa]	55	50	48
Slurry penetration depth [cm]	24	23	24.5
Duration of the experiment [s]	130	130	130
Filtrate water volume [kg]	7.37	7.07	7.27

Experiment No.:	r-VIa	r-VIb	r-VIc
Date of experiment:	24.01.2018	24.01.2018	30.01.2018
Soil properties			
Grain size of the soil [mm]	1-2	1-2	1-2
Number of installed layers	4	4	4
Height of layers [cm]	10	10	10
Actual weight of soil sample [kg]	35.22	35.22	35.22
Height of the soil sample [cm]	39.1	39.1	39.1
Density of the sample [g/cm³]	1.57	1.57	1.57
Actual bulk density ρ [g/cm^3]	1.57	1.57	1.57
Porosity n: $n = 1 - \rho_d/\rho$ [–]	0.41	0.41	0.41
max ρ_d = mass of the closest compact soil [g/cm^3]	1.65	1.65	1.65
min ρ_d = mass of the least compact soil [g/cm^3]	1.43	1.43	1.43
Actual compactness of the ground D [–]	0.63	0.63	0.63
Water permeability test			
Pressure in s-cylinder (pressure gauge) [bar]	0.5	0.5	0.5
Back-Pressure [bar]	0	0	0
Height of the water in the s-cylinder before start[cm]	61.3	63.5	63.5
Height of the water in the s-cylinder at the end [cm]	11	11	8
Duration of the experiment [s]	17	17	18
Slurry properties			
Type of bentonite	B1	B1	B1
Concentration [%]	6	6	6
Date of mixing	23.01.2018	23.01.2018	29.01.2018
pH-value [-]	8.99	8.99	9.35
Density [g/cm^3]	1.048	1.048	1.045
Yield point with ball harp [N/m²]	57.86	57.86	57.66
Marsh-time tM_{1000} [s]	58	58	59
Marsh-time tM_{1500} [s]	120	120	127
Re-penetration test			
Pressure in s-cylinder (pressure gauge) [bar]	0.5	0.5	0.5
Back-Pressure [bar]	0	0	0
Pressure at start of re-penetration [bar]	0.6	0.6	0.6
Time of primary penetration [sec]	40	40	40
Time of re-penetration [sec]	100	100	100
Height of the slurry in the s-cylinder before start[cm]	57	55.7	56.3
Pressure of the first load cell (WZ1) before start [kPa]	22	20	19
Pressure of the second load cell (WZ2) before start [kPa]	22	21	21
Height of the slurry in the s-cylinder at the end [cm]	38.5	36	38.5
Pressure of the first load cell (WZ1) at the end [kPa]		72	66
Pressure of the second load cell (WZ2) at the end [kPa]		48	52
Slurry penetration depth [cm]	30	26.5	25.5
Duration of the experiment [s]	140	140	140
Filtrate water volume [kg]	8.79	7.71	6.33

A.3.3 Diagrams

A.3.3.1 Time-dependent penetration depth

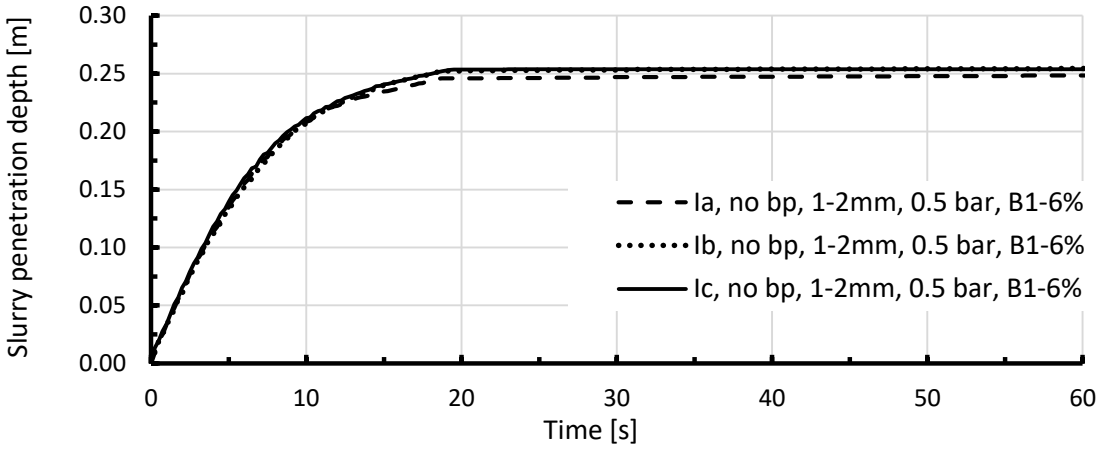

Figure A-3-7: Slurry penetration depth in combination I

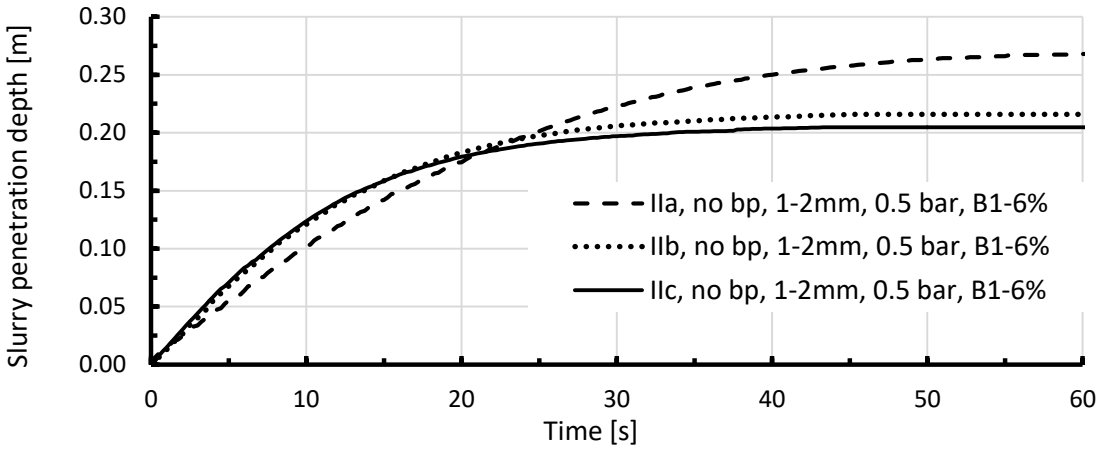

Figure A-3-8: Slurry penetration depth in combination II

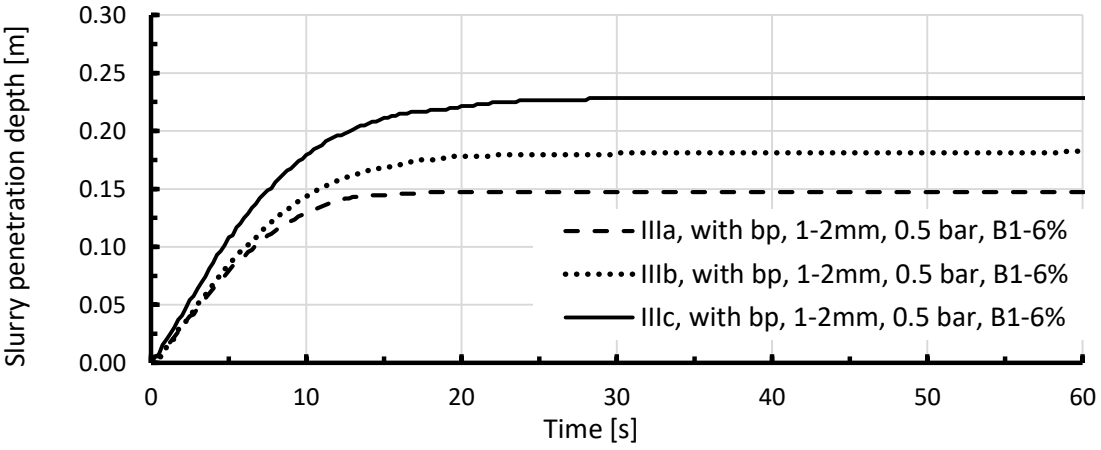

Figure A-3-9: Slurry penetration depth in combination III

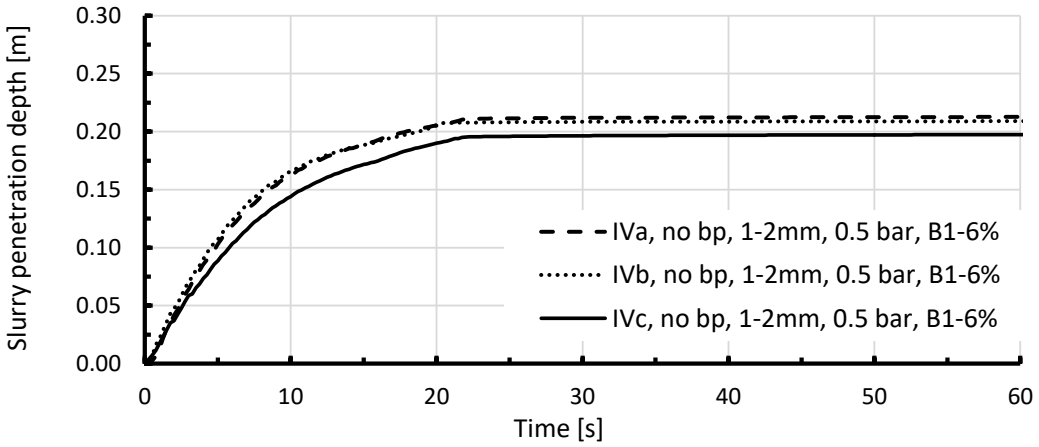

Figure A-3-10: Slurry penetration depth in combination IV

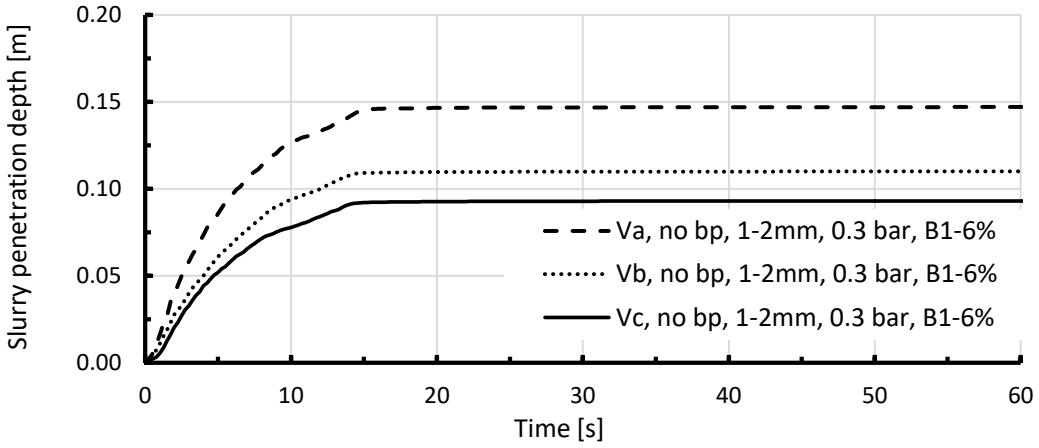

Figure A-3-11: Slurry penetration depth in combination V

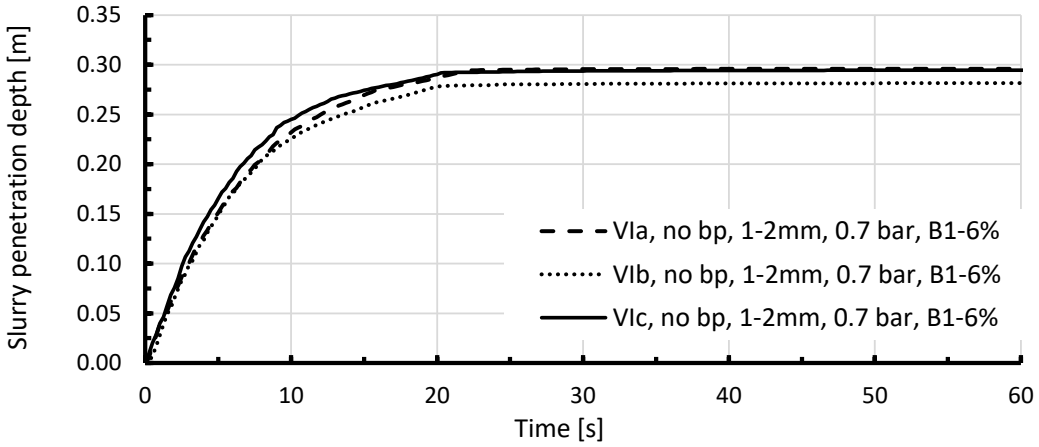

Figure A-3-12: Slurry penetration depth in combination VI

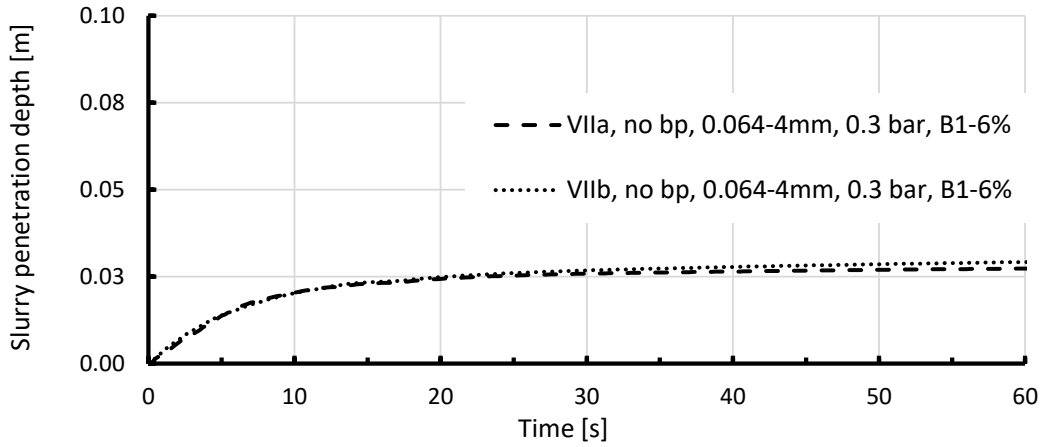

Figure A-3-13: Slurry penetration depth in combination VII

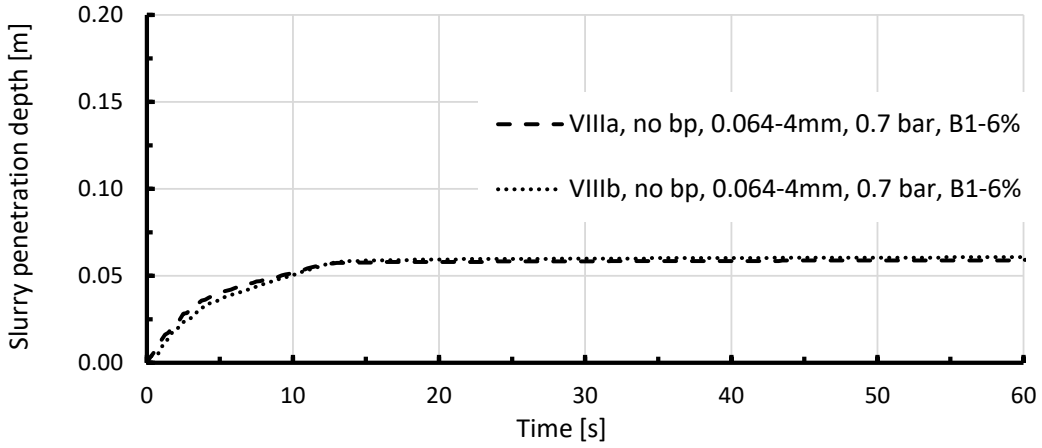

Figure A-3-14: Slurry penetration depth in combination VIII

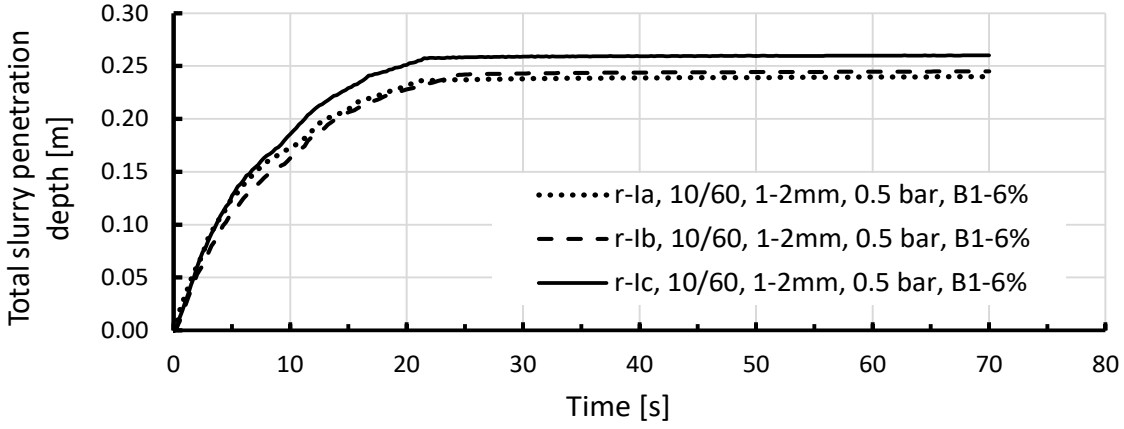

Figure A-3-15: Total slurry re-penetration depth in combination r-I 10/60

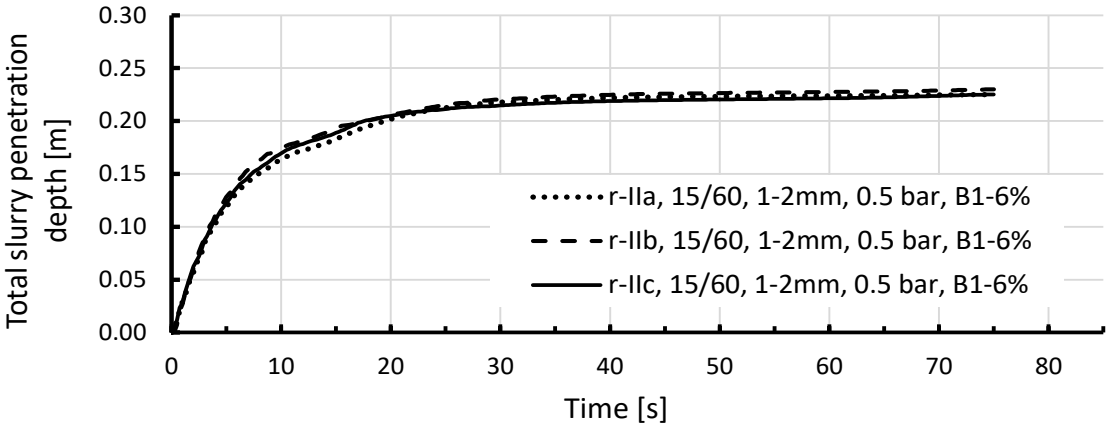

Figure A-3-16: Total slurry re-penetration depth in combination r-II 15/60

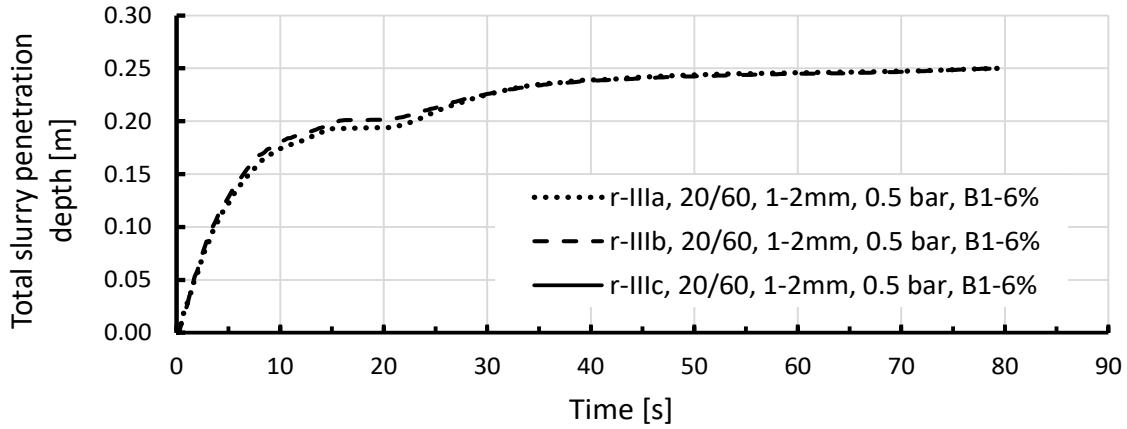

Figure A-3-17: Total slurry re-penetration depth in combination r-III 20/60

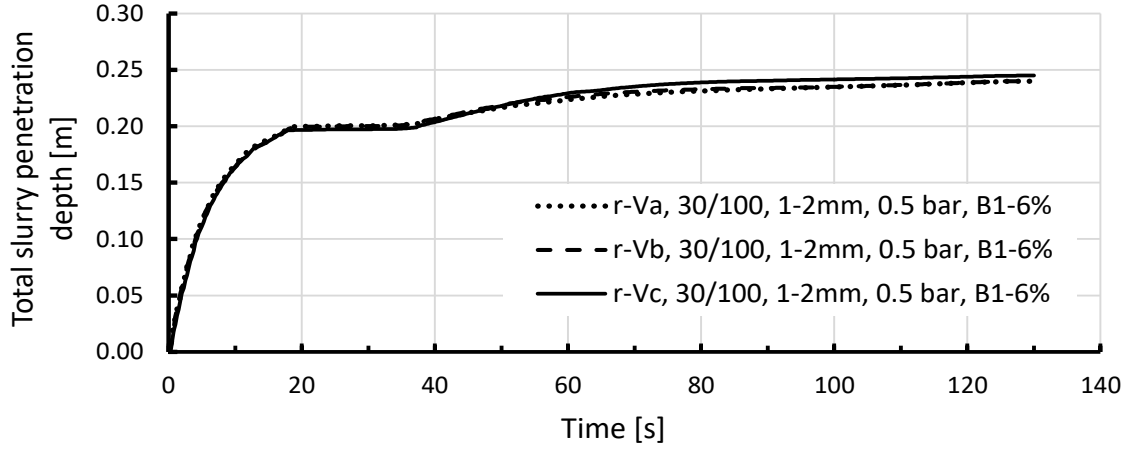

Figure A-3-18: Total slurry re-penetration depth in combination r-V 30/100

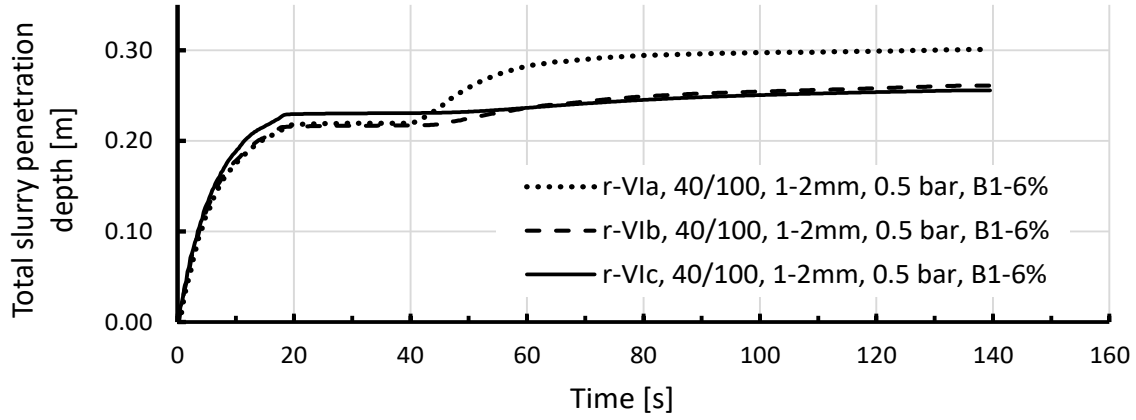

Figure A-3-19: Total slurry re-penetration depth in combination r-VI 40/100

A.3.3.2 Time-dependent development of pore pressures

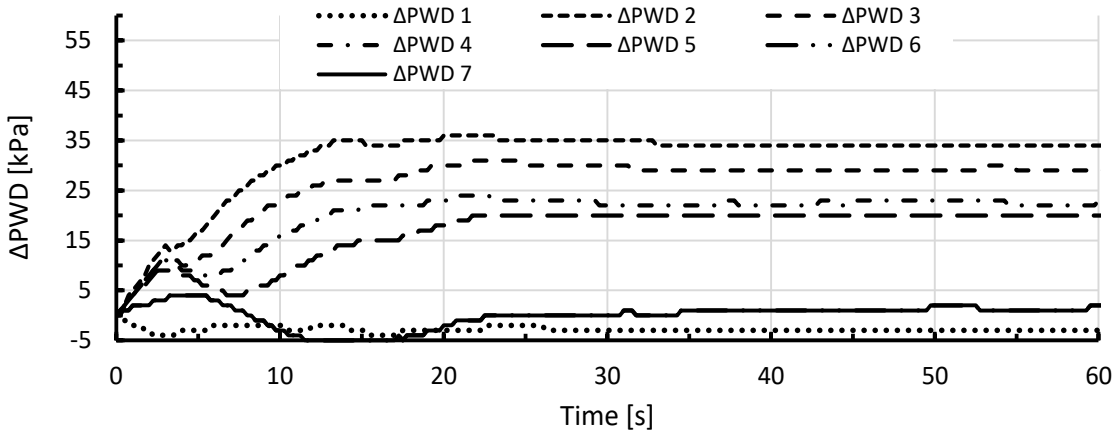

Figure A-3-20: Pore pressure development in Ia, no bp, 1-2mm, 0.5 bar, B1-6%

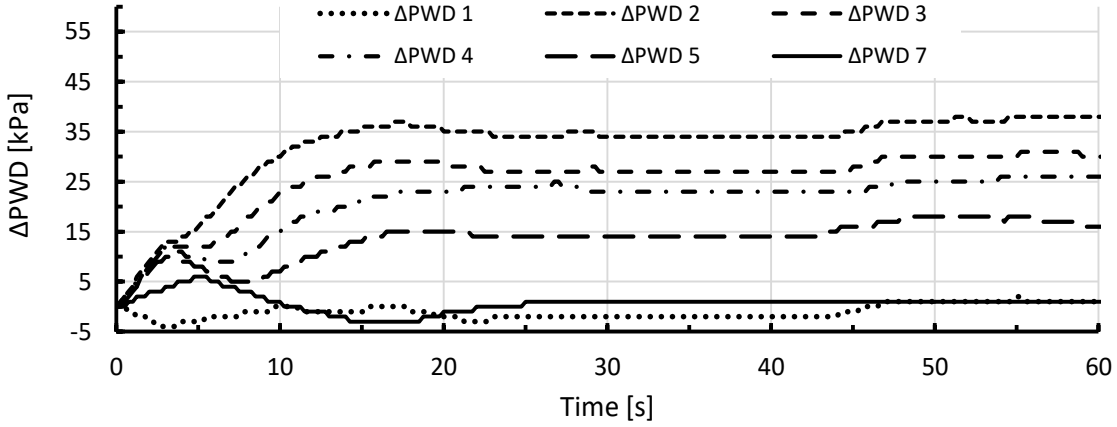

Figure A-3-21: Pore pressure development in Ib, no bp, 1-2mm, 0.5 bar, B1-6%

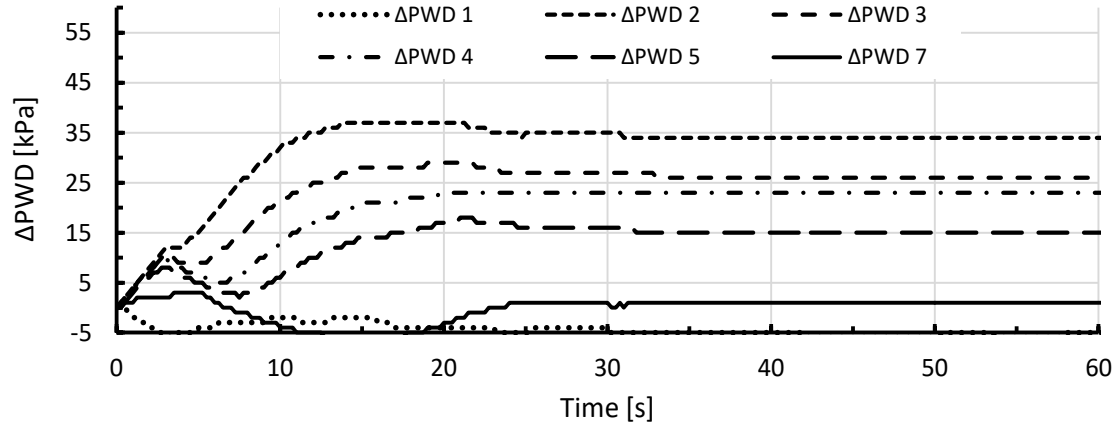

Figure A-3-22: Pore pressure development in Ic, no bp, 1-2mm, 0.5 bar, B1-6%

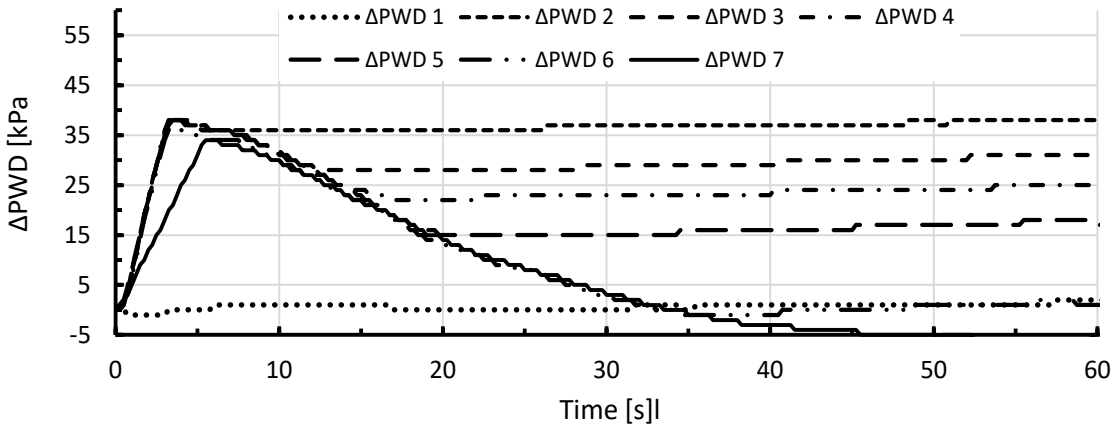

Figure A-3-23: Pore pressure development in IIa, no bp, 1-2mm, 0.5 bar, B1-6%

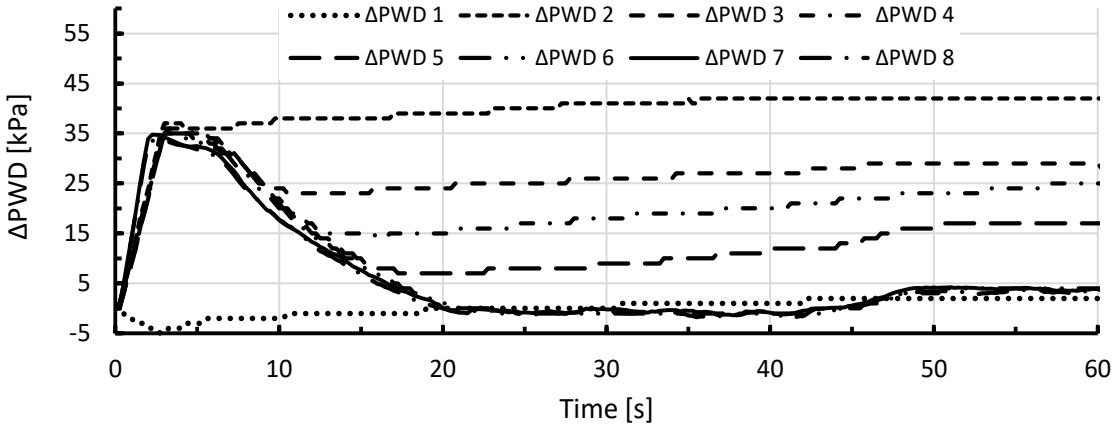

Figure A-3-24: Pore pressure development in IIb, no bp, 1-2mm, 0.5 bar, B1-6%

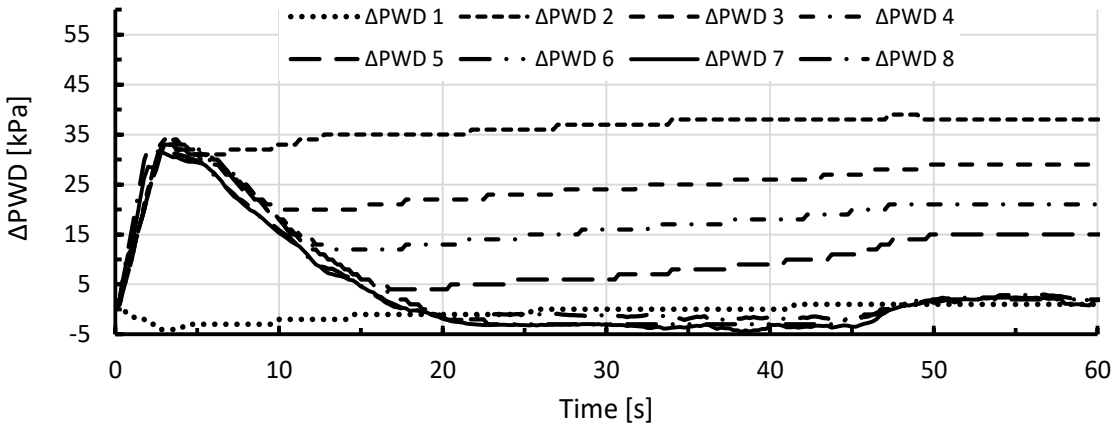

Figure A-3-25: Pore pressure development in IIc, no bp, 1-2mm, 0.5 bar, B1-6%

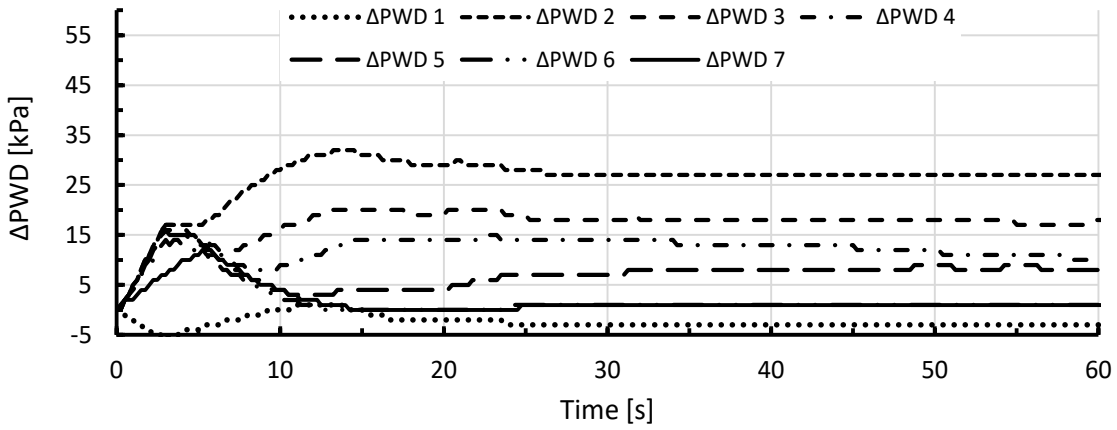

Figure A-3-26: Pore pressure development in IIIa, bp, 1-2mm, 0.5 bar, B1-6%

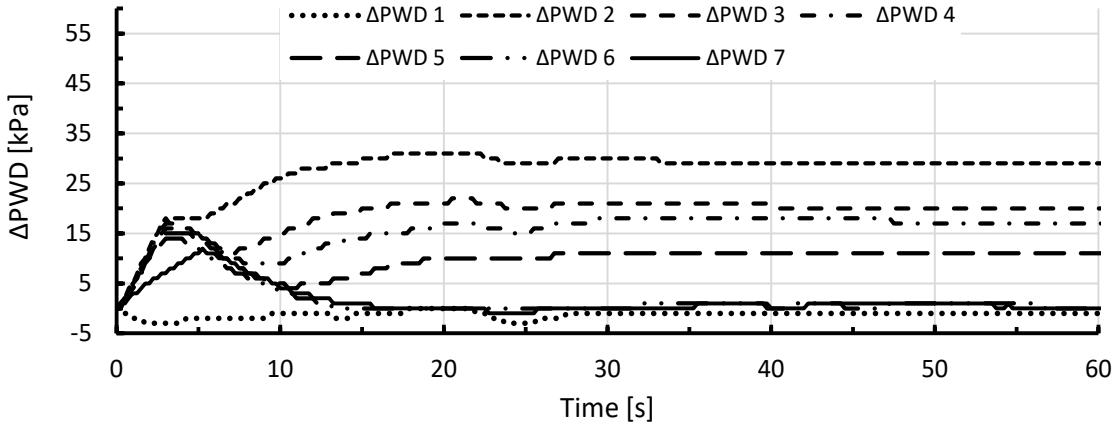

Figure A-3-27: Pore pressure development in IIIb, bp, 1-2mm, 0.5 bar, B1-6%

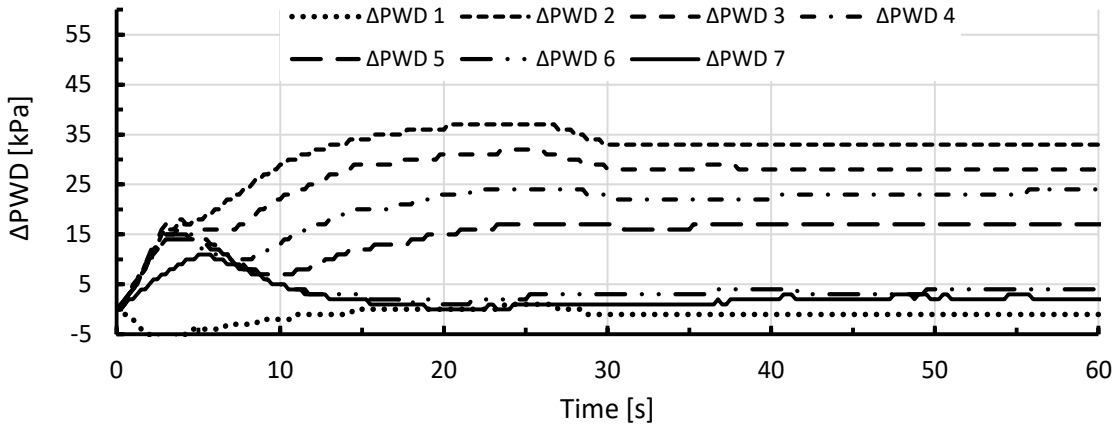

Figure A-3-28: Pore pressure development in IIIc, bp, 1-2mm, 0.5 bar, B1-6%

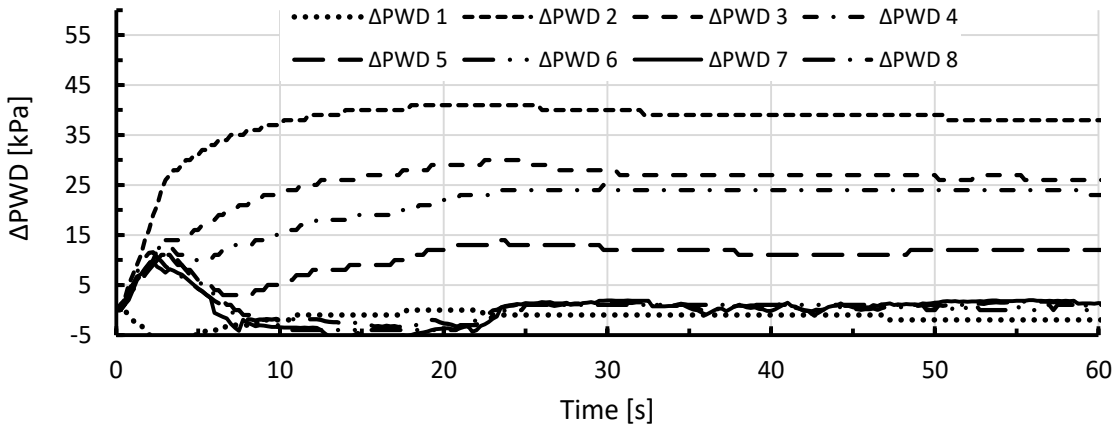

Figure A-3-29: Pore pressure development in IVa, no bp, 1-2mm, 0.5 bar, B1-6%

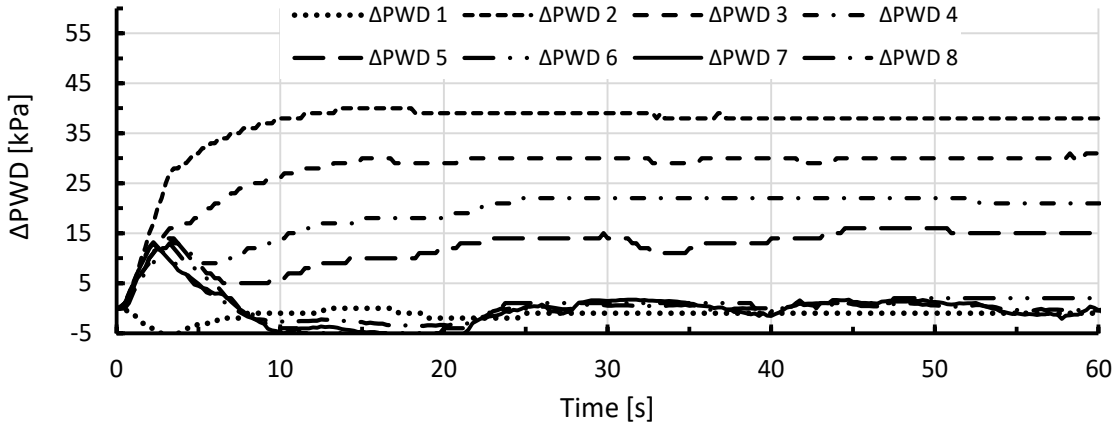

Figure A-3-30: Pore pressure development in IVb, no bp, 1-2mm, 0.5 bar, B1-6%

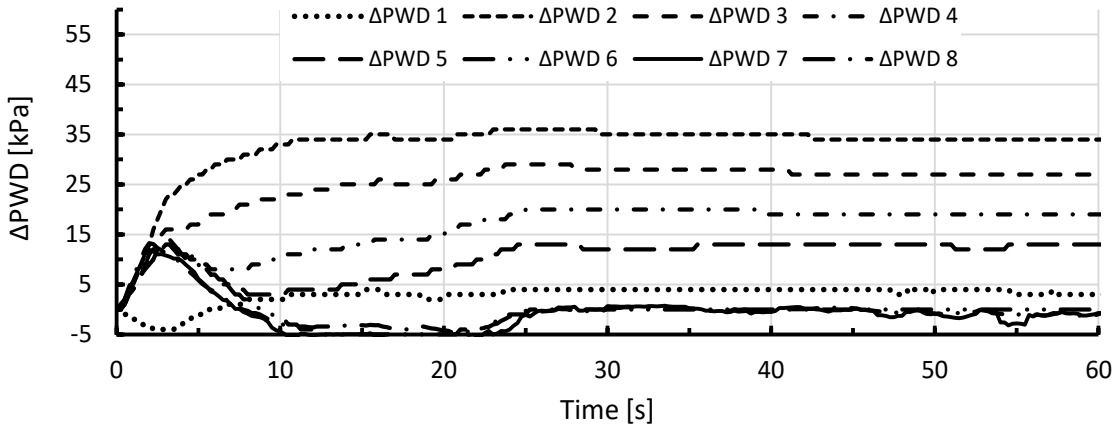

Figure A-3-31: Pore pressure development in IVc, no bp, 1-2mm, 0.5 bar, B1-6%

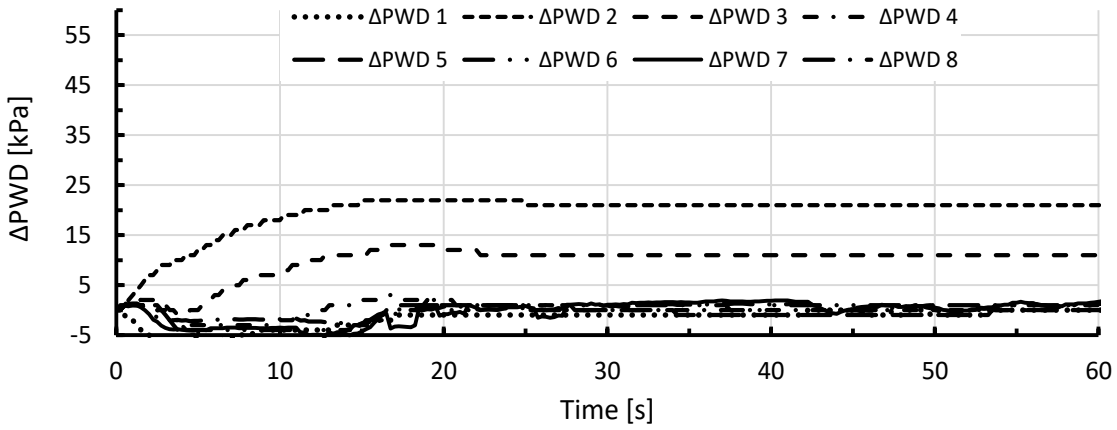

Figure A-3-32: Pore pressure development in Va, no bp, 1-2mm, 0.3 bar, B1-6%

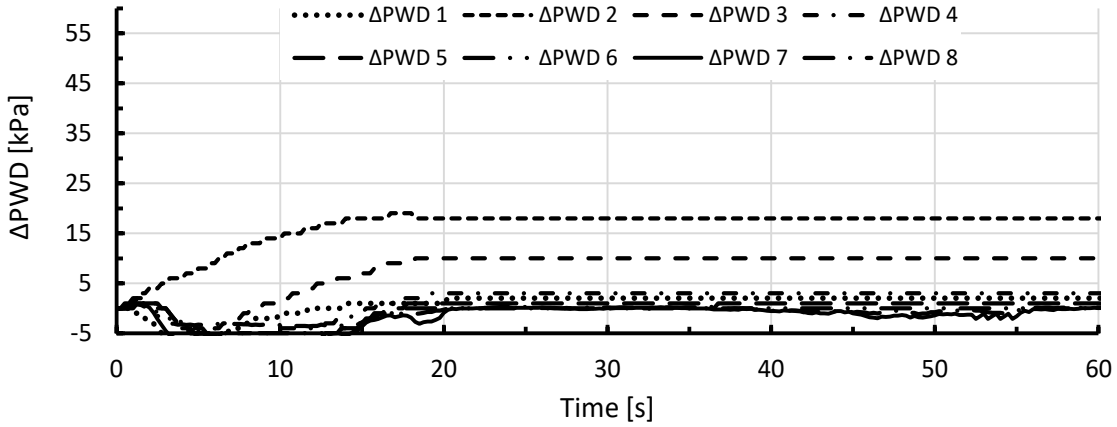

Figure A-3-33: Pore pressure development in Vb, no bp, 1-2mm, 0.3 bar, B1-6%

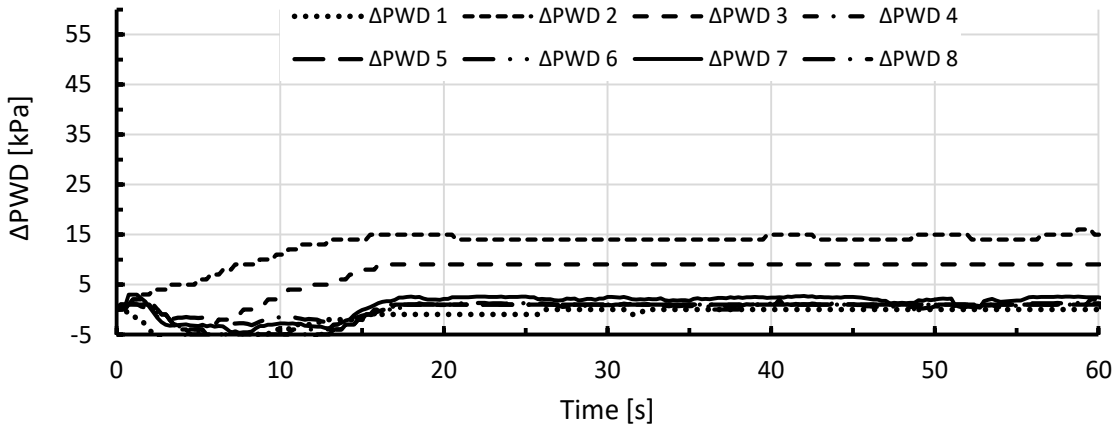

Figure A-3-34: Pore pressure development in Vc, no bp, 1-2mm, 0.3 bar, B1-6%

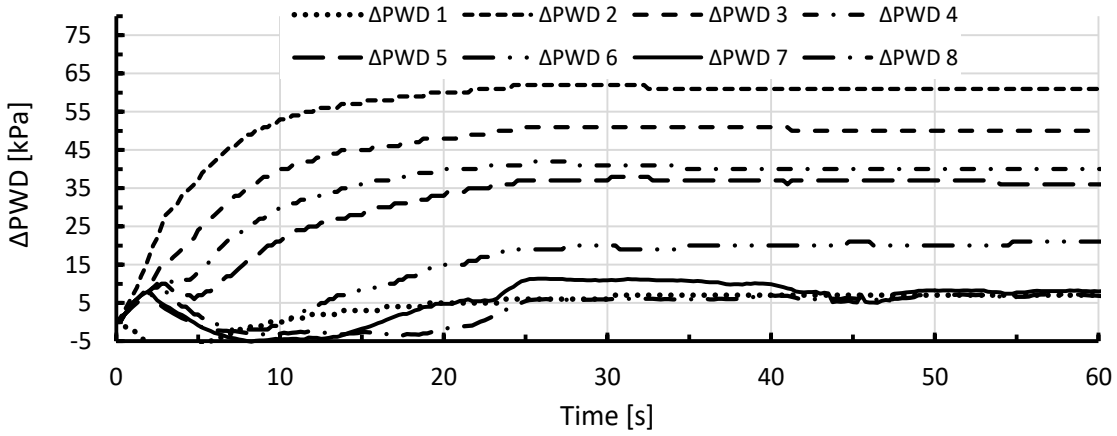

Figure A-3-35: Pore pressure development in VIa, no bp, 1-2mm, 0.7 bar, B1-6%

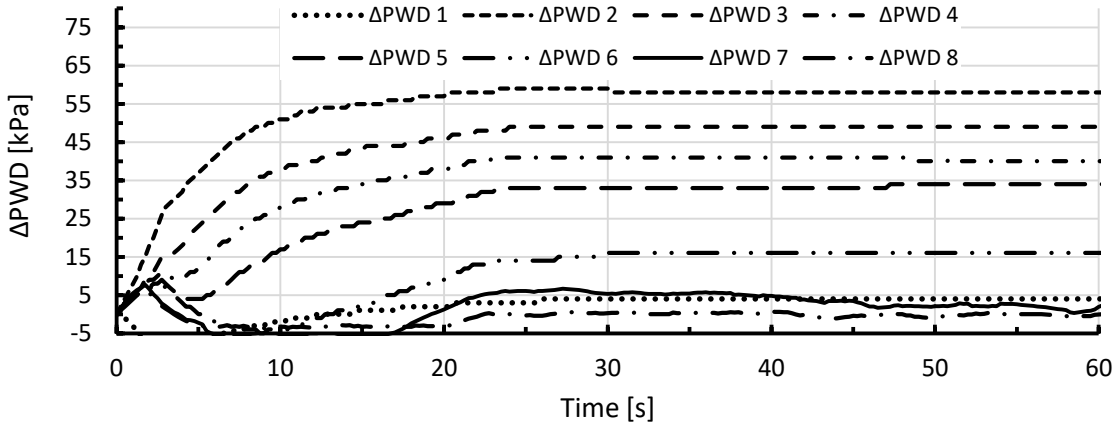

Figure A-3-36: Pore pressure development in VIb, no bp, 1-2mm, 0.7 bar, B1-6%

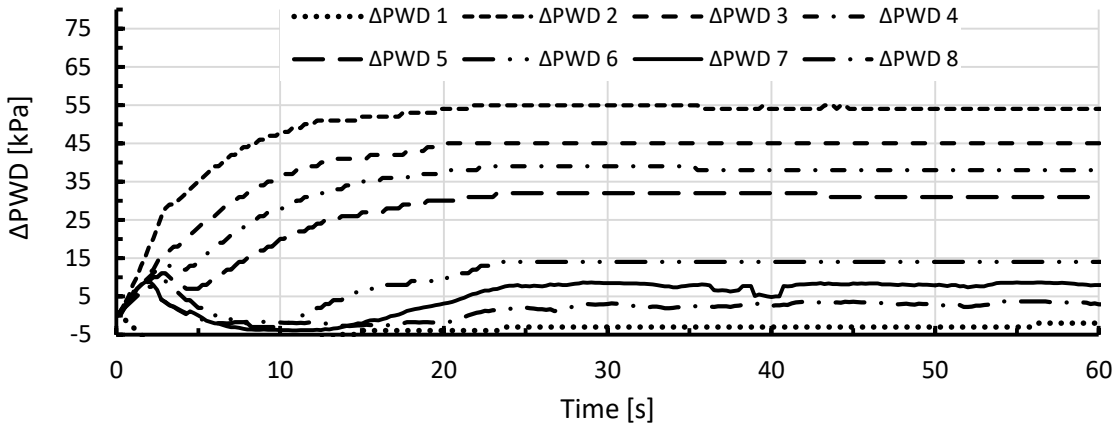

Figure A-3-37: Pore pressure development in VIc, no bp, 1-2mm, 0.7 bar, B1-6%

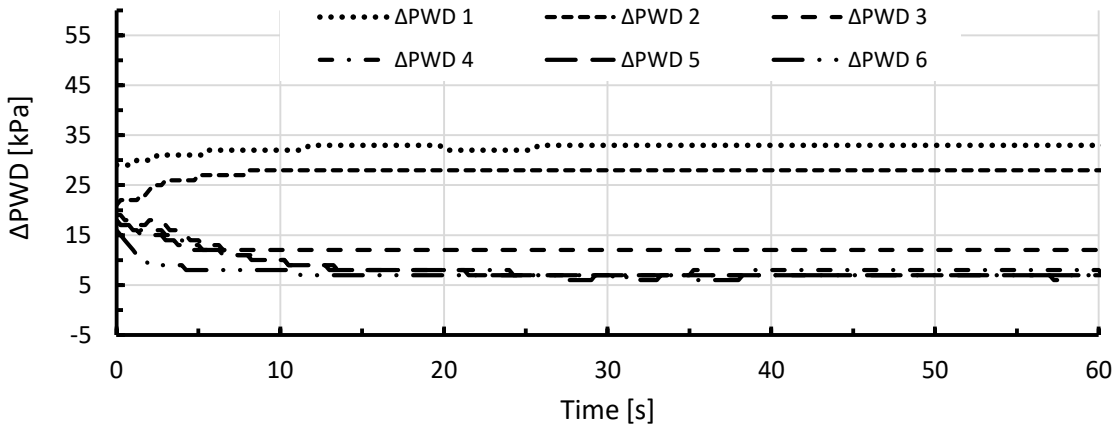

Figure A-3-38: Pore pressure development in VIIa, no bp, 0.063-4mm, 0.3 bar, B1-6%

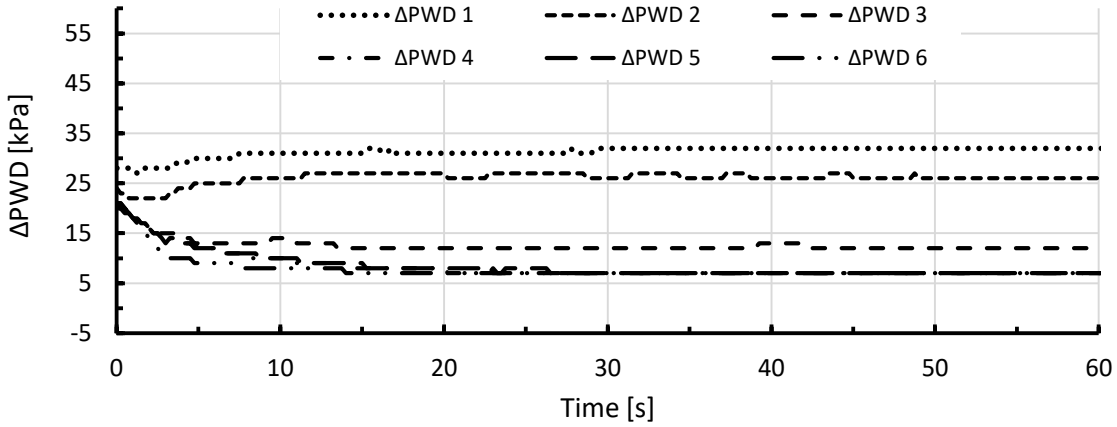

Figure A-3-39: Pore pressure development in VIIb, no bp, 0.063-4mm, 0.3 bar, B1-6%

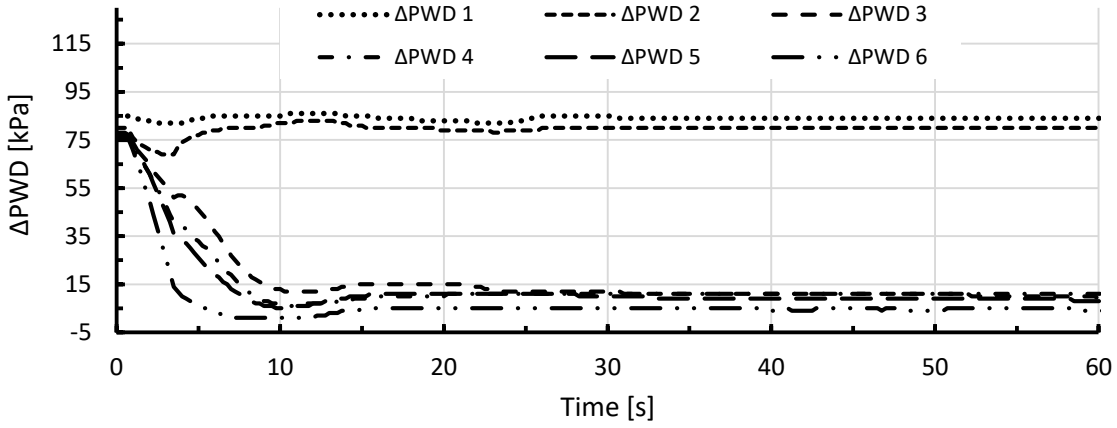

Figure A-3-40: Pore pressure development in VIIIa, no bp, 0.063-4mm, 0.9 bar, B1-6%

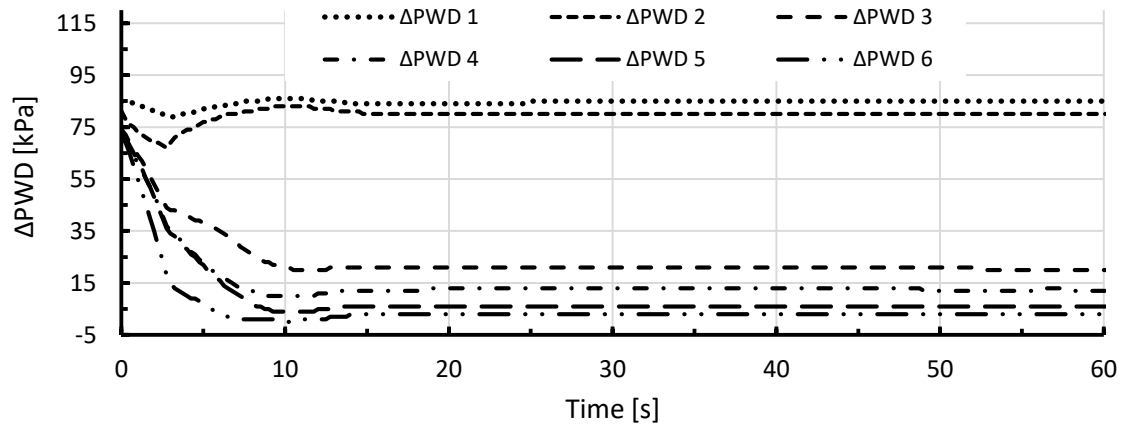

Figure A-3-41: Pore pressure development in VIIIb, no bp, 0.063-4mm, 0.9 bar, B1-6%

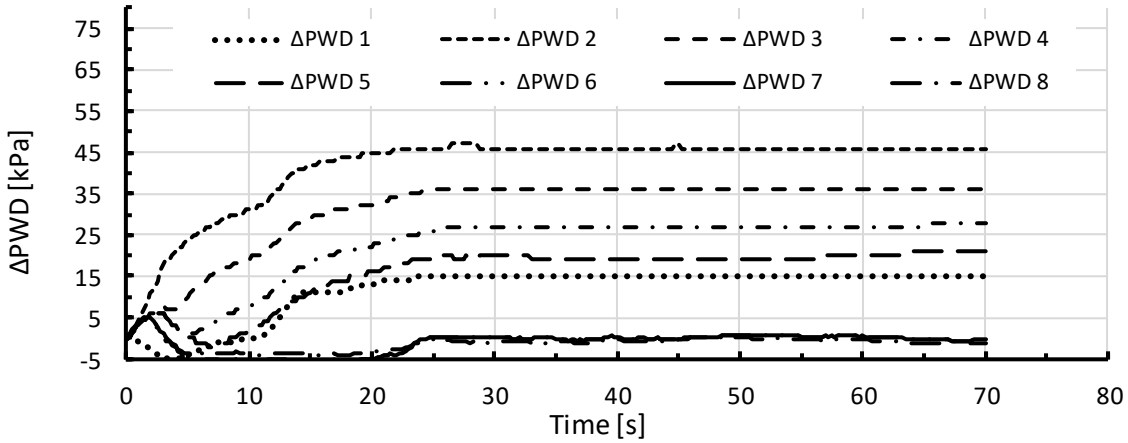

Figure A-3-42: Pore pressure development in r-Ia, 10/60, 1-2 mm, 0.5 bar, B1-6%

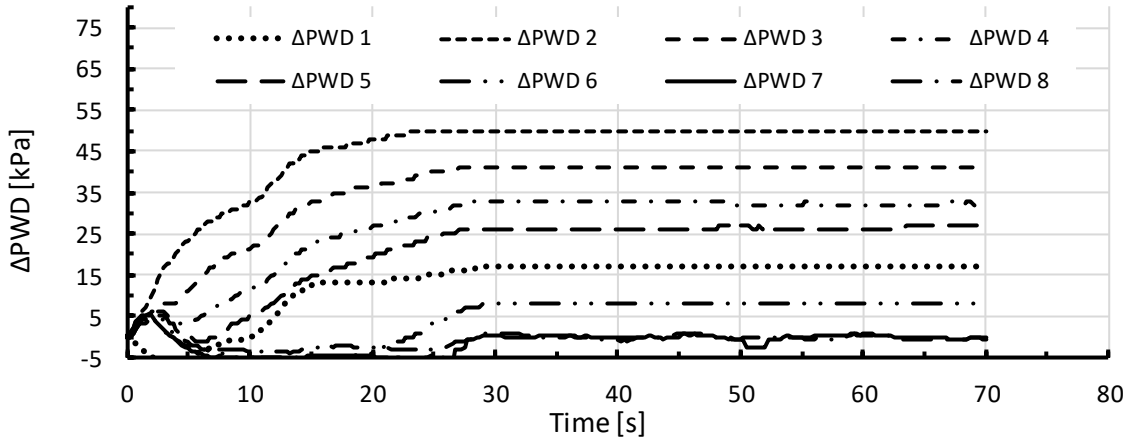

Figure A-3-43: Pore pressure development in r-Ib, 10/60, 1-2 mm, 0.5 bar, B1-6%

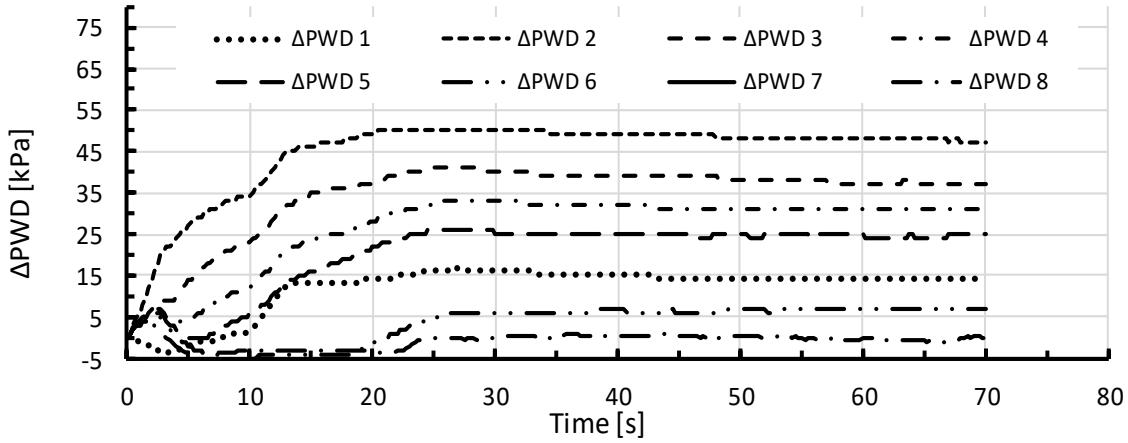

Figure A-3-44: Pore pressure development in r-Ic, 10/60, 1-2 mm, 0.5 bar, B1-6%

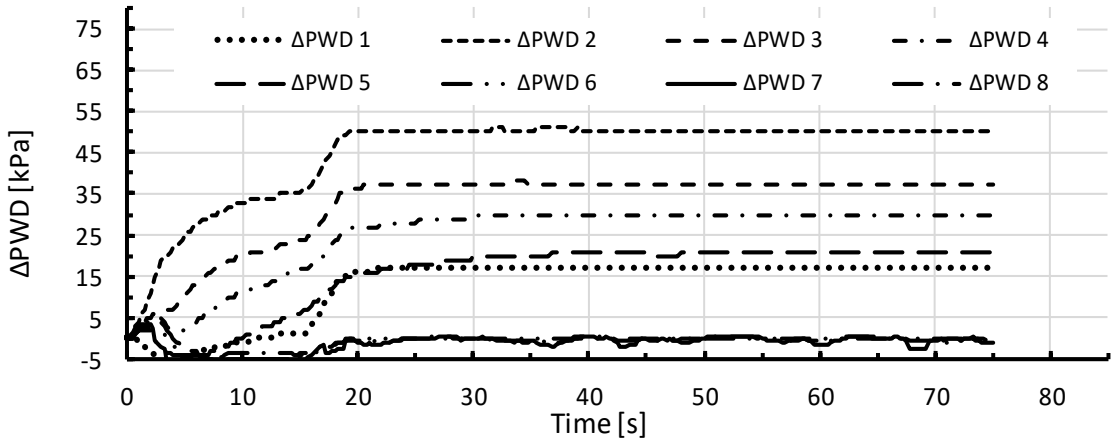

Figure A-3-45: Pore pressure development in r-IIa, 15/60, 1-2 mm, 0.5 bar, B1-6%

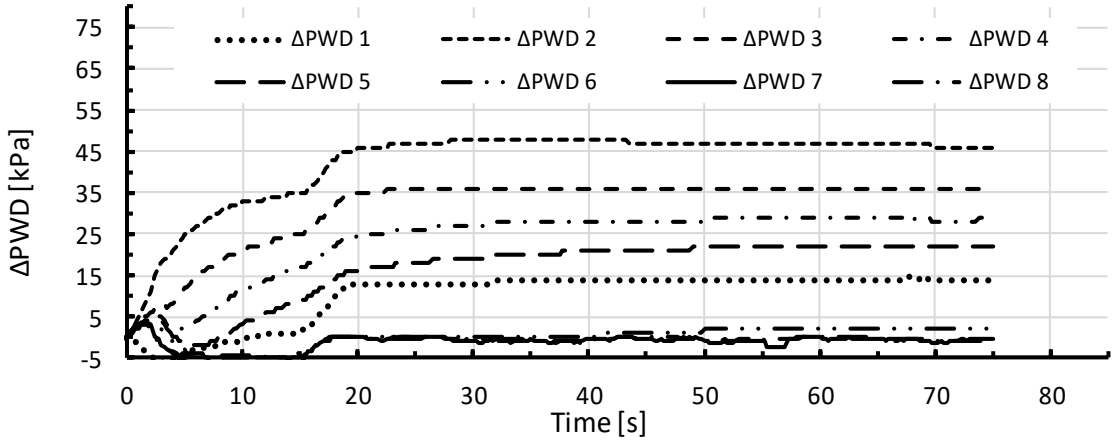

Figure A-3-46: Pore pressure development in r-IIb, 15/60, 1-2 mm, 0.5 bar, B1-6%

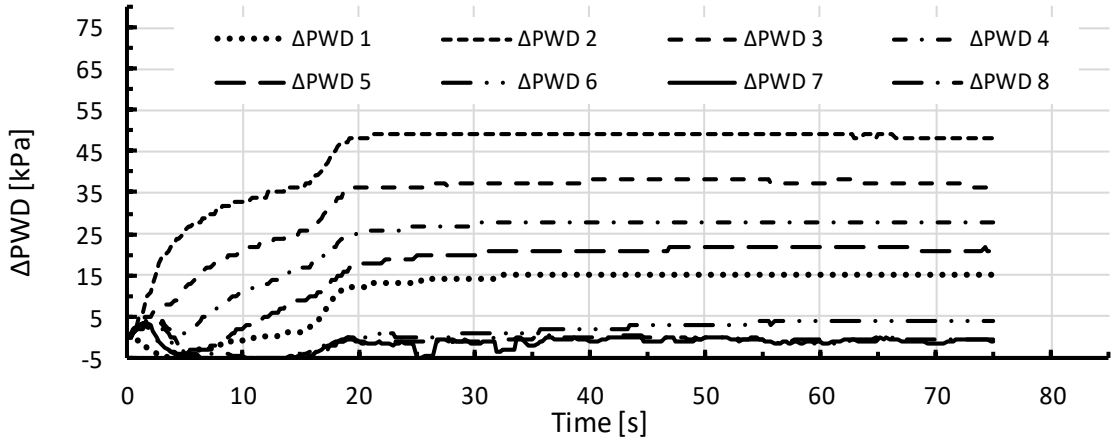

Figure A-3-47: Pore pressure development in r-IIc, 15/60, 1-2 mm, 0.5 bar, B1-6%

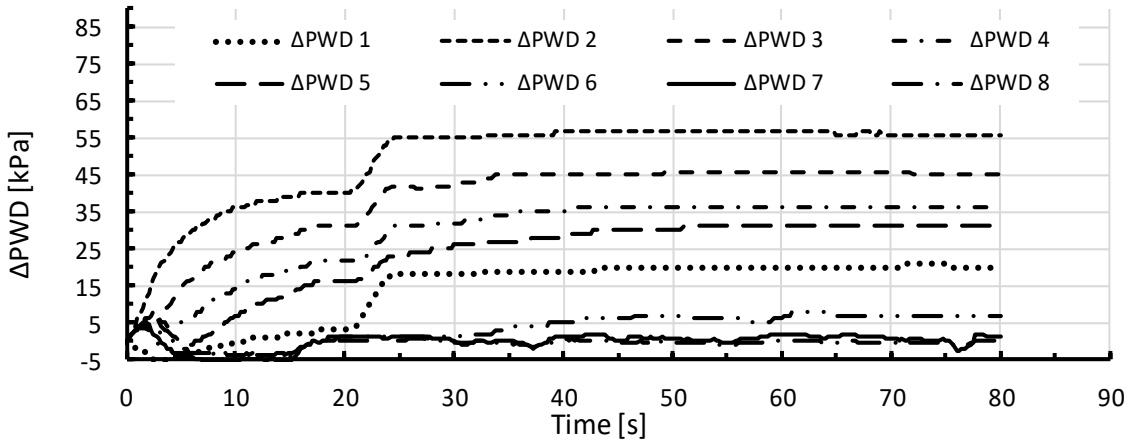

Figure A-3-48: Pore pressure development in r-IIIa, 20/60, 1-2 mm, 0.5 bar, B1-6%

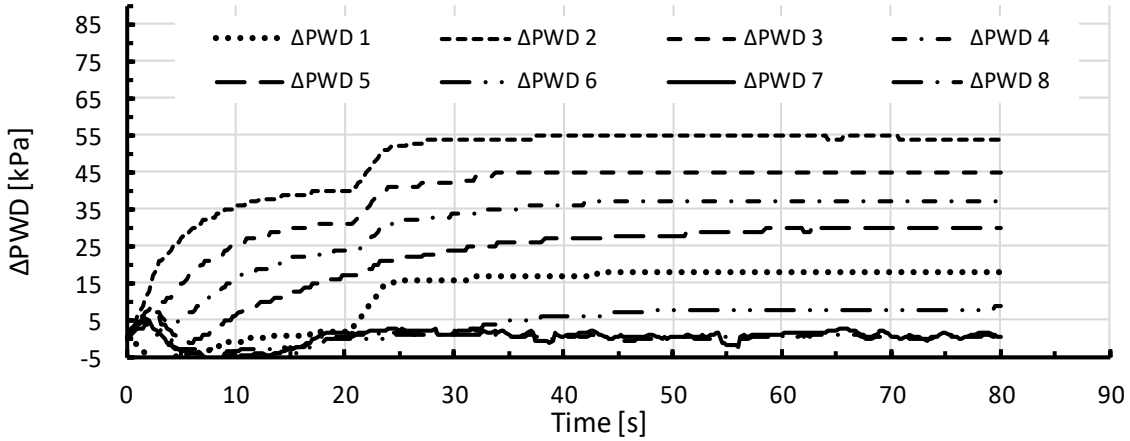

Figure A-3-49: Pore pressure development in r-IIIb, 20/60, 1-2 mm, 0.5 bar, B1-6%

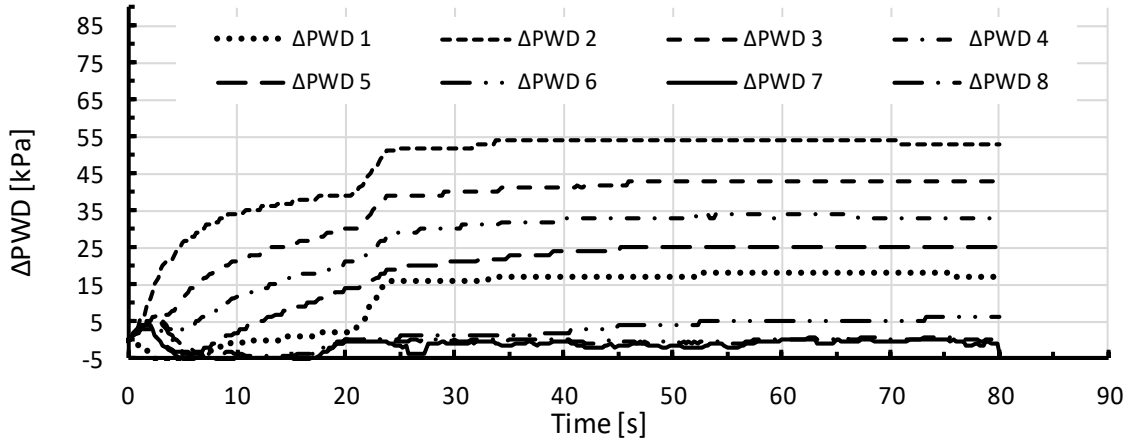

Figure A-3-50: Pore pressure development in r-IIIc, 20/60, 1-2 mm, 0.5 bar, B1-6%

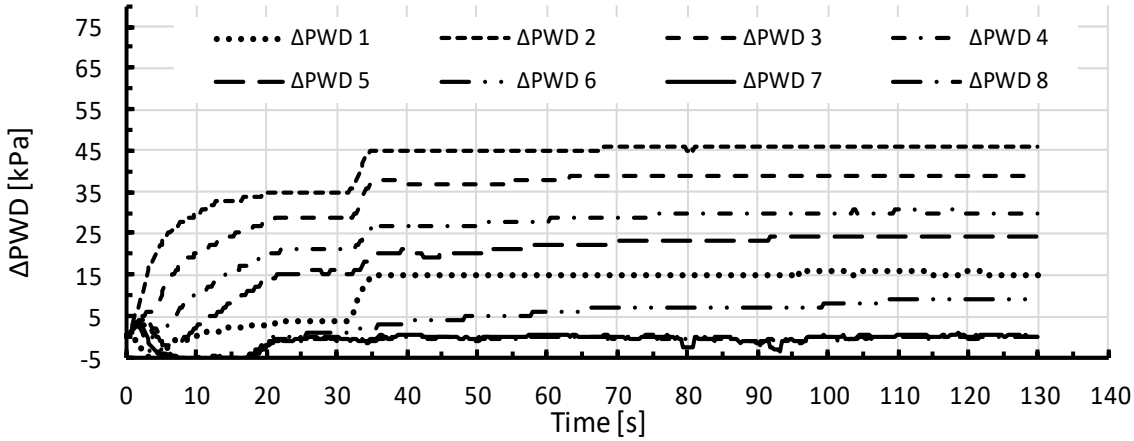

Figure A-3-51: Pore pressure development in r-Va, 30/100, 1-2 mm, 0.5 bar, B1-6%

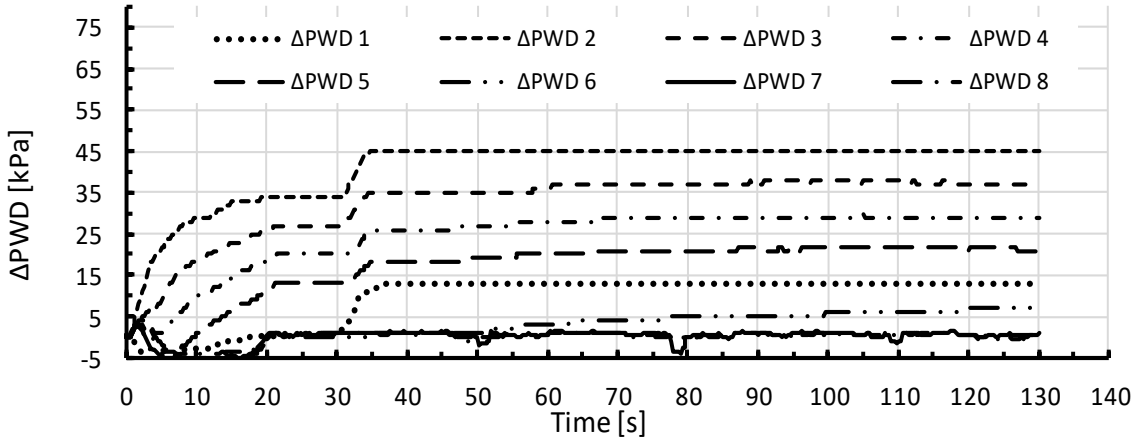

Figure A-3-52: Pore pressure development in r-Vb, 30/100, 1-2 mm, 0.5 bar, B1-6%

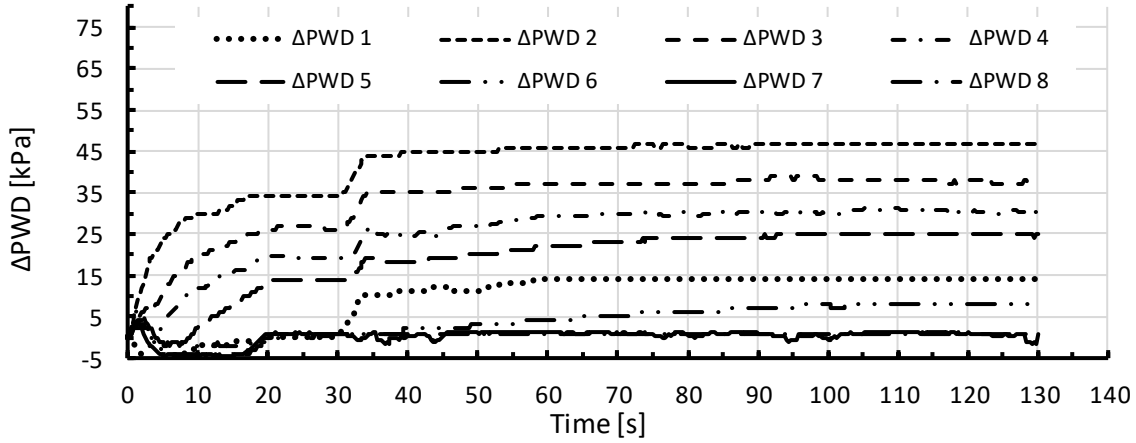

Figure A-3-53: Pore pressure development in r-Vc, 30/100, 1-2 mm, 0.5 bar, B1-6%

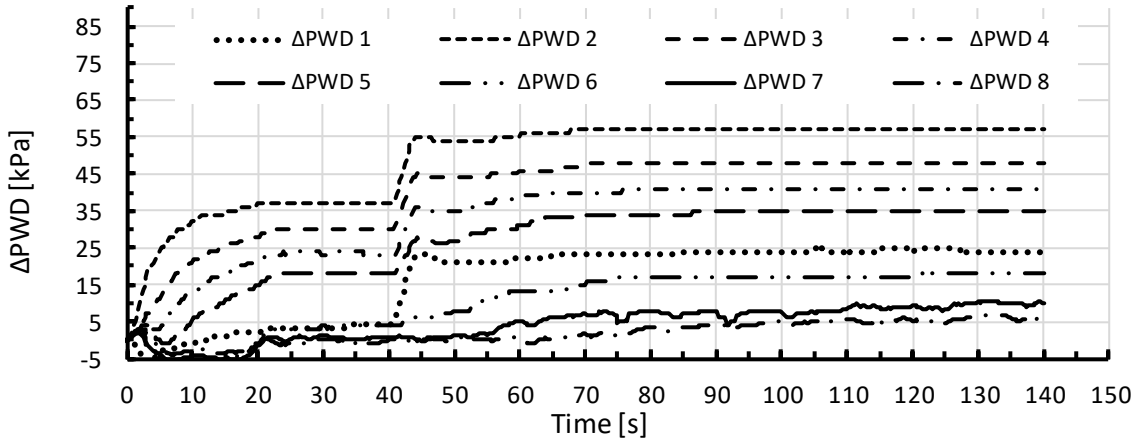

Figure A-3-54: Pore pressure development in r-VIa, 40/100, 1-2 mm, 0.5 bar, B1-6%

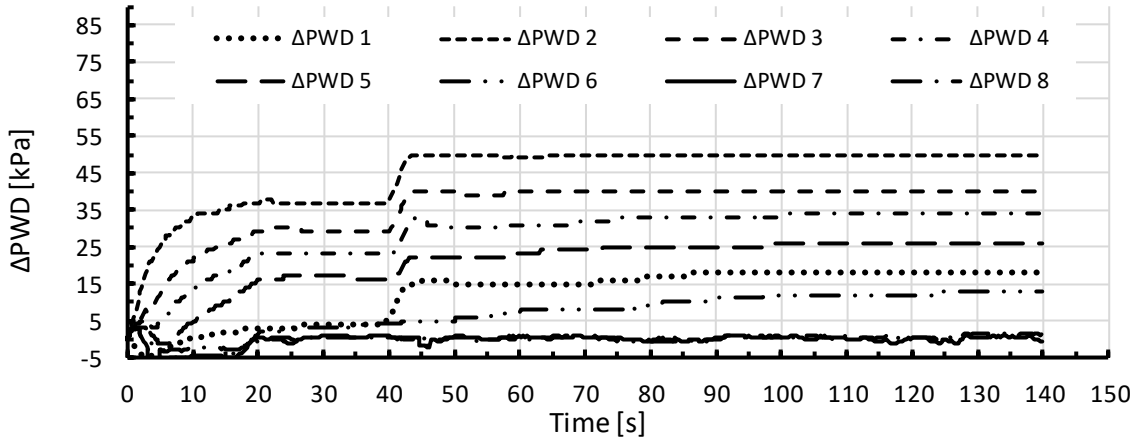

Figure A-3-55: Pore pressure development in r-VIb, 40/100, 1-2 mm, 0.5 bar, B1-6%

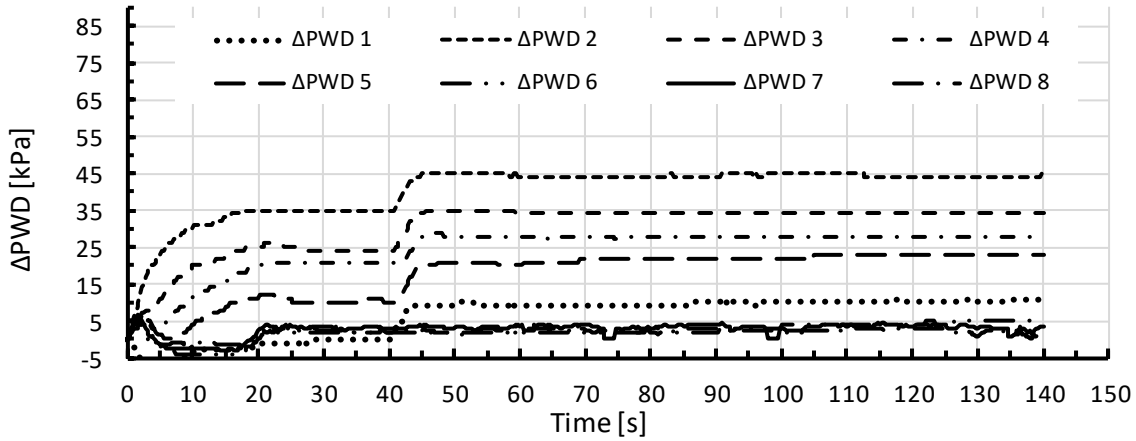

Figure A-3-56: Pore pressure development in r-VIc, 40/100, 1-2 mm, 0.5 bar, B1-6%

A.3.3.3 Time-dependent development of total stresses

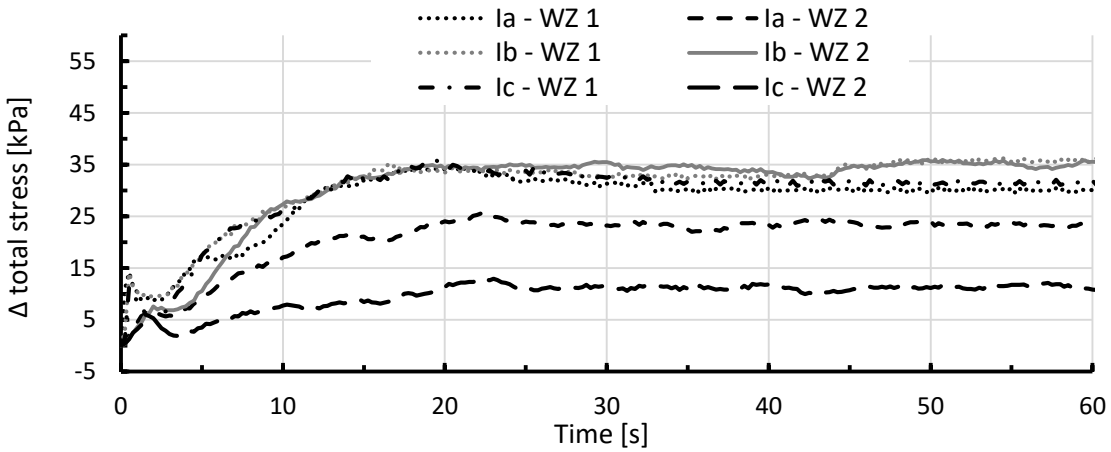

Figure A-3-57: Total stress development in combination I

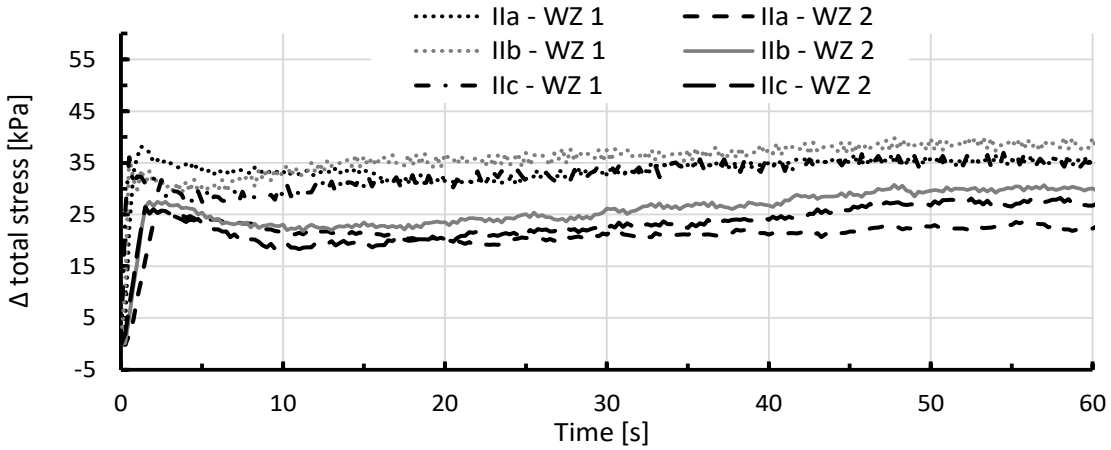

Figure A-3-58: Total stress development in combination II

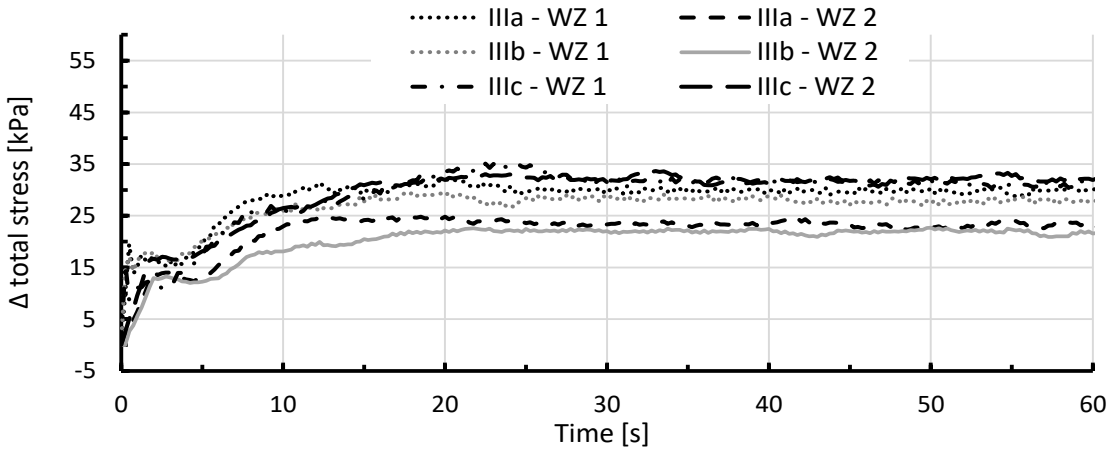

Figure A-3-59: Total stress development in combination III

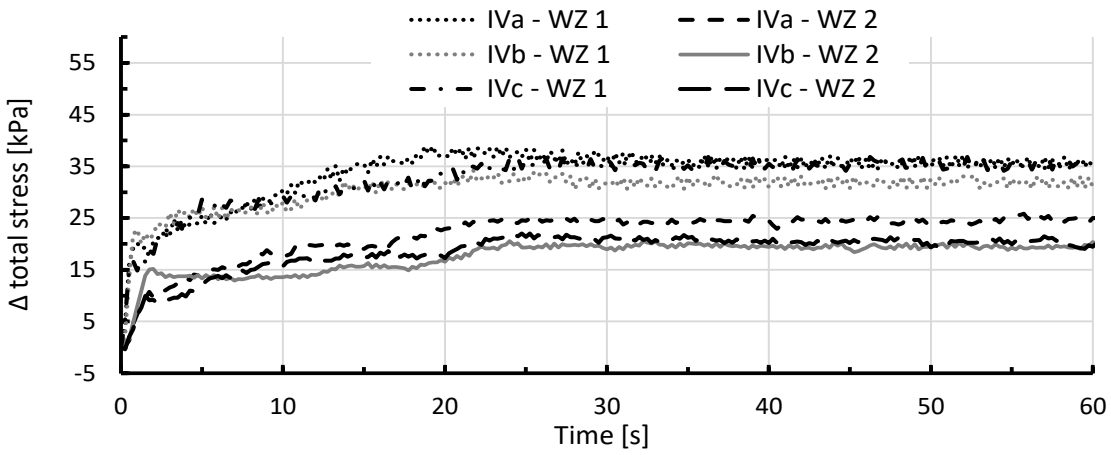

Figure A-3-60: Total stress development in combination IV

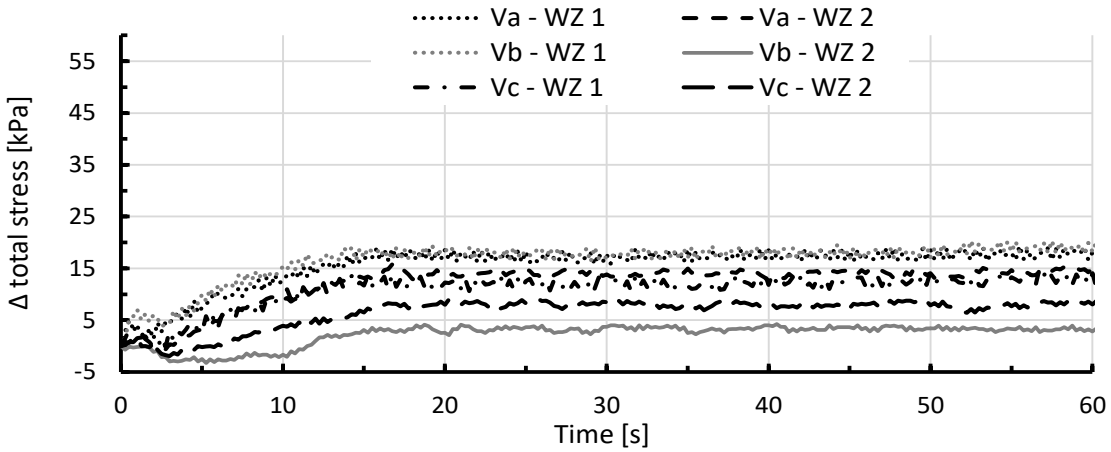

Figure A-3-61: Total stress development in combination V

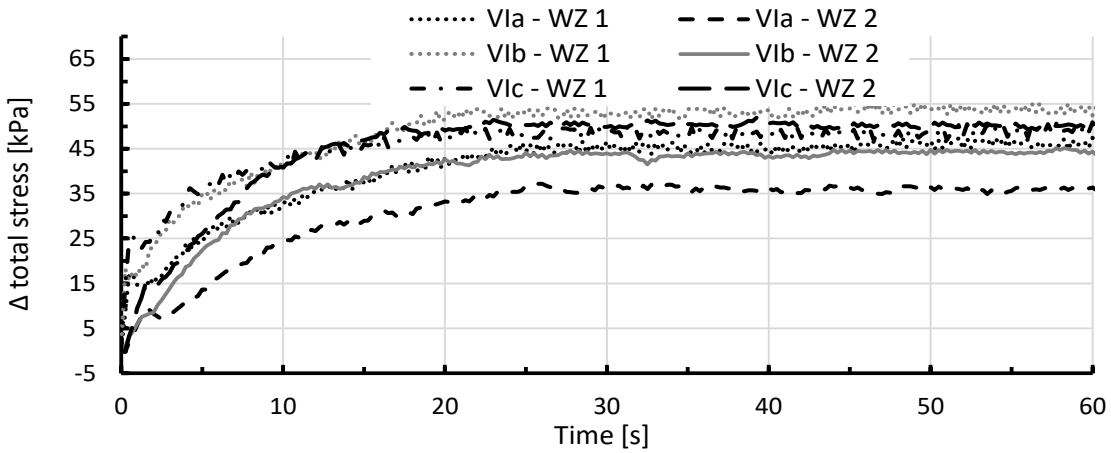

Figure A-3-62: Total stress development in combination VI

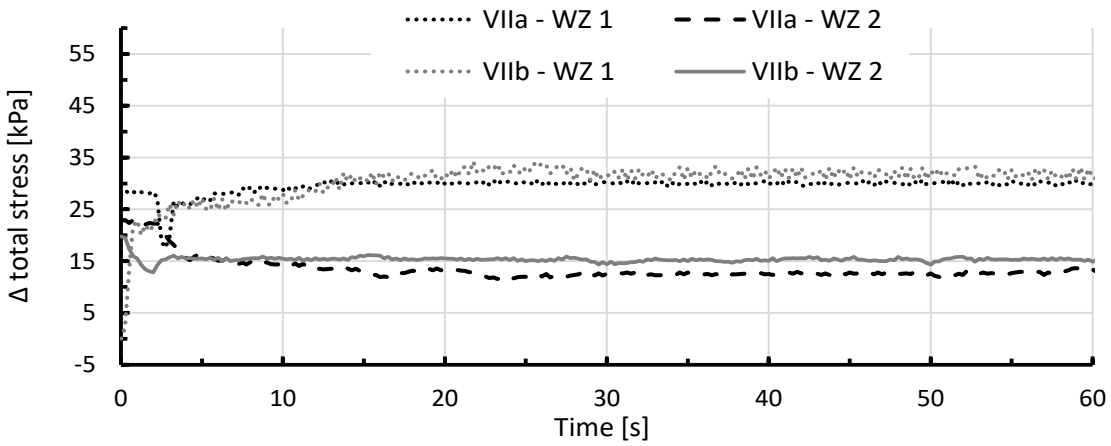

Figure A-3-63: Total stress development in combination VII

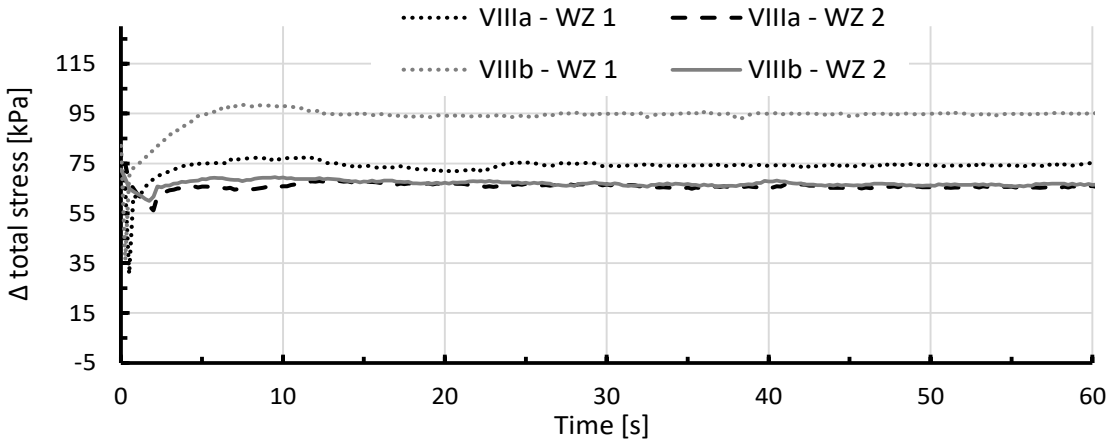

Figure A-3-64: Total stress development in combination VIII

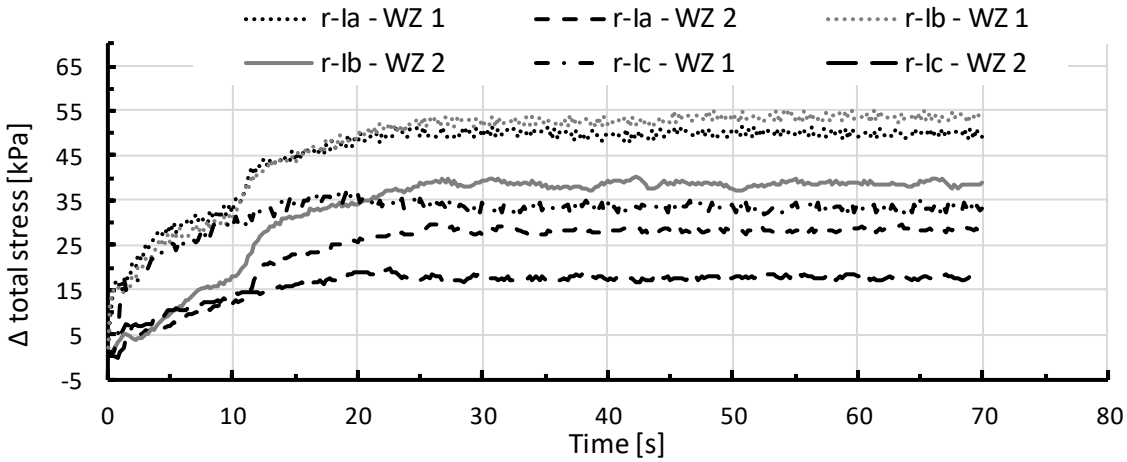

Figure A-3-65: Total stress development in combination r-I 10/60

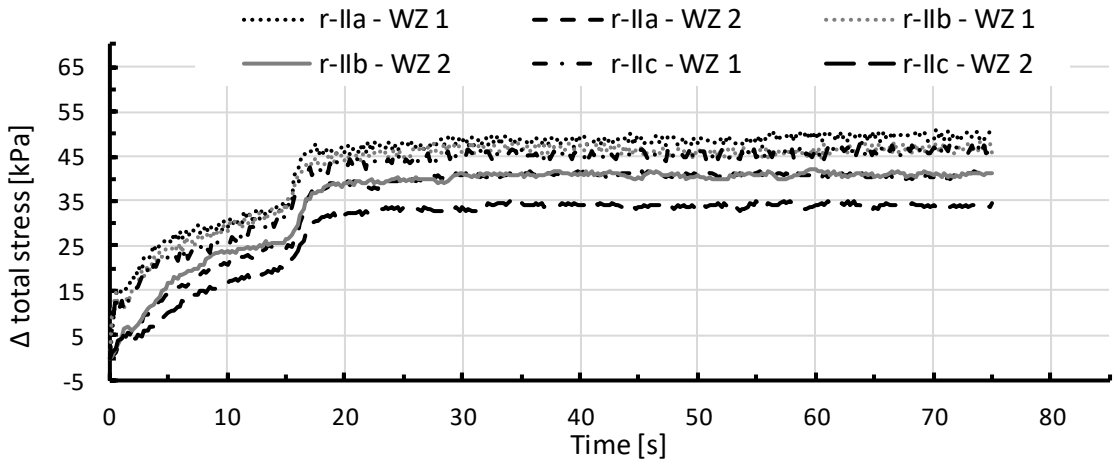

Figure A-3-66: Total stress development in combination r-II 15/60

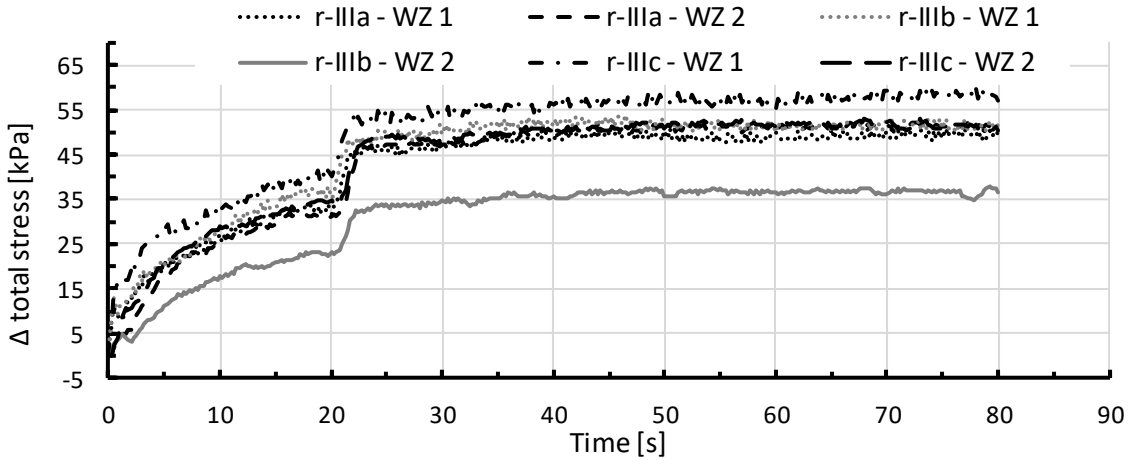

Figure A-3-67: Total stress development in combination r-III 20/60

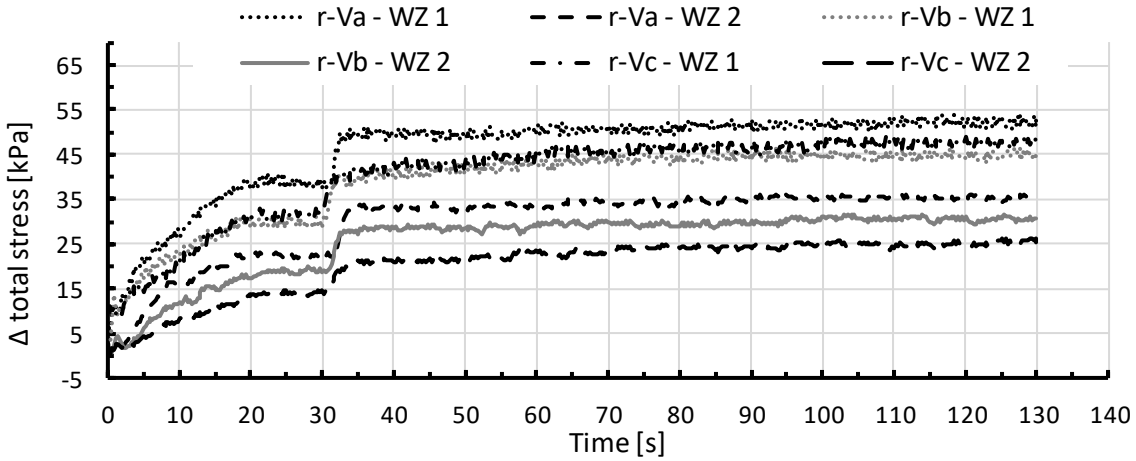

Figure A-3-68: Total stress development in combination r-V 30/100

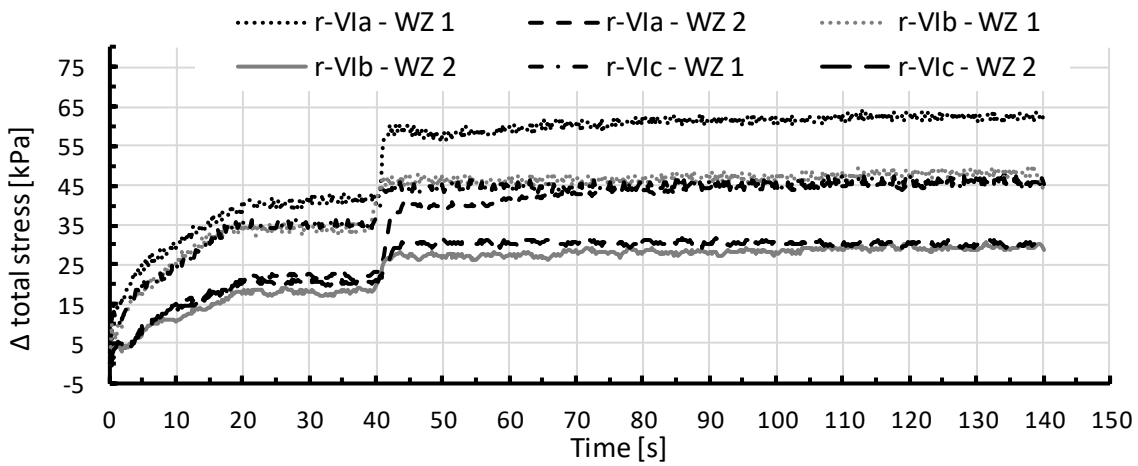

Figure A-3-69: Total stress development in combination r-VI 40/100

A.4 Case B – RUB tunnelling device

Tests for the investigation of slurry-soil interaction for a deep slurry penetration (Case B) with soil cutting were introduced in chapter 7.

A.4.1 Setup and testing procedure

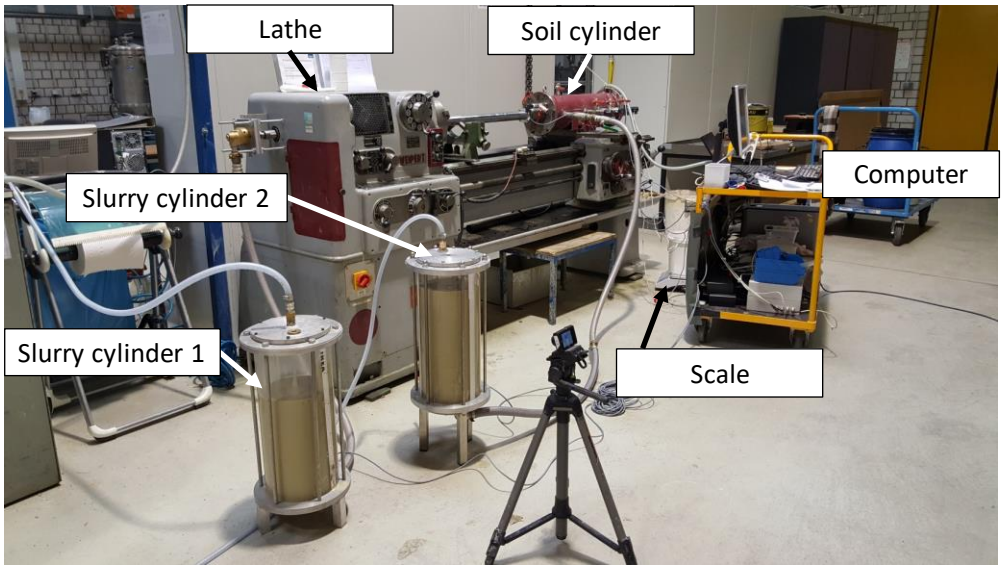

Figure A-4-1: Photo of the RUB Tunnelling device

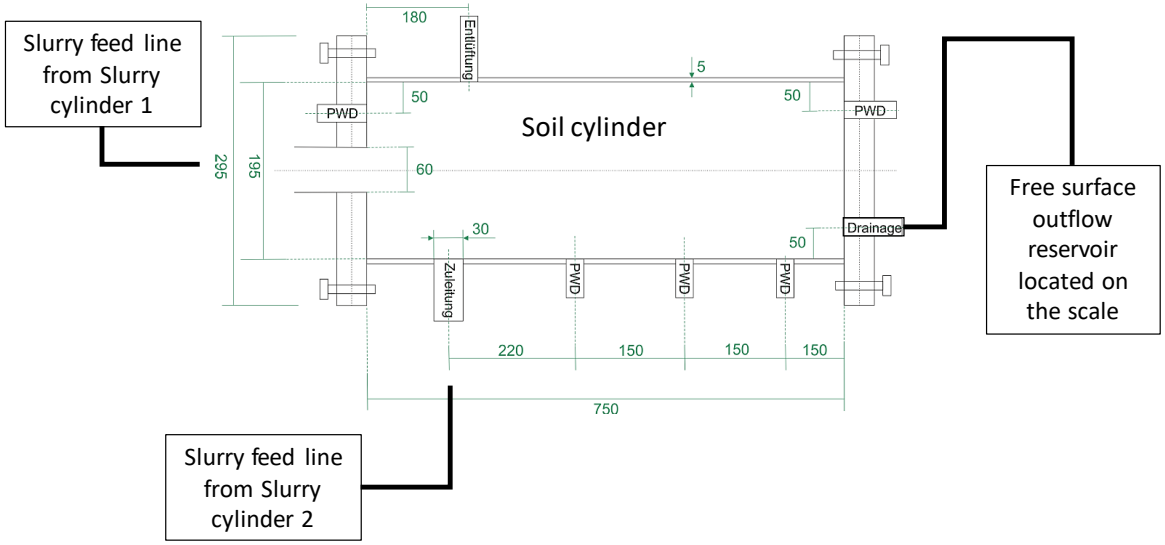

Figure A-4-2: Sketch with dimensions of the soil cylinder of the RUB tunnelling device, adapted from Küpferle (2017)

Equipment

- 2 slurry cylinders
- 1 RUB tunnelling device (Küpferle, 2018) with soil cylinder
- 1 bucket
- 3 pipes
- 1 computer connected scale
- 2 stopwatches
- 1 computer
- 2 video cameras + tripods
- 2 manometers for pressure steering*
- 6 pore water pressure sensors (PWD)* connected to the computer
- 2 total stress sensors (WZ)
- 2 video cameras + tripods
- 3 glass capillaries

Preparations

1. Slurry mixing 24 hours before the experiment
2. Check of slurry properties the day before the test starts
3. Installation of drainage grid at the bottom of soil cylinder
4. Saturated installation and compaction of the soil into the soil cylinder in vertical position
5. Installing of glass capillaries on elevations corresponding to the location of the pore pressure sensors, the capillaries are connecting the excavation axis with the respective pore pressure sensor
6. Installing the cutting wheel
7. Filling the rest of cylinder with slurry
8. Putting the soil cylinder in horizontal position and fixing on the lathe
9. Connecting slurry cylinders to the soil cylinder by pipes
10. Opening of valves on slurry pipes and pressurizing the soil cylinder
11. Opening of drainage valve enabling primary slurry penetration for 15 minutes

Procedure

12. Excavation starts by activation of lathe moving and cutting wheel rotating
13. Recording of the outflow from the set-up by scale and monitoring of pore water pressure by sensors in the set-up every 0.25 s, Recording the slurry levels in the cylinders
14. Defined length of soil is excavated, excavation stops automatically to avoid any damage of the device

A.4.2 Testing protocols

Experiment No.:	rc-Ia	rc-Ib	rc-Ic
Date of experiment:	21.02.2018	21.02.2018	06.06.2018
Soil properties			
Grain size of the soil [mm]	1-2	1-2	1-2
Actual weight of soil sample [kg]	25	25	25
Remaining height in the soil container [cm]	19.5	20.25	19
Density of the sample [g/cm³]	1.57	1.57	1.57
Grain density ρc [g/cm^3]	2.65	2.65	2.65
Porosity n: $n = 1 - \rho_d/\rho$ [–]	0.394	0.4	0.41
Slurry properties			
Type of bentonite	B1	B1	B1
Concentration [%]	6	6	6
Date of mixing	20.02.2018	20.02.2018	05.06.2018
pH-value [-]	10.61	10.61	10.4
Density [g/cm^3]	1.031	1.031	1.032
Yield point with ball harp [N/m²]	57,78	57,78	58.55
Marsh-time tM_{1000} [s]	90	90	114
Marsh-time tM_{1500} [s]	not determinable	not determinable	not determinable
Slurry filling - primary penetration			
Pressure in s-cylinder 1 (pressure gauge) [bar]	0.45	0.44	0.4
Pressure in s-cylinder 2 (pressure gauge) [bar]	0.39	0.39	0.32
Height of the slurry in the s-cylinder 1 before start[cm]	0.5	2	14.5
Height of the slurry in the s-cylinder 2 before start[cm]	13.5	25.2	26
Height of the water in the s-cylinder 1 at the end [cm]	4.2	11	20
Height of the water in the s-cylinder 2 at the end [cm]	16.2	25.5	26.3
Outflow [kg]	3.483	2.107	1.406
Duration of the experiment [s]	900	900	900
Excavation			
Pressure in s-cylinder 1 (pressure gauge) [bar]	0.52	0.44	0.64
Pressure in s-cylinder 2 (pressure gauge) [bar]	0.42	0.39	0.44
Chamber pressure [bar]	0.23	0.21	0.27
Slurry discharge from the set-up at [min]	45	45	48
Excavation path [mm]	465	465	465
RPM [-]	71	71	71
PR [0.1 mm/rev]	0.1	0.1	0.1
Outflow [kg]	6.663	6.474	6.574

Experiment No.:	rc-IIa	rc-IIb	rc-IIc
Date of experiment:	21.02.2018	20.02.2018	20.02.2018
Soil properties			
Grain size of the soil [mm]	1-2	1-2	1-2
Actual weight of soil sample [kg]	25	25	25
Remaining height in the soil container [cm]	21.5	19.5	19.7
Density of the sample [g/cm³]	1.57	1.57	1.57
Grain density ρc [g/cm^3]	2.65	2.65	2.65
Porosity n: $n = 1 - \rho_d/\rho$ [–]	0.38	0.4	0.41
Slurry properties			
Type of bentonite	B1	B1	B1
Concentration [%]	6	6	6
Date of mixing	18.02.2018	19.02.2018	19.02.2018
pH-value [-]	10.69	10.75	10.75
Density [g/cm^3]	1.035	1.031	1.031
Yield point with ball harp [N/m²]	48.34	57,78	57,78
Marsh-time tM_{1000} [s]	82	96	96
Marsh-time tM_{1500} [s]	not determinable	not determinable	not determinable
Slurry filling - primary penetration			
Pressure in s-cylinder 1 (pressure gauge) [bar]	0.73	0.69	0.64
Pressure in s-cylinder 2 (pressure gauge) [bar]	0.59	0.39	0.58
Height of the slurry in the s-cylinder 1 before start[cm]	6	8.7	0
Height of the slurry in the s-cylinder 2 before start[cm]	4.3	7.2	9.3
Height of the water in the s-cylinder 1 at the end [cm]	16.9	21.5	9.5
Height of the water in the s-cylinder 2 at the end [cm]	7	7.2	11.3
Outflow [kg]	3.895	4.077	3.483
Duration of the experiment [s]	900	900	900
Excavation			
Pressure in s-cylinder 1 (pressure gauge) [bar]	0.73	0.73	0.69
Pressure in s-cylinder 2 (pressure gauge) [bar]	0.6	0.59	0.61
Chamber pressure [bar]	0.43	0.43	0.41
Slurry discharge from the set-up at [min]	28	40	40
Excavation path [mm]	460.5	465	465
RPM [-]	71	71	71
PR [0.1 mm/rev]	0.1	0.1	0.1
Outflow [kg]	11.101	8.913	12.704

Experiment No.:	rc-IIIa	rc-IIIb	rc-IIIc
Date of experiment:	22.03.2017	23.03.2017	30.03.2017
Soil properties			
Grain size of the soil [mm]	0.063-4	0.063-4	0.063-4
Actual weight of soil sample [kg]	29.9	29.65	29.83
Remaining height in the soil container [cm]	20	21	21
Density of the sample [g/cm³]	1.88	1.94	1.91
Grain density ρc [g/cm³]	2.65	2.65	2.65
Porosity n: $n = 1 – \rho_d/\rho$ [–]	0.353	0.358	0.354
Slurry properties			
Type of bentonite	B1	B1	B1
Concentration [%]	6	6	6
Date of mixing	21.03.2017	22.03.2017	29.03.2017
pH-value [-]	10.513	10.807	10.803
Density [g/cm³]	1.038	1.039	1.039
Yield point with ball harp [N/m²]	47.877	47.873	47.873
Marsh-time tM_{1000} [s]	49	53	59
Marsh-time tM_{1500} [s]	116	118	120
Slurry filling - primary penetration			
Pressure in s-cylinder 1 (pressure gauge) [bar]	0.35	0.38	0.38
Pressure in s-cylinder 2 (pressure gauge) [bar]	0.35	0.38	0.38
Height of the slurry in the s-cylinder 1 before start[cm]			
Height of the slurry in the s-cylinder 2 before start[cm]			
Height of the water in the s-cylinder 1 at the end [cm]			
Height of the water in the s-cylinder 2 at the end [cm]			
Outflow [kg]	0.29	not measured	0.29
Duration of the experiment [s]	848	not measured	889
Excavation			
Pressure in s-cylinder 1 (pressure gauge) [bar]	0.34	0.37	0.34
Pressure in s-cylinder 2 (pressure gauge) [bar]	0.34	0.37	0.34
Chamber pressure [bar]	0.20	0.23	0.24
Slurry discharge from the set-up at [min]			
Excavation path [mm]	457	457	457
RPM [-]	71	71	71
PR [0.1 mm/rev]	0.1	0.1	0.1
Outflow [kg]	4.46	4.12	4.32

Experiment No.:	rc-IVa	rc-IVb	rc-IVc
Date of experiment:	08.02.2017	21.02.2017	02.03.2017
Soil properties			
Grain size of the soil [mm]	0.063-4	0.063-4	0.063-4
Actual weight of soil sample [kg]	29.4	27.75	29.16
Remaining height in the soil container [cm]	22	22	21
Density of the sample [g/cm³]	1.81	1.92	1.89
Grain density ρc [g/cm³]	2.65	2.65	2.65
Porosity n: $n = 1 - \rho_d/\rho$ [–]	0.364	0.399	0.369
Slurry properties			
Type of bentonite	B1	B1	B1
Concentration [%]	6	6	6
Date of mixing	07.02.2017	20.02.2017	01.03.2017
pH-value [-]	10.56	10.49	10.51
Density [g/cm³]	1.0397	1.038	1.038
Yield point with ball harp [N/m²]	47.886	47.878	47.878
Marsh-time tM_{1000} [s]	50	49	48
Marsh-time tM_{1500} [s]	124	111	116
Slurry filling - primary penetration			
Pressure in s-cylinder 1 (pressure gauge) [bar]	1.04	1.03	1.03
Pressure in s-cylinder 2 (pressure gauge) [bar]	1.04	1.03	1.03
Height of the slurry in the s-cylinder 1 before start[cm]			
Height of the slurry in the s-cylinder 2 before start[cm]			
Height of the water in the s-cylinder 1 at the end [cm]			
Height of the water in the s-cylinder 2 at the end [cm]			
Outflow [kg]	0.85	0.582	0.68
Duration of the experiment [s]	560	849	885
Excavation			
Pressure in s-cylinder 1 (pressure gauge) [bar]	1.04	1.03	1.03
Pressure in s-cylinder 2 (pressure gauge) [bar]	0.76	0.89	0.88
Chamber pressure [bar]	0.76	0.89	0.88
Slurry discharge from the set-up at [min]			
Excavation path [mm]	457	447	457
RPM [-]	71	71	71
PR [0.1 mm/rev]	0.1	0.1	0.1
Outflow [kg]	4.63	5.195	5.36

A.4.3 Diagrams

A.4.3.1 Time-dependent outflow from the set-up

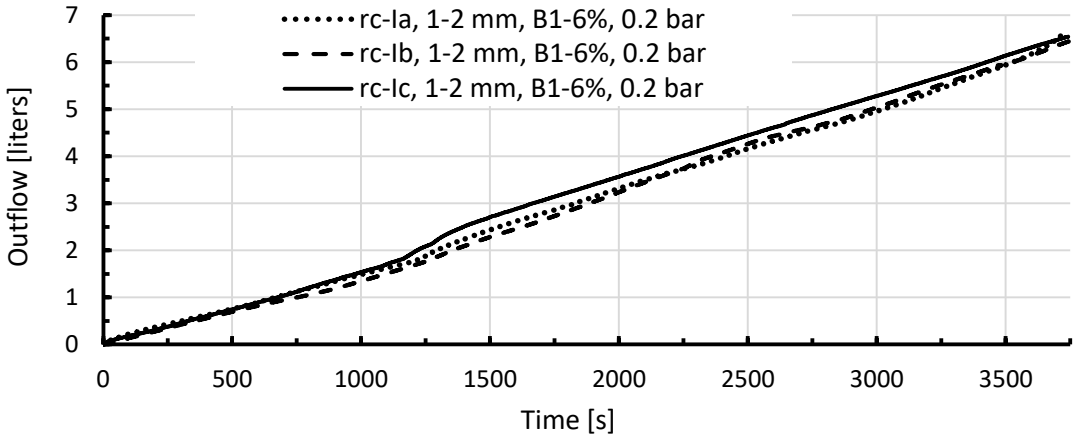

Figure A-4-3: Outflow from RUB tunnelling device during excavation in rc-I

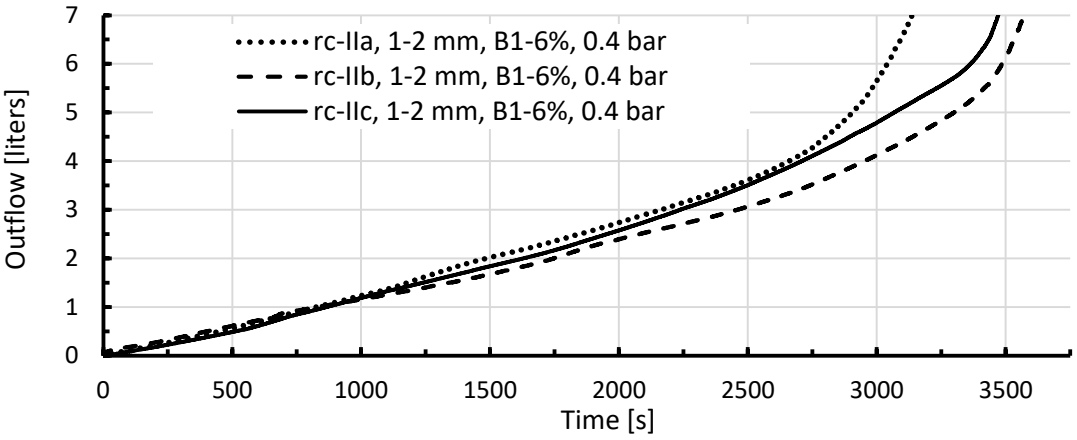

Figure A-4-4: Outflow from RUB tunnelling device during excavation in rc-II

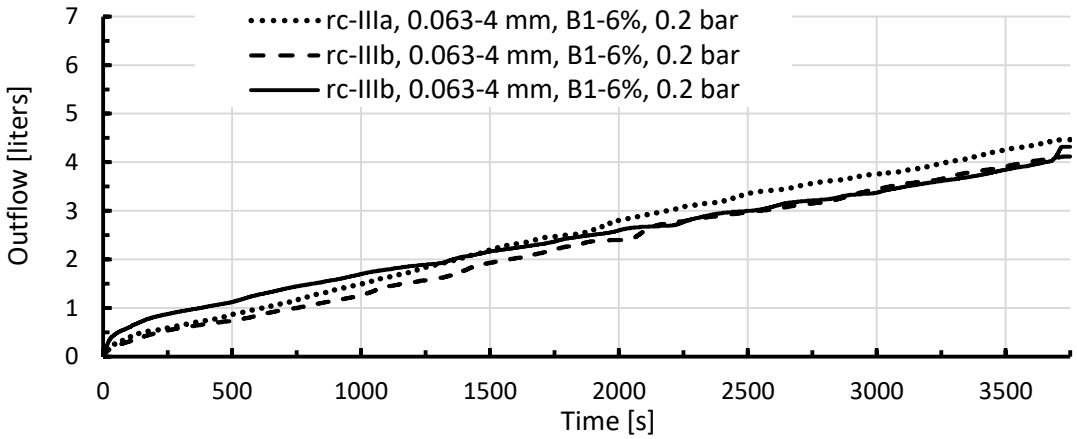

Figure A-4-5: Outflow from RUB tunnelling device during excavation in rc-III

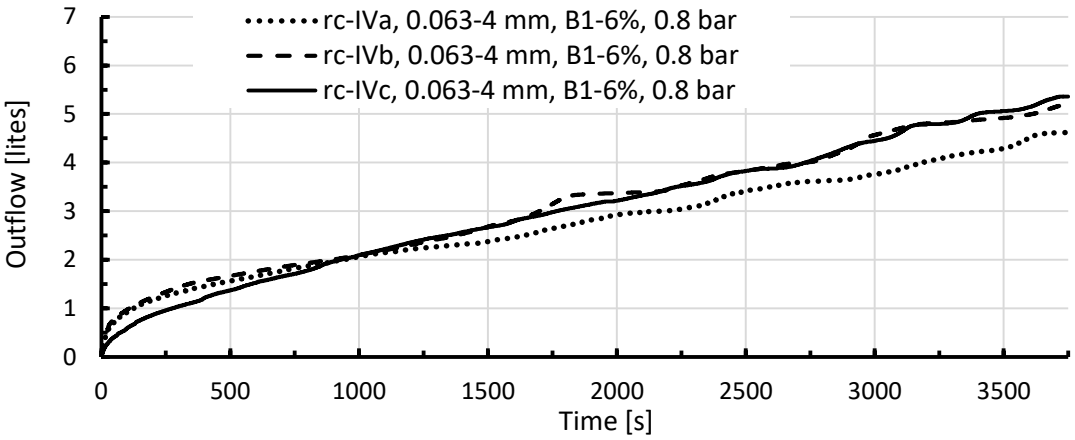

Figure A-4-6: Outflow from RUB tunnelling device during excavation in rc-IV

A.4.3.2 Time-dependent development of pore pressures

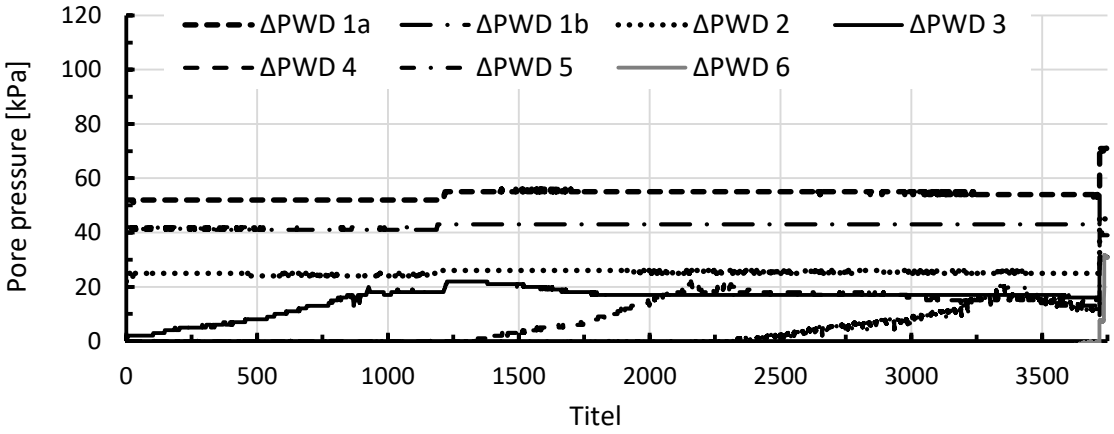

Figure A-4-7: Pore pressure development in combination rc-Ia – 0.2 bar

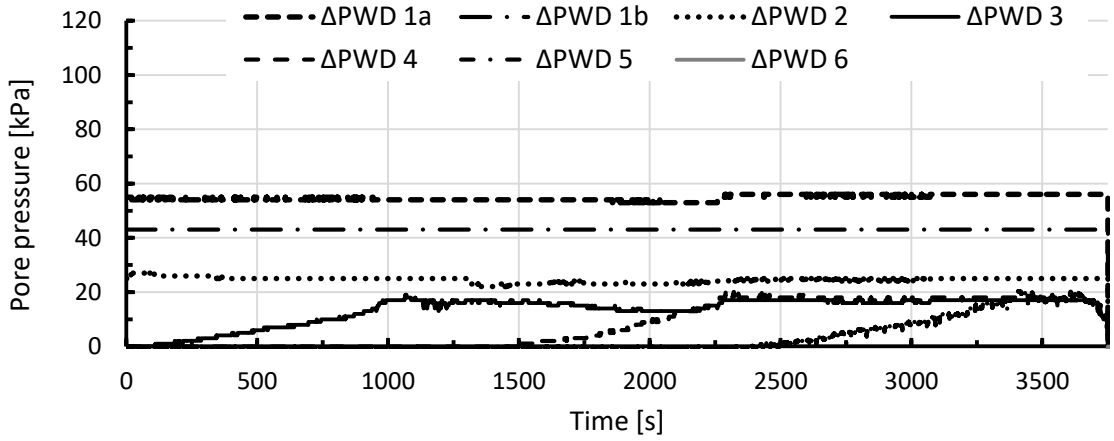

Figure A-4-8: Pore pressure development in combination rc-Ib – 0.2 bar

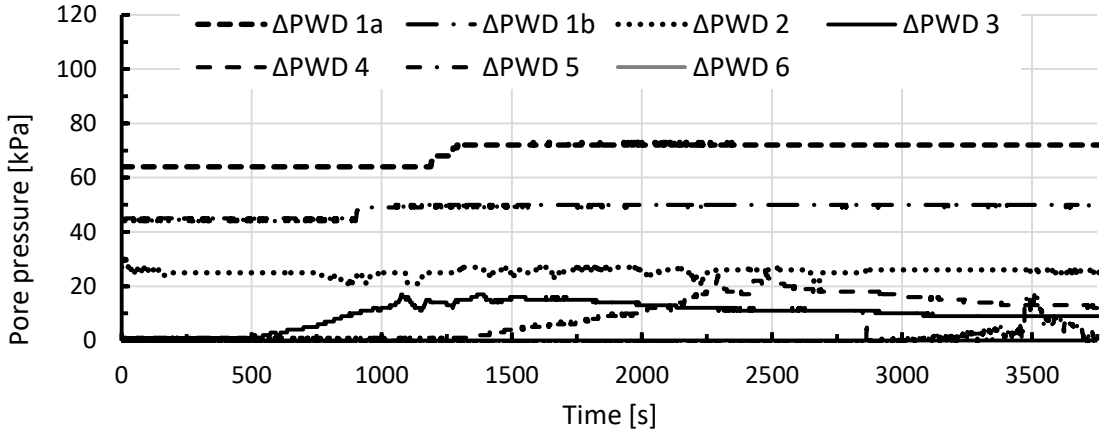

Figure A-4-9: Pore pressure development in combination rc-Ic – 0.2 bar

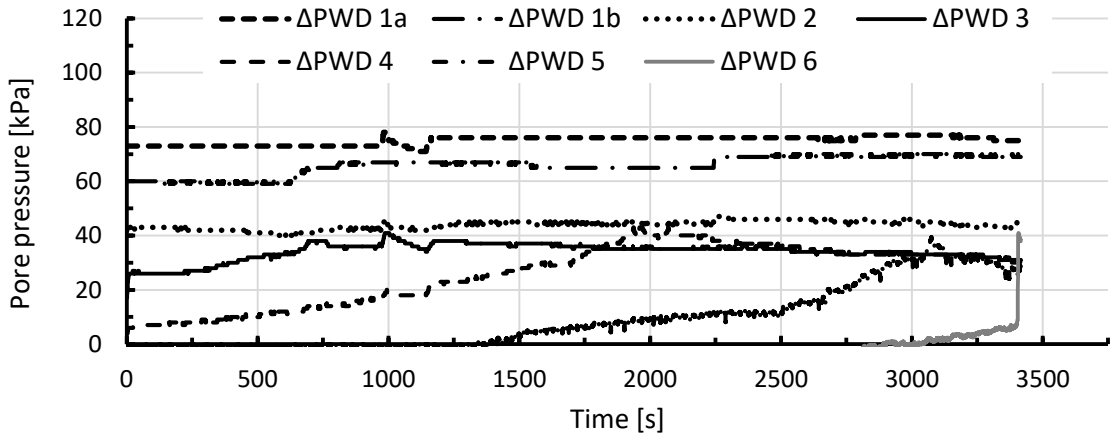

Figure A-4-10: Pore pressure development in combination rc-IIa – 0.4 bar

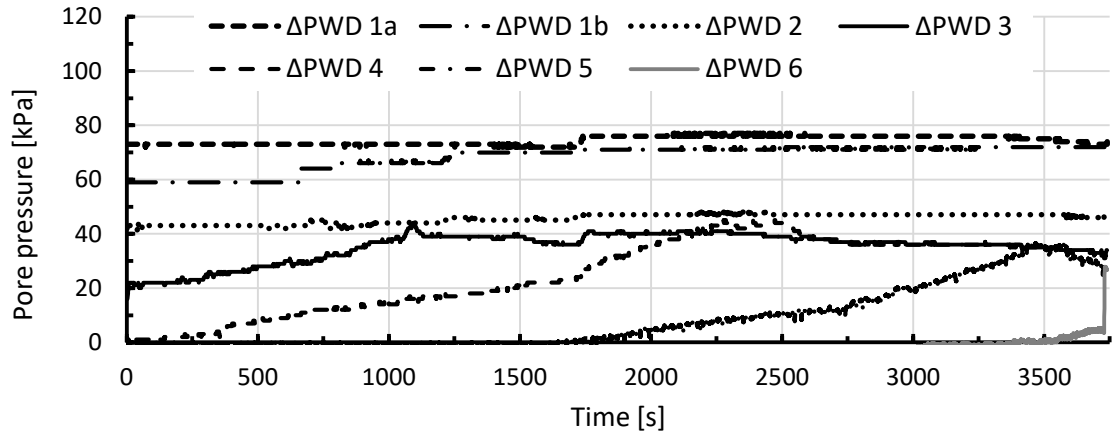

Figure A-4-11: Pore pressure development in combination rc-IIb – 0.4 bar

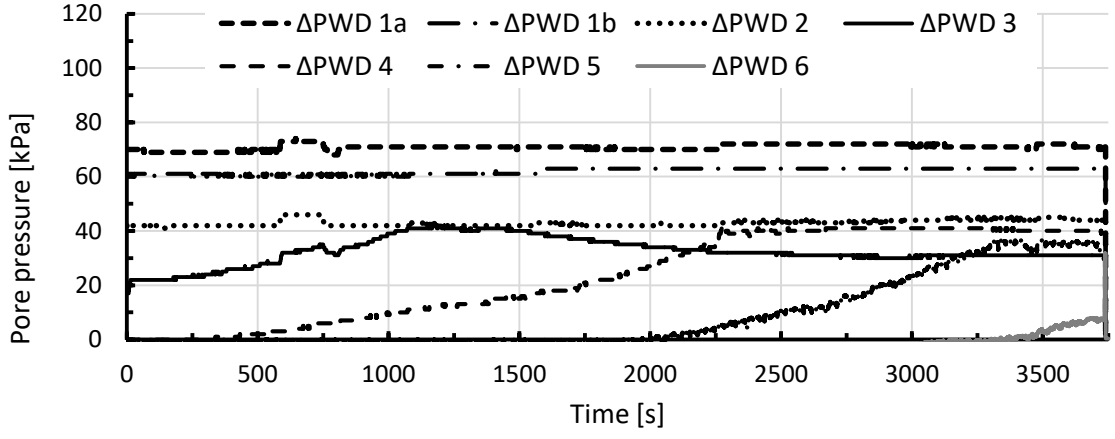

Figure A-4-12: Pore pressure development in combination rc-IIc – 0.4 bar

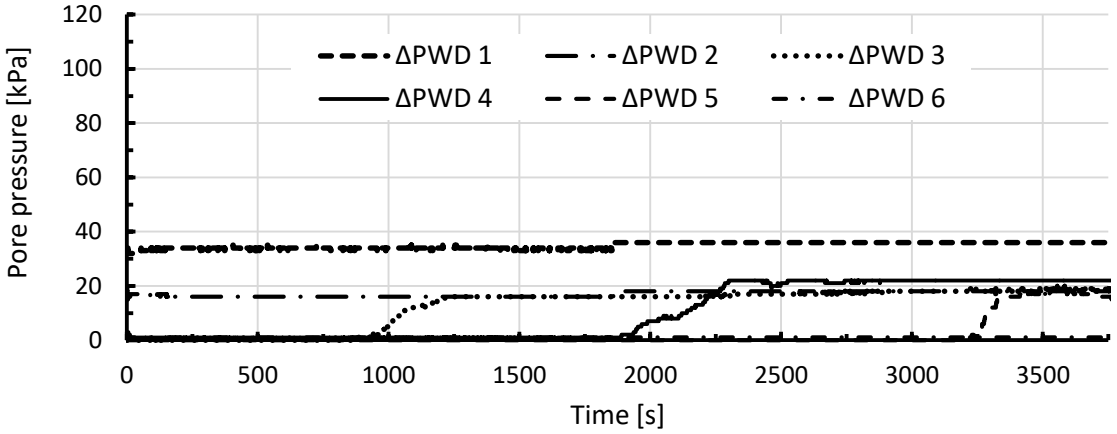

Figure A-4-13: Pore pressure development in combination rc-IIIa – 0.2 bar

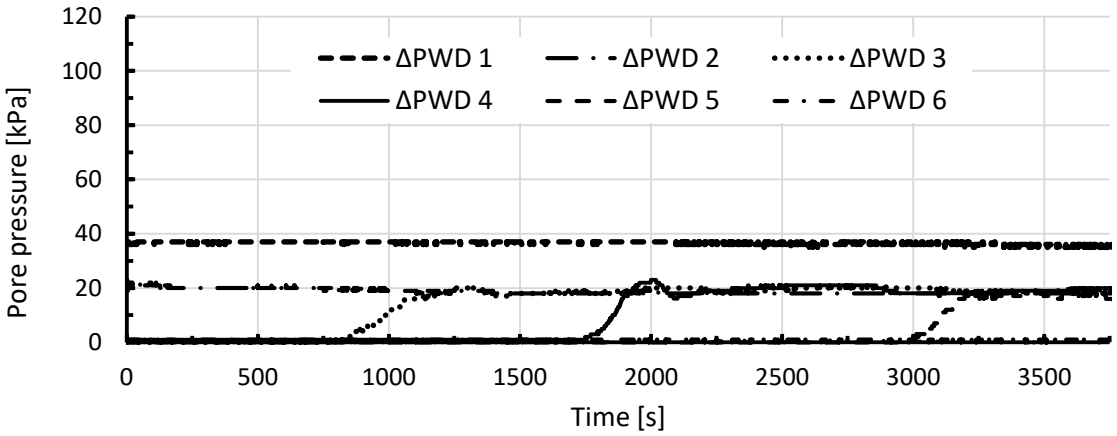

Figure A-4-14: Pore pressure development in combination rc-IIIb – 0.2 bar

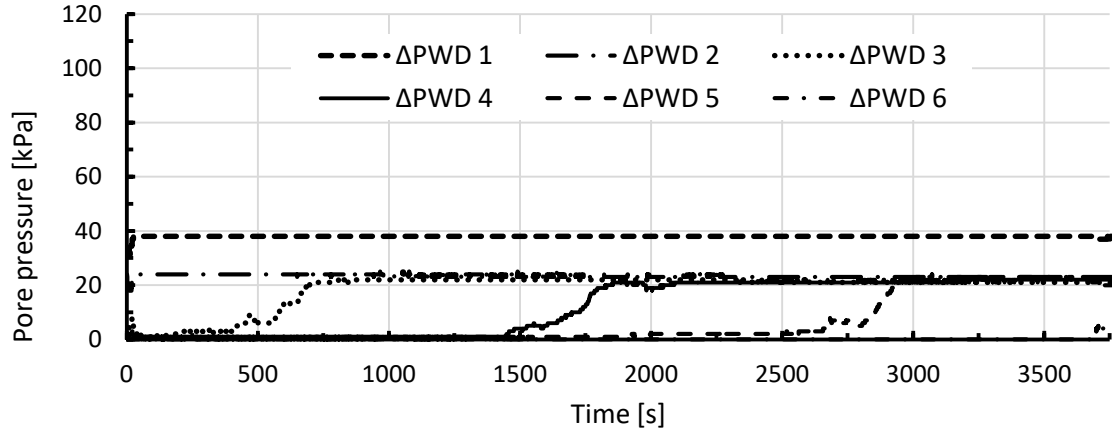

Figure A-4-15: Pore pressure development in combination rc-IIIc – 0.2 bar

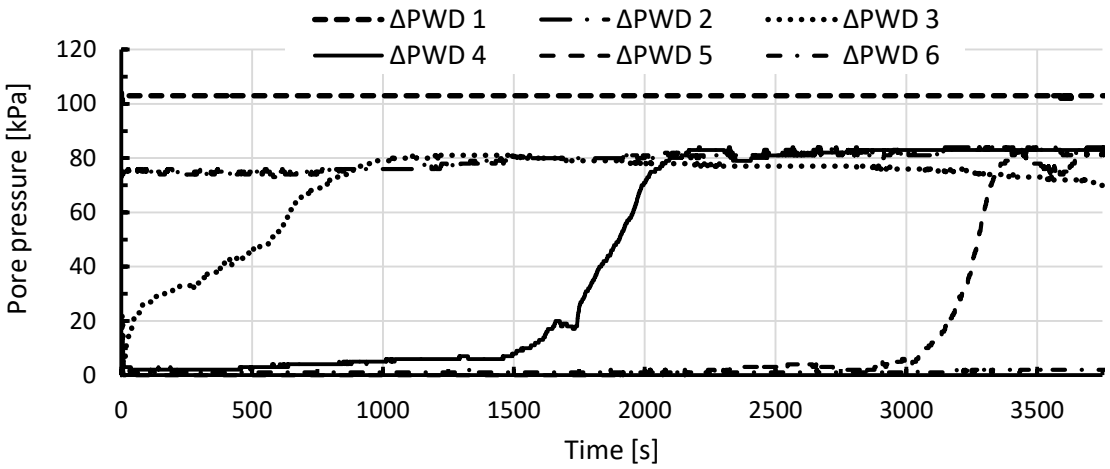

Figure A-4-16: Pore pressure development in combination rc-IIIa – 0.2 bar

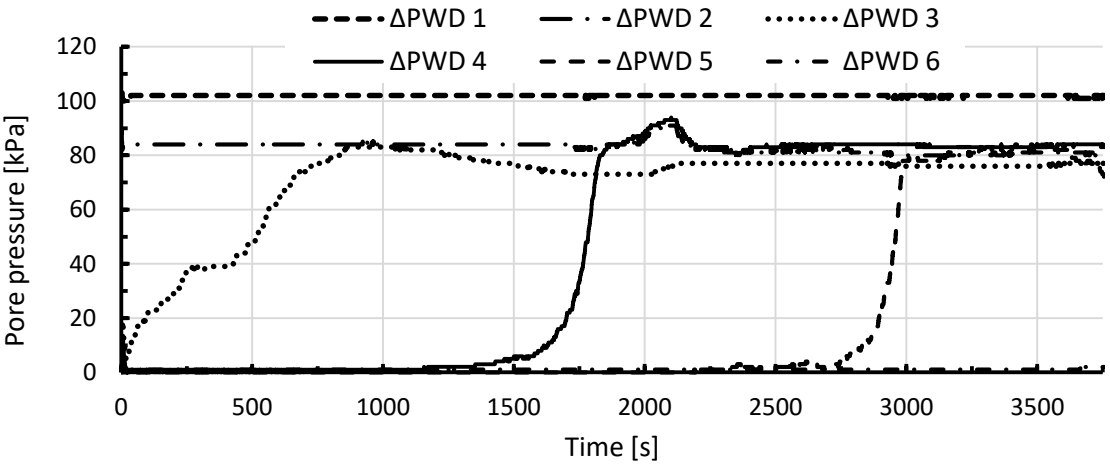

Figure A-4-17: Pore pressure development in combination rc-IIIb – 0.2 bar

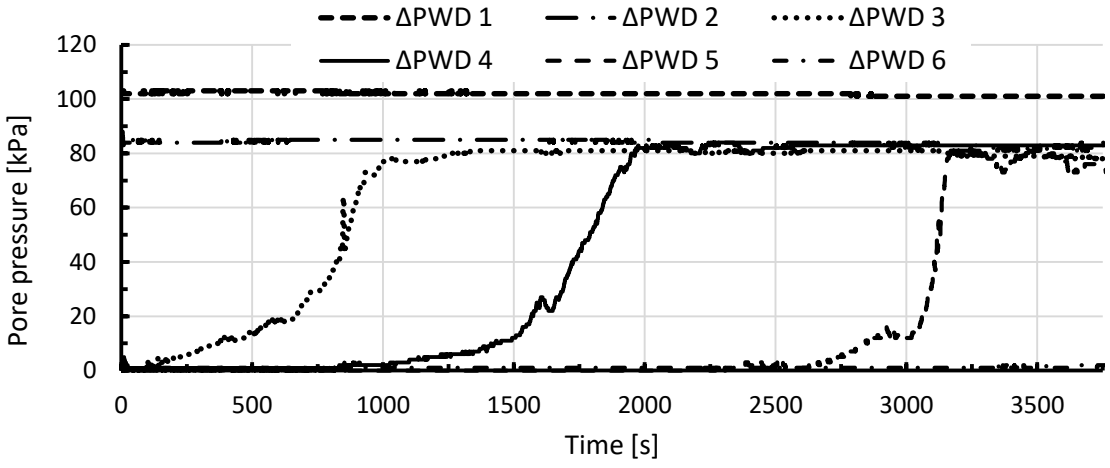

Figure A-4-18: Pore pressure development in combination rc-IIIc – 0.2 bar